

DETA GASSER

**EVOLUTION OF THE CHUGACH
METAMORPHIC COMPLEX OF SOUTHERN
ALASKA IN SPACE AND TIME**

A dissertation submitted to the

**Faculty of Natural Science
Karl Franzens University of Graz
Austria**

for the Degree of Doctor of Science

August 2010



"...und zum ersten Mal überfiel mich in diesen verzauberten Reisetagen eine Vorstellung, die mich später immer wieder einmal besucht und beglückt hat: dass Geologie die Musik der Erde sei."

Hans Cloos in *Gespräch mit der Erde*, 1947

PREAMBLE

Metamorphic rocks occur at the Earth's surface all over the world. Many of them are derived from sedimentary rocks, which once formed at the surface, and which were then buried, heated and metamorphosed, before they were finally exhumed back to the surface. In order to understand the mechanisms which lead to burial, heating, cooling and exhumation of such rocks, it is necessary to know: (a) the exact physical conditions (i.e. pressure and temperature) the rocks experienced, (b) the structures along which the rocks were buried and exhumed, and (c) the timescales on which these processes occurred.

The Eocene Chugach Metamorphic Complex (CMC) of southern Alaska is a spectacular example of a metamorphic complex exposed in a Late Cretaceous to Paleocene accretionary prism (Hudson & Plafker, 1982). The complex is exposed in a region of extreme topography: the Chugach-St. Elias mountains, which occur along the southern Alaskan margin. The presence of this metamorphic complex in a fore-arc setting has been interpreted to be the consequence of an unusual thermal event: the subduction of an oceanic spreading ridge below the margin (e.g. Sisson & Pavlis, 1993; Pavlis & Sisson, 1995). Since the CMC is remote and difficult to access, previous metamorphic and structural studies concentrated on the western and northern parts of the complex (Hudson & Plafker, 1982; Sisson & Hollister, 1988; Sisson et al., 1989; Sisson & Pavlis, 1993; Pavlis & Sisson, 1995, 2003). Apart from K/Ar and a few $^{40}\text{Ar}/^{39}\text{Ar}$ cooling ages from magmatic rocks intruding the complex (Hudson et al., 1979; Sisson et al., 1989; Bradley et al., 1993), the timing of the high-temperature history of the complex has remained largely unconstrained.

The aim of the present thesis is twofold: (1) Revealing variations in internal deformation and in the geometry of bounding fault zones across- and along-strike of the complex. For this, field work along three composite transects covering the CMC from north to south in three areas of different width of the complex was conducted. (2) Determining the timing of burial, heating, peak metamorphism, cooling and exhumation of the complex. For this, different geochronometers were applied to rocks of different metamorphic zones of the complex. Therewith, rates on which these processes occurred were calculated. Finally, structural and temporal information was integrated to derive a tectonic evolution for the complex. The results and interpretations of this thesis are complementary to and influenced by the thesis of Bruand (2010), who investigated the maximum *PT* conditions reached in the different metamorphic zones of the complex.

OUTLINE OF THESIS

This thesis is divided into six chapters and five appendixes.

In **Chapter 1**, the geological setting of the southern Alaskan margin is reviewed and summarized, since an understanding of the regional geological history is crucial for the interpretation of the results of this thesis.

In **Chapter 2**, the results of a detrital zircon study on the metasedimentary rocks of the CMC are described. Detrital zircon cores from four samples covering the CMC from west to east were analysed by LA-ICP-MS, in order to reveal (a) the maximum depositional age of the sediments, which gives a starting point for the metamorphic cycle, and (b) the provenance of the sediments, which gives an idea of the tectonic history prior to metamorphism in the CMC.

In **Chapter 3**, the applicability of garnet, monazite, allanite and xenotime as geochronometers for the prograde history of the CMC is tested. Under given circumstances, all four minerals are suitable to yield geochronological ages which date prograde points in time. A detailed description of the occurrence of these minerals is presented and the petrological context is discussed. In addition, the results of limited Sm-Nd garnet dating and U-Pb SHRIMP monazite dating are presented.

In **Chapter 4**, the results of U-Pb SHRIMP dating of metamorphic zircon are presented. The detrital zircon cores present in the rocks of the CMC are surrounded in the high-grade gneisses of the complex by small, metamorphic zircon overgrowths, which grew during partial melting under peak metamorphic conditions. Precise U-Pb SHRIMP ages of such metamorphic overgrowths from seven samples covering the CMC from west to east constrain the timing of peak metamorphism in the complex. This chapter is submitted to Geological Society of America Bulletin.

In **Chapter 5**, the results of the structural field work are described, as well as the results of $^{40}\text{Ar}/^{39}\text{Ar}$ muscovite and biotite dating, Rb/Sr isocron dating and fission track zircon dating. This information is then used, together with (a) the results of previous chapters, (b) a compilation of literature data and (c) the results of the thesis of Bruand (2010), to construct a model for the tectonic evolution of the CMC in space and time. This chapter is submitted to Tectonics.

Chapter 6 contains a summary, conclusions and outlook of this work.

Appendix A contains a progress report which was written halfway through the project and which summarizes the aims and procedures of this thesis. It was published in *Erstausgabe: Veröffentlichungen junger WissenschaftlerInnen der Universität Graz*.

Appendix B contains three research abstracts which were presented during the thesis at international conferences.

The last three appendices are not directly related to this thesis but contain the results of small side-studies which I conducted during my employment at the University of Graz, partly due to the fact that fieldwork in Alaska could only begin 10 months after the employment started. All three appendices are entirely related to my interest for the Alpine orogen.

Appendix C contains a manuscript which deals with the large-scale internal geometry of the Paleozoic of Graz. Despite a large amount of very detailed information on stratigraphy and structure of this nappe complex, large-scale profiles throughout the entire complex were lacking. I therefore compiled information on stratigraphy and structural geometry from the literature and constructed several large-scale profiles through the area. The manuscript is published in *International Journal of Earth Sciences*.

Appendix D contains a conference abstract on the structural geometry of the Paleozoic of Graz.

Appendix E finally contains a manuscript that resulted from an excursion led by PhD students for the Doctoral School of Earth Sciences of the Universities of Graz and Leoben. It contains a summary of the geological history of Styria, meant to give professional geologists and laymen alike an overview of the fascinating geology of the second-largest province of Austria.

The following manuscripts originated from this thesis and are submitted to or are published in international journals:

1. Gasser, D., Rubatto, D., Bruand, E., Stüwe, K.: Large-scale, short-lived metamorphism and magmatism in the Chugach Metamorphic Complex (CMC), southern Alaska: a zircon U-Pb SHRIMP study. Submitted to Geological Society of America Bulletin. Chapter 4
2. Gasser, D., Bruand, E., Stüwe, K., Foster, D., Schuster, R., Fügenschuh, B.: Formation of a metamorphic complex along an obliquely convergent margin: Structural and thermochronological evolution of the Chugach Metamorphic Complex, southern Alaska. Submitted to Tectonics. Chapter 5.
3. Gasser, D., Stüwe K., Fritz, H. (2010) Internal structural geometry of the Paleozoic of Graz. International Journal of Earth Sciences, 99, 1067-1081. Appendix C.

Two smaller manuscripts originated from this thesis and are published in local journals:

1. Gasser, D., Bruand, E. (2010) Tectonic and metamorphic evolution of the Chugach Metamorphic Complex, Alaska: A progress report. Erstausgabe, Veröffentlichungen junger WissenschaftlerInnen der Universität Graz. 149-158. Appendix A.
2. Gasser, D., Gusterhuber, J., Krische O., Puhr, B., Scheucher, L., Wagner, T., Stüwe, K. (2009) The Geology of Styria: An overview. Naturwissenschaftlicher Verein Steiermark, 139, 5-36. Appendix E.

The following conference contributions originated from this thesis:

1. Gasser, D., Stüwe, K. (2007) The Chugach Metamorphic Complex of southern Alaska: A test for wedge extrusion models? Geological Society of America Abstracts with Programs, Vol. 39, No. 6, p. 232. Appendix B.
2. Gasser, D., Bruand, E., Stüwe, K. (2009) Exhumation of a metamorphic complex in a strike-slip setting: observations from the Chugach Metamorphic Complex (CMC), southern Alaska. Abstract Volume 7th Swiss Geoscience Meeting, Neuchatel, p.79. Appendix B.
3. Gasser, D., Bruand, E., Stüwe, K., Rubatto, D., Foster, D., Schuster, R. (2010) Exhuming Metamorphic Rocks: Constraints from Cooling of the Chugach Metamorphic Complex, southern Alaska. Geophysical Research Abstracts Vol. 12, EGU2010-11742, 2010. Appendix B.
4. Gasser, D., Stüwe, K., Fritz, H. (2008) Journal of Alpine Geology, Vol. 49, p. 29, PANGEO 08 conference, Vienna. Appendix D.

SUMMARY

Metamorphic complexes form by various different processes in many different tectonic settings all over the world. In order to distinguish between different processes which formed a particular complex, an understanding of the spatial geometry and the temporal evolution of the complex is needed. This thesis contains the results of an interdisciplinary study conducted on the Chugach Metamorphic Complex (CMC) of southern Alaska, which aimed at constraining the evolution of the complex in space and time. The CMC is a ~10-50 km wide and ~350 km long upper amphibolite facies metamorphic complex, which consists of two macroscopically different zones: a northern schist zone and a southern gneiss zone. The complex developed in the Late Cretaceous accretionary prism of the Chugach terrane, which is exposed along the southern Alaskan margin on ~2200 km along strike.

Three across-strike composite sections were investigated by fieldwork, in order to describe the geometry of the complex in three dimensions. The three sections cover the complex from the western part where it is widest to the south-eastern part where it is narrowest. The geometry of the complex is controlled by the presence of three superimposed fabrics: The first fabric (D_1) is related to accretion of the sediments and is only recognizable in the phyllite zone surrounding the complex. The second fabric is a flat-lying foliation defined by biotite \pm sillimanite with a horizontal E-W stretching lineation, which is developed in the schist and gneiss zones (D_2). The third fabric is a steep foliation defined by biotite and melt layers with a horizontal E-W stretching lineation in the northern part and a variably W-NW-dipping stretching lineation in the southern part of the complex (D_3). It is heterogeneously developed throughout the schist and gneiss zones and is most intensely developed in the southern part of the gneiss zone. D_3 defines a foliation fan from north to south with south-dipping foliation planes in the north and north-dipping foliation planes in the south. The southern part of the gneiss zone is overprinted by numerous semi-brittle to brittle N-dipping shear zones and faults with N-side-up and dextral sense of movement, which juxtapose migmatitic gneisses against greenschist facies phyllites. These faults lead to an asymmetric shape of the complex, with a wide transition from phyllites to gneisses in the north and an abrupt transition from gneisses to phyllites in the south.

The age spectra of detrital zircon populations of four samples were investigated by LA-ICP-MS geochronology, in order to constrain the maximum depositional age of the sediments in which the CMC developed. The approach is based on the premise that the depositional age of a sequence can not be older than the youngest detrital zircon grains present in the rocks. The four samples have maximum depositional ages of 58.5 ± 1.6 Ma, 63.6 ± 1.4 Ma, 64.8 ± 0.9 Ma and 75.6 ± 0.9 Ma. The first two lie entirely within the Paleocene, whereas the last two overlap or lie within the Late Cretaceous. The oldest sample stems from deepest

in the prism. The entire age spectra of the samples revealed a predominantly Paleocene and Late Cretaceous source for the sediments, with minor contributions from Early to Middle Mesozoic, Paleozoic and Precambrian sources.

The applicability of garnet, monazite, allanite and xenotime as prograde geochronometers was investigated in the different zones of the complex. Garnet does not preserve any prograde growth zoning. A Sm-Nd age of 47.8 ± 6.3 Ma was calculated based on two garnet fractions from one sample from the gneiss zone. The age is broadly coeval with the timing of peak metamorphism based on U-Pb dating of metamorphic zircon. Monazite is absent in rocks of the phyllite zone, but is abundant as small unzoned grains in the schist zone, indicating that they grew at $\sim 550^\circ\text{C}$ and ~ 3.4 kbar. An attempt of dating these small monazites was not successful. Monazite in the gneiss zone is bigger and complexly zoned and probably crystallized during partial melting at the metamorphic peak. U-Pb SHRIMP dating of four monazite samples from the gneiss zone revealed ages ranging from 51.5 ± 0.9 Ma to 53.5 ± 0.9 Ma. Allanite is present (a) in the phyllite zone, (b) as peak metamorphic mineral in CaO-rich rocks at pressures >8 kbar, and (c) as large crystals in retrograde shear/fluid flow zones. Xenotime is ubiquitous in rocks of all metamorphic zones and its metamorphic growth conditions are difficult to constrain.

The timing of peak metamorphism was investigated by U-Pb SHRIMP dating of metamorphic zircon. Detrital zircon cores present in all samples are overgrown by narrow, light-grey, unzoned metamorphic zircon rims which probably grew during partial melting at the metamorphic peak. Six metamorphic and one magmatic zircon ages from the western and central parts of the complex range between 54.0 ± 0.9 Ma and 52.6 ± 0.8 Ma and are within error of each other. One metamorphic zircon age from the south-eastern part is 51.3 ± 0.7 Ma, which is within error of two of the seven ages from the western and central parts. The zircon ages are within error of the monazite ages from the gneiss zone. Combined with the maximum depositional age of ~ 60 - 65 Ma derived from youngest detrital zircon cores, a total of ~ 5 - 10 Ma are available for prograde metamorphism. Assuming a starting temperature of 20°C and a peak temperature of ~ 650 - 700°C , heating rates of ~ 60 - $140^\circ\text{C}/\text{Ma}$ result.

In order to constrain the cooling history of the complex, $^{40}\text{Ar}/^{39}\text{Ar}$ dating of muscovite and biotite, Rb/Sr isochron dating and zircon fission track dating was applied, and a compilation of previous $^{40}\text{Ar}/^{39}\text{Ar}$ and low-temperature geochronology was assembled. Four $^{40}\text{Ar}/^{39}\text{Ar}$ muscovite ages from the western and central parts of the complex range from 53.4 ± 2.9 Ma to 45.8 ± 2.1 Ma. Three $^{40}\text{Ar}/^{39}\text{Ar}$ muscovite ages from the south-eastern part range from 36.2 ± 2.2 Ma to 20.0 ± 1.0 Ma. Eleven $^{40}\text{Ar}/^{39}\text{Ar}$ biotite ages from the western and central part range from 50.0 ± 2.2 Ma to 46.9 ± 2.1 Ma. One $^{40}\text{Ar}/^{39}\text{Ar}$ biotite age from the south-eastern part is 15.8 ± 0.8 Ma. Eight Rb/Sr isochron ages based on biotite and whole rock measurements from the different zones are entirely within error of the $^{40}\text{Ar}/^{39}\text{Ar}$ biotite ages. Four zircon fission track ages from the western and central part of the complex range from 30.9 ± 8.6 Ma to 26.0 ± 2.8 Ma. Together with $^{40}\text{Ar}/^{39}\text{Ar}$ and low-temperature data from the literature, these ages define cooling histories for the different sections. The western and central parts of the complex cooled very rapidly after the metamorphic peak

to temperatures of $\sim 350^{\circ}\text{C}$ with rates of $\sim 30\text{-}180^{\circ}\text{C}/\text{Ma}$. Thereafter, the rocks of the gneiss zone cooled very slowly during $\sim 15\text{-}20$ Ma, until an increase in cooling rate occurred asynchronously from north to south during the last ~ 25 Ma. The rocks of the south-eastern part of the complex cooled slowly and regularly with rates of $\sim 6\text{-}10^{\circ}\text{C}/\text{Ma}$ from the peak at ~ 51 Ma to temperatures of $\sim 200\text{-}300^{\circ}\text{C}$ at $\sim 5\text{-}10$ Ma, and cooled with increased rates of $\sim 20\text{-}40^{\circ}\text{C}/\text{Ma}$ during the last $\sim 5\text{-}10$ Ma.

Based on this newly obtained structural and geochronological data and regional considerations, the following scenario for the evolution of the CMC is proposed. Rapid accretion of sediments to the southern Alaskan margin during dextral convergence led to the formation of a thick accretionary prism during the Late Cretaceous and Paleocene, which probably experienced relatively elevated temperatures due to basal friction and internal strain heating. At ~ 55 Ma, the deformational regime in the accretionary prism changed due to changing boundary conditions, and a flat-lying fabric with E-W stretching lineations developed (D_2), which indicates vertical flattening and margin-parallel stretching. This vertical flattening probably led to the compression of isotherms and elevated temperatures of $\sim 600\text{-}650^{\circ}\text{C}$ at depths of $\sim 15\text{-}20$ km. Peak metamorphic conditions were probably reached shortly after the onset of the D_2 deformation, at $\sim 55\text{-}52$ Ma. During peak metamorphism, the deformational regime changed back to dextral convergence (D_3). Fast cooling, accompanied by exhumation of parts of the gneiss zone occurred in the western and central parts of the complex. The south-eastern part of the complex experienced slower and more regular cooling after the peak, probably due to the already curved margin.

This scenario differs from scenarios previously proposed for the evolution of the CMC, which commonly infer the subduction of an oceanic spreading ridge below the complex. The results of this thesis, namely the contemporaneous peak metamorphism at least $\sim 200\text{-}350$ km along strike of the complex, together with the fast cooling reported shortly after the complex in its western and central part are difficult to explain with the model of a subducting ridge below the complex. Therefore, besides the ridge subduction model, alternative hypotheses explaining the tectonic evolution of the southern Alaskan margin should continuously be evaluated as well.

Contents

1	Geology of the southern Alaskan margin: An introduction and literature overview	21
1.1	Chugach and Prince William terranes	22
1.2	The Sanak-Baranof plutonic belt	28
1.3	Yakutat terrane	30
1.4	Plate tectonics of the Pacific basin in the Cenozoic	32
1.5	Tectonic evolution of the Southern Alaskan margin	36
2	LA-ICP-MS U-Pb ages of detrital zircons: A Paleocene maximum depositional age for the protoliths of the CMC?	41
2.1	Introduction	42
2.2	Depositional age of the CMC protoliths based on regional correlations	43
2.3	In-situ U-Pb dating of detrital zircons from the CMC	44
2.3.1	Analytical technique	45
2.3.2	Sample description	46
2.3.3	U-Pb dating: Results and data assessment	48
2.4	Discussion	56
2.4.1	Maximum depositional ages	56

2.4.2	Provenance of sediments	58
2.5	Conclusions	59
3	Testing the applicability of garnet, monazite, allanite and xenotime as prograde geochronometers in different zones of the Chugach Metamorphic Complex	73
3.1	Introduction	74
3.2	Metamorphic zones in the Chugach Metamorphic Complex	76
3.3	Garnet as possible prograde geochronometer in the Chugach Metamorphic Complex?	78
3.3.1	Sm-Nd dating: Analytical technique	79
3.3.2	Sm-Nd dating: Results and interpretation	79
3.4	Monazite, allanite or xenotime as prograde geochronometers in the Chugach Metamorphic Complex?	81
3.4.1	Analytical techniques	81
3.4.2	Distribution of monazite, allanite and xenotime throughout the CMC in varying bulk rock compositions	84
3.4.3	Chemical zoning and composition of monazites from groups 2-5	91
3.4.4	U-Pb SHRIMP dating of monazites from the gneiss zone	96
3.5	Discussion	97
3.5.1	Factors controlling the stability of REE-bearing minerals in the different groups	97
3.5.2	Monazite-in reaction between the phyllite and schist zones	101
3.5.3	Complexly zoned monazites in the gneiss zone: the result of (re)-crystal-lization during/after partial melting?	104
3.5.4	Interpretation of monazite U-Pb ages in a regional context	105
3.6	Conclusions	106

4	Large-scale, short-lived metamorphism and magmatism in the Chugach Metamorphic Complex (CMC), southern Alaska: a zircon U-Pb SHRIMP study	113
4.1	Introduction	114
4.2	Geology of the southern Alaskan margin	115
4.3	Timing and duration of metamorphism and magmatism in the Chugach Metamorphic Complex	119
4.3.1	Analytical techniques	119
4.3.2	Sample description: field occurrence, whole rock composition and petrography	121
4.3.3	Zircon description	123
4.3.4	Zircon composition and Ti-in-zircon thermometry	124
4.3.5	SHRIMP U-Pb dating of zircons	127
4.4	Discussion	130
4.4.1	Growth of metamorphic zircon rims at the metamorphic peak	130
4.4.2	Age and duration of metamorphism in the CMC	131
4.4.3	Relationship between Sanak-Baranof belt magmatism and metamorphism in the CMC	132
4.4.4	Implications for heat transfer into the CMC	133
4.5	Conclusions	137
5	Formation of a metamorphic complex along an obliquely convergent margin: Structural and thermochronological evolution of the Chugach Metamorphic Complex, southern Alaska	147
5.1	Introduction	148
5.2	Geology of the southern Alaska margin	149
5.3	Geology of the Chugach Metamorphic Complex	155

5.4	Structure of the Chugach Metamorphic Complex	157
5.4.1	Section 1	157
5.4.2	Section 2	164
5.4.3	Section 3	168
5.4.4	Structural summary and relationship with metamorphic grade . . .	171
5.5	Thermochronology	176
5.5.1	$^{40}\text{Ar}/^{39}\text{Ar}$ dating of muscovite and biotite	178
5.5.2	Rb/Sr isochron dating	179
5.5.3	Fission track zircon dating	184
5.5.4	$^{40}\text{Ar}/^{39}\text{Ar}$ and low-temperature geochronology: previous data . . .	184
5.6	Discussion	187
5.6.1	The cooling history of the Chugach Metamorphic Complex	187
5.6.2	Interpreting the cooling histories in terms of exhumation	191
5.6.3	Integration of the structural record with the metamorphic history of the Chugach Metamorphic Complex	193
5.7	Conclusions	196
5.8	Appendix - Analytical techniques	198
5.8.1	A. $^{40}\text{Ar}/^{39}\text{Ar}$ method	198
5.8.2	B. Rb/Sr isochron method	199
5.8.3	C. Fission Track zircon method	200
6	Conclusions	209
6.1	Large-scale three-dimensional geometry of the complex	209

6.2	Temporal evolution of the complex: rates of tectonic and thermal processes	210
6.3	Tectonic interpretation: Is a subducting ridge needed?	212
6.4	Outlook	214
Appendices		219
A	Tectonic and metamorphic evolution of the Chugach Metamorphic Complex, Alaska: A progress report	219
A.1	Introduction	220
A.2	Geological Setting and Project Aims	220
A.3	Field work	222
A.4	Pressure and temperature conditions of metamorphism	224
A.5	Geochronology	224
A.6	Outlook	225
B	Conference abstracts related to this thesis	227
B.1	The Chugach Metamorphic Complex of southern Alaska: A test for wedge extrusion models?	228
B.2	Exhumation of a metamorphic complex in a strike-slip setting: observations from the Chugach Metamorphic Complex (CMC), southern Alaska	229
B.3	Exhuming Metamorphic Rocks: Constraints from Cooling of the Chugach Metamorphic Complex, southern Alaska	230
C	Internal Structural Geometry of the Paleozoic of Graz	233
C.1	Introduction	234
C.2	Geological setting	234

C.3	Simplified lithological subdivision	237
C.4	Structural geometry	240
C.5	Modified tectonostratigraphy and paleogeography	245
C.6	Tectonic evolution of the Paleozoic of Graz: A discussion	247
C.6.1	Age of internal deformation and metamorphism - Variscan or Eo-Alpine?	248
C.6.2	Deformation along the borders in the Late Cretaceous and Tertiary	250
C.7	Conclusions	252
C.8	Acknowledgments	253
D	Conference abstract related to Appendix C	255
D.1	Geological profiles through the poly-phase deformed Paleozoic of Graz	256
E	Geology of Styria: An overview	257
E.1	Introduction	258
E.2	Geographical division of Styria	260
E.3	Geological division of Styria	263
E.3.1	The Austroalpine units	263
E.3.2	Neogene basins	276
E.4	Geodynamic evolution of Styria	277
E.5	Mining in Styria	284
E.6	Final remarks	288
E.7	Acknowledgments	288

Bibliography	289
Acknowledgments	309
Short CV	311

Chapter 1

Geology of the southern Alaskan margin: An introduction and literature overview

The southern Alaskan margin is part of the outermost tectonic belt of the North American Cordillera, which is a vast Phanerozoic orogen stretching from Mexico in the south up to Alaska in the north, and which formed as the result of the convergence between oceanic plates of the Pacific basin and the continent of North America (Fig. 1.1; Oldow et al., 1989; Dickinson, 2009). Large parts of this orogen consist of a vast mosaic of so-called terranes: geological provinces with uncertain paleogeographical setting relative to North America which accreted to the continent mostly during Mesozoic and Cenozoic times, and which were translated over several hundreds of kilometers and also significantly rotated relative to each other after their accretion (e.g. Coney et al., 1980). The southern Alaskan margin is a prime example for such Cordilleran tectonics, with different terranes being accreted and translated, and with the additional complication that the margin itself is curved probably due to large-scale rotations in the Cenozoic (e.g. Plafker et al., 1994; Johnston, 2001; Redfield et al., 2007). In this chapter the geology and tectonic history of this margin is summarized from the Late Cretaceous to the present, since an understanding of this history is crucial for the interpretation of the results of this thesis.

Figure 1.1 is a tectonic map of the southern Alaskan margin, with the fundamental units discussed in this chapter indicated. The Wrangellia Composite terrane to the north forms the backstop for the Late Cretaceous to present tectonic history of the southern Alaskan margin. It consists of Paleozoic to Mesozoic magmatic and metamorphic arc assemblages (Plafker et al., 1994) and is not described further. Outboard of this crystalline composite terrane, a vast, complexly deformed Mesozoic to Cenozoic accretionary prism extends from Sanak Island in the west to Baranof Island in the south-east. This accretionary prism is separated by the Contact fault system into the inboard Chugach and the outboard Prince William terrane (Fig. 1.1). Both terranes are intruded by a magmatic belt: the Sanak-Baranof plutonic belt (Fig. 1.1). Farther outboard, in the corner where the strike of the margin turns from east-west to more southeast-northwest, a younger terrane collides with the margin, the Yakutat terrane (Fig. 1.1). The geology of these three terranes and of the

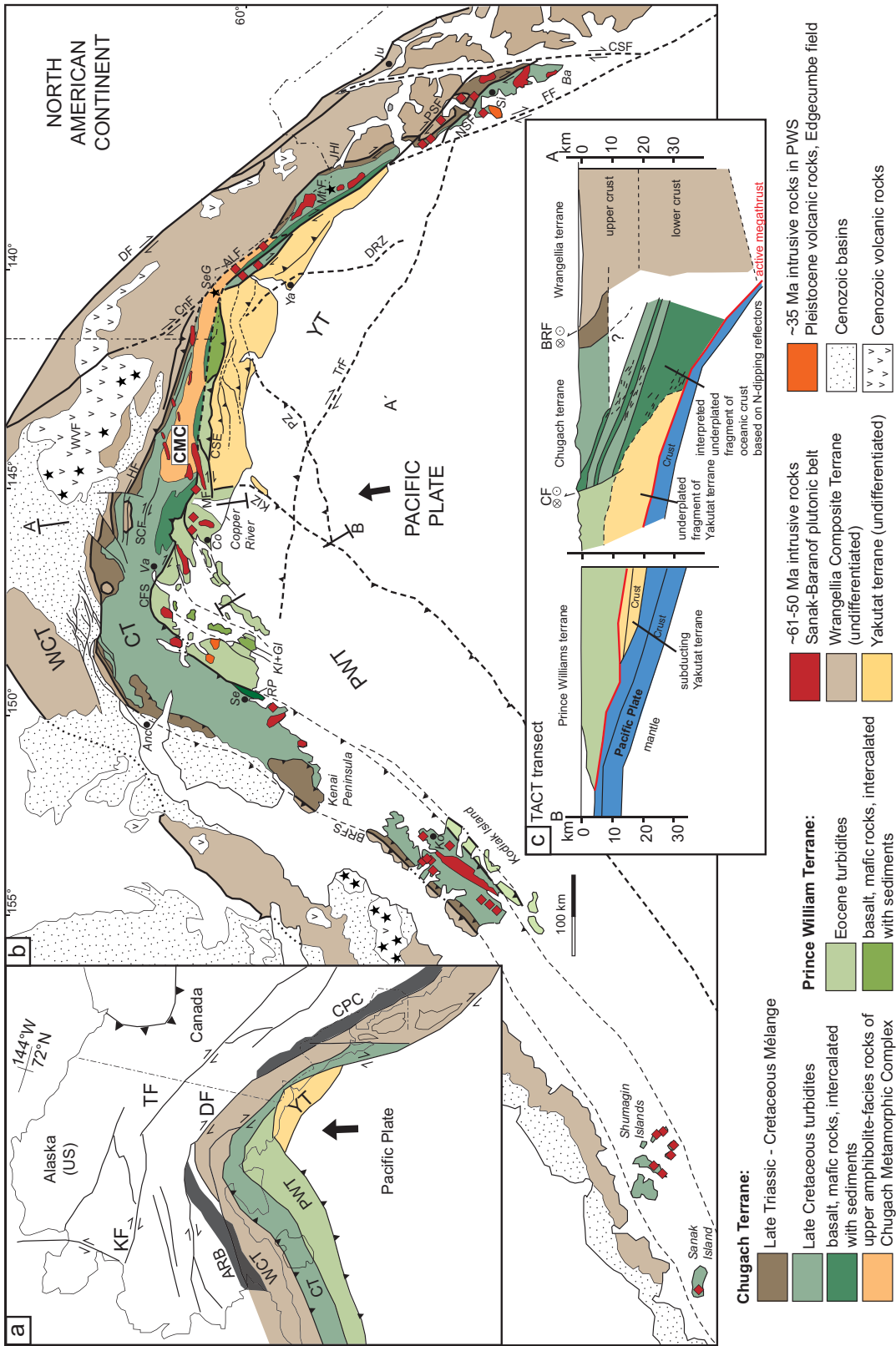
magmatic belt intruding them is described in the sections below. In addition, the magnetic anomalies preserved on the oceanic Pacific plate are described (Fig. 1.2) and the plate tectonic history of the Pacific Basin is summarized, since the relative motions between the oceanic plates of this basin and the North American continent are the driving forces for deformation along the Alaskan margin. Finally, a short summary of the tectonic evolution of the Alaskan margin is given in the last section and displayed in Figure 1.3.

1.1 Chugach and Prince William terranes

The Chugach and Prince William terranes consist of similar rocks and are the result of the same tectonic process: they constitute older and younger parts of a continuously forming accretionary prism which is separated by a syn- to post-accretionary fault system, the Contact Fault System, into the inner Chugach and the outer Prince William terrane (Fig. 1.1; e.g. Plafker et al., 1994; Bol & Gibbons, 1992). This large-scale accretionary prism is emplaced against the northerly adjacent Wrangellia Composite Terrane along the Border Range Fault System, which is a fundamental, long-lived tectonic boundary with a complex deformational history (1.1; Pavlis & Roeske, 2007).

Mélange facies and turbidite sequence The accretionary prism is built of two parts: an inboard, narrow mélange facies and an outboard, wide turbidite sequence (Fig. 1.1). The mélange facies consists of strongly disrupted rocks of Late Paleozoic to Cretaceous age which were accreted during two pulses in the Late Jurassic and Late Cretaceous (Amato & Pavlis, 2010). The change from mélange facies accretion to turbidite sequence accretion occurred during the Late Cretaceous probably as the result of massive uplift in the hinterland which fed enormous amounts of sediments onto the subducting plate (Kusky et al., 1997a). The turbidite sequence, which builds up most of the Chugach and Prince William terranes (Fig. 1.1), consists of intercalated conglomerates, impure sandstones (graywackes), marls, claystones and mafic volcanic rocks (Nilsen & Zuffa, 1982; Plafker et al., 1994). Sparse

Figure 1.1 (following page): (a) Tectonic sketch map of Alaska with major faults of the Northern Cordillera indicated. (b) Geological map of the southern Alaska margin, modified from Plafker et al. 1994. (c) Crustal profile through the southern Alaska margin, after Fuis et al. (2008). Geographical names are in italics, geological names in regular font. Abbreviations: WCT=Wrangellia Composite terrane, CT=Chugach terrane, PWT=Prince William terrane, YT=Yakutat terrane, CPC=Coast Plutonic Complex, CMC=Chugach Metamorphic Complex, Ko=Kodiak, Se=Seward, Anc=Anchorage, Va=Valdez, Co=Cordova, Ya=Yakutat, Si=Sitka, Ju=Juneau, Ba=Baranof Island, BRFS=Border Range Fault System, CFS=Contact Fault System, KIZ=Kayak Island Zone, CSE=Chugach-St-Elias-Fault, PZ=Pamplona Zone, TrF=Transition Fault, FF=Fairweather Fault, DF=Denali Fault, TF=Tintina Fault, KF=Kaltag Fault, SCF=Stuart Creek Fault, RO=Resurrection Peninsula, KI=Knight Island, GI=Glacier Island, CSF=Chatham Strait Fault, NSF=Neva Strait Fault, PSF=Peril Strait Fault, ALF=Art Lewis Fault, CnF=Connection Fault, HF=Hanagita Fault, MF=Martin Fault, ARB=Alaska Range Belt, MtF=Mount Fairweather, JHI=John Hopkins Inlet, WVF=Wrangell volcanic field, SeG=Seward Glacier.



fossil ages in these rocks range from Late Cretaceous in the Chugach terrane to Eocene in the Prince William terrane (Fig. 1.3). The Late Cretaceous rocks extend from Sanak Island in the west to Baranof Island in the east (Shumagin Fm, Kodiak Fm, Valdez group and Sitka greywacke, Fig. 1.3). Detrital zircons from the Sitka Greywacke confirm a Late Cretaceous age for these rocks (Häussler et al., 1995). Paleocene rocks occur on Kodiak Island (Ghost Rock Fm) and Paleocene to Eocene rocks occur on Kodiak Island (Sitkalidak Fm) and in Prince William Sound (Orca group, Fig. 1.3; Plafker et al., 1994). The sediments show a very narrow range of ϵNd , Sr and Pb compositions indicating a relatively homogenous source, probably a fastly exhuming continental magmatic arc (Nilsen & Zuffa, 1982; Farmer et al., 1993; Sample & Reid, 2003).

Belts of mafic rocks Mafic rocks occur intercalated with the sediments all over the accretionary prism, but are especially abundant in several areas: Along a narrow belt stretching from Valdez down to Baranof Island, on the Resurrection Peninsula, and on Knight and Glacier Islands in Prince William Sound (Fig. 1.1). (1) The belt from Valdez to Baranof Island consists of metamorphosed mafic rocks intercalated with sediments. Since these rocks are highly deformed and partly metamorphosed up to amphibolite-facies, primary textures are difficult to observe and the exact nature of these rocks is not well known. (2) The mafic rocks exposed on the Resurrection Peninsula occur in a 21 km long and up to 6 km wide fault-bounded block consisting of gabbro, sheeted mafic dikes and pillow basalts (Tysdal et al., 1977; Crowe et al., 1992; Kusky & Young, 1999; Kusky et al., 2004). The fact that the pillow basalts are intercalated with thin turbidites requires that the sequence formed relatively close to the margin which shed the sediments. (3) Similar pillow basalts, sheeted dikes and small gabbro plutons are exposed on Knight and Glacier Islands farther outboard in the Prince William terrane, suggesting that similar packages of mafic rocks were accreted during two different periods to the margin (Fig. 1.1; e.g. Tysdal et al., 1977). The geochemistry of the mafic rocks in the Valdez group, on the Resurrection Peninsula and on the Knight and Glacier Islands does not uniquely define their source and is compatible with either a MORB or a primitive-arc source (Lull & Plafker, 1990; Kusky et al., 2004). So they were interpreted as having formed (a) at an intra-oceanic island-arc (Lull & Plafker, 1990), or (b) at a leaky transform fault (Tysdal et al., 1977) or (c) at a real oceanic spreading ridge, with the arc-like signatures being the result of contamination of the mafic rocks by partial melting of the overlying sediments (e.g. Lytwyn et al., 1997; Kusky et al., 2004).

The Border Range Fault System The accretionary prism of the Chugach and Prince William terranes is bounded and transected by major fault zone systems. In the north, the Border Range Fault System (BRFS) juxtaposes the accretionary complex against the Wrangellia Composite terrane (Fig. 1.1). The BRFS has a long and complex deformational history which varies greatly along strike (Pavlis & Roeske, 2007). In the west, on Kodiak Island, the BRFS juxtaposes mid-crustal plutonic rocks inboard against Jurassic blueschist-facies sediments of the *mélange* facies of the Chugach terrane outboard, indicating that the

fault has an important thrust component that was active prior to ~150 Ma. In addition, the fault is pinned by ~58-62 Ma old plutons, limiting any strike-slip motion along this part of the fault to before this period (Pavlis & Roeske, 2007). Farther to the north-east, on the Kenai Peninsula, the BRFS is buried below Tertiary and Quaternary sediments. However, thrust faults with east-side up components follow the trace of the BRFS and suggest Miocene to recent reactivation of it (Bruhn & Häussler, 2006; Pavlis & Roeske, 2007). From north-east of Anchorage in the west to the Canadian border in the east the BRFS is well-exposed and the kinematics of it are best studied. In the hinge of the Alaskan orocline, a complex, wide network of brittle dextral faults, probably active from ~55-45 Ma, overprint an older, Late Cretaceous thrust- and strike-slip history related to subduction, leading to a complex map pattern with units from the inboard arc terrane being mixed with units from the outboard accretionary prism (Fig. 1.1). From the Copper River to the Canadian border, several strands of dextral strike-slip faults (the Hanagita fault system of Roeske et al., 2003) overprint the older BRFS and were active from ~85-52 Ma, probably accumulating dextral displacements of up to ~500 km or maybe even >1000 km (Pavlis & Roeske, 2007). In Canada the trace of the BRFS turns into a more south-easterly direction and runs south-eastwards down to Baranof Island (Fig. 1.1). In this region, the BRFS is overprinted by a major dextral Tertiary strike-slip system which was probably active at least until ~42 Ma (Smart et al., 1996; Sisson et al., 2003). In addition it is cut or reactivated by several Neogene to recent dextral strike-slip faults such as the Art Lewis and Connection faults, Peril Strait Fault, the Chatham Strait Fault, the Neva Strait Fault or the Fairweather Fault (Fig. 1.1; Pavlis & Roeske, 2007).

Internal deformation Outboard of the BRFS, the Chugach and Prince William terranes are internally highly deformed, folded, sheared and cross-cut by many brittle faults (e.g. Häussler & Nelson, 1993; Kusky et al., 1997b; Häussler et al., 2003b). In the north, the dextral Stuart Creek Fault/Bremner shear zone cross-cut rocks of the Chugach terrane (Fig. 1.1; Pavlis et al., 2003). Farther south, faults belonging to the Contact Fault System (CFS) separate rocks from the Chugach and Prince William terranes. West of Prince William Sound, the CFS consists of steeply to moderately west dipping thrust faults, overprinted by younger dextral strike-slip faults and out-of-sequence thrusts (e.g. Sample & Moore, 1987; Bol & Gibbons, 1992; Rowe et al., 2009). In the eastern Prince William Sound the CFS consists of several syn- to post-accretionary fault strands with different kinematics compatible with a dextral transpressive system (Fig. 1.1; Bol & Roeske, 1993). One of these faults cuts an ~35 Ma old pluton (Häussler & Nelson, 1993). Farther to the east, faults related to the CFS are pinned by a ~54-50 Ma pluton (Fig. 1.1) and disappear below the extensive Bagley icefield. However, a dextral fault strand splays off from beneath the Bagley icefield towards the SW (Martin fault, Bruhn et al., 2004) indicating that dextral offset may have occurred still after intrusion of the pluton. Thermochronology suggests that faults below the Bagley icefield might have been reactivated during the Pleistocene as south-dipping backthrusts during the Yakuat collision (e.g. Berger et al., 2008a). A gradient in metamorphism from greenschist facies to amphibolite facies along the ridge

south of Bagley icefield to the Canadian border suggests that considerable dip-slip motion occurred on parts of the Contact fault system in this area (Plafker et al., 1994). The Contact Fault System is completely buried below the Seward glacier in Canada, and is towards SE cut by or joins into several anastomosing dextral shear zones and brittle faults related to the Fairweather Fault.

Sub-surface structure Two major seismic reflexion and refraction studies are available for the Chugach and Prince William terranes: the EDGE transect crossing the western part of the terranes between Kodiak Island and Kenai Peninsula, and the TACT transect crossing the eastern part of the terranes west of Copper River and in the Prince William Sound (Fig. 1.1c shows the TACT-transect; Fuis & Plafker, 1991; Plafker et al., 1994; Fuis et al., 2008). Both transects show slightly north-dipping reflectors below the Chugach terrane at depths of ~10-25 km (Fig. 1.1c). These reflectors and their velocity structure have been interpreted as representing underplated sediments in the EDGE transect, and a package of underplated sediments and offscraped oceanic crust in the TACT transect (Fig. 1.1c; Fuis et al., 1991; Fuis & Plafker, 1991; Plafker et al., 1994; Fuis et al., 2008). The TACT transect further reveals that the Prince William terrane is underlain by underplated Yakutat terrane in the Copper River area and subducting Yakutat terrane in the Prince William Sound area (Fig. 1.1c; Fuis et al., 2008).

Metamorphism The landward *mélange* facies of the accretionary prism contains greenschist to blueschist-facies schists (e.g. Plafker et al., 1994). Since most of their metamorphic history is older than Late Cretaceous, they are not described in more detail further. The turbidite sequence of the accretionary prism is mostly metamorphosed to phrenite-pumpellyite to greenschist-facies grade from Sanak Island in the west to Copper River in the east. On Kodiak Island, the prism reached temperatures of ~200-250°C at pressures of ~3 kbar probably during accretion, and was then exhumed through fission track and apatite closure temperatures around ~44-25 Ma (Sample & Moore, 1987; Clendenen et al., 2003).

East of the Copper River, a large-scale metamorphic complex is developed in the accretionary prism: the Chugach Metamorphic Complex (CMC, Fig.1.1; Hudson & Plafker, 1982). According to Hudson & Plafker (1982), the CMC west of the U.S.-Canadian border consists of two macroscopically different zones: An outer schist zone composed of fine-grained biotite-quartz-plagioclase schist, which surrounds an inner gneiss zone composed of layered migmatitic gneisses. Pressure-temperature estimates for the metamorphism in this complex are sparse. The only values stem from five localities distributed throughout the northern and western parts of the complex: these samples reached temperatures of ~500-650°C and pressures of ~2.5-3.5 kbar, indicating that metamorphism occurred at ~9-13 km depth (Sisson & Hollister, 1988; Sisson et al., 1989). In the absence of more petrological data from the remaining complex these values have since been cited for the entire complex and the area has been interpreted as resulting from an unusual low-pressure-

high-temperature metamorphic event which affected the accretionary prism (e.g. Sisson & Hollister, 1988; Sisson et al., 1989; Sisson & Pavlis, 1993; Pavlis & Sisson, 1995; Bradley et al., 2003). Structural studies in the northern and western parts of the CMC suggest that the metamorphism was accompanied by two distinct fabric generations overprinting the earlier accretionary structures: a first, flat-lying foliation with an orogen-parallel stretching lineation is overprinted by a second, steep foliation (regionally termed D₂ and D₃ events; Pavlis & Sisson, 1995, 2003).

Paleomagnetism Paleomagnetic studies of volcanic rocks, sedimentary rocks or dikes allow calculating the latitude at which the rocks were magnetized, and, provided that the exact age of the rocks (i.e. the time of magnetization) is known, relative displacements and rotations between rocks with different paleolatitudes can be calculated. Such paleomagnetic studies of Alaska suggest that most terranes inboard of the BRFS were at their present position relative to North America by Latest Cretaceous to Paleocene. However, according to paleomagnetic studies, the western part of Alaska rotated $\sim 44 \pm 11^\circ$ counter clockwise between ~ 65 - 35 Ma to form the Alaskan orocline (Coe et al., 1985). Several, quite differing models have been proposed to explain this rotation: from large-scale mega-kinking around a vertical axis due to the convergence of Eurasia and North America following the opening of the North Atlantic (Coe et al., 1989), via the buckling and 'derailing' of a northwards moving ribbon continent against stable Eurasia (Johnston, 2001), to an orogenic stream which flows upwards from western North America, encounters a back stop and flows around a corner towards the free surface of the Aleutian subduction zone (Redfield et al., 2007).

Apart from this counter-clockwise rotation of western Alaska, two paleomagnetic studies also suggest that large northward displacements of the Chugach and Prince William terranes may have occurred relative to the inboard terranes after ~ 62 - 57 Ma. Volcanic rocks from the Ghost Rock Fm on Kodiak Island sampled on two different locations show magnetizations which formed $31 \pm 9^\circ$ and $16 \pm 9^\circ$ farther south relative to North America (Plumley et al., 1983; Coe et al., 1985). Magnetizations of the pillow basalts and sheeted dikes of the Resurrection ophiolite indicate formation $13 \pm 9^\circ$ farther south relative to North America (Bol & Coe, 1992). These two studies suggest that considerable dextral strike-slip displacement must have occurred between these rocks and the inboard Wrangellia composite terrane since ~ 62 - 57 Ma. In the case of the Ghost Rock Fm, this must have occurred on dextral faults outboard of the BRFS (Sample & Moore, 1987), since the BRFS itself is pinned by ~ 62 Ma plutons (Pavlis & Roeske, 2007). Farther east, such displacement could have been taken up by the dextral Hanagita fault system and several dextral strike-slip faults related to the Contact fault system which were probably active after ~ 62 - 57 Ma (Fig. 1.3). Nevertheless, the paleomagnetic results have been questioned since the values scatter considerably which is difficult to explain by differential northward displacement of the three sample locations. Instead the magnetizations could be secondary and not related to the original magnetization (see a discussion in Häussler et al., 2003a). However, a recent study supports evidence for displacement of the Ghost Rock Fm after ~ 62 - 57 Ma (Roeske et al., 2009).

1.2 The Sanak-Baranof plutonic belt

The metasedimentary rocks of the Chugach and Prince William terranes are intruded by a suite of magmatic rocks which occur from Sanak Island in the west down to Baranof Island in the south-east: the Sanak-Baranof plutonic belt (Fig. 1.1; Hudson et al., 1979). The belt consists of several widely spaced plutons which are somewhat more frequent in the eastern part of the belt (Farris & Paterson, 2009). Large and well-studied plutons occur on Kodiak Island (Hill et al., 1981; Farris et al., 2006; Ayuso et al., 2009), on the Kenai Peninsula and in eastern Prince William Sound (Barker et al., 1992; Lytwyn et al., 2000), throughout the Chugach Metamorphic Complex and in the Fairweather corridor (Harris et al., 1996; Sisson et al., 2003) and on Baranof Island (Fig. 1.1). The plutonic belt is insofar unusual as it represents magmatic activity in an extreme fore-arc location relative to the coeval magmatic arc which was active farther landwards. Even though the exact location of the accretionary prism relative to the inboard arc terranes at the time of intrusion is not well known, magmatic arcs of similar age extend farther inboard all the way from the Aleutian Islands down to British Columbia (the Kuskokwim/Alaska Range and Kluane/Coast Plutonic belts, Fig. 1.1a; Wallace & Engebretson, 1984; Gehrels et al., 2009), suggesting that indeed the Sanak-Baranof plutonic belt was somewhere seawards of a more landward 'real' magmatic arc during its formation.

Petrology and Geochemistry The plutons are dominantly granodiorites, tonalites and quartz diorites. Minor granites and gabbros are present, as well as a range of hypabyssal andesitic to rhyolitic dikes and sills (Plafker et al., 1994; Bradley et al., 2003). The occurrence of kyanite and garnet in metapelitic xenoliths found in some plutons point to an origin of these melts at depths of ~6-8 kbar (Hill et al., 1981; Ayuso et al., 2009). Most plutonic rocks show calc-alkaline major-element compositions, whereas trace-element compositions as well as Sr, Pb, Nd and O isotopic compositions vary considerably between the different plutons. The trace-element and isotopic compositions of some plutons fully overlap with the trace-element and isotopic compositions of the sediments surrounding them, suggesting that they are entirely derived from partial melting of the sediments, e.i. the plutons in the Cordova area in the eastern Prince William Sound (Barker et al., 1992), or parts of the Kodiak batholith (Ayuso et al., 2009). The trace-element and isotopic compositions of other plutons and many dikes have lower chondrite normalized trace-element compositions, lower $^{87}\text{Sr}/^{86}\text{Sr}$ values, lower $^{207}\text{Pb}/^{204}\text{Pb}$ values, lower $^{206}\text{Pb}/^{204}\text{Pb}$ values, lower $\delta^{18}\text{O}$ values, and higher ϵNd values relative to the composition of the surrounding sediments. This could be due to different sedimentary compositions deeper down in the prism where the melts originated (Barker et al., 1992) and/or suggest that besides the partial melting of sediments, a second, more mafic and isotopically depleted source for the melts was present (Hill et al., 1981; Harris et al., 1996; Lytwyn et al., 2000; Sisson et al., 2003; Ayuso et al., 2009). A characterization and geodynamic interpretation of this additional mafic source is not straightforward, amongst others due to complex fractionation and assimilation processes, and several possibilities exist (e.g. Ayuso et al., 2009): The mafic endmember could

have originated (1) from partial melting of older mafic rocks intercalated with the sediments in deeper parts of the accretionary prism, (2) from the depleted, metasomatized mantle-wedge of the upper plate which was underlying the accretionary prism, (3) from melting and devolatilization of the subducting oceanic crust (altered MORB and sediments), or (4) from the upwelling mantle of the subducting plate during the formation of a slab window. There is no clear evidence for the direct contribution of the last possibility, and the calc-alkalic nature similar to island-arc tholeiitic basalt and the trace-element and isotopic composition of the most mafic plutonic rocks resembles standard sources of continental arcs such as the metasomatized mantle wedge of the upper plate and the oceanic crust of the down-going plate (Ayuso et al., 2009).

Age relationships A range of K/Ar, $^{40}\text{Ar}/^{39}\text{Ar}$, Rb-Sr and U-Pb ages were obtained on rocks from the Sanak-Baranof plutonic belt (Sisson et al., 1989; Bradley et al., 1993; Häussler et al., 1995; Bradley et al., 2000, 2003; Sisson et al., 2003; Farris et al., 2006). Concordant U-Pb ages are generally best to date the time of intrusion, since the other systems represent cooling ages below a certain closure temperature range, which can be considerably lower than the temperature of intrusion. Therefore, cooling ages always only represent minimum ages of intrusion. 15 U-Pb ages of variable quality are published from rocks of the Sanak-Baranof belt. They were all obtained by U-Pb TIMS methods and represent either concordant fractions or lower intercepts of discordant fractions, mainly from zircon, but also from monazites. The Sanak and Shumagin plutons give ages of 61.1 ± 0.5 Ma (Bradley et al., 2000), the Kodiak pluton gives 6 ages ranging from 58.4 ± 0.2 Ma to 59.1 ± 0.2 Ma (Farris et al., 2006), one discordant monazite from the Kenai Peninsula gives an age of 56 ± 0.3 Ma (Bradley et al., 2000), discordant zircons, monazites and xenotimes from a sill in the CMC range from ~ 50 -65 Ma (Sisson et al., 2003), two plutons in the Fairweather corridor give ages of 49 ± 7 Ma and 54 ± 1 Ma (Sisson et al., 2003) and three plutons on Baranof Island finally give ages of 50.1 ± 0.1 , 50.5 ± 0.5 and 51.6 ± 0.3 Ma (Bradley et al., 1993, 2003). These ages reveal a general decrease in age of the intrusions from ~ 61 Ma in the west to ~ 50 Ma in the east, but considerable sections of the belt do not show a decrease in age at all, or some complications with younger ages in the west than in the east. The age relationships of the Sanak-Baranof belt are discussed in more detail in Chapter 4 of this thesis.

Younger plutons Several plutons occur in the Chugach and Prince William terranes which are petrologically or geochronologically not directly related to the Sanak-Baranof plutonic belt. In western Prince William Sound, a series of mainly granitic rocks have K-Ar ages of ~ 34 -38 Ma (Plafker et al., 1994). Even though U-Pb ages of these intrusions are lacking, the K-Ar ages are considerably younger than K-Ar ages of the surrounding rocks, indicating that the plutons intruded after that the surrounding rocks cooled below the K-Ar blocking temperature. Another set of somewhat different plutons occurs in the Fairweather corridor. Several massive bodies of layered gabbros, some of which contain ultramafic cumulates, un-

derlie the mountainous Fairweather Range (Fig.1.1; Loney & Himmelberg, 1983; Plafker et al., 1994). Only K/Ar and $^{40}\text{Ar}/^{39}\text{Ar}$ ages from these rocks exist and scatter widely between 41 and 19 Ma, and an interpretation of these ages in terms of cooling, excess Ar etc. is difficult. A small diorite plug in John Hopkins Inlet which might be related to these intrusions gave an age of 42 ± 0.1 Ma, suggesting that these rocks might be considerably younger than the intrusions of the Sanak-Baranof belt (Sisson et al., 2003). However, U-Pb ages from the large-scale gabbro intrusions itself would be needed in order to evaluate a potential relationship with the more felsic Sanak-Baranof intrusions.

1.3 Yakutat terrane

Lithologies The Yakutat terrane is a fault-bound block or micro-plate which actively collides with the units farther inboard along the southern Alaskan margin. It consists of an eastern continental and a western oceanic basement which are separated by the Dangerous River Zone (Fig. 1.1). The continental basement consists of up to greenschist facies mélangé and turbidites intruded by Tertiary plutons, similar to the turbidite sequence of the Chugach terrane (Plafker et al., 1994). The oceanic basement consists of thick (~24-27 km) basaltic oceanic crust of Early Eocene age which either represents crust doubled by underthrusting (e.g. Eberhart-Phillips et al., 2006), or that originated on a thick oceanic plateau (Davis & Plafker, 1986; Christeson et al., in press). Both basement types are unconformably overlain by Eocene to Oligocene sedimentary rocks of the Tonkun and Stillwater, Kulthieth and Paul Creek formations. These sediments document the evolution of deep marine, volcanoclastic strata via slope and shelf deposits to shallow-marine and non-marine strata during a subtropical climate in the Eocene and Oligocene. These sediments are unconformably overlain by the late Miocene to recent Yakataga formation, which documents the influx of large amounts of glaci-marine sediments related to uplift and glaciation in the hinterland (e.g. Plafker et al., 1994; Perry et al., 2009). A detrital zircon study on the Eocene to recent overlap sequences suggests that the Eocene and Oligocene strata were derived from the same hinterland - probably the Coast Plutonic Complex - whereas the younger Miocene to Pleistocene strata of the Yakataga formation were derived from a different source - probably the exhuming Chugach-St. Elias mountains (Perry et al., 2009).

Bounding fault zones The Yakutat terrane is bounded by several different fault zones (Fig. 1.1). Coupling between the Pacific plate and the Yakutat block in the south across the Transition fault has been a matter of debate and everything from underthrusting of the Pacific plate below the Yakutat terrane, to left-lateral or right-lateral offset has been proposed (e.g. Pavlis et al., 2004; Eberhart-Phillips et al., 2006; Gulick et al., 2007). The most recent seismic survey of the fault suggests that it is a steep dextral strike-slip fault along which no underthrusting of the Pacific plate below the Yakutat block occurred (Christeson et al., in press). The Kayak Island Zone in the west is a complexly deformed area where the struc-

tures of the Aleutian megathrust (thrusts as well as normal faults) encounter the continental margin (Bruhn et al., 2004). The Chugach-St.Elias fault in the north is a N-dipping thrust fault which separates the Yakutat sediments from older rocks of the Prince Williams and Chugach terranes to the north (Bruhn et al., 2004). The Fairweather Fault to the east finally is an active dextral strike-slip fault (McAleer et al., 2009).

Internal deformation The sedimentary rocks overlying the Yakutat basement are relatively undeformed south of the Pamplona Zone, but build up a complex fold-and-thrust belt, consisting of several thrust-bounded and internally folded sheets, north of the Pamplona Zone and along a narrow corridor along the Fairweather Fault (Fig. 1.1; e.g. Meigs et al., 2008). Formation of this fold-and-thrust belt probably started in the late Miocene and increased in the Pliocene (at ~5-6 Ma), leading to surface uplift and the formation of the spectacular highly-glaciated Chugach-St.Elias mountains with peaks exceeding 5000 m altitude standing only ~50 km from the coast (e.g. Berger et al., 2008a). Total amount of shortening is estimated to a minimum of ~82 km in the central part of the belt (Meigs et al., 2008). Pleistocene exhumation revealed by low-temperature thermochronology is strongest in a narrow belt just south of the Chugach-St.Elias fault which corresponds to the glacier equilibrium line altitude, suggesting that glaciers play an important role in focusing the locus of exhumation in this actively deforming wedge (Berger et al., 2008a,b; Berger & Spotila, 2008). In addition, thermochronology showed that Pleistocene exhumation also affected older rocks north of the Chugach-St.Elias fault south of the Bagley Icefield, indicating that a young structure must be located below this icefield (Fig. 1.1; Berger et al., 2008a). The thermochronological signal of rivers draining the area below the Seward glacier suggests that this area is also strongly affected by young (< ca. 3 Ma) exhumation (Enkelmann et al., 2009, 2010). Similarly, Pleistocene exhumation is also focused in- and outboard of the Fairweather fault zone farther east, indicating that transpression occurs in this region which is partitioned into strike-slip along the major fault and diffuse uplift in a corridor surrounding the fault (McAleer et al., 2009).

Total amount of displacement Two different views about the total amount of displacement of the Yakutat terrane relative to the inboard terranes exist. Seismic investigations suggest that the thick oceanic crust of the Yakutat terrane underthrusts the southern Alaskan margin at least until the Alaska Range ~650 km farther inboard (Ferris et al., 2003). This is in good agreement with the restoration of the Dangerous River Zone to the Chatham Strait Fault, which requires ~600 km of southward restoration (Plafker et al., 1994), and with the probable origin of the Yakutat cover sediments from the northern Coast Plutonic Complex (Perry et al., 2009). Using the current speed of the Pacific Plate relative to North America (~5-6 mm/y), and assuming that the Yakutat terrane was coupled to the Pacific Plate would suggest that this northward transport of the terrane was ongoing since ~11-13 Ma (Koons et al., in press). However, correlating the thickened oceanic basement of the Yakutat terrane with a basaltic oceanic plateau of identical age which occurs along the margin offshore

Washington and Oregon (Siletzia, e.g. Häussler et al., 2003a) requires a much larger lateral transport of the terrane (>1000 km; Davis & Plafker, 1986; Christeson et al., in press). This suggests that also more time was needed to accomplish this transport and that northward transport of the terrane may have initiated as early as ~25 Ma, which would correspond to the time of onset of volcanism in the Wrangell volcanic field (Fig. 1.1; e.g. Richter et al., 1990).

1.4 Plate tectonics of the Pacific basin in the Cenozoic

The relative motions between oceanic plates of the Pacific basin and the continent of North America are the driving forces for the tectonic evolution of the North American margin. It is therefore crucial to understand these relative motions and how they changed through time. However, understanding relative plate motions is not straightforward. Magnetic anomalies produced during seafloor spreading are commonly used to reconstruct the growth history of two adjacent oceanic plates and relative motions between these two plates are calculated. However, as soon as subduction zone boundaries are involved, much of this spreading record gets lost and relative motions between the convergent plates are very difficult to reconstruct. Since the Pacific basin has been surrounded by subduction zone boundaries for most of its Cenozoic history, much information from that oceanic basin is lost and reconstructions rely on several indirect techniques. In order to reveal relative motions between plates which are only linked by a subduction zone boundary, indirect links are constructed via several other spreading ridge connections - the most famous connection for the Pacific-North American case is the link from the Pacific plate via Antarctica to the North Atlantic spreading system (e.g. Atwater, 1989). Uncertainties in the seafloor record and in within-plate deformations of course propagate from one connection to the other, ending up in considerable uncertainties in the relative motions between the plates of interest.

This so-called plate-circuit technique only allows to investigate *relative* motions between plates, and not their absolute positions on the globe. In order to get more absolute reconstructions, it has been assumed that certain hot-spots are fixed in the mantle, and that the trace of hot-spot chains (such as the Emperor and Hawaiian chains, Fig. 1.2) are the result of the motion of the plate over a fixed hot-spot. Together with the plate-circuit approach, this allows to fix the entire plate system relative to the hot-spots in the mantle. However, there is increasing evidence that the hot-spots are actually not fixed relative to each other, but that they have relative motions comparable to relative motions between plates, making them not suitable for absolute plate reconstructions (e.g. Doubrovine & Tarduno, 2008). Other information about the absolute motion of plates on the globe may come from paleomagnetic studies, which can provide the paleolatitude of a sample given its exact age and orientation of bedding is known during its formation and no secondary magnetization occurred afterwards. However, since only paleolatitude and not longitude can be derived, paleomagnetism alone is not sufficient for reconstructing relative plate motions. Finally, relative motions be-

tween oceanic and continental plates may be derived from geological evidence preserved on the continents, such as forearc magmatism, magmatic arcs, accretionary prisms or back-arc basins, given that those features are correctly interpreted in terms of plate tectonic processes which shaped them, which is not always obvious. So keeping all the uncertainties and assumptions related with plate tectonic reconstructions in mind, the plate tectonic history of the northern Pacific basin during the Cenozoic is summarized below.

Magnetic anomalies on the Pacific plate Today, the northern Pacific basin is underlain by the vast oceanic Pacific plate, and only offshore southern British Columbia, Washington and Oregon small remnants of a once much larger plate are present, the Juan de Fuca and Explorer plates (Fig. 1.2; Atwater, 1989). Information from magnetic anomalies for the northern Pacific basin therefore mainly comes from the Pacific oceanic plate (Fig. 1.2). The central part of the northern Pacific plate east of the Emperor-Hawaiian seamount chain is dominated by an absence of magnetic anomalies, the so-called Cretaceous quiet period (Fig. 1.2; Atwater, 1989). The first magnetic anomaly after this quiet period is chron 34, which corresponds to an age of ~84 Ma (Fig. 1.2; chron-age correlations after Mueller et al., 2008). From chron 34 to chron 24 (~84-53 Ma), anomalies are relatively straight and regular, and their geometry points to the existence of three oceanic plates separated by two spreading ridges during that period: the Pacific plate in the southwest, the Farallon plate (now Juan de Fuca and Explorer plates) in the east and the Kula plate (Kula = 'all gone' in Athapascan) in the north. The Great Magnetic Bight (Fig. 1.2) tracks the location of the triple junction between the three plates. However, since the anomalies are only preserved on the Pacific plate and not on the Farallon or Kula plates, symmetric spreading has to be assumed to calculate relative plate motions between the three plates for that time period (Engebretson et al., 1984).

The relatively stable spreading situation recorded in chrons 34-24 changed abruptly at chron 24 (at ~53 Ma; Fig. 1.2). Changes occurred both in Pacific-Kula and Pacific-Farallon spreading. Most of the information regarding Pacific-Kula spreading is subducted below the Aleutian trench, but some critical but controversial observations remain, which lead to two differing views about Pacific-Kula spreading after ~53 Ma. The T-shaped anomaly 24 at the northeastern end of the Great Magnetic Bight could be explained by the cessation of Pacific-Kula spreading at that time (e.g. Byrne, 1979) or by a northeastward jump of the triple junction and continuation of Pacific-Kula spreading after that time (Engebretson et al., 1984; Atwater, 1989). Controversial evidence for the second case comes from a narrow strip of seafloor exposed at the northwestern end of the Pacific plate just offshore the Aleutian trench. There, Pacific-Kula magnetic anomalies rotate anti-clockwise at chron 24 and anomalies are preserved until chron 18 (~40 Ma). A fault trending parallel to chron 18 is interpreted as representing the Pacific-Kula spreading ridge and an anomaly northwest of this fault is interpreted as anomaly chron 20 from the Kula plate (Fig. 1.2; Lonsdale, 1988). If this interpretation is correct, Pacific-Kula spreading would have changed direction at ~53 Ma and would have continued to spread highly asymmetric until ~40 Ma. However,

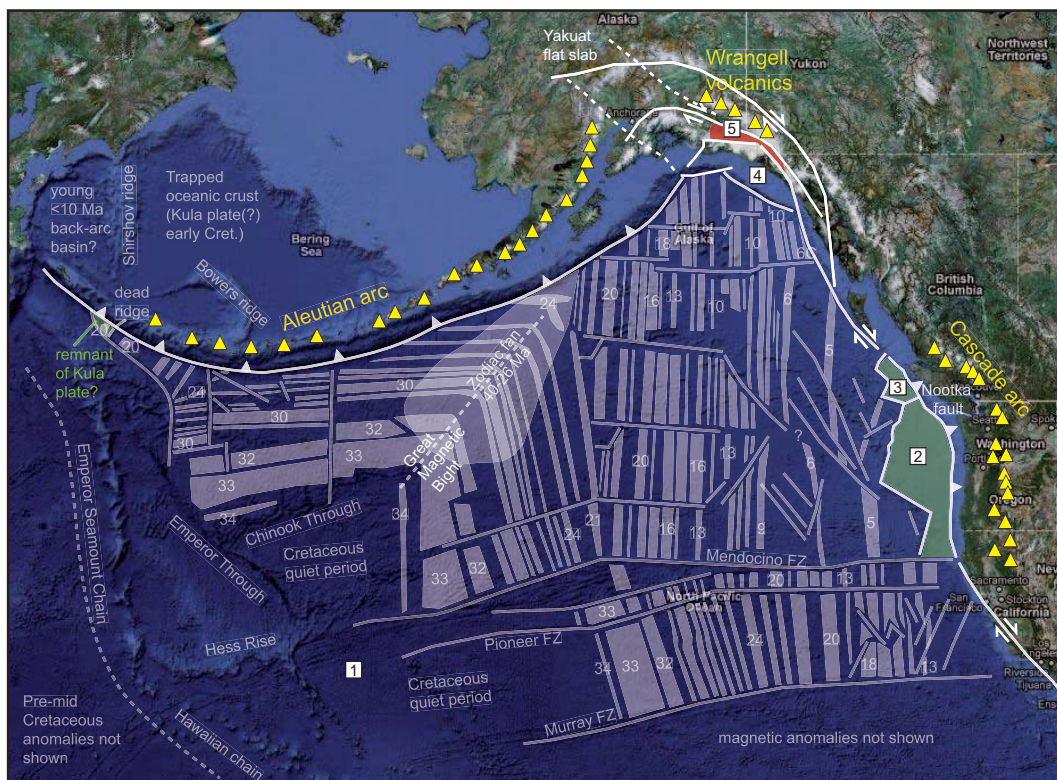


Figure 1.2: Satellite image (from maps.google.com) of the northern Pacific basin with the present-day plate tectonic situation and the magnetic anomalies on the Pacific oceanic plate (after Atwater, 1989) indicated. The complex magnetic anomalies after chron 11 on the Pacific plate are not shown in detail. (1) Pacific plate, (2) Juan de Fuca plate, (3) Explorer plate (separated from the Juan de Fuca plate by the Nootka fault), (4) Yakutat terrane, (5) Chugach Metamorphic Complex.

the observations come from a very narrow, highly fractured region with considerable topography just offshore the Aleutian trench, and is therefore questionable (Atwater, 1989; Norton, 1995). So either the Pacific-Kula spreading ceased at ~53 Ma, and only the Pacific and Farallon plates remained in the Pacific basin after that time, or Pacific-Kula spreading continued until ~40 Ma when it finally ceased. This uncertainty in relative plate motions in the Pacific basin from ~53-40 Ma leaves of course great uncertainty in the plate configuration along the margins of the Pacific basin, i.e. which plate interacted at which time and with which direction and speed with the North American margin.

Besides the changes observed in the Pacific-Kula spreading at chron 24 also major changes in Pacific-Farallon spreading occurred between chrons 24-21 (~53-48 Ma). Magnetic anomalies east of chron 24 are rotated 20° clockwise and new W-E fracture zones developed in the former straight eastern segment of the Great Magnetic Bight. This rotation is attributed to either a reorganization related to the change in Pacific-Kula spreading or to a break-up of the Farallon plate into a southern part and a northern part along the Murray FZ (with the

northern part termed Vancouver plate by some workers; Atwater, 1989). The complex fracture zones in chron 18 and younger chrons between the Murray and Pioneer FZ offshore San Francisco are attributed to oblique transpression between the southern and northern Farallon plates (Fig. 1.2). After the chron 24-21 reorganization, Pacific-Farallon/Vancouver spreading continued relatively undisturbed until at least chron 11 (from ~48-29 Ma, Fig. 1.2). The bend in the Emperor-Hawaiian seamount chain, which occurred between ~43-47 Ma, did not leave an imprint in Pacific Farallon spreading. The proposed cessation of Pacific-Kula spreading at chron 18 (~40 Ma) did not leave an imprint in Pacific-Farallon spreading either (Norton, 1995). An important feature dating from that stable spreading time period is the presence of the massive Zodiak fan, which was deposited ontop of the Great Magnetic Bight region from ~40-23 Ma (Atwater, 1989). The presence of this huge clastic fan implies that a continental landmass was close to it during the time of sedimentation, and that therefore only limited (~500 km) relative displacement between the Fan and adjacent continental landmasses (probably Alaska) could have taken place since the deposition of the fan (~40-23 Ma Stevenson et al., 1983). This geologic constraint is generally not taken into account in plate tectonic reconstructions which place the fan >1000 km away from any potential source areas during the time of its deposition (Atwater, 1989).

After chron 11 (~29 Ma), the magnetic anomalies on the Pacific plate document a complex history of spreading between the Farallon/Vancouver (now termed Juan de Fuca) and the Pacific plate, involving jumps and clockwise rotation of spreading segments, and spreading slowed considerably. Finally, the northern Explorer plate broke off from the Juan de Fuca plate along the Nootka fault (Fig. 1.2; Atwater, 1989).

Relative motions between the oceanic plates of the Pacific basin and North America based on plate tectonic reconstructions Engebretson et al. (1985) calculated relative plate motions between the oceanic plates of the Pacific basin and North America based on the observed magnetic anomalies, assuming symmetric spreading between Pacific, Farallon and Kula plates, assuming fixed hot-spots and connecting the Pacific with the Atlantic spreading system via fixed hot-spots. In addition, their reconstruction assumes cessation of Kula-Pacific spreading at chron 18 (~40 Ma), something which could as well have taken place already at chron 24 (~53 Ma, see discussion above). Their results show that in general, the Farallon plate moved east to north-east relative to North America since at least chron 34 (~84 Ma), whereas the Kula plate moved north-northwest with much greater speed relative to North America. After chron 18 (~40 Ma), the Pacific plate coupled to the Kula plate and moved northwestwards relative to North America, whereas the Farallon plate was still moving eastwards. Great uncertainties are associated with the exact location of the intersection between the Kula-Farallon ridge and the North American margin before chron 18 (~40 Ma). Estimations range from southern Mexico to Vancouver Island, with a general northward movement from ~84-40 Ma. The ridge between the Pacific and Farallon plates after ~40 Ma is shown to have intersected the margin basically at the same location as today, in the vicinity of Vancouver Island (Fig. 1.2).

Since the reconstructions of Engebretson et al. (1985), increasing evidence suggests that the Pacific and North Atlantic hot-spots are not fixed relative to each other and therefore reconstructions based on this assumption may be incorrect (e.g. Atwater, 1989; Norton, 1995; Doubrovine & Tarduno, 2008). Doubrovine & Tarduno (2008) therefore presented a revised reconstruction solely based on plate-circuit connections, and they compare their results with the results of Engebretson et al. (1985). In order to make the models comparable, they also assume a chron 18 (~40 Ma) cessation of Pacific-Kula spreading. Differences between the different models are biggest for the time before ~46-39 Ma, where the Engebretson et al. (1985)-model shows northeastward motion of the Pacific plate relative to North America, and the Doubrovine & Tarduno (2008)-model shows northward motion. In addition, the Doubrovine & Tarduno (2008)-model places the Pacific-Farallon-Kula triple junction much closer to the North American continent during the time of its existence between chron 34 and chron 24 (~84-53 Ma), limiting the possible locations of the intersection of the Kula-Farallon ridge and the North American margin to an area between northern California and southern British Columbia. Doubrovine & Tarduno (2008) calculated relative velocities between the oceanic plates and North America from ~84-0 Ma for three locations along the margin: southern Alaska, Vancouver Island and California. For all three locations convergence varies between nearly orthogonal and highly dextrally oblique and relative velocities significantly decrease after the cessation of Pacific-Kula spreading (in their model at ~40 Ma).

1.5 Tectonic evolution of the Southern Alaskan margin

The geology of the southern Alaskan margin as summarized above allows reconstructing the tectonic evolution of the margin in several episodes:

Late Cretaceous to Eocene accretion The Late Cretaceous to Eocene turbidite sequence of the Chugach and Prince William terranes was deposited and accreted probably somewhere south of its present location, with the sediments most likely derived from the exhuming Coast Plutonic Complex (Nilsen & Zuffa, 1982; Plafker et al., 1994; Sample & Reid, 2003). In addition to the high input of clastic sediments into the evolving accretionary prism, periods of increased mafic volcanism are indicated by the presence of mafic rocks in the prism. The interpretation of these mafic rocks is not unambiguous: some of them could represent volcanoclastic sediments derived from the arc, others probably represent sub-marine basaltic lava-flows and hypabyssal sills either derived from an intra-oceanic island-arc (Lull & Plafker, 1990), from a leaky transform fault (Tysdal et al., 1977) or from a proper oceanic spreading ridge (e.g. Bradley et al., 2003) which was present close to the margin.

Paleoposition and dextral transport of the prism during accretion Contemporaneous with accretion, dextral northward motion of the prism probably took place along the inboard Hanagita fault zone from ~70-51 Ma. The total amount of displacement during that period is not well constrained and varies from ~500 km to >1000 km (Roeske et al., 2003; Pavlis & Roeske, 2007). The uncertain location of the accretionary prism relative to the inboard margin produces uncertainties with respect to on which oceanic plate the accretionary prism formed. Plate tectonic reconstructions for the time period of interest show that the Kula-Farallon spreading ridge intersected the margin somewhere between Northern California and Vancouver Island, with the Farallon plate to the south subducting relatively orthogonal below the margin, and the Kula plate to the north subducting dextral obliquely below the margin (Engebretson et al., 1985; Doubrovine & Tarduno, 2008). If the accretionary prism was located north of at least Vancouver Island during its formation, it moved dextrally with the Kula plate northwards, and if it was located to the south of it (as suggested for example by Cowan, 2003) it originated on the Farallon plate and must have overridden the Kula-Farallon boundary in order to reach its present position. A third possibility would be that the prism formed on the Resurrection plate introduced by (Häussler et al., 2003a) in order to explain the Sanak-Baranof plutonic belt as described in the next paragraph.

The Sanak-Baranof plutonic belt and the ridge subduction model The accretionary prism of the Chugach and Prince William terranes is intruded by the ~2100 km long Sanak-Baranof plutonic belt (Fig. 1.1). These plutons intruded the accretionary prism at a time when coeval "normal" arc magmatism was still ongoing farther inboard (e.g. Wallace & Engebretson, 1984), which suggests that the plutons formed in an extreme fore-arc position. The geochemical composition of the plutons points to an origin from mainly melted sediments, with an additional component derived from a more mafic source. Marshak & Karig (1977) were the first to propose that the subduction of an oceanic spreading ridge below the prism could have been responsible for this near-trench melting event, a model which thereafter has been taken up and fine-tuned by many workers (e.g. Bradley et al., 1993; Sisson et al., 1989; Sisson & Pavlis, 1993; Pavlis & Sisson, 1995; Bradley et al., 2003; Häussler et al., 2003a; Farris et al., 2006; Madsen et al., 2006; Farris & Paterson, 2009). However, several uncertainties related to this model remain:

(1) Bradley et al. (1993, 2000, 2003) and Farris et al. (2006) revealed an W-E decreasing gradient in age of the plutons, which they interpreted as tracking the location of the subducting ridge below the margin. However, identical ages of plutons ~200 km apart from each other (e.g. the Sanak and Shumagin plutons, Chap. 4) and complications with younger ages in the west than in the east, contrary to what would be expected by the simple subduction of an west-east-migrating ridge (Sisson et al., 2003) suggests that the model of a single, punctual west-east migrating ridge might be an oversimplification. (2) The geochemical compositions of both the mafic rocks intercalated with the sediments (Lull & Plafker, 1990; Lytwyn et al., 1997) and the mafic end-member in the plutons (Ayuso et al., 2009) are more calc-alkaline and show different trace-element and isotopic compositions than what would

be expected if they originated at an oceanic spreading ridge. So either the mafic components have been complexely altered by the assimilation of sediments or they did not originate at an oceanic spreading ridge - but for example in the depleted mantle wedge underlying the accretionary prism or by partial melting of the subducting oceanic crust (Ayuso et al., 2009). Therefore, the geochemical composition of the plutons does not uniquely require the presence of a subducting spreading ridge. (3) Great uncertainties also exist with respect to which oceanic spreading ridge actually subducted below the margin. Since plate tectonic reconstructions based on the magnetic anomaly record of the Pacific plate only invoke three plates in the Pacific basin at that time, and only the Kula-Farallon ridge likely intersected the North American margin (Engebretson et al., 1985; Doubrovine & Tarduno, 2008), early workers (e.g. Bradley et al., 1993; Sisson & Pavlis, 1993; Pavlis & Sisson, 1995; Harris et al., 1996) inferred that it must have been this Kula-Farallon ridge which produced the plutonic belt. However, this Kula-Farallon ridge probably intersected the margin considerably to the south of the present position of the Sanak-Baranof belt and was slowly north-moving, the contrary to what the age gradient in the plutonic rocks infers. So either the terrane must have been located to the south of this ridge and moved faster northwards than the ridge in order to produce the southward younging age trend (e.g. Cowan, 2003), or, if the terrane was not located that far south, a second oceanic spreading ridge must have been present between so far unknown oceanic plates. This second possibility was developed by Häussler et al. (2003a). They assumed that the accretionary prism was in its present position when the intrusions of the Sanak-Baranof belt formed, and therefore introduced the additional Resurrection plate between the Kula and Farallon plates with the Kula-Resurrection ridge being responsible for the Sanak-Baranof belt (Fig. 1.3).

In conclusion, the model of a subducting spreading ridge below the southern Alaskan margin in the Eocene includes the following assumptions: (1) the ridge somehow produced a non-linear age distribution along the belt, (2) the geochemical signal of the plutons, which is more an arc-like than a spreading-ridge signal, was altered by the assimilation of sediments, and (3) either a large northward transport of the accretionary prism occurred after intrusion of the belt or an additional oceanic plate must have been present.

The chron 24-21 (~53-48 Ma) plate reorganization Contemporaneous with the younger part of the Sanak-Baranof plutonic belt, a plate reorganization is indicated by the magnetic anomalies on the Pacific plate. Unfortunately, what exactly happened during this reorganization of magnetic anomalies is not well constrained and two different interpretations are available: either the Kula-Pacific spreading stopped (Byrne, 1979; Atwater, 1989; Norton, 1995) or both the Kula-Pacific and the Pacific-Farallon ridges changed their direction and continued spreading - in the case of Kula-Pacific spreading until ~40 Ma (Lonsdale, 1988; Atwater, 1989). In the first case, a drop in plate convergence is expected along the margin since the Pacific plate moved much slower northwards relative to North America than the Kula plate; in the second case, an increase in plate convergence is predicted due to the reorganization and increased Pacific-Kula spreading (Engebretson et al., 1985; Doubrovine

& Tarduno, 2008). These two differing models lead to considerable uncertainties about the relative plate motions between the oceanic plates and the continental margin from ~53-40 Ma.

The accretion of the Yakutat terrane After the intrusion of the Sanak-Baranof belt at ~61-50 Ma and the plate tectonic reorganization at ~53-48 Ma a less well-defined and less active period followed. Some accretion of sediments may have occurred in the outer parts of the Prince William terrane, and the large Zodiac fan was deposited on the Pacific plate. Dextral strike-slip motion may have occurred on the Contact fault. The time at which the Yakutat terrane broke off from the continental margin and was transported northwards is not well defined. Plate tectonic reconstructions show margin-parallel motion of the Pacific plate since at least ~40 Ma (Dobrovine & Tarduno, 2008), Wrangell volcanism initiated at ~25 Ma (Richter et al., 1990) and retrodeformation of ~650 km of underthrust Yakutat oceanic crust with current underthrusting rates suggests that this underthrusting is going on since at least ~11-13 Ma. Finally, the formation of the fold-and-thrust belt of the Yakutat terrane started at ~5-6 Ma (e.g. Berger et al., 2008a; Meigs et al., 2008) which led to the formation of high topography and glaciation in the Chugach-St. Elias Mountains.

Summary The southern Alaskan margin shows a complex Late Cretaceous to recent geological history controlled by oblique convergence between various oceanic plates and the curved continental margin. Key features involved in the tectonic history of this margin are (1) sedimentation and accretion of large amounts of volcanoclastic detritus shed onto the subducting oceanic plates, forming the vast accretionary prism of the Chugach and Prince William terranes, (2) unknown amounts of dextral displacement of this accretionary prism relative to the inboard crystalline terranes, (3) metamorphism and partial melting of these sediments at depth and mixing with mafic melts, possibly caused by the interaction of this accretionary prism with subducting oceanic ridges or transform faults, and (4) the still-ongoing collision of the Yakutat terrane with the inboard accretionary prism which causes volcanism, deformation and uplift in the corner of the Alaskan orocline.

In this context, the following chapters of this thesis explore the spatial and temporal evolution of a part of this southern Alaskan margin, the Chugach Metamorphic Complex, in more detail.

Chapter 2

LA-ICP-MS U-Pb ages of detrital zircons: A Paleocene maximum depositional age for the protoliths of the CMC?

Abstract Knowing the depositional age range of the sediments in which the Chugach Metamorphic Complex developed is crucial for inferring the time available for prograde metamorphism in the metamorphic complex. Since biostratigraphic information from the metamorphic rocks is lacking, four samples covering the CMC from west to east-southeast were analysed by U-Pb LA-ICP-MS geochronology on detrital zircon. Youngest detrital zircon populations determined by several statistical methods reveal a Paleocene maximum depositional age for three of the four samples. These ages limit the time available for prograde metamorphism in the CMC to ~5-10 Ma. The Paleocene maximum depositional ages are slightly younger than the Late Cretaceous depositional age derived from biostratigraphy for sediments of the Valdez Group of the Chugach terrane, which are exposed along strike of the CMC to the west. They are also slightly younger than the Late Cretaceous maximum depositional age derived from U-Pb zircon geochronology for sediments of the Sitka Greywacke, which are exposed along strike of the CMC to the south-east. The age populations of all four samples are dominated by Paleocene and Cretaceous zircon grains, with minor contributions from Jurassic, Triassic, Paleozoic and Precambrian sources.

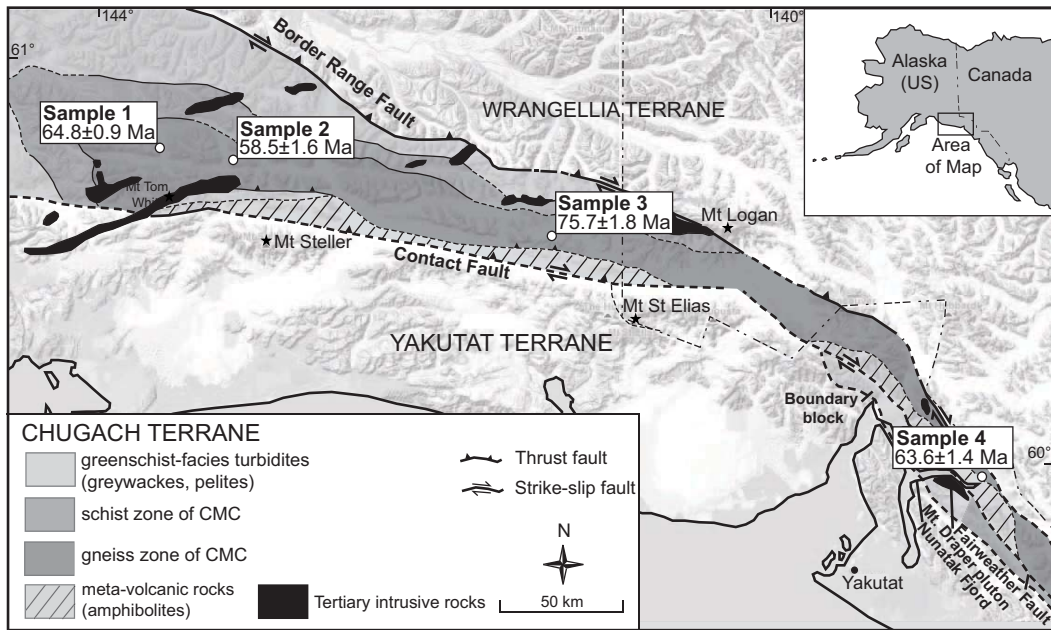


Figure 2.1: Geological map of Chugach Metamorphic Complex with the four sample localities indicated. The maximum depositional age for each sample is given based on mean ages of the youngest three or more zircon grains which overlap at 2σ ($YC2\sigma(3+)$), Tab. 2.1, see text for explanation).

2.1 Introduction

The depositional age of sedimentary rocks is traditionally determined using their fossil record. Since species evolve through time and varying species associations existed throughout much of Earth's history, the fossil record is generally a very powerful tool to infer the time of sediment deposition. However, as soon as the sediments are metamorphosed, the carbonaceous or siliceous fossils are altered and recrystallize, and crucial age information is lost. Therefore, alternative tools have to be used to constrain the depositional age of metamorphosed sediments. Over the past decade, U-Pb geochronology on detrital zircon grains has been increasingly used to constrain the maximum depositional age of sedimentary rocks, either where biostratigraphic age control is lacking or in order to refine biostratigraphic information (e.g. Barbeau et al., 2005; Surpless et al., 2006; DeCelles et al., 2007; Dickinson & Gehrels, 2009; Jones et al., 2009). The approach is based on the premise that the depositional age of the sediments can not be older than the youngest detrital zircon grains found in the rocks. In addition to the information on the maximum depositional age of the sequence, also valuable information on the provenance of the rocks can be inferred from the total age spectra revealed by U-Pb geochronology on detrital zircon grains (e.g. Carrapa, 2010).

The Chugach Metamorphic Complex (CMC) of southern Alaska is developed in metasedimentary rocks, but no fossils are preserved in this upper-amphibolite facies metamorphic complex. Therefore, the depositional age of the sedimentary protolith is not directly known and has to be inferred from regional correlations with lower-grade sedimentary rocks. Knowing the depositional age of the protolith of the CMC is important, since the depositional age limits the maximum time available for prograde metamorphism in the complex. This in turn may help to constrain the mechanisms which led to metamorphism in the complex. In this chapter, possible depositional ages of the metasediments of the CMC based on regional correlations are first reviewed, and then the results of U-Pb geochronology of detrital zircons from four samples covering the entire CMC from west to the south-east are presented.

2.2 Depositional age of the CMC protoliths based on regional correlations

The metamorphic rocks of the CMC plunge below lower-grade (phrenite-pumpellyite- to greenschist-facies) metasedimentary rocks just east of Copper River (Fig. 1.1). These lower-grade rocks are part of the turbidite sequence of the Chugach terrane, which consists of intercalated conglomerates, impure sandstones, marls, claystones and mafic volcanic rocks (e.g. Plafker et al., 1994). In the area west of Copper River, the turbidite sequence is termed Valdez Group, after outcrops close to Valdez in Prince William Sound (Fig. 1.1; Tysdal & Plafker, 1978). The depositional age of the Valdez Group is constrained by fossil bivalves belonging to different species of the Inoceramidae family, which have been found at 16 localities within the Valdez Group mostly in the western Chugach Mountains and on the Kenai Peninsula (Fig. 1.1). The fossils point to a mostly Maastrichtian (Late Cretaceous, ~70-65 Ma, timescale after Gradstein et al. (2004) or possibly Campanian (Late Cretaceous, ~83-70 Ma) depositional age of the Valdez Group (Plafker et al., 1994). Similar bivalves of Late Cretaceous age have been found on the Shumagin Islands and on Kodiak Island, suggesting that the Late Cretaceous turbidite sequence is continuous along the margin to the west. Since the metamorphic rocks of the CMC are exposed along-strike of the Valdez Group turbidites, a Late Cretaceous depositional age for the protoliths of the metamorphic rocks is generally assumed (e.g. Hudson & Plafker, 1982).

Along-strike of the CMC to the south-east, lower-grade sedimentary rocks similar to the Valdez Group are exposed on Baranof Island: the so-called Sitka Greywacke (Plafker et al., 1994). No age-diagnostic fossils have been found in this unit, but Häussler et al. (2005) dated detrital zircons from seven samples along an east-west transect covering the entire width of the unit across strike (~15 km). They determined maximum depositional ages of ~97-105 Ma for the eastern part and ~72-74 Ma for the western part of the unit, suggesting that the unit actually consists of an eastern older part, and a western younger part which is correlative in age with the Valdez Group farther west.

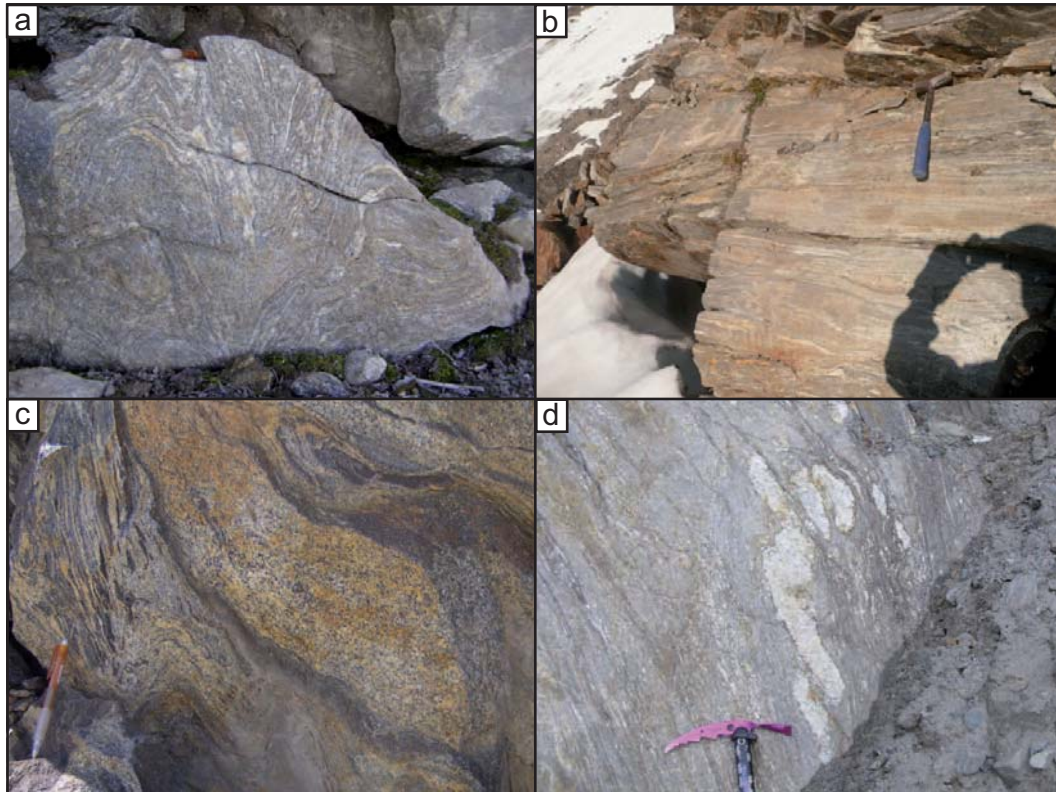


Figure 2.2: Field photographs of the four sample localities. **(a)** Outcrop of sample 1, which is a layered and folded metagreywacke. Width of outcrop ca. 50 cm, pencil for scale in upper left. **(b)** Outcrop of sample 2, which is a strongly foliated quartzofeldspathic gneiss. Hammer and shadow for scale. **(c)** Outcrop of sample 3, which is a strongly migmatized metapelite. Pencil for scale. **(d)** Outcrop of sample 4, which is a highly sheared metapelite. Ice axe for scale.

2.3 In-situ U-Pb dating of detrital zircons from the CMC

In order to reveal the maximum depositional age of the rocks of the CMC and in order to compare this age with the biostratigraphic age of the Valdez Group and the maximum depositional ages of the Sitka Greywacke, four samples covering the entire CMC from west to south-east were selected for in-situ U-Pb dating of detrital zircons by LA-ICP-MS. The sample locations are shown in Fig. 2.1.

Table 2.1: Summary of all detrital zircon samples

Nr.	Field-Nr.	Latitude (°N)	Longitude (°W)	YSG	YPP	YC1 σ (2+)	YC2 σ (3+)
1	F20	60.7970	143.7213	60.1 \pm 2.2	65	63.2 \pm 0.7 (7), 0.4	64.8 \pm 0.9 (21), 0.9
2	KB3	60.7380	143.3014	56.1 \pm 1.0	63	56.7 \pm 0.9 (5), 0.5	58.5 \pm 1.6 (11), 1.2
3	BG6	60.5399	141.3949	70.5 \pm 8.5	75	75.6 \pm 0.9 (16), 1	75.7 \pm 1.8 (13), 1
4	N28	59.8151	138.8827	58.1 \pm 3.4	63	62.1 \pm 0.9 (9), 0.4	63.6 \pm 1.4 (15), 0.9

YSG: youngest single detrital zircon grain, YPP: youngest graphical age peak on age distribution plot, YC1 σ (2+): Mean age of the youngest two or more single detrital zircon ages which overlap in 1 σ , number of included analyses given in parantheses, last value is MSWD of mean age, YC2 σ (3+): Mean age of the youngest three or more single detrital zircon ages which overlap in 2 σ , number of included analyses given in parantheses, last value is MSWD of mean age, after Dickinson & Gehrels (2009).

2.3.1 Analytical technique

Zircon grains were extracted from ~1-2 kg of material per sample by crushing, sieving, magnetic and heavy liquid separation, and were then handpicked, mounted in epoxy and polished to expose the grain centers. The internal zoning of the zircons was investigated by Cathodoluminescence (CL) imaging, carried out at the University of Graz, with a JEOL JSM-6310 scanning electron microprobe working at 15 kV, ~6 nA and 15 mm working distance. Isotopic ratios were measured by LA-ICP-MS at the Department of Lithospheric Research, University of Vienna, using a 193 nm solid state Nd:YAG laser (NewWave UP193-SS) coupled to a multi-collector ICP-MS (Nu Instruments Plasma HR) equipped with a U-Pb collector block. Detrital zircons were ablated in a He atmosphere depending on the size and zoning of the cores by 50 μ m, 35 μ m, or 25 μ m spots or lines. Each fifth to sixth analysis two to four measurements on the zircon standard Plesovice (337 \pm 1 Ma, Sláma et al., 2008) were conducted. On the standard zircon, a 25 μ m wide and 200 μ m long line was ablated in four line passes per analysis. Each analysis (on sample and standard) consisted of 40 s of gas and Hg blank measurement followed by 160 s of material ablation. Isotopes were transported in a mixed He-Ar gas. All measurements were made in static mode, using Faraday detectors for ^{238}U and ^{232}Th and ion counters for ^{208}Pb , ^{207}Pb , ^{206}Pb and ^{204}Pb .

Raw data from the mass spectrometer were evaluated using LamTool (Kosler and Klötzli, unpublished). All masses were corrected for blank values, including ^{204}Hg interferences on ^{204}Pb . ^{235}U was calculated from ^{238}U using a $^{238}\text{U}/^{235}\text{U}$ value of 137.88 (Jaffey et al., 1971). Standard corrected ratios were corrected for common Pb using measured ^{204}Pb concentrations and assuming an initial Pb composition from Stacey & Kramers (1975) using the apparent $^{207}\text{Pb}/^{206}\text{Pb}$ age. The uncertainties reported on single $^{206}\text{Pb}/^{238}\text{U}$, $^{207}\text{Pb}/^{235}\text{U}$ and $^{207}\text{Pb}/^{206}\text{Pb}$ ages in Table 2.2 are 2 σ and include only analytical uncertainty and uncertainty resulting from the standardization. Additional external errors such as errors on the decay

constants, the composition of common Pb, and the age of the standard are not considered but would add another ~1% of uncertainty to the single ages. Further data evaluation was done using the software Isoplot/Ex (Ludwig, 2003).

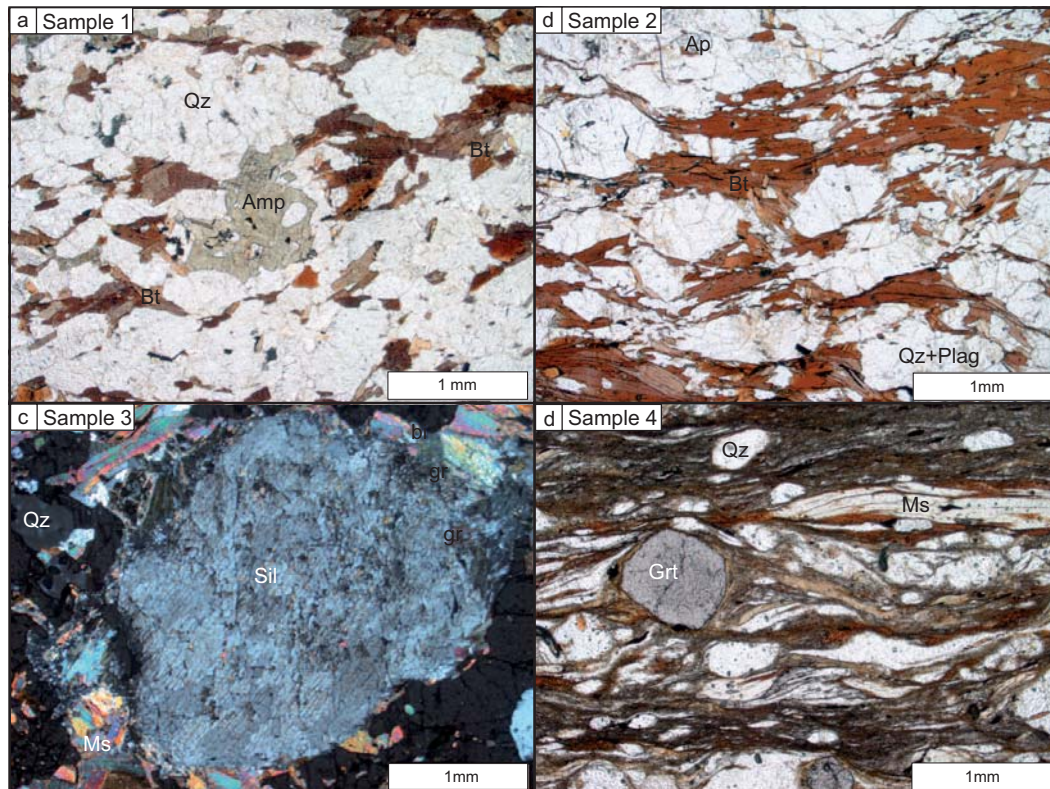


Figure 2.3: Representative thin section photographs of the four samples. **(a)** Sample 1 is a migmatitic meta-greywacke with amphiboles in its leucosome. **(b)** Sample 2 is a quartzofeldspathic gneiss. **(c)** Sample 3 is a metapelite with sillimanite and garnet. **(d)** Sample 4 is a mylonitic metapelite with sillimanite and garnet.

2.3.2 Sample description

Sample 1 is from the western part of the gneiss zone of the CMC (Fig. 2.1, Tab. 2.1). It is from a layered and folded gneiss which is exposed along the western side of the Fan glacier (see Chap. 5, Fig. 2.2a). It is a metagreywacke consisting of biotite, quartz, plagioclase, hornblende, epidote and titanite (Fig. 2.3a). Sample 2 is located ~24 km to the east of sample 1 in the gneiss zone of the CMC (Fig. 2.1, Tab. 2.1). It is a strongly foliated and layered quartzofeldspathic gneiss exposed at the eastern side of the Bremner glacier (see Chap. 5, Fig. 2.2b). It consists of biotite, quartz, plagioclase and titanite (Fig. 2.3b). Sample 3 is located ~107 km to the east-south-east of sample 2 (Fig. 2.1, Tab. 2.1) and comes from the southern end of the gneiss zone exposed on Nunataks between the Jeffries glacier in

the north and the Bagley icefield in the south (see Chap. 5). It is a strongly migmatized metapelite (Fig. 2.2c) and consists of biotite, quartz, plagioclase, garnet, sillimanite and muscovite (Fig. 2.3c). Sample 4 is located ~165 km to the south-east of sample 3 (Fig. 2.1, Tab. 2.1) and is located in the narrow part of the Chugach terrane exposed along the Nunatak glacier (see Chap. 5). It also belongs to the gneiss zone and comes from a fine-grained, highly sheared metapelite (Fig. 2.2d). It consists of biotite, quartz, plagioclase, garnet, sillimanite, muscovite and chlorite (Fig. 2.3d).

Zircons separated from all four samples are generally ~50-200 μm in length. They show subrounded, short-prismatic and a few long-prismatic shapes. CL-images reveal oscillatory, patchy or sector zoning of most grains, and ~80% of the grains show thin, light- to dark-grey, unzoned rims (Fig. 2.4, see Chap. 4).

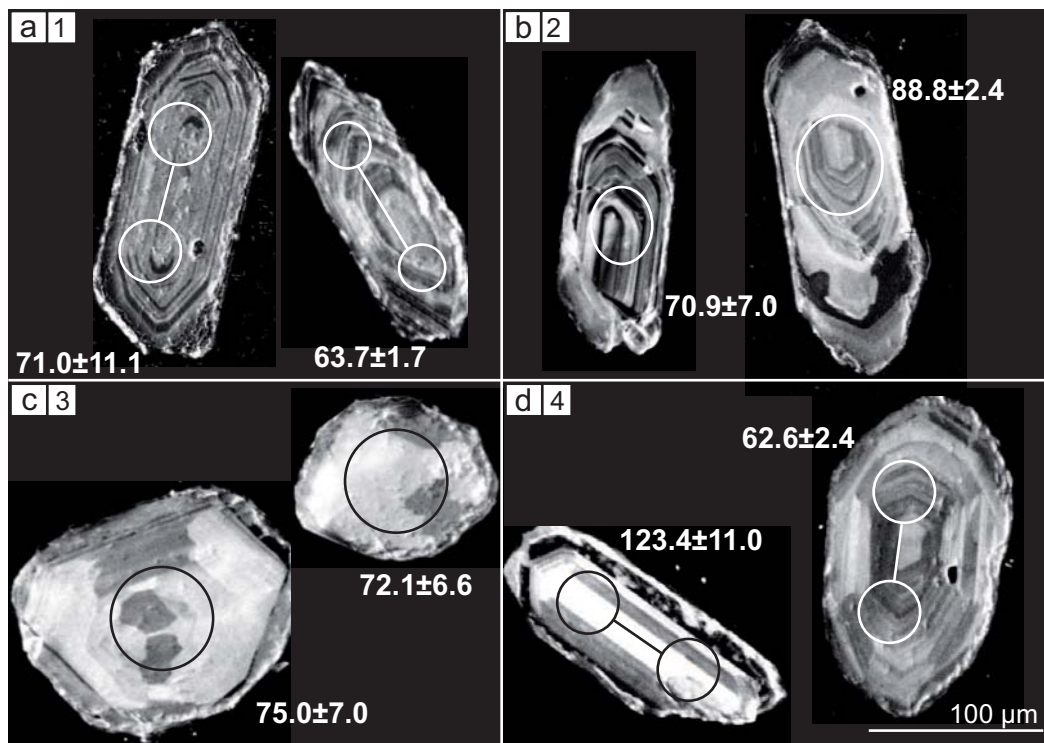


Figure 2.4: Representative CL-images of zircons separated from the four samples 1-4 (a-d). Note the narrow, light-grey, unzoned rims present on many grains. They formed during partial melting in the gneiss zone of the CMC (see Chap. 4).

2.3.3 U-Pb dating: Results and data assessment

A total of 97-100 zircon cores were analysed from each sample. Standard- and common Pb corrected isotopic ratios as well as calculated $^{206}\text{Pb}/^{238}\text{U}$, $^{207}\text{Pb}/^{235}\text{U}$ and $^{207}\text{Pb}/^{206}\text{Pb}$ ages for each measurement and each sample are given in table 2.2. The low ^{207}Pb intensities measured in >90% of the grains indicate that most of them are <1000 Ma. These low ^{207}Pb intensities produce large analytical errors on $^{207}\text{Pb}/^{204}\text{Pb}$ ratios and subsequently on calculated $^{207}\text{Pb}/^{206}\text{Pb}$ and to a lower degree on $^{207}\text{Pb}/^{235}\text{U}$ ages. Therefore, for ages <1000 Ma, $^{206}\text{Pb}/^{238}\text{U}$ ages are generally most precisely measurable and are generally used for the interpretation of detrital zircon populations, even though they have to be interpreted as minimum ages (e.g. Häussler et al., 2005; Dickinson & Gehrels, 2009; Amato & Pavlis, 2010). However, given the large errors on $^{207}\text{Pb}/^{206}\text{Pb}$ ages, discordance of the ages can not be assessed on an individual grain basis and the viability/geological significance of the determined $^{206}\text{Pb}/^{235}\text{U}$ ages can therefore not be checked. In addition, the ^{204}Pb -based common Pb correction led to large (>10%) corrections on ~50% of all measured $^{207}\text{Pb}/^{204}\text{Pb}$ ratios, adding an additional uncertainty on these measurements.

We therefore applied the following approach for the assessment of our age data: We first discarded all measurements where the common Pb correction on the isotopic ratios was >10% in order to avoid this additional uncertainty. We then sorted the remaining analyses according to the $^{206}\text{Pb}/^{238}\text{U}$ ages. For ages >1000 Ma, we evaluated the discordance of the measurements by simply comparing the $^{206}\text{Pb}/^{238}\text{U}$ to the $^{207}\text{Pb}/^{206}\text{Pb}$ ages, and analyses with >10% discordance were discarded. For ages <1000 Ma, we plotted all remaining measurements on Concordia plots using the software Isoplot/Ex (Ludwig, 2003) and excluded measurements with errors of >30% on the $^{206}\text{Pb}/^{238}\text{U}$ ages and measurements with very low probability of concordance (i.e. measurements which did not touch the Concordia curve). For the remaining analyses, we present Concordia curves as well as age probability plots superimposed on age histograms for each sample and each age group. The histograms give an impression of how many analyses are incorporated within one area but they do not consider the individual errors on each measurement, whereas the age probability plots incorporate each age and its uncertainty as a normal distribution, and sum all ages from a sample into a single curve. In a second assessment, we analysed the measurements with >10% common Pb correction, also sorted them according to $^{206}\text{Pb}/^{238}\text{U}$ age, excluded the analyses with >30% error on the $^{206}\text{Pb}/^{238}\text{U}$ age and excluded the discordant analyses (for grains >1000 Ma by comparison with the corresponding $^{207}\text{Pb}/^{206}\text{Pb}$ age, for grains <1000 Ma graphically by Concordia plots). The age distribution of the remaining concordant ages was then compared with the age distribution derived from the measurements with <10% common Pb correction. The results are discussed for each sample below.

Results for sample 1 A total of 97 analyses were made on zircon cores from sample 1. 55 measurements were excluded in a first assessment of the data due to >10% common Pb correction. From the remaining 42 analyses, one gave an age of >1000 Ma, but which is

>30% discordant. From the other 41 analyses, none has an error of >30% on the $^{206}\text{Pb}/^{238}\text{U}$ age but two do not touch the Concordia line and are therefore excluded. A total of 39 concordant analyses remain. The following age distribution is obvious from Fig. 2.5: 97% of all zircon cores (38 measurements) show ages <130 Ma, with a major peak from ~60-85 Ma, no ages from ~85-100 Ma and four scattered ages from ~100-130 Ma. The remaining 3% (1 measurement) gives an age of ~500 Ma.

In a second assessment, the 55 measurements excluded before due to high common Pb-correction were screened in addition. One analysis was excluded for >30% error on the $^{206}\text{Pb}/^{238}\text{U}$ age and 44 measurements do not lie on the Concordia line and are therefore excluded. From the remaining ten concordant ages two are ~110-140 Ma, the other eight ages lie between ~60 and ~70 Ma. They are included in the Histogram/relative age plot in Fig. 2.9 and 2.10 and do not alter the age distribution as plotted in Fig. 2.5 significantly (compare Fig. 2.5b with Fig. 2.9a).

Results for sample 2 A total of 100 analyses were made on zircon cores from sample 2. 45 measurements were excluded in a first assessment of the data due to >10% common Pb correction. From the remaining 55 analyses, two gave an age of >1000 Ma, and both are concordant. From the other 53 analyses six have errors of >30% on their $^{206}\text{Pb}/^{238}\text{U}$ ages and two are discordant and they are therefore excluded. 47 concordant ages are remaining for sample 2. The Concordia plots, histograms and age probability plots displayed in Fig. 2.6 reveal the following: 87% of the zircon cores (41 measurements) lie in the range of ~50-100 Ma with a major peak at ~62 Ma, 9% (4 measurements) lie in the range of ~120-200 Ma, and 4% (2 measurements) are ~1800 Ma.

From the 45 measurements excluded before due to high common Pb correction, five measurements have >30% error on the $^{206}\text{Pb}/^{238}\text{U}$ age and 32 analyses are discordant, leaving eight additional concordant ages. One of these eight ages is ~190 Ma, the other seven lie in the range of ~50-70 Ma. They do not alter the age distribution as displayed in Fig. 2.6 significantly (compare Fig. 2.6b with Fig. 2.9b).

Results for sample 3 A total of 99 analyses were made on zircon cores from sample 3. In 48 measurements, the common Pb correction was >10% on the $^{207}\text{Pb}/^{204}\text{Pb}$ ratio, and these measurements were therefore excluded. From the remaining 51 analyses, three gave $^{206}\text{Pb}/^{238}\text{U}$ ages of >1000 Ma, with discordance <10%. The other 48 analyses gave $^{206}\text{Pb}/^{238}\text{U}$ ages of <400 Ma, with 11 analyses having an error of >30% on the $^{206}\text{Pb}/^{238}\text{U}$ age and one analysis plotting off the Concordia curve and being therefore excluded. So a total of three concordant ages >1000 Ma and 36 concordant ages <400 Ma remain for sample 3. These analyses are plotted in Fig. 2.7. The following age distribution is obvious: 72% of the zircon cores (28 measurements) show ages of ~60-120 Ma, with a major peak at ~73 Ma, and second peaks at ~83 Ma and ~98 Ma. 21% of the zircon cores (8 measurements)

show ages of ~160-380 Ma with a broad peak from ~160-230 Ma. The remaining 7% of the zircon cores (3 measurements) give ages of ~1300-1600 Ma and one age of ~2300 Ma.

From the 48 measurements excluded before due to high common Pb correction, one analysis yielded an age of >1000 Ma, but with a discordance of >10%, and is therefore discarded. From the remaining 47 measurements, 12 were excluded due to high errors, and 27 analyses do not lie on the Concordia line, leaving a total of eight additional concordant analyses. All eight analyses fall into the dominant ~60-120 Ma interval of sample 3 and do not alter the age distribution significantly (compare Fig. 2.7c with Fig. 2.9c).

Results for sample 4 A total of 99 analyses were made on zircon cores from sample 4, and 47 measurements are in a first assessment excluded due to >10% common Pb correction. From the remaining 52 analyses, one has an age of >1000 Ma, and shows >10% discordance. From the other 51 measurements, three have >30% error on their $^{206}\text{Pb}/^{238}\text{U}$ ages and one analysis is discordant, leaving 47 concordant ages. From figure 2.8, the following age distribution is obvious: From the 47 concordant analyses, 92% (43 analyses) fall in the age range ~60-140 Ma with a pronounced peak at ~64 Ma and a smaller peak at ~98 Ma. The remaining 8% (4 analyses) are scattered between ~140 and ~230 Ma.

From the 47 measurements excluded before due to high common Pb correction, one analysis yielded an age of >1000 Ma, but with a discordance of >10%, and is therefore discarded. From the remaining 46 measurements, one was excluded due to high errors, and 38 measurements are discordant, leaving 8 additional concordant ages for this sample. Two of them lie between ~200-360 Ma, and the others between ~60 and ~80 Ma, not changing the general age distribution of sample 4 significantly (compare Fig. 2.8d with Fig. 2.9d).

Summary From the initially 97-100 analyses conducted per sample, 47-55 concordant analyses per sample remained. A few Precambrian, Paleozoic, Triassic and Jurassic grains occur in all samples, but the vast majority of grains are of Lower Cretaceous and Paleocene age (Fig. 2.10).

Sample 1

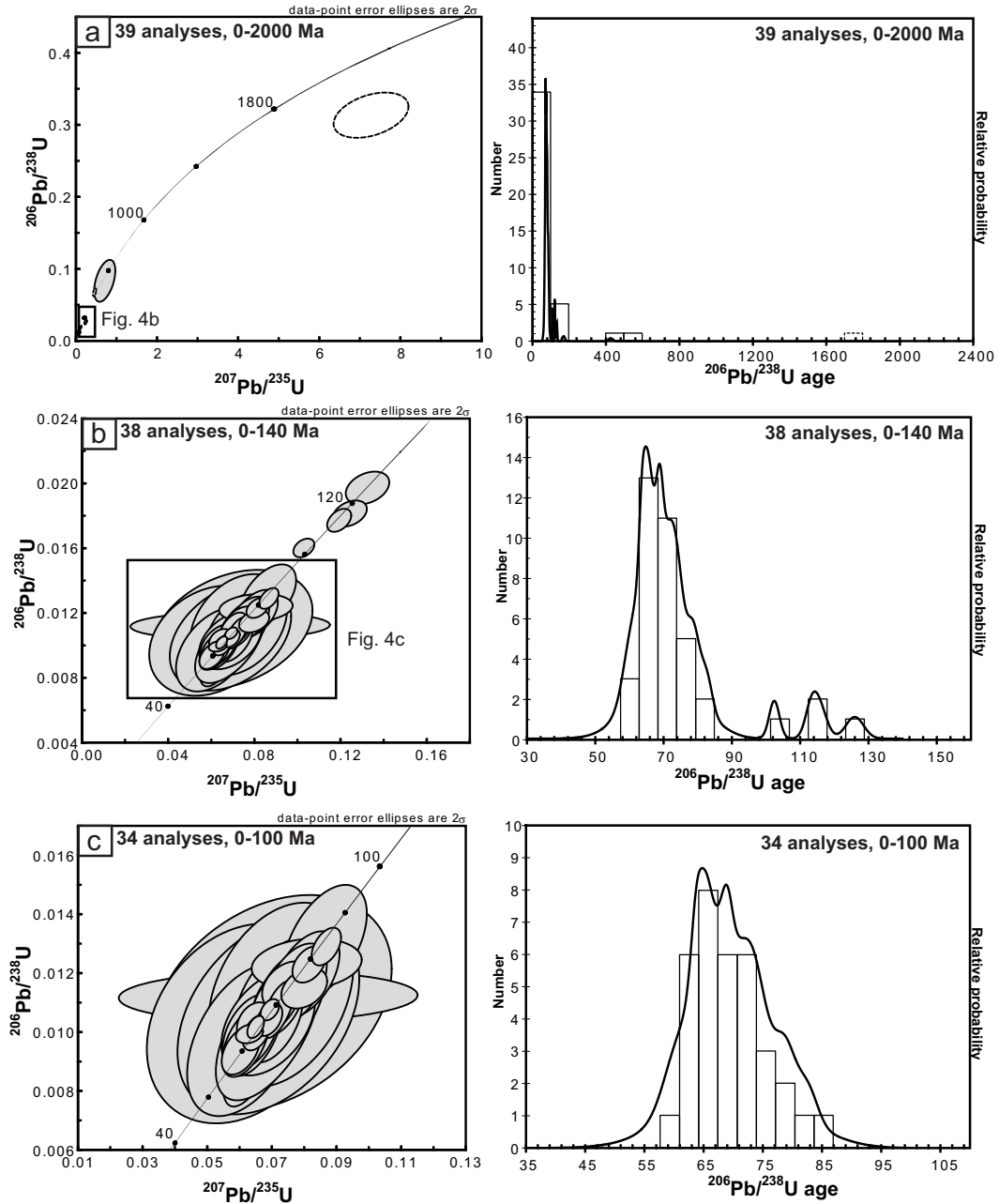


Figure 2.5: Concordia plot, Histogram and relative age probability plots for sample 1. Only the concordant analyses with common Pb corrections <10% are shown. Discordant analyses with <10% common Pb correction are stippled. From the original 97 analyses, 55 measurements were excluded due to >10% common Pb correction and three discordant analyses were excluded (stippled ellipses in (a)). The number of analyses gives only the concordant analyses.

Sample 2

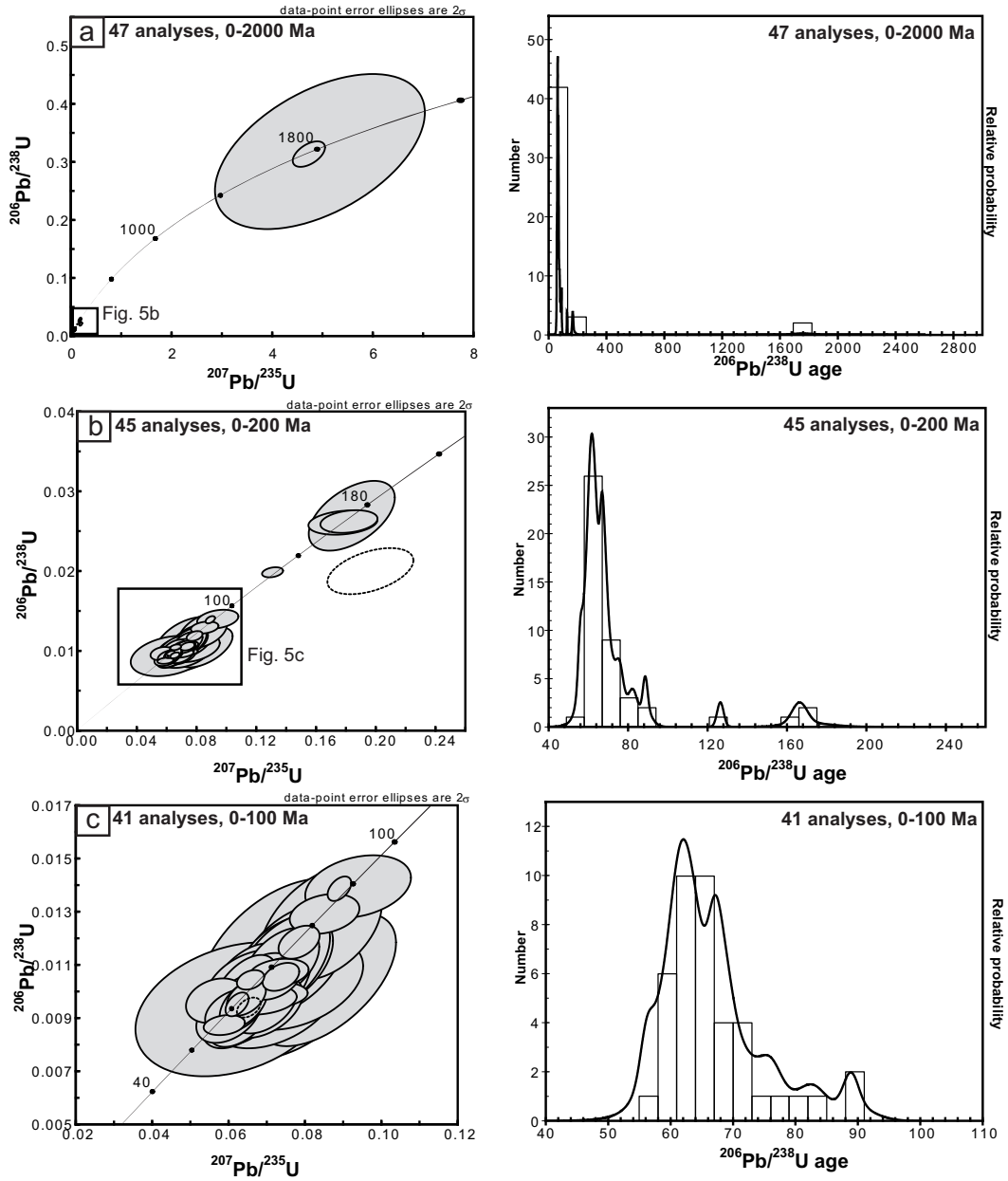


Figure 2.6: Concordia plot, Histogram and relative age probability plots for sample 2. From the original 100 analyses, 45 measurements were excluded due to >10% common Pb correction, six were excluded due to >30% error on their $^{206}\text{Pb}/^{238}\text{U}$ ages and two discordant analyses were excluded (stippled ellipses in (b) and (c)). The number of analyses gives only the concordant analyses.

Sample 3

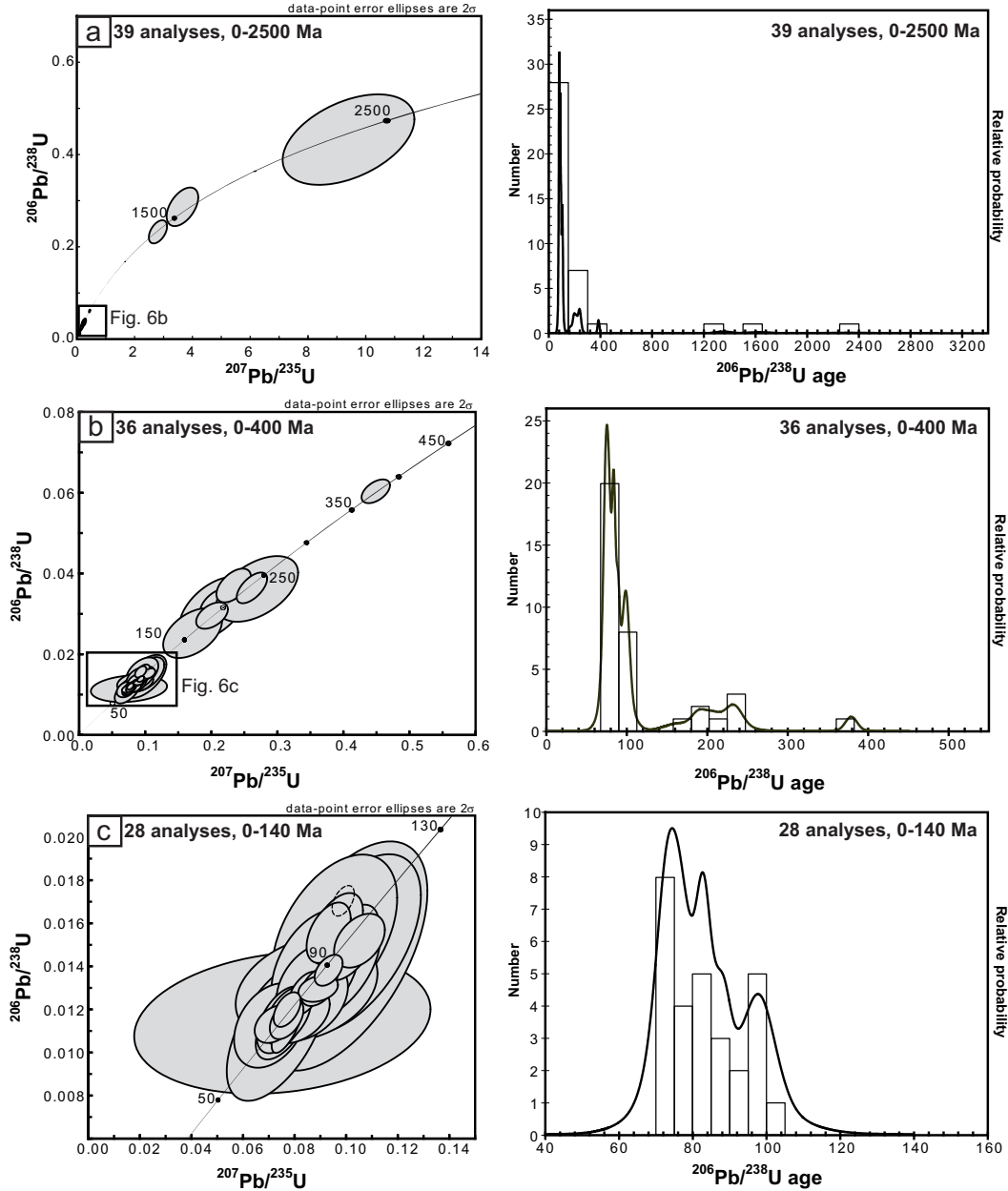


Figure 2.7: Concordia plot, Histogram and relative age probability plots for sample 3. From the original 99 analyses, 48 measurements were excluded due to $>10\%$ common Pb correction, 11 analyses were excluded due to $>30\%$ error on their $^{206}\text{Pb}/^{238}\text{U}$ ages, and one discordant analysis was excluded (stippled ellipse in (c)). The number of analyses gives only the concordant analyses.

Sample 4

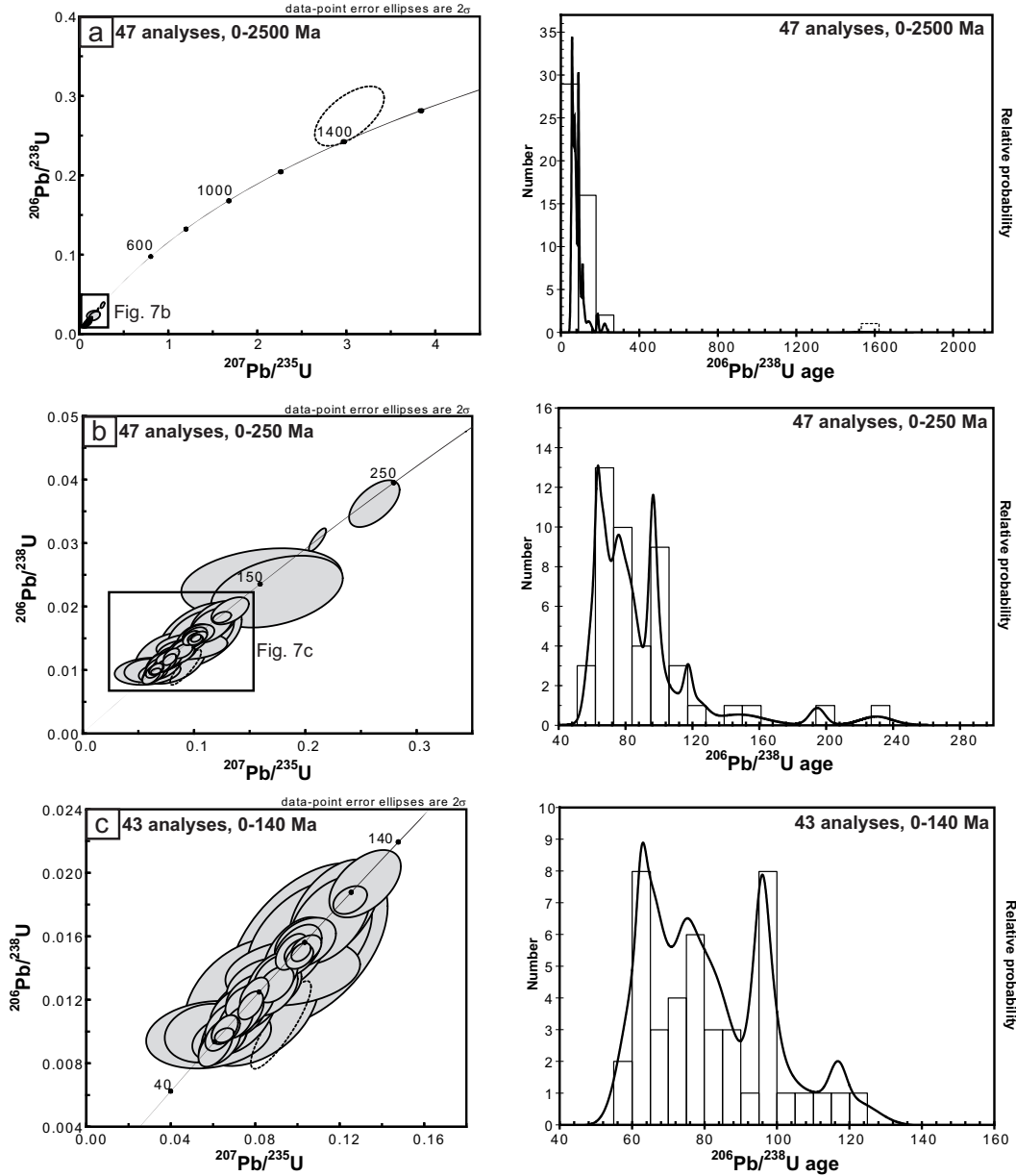


Figure 2.8: Concordia plot, Histogram and relative age probability plots for sample 4. From the original 99 analyses, 47 measurements were excluded due to >10% common Pb correction, three analyses were excluded due to >30% error on their $^{206}\text{Pb}/^{238}\text{U}$ ages, and two discordant analyses were excluded (stippled ellipses in (a)-(c)). The number of analyses gives only the concordant analyses.

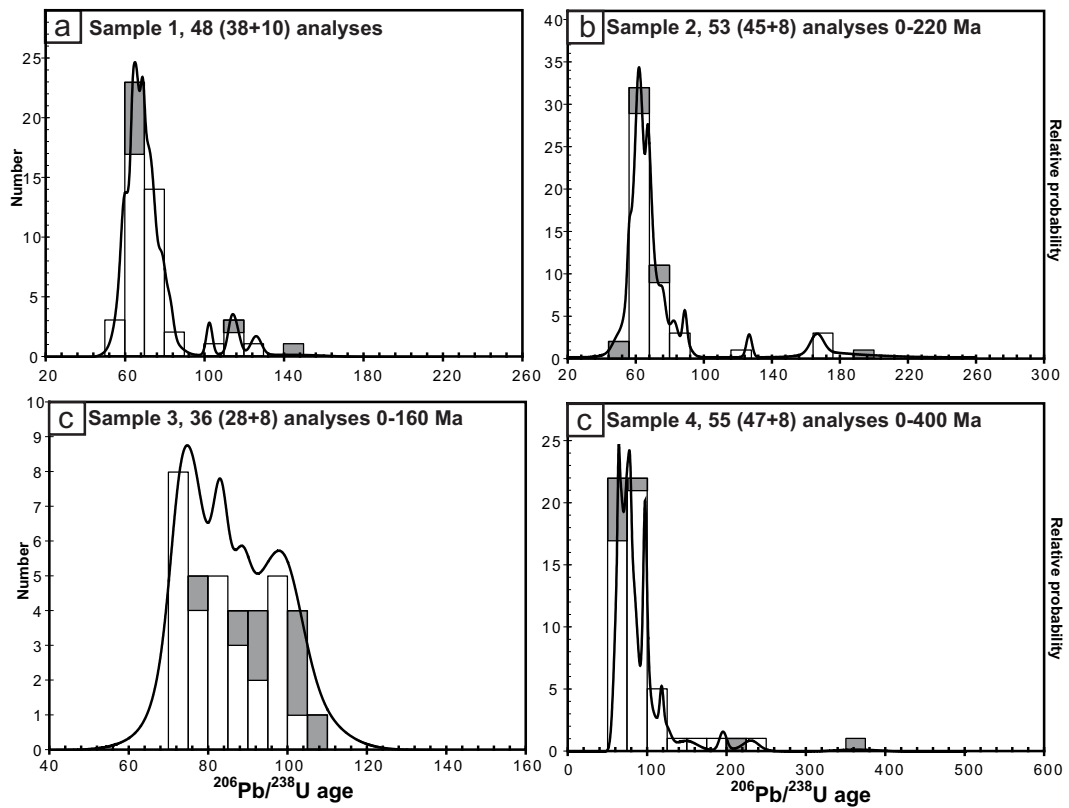


Figure 2.9: Histogram and relative age probability plots showing the additional concordant analyses from measurements with common Pb corrections of >10%. The additional analyses are displayed in grey. They do not alter the age distribution of the samples significantly: compare (a) with Fig. 2.5b, (b) with Fig. 2.6b, (c) with Fig. 2.7c and (d) with Fig. 2.8b. The additional analyses are therefore included in the discussion of the age distribution of the four samples.

2.4 Discussion

2.4.1 Maximum depositional ages

The youngest detrital zircon grains found in a sedimentary sequence generally indicate a maximum depositional age for the sequence, since the sequence can not be older than the youngest detrital grains (e.g. Barbeau et al., 2005; DeCelles et al., 2007; Jones et al., 2009; Dickinson & Gehrels, 2009). Dickinson & Gehrels (2009) compared youngest detrital zircon ages from 58 samples (with a mean of 92 concordant analyses per sample, using $^{206}\text{Pb}/^{238}\text{U}$ ages and graphically investigated concordance) with depositional ages independently known from biostratigraphy, and showed that the depositional ages derived from both methods overlap indeed very well. However, they also showed that there are statistically less and more robust methods to define the youngest detrital zircon age. They distinguished four alternative measures of youngest detrital zircon ages from the least to the most statistically robust: (1) YSG: youngest single grain age with 1σ -uncertainty, statistically least robust since not reproduced, (2) YPP: youngest graphical age peak on an age-probability plot, statistically more robust than YSG, but can be considerably older than the actual depositional age, (3) YC $1\sigma(2+)$: mean age of the youngest two or more grains that overlap in age at 1σ , interpreted to be as robust as YPP and can be used interchangeably, and (4) YC $2\sigma(3+)$: mean age of the youngest three or more grains that overlap in age at 2σ . This value is the statistically most robust value, but also the most conservative estimate for the depositional age of the sediments and can therefore be considerably older than the actual depositional age.

In Table 2.1 we report all four different methods of calculating maximum depositional ages based on our $^{206}\text{Pb}/^{238}\text{U}$ ages with $<10\%$ common Pb correction (Figs. 2.5-2.8, Tab. 2.2). For sample 1, the different methods range from 60.1 ± 2.2 Ma to 64.8 ± 0.9 Ma, with the latter being based on 21 overlapping analyses (Tab. 2.1). For sample 2, the methods range from 56.1 ± 1.0 Ma to 58.5 ± 1.6 Ma, with the latter being based on 11 overlapping measurements (Tab. 2.1). For sample 3, the methods range from 70.5 ± 8.5 Ma to 75.7 ± 1.8 Ma, with the latter being based on 13 overlapping analyses (Tab. 2.1). For sample 4, the methods range from 58.1 ± 3.4 Ma to 63.6 ± 1.4 Ma, with the latter being based on 15 measurements (Tab. 2.1). Since the YC $2\sigma(3+)$ values are based on multiple analyses overlapping in 2σ (11-21 analyses per sample), we consider these values as robust and not influenced by partial lead loss or mixing of different domains. We therefore consider only these values in our further discussion of maximum depositional ages.

The YC $2\sigma(3+)$ values for samples 2 and 4 are youngest (59.7 ± 1.5 Ma and 63.6 ± 1.4 Ma, respectively) and fall entirely within the Danian stage of the Paleocene epoch following the time scale of Gradstein et al. (2004). So for these two samples, a Paleocene maximum depositional age is indicated by the youngest detrital zircon population. The YC $2\sigma(3+)$ value for sample 1 (64.8 ± 0.9 Ma) overlaps with the YC $2\sigma(3+)$ value of sample 4, but also with

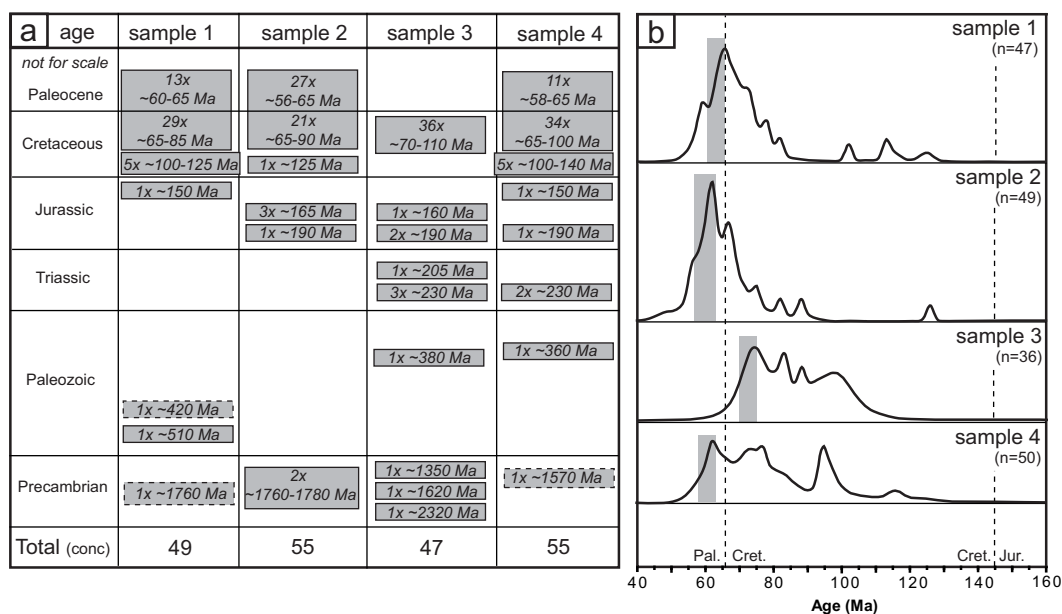


Figure 2.10: Summary of age distribution of detrital zircon grains from the four samples. **(a)** General age distribution showing the relative contribution of Precambrian, Paleozoic, Triassic, Jurassic, Cretaceous and Paleocene grains for each sample. Both concordant analyses with <10% common Pb correction and concordant analyses with >10% common Pb correction are included. **(b)** Normalized age probability plots (each curve contains the same area) for the Cretaceous and Paleocene populations of each sample, constructed with the macro NORMALIZED PROB PLOT.xls provided by the Arizona LaserChron Center, <http://sites.google.com/a/laserchron.org/laserchron/home>. The range of maximum depositional ages as derived from different statistical methods (Tab. 2.1) is indicated by grey bars.

the numerical age of 65.5 ± 0.3 Ma given to the Paleocene-Late Cretaceous boundary by Gradstein et al. (2004). For this sample, a latest Cretaceous to earliest Paleocene maximum depositional age is therefore indicated. The $YC2\sigma(3+)$ value for sample 3 is considerably older (75.7 ± 1.8 Ma), which lies entirely within the Campanian stage of the Late Cretaceous epoch following Gradstein et al. (2004). This suggests a Late Cretaceous maximum depositional age for this sample.

The analysis of the youngest detrital zircon populations of four samples covering the CMC from west to south-east as described above suggests that at least parts of the sediments incorporated into the CMC have a Paleocene depositional age and are therefore slightly younger than the age derived by biostratigraphy for the Valdez Group of the Chugach terrane (~83-65 Ma; Plafker et al., 1994). They are also younger than the maximum depositional ages derived for the Sitka Greywacke (~105-74 Ma; Häussler et al., 2003a). This restricts the time available for prograde metamorphism in the CMC to only ~5-10 Ma (see Chap. 3 and 4). The sample with the oldest maximum depositional age (sample 3) is also the sample which recorded the highest pressures during CMC metamorphism (~13 kbar, Bruand, 2010), suggesting that deeper parts of the prism might consist of older (Late Cretaceous) sediments.

2.4.2 Provenance of sediments

In addition to the information on maximum depositional ages, the total age distribution of detrital zircon populations may also give some information on the source from which the sediments are derived (e.g. Carrapa, 2010). However, this requires that the age distribution measured represents statistically well enough the age distribution actually present in the sample, which generally needs a large (>100) number of single analyses (e.g. Vermeesch, 2004). In addition, age probability plots do generally not *quantitatively* reflect the original distribution of the sediments, even when >100 analyses are incorporated into the plots (Andersen, 2005). So an age probability plot of a sample with less than 100 analyses at best describes qualitatively the age distribution in the source of the sediments. In addition, with less than 100 analyses, in general only the presence of a certain population can be proved, whereas it is more difficult to argue for the absence of a certain population, since this absence could be just the result of missing it due to limited analyses.

In our case, 55 concordant analyses for samples 2 and 4 and 49 and 47 concordant analyses for samples 1 and 3 remained (Fig. 2.10a, both concordant analyses with <10% and >10% common Pb correction included). For samples 2 and 4 the 55 measurements are according to Vermeesch (2004) sufficient to be certain at >95% confidence level that no fraction contributing more than 10% to the total age fraction was missed. For samples 1 and 3 with 49 and 47 analyses we are at >90% confidence level certain that no fraction contributing >10% to the total age fraction was missed. In other words, the age distributions of samples 2 and 4 reasonably well describe all age populations which contribute >10% to the total distribution, whereas for samples 1 and 3 there is a greater chance that an age population of >10% is missed. Given these limitations, a qualitative discussion of the age distribution derived from the four samples is given below.

Fig. 2.10a contains a summary of all ages found in the different samples. Each sample contains 1-3 Precambrian grains indicating that the source terrane(s) for the sediments contain(s) at least some Precambrian rocks. Samples 1, 3 and 4 contain 1-2 Paleozoic grains which spread in age from Cambrian to Devonian, indicating that a minor part of the source terrane(s) probably consisted of variable Paleozoic rocks. Samples 3 and 4 contain 2-4 Triassic grains, and all four samples contain 1-4 Jurassic grains indicating minor contributions from Early and Middle Mesozoic rocks. However, the bulk of the grains are Cretaceous and Paleocene in age, notably 95%, 89%, 76% and 90% of all concordant grains for samples 1-4, respectively (Fig. 2.10). In order to compare these Cretaceous to Paleocene populations between the samples, we constructed normalized age probability plots as displayed in Fig. 2.10b. From these plots it is qualitatively visible that samples 1 and 2 have a very similar distribution, with a relatively narrow population from ~60-85 Ma and only few ages from ~90-140 Ma. Samples 3 and 4 have equally a similar distribution but different from the distribution of samples 1 and 2: they show a much broader age population from ~60(70)-120 Ma. This could indicate that samples 1 and 2, located more to the west, received their detritus mainly from an ~60-85 Ma source, whereas samples 3 and 4, located more to the

east-south-east, received their detritus from a source which had in addition to the ~60-85 Ma component also a slightly older component of ~85-120 Ma. However, in order to resolve these differences more rigorously, about the double amount of analyses would be necessary in order to get more representative age probability distributions (Vermeesch, 2004) and the differences between the samples could as well be due to the insufficient amount of concordant analyses.

2.5 Conclusions

U-Pb LA-ICP-MS dating of detrital zircons from four samples covering the CMC from west to the south-east revealed the following: (1) Three of the four samples show Paleocene (~60-65 Ma) maximum depositional ages based on several overlapping youngest grains. These ages are slightly younger than the Late Cretaceous depositional age proposed based on biostratigraphy for the sediments of the Valdez Group in which the CMC formed, and they are also slightly younger than the maximum depositional ages proposed for the youngest part of the Sitka Greywacke based on youngest detrital zircon populations. The Paleocene maximum depositional ages limit the time available for prograde metamorphism in the CMC to only ~5-10 Ma (see Chap. 4). (2) The age distribution of all samples is dominated by Paleocene to Cretaceous ages (~60-140 Ma), with very minor contributions of Jurassic, Triassic, Paleozoic and Precambrian ages. The two westernmost samples seem to have a slightly different Paleocene to Cretaceous distribution than the two easternmost samples. This could be either due to slightly different sources, or be an artefact of insufficient amount of concordant analyses.

Acknowledgments U. Klötzli is thanked for help with the zircon separation and mounting, the LA-ICP-MS analyses and the data assessment. F. Biedermann helped with the mount preparation. A. Oswald is thanked for assistance during analytical work - without her the 82 h non-stop analytical session would not have been possible. C. Carson is thanked for hints regarding detrital zircon analyses.

Table 2.2: Isotopic measurements of detrital zircon samples

File name	$^{207}\text{Pb}/^{235}\text{U}$ ratio	RSE (%)	$^{206}\text{Pb}/^{238}\text{U}$ ratio	2RSE (%)	Rho	$^{207}\text{Pb}/^{206}\text{Pb}$ ratio	2RSE (%)	$^{207}\text{Pb}/^{238}\text{U}$ age (Ma)	2RSE (Ma)	$^{206}\text{Pb}/^{238}\text{U}$ age (Ma)	2RSE (Ma)	2RSE (%)	$^{207}\text{Pb}/^{206}\text{Pb}$ age (Ma)	2RSE (Ma)	Quality*
Sample 1 (F20), analyses with <10% common Pb correction															
100206_F20_B_39_a	0.0605	7.9	0.0094	7.2	0.4553	0.0461	2.5	59.7	4.6	60.1	4.3	7.2	0.9	30.3	conc
100206_F20_A_42_b	0.0620	9.6	0.0097	10.1	0.5321	0.0463	5.9	61.1	5.7	62.0	6.2	10.0	14.1	75.2	conc
100206_F20_A_26_a	0.0616	23.4	0.0097	21.7	0.4460	0.0461	13.9	60.7	13.8	62.4	13.5	21.6	4.8	154.6	conc
100206_F20_A_06_a	0.0648	10.5	0.0099	11.2	0.5794	0.0474	8.8	63.8	6.5	63.3	7.1	11.2	67.6	131.9	conc
100206_F20_C_12_a	0.0632	5.4	0.0099	2.7	0.2484	0.0463	3.6	62.2	3.2	63.7	1.7	2.7	12.1	48.4	conc
100206_F20_B_05_a	0.0654	5.3	0.0100	5.0	0.4398	0.0475	4.2	64.3	3.3	64.0	3.2	4.9	72.9	84.4	conc
100206_F20_A_07_a	0.0636	11.2	0.0100	10.4	0.4453	0.0460	7.8	62.6	6.8	64.2	6.7	10.4	0.0	87.5	conc
100206_F20_D_02_a	0.0687	18.9	0.0101	19.4	0.5863	0.0492	20.4	67.5	12.3	64.5	12.4	19.3	156.8	287.4	conc
100206_F20_A_04_a	0.0651	3.2	0.0102	3.0	0.4653	0.0463	1.4	64.0	2.0	65.2	2.0	3.0	14.3	23.8	conc
100206_F20_B_10_a	0.0601	39.0	0.0103	27.0	0.2551	0.0441	24.5	59.3	22.4	66.0	17.7	26.8	0.0	203.5	conc
100206_F20_C_19_a	0.0690	17.1	0.0103	14.2	0.4137	0.0493	8.0	67.7	11.2	66.1	9.3	14.1	162.0	169.9	conc
100206_F20_B_12_a	0.0676	15.4	0.0103	22.5	0.7321	0.0484	28.4	66.4	9.9	66.1	14.8	22.4	118.2	339.6	conc
100206_F20_B_04_a	0.0710	9.9	0.0103	10.6	0.5401	0.0496	7.1	69.7	6.6	66.1	7.0	10.6	176.0	165.2	conc
100206_F20_B_26_a	0.0646	6.7	0.0103	5.3	0.3249	0.0455	5.0	63.6	4.1	66.3	3.5	5.3	0.0	42.5	conc
100206_F20_A_35_a	0.0692	4.9	0.0104	4.4	0.3980	0.0480	4.1	68.0	3.2	66.9	2.9	4.3	97.2	96.1	conc
100206_F20_A_29_a	0.0691	33.2	0.0106	26.0	0.3679	0.0483	22.0	67.8	21.8	67.7	17.5	25.8	114.9	283.0	conc
100206_F20_C_23_a	0.0695	3.4	0.0108	2.7	0.4038	0.0472	2.2	68.2	2.2	69.0	1.9	2.7	58.0	51.9	conc
100206_F20_A_32_a	0.0721	5.7	0.0108	7.4	0.6438	0.0492	4.7	70.6	3.9	69.0	5.0	7.3	158.1	109.8	conc
100206_F20_C_42_a	0.0701	43.2	0.0110	27.4	0.3166	0.0472	23.3	68.8	28.7	70.4	19.2	27.2	58.2	268.0	conc
100206_F20_C_07_a	0.0714	9.4	0.0110	11.6	0.6212	0.0463	3.1	70.0	6.3	70.6	8.2	11.6	12.2	42.7	conc
100206_F20_A_39_a	0.0705	7.5	0.0110	7.4	0.4935	0.0466	3.8	69.2	5.0	70.7	5.2	7.4	29.7	58.6	conc
100206_F20_C_32_a	0.0721	9.1	0.0111	8.9	0.4394	0.0476	8.5	70.7	6.2	70.9	6.3	8.9	77.2	134.2	conc
100206_F20_A_09_a	0.0725	16.4	0.0111	15.8	0.4819	0.0476	1.8	71.1	11.2	71.0	11.1	15.7	81.7	42.4	conc
100206_F20_C_33_a	0.0727	7.5	0.0111	7.8	0.5207	0.0479	3.1	71.3	5.2	71.2	5.5	7.7	95.0	73.1	conc
100206_F20_A_38_a	0.0690	54.6	0.0112	6.3	0.0574	0.0456	41.2	67.8	35.8	71.8	4.5	6.2	0.0	377.3	conc
100206_F20_A_15_a	0.0729	25.2	0.0113	22.8	0.3209	0.0461	21.1	71.5	17.4	72.2	16.3	22.6	3.9	223.6	conc
100206_F20_A_20_a	0.0801	7.2	0.0115	4.9	0.3393	0.0499	5.0	78.2	5.4	73.7	3.6	4.9	189.1	116.2	conc
100206_F20_D_15_a	0.0749	8.4	0.0116	5.8	0.3435	0.0477	5.0	73.4	6.0	74.2	4.3	5.8	82.7	98.8	conc
100206_F20_A_38_b	0.0775	10.2	0.0116	9.7	0.4773	0.0483	2.8	75.8	7.4	74.5	7.2	9.6	116.1	65.0	conc
100206_F20_C_13_a	0.0807	10.5	0.0120	10.0	0.4789	0.0495	3.2	78.8	7.9	76.7	7.6	10.0	173.2	74.3	conc
100206_F20_C_38_a	0.0815	5.1	0.0123	4.1	0.4007	0.0485	3.4	79.6	3.9	78.8	3.2	4.1	124.8	79.4	conc
100206_F20_D_14_a	0.0809	17.1	0.0123	5.8	0.1697	0.0481	13.9	79.0	13.0	78.9	4.6	5.8	102.6	200.7	conc
100206_F20_B_02_a	0.0869	4.3	0.0129	4.1	0.4797	0.0485	1.7	84.6	3.5	82.7	3.4	4.1	122.1	40.3	conc
100206_F20_B_24_a	0.0865	12.2	0.0131	12.0	0.4930	0.0475	3.3	84.3	9.9	83.8	10.0	12.0	76.9	76.3	conc

Continues on following page

Table 2.2: Isotopic measurements of detrital zircon samples

File name	$^{207}\text{Pb}/^{235}\text{U}$ ratio	RSE (%)	$^{206}\text{Pb}/^{238}\text{U}$ ratio	2RSE (%)	Rho	$^{207}\text{Pb}/^{206}\text{Pb}$ ratio	2RSE (%)	$^{207}\text{Pb}/^{238}\text{U}$ age (Ma)	2RSE (Ma)	$^{206}\text{Pb}/^{238}\text{U}$ age (Ma)	2RSE (Ma)	2RSE (%)	$^{207}\text{Pb}/^{206}\text{Pb}$ age (Ma)	2RSE (Ma)	Quality*
100206_F20_C_04_a	0.1032	3.9	0.0160	2.9	0.3793	0.0467	3.7	99.7	3.0	102.4	3.0	2.9	31.5	45.3	conc
100206_F20_B_33_a	0.1195	3.8	0.0177	3.3	0.4274	0.0490	4.1	114.6	3.7	113.3	3.7	3.2	146.7	65.3	conc
100206_F20_B_09_a	0.1245	5.2	0.0181	3.6	0.3523	0.0497	5.8	119.1	4.2	115.9	4.2	3.6	183.1	85.9	conc
100206_F20_D_24_a	0.1326	6.2	0.0197	4.2	0.3372	0.0485	7.4	126.5	5.2	126.0	5.2	4.1	124.2	82.3	conc
100206_F20_B_01_a	0.2406	10.6	0.0256	10.4	0.5182	0.0677	20.8	218.9	16.7	163.1	16.7	10.3	858.6	184.5	disc
100206_F20_D_05_a	0.4594	6.9	0.0672	6.8	0.5098	0.0491	22.2	383.8	27.6	419.3	27.6	6.6	153.9	146.0	disc
100206_F20_A_14_a	0.7185	29.4	0.0831	28.5	0.4837	0.0634	4.3	549.8	140.9	514.8	140.9	27.4	722.4	92.2	conc
100206_F20_B_22_a	7.2807	10.4	0.3137	8.2	0.3813	0.1692	6.3	2146.4	126.1	1758.9	126.1	7.2	2550.1	105.9	disc
Sample 1 (F20), analyses with >10% common Pb correction															
100206_F20_C_31_a	0.0525	11.4	0.0091	9.9	0.4324	0.0419	5.7	51.9	5.7	58.2	5.7	9.8	0.0	0.0	conc
100206_F20_C_24_a	0.0578	12.0	0.0092	11.5	0.4437	0.0438	6.7	57.0	6.8	58.8	6.8	11.5	0.0	66.0	conc
100206_F20_A_01_a	0.0612	6.4	0.0092	4.6	0.2310	0.0480	3.8	60.3	2.7	59.2	2.7	4.6	99.1	108.8	conc
100206_F20_A_42_a	0.0599	19.0	0.0096	17.8	0.4290	0.0456	14.1	59.0	10.9	61.5	10.9	17.7	0.0	143.5	conc
100206_F20_C_26_a	0.0685	14.0	0.0103	12.6	0.4491	0.0490	5.9	67.3	8.2	66.0	8.2	12.5	149.8	139.5	conc
100206_F20_C_01_a	0.0660	8.5	0.0106	8.4	0.4942	0.0451	5.5	64.9	5.7	67.7	5.7	8.3	0.0	38.9	conc
100206_F20_B_11_a	0.0666	13.0	0.0106	12.4	0.4771	0.0456	3.1	65.5	8.4	67.9	8.4	12.4	0.0	23.9	conc
100206_F20_A_08_a	0.0663	21.8	0.0108	20.2	0.4126	0.0451	17.1	65.2	13.9	69.0	13.9	20.1	0.0	160.2	conc
100206_F20_A_28_a	0.0842	44.4	0.0172	27.8	0.2037	0.0365	29.7	82.1	30.3	110.1	30.3	27.5	0.0	32.4	conc
100206_F20_A_02_a	0.1313	24.7	0.0231	24.6	0.4948	0.0411	24.1	125.2	35.7	147.1	35.7	24.3	0.0	121.2	conc
100206_F20_D_18_a	0.0471	16.9	0.0092	10.7	0.2777	0.0377	7.7	46.7	6.2	58.8	6.2	10.6	0.0	0.0	disc
100206_F20_B_20_a	0.0500	9.8	0.0095	7.5	0.2957	0.0384	9.7	49.5	4.5	60.9	4.5	7.4	0.0	0.0	disc
100206_F20_B_17_a	0.0424	12.6	0.0098	9.3	0.2384	0.0317	10.3	42.2	5.8	62.7	5.8	9.2	0.0	0.0	disc
100206_F20_B_35_a	0.0516	15.3	0.0102	13.1	0.2675	0.0367	14.1	51.1	8.5	65.2	8.5	13.0	0.0	0.0	disc
100206_F20_B_18_a	-0.0595	13.0	0.0104	12.3	0.3675	-0.0419	12.2	-62.3	8.2	66.8	8.2	12.3	0.0	0.0	disc
100206_F20_C_27_a	0.0634	5.5	0.0104	4.4	0.3183	0.0442	4.9	62.4	2.9	66.9	2.9	4.4	0.0	8.9	disc
100206_F20_A_22_a	0.0609	6.6	0.0106	5.2	0.3065	0.0419	5.4	60.0	3.5	67.7	3.5	5.2	0.0	0.0	disc
100206_F20_C_02_a	0.0036	27.6	0.0109	22.9	0.1419	0.0024	25.0	3.7	16.0	70.2	16.0	22.8	0.0	0.0	disc
100206_F20_A_13_a	0.0142	67.9	0.0110	24.5	0.1649	0.0093	42.2	14.4	17.2	70.6	17.2	24.4	0.0	0.0	disc
100206_F20_C_21_a	0.0124	9.3	0.0111	7.7	0.4212	0.0081	2.7	12.5	5.4	70.9	5.4	7.6	0.0	0.0	disc
100206_F20_C_40_a	0.0262	8.5	0.0111	5.4	0.2982	0.0174	5.2	26.3	3.8	70.9	3.8	5.4	0.0	0.0	disc
100206_F20_D_40_a	0.0362	4.5	0.0111	3.7	0.4313	0.0238	2.5	36.1	2.6	71.2	2.6	3.6	0.0	0.0	disc
100206_F20_A_16_a	0.0250	15.3	0.0112	14.9	0.4988	0.0161	6.4	25.1	10.6	71.6	10.6	14.8	0.0	0.0	disc
100206_F20_A_34_a	0.0213	12.6	0.0113	9.6	0.4030	0.0136	4.7	21.4	6.9	72.5	6.9	9.5	0.0	0.0	disc
100206_F20_C_36_a	0.0455	7.3	0.0114	6.2	0.4325	0.0292	2.7	45.2	4.5	72.8	4.5	6.2	0.0	0.0	disc
100206_F20_A_33_a	0.0553	9.3	0.0115	7.8	0.3476	0.0354	6.6	54.7	5.7	73.5	5.7	7.7	0.0	0.0	disc

Continues on following page

Table 2.2: Isotopic measurements of detrital zircon samples

File name	$^{207}\text{Pb}/^{235}\text{U}$ ratio	RSE (%)	$^{206}\text{Pb}/^{238}\text{U}$ ratio	2RSE (%)	Rho	$^{207}\text{Pb}/^{206}\text{Pb}$ ratio	2RSE (%)	$^{207}\text{Pb}/^{238}\text{U}$ age (Ma)	2RSE (Ma)	$^{206}\text{Pb}/^{238}\text{U}$ age (Ma)	2RSE (Ma)	$^{207}\text{Pb}/^{206}\text{Pb}$ age (Ma)	2RSE (Ma)	Quality*	
100206_F20_D_37_a	0.0545	21.2	0.0115	20.4	0.3631	0.0348	19.8	53.8	11.1	73.6	14.9	20.3	0.0	disc	
100206_F20_C_37_a	-0.3278	25.8	0.0115	16.0	0.3551	-0.1968	13.1	-403.3	-128.7	74.0	11.8	15.9	0.0	disc	
100206_F20_B_14_a	0.0536	11.6	0.0115	11.1	0.4791	0.0336	7.8	53.0	6.0	74.0	8.2	11.0	0.0	disc	
100206_F20_C_15_a	0.0518	13.4	0.0116	12.9	0.4854	0.0322	4.3	51.2	6.7	74.2	9.5	12.9	0.0	disc	
100206_F20_C_08_a	0.0062	7.0	0.0117	5.6	0.3964	0.0338	5.4	6.3	0.4	74.7	4.2	5.6	0.0	disc	
100206_F20_B_08_a	0.0617	11.8	0.0117	12.3	0.5880	0.0384	9.3	60.7	7.0	74.8	9.1	12.2	0.0	disc	
100206_F20_A_03_a	0.0614	10.1	0.0119	9.7	0.4814	0.0373	4.5	60.5	6.0	76.0	7.3	9.6	0.0	disc	
100206_F20_D_11_a	0.0513	9.1	0.0121	4.6	0.2523	0.0313	4.5	50.8	4.5	77.6	3.5	4.6	0.0	disc	
100206_F20_B_38_a	0.0188	12.8	0.0123	9.5	0.2497	0.0111	10.3	18.9	2.4	78.9	7.4	9.4	0.0	disc	
100206_F20_A_37_a	0.0640	7.0	0.0123	6.9	0.4927	0.0378	4.8	63.0	4.3	78.9	5.4	6.8	0.0	disc	
100206_F20_C_10_a	0.0426	5.7	0.0124	3.7	0.2899	0.0249	3.9	42.3	2.3	79.2	2.9	3.7	0.0	disc	
100206_F20_C_03_a	0.0614	5.1	0.0125	4.5	0.4313	0.0355	3.6	60.5	3.0	80.0	3.6	4.5	0.0	disc	
100206_F20_B_28_a	0.0717	3.5	0.0126	3.4	0.5029	0.0414	1.8	70.3	2.4	80.5	2.7	3.3	0.0	disc	
100206_F20_A_12_a	0.0628	14.5	0.0126	11.9	0.2729	0.0365	11.7	61.8	8.7	80.9	9.6	11.9	0.0	disc	
100206_F20_B_34_a	0.0455	279.0	0.0127	278.8	0.4889	0.0261	275.7	45.2	123.9	81.3	225.2	277.2	0.0	793.5	
100206_F20_A_24_a	0.0629	9.7	0.0127	9.3	0.4894	0.0360	3.7	62.0	5.8	81.4	7.5	9.3	0.0	disc	
100206_F20_C_22_a	0.0241	9.5	0.0128	4.3	0.2486	0.0136	6.2	24.1	2.3	82.0	3.5	4.3	0.0	disc	
100206_F20_C_39_a	0.0451	6.0	0.0135	4.9	0.3900	0.0243	4.6	44.8	2.6	86.2	4.2	4.9	0.0	disc	
100206_F20_A_21_a	0.0540	29.5	0.0136	29.6	0.6378	0.0290	28.9	53.4	15.3	87.0	25.5	29.4	0.0	disc	
100206_F20_B_37_a	-0.1119	8.4	0.0142	7.0	0.3170	-0.0570	7.3	-120.5	-10.7	91.1	6.4	7.0	0.0	disc	
100206_F20_B_23_a	0.0236	9.1	0.0162	7.6	0.4289	0.0107	4.9	23.7	2.1	103.4	7.8	7.5	0.0	disc	
100206_F20_C_35_a	0.0483	14.5	0.0173	12.4	0.4399	0.0197	4.6	47.9	6.8	110.7	13.6	12.3	0.0	disc	
100206_F20_B_31_a	0.0137	6.0	0.0174	4.9	0.4436	0.0057	3.0	13.9	0.8	111.3	5.4	4.9	0.0	disc	
100206_F20_C_41_a	0.0814	10.9	0.0175	10.3	0.4791	0.0340	4.3	79.5	8.4	111.8	11.5	10.2	0.0	disc	
100206_F20_A_45_a	0.0625	9.3	0.0175	9.8	0.5586	0.0257	5.4	61.5	5.6	111.8	10.9	9.7	0.0	disc	
100206_F20_A_19_a	0.0625	10.9	0.0176	10.6	0.4907	0.0260	5.0	61.5	6.5	112.4	11.8	10.5	0.0	disc	
100206_F20_B_16_a	0.0280	10.6	0.0178	9.8	0.5506	0.0113	5.8	28.0	2.9	113.7	11.1	9.7	0.0	disc	
100206_F20_B_19_a	0.1652	7.9	0.0312	7.9	0.5061	0.0385	1.7	155.2	11.4	197.8	15.4	7.8	0.0	disc	
100206_F20_C_05_a	0.3520	14.7	0.0561	14.9	0.5585	0.0457	13.3	306.2	38.9	352.0	51.2	14.5	0.0	138.0	
Sample 2 (KB3), analyses with <10% common Pb correction															
100204_KB3_A_25_a	0.0590	7.5	0.0087	3.5	0.2378	0.0489	6.4	58.2	4.2	56.1	2.0	3.5	143.5	144.1	conc
100204_KB3_A_44_a	0.0662	32.5	0.0091	45.6	0.7024	0.0519	13.3	65.1	20.5	58.2	26.4	45.4	280.0	279.2	1.e.
100207_KB3_B_50_b	0.0601	11.4	0.0091	9.2	0.4032	0.0489	6.2	59.3	6.6	58.3	5.4	9.2	141.4	140.3	conc
100204_KB3_A_13_a	0.0629	12.7	0.0092	12.0	0.4714	0.0491	3.2	61.9	7.6	59.0	7.0	11.9	154.7	74.0	conc
100204_KB3_A_47_a	0.0637	11.5	0.0092	11.7	0.5095	0.0499	4.6	62.7	7.0	59.3	6.9	11.6	188.3	107.1	conc

Continues on following page

Table 2.2: Isotopic measurements of detrital zircon samples

File name	$^{207}\text{Pb}/^{235}\text{U}$ ratio	RSE (%)	$^{206}\text{Pb}/^{238}\text{U}$ ratio	2RSE (%)	Rho	$^{207}\text{Pb}/^{206}\text{Pb}$ ratio	2RSE (%)	$^{207}\text{Pb}/^{238}\text{U}$ age (Ma)	2RSE (Ma)	$^{206}\text{Pb}/^{238}\text{U}$ age (Ma)	2RSE (Ma)	2RSE (%)	$^{207}\text{Pb}/^{206}\text{Pb}$ age (Ma)	2RSE (Ma)	Quality*
100207_KB3_C_24_a	0.0615	9.9	0.0093	7.4	0.3729	0.0489	5.7	60.6	5.8	59.4	4.4	7.3	141.4	133.0	conc
100204_KB3_A_56_a	0.0614	34.0	0.0093	22.2	0.2987	0.0460	19.5	60.5	20.0	59.8	13.2	22.1	0.0	204.5	conc
100204_KB3_A_02_a	0.0654	3.9	0.0094	3.3	0.4217	0.0500	2.2	64.3	2.4	60.3	2.0	3.2	192.8	52.2	disc
100204_KB3_A_18_a	0.0695	11.7	0.0094	10.2	0.4336	0.0537	5.0	68.2	7.7	60.5	6.1	10.1	356.7	113.5	conc
100204_KB3_A_37_a	0.0623	4.0	0.0095	3.9	0.4770	0.0473	2.5	61.4	2.4	61.1	2.4	3.9	66.1	60.4	conc
100204_KB3_A_11_a	0.0641	7.9	0.0095	7.9	0.4955	0.0485	1.4	63.1	4.9	61.1	4.8	7.8	122.1	32.5	conc
100204_KB3_A_58_a	0.0695	10.2	0.0095	9.5	0.4427	0.0526	6.8	68.3	6.7	61.1	5.8	9.4	311.9	155.9	conc
100207_KB3_B_03_b	0.0633	10.0	0.0096	9.3	0.4620	0.0475	2.8	62.3	6.1	61.4	5.7	9.2	76.3	65.4	conc
100207_KB3_C_09_a	0.0567	11.1	0.0097	7.1	0.2488	0.0436	6.3	56.0	6.1	61.9	4.4	7.0	0.0	8.4	conc
100204_KB3_A_38_a	0.0684	11.4	0.0097	4.7	0.2064	0.0527	9.7	67.2	7.4	62.1	2.9	4.7	317.8	221.2	conc
100204_KB3_A_01_a	0.0721	19.4	0.0097	15.6	0.4019	0.0502	5.1	70.7	13.2	62.2	9.6	15.5	205.4	119.7	conc
100204_KB3_A_10_a	0.0680	70.6	0.0097	69.6	0.4173	0.0516	78.2	66.8	45.7	62.3	43.1	69.3	268.4	733.5	l.e.
100207_KB3_C_23_a	0.0647	6.4	0.0098	5.6	0.4372	0.0478	4.3	63.7	4.0	62.6	3.5	5.6	89.0	94.1	conc
100207_KB3_B_29_a	0.0702	12.4	0.0099	4.3	0.1743	0.0529	11.5	68.9	8.3	63.2	2.7	4.3	323.0	264.5	conc
100204_KB3_A_04_a	0.0673	14.2	0.0099	16.0	0.5642	0.0486	5.0	66.2	9.1	63.7	10.1	15.9	127.5	118.5	conc
100204_KB3_A_46_a	0.0643	10.9	0.0100	11.2	0.5163	0.0472	3.6	63.2	6.7	64.2	7.2	11.2	56.8	69.7	conc
100204_KB3_A_53_a	0.0685	11.2	0.0101	10.9	0.4052	0.0487	10.5	67.3	7.3	64.8	7.0	10.8	133.7	182.0	conc
100207_KB3_C_34_a	0.0670	14.1	0.0101	14.5	0.5129	0.0472	4.7	65.8	9.0	64.8	9.3	14.4	59.9	83.6	conc
100207_KB3_B_21_a	0.0688	12.4	0.0101	12.6	0.5093	0.0485	4.7	67.5	8.1	64.9	8.1	12.5	125.5	111.5	conc
100207_KB3_B_48_a	0.0648	13.3	0.0101	13.3	0.4999	0.0467	2.6	63.7	8.2	65.1	8.6	13.2	31.9	46.1	conc
100207_KB3_C_23_b	0.0661	14.8	0.0102	10.8	0.3633	0.0491	22.6	65.0	9.3	65.5	7.0	10.7	152.8	305.3	conc
100207_KB3_B_39_a	0.0779	18.2	0.0103	13.8	0.3804	0.0555	8.9	76.2	13.3	66.0	9.1	13.8	432.0	199.5	conc
100204_KB3_A_24_a	0.0706	12.9	0.0103	12.7	0.4936	0.0504	4.3	69.3	8.6	66.1	8.3	12.6	215.7	99.1	conc
100204_KB3_A_48_a	0.0674	78.8	0.0104	78.6	0.4236	0.0467	78.4	66.3	50.6	66.5	52.0	78.2	33.2	637.9	l.e.
100207_KB3_C_19_a	0.0659	4.4	0.0104	2.8	0.3244	0.0457	2.1	64.8	2.8	66.9	1.9	2.8	0.0	16.7	conc
100207_KB3_B_28_a	0.0855	17.6	0.0104	19.6	0.5566	0.0595	10.0	83.3	14.1	67.0	13.1	19.5	584.2	218.3	conc
100204_KB3_A_04_b	0.0721	7.8	0.0105	6.1	0.3908	0.0496	4.4	70.7	5.4	67.2	4.1	6.1	174.5	102.6	conc
100204_KB3_A_39_a	0.0738	5.3	0.0106	4.1	0.3794	0.0507	2.9	72.3	3.7	67.7	2.7	4.0	227.0	66.9	conc
100207_KB3_C_22_a	0.0733	8.6	0.0107	4.0	0.2329	0.0499	7.6	71.8	6.0	68.6	2.7	4.0	192.6	177.7	conc
100207_KB3_C_32_a	0.0758	26.0	0.0108	25.8	0.3808	0.0507	25.7	74.2	18.6	69.5	17.8	25.6	225.2	365.4	conc
100204_KB3_A_14_a	0.0744	13.4	0.0110	13.8	0.5172	0.0487	7.2	72.9	9.4	70.8	9.7	13.8	135.2	147.7	conc
100207_KB3_B_11_a	0.0740	10.8	0.0111	9.9	0.4588	0.0484	2.2	72.5	7.6	70.9	7.0	9.9	121.3	51.9	conc
100207_KB3_B_27_a	0.0745	14.2	0.0111	13.1	0.4621	0.0487	2.9	72.9	10.0	71.0	9.3	13.0	133.9	67.0	conc
100207_KB3_B_11_b	0.0766	15.6	0.0112	15.2	0.4893	0.0504	4.8	75.0	11.3	71.8	10.9	15.2	215.6	110.6	conc
100207_KB3_C_11_a	0.0786	5.6	0.0119	4.3	0.3831	0.0482	4.0	76.8	4.1	76.0	3.2	4.3	110.7	95.5	conc
100204_KB3_A_08_a	0.0821	39.9	0.0119	38.4	0.4812	0.0509	12.4	80.1	30.8	76.2	29.1	38.2	238.1	250.4	l.e.

Continues on following page

Table 2.2: Isotopic measurements of detrital zircon samples

File name	$^{207}\text{Pb}/^{235}\text{U}$ ratio	RSE (%)	$^{206}\text{Pb}/^{238}\text{U}$ ratio	2RSE (%)	Rho	$^{207}\text{Pb}/^{206}\text{Pb}$ ratio	2RSE (%)	$^{207}\text{Pb}/^{238}\text{U}$ age (Ma)	2RSE (Ma)	$^{206}\text{Pb}/^{238}\text{U}$ age (Ma)	2RSE (Ma)	$^{207}\text{Pb}/^{206}\text{Pb}$ age (Ma)	2RSE (Ma)	Quality*	
100204_KB3_A_03_a	0.0870	12.4	0.0123	12.4	0.5003	0.0505	3.8	84.7	10.0	78.8	9.7	217.7	87.1	conc	
100207_KB3_B_17_a	0.0824	48.2	0.0124	50.2	0.5198	0.0481	5.3	80.4	37.3	79.7	39.7	103.4	112.1	1.e.	
100204_KB3_A_31_a	0.0830	14.6	0.0125	14.5	0.4955	0.0483	0.8	81.0	11.4	79.8	11.5	113.0	19.9	conc	
100207_KB3_B_35_a	0.0852	8.7	0.0129	4.8	0.2721	0.0479	6.4	83.0	7.0	82.8	3.9	96.3	120.6	conc	
100207_KB3_B_47_a	0.0891	2.9	0.0139	2.7	0.4732	0.0469	1.4	86.7	2.4	88.8	2.4	45.4	33.8	conc	
100204_KB3_A_12_a	0.0940	12.0	0.0140	6.9	0.2870	0.0489	6.8	91.2	10.5	89.3	6.1	143.6	148.2	conc	
100207_KB3_C_08_a	0.1126	110.8	0.0164	82.8	0.3738	0.0499	34.2	108.4	114.3	104.7	86.0	188.1	417.7	1.e.	
100207_KB3_B_33_a	0.1307	4.3	0.0198	2.6	0.3025	0.0480	2.7	124.7	5.1	126.7	3.3	98.9	63.2	conc	
100207_KB3_C_29_a	0.1960	12.0	0.0200	11.8	0.4662	0.0721	11.5	181.7	19.9	127.7	14.9	988.9	236.4	disc	
100207_KB3_B_41_a	0.1778	10.6	0.0261	4.8	0.2263	0.0501	8.0	166.2	16.3	166.0	7.9	200.8	185.6	conc	
100207_KB3_B_19_a	0.1817	8.6	0.0262	4.4	0.2570	0.0506	6.4	169.5	13.4	166.9	7.3	220.7	149.0	conc	
100204_KB3_A_43_a	0.1835	12.8	0.0270	13.3	0.5193	0.0496	1.8	171.1	20.2	171.4	22.5	175.7	42.1	conc	
100204_KB3_A_27_a	4.7288	5.6	0.3136	5.7	0.5217	0.1087	3.5	1772.4	46.6	1758.6	87.5	1778.5	64.7	conc	
100204_KB3_A_27_b	4.9455	34.4	0.3181	34.4	0.5028	0.1130	33.5	1810.1	299.1	1780.6	536.9	1848.6	641.7	conc	
Sample 2 (KB3), analyses with >10% common Pb correction															
100204_KB3_A_20_a	0.0451	15.5	0.0077	12.8	0.4128	0.0431	4.9	44.8	6.8	49.5	6.3	12.8	0.0	conc	
100204_KB3_A_52_a	0.0436	28.2	0.0079	28.0	0.4651	0.0399	27.3	43.3	11.9	50.7	14.1	27.9	0.0	conc	
100204_KB3_A_49_a	0.0516	17.3	0.0088	9.6	0.2122	0.0416	14.3	51.1	8.6	56.2	5.4	9.6	0.0	conc	
100204_KB3_A_29_a	0.0565	14.0	0.0090	13.1	0.4451	0.0454	11.1	55.8	7.6	57.6	7.5	13.0	0.0	conc	
100207_KB3_B_50_a	0.0603	24.8	0.0092	21.6	0.4084	0.0470	14.7	59.4	14.3	59.2	12.7	21.5	49.4	183.3	conc
100204_KB3_A_21_a	0.0607	14.0	0.0108	13.7	0.4884	0.0404	6.6	59.8	8.1	69.5	9.4	13.6	0.0	conc	
100207_KB3_C_03_a	0.0603	21.4	0.0109	20.9	0.4244	0.0403	20.1	59.5	12.4	69.6	14.5	20.8	0.0	conc	
100204_KB3_A_51_a	0.1820	20.4	0.0300	19.8	0.4830	0.0439	7.8	169.8	32.0	190.5	37.2	19.5	0.0	conc	
100207_KB3_C_04_a	0.0395	5.9	0.0083	4.3	0.3387	0.0345	4.5	39.3	2.3	53.5	2.3	4.3	0.0	disc	
100204_KB3_A_41_a	0.0478	12.0	0.0089	6.1	0.1622	0.0386	9.5	47.4	5.6	57.0	3.5	6.1	0.0	disc	
100207_KB3_C_10_a	-0.0893	10.6	0.0094	8.2	0.5366	-0.0679	7.5	-95.0	-10.6	60.5	4.9	8.2	0.0	disc	
100207_KB3_B_43_a	-0.0239	24.5	0.0096	18.5	0.3892	-0.0183	14.8	-24.5	-6.1	61.7	11.3	18.4	0.0	disc	
100207_KB3_B_51_a	-0.0763	7.7	0.0098	5.0	0.2798	-0.0566	5.7	-80.6	-6.5	63.0	3.1	4.9	0.0	disc	
100207_KB3_C_31_a	0.0788	8.8	0.0098	9.0	0.5125	0.0574	5.5	77.0	6.5	63.1	5.6	8.9	0.0	disc	
100207_KB3_B_14_a	0.0099	4.7	0.0099	2.1	0.2630	0.0071	2.9	10.0	0.5	63.8	1.3	2.1	0.0	disc	
100207_KB3_C_17_a	-0.0242	43.4	0.0100	38.6	0.3761	-0.0176	33.9	-24.8	-10.9	64.3	24.7	38.4	0.0	1.e.	
100207_KB3_B_10_a	-0.0081	5.1	0.0101	4.0	0.3910	-0.0058	3.9	-8.3	-0.4	64.6	2.6	4.0	0.0	disc	
100207_KB3_B_13_a	-0.0201	11.8	0.0101	10.3	0.3626	-0.0146	9.8	-20.7	-2.5	65.0	6.6	10.2	0.0	disc	
100207_KB3_B_18_a	-0.0117	12.8	0.0101	11.1	0.3330	-0.0084	11.2	-11.9	-1.5	65.1	7.2	11.1	0.0	disc	
100207_KB3_C_07_a	0.0307	56.9	0.0101	50.5	0.2911	0.0212	52.3	30.7	17.2	65.1	32.7	50.3	0.0	1.e.	

Continues on following page

Table 2.2: Isotopic measurements of detrital zircon samples

File name	$^{207}\text{Pb}/^{235}\text{U}$ ratio	RSE (%)	$^{206}\text{Pb}/^{238}\text{U}$ ratio	2RSE (%)	Rho	$^{207}\text{Pb}/^{206}\text{Pb}$ ratio	2RSE (%)	$^{207}\text{Pb}/^{238}\text{U}$ age (Ma)	2RSE (Ma)	$^{206}\text{Pb}/^{238}\text{U}$ age (Ma)	2RSE (Ma)	$^{207}\text{Pb}/^{206}\text{Pb}$ age (Ma)	2RSE (Ma)	Quality*
100207_KB3_B_46_b	0.0156	15.6	0.0104	13.6	0.4698	0.0109	9.4	15.8	2.4	66.7	9.0	13.5	0.0	disc
100207_KB3_C_16_a	-0.0006	7.1	0.0105	2.9	0.2252	-0.0004	4.8	-0.6	0.0	67.5	2.0	2.9	0.0	disc
100207_KB3_B_31_a	-0.0918	13.2	0.0107	12.6	0.5034	-0.0618	5.0	-97.8	-13.5	68.3	8.6	12.6	0.0	disc
100204_KB3_A_45_a	-0.0174	48.6	0.0107	48.1	0.3655	-0.0118	47.9	-17.8	-8.8	68.5	32.8	47.8	0.0	1.e.
100207_KB3_B_46_a	0.0342	6.6	0.0109	5.2	0.3625	0.0231	5.3	34.1	2.2	69.8	3.6	5.2	0.0	disc
100207_KB3_B_01_a	0.0155	14.9	0.0109	12.0	0.2246	0.0104	13.0	15.6	2.3	69.9	8.3	11.9	0.0	disc
100204_KB3_A_35_a	0.0397	4.3	0.0110	4.1	0.4916	0.0261	2.4	39.5	1.7	70.5	2.9	4.1	0.0	disc
100204_KB3_A_40_a	0.0519	27.2	0.0110	15.5	0.2920	0.0334	6.8	51.4	13.6	70.8	10.9	15.4	0.0	disc
100204_KB3_A_42_a	0.0584	5.4	0.0111	4.5	0.4144	0.0384	3.2	57.7	3.0	71.0	3.2	4.5	0.0	disc
100207_KB3_C_05_a	0.0405	5.4	0.0114	4.3	0.3105	0.0261	4.3	40.3	2.1	72.8	3.1	4.3	0.0	disc
100204_KB3_A_50_a	0.0437	341.7	0.0114	342.2	0.5265	0.0277	336.7	43.5	146.3	72.9	248.0	340.4	0.0	985.4
100204_KB3_A_50_b	0.0502	5.8	0.0122	5.7	0.4973	0.0301	2.0	49.7	2.8	78.0	4.4	5.7	0.0	disc
100204_KB3_A_55_a	0.0730	5.9	0.0125	5.7	0.4854	0.0419	3.7	71.5	4.0	80.1	4.5	5.7	0.0	disc
100207_KB3_B_38_a	0.0431	4.4	0.0137	3.9	0.4745	0.0228	1.6	42.9	1.9	87.7	3.4	3.9	0.0	disc
100207_KB3_B_42_a	0.0357	4.3	0.0139	3.6	0.4483	0.0191	2.2	35.6	1.5	88.8	3.2	3.5	0.0	disc
100207_KB3_C_33_a	0.0721	11.1	0.0150	9.8	0.4301	0.0351	7.8	70.7	7.5	95.7	9.3	9.7	0.0	disc
100207_KB3_B_08_b	-0.0660	54.3	0.0166	53.4	0.7266	-0.0288	52.1	-69.3	-39.0	106.1	56.2	53.0	0.0	1.e.
100207_KB3_B_20_a	0.0469	5.2	0.0171	4.5	0.4798	0.0197	3.7	46.6	2.4	109.4	4.9	4.5	0.0	disc
100207_KB3_B_49_a	0.0705	8.6	0.0180	6.0	0.3119	0.0286	6.2	69.2	5.7	114.9	6.9	6.0	0.0	disc
100207_KB3_B_03_a	0.0687	11.8	0.0200	11.3	0.4833	0.0248	3.2	67.4	7.7	127.4	14.3	11.2	0.0	disc
100207_KB3_C_28_a	0.0989	10.0	0.0286	9.7	0.4919	0.0249	5.5	95.8	9.1	181.9	17.4	9.6	0.0	disc
100207_KB3_C_21_a	0.0498	9.0	0.0311	7.1	0.2717	0.0117	7.3	49.4	4.4	197.4	13.8	7.0	0.0	disc
100204_KB3_A_06_a	0.2512	3.3	0.0408	3.0	0.4589	0.0447	1.9	227.6	6.7	257.6	7.5	2.9	0.0	disc
100204_KB3_A_05_a	0.3377	7.7	0.0548	7.8	0.5379	0.0448	6.5	295.4	19.8	343.8	26.2	7.6	0.0	disc
100207_KB3_B_15_a	0.4090	8.8	0.0701	8.8	0.5054	0.0421	1.9	348.2	26.0	436.6	37.3	8.5	0.0	disc
Sample 3 (BG6), analyses with <10% common Pb correction														
100205_BG6_A_17_a	0.0732	21.7	0.0110	24.2	0.5766	0.0473	11.4	71.7	15.0	70.5	17.0	24.1	61.9	156.5
100205_BG6_B_14_a	0.0810	86.8	0.0113	85.6	0.4933	0.0519	21.1	79.1	66.1	72.1	61.4	85.1	281.1	351.3
100205_BG6_B_28_a	0.0707	16.1	0.0113	14.2	0.3409	0.0461	13.0	69.3	10.8	72.1	10.2	14.2	4.7	145.8
100205_BG6_B_26_a	0.0774	6.5	0.0113	9.3	0.7270	0.0488	3.4	75.7	4.7	72.1	6.6	9.2	140.6	80.8
100205_BG6_C_05_a	0.0753	11.1	0.0113	11.8	0.5559	0.0479	7.6	73.7	7.9	72.4	8.5	11.7	96.2	133.6
100205_BG6_A_10_a	0.0755	82.8	0.0113	36.0	0.2175	0.0487	100.4	73.9	59.0	72.5	26.0	35.8	131.0	788.2
100205_BG6_D_33_a	0.0723	8.7	0.0113	6.4	0.3504	0.0461	4.6	70.9	6.0	72.5	4.6	6.3	1.0	54.1
100205_BG6_C_22_a	0.0754	62.3	0.0114	23.7	0.1904	0.0497	18.6	73.8	44.3	73.0	17.2	23.6	181.3	282.8
100205_BG6_A_09_a	0.0730	32.1	0.0114	32.2	0.5048	0.0470	29.7	71.5	22.2	73.3	23.5	32.0	51.7	320.0

Continues on following page

Table 2.2: Isotopic measurements of detrital zircon samples

File name	$^{207}\text{Pb}/^{235}\text{U}$ ratio	RSE (%)	$^{206}\text{Pb}/^{238}\text{U}$ ratio	2RSE (%)	Rho	$^{207}\text{Pb}/^{206}\text{Pb}$ ratio	2RSE (%)	$^{207}\text{Pb}/^{238}\text{U}$ age (Ma)	2RSE (Ma)	$^{206}\text{Pb}/^{238}\text{U}$ age (Ma)	2RSE (Ma)	2RSE (%)	$^{207}\text{Pb}/^{206}\text{Pb}$ age (Ma)	2RSE (Ma)	Quality*
100205_BG6_A_15_a	0.0753	10.6	0.0115	11.0	0.5192	0.0475	3.6	73.8	7.6	73.8	8.1	11.0	73.2	78.5	conc
100205_BG6_C_39_a	0.0770	6.9	0.0116	6.6	0.4658	0.0478	4.1	75.4	5.0	74.0	4.9	6.6	91.7	93.0	conc
100205_BG6_D_03_a	0.0776	9.5	0.0117	9.4	0.4948	0.0480	4.8	75.9	7.0	75.0	7.0	9.4	98.4	104.3	conc
100205_BG6_D_20_a	0.0814	12.4	0.0117	9.2	0.3704	0.0490	7.0	79.4	9.5	75.3	6.9	9.1	146.3	151.3	conc
100205_BG6_A_24_a	0.0773	5.5	0.0120	5.5	0.4996	0.0470	4.3	75.6	4.0	76.8	4.2	5.5	50.8	75.7	conc
100205_BG6_B_16_a	0.1032	130.9	0.0120	74.1	0.2831	0.0600	103.5	99.7	124.9	76.9	56.6	73.6	603.4	993.5	l.e.
100205_BG6_C_13_a	0.0858	14.2	0.0123	11.9	0.3943	0.0494	8.8	83.6	11.4	79.1	9.4	11.9	166.1	180.1	conc
100205_BG6_D_27_a	0.0850	13.4	0.0126	12.8	0.4789	0.0487	2.3	82.8	10.6	80.7	10.3	12.7	131.3	54.6	conc
100205_BG6_C_31_a	0.0843	6.5	0.0127	6.5	0.5044	0.0479	2.6	82.1	5.1	81.6	5.3	6.5	94.1	61.3	conc
100205_BG6_A_21_a	0.0847	26.5	0.0130	15.5	0.2915	0.0474	19.2	82.5	21.0	83.0	12.7	15.4	69.7	236.1	conc
100205_BG6_A_28_b	0.0893	7.0	0.0130	3.9	0.2760	0.0503	6.2	86.8	5.8	83.0	3.2	3.8	206.8	144.0	conc
100205_BG6_B_15_a	0.0896	6.4	0.0131	5.7	0.4450	0.0490	2.3	87.2	5.4	83.8	4.8	5.7	146.5	54.1	conc
100205_BG6_A_22_a	0.1000	42.8	0.0132	42.4	0.4117	0.0546	42.1	96.7	39.5	84.8	35.7	42.1	396.5	568.3	l.e.
100205_BG6_A_28_a	0.0852	11.5	0.0133	10.5	0.4531	0.0465	6.8	83.1	9.2	85.2	8.9	10.4	25.6	91.1	conc
100205_BG6_A_32_a	0.0933	4.7	0.0138	4.3	0.4539	0.0492	3.1	90.6	4.1	88.5	3.8	4.2	155.3	73.5	conc
100205_BG6_A_36_a	0.0883	16.0	0.0139	15.8	0.4075	0.0464	15.5	86.0	13.2	89.3	14.0	15.7	18.3	177.4	conc
100205_BG6_C_24_a	0.0950	15.9	0.0141	15.4	0.4855	0.0491	2.1	92.1	14.0	90.3	13.8	15.3	150.5	48.5	conc
100205_BG6_B_33_a	0.0998	64.3	0.0144	81.5	0.6337	0.0516	41.2	96.5	59.3	91.9	74.4	80.9	266.5	504.6	l.e.
100205_BG6_A_26_b	0.0990	26.9	0.0145	30.1	0.5608	0.0489	5.9	95.9	24.6	92.7	27.7	29.9	143.9	138.9	conc
100205_BG6_C_19_a	0.1025	21.1	0.0151	22.6	0.5352	0.0493	4.0	99.1	19.9	96.4	21.6	22.4	160.2	93.3	conc
100205_BG6_C_25_a	0.1012	9.2	0.0151	9.5	0.5186	0.0485	3.4	97.9	8.6	96.7	9.1	9.4	121.5	80.6	conc
100205_BG6_D_28_a	0.1053	7.6	0.0152	6.8	0.3979	0.0494	6.2	101.6	7.3	97.2	6.5	6.7	167.8	145.4	conc
100205_BG6_B_23_a	0.0956	20.7	0.0155	19.5	0.4503	0.0443	14.0	92.7	18.3	99.2	19.2	19.4	0.0	109.5	conc
100205_BG6_A_23_a	0.0933	7.5	0.0156	7.4	0.4650	0.0436	7.1	90.6	6.5	99.6	7.3	7.3	0.0	16.8	conc
100205_BG6_C_27_a	0.0963	8.8	0.0157	8.7	0.5004	0.0446	7.1	93.3	7.8	100.7	8.7	8.6	0.0	44.3	conc
100205_BG6_C_38_a	0.1269	27.6	0.0162	31.6	0.5726	0.0545	8.0	121.3	31.5	103.6	32.5	31.3	390.5	179.7	l.e.
100205_BG6_A_30_a	0.0989	4.9	0.0168	4.8	0.4858	0.0434	3.5	95.7	4.5	107.2	5.1	4.8	0.0	0.0	disc
100205_BG6_C_37_a	0.1300	41.7	0.0188	37.9	0.4543	0.0506	5.7	124.1	48.8	120.0	45.1	37.6	220.8	132.6	l.e.
100205_BG6_C_34_a	0.1396	133.7	0.0199	132.0	0.4933	0.0500	14.1	132.7	167.9	126.9	165.9	130.7	196.3	247.1	l.e.
100205_BG6_C_17_a	0.1634	25.8	0.0224	40.5	0.7844	0.0510	13.3	153.7	36.8	142.7	57.1	40.1	241.4	261.2	l.e.
100205_BG6_B_19_a	0.6171	40.9	0.0228	40.6	0.3442	0.1941	40.6	488.0	159.8	145.5	58.4	40.0	2777.2	719.3	l.e.
100205_BG6_C_09_a	0.1711	21.2	0.0252	20.0	0.4713	0.0503	4.0	160.4	31.5	160.5	31.7	19.8	210.9	93.7	conc
100205_BG6_C_18_a	0.2006	9.7	0.0296	9.1	0.4652	0.0492	7.3	185.7	16.5	188.0	16.8	8.9	157.6	160.4	conc
100205_BG6_B_17_a	0.2033	20.7	0.0313	20.7	0.5281	0.0471	20.0	187.9	35.5	198.4	40.5	20.4	56.2	237.3	conc
100205_BG6_A_33_a	0.2073	9.7	0.0324	9.6	0.5075	0.0464	9.1	191.2	16.8	205.5	19.5	9.5	15.9	110.3	conc
100205_BG6_B_25_a	0.2692	18.7	0.0362	18.4	0.4908	0.0533	4.1	242.0	40.4	229.0	41.4	18.1	342.0	94.0	conc

Continues on following page

Table 2.2: Isotopic measurements of detrital zircon samples

File name	$^{207}\text{Pb}/^{235}\text{U}$ ratio	RSE (%)	$^{206}\text{Pb}/^{238}\text{U}$ ratio	2RSE (%)	Rho	$^{207}\text{Pb}/^{206}\text{Pb}$ ratio	2RSE (%)	$^{207}\text{Pb}/^{238}\text{U}$ age (Ma)	2RSE (Ma)	$^{206}\text{Pb}/^{238}\text{U}$ age (Ma)	2RSE (Ma)	$^{207}\text{Pb}/^{206}\text{Pb}$ age (Ma)	2RSE (Ma)	Quality*
100205_BG6_B_18_a	0.2613	7.1	0.0364	8.6	0.6030	0.0522	4.7	235.7	15.0	230.6	19.5	293.4	107.3	conc
100205_BG6_A_39_a	0.2333	9.1	0.0370	9.2	0.5244	0.0467	5.8	212.9	17.6	234.4	21.3	35.8	84.6	conc
100205_BG6_B_21_a	0.4483	3.9	0.0604	4.0	0.5053	0.0535	0.6	376.1	12.4	378.2	14.6	352.1	14.6	conc
100205_BG6_B_06_a	2.8120	9.2	0.2320	8.9	0.4756	0.0876	5.3	1358.7	69.0	1345.0	107.7	1373.0	101.2	conc
100205_BG6_A_05_a	3.6604	12.2	0.2864	12.0	0.4925	0.0926	2.8	1562.8	97.4	1623.6	171.8	1479.6	53.7	conc
100205_BG6_B_34_a	9.4092	19.8	0.4327	18.5	0.4489	0.1582	12.6	2378.7	183.6	2317.8	361.5	2436.7	215.8	conc
Sample 3 (BG6), analyses with >10% common Pb correction														
100205_BG6_B_07_a	0.0673	26.2	0.0119	20.0	0.1334	0.0386	24.7	66.2	16.8	76.2	15.1	19.9	53.7	conc
100205_BG6_D_21_a	0.0923	19.5	0.0134	17.2	0.4319	0.0500	12.8	89.7	16.7	85.8	14.7	196.3	234.4	conc
100205_BG6_A_13_a	0.0850	10.3	0.0143	9.0	0.3120	0.0433	9.0	82.9	8.2	91.3	8.2	0.0	29.0	conc
100205_BG6_B_36_a	0.0902	9.0	0.0144	7.5	0.3873	0.0464	6.3	87.7	7.5	92.2	6.9	18.9	81.7	conc
100205_BG6_A_27_a	0.0950	10.8	0.0157	10.5	0.4680	0.0436	10.0	92.1	9.5	100.4	10.5	0.0	49.9	conc
100205_BG6_A_35_a	0.0928	11.9	0.0158	14.6	0.6414	0.0421	3.7	90.2	10.3	100.9	14.6	0.0	0.0	conc
100205_BG6_B_11_a	0.0877	10.1	0.0159	8.3	0.2962	0.0406	8.2	85.4	8.3	101.5	8.3	0.0	0.0	conc
100205_BG6_C_35_a	0.0996	14.3	0.0167	13.9	0.4677	0.0429	10.3	96.4	13.2	107.0	14.7	0.0	33.3	conc
100205_BG6_A_03_a	-0.0606	62.9	0.0087	60.0	0.2402	-0.0521	61.8	-63.4	-41.2	55.7	33.3	59.7	0.0	l.e.
100205_BG6_A_37_a	0.0639	82.1	0.0088	37.3	0.2237	0.0348	38.8	62.9	50.1	56.8	21.1	37.1	57.5	l.e.
100205_BG6_C_28_a	0.0467	62.8	0.0099	43.9	0.3408	0.0343	24.9	46.3	28.5	63.5	27.7	43.6	0.0	l.e.
100205_BG6_C_30_a	0.0814	49.0	0.0125	43.8	0.3824	0.0474	38.2	79.5	37.5	80.1	34.9	43.6	394.3	l.e.
100205_BG6_C_12_a	-0.1887	62.2	0.0128	44.2	0.0815	-0.1043	60.0	-212.3	-147.8	82.1	36.1	44.0	0.0	l.e.
100205_BG6_A_20_a	-0.1254	17.4	0.0139	14.4	0.4334	-0.0653	10.8	-136.1	-25.4	88.7	12.7	14.3	0.0	disc
100205_BG6_C_04_a	-0.1865	29.7	0.0142	17.6	0.3385	-0.1053	21.6	-209.6	-69.3	90.9	15.9	17.5	0.0	disc
100205_BG6_A_34_a	0.0848	5.7	0.0160	5.2	0.4615	0.0384	3.9	82.7	4.5	102.6	5.3	5.2	0.0	disc
100205_BG6_A_11_a	0.0785	11.1	0.0168	10.9	0.4973	0.0337	4.1	76.7	8.2	107.6	11.6	10.8	0.0	disc
100205_BG6_D_22_a	0.0823	9.1	0.0170	10.0	0.6196	0.0349	6.2	80.3	7.0	108.6	10.8	9.9	0.0	disc
100205_BG6_B_09_a	0.0803	22.0	0.0171	17.5	0.4085	0.0343	12.2	78.5	16.6	109.0	18.9	17.3	0.0	disc
100205_BG6_A_26_a	0.0977	3.9	0.0183	3.7	0.5048	0.0390	1.4	94.7	3.5	116.6	4.3	3.7	0.0	disc
100205_BG6_D_30_a	-0.0158	23.3	0.0188	20.1	0.4890	-0.0066	22.2	-16.1	-3.8	119.9	23.9	19.9	0.0	disc
100205_BG6_B_03_a	0.0886	22.4	0.0193	12.2	0.1966	0.0332	15.5	86.2	18.5	123.0	14.9	12.1	0.0	disc
100205_BG6_C_08_a	0.0613	7.3	0.0195	7.3	0.5242	0.0229	5.1	60.4	4.3	124.5	9.0	7.2	0.0	disc
100205_BG6_C_01_a	-0.0825	10.9	0.0196	9.7	0.4546	-0.0309	4.1	-87.4	-10.0	125.1	12.0	9.6	0.0	disc
100205_BG6_B_02_a	0.1105	21.4	0.0213	18.7	0.4356	0.0379	10.3	106.4	21.6	136.0	25.1	18.5	0.0	disc
100205_BG6_B_08_a	0.0430	63.7	0.0231	62.1	0.4908	0.0140	30.7	42.8	26.7	147.0	90.2	61.4	0.0	l.e.
100205_BG6_A_12_a	-0.0439	59.8	0.0241	55.3	0.4477	-0.0133	37.4	-45.6	-27.9	153.2	83.8	54.7	0.0	l.e.
100205_BG6_B_05_a	0.0494	17.8	0.0241	17.4	0.5863	0.0147	16.1	48.9	8.5	153.7	26.5	17.2	0.0	disc

Continues on following page

Table 2.2: Isotopic measurements of detrital zircon samples

File name	$^{207}\text{Pb}/^{235}\text{U}$ ratio	RSE (%)	$^{206}\text{Pb}/^{238}\text{U}$ ratio	2RSE (%)	Rho	$^{207}\text{Pb}/^{206}\text{Pb}$ ratio	2RSE (%)	$^{207}\text{Pb}/^{238}\text{U}$ age (Ma)	2RSE (Ma)	$^{206}\text{Pb}/^{238}\text{U}$ age (Ma)	2RSE (Ma)	2RSE (%)	$^{207}\text{Pb}/^{206}\text{Pb}$ age (Ma)	2RSE (Ma)	Quality*
100205_BG6_A_01_a	0.0628	12.9	0.0256	13.8	0.6714	0.0178	10.7	61.8	7.8	163.2	22.2	13.6	0.0	0.0	disc
100205_BG6_D_40_a	0.0912	13.2	0.0261	6.9	0.2721	0.0252	9.5	88.6	11.2	166.1	11.3	6.8	0.0	0.0	disc
100205_BG6_A_18_a	0.1348	11.6	0.0271	11.4	0.4981	0.0365	4.4	128.4	14.0	172.3	19.4	11.2	0.0	0.0	disc
100205_BG6_B_30_a	0.0527	10.4	0.0274	9.9	0.4439	0.0139	8.8	52.1	5.3	174.4	17.0	9.8	0.0	0.0	disc
100205_BG6_B_24_a	0.1629	6.3	0.0286	6.3	0.5289	0.0412	3.5	153.3	8.9	182.0	11.3	6.2	0.0	0.0	disc
100205_BG6_B_13_a	0.1561	4.1	0.0287	3.8	0.4794	0.0394	1.9	147.3	5.6	182.7	6.8	3.7	0.0	0.0	disc
100205_BG6_A_40_a	0.1398	9.5	0.0294	8.2	0.4459	0.0347	5.6	132.9	11.8	186.9	15.1	8.1	0.0	0.0	disc
100205_BG6_A_08_a	0.1206	9.5	0.0297	7.1	0.4606	0.0274	7.6	115.6	10.3	188.6	13.1	7.0	0.0	0.0	disc
100205_BG6_B_35_a	0.1780	8.7	0.0299	8.6	0.4955	0.0431	4.6	166.3	13.3	190.0	16.0	8.4	0.0	0.0	disc
100205_BG6_A_06_a	0.1875	8.2	0.0331	8.2	0.5326	0.0408	7.6	174.5	13.2	210.1	17.0	8.1	0.0	0.0	disc
100205_BG6_D_37_a	0.2303	48.4	0.0375	47.4	0.4815	0.0433	38.9	210.4	92.3	237.5	110.5	46.5	0.0	304.5	l.e.
100205_BG6_B_29_a	0.2393	8.9	0.0442	8.7	0.5145	0.0392	5.1	217.9	17.5	278.5	23.7	8.5	0.0	0.0	disc
100205_BG6_A_41_a	0.2226	34.6	0.0443	26.1	0.3644	0.0363	19.0	204.0	64.0	279.4	71.4	25.6	0.0	0.0	disc
100205_BG6_C_03_a	0.3297	280.5	0.0485	185.2	0.2550	0.0536	144.8	289.3	871.7	305.4	554.0	181.4	355.8	1057.9	l.e.
100205_BG6_C_29_a	0.2759	10.3	0.0528	10.3	0.5055	0.0378	3.6	247.4	22.7	331.5	33.3	10.1	0.0	0.0	disc
100205_BG6_C_40_a	0.3581	51.0	0.0557	48.0	0.4010	0.0466	43.4	310.8	137.3	349.6	163.5	46.8	30.7	417.0	l.e.
100205_BG6_B_20_a	0.4965	33.7	0.0673	33.9	0.5152	0.0517	29.4	409.3	114.0	419.9	137.9	32.8	274.2	418.1	l.e.
100205_BG6_C_15_a	0.4527	11.6	0.0733	11.2	0.4694	0.0446	9.6	379.2	36.7	456.0	49.4	10.8	0.0	70.1	disc
100205_BG6_C_10_a	1.2897	6.1	0.1523	6.3	0.5258	0.0613	2.4	841.2	34.8	913.8	53.4	5.8	649.9	51.5	disc
100205_BG6_B_22_a	5.2558	11.6	0.3692	11.6	0.5030	0.1031	1.0	1861.7	98.9	2025.5	201.8	10.0	1681.4	18.3	disc
Sample 4 (N28), analyses with <10% common Pb correction															
100204_N28_C_27_a	0.0613	10.8	0.0090	11.5	0.5351	0.0489	3.5	60.4	6.3	58.1	6.7	11.5	141.4	81.1	conc
100204_N28_B_07_a	0.0632	12.7	0.0092	11.8	0.4665	0.0500	2.8	62.2	7.6	59.2	7.0	11.8	193.3	65.7	conc
100204_N28_C_35_a	0.0631	16.6	0.0095	11.6	0.3475	0.0474	8.0	62.2	10.0	61.2	7.0	11.5	71.3	125.7	conc
100204_N28_C_24_a	0.0630	8.5	0.0097	8.0	0.4432	0.0476	6.0	62.0	5.1	62.4	4.9	7.9	77.6	107.4	conc
100204_N28_D_14_a	0.0655	5.6	0.0098	3.9	0.3474	0.0485	3.8	64.5	3.5	62.6	2.4	3.9	123.6	89.9	conc
100204_N28_C_05_a	0.0581	41.5	0.0098	17.8	0.1845	0.0437	24.9	57.3	23.2	62.8	11.1	17.7	0.0	197.5	conc
100204_N28_C_18_a	0.0570	28.0	0.0099	15.3	0.1617	0.0428	19.0	56.3	15.3	63.4	9.7	15.2	0.0	118.3	conc
100204_N28_D_22_a	0.0652	13.1	0.0099	13.3	0.5155	0.0472	10.9	64.1	8.1	63.8	8.4	13.2	58.3	149.6	conc
100204_N28_D_07_a	0.0658	7.7	0.0101	7.4	0.4795	0.0470	2.0	64.7	4.8	64.9	4.8	7.4	50.4	47.2	conc
100204_N28_C_29_a	0.0662	8.2	0.0101	7.1	0.4091	0.0472	5.3	65.1	5.2	64.9	4.6	7.1	58.6	90.6	conc
100204_N28_B_08_a	0.0923	12.6	0.0104	21.7	0.8628	0.0622	11.9	89.6	10.8	66.8	14.4	21.6	679.5	257.2	disc
100204_N28_D_04_a	0.0667	12.5	0.0104	10.9	0.4357	0.0473	10.2	65.6	8.0	66.9	7.3	10.9	62.8	144.2	conc
100204_N28_C_06_a	0.0721	7.8	0.0106	7.8	0.4996	0.0493	5.4	70.7	5.3	67.9	5.3	7.7	159.8	126.8	conc

Continues on following page

Table 2.2: Isotopic measurements of detrital zircon samples

File name	$^{207}\text{Pb}/^{235}\text{U}$ ratio	RSE (%)	$^{206}\text{Pb}/^{238}\text{U}$ ratio	2RSE (%)	Rho	$^{207}\text{Pb}/^{206}\text{Pb}$ ratio	2RSE (%)	$^{207}\text{Pb}/^{238}\text{U}$ age (Ma)	2RSE (Ma)	$^{206}\text{Pb}/^{238}\text{U}$ age (Ma)	2RSE (Ma)	2RSE (%)	$^{207}\text{Pb}/^{206}\text{Pb}$ age (Ma)	2RSE (Ma)	Quality*
100204_N28_C_30_a	0.0724	11.1	0.0108	10.6	0.4801	0.0488	2.6	71.0	7.6	69.5	7.3	10.6	139.8	61.9	conc
100204_N28_D_27_a	0.0732	18.8	0.0110	18.0	0.4741	0.0480	9.2	71.8	13.0	70.4	12.6	17.9	99.0	151.9	conc
100204_N28_C_38_a	0.0756	9.4	0.0111	10.1	0.5355	0.0496	7.1	74.0	6.7	71.3	7.1	10.0	174.7	165.0	conc
100204_N28_C_11_a	0.0722	15.3	0.0112	12.2	0.3639	0.0471	8.1	70.7	10.5	71.7	8.7	12.1	52.1	117.4	conc
100204_N28_D_10_a	0.0780	6.2	0.0116	6.2	0.4987	0.0482	3.4	76.2	4.6	74.6	4.6	6.2	108.4	80.3	conc
100204_N28_B_09_a	0.0785	11.4	0.0117	10.6	0.4671	0.0485	2.7	76.7	8.4	75.2	8.0	10.6	121.6	63.8	conc
100204_N28_B_14_a	0.0750	9.7	0.0118	7.5	0.3839	0.0467	5.3	73.5	6.9	75.7	5.6	7.4	35.0	78.1	conc
100204_N28_D_38_a	0.0795	13.6	0.0118	12.2	0.4497	0.0490	9.3	77.7	10.2	75.8	9.2	12.1	147.7	176.3	conc
100204_N28_D_34_a	0.0786	33.2	0.0119	27.8	0.3132	0.0471	30.6	76.8	24.5	76.0	21.0	27.7	53.6	328.5	conc
100204_N28_B_10_a	0.0807	14.5	0.0122	10.0	0.3456	0.0484	7.4	78.8	11.0	78.3	7.8	10.0	117.5	141.9	conc
100204_N28_B_11_a	0.0797	7.0	0.0123	7.0	0.5048	0.0470	4.5	77.9	5.2	79.1	5.5	7.0	49.2	76.8	conc
100204_N28_C_15_a	0.1115	56.9	0.0124	56.5	0.4728	0.0640	56.3	107.3	58.0	79.7	44.7	56.1	742.1	812.8	l.e.
100204_N28_B_03_a	0.0893	10.0	0.0126	10.0	0.4985	0.0519	7.7	86.9	8.3	80.4	8.0	9.9	282.2	177.0	conc
100204_N28_A_13_a	0.0843	17.2	0.0129	11.2	0.3258	0.0481	6.8	82.2	13.6	82.5	9.2	11.1	102.2	127.8	conc
100204_N28_C_03_a	0.0898	7.9	0.0130	7.2	0.4572	0.0492	4.2	87.3	6.6	83.0	5.9	7.2	155.6	98.9	conc
100204_N28_B_27_a	0.0868	10.1	0.0133	10.4	0.5160	0.0466	1.7	84.5	8.2	85.0	8.8	10.3	29.1	34.5	conc
100204_N28_D_31_a	0.0898	9.5	0.0135	8.5	0.4440	0.0486	1.7	87.3	8.0	86.2	7.2	8.4	128.7	39.6	conc
100204_N28_B_20_a	0.0886	37.6	0.0136	37.9	0.5042	0.0480	5.0	86.2	31.1	87.0	32.7	37.6	99.8	106.6	l.e.
100204_N28_D_23_a	0.0979	26.6	0.0137	12.5	0.2354	0.0516	19.8	94.9	24.1	88.0	10.9	12.4	267.9	334.0	conc
100204_N28_D_24_a	0.1012	5.3	0.0147	4.2	0.3961	0.0501	2.8	97.9	4.9	94.1	3.9	4.2	200.9	64.4	conc
100204_N28_B_23_a	0.0992	12.5	0.0150	12.2	0.4894	0.0490	2.8	96.0	11.5	95.8	11.6	12.2	146.7	65.7	conc
100204_N28_D_08_a	0.1018	3.7	0.0150	3.2	0.4315	0.0487	1.9	98.4	3.4	96.0	3.0	3.1	132.7	45.4	conc
100204_N28_D_05_a	0.1024	6.6	0.0150	4.9	0.3686	0.0496	4.1	98.9	6.2	96.1	4.6	4.8	176.5	95.6	conc
100204_N28_B_13_b	0.0973	6.4	0.0150	6.2	0.4897	0.0472	4.1	94.3	5.7	96.2	5.9	6.1	59.0	76.5	conc
100204_N28_C_22_a	0.1000	9.4	0.0151	8.9	0.4769	0.0483	1.3	96.8	8.6	96.6	8.6	8.9	115.3	31.4	conc
100204_N28_D_13_a	0.1043	5.6	0.0152	4.7	0.4150	0.0497	4.1	100.7	5.4	97.4	4.5	4.6	180.1	94.9	conc
100204_N28_B_23_b	0.1053	29.2	0.0155	27.4	0.4692	0.0507	11.0	101.6	28.2	98.9	26.9	27.2	225.6	230.6	conc
100204_N28_D_40_a	0.1038	11.3	0.0156	8.3	0.3670	0.0488	4.5	100.3	10.8	99.8	8.2	8.2	140.2	106.8	conc
100204_N28_C_32_a	0.1058	22.9	0.0157	19.8	0.4317	0.0499	4.5	102.1	22.3	100.7	19.8	19.6	191.4	105.4	conc
100204_N28_D_37_a	0.1153	13.6	0.0170	13.2	0.4870	0.0494	5.6	110.8	14.3	108.8	14.3	13.1	165.4	131.0	conc
100204_N28_B_06_a	0.1176	14.8	0.0177	14.7	0.4954	0.0486	3.6	112.9	15.8	113.0	16.5	14.6	129.8	85.2	conc
100204_N28_C_31_a	0.1250	5.3	0.0183	3.9	0.3712	0.0500	3.1	119.6	6.0	116.9	4.5	3.9	196.0	73.1	conc
100204_N28_B_15_a	0.1321	10.4	0.0193	9.0	0.5100	0.0496	61.0	126.0	12.4	123.4	11.0	8.9	174.3	596.0	conc
100204_N28_C_25_a	0.1743	27.7	0.0224	20.7	0.3733	0.0566	17.1	163.1	41.8	142.6	29.2	20.5	477.6	384.1	conc
100204_N28_C_33_a	0.1603	36.7	0.0238	18.7	0.2551	0.0491	18.1	151.0	51.5	151.5	28.0	18.5	151.5	264.1	conc
100204_N28_D_28_a	0.1517	202.5	0.0241	93.7	0.2313	0.0503	7.2	143.4	277.5	153.3	141.9	92.6	210.2	167.8	l.e.

Continues on following page

Table 2.2: Isotopic measurements of detrital zircon samples

File name	$^{207}\text{Pb}/^{235}\text{U}$ ratio	RSE (%)	$^{206}\text{Pb}/^{238}\text{U}$ ratio	2RSE (%)	Rho	$^{207}\text{Pb}/^{206}\text{Pb}$ ratio	2RSE (%)	$^{207}\text{Pb}/^{238}\text{U}$ age (Ma)	2RSE (Ma)	$^{206}\text{Pb}/^{238}\text{U}$ age (Ma)	2RSE (Ma)	$^{207}\text{Pb}/^{206}\text{Pb}$ age (Ma)	2RSE (Ma)	Quality*
100204_N28_D_12_a	0.2106	2.9	0.0306	4.8	0.8102	0.0510	0.7	194.1	9.1	194.1	4.7	241.4	16.8	conc
100204_N28_C_26_a	0.2617	7.1	0.0362	8.3	0.5873	0.0522	2.8	236.0	18.8	229.5	8.2	293.8	63.6	conc
100207_N28_A_05_a	3.0320	10.5	0.2748	11.2	0.6044	0.0804	8.3	1415.7	155.1	1565.3	9.9	1206.8	163.5	disc
Sample 4 (N28), analyses with > 10% common Pb correction														
100204_N28_B_02_a	0.0564	16.3	0.0097	13.8	0.4232	0.0427	5.1	55.7	8.8	62.1	8.5	0.0	0.0	conc
100207_N28_B_38_a	0.0663	8.4	0.0111	7.7	0.3485	0.0433	7.8	65.1	5.3	71.2	5.5	0.0	0.0	conc
100204_N28_D_02_a	0.0686	26.2	0.0114	25.1	0.4583	0.0431	18.6	67.3	17.1	73.1	18.2	0.0	0.0	conc
100207_N28_B_32_a	0.0697	7.7	0.0115	7.0	0.4535	0.0441	3.3	68.4	5.1	73.8	5.2	0.0	0.0	conc
100204_N28_C_04_a	0.0694	11.9	0.0116	11.3	0.4013	0.0429	11.2	68.2	7.9	74.5	8.4	0.0	0.0	conc
100204_N28_B_01_a	0.0756	5.4	0.0121	4.1	0.3601	0.0455	3.0	74.0	3.9	77.3	3.1	0.0	0.0	conc
100204_N28_B_18_a	0.2082	32.5	0.0344	26.8	0.4144	0.0446	18.9	192.0	57.0	218.1	57.4	0.0	0.0	conc
100204_N28_D_06_a	0.3776	17.7	0.0578	18.6	0.5535	0.0459	5.9	325.3	49.3	362.4	65.5	0.0	0.0	conc
100204_N28_D_32_a	0.0124	38.9	0.0071	23.5	0.2430	0.0129	24.8	12.5	4.8	45.7	10.7	0.0	0.0	disc
100204_N28_D_09_a	0.0358	16.8	0.0085	10.9	0.2794	0.0305	13.0	35.8	5.9	54.9	6.0	0.0	0.0	disc
100207_N28_A_12_a	0.0167	16.3	0.0091	8.8	0.2656	0.0133	16.3	16.8	2.7	58.7	5.2	0.0	0.0	disc
100204_N28_C_28_a	-0.0165	188.1	0.0092	26.6	0.0601	-0.0134	134.8	-16.9	-32.0	59.0	15.6	0.0	0.0	disc
100207_N28_A_08_a	-0.1791	18.9	0.0107	12.2	0.2294	-0.1203	14.0	-200.4	-41.8	68.8	8.4	0.0	0.0	disc
100204_N28_D_26_a	0.0624	7.6	0.0111	6.2	0.3936	0.0407	4.8	61.4	4.5	71.3	4.4	0.0	0.0	disc
100207_N28_B_35_a	0.0242	31.8	0.0113	15.3	0.0780	0.0157	30.3	24.2	7.6	72.3	11.0	0.0	0.0	disc
100204_N28_D_33_a	0.0351	17.0	0.0127	13.9	0.4321	0.0200	8.5	35.0	5.9	81.1	11.2	0.0	0.0	disc
100204_N28_C_20_a	0.0228	17.0	0.0127	15.4	0.3781	0.0130	14.0	22.8	3.8	81.4	12.4	0.0	0.0	disc
100204_N28_D_01_a	-0.0176	18.9	0.0129	18.1	0.4967	-0.0100	7.0	-18.0	-3.4	82.4	14.8	0.0	0.0	disc
100204_N28_D_41_a	0.0164	30.0	0.0130	19.4	0.2814	0.0093	15.7	16.5	4.9	83.1	16.1	0.0	0.0	disc
100204_N28_D_18_a	0.0675	4.2	0.0132	3.8	0.4622	0.0371	2.5	66.3	2.7	84.5	3.2	0.0	0.0	disc
100204_N28_B_21_a	0.0304	11.1	0.0132	10.6	0.4824	0.0169	4.7	30.4	3.3	84.7	8.9	0.0	0.0	disc
100204_N28_D_29_a	0.0254	5.8	0.0135	4.0	0.3663	0.0136	2.9	25.4	1.5	86.3	3.5	0.0	0.0	disc
100207_N28_B_28_a	-0.2137	38.3	0.0136	31.3	0.3354	-0.1148	30.7	-244.1	-106.2	87.0	27.0	0.0	0.0	disc
100204_N28_D_15_a	0.0542	6.4	0.0137	5.3	0.3907	0.0286	4.9	53.6	3.3	87.5	4.6	0.0	0.0	disc
100207_N28_A_03_a	-0.0765	27.2	0.0140	14.9	0.1294	-0.0398	21.2	-80.8	-22.9	89.7	13.3	0.0	0.0	disc
100204_N28_C_21_a	0.0505	12.5	0.0141	11.3	0.4181	0.0260	9.1	50.0	6.1	90.4	10.1	0.0	0.0	disc
100204_N28_B_04_a	0.0590	11.8	0.0143	11.1	0.4719	0.0294	3.0	58.2	6.7	91.7	10.1	0.0	0.0	disc
100207_N28_A_04_a	-0.0603	64.0	0.0147	60.8	0.3003	-0.0299	60.6	-63.1	-41.7	93.8	56.7	0.0	0.0	1.e.
100207_N28_B_34_a	0.0438	10.6	0.0147	8.6	0.3100	0.0216	8.7	43.5	4.5	93.9	8.0	0.0	0.0	disc
100204_N28_C_36_a	0.0757	5.1	0.0149	4.9	0.4930	0.0367	3.1	74.1	3.7	95.6	4.7	0.0	0.0	disc
100204_N28_B_12_a	-0.0481	4.9	0.0153	4.2	0.4725	-0.0229	2.1	-50.0	-2.5	97.8	4.0	0.0	0.0	disc

Continues on following page

Table 2.2: Isotopic measurements of detrital zircon samples

File name	$^{207}\text{Pb}/^{235}\text{U}$ ratio	RSE (%)	$^{206}\text{Pb}/^{238}\text{U}$ ratio	2RSE (%)	Rho	$^{207}\text{Pb}/^{206}\text{Pb}$ ratio	2RSE (%)	$^{207}\text{Pb}/^{238}\text{U}$ age (Ma)	2RSE (Ma)	$^{206}\text{Pb}/^{238}\text{U}$ age (Ma)	2RSE (Ma)	$^{207}\text{Pb}/^{206}\text{Pb}$ age (Ma)	2RSE (Ma)	Quality*
100204_N28_B_24_a	0.0929	10.3	0.0155	10.3	0.4993	0.0432	8.8	90.2	8.9	98.9	10.1	10.2	10.1	disc
100204_N28_B_05_a	0.0836	2.9	0.0156	2.7	0.4919	0.0389	0.7	81.5	2.3	99.6	2.7	2.7	2.7	disc
100207_N28_B_30_a	0.0094	13.7	0.0164	12.8	0.4807	0.0042	4.1	9.5	1.3	104.6	13.3	12.7	13.3	disc
100207_N28_B_36_a	0.0492	17.1	0.0166	16.0	0.4840	0.0218	6.2	48.7	8.1	106.2	16.9	15.9	16.9	disc
100207_N28_B_31_a	0.0544	7.1	0.0166	5.1	0.3335	0.0237	4.5	53.8	3.7	106.2	5.3	5.0	5.3	disc
100204_N28_C_16_a	-0.0156	19.0	0.0221	13.1	0.2787	-0.0052	10.9	-15.9	-3.0	140.9	18.3	13.0	18.3	disc
100207_N28_B_26_a	0.0225	14.0	0.0233	10.4	0.2564	0.0070	11.3	22.6	3.1	148.3	15.3	10.3	15.3	disc
100204_N28_D_03_a	0.0952	10.9	0.0237	10.4	0.4831	0.0285	3.8	92.3	9.6	151.2	15.5	10.2	15.5	disc
100204_N28_D_21_a	0.0630	12.1	0.0248	9.6	0.4025	0.0186	4.8	62.0	7.3	158.2	15.0	9.5	15.0	disc
100204_N28_D_19_a	0.0793	3.3	0.0262	2.9	0.4654	0.0220	1.1	77.5	2.4	166.8	4.7	2.8	4.7	disc
100204_N28_C_02_a	0.0933	6.4	0.0297	6.0	0.5213	0.0230	3.0	90.6	5.6	188.6	11.1	5.9	11.1	disc
100207_N28_A_01_a	-0.1823	14.9	0.0311	14.6	0.5045	-0.0431	12.1	-204.4	-33.8	197.5	28.4	14.4	28.4	disc
100204_N28_D_16_a	0.1551	8.3	0.0312	8.4	0.5057	0.0356	1.3	146.4	11.4	197.9	16.4	8.3	16.4	disc
100207_N28_B_29_a	0.0580	8.2	0.0322	8.2	0.5103	0.0129	2.8	57.3	4.6	204.4	16.5	8.0	16.5	disc
100204_N28_C_19_a	0.1785	11.0	0.0324	10.9	0.5114	0.0400	7.5	166.7	17.0	205.6	22.1	10.7	22.1	disc
100204_N28_D_36_a	2.6574	11.8	0.2534	11.6	0.4937	0.0751	1.6	1316.7	87.2	1456.2	151.6	10.4	151.6	disc

*conc=concordant; for ages >1000 Ma based on a comparison of $^{206}\text{Pb}/^{238}\text{U}$ ages with $^{206}\text{Pb}/^{207}\text{Pb}$ ages and a discordance of <10%, for ages <1000 Ma based on Concordia plots: only measurements which touch the Concordia line are considered concordant, i.e.=large error, >30% error on the $^{206}\text{Pb}/^{238}\text{U}$ age.

Chapter 3

Testing the applicability of garnet, monazite, allanite and xenotime as prograde geochronometers in different zones of the Chugach Metamorphic Complex

Abstract In this chapter, the occurrence of garnet, monazite, allanite and xenotime in the Chugach Metamorphic Complex of Alaska is investigated in order to reveal the applicability of these minerals as prograde geochronometers. Garnet is ubiquitous throughout the complex, but element zoning reveals that the garnets do not preserve prograde growth zoning. Garnets of one sample from the gneiss zone give an Sm-Nd age of 47.8 ± 6.3 Ma, which is within error of U-Pb zircon ages from peak metamorphic zircon overgrowths. No monazite is present in the rocks of the phyllite zone. Small, unzoned monazite is abundant above $\sim 550^\circ\text{C}$ and 3.4 kbar in the schist zone. An attempt of dating these small monazites was not successful. Large, complexly zoned monazites are present in the gneiss zone. U-Pb SHRIMP dating of four samples from the gneiss zone range from 51.5 ± 0.9 Ma to 53.5 ± 0.9 Ma and lie within error of U-Pb zircon peak ages. Allanite is present (a) in the low-grade phyllites, (b) as peak mineral in the gneiss zone at pressures above ~ 8 kbar in CaO-rich bulk compositions, and (c) as retrograde minerals in fluid-flow zones. Allanite might therefore be a powerful potential geochronometer to date prograde metamorphism in the phyllite zone, the peak pressure in the gneiss zone or retrograde fluid flow. Xenotime is present in all metamorphic zones, but its growth history is difficult to constrain, which limits its applicability as a geochronometer.

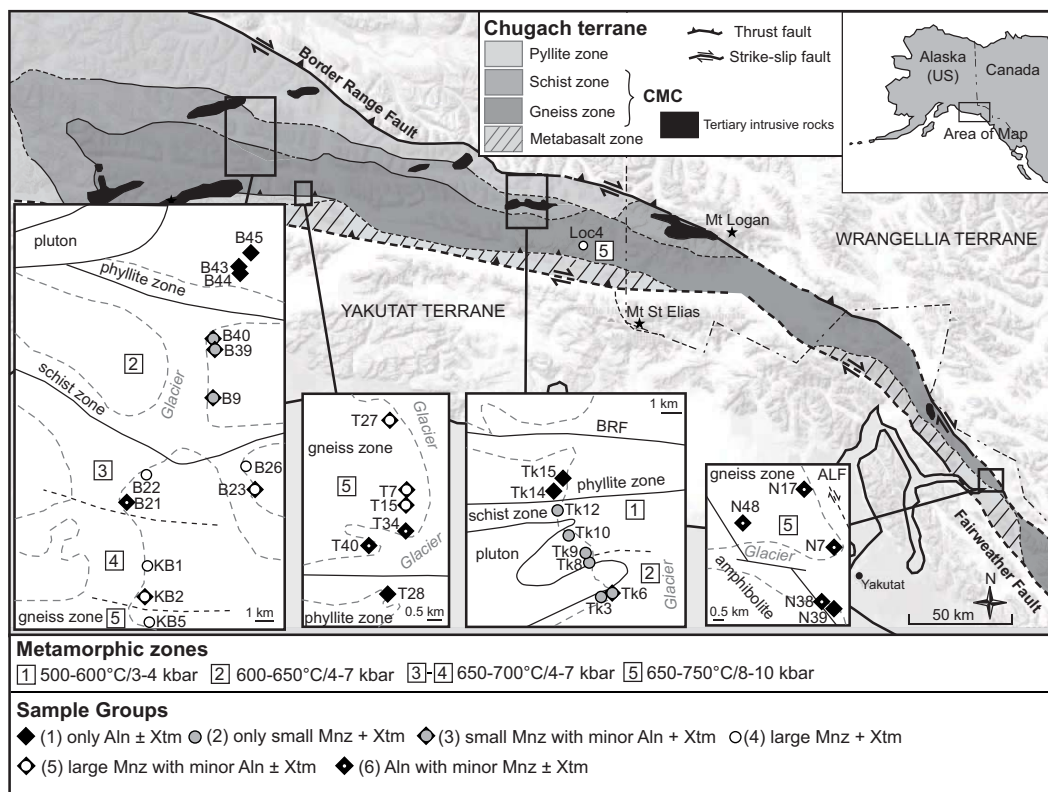


Figure 3.1: Geological Map of the Chugach Metamorphic Complex (after Hudson & Plafker, 1982). Small insets show the localities of the 32 samples described in this chapter. Note that sample Loc4 is outside of the small inset maps. (1)-(5) metamorphic zones as defined by the mineralogy of (calcareous) metapelites after Bruand (2010). (1) Andalusite-bearing schist zone, (2) sillimanite-garnet-bearing schist zone, (3) northern migmatite zone with Sil+Grt+Liq±Kfs, (4) central migmatite zone with Grt+Liq±Kfs, (5) southern migmatite zone with Grt+Ms+Liq±Kfs±Sil. The 32 samples are divided into six groups depending on the occurrence of monazite, allanite and xenotime (see text for further explanation).

3.1 Introduction

The retrograde part of the evolution of a metamorphic complex, i.e. the timing of its cooling and exhumation, is often well constrained by several geo- and thermochronological systems (e.g. Chap. 5). The timing of its heating and burial however, is much more difficult to constrain (e.g. Foster & Parrish, 2003). Similar to dating of cooling and exhumation, geochronometers have to be found which can be linked with particular points in the prograde *PT* space. One possibility is to date major rock-forming phases which were simultaneously used to deduce the *PT* information, such as garnet (e.g. Mezger et al., 1989; Vance & Harris, 1999; Vance & Mahar, 1998; Vance et al., 2003). Another possibility is to date accessory minerals, which can be linked to the prograde evolution of the major phases in the rock by

textural or microchemical analyses (e.g. Wing et al., 2003; Foster & Parrish, 2003; Vance et al., 2003; Foster et al., 2004; Janots et al., 2009).

A well-studied and widely-used accessory mineral in the geochronology of prograde metamorphism is monazite ((LREE, Th, U)PO₄), since it incorporates relatively high concentrations of U and Th, has typically low concentrations of common Pb and is highly resistant to diffusive Pb-loss, making it suitable for U-Pb geochronology (e.g. Parrish, 1990; Harrison et al., 2002). However, linking monazite formation ages with the *PT* evolution of the host rock is not always straightforward (e.g. Vance et al., 2003). Monazite may occur as detrital grains at or below greenschist facies, and may be stable as metamorphic monazite in rocks of appropriate bulk composition at all metamorphic grades at and above greenschist facies (e.g. Spear & Pyle, 2003). Due to this large potential stability range of monazite in metamorphic rocks, the formation conditions of monazite in a particular sample have to be investigated prior to or accompanying the geochronological analyses. This can be done by studying natural samples of similar bulk composition occurring over a range of metamorphic conditions and/or by studying samples with variable bulk composition but similar metamorphic grade (e.g. Smith & Barreiro, 1990; Kingsbury et al., 1993; Wing et al., 2003; Foster et al., 2004; Kohn & Malloy, 2004; Fitzsimons et al., 2005; Rasmussen et al., 2006; Janots et al., 2006, 2008; Kim et al., 2009). A different approach is to chemically classify zoned monazites and to relate the composition and age of these zones to the composition of major phases such as garnet in the same sample (e.g. Williams et al., 1999; Foster et al., 2000; Pyle et al., 2001; Pyle & Spear, 2003; Gibson et al., 2004; Kohn et al., 2005; Williams et al., 2006, 2007).

Another, but less-studied and less widely-used accessory mineral in the geochronology of prograde metamorphism is allanite ((Ca,REE,Th)₂Al₂(Fe,Al)₃Si₃O₁₂(OH)), an epidote-group mineral. It occurs in a wide range of rock types and under a variety of metamorphic conditions (e.g. Smith & Barreiro, 1990; Finger et al., 1998; Hermann, 2002; Wing et al., 2003; Krenn et al., 2008; Janots et al., 2006, 2007, 2008). It recently became possible to date allanite in-situ (Gregory et al., 2007), which has proven useful in dating prograde mineral sequences (e.g. Janots et al., 2009). Besides monazite and allanite, xenotime (YPO₄) is also a wide-spread accessory mineral in metamorphic rocks and may incorporate a considerable amount of REE as well as Th and U, making it a potential geochronometer (e.g. Hetherington et al., 2008). Indeed, xenotime dating has been successfully applied in a range of different metamorphic and fluid flow studies (e.g. Rasmussen et al., 2007, 2009; Wall et al., 2008).

In this chapter, the occurrence of garnet, monazite, allanite and xenotime in different zones of the Chugach Metamorphic Complex is investigated in order to test the applicability of these minerals as prograde geochronometers. Firstly, the petrology of garnet in the CMC is shortly reviewed and limited Sm-Nd dating is presented. Secondly, the results of a search for monazite, allanite and xenotime in the different metamorphic zones of the CMC and in different bulk compositions is presented, followed by a chemical characterization and U-Pb SHRIMP dating of monazites from the gneissic core. Finally, the petrological context for

the distribution of monazite, allanite and xenotime is discussed and implications for dating the prograde history of the CMC are evaluated. Mineral abbreviations used throughout this chapter are according to Whitney & Evans (2010).

3.2 Metamorphic zones in the Chugach Metamorphic Complex

The Chugach Metamorphic Complex (CMC) of southern Alaska is a ~10-50 km wide and ~350 km long upper amphibolite facies metamorphic complex which developed in a Late Cretaceous to Paleocene accretionary prism (Fig. 3.1; Hudson & Plafker, 1982). The accretionary prism consists of greenschist-facies conglomerates, impure sandstones, marls and claystones, which are intercalated with mafic volcanic rocks (e.g. Nilsen & Zuffa, 1982). This original layering of different sedimentary and volcanic rocks in the accretionary prism leads to the presence of pelitic, calcareous, quarzo-feldspatic and basic protoliths within the metamorphic complex. The complex consists of two macroscopically different zones: a northern schist zone composed of fine-grained biotite-quartz-plagioclase schist, and a southern gneiss zone composed of layered migmatitic gneisses (Fig. 3.1; Hudson & Plafker, 1982).

The mineralogy observed in the CMC varies depending on metamorphic grade and on the bulk rock composition. In the schist zone, metapelitic to CaO-rich metapelitic rocks show two different metamorphic zones: a structurally higher andalusite-bearing zone (zone 1, Figs. 3.1, 3.2a) and a structurally lower (western part of the complex, Fig. 3.1) or contact-metamorphic (central part of the complex, Fig. 3.1) garnet-sillimanite-bearing zone (zone 2, Figs. 3.1, 3.2b; Bruand, 2010). In the gneiss zone of the western part of the complex, high-CaO metapelites define three different zones: a northern zone where the peak paragenesis is defined by garnet, sillimanite, melt and minor K-feldspar (zone 3, Fig. 3.1), a central zone where sillimanite disappears and only garnet, melt and minor K-feldspar are stable (zone 4, Figs. 3.1, 3.2c) and a southern zone where muscovite appears together with garnet, melt and minor K-feldspar (zone 5, Fig. 3.1; Bruand, 2010). Farther east in the gneiss zone, only zone 5 is present, where sillimanite is stable in addition in metapelitic rocks. Staurolite was found as small (<50 μm), retrograde crystals in several samples both in the schist and gneiss zones, and as large (>1 mm) crystals in one sample of the south-eastern part of the complex (sample N48, Fig. 3.2d; Bruand, 2010). Metabasic rocks occur mainly in the southern and eastern parts of the complex (Fig. 3.1). They contain abundant amphibole and garnet (Fig. 3.2e; Bruand, 2010). Close to major faults, rocks are highly altered and destabilized into chlorite, muscovite and epidote (Fig. 3.2f).

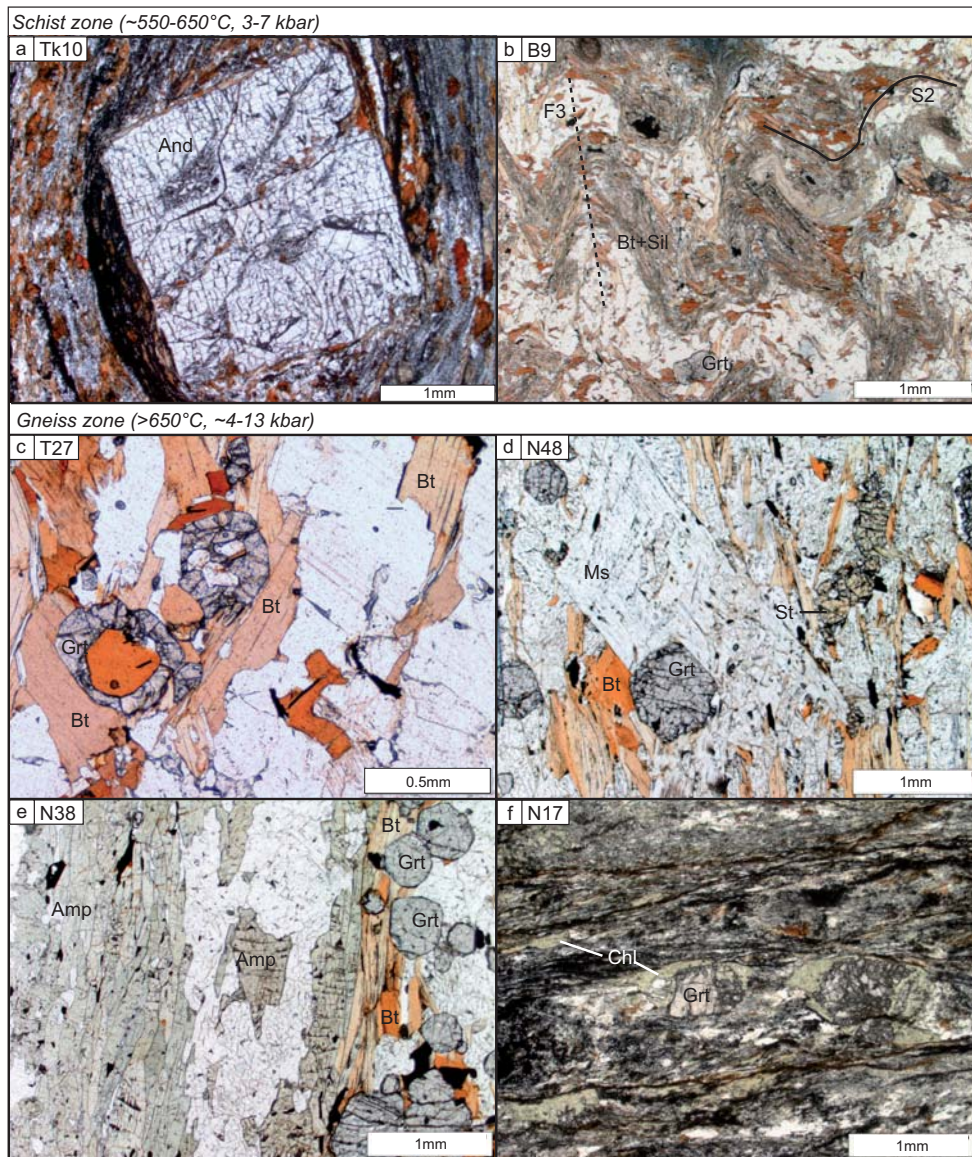


Figure 3.2: Representative thin section photographs of the different mineralogies observed in the CMC. The sample numbers are given in the upper left of the images. **(a)** Andalusite crystal representative for zone 1 of the schist zone of the CMC. **(b)** Fine-grained biotite-sillimanite matrix with garnet representative for zone 2 of the schist zone of the CMC. The foliation defined by biotite and sillimanite (S_2 after Pavlis & Sisson, 1995) is folded into tight, upright folds (F_3). **(c)** Coarse-grained biotite-quartz-plagioclase matrix with garnet representative for the metapelitic to calcareous metapelitic bulk rock compositions in the gneiss zone of the CMC. **(d)** Sample N48 from the south-eastern part of the CMC (metamorphic zone 5) contains biotite, staurolite, garnet, and late muscovite. **(e)** Amphibole-garnet-biotite matrix representative for meta-basic samples from the south-eastern part of the CMC. **(f)** Highly altered (chlorite-muscovite-epidote) matrix of samples exposed close to the Art-Lewis Fault (Fig. 3.1).

Based on the observed mineralogy, *PT* conditions derived from classical thermobarometry (biotite-garnet, graphite), average *PT* calculations (THERMOCALC) and pseudosection modelling (THERMOCALC) are the following: ~400-550°C in the phyllite zone, ~500-600°C and ~3-4 kbar in zone 1, ~600-650°C and ~4-7 kbar in zone 2, ~650-700°C and ~4-7 kbar in zones 3-4 and ~650-750°C and ~8-13 kbar in zone 5 (Fig. 3.1; Bruand, 2010).

3.3 Garnet as possible prograde geochronometer in the Chugach Metamorphic Complex?

During metamorphism, garnet growth may begin before the rocks reach their metamorphic peak, and under certain circumstances the cores of these garnets may preserve prograde growth zoning (e.g. Spear, 1993). Dating these prograde garnet cores may reveal temporal information on the prograde metamorphic history (e.g. Vance & Mahar, 1998; Vance & Harris, 1999; Vance et al., 2003; Stowell & Tinkham, 2003). However, if the garnets stayed at elevated temperatures (close to or above the solidus), a potential growth zoning may be equilibrated by diffusion and information on the prograde history of the samples may be lost (e.g. Spear, 1993).

Garnet is ubiquitous throughout the schist and gneiss zones of the CMC in rocks with appropriate bulk composition. Element mapping of garnets from the entire CMC revealed considerable differences between garnets from the western/central parts and the south-eastern part of the CMC (Bruand, 2010). Garnets from the western and central parts of the complex have very homogenous core compositions, and show only a slight decrease in Mg and an increase in Mn in the outermost rims (Bruand, 2010). This suggests that these garnets equilibrated at high temperatures and do not preserve any information on the prograde part of the metamorphic history. In contrast, garnets from the south-eastern CMC show strong internal zoning in Fe, Ca, Mg and Mn, suggesting that these garnets conserve growth zoning (Bruand, 2010). However, garnet isopleths ($\text{Ca}/(\text{Ca}+\text{Fe}+\text{Mg})$), plotted on a pseudosection for the bulk composition of these samples, indicate that the growth zoning of these garnets probably formed *after* the metamorphic peak on the retrograde part during decompression (Bruand, 2010). This interpretation is supported by the observation that the garnets grow across the foliation (Figs. 3.2d, 3.3b). Therefore, the garnets of the CMC are probably not suitable as prograde geochronometers.

Nevertheless, an attempt of obtaining a Sm-Nd garnet age for one sample was made. Sample N48 (Figs. 3.1, 3.2d) contains abundant, relatively inclusion-free garnets and it was therefore selected for Sm-Nd isotopic dating. The garnets are 0.2-1.5 mm in size, euhedral and grow across the foliation (Figs. 3.2d, 3.3a and b). They conserve growth zoning and contain ~ μm inclusions of ilmenite and graphite (Figs. 3.3a-b). In a few crystals ~ μm inclusions of monazite were observed in BSE mode. No attempt was made of separating garnet cores from garnet rims due to the small size of the garnets.

Table 3.1: Sm-Nd isotope data for sample N48

Analysis	Sm (ppm)	Nd (ppm)	$^{147}\text{Sm}/^{144}\text{Nd}$	$^{143}\text{Nd}/^{144}\text{Nd}$	$\pm 2\sigma$
N48 WR	4.70	21.8	0.1303	0.512629	0.000003
N48 Grt1	1.51	5.31	0.1716	0.512623	0.000002
N48 Grt2	1.05	2.20	0.2883	0.512659	0.000004

3.3.1 Sm-Nd dating: Analytical technique

Mechanical and chemical sample preparation for Sm-Nd isotope analyses was performed at the Geological Survey of Austria in Vienna. The garnets were separated by standard methods of crushing, grinding, sieving and magnetic separation, were then hand-picked under the binocular from the sieve fraction 0.2-0.3 mm and finally cleaned in water and acetone. Whole rock powder was obtained by milling a matchbox-sized sample. About 100 mg of whole rock powder and two 100 mg fractions of garnet were prepared for dissolution. The two garnet fractions (Grt1 and Grt2) were leached in 6n HCL at 70°C for 30 minutes. Garnet fraction Grt2 was then crushed in an agate mortar and additionally leached in H₂SO₄ at 140°C for 24h in order to remove potential phosphate inclusions (Anczkiewicz & Thirlwall, 2003). The chemical sample preparation follows the procedure described by Sölva et al. (2005). Isotopic measurements were done at the Department of Geological Sciences at the University of Vienna. Spiked Sm and Nd ratios were measured at a Finnigan® MAT 262, whereas unspiked Nd ratios were analysed at a ThermoFinnigan® Triton TI TIMS. All elements were run from Rhenium double filaments. During the periods of measurements the La Jolla standard yielded $^{143}\text{Nd}/^{144}\text{Nd} = 0.511846 \pm 2$ (n=7) on the Triton TI. The error on the $^{147}\text{Sm}/^{144}\text{Nd}$ measurement is taken as $\pm 1\%$ (2σ). Calculation of isochron ages was done with the software Isoplot/Ex (Ludwig, 2003).

3.3.2 Sm-Nd dating: Results and interpretation

The results of the Sm-Nd measurements are given in table 3.1 and are displayed in figure 3.3c. The whole rock contains 4.7 ppm Sm and 21.8 ppm Nd, resulting in a $^{147}\text{Sm}/^{144}\text{Nd}$ ratio of 0.130 (Tab. 3.1). The garnets contain lower Sm (1.5 and 1.0) and Nd (5.3 and 2.2) contents, resulting in $^{147}\text{Sm}/^{144}\text{Nd}$ ratios of 0.172 and 0.288 (Tab. 3.1). Comparing the two garnet fractions, Grt2 (additionally leached) shows lower REE contents than Grt1, indicating that tiny REE-rich inclusions have been partly or entirely (?) dissolved by leaching in H₂SO₄. The REE-rich phosphate inclusions probably are monazite, which has been observed as tiny inclusions in garnet of this sample.

The three data points derived from whole rock measurements and two garnet fractions do not define an isochron (Fig. 3.3c). Combining the whole rock measurement with Grt2 gives

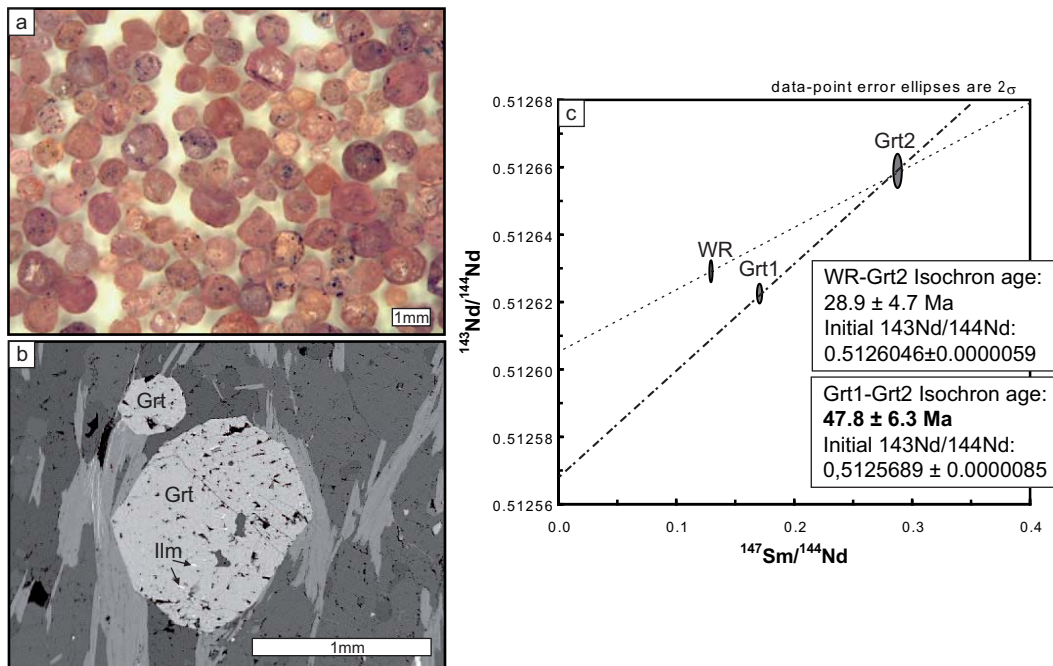


Figure 3.3: (a) Photograph of garnet separate from sample N48 used for Sm-Nd isotope dating. Black spots are graphite inclusions which do not affect the isotope measurements. (b) BSE image of garnet crystal from sample N48, showing $\sim\mu\text{m}$ inclusions of ilmenite. Similar $\sim\mu\text{m}$ inclusions of monazite were also detected. (c) Isochron diagram showing whole rock and Grt1 and Grt2 fractions. They do not lie on an isochron. The isochron age defined by the two garnet fractions is broadly coeval with U-Pb ages obtained from metamorphic zircon from this region.

an age of 28.9 ± 4.7 Ma. Combining Grt1 with Grt2 gives an age of 47.8 ± 6.3 Ma (Fig. 3.3c). This second age is broadly coeval with a U-Pb age of metamorphic zircon from the same region, which is 51.3 ± 0.7 Ma (Chap. 4). We therefore interpret this second age as approximating the formation age of the garnet. The relatively high error on the age results from the low spread in the $^{147}\text{Sm}/^{144}\text{Nd}$ ratio of the two fractions. The whole rock shows the lowest $^{147}\text{Sm}/^{144}\text{Nd}$ ratio and is situated above the Grt1-Grt2 isochron, suggesting that it contains a REE-rich component with a high $^{143}\text{Nd}/^{144}\text{Nd}$ ratio, which is under-represented in the garnet fractions. This component may be derived from detrital zircon cores which are abundant in the rocks of the CMC. These detrital zircon cores show dominantly ages of ~ 60 - 120 Ma (Chap. 2), and are overgrown by tiny ~ 51 Ma old metamorphic rims (Chap. 4).

The ϵNd value of the whole rock gives some information on the provenance of the sediments in which the CMC developed. The ϵNd value of sample N48 is -0.17 , and recalculated to

50 Ma is 0.25. This is similar or even less radiogenic than the ϵNd values measured by Farmer et al. (1993) for lower-grade metasedimentary rocks of the Valdez Group which are exposed along-strike of the CMC farther west. Such a ϵNd value is in agreement with the provenance of the sediments from a continental magmatic Mesozoic arc, probably the Coast Plutonic Complex exposed to the south-east of the CMC (Farmer et al., 1993).

In summary, the garnets of the CMC are not suited for obtaining a prograde growth age, because their compositions either equilibrated at the metamorphic peak (western and central parts of the complex) or because they conserve growth zoning from the retrograde part of the PT path (south-eastern part of the complex). In order to obtain a prograde garnet age the following criteria must fulfil: (1) The presence of prograde growth zoning in garnet has first to be shown by detailed petrological and thermobarometric work, (2) The garnets should preferentially be big, so that cores and rims can be separated, (3) The garnets should be inclusion-free, especially of REE-rich inclusions which can heavily disturb the Sm-Nd systematics, (4) in order to obtain a precise age, a considerable spread in $^{147}\text{Sm}/^{144}\text{Nd}$ ratios between the different fractions is needed, and (5) if the whole rock fraction is analysed as well, the presence of isotopically older REE-bearing phases such as zircon or monazite can disturb the Sm-Nd systematics and make the analysis useless for isochron calculation.

3.4 Monazite, allanite or xenotime as prograde geochronometers in the Chugach Metamorphic Complex?

In order to test the applicability of monazite, allanite or xenotime as prograde geochronometers in the different zones of the CMC, the distribution of these REE-bearing accessory minerals was revealed first. A total of 32 samples from the different metamorphic zones and with varying bulk rock compositions were studied for this purpose (Fig. 3.1, Tab. 3.2). The chemical zonation of monazite was then studied, and four monazite samples were dated by U-Pb SHRIMP. The results of these investigations are described below.

3.4.1 Analytical techniques

Major element bulk rock compositions of all samples were obtained with a Siemens Pioneer S4 WD-XRF at the Department of Earth Sciences, University of Graz. Identification and high-contrast BSE imaging of accessory minerals was done on polished thin sections at the Department of Earth Sciences, University of Graz, with a JEOL JSM-6310 scanning electron microscope, equipped with an IDIX EDX system for mineral identification, working at 15 kV, ~6 nA and 15 mm working distance.

Element mapping and quantitative chemical analyses of monazites were obtained on a JEOL JXA 8200 microprobe at the Department for Applied Geosciences, University of Leoben. Monazite element maps were obtained with 30 kV, ~10 nA, step size of ~0.2-0.4 μm and dwell times of 20-50 ms. Quantitative analyses of monazites were obtained using synthetic and natural mineral standards and a ZAF data correction scheme. Accelerating voltage was ~20 kV and beam current was 50 nA. $K\alpha$ X-ray lines were used for Si, P and Ca, $L\alpha$ X-ray lines were used for Y, Ce, Dy, La, Pr, Nd, Eu, Ho, Tb and Er and $L\beta$ X-ray lines were used for Sm and Gd.

Trace-element composition of garnet from one sample was measured with LA-ICP-MS at the Research School of Earth Sciences (RSES), ANU, using a pulsed 193 nm ArF Excimer laser with 100 mJ energy at a repetition rate of 5 Hz, coupled to an Agilent 7500 quadrupole ICP-MS. A spot size of 47 μm was used. External calibration was performed relative to NIST 612 glass (Pearce et al., 1996) and internal standardisation was based on Si. Accuracy and reproducibility were evaluated by repeated analyses of a BCR-2G secondary glass standard.

Monazites were separated for U-Pb SHRIMP dating from fist-sized samples by crushing, sieving, magnetic and heavy liquid separation, and then handpicked, mounted in epoxy and polished to expose the grain centers. BSE imaging of the separated monazite grains was done at the Electron Microscope Unit, Australian National University (ANU), with a Cambridge S360 scanning electron microscope working at 15 kV, ~2 nA and a working distance of ~17 mm. U-Pb analyses on monazites were performed with a sensitive high-resolution ion microprobe (SHRIMP II) at the Research School of Earth Sciences (RSES), ANU, using a beam size of ~20 μm . The data were collected in sets of six scans throughout the masses and a reference monazite S440 (424.9 ± 0.4 Ma, Aleinikoff et al., 2006) was analysed each fourth analysis. Energy filtering was applied to eliminate the molecular interference on ^{204}Pb (Rubatto et al., 2001) and to reduce any matrix effect. The analyses were corrected for common Pb based on ^{204}Pb and ^{207}Pb measurements following Williams (1998). The two correction methods deliver results indistinguishable within error. Th-Pb ages, despite being less precise, are generally in agreement with the U-Pb ages. Here ^{204}Pb corrected data are presented in the tables and plotted on Concordia diagrams, and Concordia ages (Ludwig, 1998) are calculated, as well as $^{206}\text{Pb}/^{238}\text{U}$ weighted average ages. The common Pb composition was according to the Stacey & Kramers (1975) model. U-Pb data were collected over one analytical session using the same standard, with the session having a calibration error of 2.7% (2σ), which was propagated to single analyses. Additionally, a 1% error was added to the final Concordia and average ages to account for external errors. Data evaluation and age calculation were done using the software Squid1 and Isoplot/Ex (Ludwig, 2003), respectively.

Table 3.2: List of all samples studied for accessory mineralogy

Sample	Lat (°N)	Long (°W)	Metamorphic Zone	REE- Group*	Mineralogy Qz+Plag+Bt	Mnz ¹	Mnz(i) ²	Xtm	Ap	Ep/Aln ³	Zrn	Ilm	Ttn	Py	Hem	Rt	T ⁴ (°C)	P ⁴ (kbar)	Mnz U-Pb age (Ma)
B43	60.9263	143.2130	phyll.	1	Ms			x	x	x	x	x		x	x	515			
B44	60.9263	143.2130	phyll.	1	Ms				x	x	x	x		x	x	535			
B45	60.9328	143.2025	phyll.	1	Ms			x	x	x	x	x		x		547			
T28	60.6704	142.9123	phyll.	1						x	x		x			432			
Tk14	60.6941	141.5803	phyll.	1	Ms				x	x	x	x				536			
Tk15	60.6965	141.5739	phyll.	1	Ms				x	x	x	x			x	526			
Tk12	60.6878	141.5807	1	2	And-Ms-Grt	x		x	x	x	x	x				543	3.4		
Tk10	60.6820	141.5716	2	2	And-Ms-Grt	x		x	x	x	x	x				645	5.9		
Tk9	60.6752	141.5608	2	2	And-Ms-Grt	x		x	x	x	x	x				>640			
Tk8	60.6731	141.5605	2	2	(And)Sil-Ms-Grt	x		x	x	x	x	x							
Tk6	60.6642	141.5488	2	3	(And)Sil-Ms	x		x	x	xr	x	x							
Tk3	60.6642	141.5488	2	2	(And)Sil-Ms-Grt	x		x	x	x	x	x							
B39	60.8858	143.2384	2	3	Grt-Sil-Ms	x		x	x	xp ² ,xr	x	x				658	6.4		
B40	60.8883	143.2384	2	3	Grt-Sil-Ms	x		x	x	xr	x	x				597			
B9-2	60.8583	143.2362	2	3	Grt-Sil-Ms	x		x	x	xr	x	x				632	6.8		
B21	60.8124	143.3148	3	6	Grt-Sil-Ms	x		x	x	x	x	x						51.5±0.9	
B22	60.8124	143.3148	3	4	Grt-Sil	x		x	x	x	x	x							
B23	60.8110	143.1928	3	5	Grt-Sil	x		x	x	x,xr	x	x	x						
B26	60.8236	143.2033	3	4	Grt-Sil-Ms	x		x	x	x	x	x	x						
KB1	60.7643	143.2881	4	4	Grt-Ms	x		x	x	x	x	x						52.7±0.8	
KB2	60.7643	143.2881	4	5	Grt	x		x	x	xr	x	x							
KB5	60.7381	143.3015	5	4	Ms	x		x	x	x	x	x						53.5±0.9	
T7	60.6960	142.9031	5	5	Amph-Grt	xu		x	x	x	x	x							
T15a	60.6946	142.9069	5	5	Grt-Ms-Chl	x		x	x	x,xr	x	x							
T27	60.7146	142.9147	5	5	Grt-Ms	x		x	x	xr	x	x						52.4±0.7	
T40	60.6828	142.9238	5	6	Ms	xu		x	x	x	x	x							
Loc4	60.5544	141.3030	5	4	Grt-Sil-Ms	x		x	x	x	x	x							
N7	59.8116	138.8131	5	6	Grt-Ms-Chl	xu			x	x	x	x							
N17	59.8330	138.8322	5	6	Grt-Ms-Chl	xu			x	x	x	x							
N38	59.7914	138.8207	5	6	Amph-Grt	xu			x	x	x	x							
N39	59.7914	138.8207	5	1	Amph-Grt	xu			x	x	x	x							
N48	59.8210	138.8783	5	6	Grt-Sil-St	x		x	x	x	x	x							

*REE-group as described in text and figure 3.1. x=mineral is present in matrix. ¹xu=mineral is metastable, ²(i)=mineral occurs as inclusion in garnet and/or andalusite, ³xr=mineral occurs as retrograde fibres around monazite, ⁴PT data from Bruand (2010)

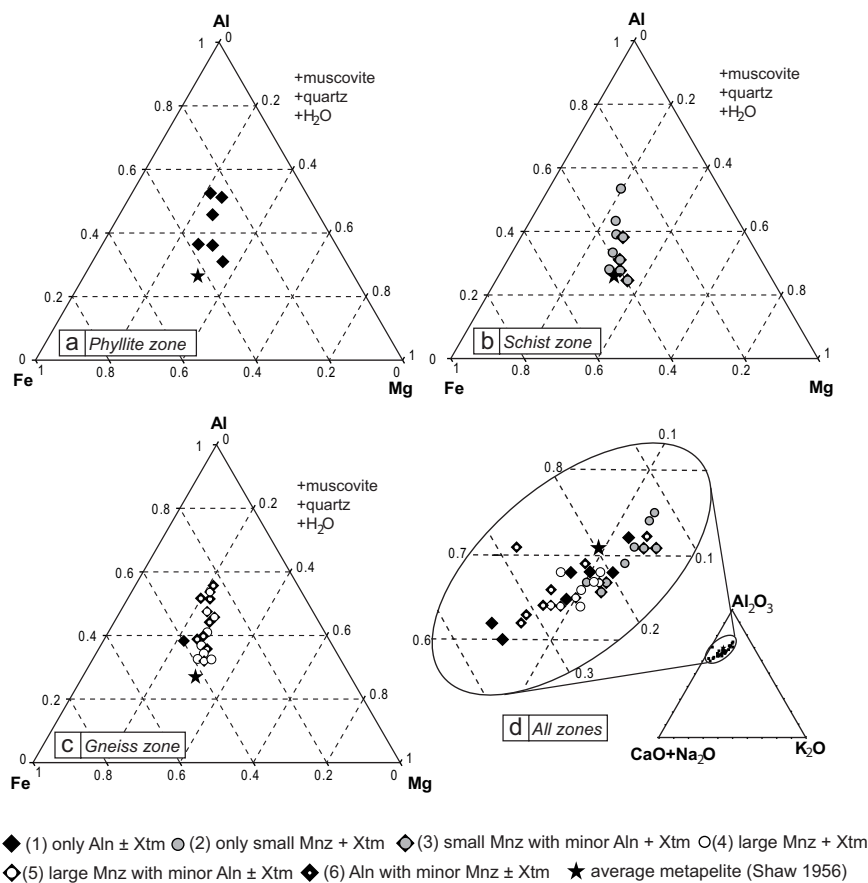


Figure 3.4: Bulk rock compositions of all samples investigated. **(a)** AFM diagram of samples from the phyllite zone. **(b)** AFM diagram of samples from the schist zone. **(c)** AFM diagram of samples from the gneiss zone. **(d)** Al_2O_3 - $\text{CaO}+\text{Na}_2\text{O}$ - K_2O ternary diagram of all samples. No simple relationship between bulk rock composition and dominant REE-bearing accessory phase is observed in the gneiss zone, but there is a tendency of large, complex monazites (group 4) being developed in compositions close to an average pelite composition.

3.4.2 Distribution of monazite, allanite and xenotime throughout the CMC in varying bulk rock compositions

From the 32 samples studied, 6 samples come from the phyllite zone outside of the CMC, 9 samples are from the schist zone of the CMC and 17 samples come from the gneiss zone (Fig. 3.1, Tab. 3.2). The studied samples are representative for the variation in mineralogy observed in the entire CMC (Fig. 3.2, Tab. 3.2). Sample T28 is the lowest-grade sample, and contains only quartz and plagioclase as major phases. The remaining five phyllite zone samples contain quartz, plagioclase, biotite and muscovite. In the schist and gneiss zone, apart from quartz, plagioclase and biotite, typical metapelitic assemblages with garnet and andalusite/sillimanite as major phases are present in 14 samples. Nine samples show

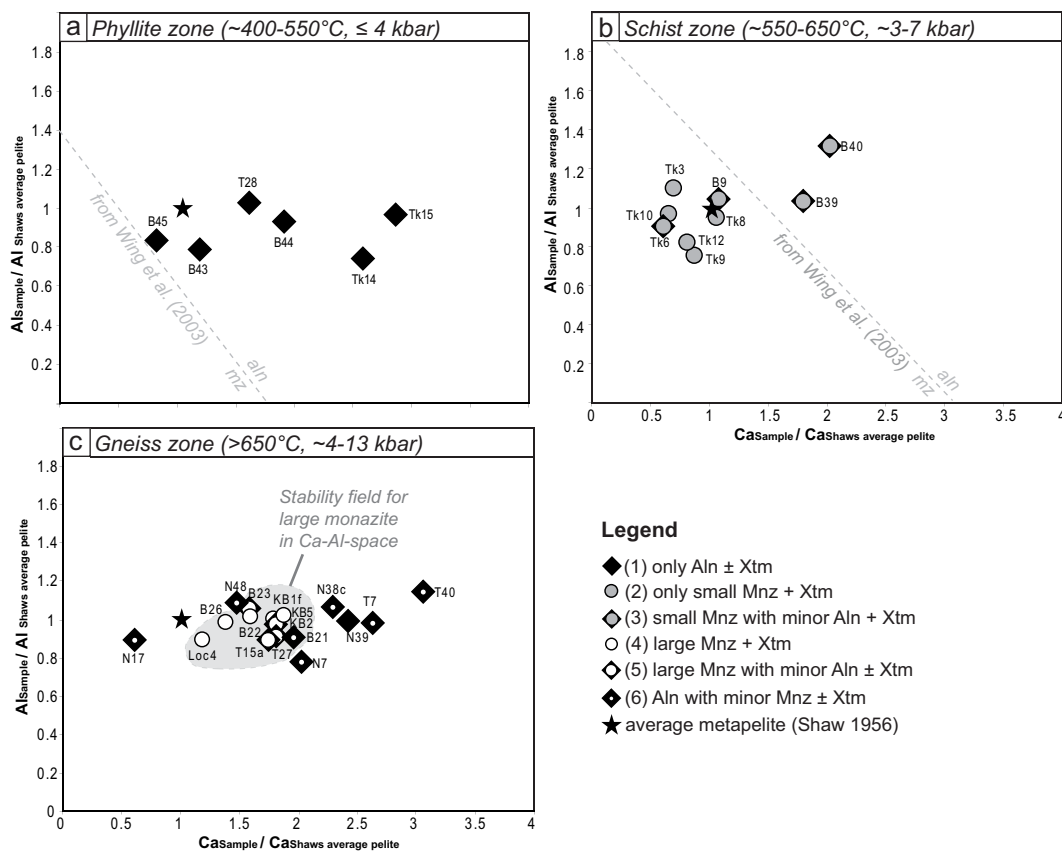


Figure 3.5: Bulk rock Ca versus Al contents relative to the average pelite composition of Shaw (1956) for the 32 samples from the three different metamorphic zones of the CMC. **(a)** In the phyllite zone, only allanite is present, **(b)** in the schist zone, mainly relatively small (<50 μm) monazite with minor allanite is present, and **(c)** in the gneiss zone both allanite and relatively large (~20-100 μm) monazite occur depending on the bulk composition, the mineralogy and the metamorphic and the fluid history of the samples (see text for explanation). Note that for the schist zone, our Mnz/Aln stability field does not correspond to the Mnz/Aln field shown by Wing et al. (2003) for rocks of similar metamorphic grade (see text for explanation).

only garnet, and/or muscovite as additional major phases, and are more likely derived from greywacke protoliths, or in the case of sample T40, represent an orthogneiss (Chap. 4). Finally, three samples contain amphiboles and garnet, and are derived from basic volcanic rocks (Tab. 3.2).

Most of the 32 samples studied have bulk rock compositions with SiO₂, Al₂O₃, Fe₂O₃ and MgO values similar to average pelites (e.g. Shaw, 1956) but with generally higher CaO, Na₂O and lower K₂O values (Tab. 3.3, Figs. 3.4 and 3.5). In AFM diagrams, the compositions of samples from the phyllite, schist and gneiss zones show similar variations (Fig. 3.4a-c): The Al-component varies most, between 0.2 and 0.6, and is in general similar or higher than the average pelite composition of Shaw (1956). The Fe- and Mg-components

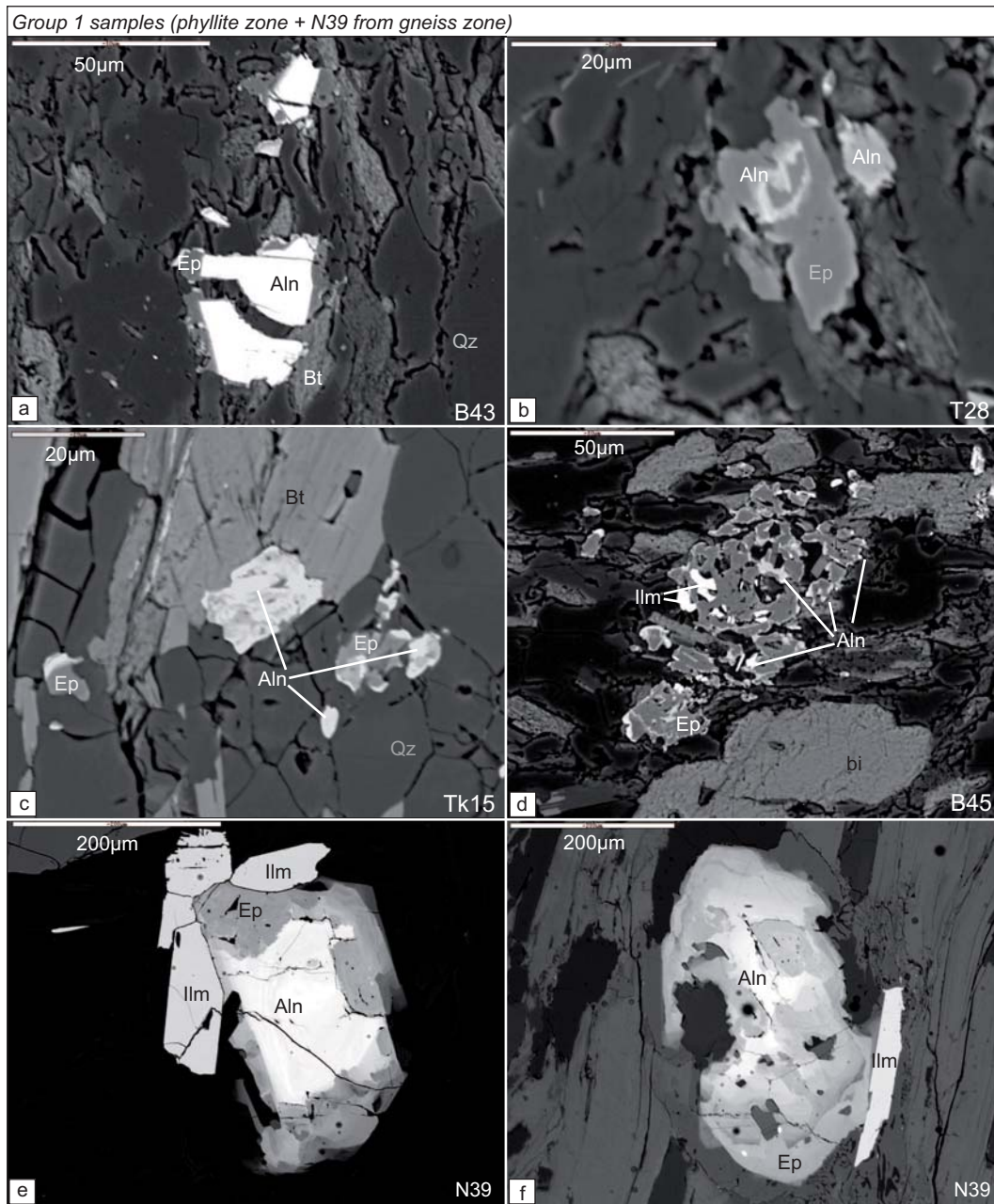


Figure 3.6: Representative BSE images of samples from group 1. Sample numbers are given in the lower right corner of each image. Allanite/Epidote is the main REE-bearing phase in these samples. In the phyllite zone, allanite occurs either as (a) single crystals or as (b-d) irregular small patches on epidote crystals. The only sample from the gneiss zone in this group contains large, strongly zoned allanite crystals (e-f).

vary less: between 0.2 and 0.4, which is similar or slightly lower than the average pelite composition of Shaw (1956). Relative to the average pelite composition of Shaw (1956),

the Al₂O₃ composition varies between 0.8 and 1.2 (Fig. 3.5), whereas the CaO composition varies between 0.5 and 3.5 (Fig. 3.5). Samples with bulk rock compositions considerably different from the remaining samples are B40, with very low SiO₂, but high Al₂O₃, Fe₂O₃, MgO, K₂O and TiO₂, Samples T7 and N39 with high Fe₂O₃, sample T40 with high CaO and Na₂O and sample N7 and B45 with high SiO₂ (Tab. 3.3).

The search for monazite, allanite and xenotime in the 32 samples of varying metamorphic grade, mineralogy and bulk rock composition revealed that the samples belong to six different groups based on the observed occurrence of these accessory minerals. The six groups are:

Group 1 Samples from the first group contain allanite ± xenotime but no monazite (Tab. 3.2, Figs. 3.1, 3.4-3.6). All samples from the phyllite zone outside of the CMC belong to this group, as well as one metavolcanic sample from the gneiss zone exposed in the south-eastern part of the complex (sample N39, Fig. 3.1, Tab. 3.2). The phyllite zone samples contain allanite either as large (~20-50 μm) single crystals (Fig. 3.6a) or as irregular small (~μm) allanite patches or rims on epidote (Fig. 3.6b-d). Xenotime was observed in two of the six phyllite samples (Tab. 3.2) as very small crystals (~5-10 μm) in the matrix. Additional accessory minerals are zircon, ilmenite, and apatite in all phyllite samples, whereas titanite, pyrite and hematite were observed in some of the phyllite samples (Tab. 3.2). Sample N39 from the gneiss zone contains several large (~100-400 μm) allanite crystals in the quartz-plagioclase matrix, as inclusions in biotite or adjacent to garnet or ilmenite (Fig. 3.6e-f). The allanite crystals are often surrounded by clinozoisite and are strongly zoned in calcium, iron and REE following the substitution reaction $Fe^{3+} = REE^{3+} + Fe^{2+}$ (Bruand, 2010). Ilmenite, pyrite, zircon, apatite and rutile are additional accessory minerals in this sample (Tab. 3.2).

Group 2 Samples from the second group contain small monazite + xenotime, but no allanite (Tab. 3.2, Figs. 3.1, 3.4, 3.5, 3.7). Five samples from the schist zone belong to this group (Fig. 3.1, Tab. 3.2). The monazites in these samples are euhedral and very small: the majority is ~5-20 μm in length with a few being ~20-50 μm in length. Most grains lay in the matrix (Fig. 3.7a), are associated with apatite, or occur as inclusions in andalusite (Tk10, Tk9, Fig. 3.7b) and garnet (Tk10, Tk9, Fig. 3.7c). Xenotime occurs in all samples of this group as ~5-30 μm crystals in the matrix (Fig. 3.7a) or associated with zircon. Zircon, apatite and ilmenite are present in all samples, whereas pyrite and hematite occur in some of the samples (Tab. 3.2).

Group 3 Samples from the third group contain small monazite + xenotime, but in contrast to group 2 also contain minor allanite (Tab. 3.2, Figs. 3.1, 3.4, 3.5, 3.7). Four samples from the schist zone belong to this group (Fig. 3.1, Tab. 3.2). The size and distribution of mon-

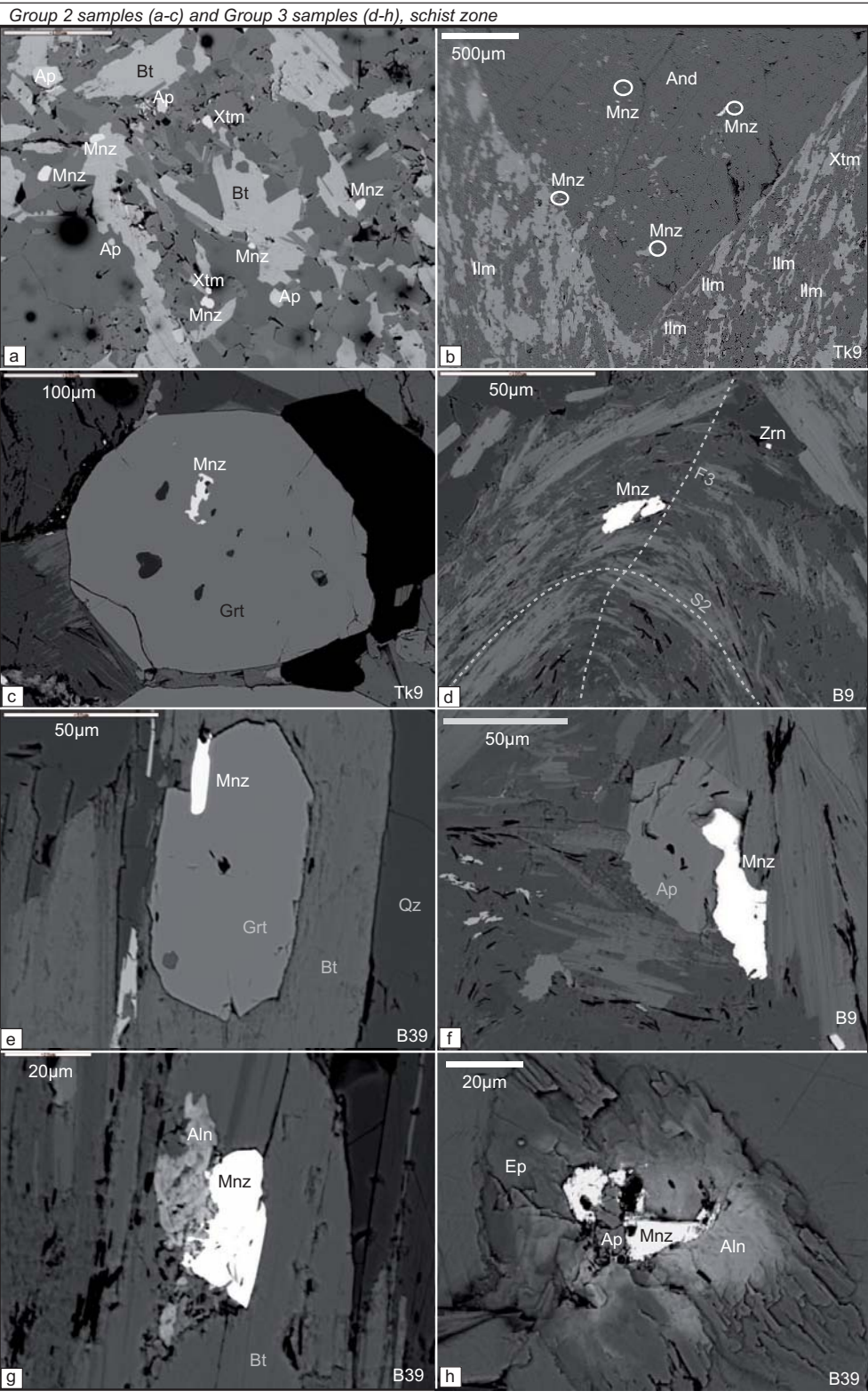
azite and xenotime is comparable to group 2 samples. Monazite occurs predominantly in the matrix. About 70% of the grains are elongated parallel to the main foliation (regionally termed S_2 , Pavlis & Sisson, 1995) and they are folded with F_3 (Fig. 3.7d). Inclusions of monazite in garnet occur (Fig. 3.7e). Again, about 10% of the monazites are associated with apatite (Fig. 3.7f). Xenotime is present in all samples, but is generally small (~ 5 - $20 \mu\text{m}$) and only a few grains were observed per thin section. Allanite occurs in samples of this group exclusively in association with monazite as fibres/patches (Fig. 3.7g-h).

Group 4 Samples from the fourth group contain large monazite + xenotime, but no allanite (Tab. 3.2, Figs. 3.1, 3.4, 3.5, 3.8). Five samples from the gneiss zone belong to this group (Fig. 3.1, Tab. 3.2). The monazites are located at grain boundaries or within biotite (Fig. 3.8a) and are larger than the monazites observed in group 2 and 3 with sizes ranging from ~ 10 to $100 \mu\text{m}$ (with a majority of ~ 20 - $50 \mu\text{m}$). 10-20% of the monazites are associated with apatite (Fig. 3.8b). Minor small crystals of xenotime (~ 5 - $15 \mu\text{m}$) were observed in all samples. All five samples contain apatite, zircon and ilmenite and some samples contain pyrite as additional accessory minerals (Tab. 3.2).

Group 5 Samples from the fifth group contain large monazite \pm xenotime, but in contrast to group 2 also contain minor allanite (Tab. 3.2, Figs. 3.1, 3.4, 3.5, 3.8). Five samples from the gneiss zone belong to this group. The monazites occur in these samples in similar locations and of similar size as in group 4, but in addition $\sim 25\%$ of the monazites have irregular boundaries and are surrounded by fine-grained allanite-epidote fibers which grow on biotite (Fig. 3.8c). A single allanite crystal is present in one sample (B23) and several large (~ 50 - $200 \mu\text{m}$) elongated allanite crystals occur along a fine-grained, altered, muscovite/chlorite-bearing zone in sample T15 (Fig. 3.8d). Again, about 10-20% of the monazites are associated with apatite (Fig. 3.8c, inset). Minor xenotime is present in all samples of this group except for sample T7. Zircon, apatite and ilmenite are present in all samples, whereas pyrite and/or hematite are present in some samples (Tab. 3.2).

Group 6 Samples from the sixth group contain large allanite \pm xenotime, and additionally small, metastable monazites (Tab. 3.2, Figs. 3.1, 3.4, 3.5, 3.9). Seven samples from the gneiss zone belong to this group. In all samples, relatively large (~ 20 - $300 \mu\text{m}$) allanite crystals are present in the matrix (9a). Monazites occur in these samples in minor quantities, smaller than in groups 4 and 5 and often with very irregular boundaries, indicating that they

Figure 3.7 (following page): Representative BSE images of group 2 and 3 samples from the schist zone. Sample numbers are given in the lower right corner of each image. In group 2, monazite occurs (a) in the matrix, (b) as inclusions in andalusite, and (c) as inclusions in garnet. In group 3, monazite occurs (d) in the matrix (parallel to S_2 , folded with F_3), (e) as inclusions in garnet, (f) associated with apatite, and (g-h) associated with allanite/epidote.



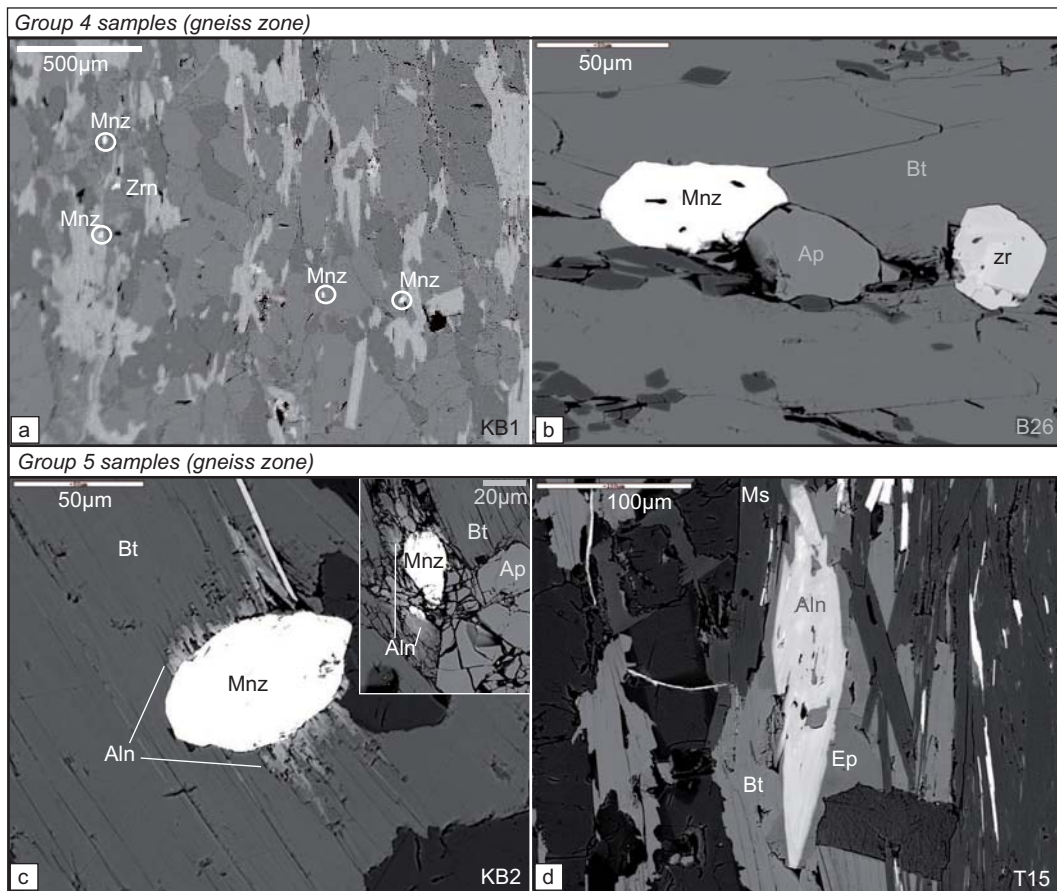


Figure 3.8: Representative BSE images of group 4 and 5 samples from the gneiss zone. Sample numbers are given in the lower right corner of each image. In group 4, monazite occurs as (a) large monazite crystals in the matrix, and (b) associated with apatite. In group 5, monazites are (c) surrounded by fine-grained allanite/epidote fibres \pm apatite (inset). (d) In sample T15, large allanite crystals are present in an altered (muscovite + chlorite) fluid-infiltration zone.

are metastable (Fig. 3.9b-f). Allanite/Epidote coronas around monazites are present in samples B21, T40, N48 and N7 (Fig. 3.9b-f). Epidote-plagioclase symplectites are present around some of the allanites and some of the monazite-allanite pairs (Fig. 3.9a-c). In sample N7, apatite is closely associated with monazite and allanite (Fig. 3.9d-e). In sample N17, complex allanite-epidote coronas occur around apatite (Fig. 3.9g). Sample N48 contains small (a few μm) monazite inclusions in garnet. Xenotime was only found in one sample (B21) of this group (Fig. 3.9h, Tab. 3.2). Apatite and zircon are present in all samples, whereas ilmenite, titanite and pyrite occur in some of the samples (Tab. 3.2).

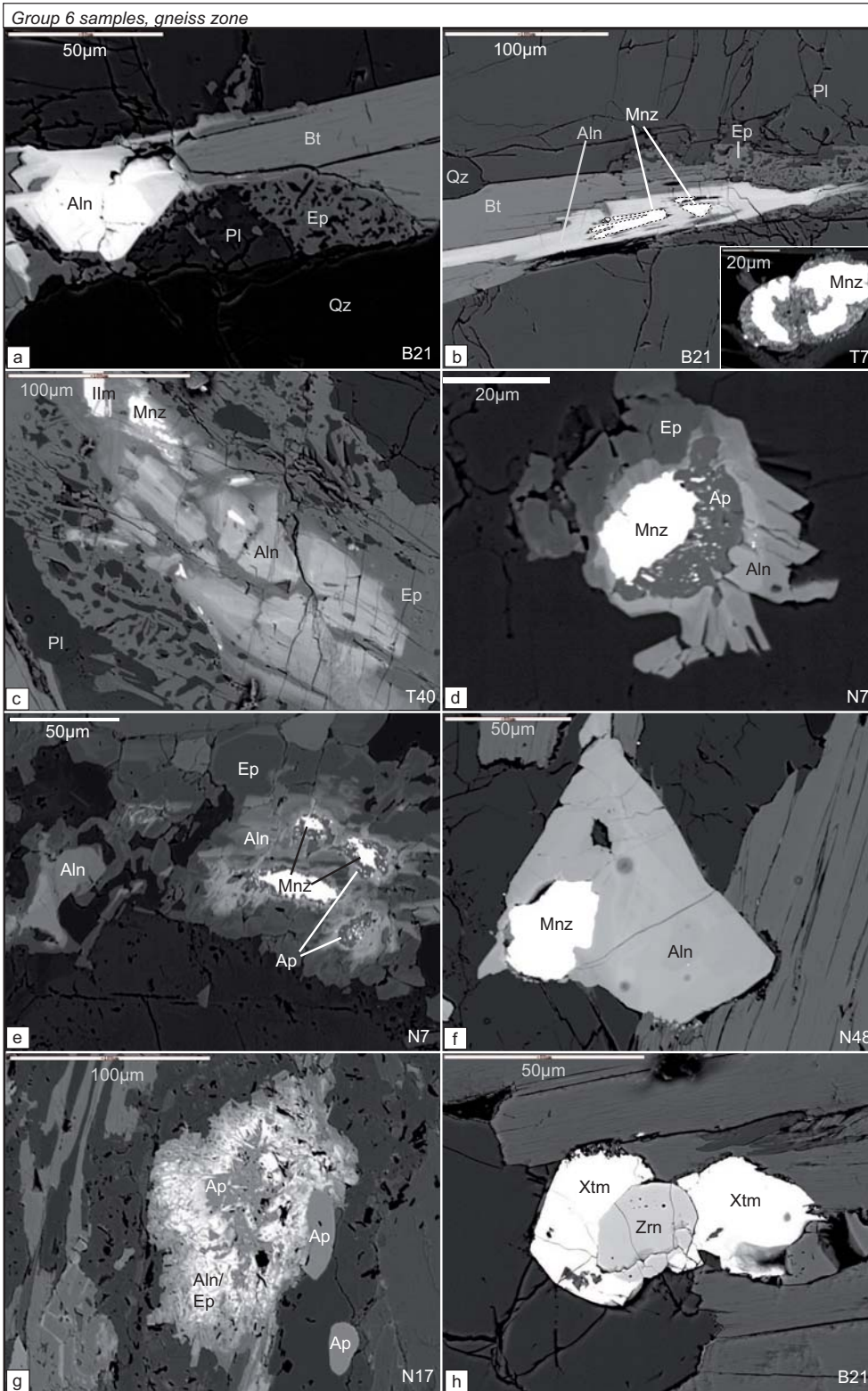
3.4.3 Chemical zoning and composition of monazites from groups 2-5

In order to investigate the suitability of monazite in the different groups described above for U-Pb dating, we investigated the chemical zonation and composition of the stable monazites from groups 2 and 3 (schist zone) and groups 4-5 (gneiss zone).

Groups 2 and 3 (schist zone) High-contrast BSE images of the small monazites of groups 2 and 3 revealed that 60-100% of the grains showed no zoning in BSE brightness and ~0-40% of the grains show two or three weak different zones of brightness (Fig. 3.10a). Since monazites from sample B39 show most variations in BSE brightness, they were selected for elemental mapping and chemical analyses by electron microprobe. Elemental maps for Y and Th (Fig. 3.10b) show weak variations in Y and stronger variations in Th content, with the light zones in BSE images corresponding to high contents of Th. Representative chemical analyses from different zones of these grains are shown in Tab. 3.4, together with the average composition from 38 analyses from monazite grains from sample B39. All analyses from B39 are also plotted on compositional diagrams on Fig. 3.11.

Groups 4 and 5 (gneiss zone) High-contrast BSE images of the bigger monazites of groups 4 and 5 revealed that they are zoned more often and more strongly than the small monazites from the schist zone: ~30-80% of the grains showed two or more different BSE zones (Figs. 3.12, 3.13). Sample T27 showed particularly strong zoning and was therefore selected for elemental mapping and chemical analyses (Fig. 3.12). The maps revealed that the strong BSE zoning is the result of variations in both Y and Th content: bright BSE zones correspond to high Th and low Y content, dark zones correspond to low Th and high Y content. There is a tendency of the bright BSE zones forming cores and the dark zones forming rims (Fig. 3.12a-c), but often the zoning is very patchy with no clear core-rim structures developed (Figs. 3.12d, 3.13). Chemical analyses from the bright and dark zones shown in Fig. 3.12 are shown in Tab. 3.5, together with the average composition from 33 analyses from monazites of sample T27. All analyses from T27 are also plotted on Fig. 3.11. These diagrams show that T27 clearly contains two different monazite compositions which correspond to the bright and dark BSE zones: the bright zones (with a tendency of being cores) have high but variable Th, and high La, Ce and Pr contents, whereas the dark zones (with a tendency of being rims) have high Y, Sm, Nd, and Gd and low Th, La and Ce contents (Fig. 3.11).

Figure 3.9 (following page): Representative BSE images of group 6 samples from the gneiss zone. Sample numbers are given in the lower right corner of each image. **(a)** A large allanite crystal representative for the allanites which are present in all samples from this group. **(b-f)** Unstable monazite grains are surrounded by allanite/epidote coronas in several samples. Note the symplectite texture of plagioclase and epidote in **(a-c)**. **(g)** Complex allanite/epidote overgrowths on apatite crystal, no relicts of monazite were observed in this association. **(h)** Large xenotime crystals associated with zircon in sample B21.



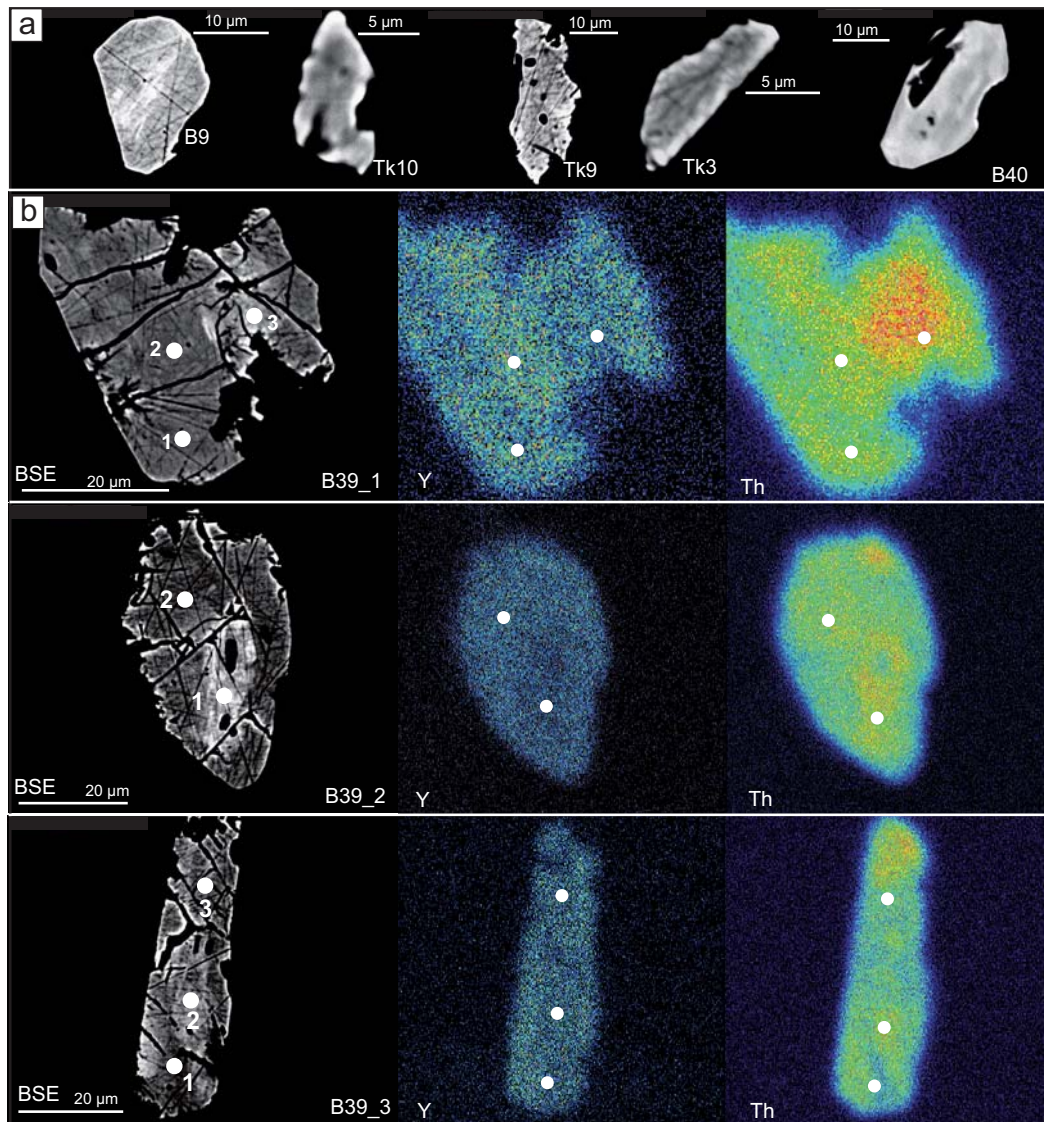


Figure 3.10: (a) Representative high-contrast BSE images of monazites from groups 2 and 3 (schist zone). The monazites are generally very small (~5-50 μm) and show no or only very weak zoning in BSE. Scratches on grains are from imperfect polishing of thin sections. (b) BSE image and corresponding element maps (Y, Th) for three selected grains from sample B39. Grains show relatively homogenous Y content but variations in Th content. Bright BSE zones correspond to zones with high Th content. White dots are the location of EMP analyses shown in Tab. 3.4.

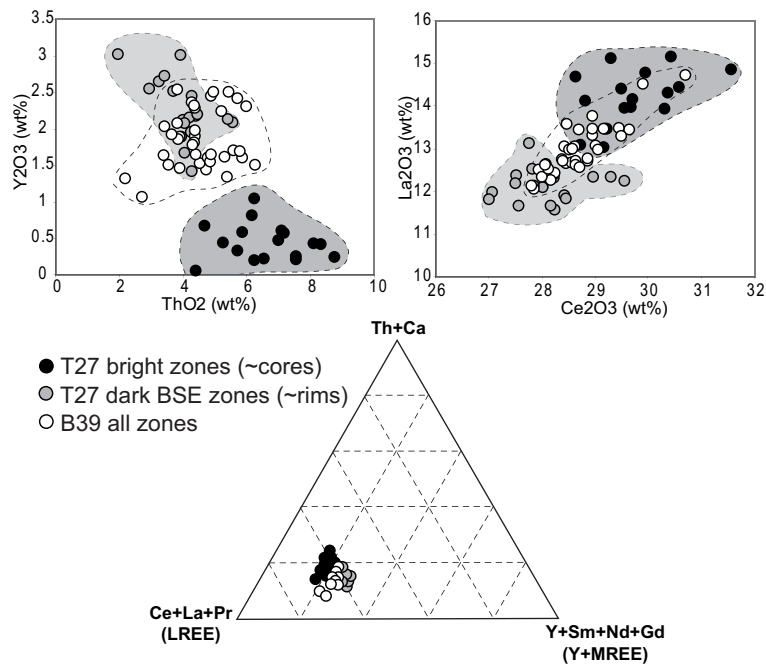
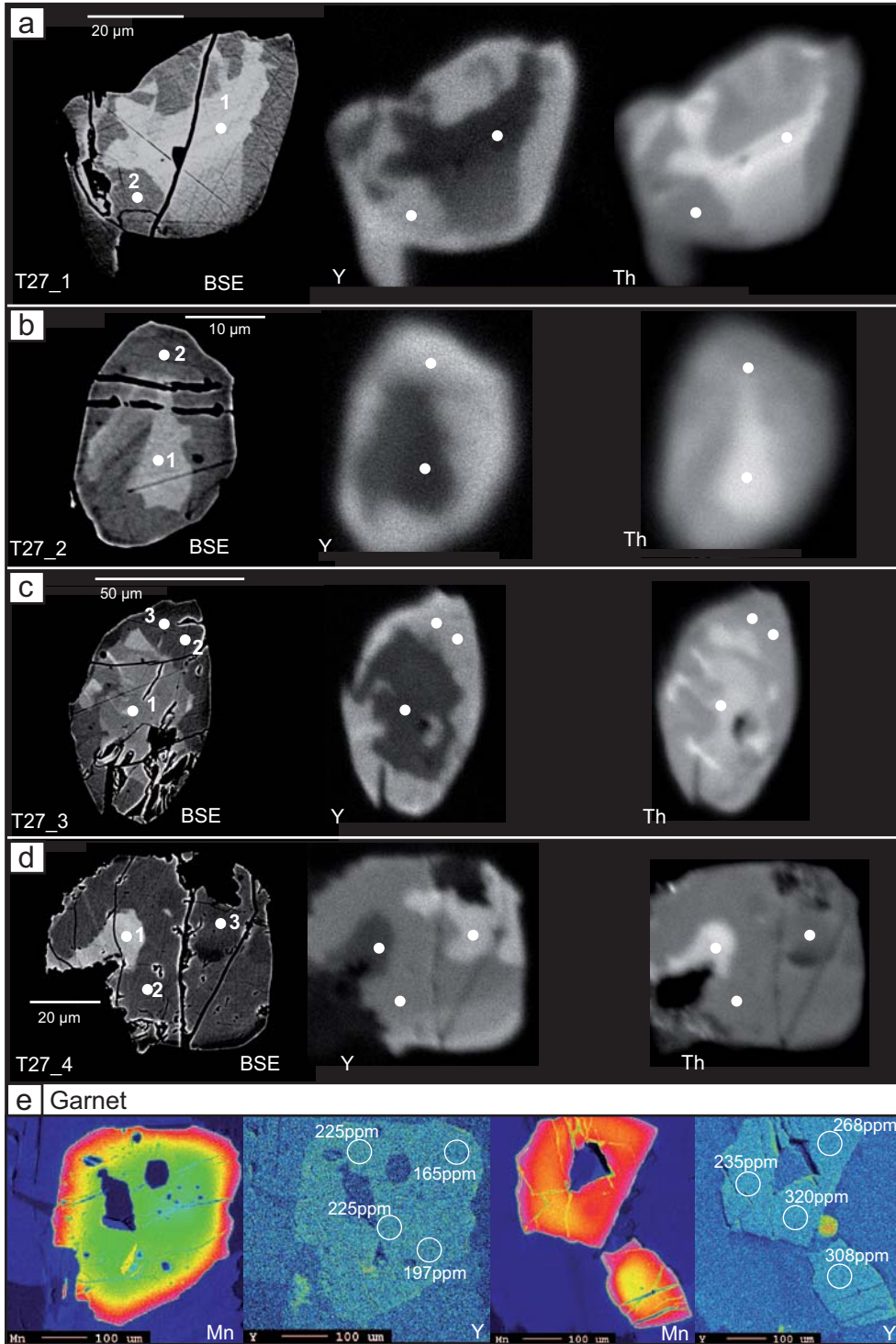


Figure 3.11: Monazite compositional diagrams, showing the different compositions of monazites from the schist zone (sample B39) and from the gneiss zone (sample T27). Sample T27 contains two distinctly different zones (bright and dark in BSE respectively). The composition of B39 is intermediate to the two zones of sample T27.

Y zoning in monazite has often been linked to reactions involving major silicates such as garnet, since garnet is another major source or sink for Y (e.g. Foster & Parrish, 2003). We therefore mapped garnets of sample T27 for Y and analysed the trace element composition by LA-ICP-MS. The element maps reveal that the garnets are homogenous and relatively low in Y, with values of ~150-350 ppm (Fig. 3.12e). The garnets are unzoned in Ca and Fe, but show slightly decreasing values of Mg and increasing values of Mn towards the rim (Fig. 3.12e, Mn shown as example, Bruand, 2010).

Figure 3.12 (following page): Representative high-contrast BSE images of monazites with corresponding element maps (Y, Th) from sample T27 from the gneiss zone. The BSE zoning is a combination of variations in Y and Th content. Bright zones correspond to high Th and low Y content, dark zones correspond to low Th and high Y content. White spots correspond to EMP analyses given in Tab. 3.5. **(a-c)** There is a tendency of high Y rims and high Th cores, but often the zoning is patchy **(d)** and no clear core-rim structures are observed. **(e)** Mn and Y element maps for three garnet grains from sample T27. LA-ICP-MS spot measurements of Y content are shown. The garnets have relatively low and homogenous Y contents. They show a strong rimward increase in manganese and slightly irregular grain boundaries, suggesting that diffusional exchange and resorption of garnet occurred after the metamorphic peak, which could have caused the growth of Y-rich rims on monazite.



3.4.4 U-Pb SHRIMP dating of monazites from the gneiss zone

In order to get precise age information from the monazites grown in the schist and gneiss zones of the CMC, three samples from the schist zone (groups 2 and 3) and four samples from the gneiss zone (groups 4 and 5) were selected for U-Pb SHRIMP dating. The attempt of dating the small monazites from the three schist samples (B39, Tk9, Tk10) was not successful. The heavy mineral separates after sample processing did not contain any monazites, despite having recognized >40 grains/per thin section. There are two possible explanations for that: (1) the grains observed in thin sections are mostly <50 μm and they might therefore be lost during standard mineral separation. (2) Most grains are hosted by biotite - since we did not mill the samples after crushing, they might have stayed in the biotite. Therefore, additional milling would probably increase the chance of separating monazites from these fine-grained samples.

The four samples from the gneiss zone (B21, KB5, KB1, T27) all yielded >50 grains of monazites per sample, typically ~50-200 μm in size. BSE images of the separated monazite grains from the four samples are displayed on Fig. 3.13. The separated grains from the four gneiss samples show a tendency to bright BSE cores and dark BSE rims as already observed on monazite crystals in thin section from sample T27 (Fig. 3.12). We dated 13-18 spots on 10-11 crystals from each sample covering zones with different BSE brightness (Fig. 3.13). No differences in age between zones of different BSE brightness (and hence composition) could be detected at this level of precision (Fig. 3.13). For samples B21 and KB5, one discordant analysis was excluded from the age calculation (Tab. 3.6, Fig. 3.14, the discordant analyses are shown in the table but not in the plots). For sample KB5, five analyses were excluded from the age calculation, due to high common Pb, large error on the isotopic ratios and/or discordance (Tab. 3.6, Fig. 3.14). For sample T27, two analyses are excluded due to high error on the isotopic ratio (Tab. 3.6). With the remaining analyses, Concordia ages could be calculated for B21, KB1 and KB5, whereas for sample T27 a weighted average $^{206}\text{Pb}/^{238}\text{U}$ age is reported (Fig. 3.14). The ages vary between 51.5 ± 0.9 Ma and 53.5 ± 0.9 Ma (Fig. 3.14, Tab. 3.2). The ages of KB1, KB5 and T27 are within error of each other, whereas the age of sample B21 is slightly younger than the age of KB5, but is within error of the ages of KB1 and T27 (Fig. 3.14).

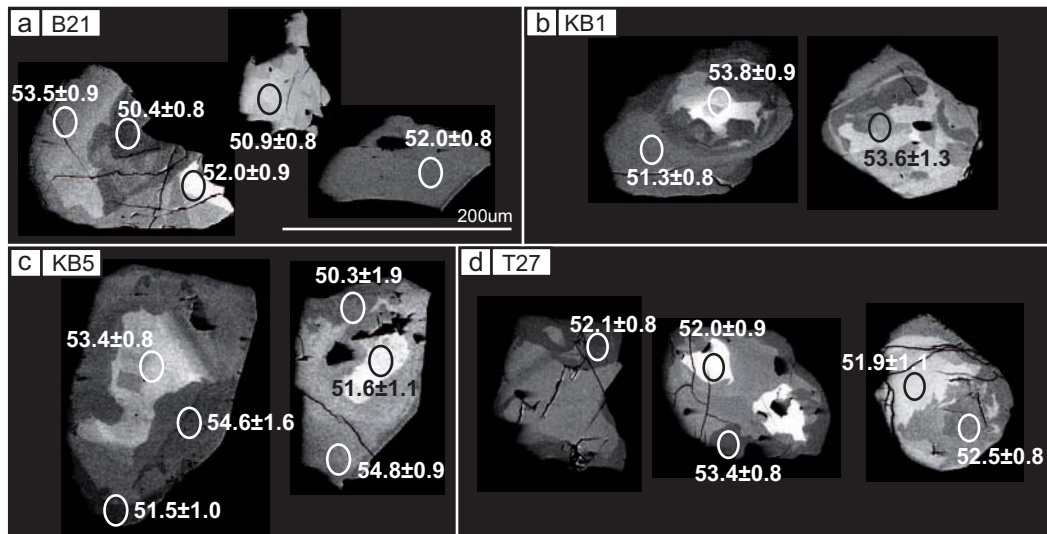


Figure 3.13: Representative BSE images of separated monazite grains from the four gneiss samples with SHRIMP spots and $^{206}\text{Pb}/^{238}\text{U}$ single ages (1σ -errors). The scale is the same for all grains. Note that domains with different BSE brightness do not show differences in age at the resolution of the U-Pb SHRIMP dating method. All single spot ages from each sample are shown in Table 3.6.

3.5 Discussion

3.5.1 Factors controlling the stability of REE-bearing minerals in the different groups

The stability of monazite versus allanite in metamorphic rocks depends on many factors such as the *PT* conditions, the bulk rock composition, and the water activity (e.g. Smith & Barreiro, 1990; Kingsbury et al., 1993; Finger et al., 1998; Rubatto et al., 2001; Wing et al., 2003; Kohn & Malloy, 2004; Foster et al., 2004; Fitzsimons et al., 2005; Rubatto et al., 2006; Rasmussen et al., 2006; Tomkins & Pattison, 2007; Janots et al., 2006, 2007; Krenn et al., 2008; Berger et al., 2009; Kim et al., 2009). In metapelitic rocks of variable composition, the following general succession of allanite versus monazite has been observed in many regional studies: Monazite is stable under low-grade (<300-450°C) conditions, is replaced by allanite under medium-grade conditions (>300-500°C, depending on pressure and bulk rock composition), and reappears under higher-grade conditions (>550-700°C, depending on pressure and bulk rock composition; e.g. Wing et al., 2003; Janots et al., 2007, 2008; Tomkins & Pattison, 2007). The 32 samples studied from the CMC belong to six different groups based on the occurrence of monazite, allanite and xenotime in these samples. The factors controlling the stability of these minerals in the different groups are discussed in the following.

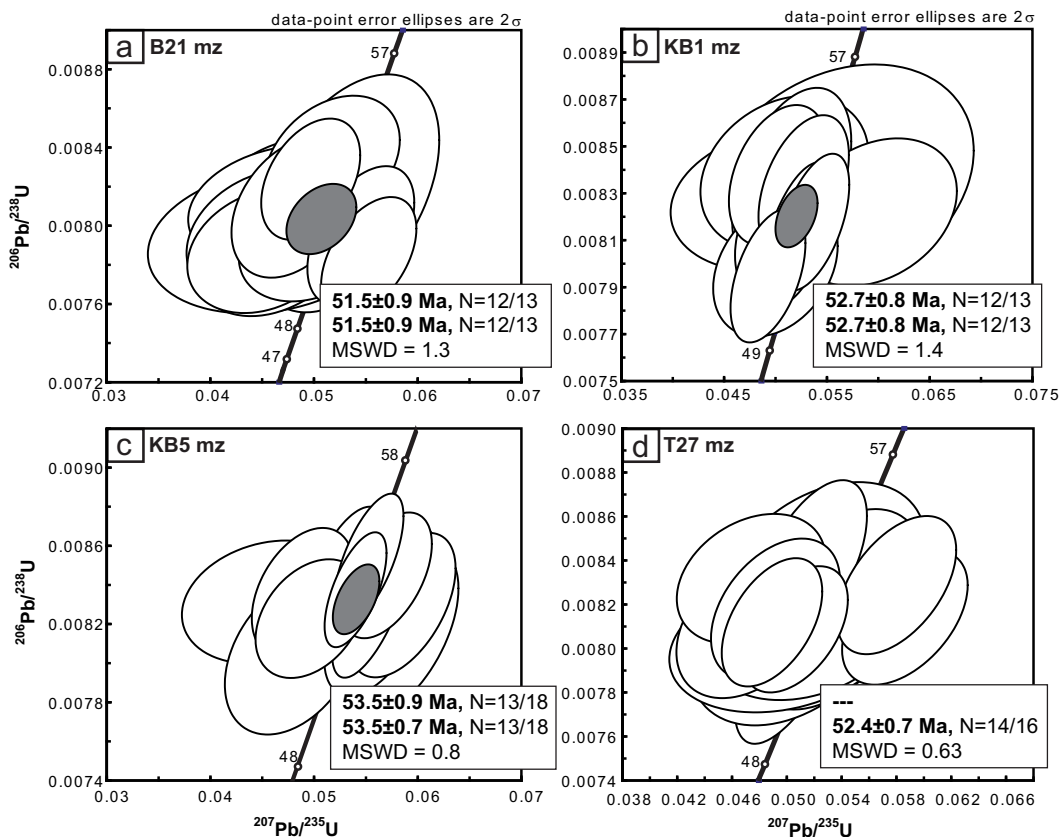


Figure 3.14: Concordia diagrams of monazites from the four gneiss samples (a) B21, (b) KB5, (c) KB1 and (d) T27. The localities of the samples are displayed on Fig. 3.1. Upper age in box is Concordia age calculated after Ludwig (1998) with the software Isoplot (Ludwig, 2003). Lower age in box is weighted average $^{206}\text{Pb}/^{238}\text{U}$ age with corresponding MSWD. The error is given at 95% confidence interval. N denotes number of analyses included in age calculation versus total number of analyses given in Table 3.6. Only analyses included in the age calculation are shown on the plots.

Group 1

Samples from this group contain only $\text{Aln} \pm \text{Xtm}$ (Fig. 3.6, Tab. 3.2). Except for one sample (N39, Tab. 3.2) all samples from this group come from the low-grade phyllite zone, which experienced temperatures of $\sim 400\text{--}550^\circ\text{C}$ at pressures of <3.4 kbar (Bruand, 2010). These conditions correspond to the allanite stability field in metapelitic rocks shown by many workers (e.g. Smith & Barreiro, 1990; Kingsbury et al., 1993; Wing et al., 2003; Kohn & Malloy, 2004; Tomkins & Pattison, 2007; Janots et al., 2007, 2008; Kim et al., 2009), indicating that metamorphic grade is the controlling factor stabilizing allanite in these phyllite zone samples. The bulk rock composition of these phyllites varies considerably with CaO-contents $\sim 2\text{--}3$ times the CaO-content of average pelites (Fig. 3.4a, 3.5a). This variation in CaO-content does not seem to influence the stability of allanite, which is

present in all samples, but might have an influence on the stability of xenotime, which is only present in samples B45 and B43 which have a relatively low CaO-content close to an average pelite composition (Fig. 3.5a).

Sample N39 from the gneiss zone also belongs to group 1. It is derived from the south-eastern part of the complex which experienced peak metamorphic conditions of $\sim 650^{\circ}\text{C}$ and $\sim 8\text{-}10$ kbar. The medium-grade stability field of allanite discussed above depends on the temperature and pressures reached and the bulk rock molar content of Ca (Janots et al., 2007). Considering the Mg-equivalent of allanite, Janots et al. (2007) showed that at conditions of $\sim 650^{\circ}\text{C}$ and $\sim 8\text{-}10$ kbar, allanite is stable at Ca molar contents $>1\%$. Sample N39 has a Ca molar content of 4.9% which is entirely within the stability field of allanite after Janots et al. (2007). The zonation into a REE-rich core and a Ca-rich epidote rim often observed in sample N39 (Fig. 3.6e-f) is typical for prograde growth of allanite/epidote during increasing temperature (e.g. Janots et al., 2006, 2007). We therefore interpret the allanite crystals observed in sample N39 as representing prograde growth zoning in an allanite field stabilized by relatively high pressures and high CaO-content.

Groups 2 and 3

Samples from these groups all contain small, unzoned monazites and xenotime, with samples from group 3 containing additional minor allanite fibres (Fig. 3.7). All samples come from the schist zone, which experienced metamorphic conditions of $\sim 550\text{-}650^{\circ}\text{C}$ and $\sim 3.4\text{-}6$ kbar (Bruand, 2010). These conditions overlap with the higher-grade monazite stability field observed by many workers in metapelitic rocks (e.g. Smith & Barreiro, 1990; Kingsbury et al., 1993; Wing et al., 2003; Kohn & Malloy, 2004; Tomkins & Pattison, 2007; Janots et al., 2008; Kim et al., 2009), indicating that metamorphic grade is the controlling factor in stabilizing monazites in these rocks. The transition between the allanite-bearing phyllite zone samples and the monazite-bearing schist zone samples is discussed in more detail in a separate paragraph below.

Groups 4 and 5

Samples from these groups contain large, complexly zoned monazites \pm xenotime, and samples from group 5 contain additional fibrous allanite (Fig. 3.8). All samples are derived from the gneiss zone, with a tendency towards more northern locations, and therewith lower pressures (Fig. 3.1; Bruand, 2010). They all have bulk rock compositions close to an average metapelite both in AFM space (especially group 4, Fig. 3.4c) and in Al/Ca-space, with a CaO content maximally ~ 2 times the CaO content of an average metapelite (Fig. 3.5c). They experienced metamorphic conditions of $\sim 650\text{-}700^{\circ}\text{C}$ and $\sim 4\text{-}7$ kbar, and water-saturated partial melting occurred in these rocks (Bruand, 2010). The presence of com-

plexly zoned monazite in metapelitic rocks which experienced partial melting has been documented widely in the literature (e.g. Rubatto et al., 2001; Pyle & Spear, 2003; Kohn et al., 2005). The reason for the complex zoning present in the samples of these groups is discussed in a separate paragraph below.

Group 6

Samples from this group contain allanite as well as minor metastable monazite \pm xenotime (Fig. 3.9). All samples are from the gneiss zone, and except for sample B21 are exclusively derived from the southern gneiss zone which experienced higher pressures (\sim 8-10 kbar and \sim 600-700°C compared to \sim 4-7 kbar and \sim 650-700°C farther north, Fig. 3.1; Bruand, 2010). Compositionally, the samples from this group vary considerably, both in AFM and Al/Ca-space (Fig. 3.4c, 3.5c). Also mineralogically, they are very different: a typical metapelite (N48), a metagreywacke (B21), an amphibolite (N38), an orthogneiss (T40) and two highly altered metasedimentary rocks (N7, N17) belong to this group. This variety in bulk rock composition and mineralogy suggest that also their REE-bearing minerals probably show a variable history and therefore these samples are discussed separately in the following.

The metapelitic sample N48 contains (i) small monazite inclusions in garnet, (ii) metastable monazites in the matrix partly overgrown by allanite (Fig. 3.9f), as well as (iii) large stable allanites in the matrix. It experienced \sim 8-10 kbar and \sim 650°C and has a CaO-content of 3.3 mol%, indicating that it was situated in the allanite stability field of Janots et al. (2007) during peak metamorphic conditions. The monazites in this sample grew probably before or together with garnet, possibly during lower pressures, and might then have been replaced by allanite during higher pressures (Fig. 3.9f).

The metagreywacke sample B21 contains (i) relatively large, stable monazites, (ii) large, stable allanites and (iii) unstable monazites surrounded by allanite crystals (Fig. 3.9a-b). The allanite crystals and coronas are always associated with epidote and biotite, but not all monazites located in biotite show allanite coronas. The bulk rock composition of B21 is relatively CaO-rich (3.8 mol%), but is not very different from gneiss samples from group 4 and 5 where no allanite is present (Fig. 3.5c). It experienced peak metamorphic conditions of \sim 4-7 kbar at \sim 650°C, which is even with high CaO-content in the stability range of monazite after Janots et al. (2007, 2008). The sample does not contain any signs of retrograde alteration which could have caused the allanite growth. So the only difference compared to samples where large monazites and no allanites are preserved (groups 4 and 5) seems to be the absence of garnet. Garnet may incorporate Ca, and therewith forcing the REE into monazite, whereas during the absence of garnet, Ca could be taken up in allanite and epidote.

The amphibolitic sample N38 is very similar to sample N39 of group 1, and equally contains large allanite crystals which we interpret to have formed at the metamorphic peak under

conditions of ~650°C and ~8-10 kbar in a CaO-rich bulk composition (Bruand, 2010). The few metastable monazites may be remnants of a minor monazite growth episode during lower pressures.

The orthogneissic sample T40 with its high CaO-content (6.3 mol%) and peak metamorphic conditions of ~7-8 kbar and ~650-700°C (Bruand, 2010) lies in the stability field for allanite after Janots et al. (2007). The only present (unstable) monazite grain in this sample (Fig. 3.9c) could possibly represent a primary magmatic monazite.

The two altered samples N7 and N17 (Fig. 3.2f) are both derived from close to a major Neogene fault (Fig. 3.1). The peak paragenesis of biotite and garnet in these samples is strongly retrogressed into chlorite, muscovite and epidote, and calcite is present in small fissures, indicating the influx of calcareous fluids. Monazite-apatite-allanite textures as observed in sample N7 (Fig. 3.9d-e) were described by Finger et al. (1998) and Krenn et al. (2008). In the first case, they formed during amphibolite-facies on primary magmatic monazite in an orthogneiss, and in the second case they formed retrogradely during greenschist facies on amphibolite-facies monazite. Since samples N7 and N17 show such a strong retrograde overprint, we interpret that the apatite-allanite coronas found in these samples probably formed during this retrograde event. The influx of carbonate-rich fluids could have enabled the transformation of monazite into apatite, allanite and epidote according to reactions described in Finger et al. (1998).

In summary, allanite-monazite textures observed in the different samples of group 6 may be the result of either prograde replacement of monazite by allanite due to an increase in pressure in relatively CaO-rich bulk compositions, or be the result of a retrograde overprint which affected the samples due to the activity of a major fault.

3.5.2 Monazite-in reaction between the phyllite and schist zones

Since all phyllite zone samples contain allanite but no monazite, and all schist zone samples contain mainly monazite with only very minor allanite, a monazite-in reaction, controlled by an increase in metamorphic grade, must have occurred between the two metamorphic zones. Possible reactions and the influence of bulk rock composition on these reactions are discussed in detail below.

Exact physical conditions and possible reactions

The highest-grade sample of the phyllite zone containing allanite is sample B45, which registered a peak temperature of $547 \pm 30^\circ\text{C}$ (Tab. 3.2; Bruand, 2010). The lowest-grade sample of the schist zone in which monazite was detected is sample Tk12, which regis-

tered a maximum temperature of $543 \pm 23^\circ\text{C}$ at 3.4 ± 0.9 kbar (Tab. 3.2; Bruand, 2010). The bulk rock composition of both samples is very similar and close to an average metapelite composition (Tab. 3.3, Fig. 3.5), indicating that the two samples are comparable. Whereas sample B45 only contains quartz, plagioclase, muscovite and biotite as major phases, andalusite and garnet occur in addition in sample Tk12. These observations suggest that the monazite-in reaction occurred in these rocks at $\sim 540^\circ\text{C}$ ($\pm 30^\circ$) close to or at the andalusite- and garnet-in reactions at pressures of < 3.4 kbar.

Such a monazite-in reaction close to or at the andalusite- and garnet-in isograds has been reported by many workers in metamorphosed metapelitic rocks (e.g. Smith & Barreiro, 1990; Kingsbury et al., 1993; Wing et al., 2003; Kohn & Malloy, 2004; Tomkins & Pattison, 2007; Janots et al., 2008; Kim et al., 2009). However, the exact reactions which lead to monazite growth and the role of the major silicate phases versus the role of other accessory phases during these reactions is debated and different propositions have been made. Most workers agree that the REE necessary for formation of the monazite probably come from the breakdown of allanite (e.g. Smith & Barreiro, 1990; Wing et al., 2003; Tomkins & Pattison, 2007; Janots et al., 2008). However, Kohn & Malloy (2004) suggested that if the major silicate phases (especially micas and garnet) incorporated high but not unrealistic REE contents during lower grades, these REE liberated from major phases could be sufficient to produce monazite without another REE-rich precursor.

In our case, only very minor mica and no garnet is present in the phyllites, suggesting that the REE necessary for monazite formation were probably derived from a REE-rich precursor such as allanite and/or xenotime. However, in our samples no direct breakdown of allanite to monazite was observed. Textures such as described by Wing et al. (2003), Tomkins & Pattison (2007), Janots et al. (2008) or Kim et al. (2009) with pseudomorphs of small monazites after allanite or clusters of monazites with the shape of allanites were not found in our samples. Only in one sample from the schist zone (B39), a monazite crystal is tightly associated with an allanite crystal (Fig. 3.7g), but it is not unambiguous whether the monazite progradly replaces the allanite or whether the allanite retrogradly replaces the monazite. Other monazites in the same sample are surrounded by allanite fibres, indicating that this sample probably experienced retrograde allanite growth. The monazites in all the other schist samples are dispersed throughout the matrix of the sample and are generally not associated with an allanite precursor.

Whether or not the aluminosilicates play a major role in the formation of the monazite is also debated. Wing et al. (2003) proposed the following reaction for the formation of monazite at the aluminosilicate-in isograds: $3 \text{ allanite} + \text{apatite} + \text{muscovite} + 4 \text{ aluminosilicate} + 3 \text{ quartz} = 3 \text{ monazite} + \text{biotite} + 8 \text{ plagioclase} + 2 \text{ H}_2\text{O}$. However, Tomkins & Pattison (2007) observed that the monazite-in reaction in their rocks did occur slightly below the aluminosilicate-in reaction and proposed the following general formation mechanism: $\text{allanite} + \text{apatite} = \text{monazite} + \text{plagioclase} + \text{magnetite}$. Similarly, Janots et al. (2008) did not observe a clear link with the aluminosilicate-in reaction and proposed the following generalized prograde reaction: $\text{allanite} + \text{apatite} + \text{Al-Fe-Mg phases} = \text{monazite} + \text{anorthite} +$

Al-Fe-Mg phases². In addition, Wing et al. (2003) and Kim et al. (2009) proposed that Thoriumsilicate (ThSiO₄) may contribute to the relatively high Th-contents of monazite relative to allanite.

In our case, the rare observation of monazite inclusions both in andalusite (Fig. 3.7b) and garnet (Fig. 3.7c, e) indicates that the monazite-in reaction probably occurred before the formation of andalusite and garnet, similarly to what has been observed by Tomkins & Pattison (2007). In addition, the monazites of sample B39 from the schist zone are relatively Y-rich (1-2.5 wt% Y₂O₃, Fig. 3.11), indicating that they probably grew before garnet which also preferentially incorporates Y (e.g. Foster & Parrish, 2003). Based on these qualitative observations it can be assumed that probably a similar reaction as the one proposed by Tomkins & Pattison (2007) or Janots et al. (2008) was responsible for the monazite formation in the schist zone samples, including apatite, plagioclase and an Al-Fe-Mg phase (muscovite, biotite) as reactants but probably neither andalusite nor garnet.

The influence of bulk rock composition on the monazite-in reaction

Wing et al. (2003) suggested that in addition to metamorphic grade, the monazite-in reaction is controlled by the CaO-content of the bulk rock, and they showed that in samples of the andalusite-, kyanite- and sillimanite-zones, allanite can be stable if the bulk rock compositions contain 2-3 times the average pelite CaO-content. Their dividing line between Mzn- and Aln-bearing samples in the Ca-Al compositional space for And/Ky/Sil-zone samples is displayed in Fig. 3.5b. Such an influence of the CaO-content is not observed in the schist-zone samples from the CMC (Fig. 3.5b). Sample B39 and B40, which both lie in the stability field for allanite after Wing et al. (2003) do contain abundant stable monazite, and allanite is only present as retrograde fibres or as instable prograde crystals (Fig. 3.7g-h). These retrograde allanite fibres are not restricted to samples from the allanite stability field of Wing et al. (2003), but also occur on samples in the monazite stability field (Fig. 3.5b).

Similarly, the equation proposed by Foster & Parrish (2003), which links the temperature of monazite growth to the CaO/SiO₂-ratio of the rock, gives monazite-in temperatures of ~670°C and ~760°C for samples B39 and B40, respectively. These temperatures are higher than the temperatures observed in these samples, suggesting that allanite and not monazite should be stable in these samples, which is not observed. This indicates that the CaO bulk rock content and the CaO/SiO₂ ratio of our samples did not essentially influence the monazite-in reaction. Janots et al. (2008) suggested that the CaO/Na₂O ratio of a sample might influence the breakdown of allanite to monazite between temperatures of ~500-650°C, with allanite being stable to higher temperatures the higher the CaO/Na₂O ratio is (their Fig. 13). The CaO/Na₂O ratio of all our schist samples is below 1.1 which is clearly in the field where allanite breaks down to monazite at temperatures of ~550°C - 600°C. So compared to the results of Janots et al. (2008) the occurrence of monazite even in our samples with high CaO content is not surprising.

Variations in the AFM space seem not to influence the monazite-in reaction between the phyllite and schist zones: Despite variations of 0.4 in the Al-component and 0.2 in the Fe- and Mg-components all samples from the phyllite zone contain allanite whereas all samples from the schist zone contain monazite (compare Fig. 3.4a with Fig. 3.4b). Similarly, Rasmussen et al. (2006) concluded that monazite growth during amphibolite facies metamorphism is not influenced by compositional variations in AFM space.

3.5.3 Complexly zoned monazites in the gneiss zone: the result of (re)-crystallization during/after partial melting?

The samples from groups 4 and 5 from the gneiss zone contain abundant, large monazite which is much more zoned in BSE images than the monazites from the schist zone. Element-mapping and chemical analyses from one representative sample (T27) revealed the presence of two compositional domains: Th-, La-, Ce-, Pr-rich and Y-poor domains and Y-, Sm-, Nd-, Gd-rich, Th-, La-, Ce- and Pr-poor domains (Fig. 3.11). The distribution of the domains is mainly patchy, with a tendency of the former constituting cores and the latter constituting rims (Fig. 3.12 and 3.13). Within error of U-Pb SHRIMP dating, no age difference is detected between the different zones (Fig. 3.13, 3.14).

Complex chemical zoning of metamorphic monazite in upper amphibolite-facies rocks and in migmatites has been reported by many workers (e.g. Fitzsimons et al., 1997; Pyle et al., 2001; Rubatto et al., 2001; Foster et al., 2002, 2004; Pyle & Spear, 2003; Gibson et al., 2004; Kohn et al., 2005). Especially the zoning in Y has been investigated extensively since Y is also incorporated in other phases such as garnet and xenotime. The partitioning of Y between the different minerals may allow drawing conclusions on the timing of monazite growth relative to garnet and/or xenotime growth (e.g. Pyle et al., 2001).

The monazites in the schist zone (B39) are relatively Y-rich (Fig. 3.11), possibly indicating growth prior to garnet growth. The monazites in the gneiss zone however (T27), show Y-poor zones which form preferentially grain cores (Fig. 3.12, 3.13). In addition, these cores show complex zoning in Th (Fig. 3.12a and c). The composition of these cores suggests that they possibly grew after garnet growth (e.g. Foster & Parrish, 2003). They could therefore represent a younger generation of monazites than the Y-rich monazites present in the schist zone. However, this would imply that the older Y-rich monazites were completely dissolved prior to precipitation of the Y-poor monazites. Samples from groups 4 and 5 experienced partial melting under water-saturated conditions (Bruand, 2010) with garnet stable both before and during the melting stage. Monazite solubility in metapelitic melts under water-saturated conditions can be relatively high (e.g. Zeng et al., 2005) suggesting that dissolution of lower-grade monazite during partial melting might be possible. The Th-rich cores could then have been crystallized during melt crystallization, with the high Th-content being the result of preferential Th incorporation into monazite (e.g. Kohn & Malloy, 2004; Kohn et al., 2005).

Y-rich zones/rims similar to the Y-rich zones of sample T27 have been described by other workers from migmatitic rocks, and have generally been interpreted as representing a monazite generation which grew during breakdown of garnet and/or in equilibrium with xenotime (e.g. Pyle & Spear, 2003; Foster & Parrish, 2003; Kohn et al., 2005). The garnets of sample T27 show a strong rimward increase in Mn and a slight decrease in Mg as well as some irregular grain boundaries (Fig. 3.12e; Bruand, 2010). Sharp rimward zoning in Mg, Fe or Mn in otherwise homogenous garnets is commonly attributed to diffusional exchange and/or net transfer reactions between garnet and biotite during cooling (e.g. Spear, 1993; Kohn et al., 2001). Whereas during diffusional exchange no garnet breakdown occurs, net transfer reactions may lead to the resorption of garnet and therewith the liberation of Y, which then could lead to the production of high-Y monazite rims (e.g. Spear, 1993; Foster & Parrish, 2003; Kohn et al., 2005). However, whether or not garnet resorption occurred in sample T27 is difficult to judge. The grain boundaries are somewhat irregular and the zoning is truncated in one of the crystals (lower-left of first crystal in Fig. 3.12e), indicating that maybe some resorption during cooling occurred. Xenotime is present in the matrix of the sample or as overgrowths on zircon, but no textural relationship with the zoned monazites or garnet were observed, making it difficult to judge at what time relative to garnet or monazite the xenotimes grew.

In summary, the complex zoning patterns in monazites of group 4 and 5 from the gneiss zone are probably the result of complex interactions between monazite, garnet, xenotime, apatite and partial melting reactions, and fully understanding them would need a more detailed investigation of the textural relationships, chemical zoning and composition and reaction history in selected samples between these important minerals. Nevertheless, the U-Pb age dating of complexly zoned monazite showed no age differences between the different zones, indicating that any possible growth history within these samples is below the temporal resolution of U-Pb SHRIMP dating. Unfortunately, no age data is available from the unzoned monazites from the schist zone, which potentially represent an older grain generation.

3.5.4 Interpretation of monazite U-Pb ages in a regional context

The four U-Pb SHRIMP ages from the zoned monazites of groups 4 and 5 cover a very narrow age range between 51.5 ± 0.9 Ma and 53.5 ± 0.9 Ma (Fig. 3.13). This indicates that the processes which formed these monazites must have occurred over a very restricted time period and, if different processes formed the different metamorphic zones, these processes occurred during shorter time scales than what is resolvable by the U-Pb SHRIMP method.

For samples KB5 and T27, U-Pb SHRIMP ages of metamorphic zircon rims are available, and they are within error of the monazite ages for the same samples (54.0 ± 0.8 Ma for KB5 and 52.6 ± 0.8 Ma for T27, Chap. 4). Four additional U-Pb SHRIMP ages of metamorphic zircons rims from the CMC and one age from a granodioritic intrusion are equally within error of all monazite ages (Chap. 4). The formation of the metamorphic zircon rim was

interpreted as being related to the partial melting event (chapter zircon), and the conformity of monazite and zircon-rim ages indicates that indeed, the monazite formation probably occurred during the same time period as the zircon-rim formation close or at the metamorphic peak. Together, zircon and monazite ages indicate a short, restricted time period from ~55 to ~51 Ma during which partial melting occurred in the CMC at least ~300 km along strike. So even if no independent age on the prograde heating and burial history of the CMC could be obtained, the maximum depositional age of ~60-65 Ma derived in the last chapter leaves only ~5-10 Ma for prograde heating and burial of the CMC. Peak temperatures reached in the CMC are ~650-700°C, and, with assuming a starting temperature of ~20°C, an average heating rate of ~60-140°C/Ma can be calculated.

3.6 Conclusions

The search for prograde datable minerals in the different zones of the CMC revealed the following:

(1) Garnet is ubiquitous throughout the CMC in rocks of appropriate bulk composition, but its internal zoning either equilibrated at the metamorphic peak, or represents growth zoning during the retrograde part of the *PT* path (Bruand, 2010). Garnet is therefore not suited to date the prograde metamorphic history of the CMC. A Sm-Nd age obtained from two garnet fractions from a sample of the south-eastern part of the CMC gives 47.8 ± 6.3 Ma, which is broadly coeval with the metamorphic peak dated by the U-Pb method on metamorphic zircon from the same area.

(2) Monazite is absent in rocks of the phyllite zone, but is abundant as small, unzoned grains in the schist zone. Textural relationships and chemical composition indicate that these monazites grew prior to garnet and andalusite due to a reaction of the form allanite + apatite + Al-Fe-Mg phases₁ = monazite + anorthite + Al-Fe-Mg phases₂ (Janots et al., 2008) at temperatures of ~550°C and pressures of ~3.5 kbar. The metamorphic conditions of this monazite-in reaction seem not to be influenced by the CaO-content or the CaO/SiO₂ ratio of the samples as suggested by Wing et al. (2003) and Foster & Parrish (2003), or by compositional variations in the AFM space. Dating these schist-zone monazites would probably reveal a prograde *PT* age, but separating the small monazites from their host rock was not successful.

(3) Samples from the gneiss zone with bulk rock compositions close to average metapelites contain abundant, large, complexly zoned monazite. The chemical composition of the monazites from one of these samples suggest that a first Th-rich, Y-poor generation grew after the formation of garnet, possibly due to the crystallization of melt, whereas a second, Th-poor, Y-rich generation possibly formed during retrograde consumption of garnet in an early stage of the cooling history. U-Pb SHRIMP ages of the two different zones are within error

of each other indicating that these complexly zoned monazites formed over a short time period close to or at the metamorphic peak. Combined with the maximum depositional age of ~60-65 Ma for the sediments in which the CMC developed, these peak metamorphic ages reveal an average heating rate of ~60-140°C/Ma for the available ~5-10 Ma between deposition and metamorphic peak.

(4) Allanite is present (a) in the low-grade phyllites, (b) as peak metamorphic mineral in samples with high CaO-content and with relatively high peak pressures (~8-10 kbar), and (c) as retrograde crystals in altered zones related to fluid flow in some gneiss samples. Allanite therefore might represent an ideal mineral to date prograde metamorphism in the phyllite zone, the timing of peak pressure metamorphism in the gneiss zone, or the timing of fluid flow related to younger faults.

(5) Xenotime is present in all metamorphic zones in samples with metapelitic bulk rock compositions. It is often present as idiomorphic overgrowth on zircon. Textural relationships between xenotime and monazite, allanite, garnet, andalusite or staurolite have not been observed and linking xenotime growth with the reaction history of the other minerals is therefore not straightforward. Its application as a geochronometer in the rocks of the CMC is therefore probably limited.

Acknowledgments U. Klötzli is thanked for pointing me to the importance of monazite-allanite-xenotime relationships in prograde metamorphic sequences at the PANGEO conference 2008. R. Schuster proposed to date garnets from the CMC after having seen our mineral separates - he did the entire handpicking, chemical treating and isotopic analyses for the Sm-Nd garnet age. Many thanks for that! D. Rubatto is thanked for guidance during U-Pb monazite dating at ANU, Canberra, and for correcting parts of this chapter. C. Carson is thanked for his hospitality in Canberra. J. Neubauer was always there when there was a problem with the SEM at the University of Graz (even on sunday mornings!). F. Zaccharini is thanked for help with the monazite analyses in Leoben.

Table 3.3: Bulk rock compositions of all samples

Nr	Metam. Zone	REE-group	LOI	SiO ₂	Al ₂ O ₃	Fe ₂ O ₃	MnO	MgO	CaO	Na ₂ O	K ₂ O	TiO ₂	P ₂ O ₅	Sum
B43	Phyl.	1	1.6	68.9	13.4	5.8	0.07	2.4	2.1	2.2	2.0	0.70	0.15	99.4
B44	Phyl.	1	1.9	61.1	15.6	7.1	0.12	3.8	3.3	2.7	2.2	0.91	0.18	99.3
B45	Phyl.	1	2.1	70.2	13.8	5.2	0.07	1.8	1.4	1.7	2.3	0.65	0.15	99.6
T28	Phyl.	1	3.4	59.9	17.3	6.7	0.13	3.0	2.9	2.7	2.5	0.76	0.19	99.6
Tk14	Phyl.	1	0.8	66.3	12.5	6.5	0.13	3.5	4.6	2.8	1.0	0.93	0.15	99.5
Tk15	Phyl.	1	0.9	60.8	16.6	6.8	0.12	3.0	5.1	4.4	0.9	0.77	0.18	99.8
Tk12	1	2	1.7	69.2	13.8	6.0	0.09	2.1	1.4	1.9	2.2	0.68	0.18	99.6
Tk10	2	2	2.2	64.4	16.3	7.3	0.10	2.6	1.2	1.5	2.9	0.84	0.24	99.7
Tk9	2	2	1.6	69.6	12.8	6.1	0.12	2.1	1.5	2.0	2.3	0.68	0.23	99.4
Tk8	2	2	1.1	66.5	16.0	5.4	0.07	2.0	1.9	3.7	2.3	0.69	0.06	100.0
Tk6	2	3	2.9	65.6	15.7	5.7	0.08	2.3	1.1	2.0	3.3	0.74	0.18	99.9
Tk3	2	2	2.5	60.0	18.6	7.8	0.10	2.9	1.2	2.3	3.2	0.97	0.20	99.9
B40	2	3	1.2	46.5	22.3	11.6	0.22	5.3	3.6	3.5	4.0	1.22	0.09	99.9
B39	2	3	1.2	60.3	17.4	7.3	0.23	2.9	3.2	2.8	3.1	0.75	0.23	99.6
B9	2	3	2.4	60.7	17.6	8.0	0.10	3.1	1.9	2.2	3.1	0.85	0.23	100.5
B21	3	6	0.7	68.1	15.2	4.5	0.07	2.0	3.3	3.3	2.0	0.59	0.17	100.0
B22	3	4	0.7	60.4	17.9	7.3	0.11	2.9	2.8	3.3	2.9	0.84	0.25	99.6
B23	3	5	1.3	60.8	17.2	6.9	0.10	2.9	2.8	3.1	2.7	0.76	0.28	98.8
B26	3	4	0.9	63.2	16.7	7.6	0.09	3.1	2.4	2.5	2.9	0.84	0.23	100.6
KB1f	4	4	1.5	61.7	16.9	6.9	0.11	2.9	3.2	3.1	2.6	0.87	0.22	100.3
KB2	4	5	1.1	62.8	16.5	6.4	0.09	2.7	3.2	3.2	2.4	0.73	0.23	99.8
KB5	5	4	1.2	62.3	17.1	6.3	0.11	2.8	3.3	3.2	2.9	0.86	0.18	100.7
T7	5	6	1.7	56.5	17.8	11.5	0.23	4.4	4.5	2.6	0.3	1.07	0.24	101.0
T15a	5	5	0.7	68.6	15.1	4.3	0.06	2.0	3.1	3.4	1.9	0.48	0.17	100.2
T27	5	5	1.0	65.9	15.4	5.3	0.09	2.2	3.2	3.1	2.2	0.61	0.31	99.7
T40	5	6	0.7	60.4	19.5	4.5	0.07	2.1	5.4	4.8	1.7	0.47	0.86	100.8
Loc4	5	4	1.8	66.3	15.3	5.8	0.10	2.3	2.1	2.7	2.4	0.68	0.20	99.9
N7	5	6	1.3	70.9	13.3	3.6	0.10	1.5	3.6	2.9	1.3	0.49	0.14	99.3
N17	5	6	3.4	66.9	15.2	5.3	0.08	1.9	1.1	2.2	2.8	0.68	0.22	99.9
N38c	5	6	0.5	59.5	18.0	8.0	0.23	3.1	4.1	3.3	1.8	0.84	0.20	99.9
N39	5	1	0.5	57.2	16.8	12.6	0.30	3.5	4.3	1.8	1.8	0.99	0.24	100.2
N48	5	6	1.2	58.8	18.4	8.0	0.17	3.3	2.8	3.2	2.4	0.86	0.24	99.4
Min.				46.5	12.5	3.6	0.06	1.5	1.1	1.5	0.3	0.47	0.06	98.8
Max.				70.9	22.3	12.6	0.30	5.3	5.4	4.8	4.0	1.22	0.86	101.0
Av.				63.1	16.3	6.8	0.12	2.8	2.8	2.8	2.3	0.78	0.22	99.9

Metamorphic zones as described in the text and the figure caption of figure 3.1. REE-groups as described in the text and in figure 3.1.

Table 3.4: Representative monazite EMP analyses of sample B39

Spot	B39	Av*							
	<u>1_1</u>	<u>1_2</u>	<u>1_3</u>	<u>2_1</u>	<u>2_2</u>	<u>3_1</u>	<u>3_2</u>	<u>3_3</u>	
SiO ₂	0.27	0.24	0.42	0.33	0.23	0.30	0.31	0.58	0.34
Y ₂ O ₃	1.86	2.28	1.60	1.69	2.50	2.08	1.60	1.50	1.80
P ₂ O ₅	29.92	30.03	29.95	29.65	30.04	29.63	29.64	29.44	29.70
Ce ₂ O ₃	29.51	28.64	28.38	27.85	28.08	28.56	28.62	29.45	28.99
ThO ₂	3.86	4.39	5.87	5.78	5.43	3.84	4.79	3.56	4.45
Dy ₂ O ₃	0.21	0.34	0.26	0.57	0.54	-	0.22	0.03	0.33
La ₂ O ₃	13.29	12.71	12.74	12.05	12.64	12.67	13.04	13.48	13.13
CaO	0.78	0.92	1.10	1.04	1.10	0.84	0.89	0.70	0.87
Sm ₂ O ₃	2.12	2.18	2.10	2.46	2.08	2.08	2.14	2.19	2.12
Pr ₂ O ₃	3.52	3.26	3.35	3.26	3.15	3.39	3.35	3.42	3.41
Gd ₂ O ₃	1.77	1.67	1.93	2.05	1.67	1.73	1.80	1.79	1.72
Nd ₂ O ₃	11.83	11.44	11.42	11.99	11.56	11.39	11.35	11.65	11.55
Eu ₂ O ₃	0.74	0.72	0.76	0.84	0.76	0.61	0.82	0.74	0.77
Ho ₂ O ₃	0.50	0.45	0.44	0.53	0.51	0.51	0.45	0.57	0.48
Tb ₂ O ₃	-	0.02	-	0.01	0.05	0.06	0.12	0.04	0.05
Er ₂ O ₃	-	0.02	-	-	0.08	-	-	-	0.02
Total	100.16	99.31	100.31	100.10	100.44	97.69	99.14	99.14	99.72

*Average compositions from 38 measurements on B39. The grains from the given analyses are displayed on Fig. 3.10. All analyses are displayed on Fig. 3.11.

Table 3.5: Representative Monazite EMP analyses of sample T27

	T27	*Av									
	<u>1_1</u>	<u>1_2</u>	<u>2_1</u>	<u>2_2</u>	<u>3_1</u>	<u>3_2</u>	<u>3_3</u>	<u>4_1</u>	<u>4_2</u>		<u>4_3</u>
SiO ₂	0.63	0.31	0.69	0.44	0.69	0.40	0.38	0.75	0.32	0.35	0.49
Y ₂ O ₃	0.20	2.12	0.26	2.19	0.44	2.15	2.52	0.60	1.66	3.00	1.38
P ₂ O ₅	29.15	28.70	28.95	29.61	29.06	29.31	29.49	29.34	29.93	30.24	29.43
Ce ₂ O ₃	30.37	28.17	29.56	27.85	30.58	28.02	28.01	28.82	29.30	27.01	28.86
ThO ₂	6.25	4.00	7.55	4.46	5.26	4.21	3.70	7.10	4.05	3.94	5.28
Dy ₂ O ₃	0.00	0.28	0.00	0.00	0.19	0.43	0.29	0.30	0.29	0.50	0.24
La ₂ O ₃	14.31	11.66	13.96	12.13	14.43	12.10	12.09	14.11	12.34	11.80	13.11
CaO	1.00	1.05	1.14	1.09	0.90	1.07	1.02	1.17	0.94	1.10	1.08
Sm ₂ O ₃	1.68	2.14	1.72	1.93	1.81	2.15	2.16	1.72	2.23	2.31	1.95
Pr ₂ O ₃	3.63	3.18	3.59	3.04	3.46	3.21	3.16	3.64	3.40	3.12	3.40
Gd ₂ O ₃	0.98	1.58	0.92	1.55	1.14	1.44	1.68	1.18	1.41	1.80	1.32
Nd ₂ O ₃	11.05	11.93	11.58	11.87	11.87	12.58	12.77	10.94	13.02	12.32	11.92
Eu ₂ O ₃	0.08	0.08	0.09	0.08	0.08	0.08	0.08	0.09	0.10	0.09	0.00
Ho ₂ O ₃	0.17	0.58	0.21	0.37	0.29	0.50	0.59	0.20	0.40	0.60	0.32
Tb ₂ O ₃	0.00	0.01	0.00	0.03	0.00	0.08	0.00	0.11	0.00	0.03	0.02
Er ₂ O ₃	0.00	0.02	0.00	0.08	0.00	0.11	0.11	0.00	0.00	0.03	0.02
Total	99.50	95.83	100.21	96.71	100.20	97.84	98.02	100.07	99.39	98.23	98.90

*Average compositions from 35 measurements on T27. The grains from the given analyses are displayed on Fig. 3.12, all measurements are displayed in Fig. 3.11

Table 3.6: Monazite U-Pb data

Label	U (ppm)	Th (ppm)	²³² Th/ ²³⁸ U	% common Pb	²⁰⁷ Pb/ ²³⁵ U	1σ %	²⁰⁶ Pb/ ²³⁸ U	1σ %	error corr.	²⁰⁶ Pb/ ²³⁸ U Age	±1 σ
Sample B21											
B21-1C	4112	38887	9.8	1.42	0.0474	8.2	0.00809	1.6	0.196	52.0	0.8
B21-2C	3196	26546	8.6	0.00	0.0552	3.4	0.00784	1.6	0.469	50.4	0.8
B21-2M	5441	64526	12.3	0.71	0.0480	5.1	0.00809	1.8	0.357	52.0	0.9
B21-2R	3080	37389	12.5	0.37	0.0517	5.1	0.00833	1.6	0.318	53.5	0.9
B21-3C	3972	38741	10.1	0.36	0.0497	3.9	0.00824	1.5	0.394	52.9	0.8
B21-4C	1603	23122	14.9	1.16	0.0455	7.0	0.00795	1.8	0.253	51.0	0.9
B21-5C	2885	53646	19.2	0.31	0.0498	5.8	0.00793	1.6	0.279	50.9	0.8
B21-6C	2626	28878	11.4	1.03	0.0466	7.6	0.00799	2.3	0.306	51.3	1.2
B21-6R	2471	22713	9.5	0.00	0.0545	3.9	0.00795	1.8	0.474	51.0	0.9
B21-7C	4336	39452	9.4	0.50	0.0451	6.6	0.00787	1.7	0.250	50.6	0.8
B21-8C*	4943	68740	14.4	1.35	0.0453	10.9	0.00836	2.1	0.197	53.6	1.1
B21-9C	2240	55502	25.6	1.04	0.0457	10.4	0.00792	1.9	0.183	50.9	1.0
B21-10C	3932	29956	7.9	0.27	0.0531	6.8	0.00817	3.0	0.446	52.4	1.6
Sample KB1											
KB1A-11R	13417	30504	2.3	0.18	0.0493	3.0	0.00795	1.5	0.486	51.0	0.7
KB1A-10R	6339	31408	5.1	0.58	0.0500	4.9	0.00798	1.5	0.306	51.3	0.8
KB1A-12R	8339	32679	4.0	0.19	0.0522	2.7	0.00813	1.5	0.567	52.2	0.8
KB1A-8C	7415	30480	4.2	0.42	0.0511	4.0	0.00816	1.5	0.389	52.4	0.8
KB1A-6C	8198	30578	3.9	0.00	0.0537	2.7	0.00818	1.5	0.544	52.5	0.8
KB1A-1C	5546	27957	5.2	0.00	0.0596	5.5	0.00822	1.6	0.285	52.8	0.8
KB1A-7C	7316	32106	4.5	0.00	0.0503	8.5	0.00827	1.5	0.177	53.1	0.8
KB1A-5C	6360	29322	4.8	0.41	0.0527	3.4	0.00833	1.5	0.436	53.5	0.8
KB1A-3C	7383	27492	3.8	0.42	0.0516	4.6	0.00835	2.0	0.426	53.6	1.0
KB1A-9C	2486	34781	14.5	0.85	0.0563	9.4	0.00836	2.4	0.257	53.6	1.3
KB1A-4C	7866	28833	3.8	0.49	0.0503	3.9	0.00838	1.5	0.374	53.8	0.8
KB1A-10C	3076	34049	11.4	0.53	0.0509	6.6	0.00839	1.6	0.244	53.8	0.9
KB1A-2C*	2023	21587	11.0	4.12	0.0199	47.6	0.00705	3.0	0.063	45.3	1.4
Sample KB5											
KB5-4C	3305	36461	11.4	0.85	0.0479	5.6	0.00804	2.1	0.371	51.6	1.1
KB5-2C	2009	27306	14.0	0.00	0.0577	4.4	0.00815	2.3	0.516	52.3	1.2
KB5-1C	6044	21853	3.7	0.25	0.0560	3.7	0.00822	1.9	0.521	52.8	1.0
KB5-9C	5172	25267	5.0	0.51	0.0496	4.3	0.00823	1.5	0.351	52.8	0.8
KB5-10C	2688	30811	11.8	0.00	0.0584	3.6	0.00830	1.8	0.508	53.3	1.0

Continues on following page

Table 3.6: Monazite U-Pb data

Label	U (ppm)	Th (ppm)	$^{232}\text{Th}/^{238}\text{U}$	% common Pb	$^{207}\text{Pb}/^{235}\text{U}$	1 σ %	$^{206}\text{Pb}/^{238}\text{U}$	1 σ %	error corr.	$^{206}\text{Pb}/^{238}\text{U}$ Age	$\pm 1\sigma$
KB5-1R	6867	22129	3.3	0.00	0.0554	2.7	0.00830	1.9	0.675	53.3	1.0
KB5-8C	4537	41541	9.5	1.13	0.0456	7.4	0.00831	1.5	0.208	53.4	0.8
KB5-7C	5012	22550	4.6	0.52	0.0489	4.1	0.00836	1.6	0.395	53.7	0.9
KB5-10R	10058	18487	1.9	0.00	0.0540	2.3	0.00838	1.4	0.635	53.8	0.8
KB5-5R	8488	20678	2.5	0.28	0.0530	3.0	0.00843	1.8	0.590	54.1	1.0
KB5-6C	5221	38398	7.6	0.60	0.0552	5.0	0.00844	1.6	0.314	54.2	0.8
KB5-3C	3660	31100	8.8	0.00	0.0569	3.1	0.00845	1.6	0.499	54.2	0.8
KB5-4M	8347	20185	2.5	0.00	0.0552	2.5	0.00853	1.6	0.652	54.8	0.9
KB5-4R*	4402	26956	6.3	1.18	0.0405	9.4	0.00784	3.7	0.391	50.3	1.9
KB5-8R*	5323	21729	4.2	4.42	0.0545	18.3	0.00802	1.9	0.103	51.5	1.0
KB5-2R*	3941	19976	5.2	2.38	0.0721	9.2	0.00827	1.6	0.178	53.1	0.9
KB5-5C*	4375	37643	8.9	1.41	0.0424	13.1	0.00828	1.6	0.124	53.1	0.9
KB5-8M*	2528	29537	12.1	1.10	0.0441	14.6	0.00851	3.0	0.202	54.6	1.6
Sample T27											
T27-11C	3291	34414	10.8	0.81	0.0497	6.8	0.00803	1.6	0.238	51.5	0.8
T27-7R	5519	31414	5.9	0.59	0.0515	5.6	0.00808	1.6	0.280	51.8	0.8
T27-6C	4057	38046	9.7	0.96	0.0504	6.0	0.00808	2.2	0.361	51.9	1.1
T27-10R	15265	21526	1.5	0.26	0.0506	3.1	0.00809	1.5	0.467	51.9	0.8
T27-1C	6439	68741	11.0	1.13	0.0472	4.5	0.00810	1.7	0.364	52.0	0.9
T27-2R	8892	28224	3.3	0.36	0.0489	3.1	0.00812	1.5	0.479	52.1	0.8
T27-4C	8999	22585	2.6	0.33	0.0513	4.0	0.00814	2.9	0.709	52.2	1.5
T27-7C	3737	28640	7.9	0.00	0.0586	3.2	0.00814	1.5	0.481	52.3	0.8
T27-9C	5246	31195	6.1	0.80	0.0535	4.9	0.00818	2.3	0.464	52.5	1.2
T27-6R	8555	27730	3.3	0.71	0.0492	3.9	0.00818	1.6	0.412	52.5	0.8
T27-3C	4515	36312	8.3	0.00	0.0580	3.1	0.00829	1.6	0.507	53.2	0.8
T27-1R	9590	18836	2.0	0.35	0.0474	4.7	0.00832	1.4	0.309	53.4	0.8
T27-8C	4677	44039	9.7	0.46	0.0525	5.9	0.00833	2.1	0.356	53.5	1.1
T27-5C	11855	27660	2.4	0.38	0.0517	3.3	0.00838	1.9	0.572	53.8	1.0
T27-1M*	1452	44155	31.4	1.57	0.0465	14.2	0.00759	3.9	0.275	48.8	1.9
T27-2C*	2796	32899	12.2	1.50	0.0444	12.3	0.00791	2.2	0.183	50.8	1.1

* denotes measurement excluded in age calculation and Concordia plots

Chapter 4

Large-scale, short-lived metamorphism and magmatism in the Chugach Metamorphic Complex (CMC), southern Alaska: a zircon U-Pb SHRIMP study

Abstract We present U-Pb SHRIMP geochronology of metamorphic and magmatic zircons from the Chugach Metamorphic Complex, southern Alaska. Seven metamorphic and magmatic zircon ages from the western and central parts of the complex range between 54.0 ± 0.9 Ma and 52.6 ± 0.8 Ma and are within error of each other. One metamorphic zircon age from the south-eastern part is 51.3 ± 0.7 Ma, which is within error of two of the seven samples from the western and central parts. Combined with previous U-Pb ages of magmatic rocks of the Sanak-Baranof belt, our data constrain the age and duration of metamorphism and magmatism to ~ 3 Ma between ~ 55 - 52 Ma on a ~ 200 km long section in the western and central part of the complex, and to ~ 2 Ma between ~ 52 - 50 Ma on a ~ 400 km long section from the south-eastern part of the complex to Baranof Island. Youngest detrital zircon grains from one of the samples (~ 63 Ma) limit the time available for prograde metamorphism to only ~ 8 Ma. Cooling ages of ~ 53 - 46 Ma from the literature for the western and central part of the complex point to fast cooling after metamorphism. Such a short metamorphic cycle simultaneously occurring over a large distance is difficult to explain by heat conduction, and advective heat sources like fluids or magmas can also be excluded. We propose that this cycle is best explained by advection of material during rapid, penetrative deformation in an actively deforming fold-and-thrust belt aided by internal heat production from strain heating.

submitted to Geological Society of America Bulletin

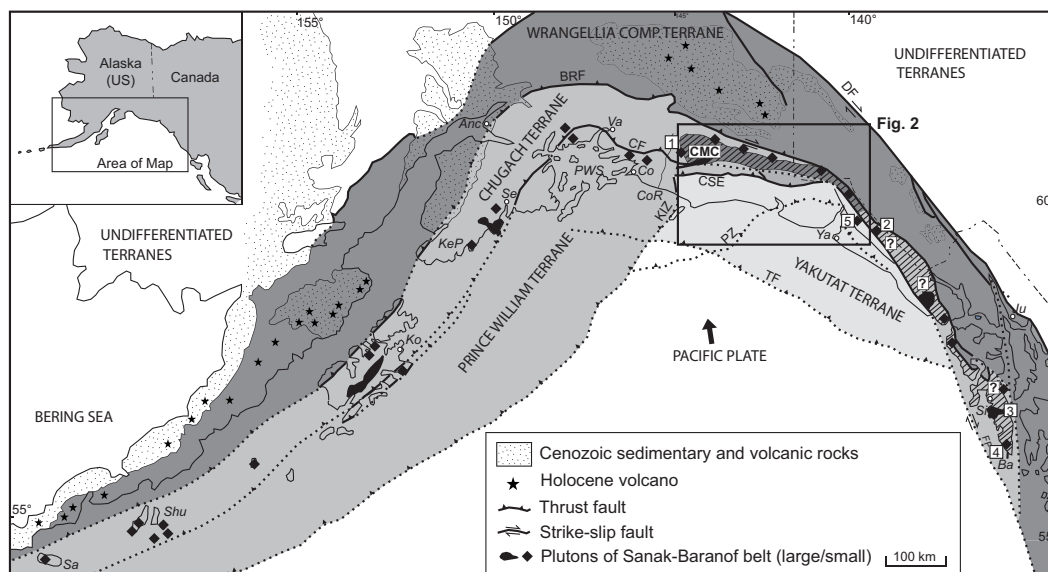


Figure 4.1: Tectonic overview map of the southern Alaskan margin with terrane names, plutons of the Sanak-Baranof belt and the Chugach Metamorphic Complex (CMC) indicated. The CMC is traditionally defined west of the U.S. Canadian border (Hudson & Plafker, 1982), but rocks of similar metamorphic grade may extend as far to the south-east as Baranof Island (Zumsteg et al., 2003). Abbreviations: CMC= Chugach Metamorphic Complex, Sa=Sanak Island, Shu=Shumagin Islands, Ko=Kodiak, KeP=Kenai Peninsula, Se=Seward, Anc=Anchorage, PWS=Prince William Sound, Va=Valdez, Co=Cordova, CoR=Copper River, Ya=Yakutat, Si=Sitka, Ju=Juneau, Ba=Baranof Island, BRF=Border Range Fault, CF=Contact Fault, KIZ=Kayak Island Zone, CSE=Chugach-St-Elias-Fault, PZ=Pamplona Zone, TF=Transition Fault, FF=Fairweather Fault, DF=Denali Fault. (1)-(5) Location of magmatic rocks dated by the U-Pb method during previous studies and plotted on Fig. 10b. (1) Tonalitic sill in Van Cleve Glacier area (Sisson et al., 2003), (2) Novatak glacier pluton (Sisson et al., 2003), (3) Crawfish Inlet pluton (Bradley et al., 1993, 2003), (4) Redfish bay pluton (Bradley et al., 2003), (5) Mt. Draper pluton (Sisson et al., 2003).

4.1 Introduction

Determining the exact timing and duration of metamorphic and magmatic events is one of the key challenges in the field of geochronology and an important factor for understanding the processes that form the Earth's crust. The duration of regional metamorphism has bearings on the different thermal and tectonic mechanisms responsible for heat transfer. Classical models of collision zones assume conductive heating (and cooling) and predict metamorphic cycles that last tens of millions of years with a pronounced asynchrony between the timing of peak metamorphism at different crustal levels (e.g. England & Thompson, 1984; Ruppel & Hodges, 1994; Huerta et al., 1996; Jamieson et al., 1998; Stuewe, 1998a). However, over the last decades, geochronological studies of natural examples of regional metamorphic complexes covering various metamorphic grades (from low-pressure/high-temperature to high-pressure/low-temperature terrains) revealed that metamorphism actually may oc-

cur over much shorter time periods and/or proceed in short-lived episodes (e.g. Wijbrans & McDougall, 1987; Chamberlain & Rumble, 1988; Treolar, 1997; Philippot et al., 2001; Rubatto & Hermann, 2001; Camacho et al., 2005; Dewey, 2005; Forster & Lister, 2005; Ague & Baxter, 2007; Beltrando et al., 2007; Lancaster et al., 2008). Such short thermal spikes associated with high rates of heating and cooling are difficult to explain by conductive processes only, and other processes such as advective ascent of magmas or fluids (e.g. Lux et al., 1986; De Yoreo et al., 1991), tectonic advection via rapid burial or exhumation of isolated crustal blocks (e.g. Rubatto & Hermann, 2001), or in-situ production of radiogenic and mechanical or chemical heat (e.g. Burg & Gerya, 2005) were postulated to contribute to the formation of regional metamorphic terrains. Metamorphism as the result of such advective or heat-producing processes is not limited by relatively slow heat conduction and can therefore be fast, short-lived and synchronous over large areas.

In this contribution we present the results of U-Pb SHRIMP zircon geochronology on a large-scale metamorphic complex which is exposed in the Late Cretaceous to Paleocene accretionary prism of southern Alaska: the Chugach Metamorphic Complex (CMC, Fig. 4.1 and 4.2; Hudson & Plafker, 1982; Sisson & Hollister, 1988; Sisson et al., 1989). No geochronological ages which would document the exact timing and duration of peak metamorphism in this complex are available so far. The only two K-Ar cooling ages from the metamorphic rocks of the CMC (51.5 ± 2 and 46.7 ± 2 Ma for hornblende and biotite, respectively; Hudson et al., 1979) suggest that a relatively short time period was available to produce the metamorphic complex in Late Cretaceous to Paleocene sedimentary rocks. Our first goal is to constrain the timing and duration of peak metamorphism in the CMC. In addition, the metamorphic rocks of the CMC are associated with magmatic rocks, which are part of a larger plutonic belt that extends from Sanak Island in the west to Baranof Island in the south-east: the Sanak-Baranof plutonic belt (Fig. 4.1; Hudson et al., 1979; Farris & Paterson, 2009). Geochronological data from these magmatic rocks suggest that there is an age gradient in the magmatism from ~ 61 Ma in the west to ~ 50 Ma in the east (Bradley et al., 1993, 2000, 2003; Häussler et al., 1995, 2003a; Sisson et al., 2003; Farris et al., 2006). In this context, our second goal is to understand the timing relationships between metamorphism and magmatism and to determine if the west-east age gradient that is present in the magmatic rocks is also recorded in the metamorphic rocks of the CMC. We finally discuss implications of our results for possible heat transfer mechanisms into the complex.

4.2 Geology of the southern Alaskan margin

The southern Alaskan margin consists of a complexly deformed accretionary prism that formed from the Late Triassic to the present due to the northward oblique subduction of oceanic plates of the Pacific basin below the North American continent. South of the present-day volcanic arc, this prism is generally subdivided into the Chugach, Prince William and Yakutat terranes (Fig. 4.1; Plafker et al., 1994). The most landward terrane - the

Chugach terrane - is bound to the north by the Border Range Fault and consists of a northern, narrow, Late Triassic to Cretaceous mélange belt (~10% of the terrane) and a southern, more homogenous Late Cretaceous to Paleogene volcano-clastic turbidite sequence (~90% of the terrane). This turbidite sequence extends from Sanak Island in the west to Baranof Island in the south-east and consists of greenschist-facies conglomerates, impure sandstones, marls and claystones, which are intercalated with mafic volcanic rocks. The turbidite sequence has been interpreted to represent a deep marine trench-fill deposit derived from a magmatic arc south-east of the current exposure (Nilsen & Zuffa, 1982; Farmer et al., 1993; Plafker et al., 1994). Several local formation or group names such as Shumagin and Kodiak Formation, Valdez Group and Sitka Greywacke have been assigned to this turbidite sequence. The Chugach Metamorphic Complex described further below is developed in the Valdez Group of the Chugach terrane (Fig. 4.1).

Mafic rocks are especially abundant in the southern Chugach terrane east of Prince William Sound and form a narrow (~1-3 km wide) belt of greenschist- to amphibolite-facies rocks, intercalated with sediments, which extends from Valdez in the west down to Baranof Island in the south-east (Fig. 4.2; Lull & Plafker, 1990). A seismic profile through the Prince William Sound region suggests that those rocks are the surface expression of an up to 10 km thick package of mafic rocks and sediments which dips from the surface northwards below the Chugach terrane down to depths of at least ~20 km (Fuis et al., 1991, 2008).

The Prince-William terrane farther seawards consists of similar turbidites of slightly younger age (mainly the Eocene Orca group), which are separated from the Chugach terrane by the syn- to post-accretionary Contact fault system (Fig. 4.1; Plafker et al., 1994). The Yakutat terrane finally consists of an oceanic and continental basement that is overlain by thick, clastic Neogene sediments. The continental basement consists of metamorphosed, Cretaceous to Paleogene turbiditic rocks similar to the rocks of the Chugach terrane. The Yakutat terrane was dextrally displaced along the Fairweather fault and now actively collides with the Chugach and Prince William terranes farther inboard (Fig. 4.1; Plafker et al., 1994).

Magmatic rocks of the Sanak-Baranof plutonic belt intrude the Chugach terrane and the northernmost part of the Prince William terrane, from Sanak Island in the west to Baranof Island in the southeast (Fig. 4.1; Hudson et al., 1979; Farris & Paterson, 2009). The belt consists of a series of tonalitic, granodioritic and granitic intrusions a few hundred meters to several kilometers in size. The plutons are insofar unusual as they intrude the accretionary prism shortly after its accretion and are therefore located in an extreme forearc-position - the corresponding coeval magmatic arc is located a few hundred kilometres farther inboard (Kuskokwim-Alaska-Range belt and Kluane belt/Coast Plutonic Complex, Plafker et al., 1994). Geochemically, the intrusions consist of sediment-derived and mantle-derived components. Apart from local complexities, some general trends can be observed in the intrusions from west to east. The western part from Sanak to Kodiak Island is characterized by wide spacing between magmatic centers, low regional metamorphic grade, and intrusions mainly derived from melted sediments, with only minor basaltic components. The eastern part from the western CMC to Baranof Island is characterized by narrow spacing between

magmatic centers, high regional metamorphic grade and higher basaltic components (up to 80%) in the melts (Fig. 4.1; Farris & Paterson, 2009). U-Pb zircon and monazite ages, K/Ar, Rb/Sr and $^{40}\text{Ar}/^{39}\text{Ar}$ ages of micas point to a broadly defined age gradient in magmatism from ~61 Ma in the west to ~50 Ma in the south-east (Bradley et al., 1993, 2000, 2003; Sisson et al., 2003; Farris et al., 2006). This age progression, the fore-arc position in the accretionary prism, the chemical composition of the igneous rocks, and the regional-scale metamorphism of the CMC have been interpreted as the result of the subduction of an active oceanic spreading ridge below the accretionary prism (Marshak & Karig, 1977; Bradley et al., 1993, 2000, 2003; Sisson & Pavlis, 1993; Häussler et al., 1995, 2003a; Harris et al., 1996; Madsen et al., 2006; Farris & Paterson, 2009). However, the unknown amount of dextral displacement of the Chugach and Prince William terranes since their intrusion by the Sanak-Baranof belt, and the fact that most magnetic anomalies from the time of interest are subducted, reveals great freedom in which oceanic ridge actually subducted below the accretionary prism in the Paleocene to Eocene Ma and therefore models which restore the situation during emplacement of the plutons vary considerably (e.g. Sisson & Pavlis, 1993; Bradley et al., 2003; Häussler et al., 2003a; Madsen et al., 2006).

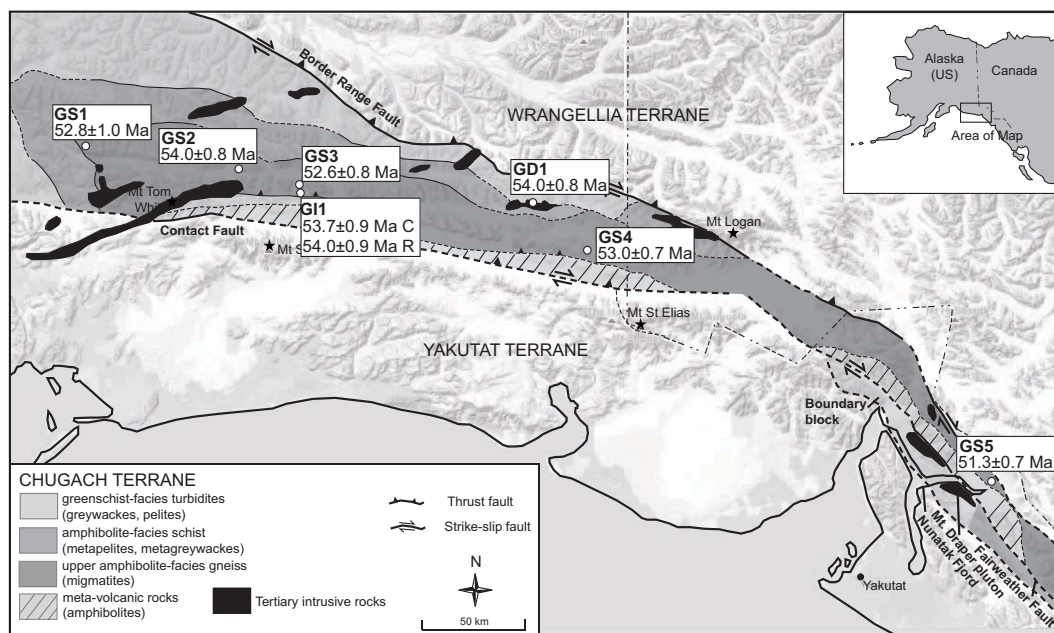


Figure 4.2: Geological Map of the Chugach Metamorphic Complex (modified from Hudson & Plafker, 1982) with localities of samples used for zircon SHRIMP U-Pb geochronology. Samples GS1-GS5 are metasedimentary migmatitic gneisses from the core of the CMC. Sample G11 is a meta-igneous gneiss, C=core age, R=rim age. Sample GD1 is from a granodioritic intrusion cross-cutting the schist zone of the CMC. Ages reported are Concordia ages ($\pm 95\%$ c.I.) except for the rim age of sample G11 for which a weighted mean $^{206}\text{Pb}/^{238}\text{U}$ age ($\pm 95\%$ c.I.) is given. Coordinates, mineralogy and PT conditions for all samples are reported in Table 4.1, ages are reported in Table 4.3.

In the eastern part of the Chugach terrane, the magmatic rocks of the Sanak-Baranof plutonic belt are accompanied by a large-scale metamorphic complex: The Chugach Metamorphic Complex (Figs. 4.1, 4.2). The area where the CMC crops out is high-alpine: peaks reach altitudes of >5000 meters and the area is covered by the 3rd largest continental ice field in the world. Access to the CMC is therefore difficult and only possible by fixed wing aircraft or helicopter assistance. The CMC was first described by Hudson & Plafker (1982) in a reconnaissance study. They define the complex between the Copper River in the west and the US-Canadian border in the east (Figs. 4.1, 4.2). In that region, the metamorphic grade of the Late Cretaceous Valdez Group increases and two macroscopically different metamorphic zones are present: An outer schist zone composed of fine-grained biotite-quartz-plagioclase schist, and an inner gneiss zone composed of layered migmatitic gneisses (Fig. 4.2). The greenschist-facies slates outside these two zones are referred to here as the phyllite zone, whereas the two others are referred to as the schist and gneiss zones, respectively. Schist and gneiss zone together define the CMC. The distribution of the schist and gneiss zone is asymmetric: there is a wide transition from phyllite to schist to gneiss in the north and an abrupt juxtaposition of gneisses against phyllites in the south (Fig. 4.2). The migmatitic core is up to ~25 km wide in the west and ~5-10 km wide in the south-east.

Information on *PT* conditions from the CMC is sparse. Sisson & Hollister (1988) and Sisson et al. (1989) analysed samples from five localities along the northern and western border of the CMC (mainly in the schist zone) and derived peak pressures of ~2.5-3.5 kbar (~9-13 km depth) and peak temperatures of ~600-660°C. These values have since been cited as being representative for the entire complex (e.g. Sisson & Pavlis, 1993; Pavlis & Sisson, 1995, 2003; Bradley et al., 2003). According to these authors, the entire CMC therefore represents an unusual low-pressure/high-temperature complex, which developed in an accretionary prism shortly after its accretion. However, a recent detailed thermobarometric study which covers a much larger area of the CMC and which extends as far to the south-east as Nunatak fjord (Fig. 4.2) obtained metamorphic conditions of ~450-550°C and <4 kbar for the phyllite zone, ~550-650°C and ~3-5 kbar for the schist zone, and >650°C and 6-13 kbar for the gneiss zone (Bruand, 2010). According to these results, the pressure increases significantly from the schist to the gneiss zone and peak metamorphic conditions in the gneisses are more typical for Barrovian type metamorphism. Partial melting occurred in this gneiss zone probably not by muscovite break-down melting, but by water-saturated melting, similarly to the process described for migmatites in Berger et al. (2008) and Rubatto et al. (2009).

4.3 Timing and duration of metamorphism and magmatism in the Chugach Metamorphic Complex

In order to study the timing and duration of metamorphism and magmatism over the entire CMC, seven samples were selected for U-Pb geochronology on zircon. Since the U-Pb closure temperature in zircon is very high (800-1000°C; Cherniak & Watson, 2003), U-Pb zircon ages generally reflect the time of mineral crystallization. During metamorphism and anatexis, small metamorphic zircon overgrowths may form on older zircon cores. The application of the SHRIMP ion microprobe allows analysing exceptionally small metamorphic overgrowths (~10 µm). Because zircon growth can occur over a wide range of *PT* conditions we strive to link the ages of such zircon overgrowths with the *PT* evolution of the host rock. Petrographic observations, zircon internal structure, Ti-in-zircon thermometry and trace elemental analyses of zircons are used to create this link.

4.3.1 Analytical techniques

Whole rock compositions of the samples used for U-Pb geochronology were obtained with a Siemens Pioneer S4 WD-XRF at the Department of Earth Sciences, University of Graz. Zircon grains were extracted from the samples by crushing, sieving, magnetic and heavy liquid separation, and then handpicked, mounted in epoxy and polished to expose the grain centers. The internal zoning of the zircons was investigated by Cathodoluminescence (CL) imaging, carried out at the Electron Microscope Unit, Australian National University (ANU), with a HITACHI S2250-N scanning electron microscope working at 15 kV, ~60 nA and ~20 mm working distance.

Trace element compositions (including Ti) of zircons were measured with LA-ICP-MS at the Research School of Earth Sciences (RSES), ANU, using a pulsed 193 nm ArF Excimer laser with 100mJ energy at a repetition rate of 5 Hz, coupled to an Agilent 7500 quadrupole ICP-MS. Spot sizes of 22 µm and 28 µm were used to analyse rims and cores, respectively. External calibration was performed relative to NIST 612 glass (Pearce et al., 1996) and internal standardisation was based on Si. Accuracy and reproducibility were evaluated by repeated analyses of a BCR-2G secondary glass standard and are within 15% and <5% for all elements except for Y. During the time-resolved analysis of the zircons, contamination resulting from fractures or mineral inclusions was monitored and only the undisturbed part of the signal was integrated.

U-Pb analyses on zircons were performed with a sensitive high-resolution ion microprobe (SHRIMP RG) at the RSES, ANU, using a beam size of ~10-20 µm. Instrumental conditions and data acquisition for zircon analysis were generally as described by Williams (1998). The data were collected in sets of six scans throughout the masses and a reference zircon was analysed each fourth to fifth analysis. Reference zircon from a granodiorite

(Temora, 417 ± 1 Ma, Black et al., 2003) was used to correct the measured $^{206}\text{Pb}/^{238}\text{U}$ ratio of our unknown samples. A zircon of known composition (SL13, U = 238 ppm) was used to determine the U content. The analyses were corrected for common Pb using three different methods based on ^{204}Pb , ^{207}Pb and ^{208}Pb measurements following Williams (1998). All three corrections returned results identical within error. Here we present data corrected by the ^{208}Pb method plotted on Concordia diagrams, and we calculate Concordia ages following Ludwig (1998). The common Pb composition was according to the Stacey & Kramers (1975) model. U-Pb data were collected over four analytical sessions using the same standard, with the different sessions having calibration errors between 1 and 1.9% (2 sigma), which was propagated to single analyses. Additionally, a 1% error was added to the final average age to account for external errors. Data evaluation and age calculation were done using the software Squid2 and Isoplot/Ex (Ludwig, 2003), respectively. Zircon rims in sample GL1 contain exceptionally high amounts of U requiring an additional matrix correction for analysis with $\text{U} > 2500$ ppm. Details of this correction are given in the data presentation.

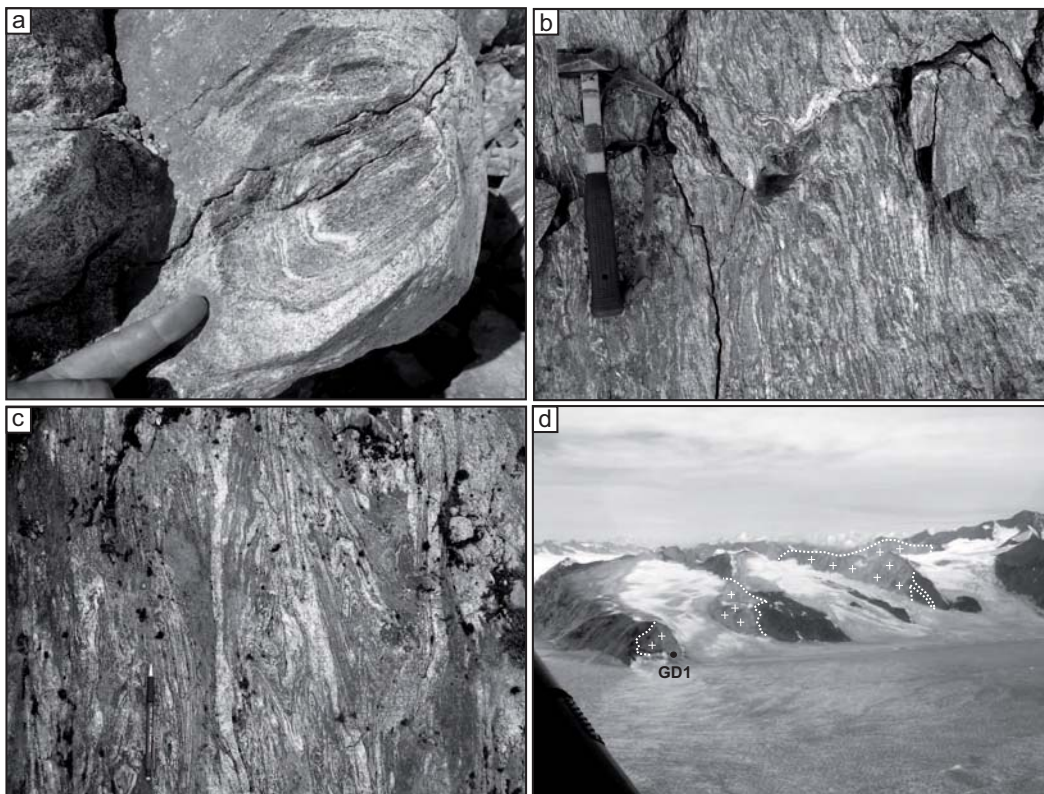


Figure 4.3: Representative field photographs of rocks from the core of the CMC sampled for zircon geochronology. **(a)** Outcrop of sample GS2 (finger for scale), **(b)** Outcrop of sample GS4 (hammer for scale), **(c)** Outcrop of sample GS5 (pencil for scale), **(d)** Granodioritic intrusion in schist zone of CMC, with sample location of GD1. Width of view ~4 km, wing of airplane in lower left corner of image.

Table 4.1: Summary of all samples used for U-Pb geochronology

Nr.	Field-Nr.	Latitude (°N)	Longitude (°W)	Rock type	Mineralogy <small>+Bt+Qz+Plag</small>	<i>PT</i> conditions
GS1	91Asn11	60.8236	144.2500	PG	Grt	650°C±50°C*
GS2	KB5	60.7380	143.3014	PG	Ms	>640°C† 730°C/7-8 kbar§**
GS3	T27	60.7146	142.9147	PG	Ms-Grt	680±30°C/7.3±1.1 kbar# 710-720°C/8-9 kbar§ 660±50°C*
GI1	T40	60.6827	142.9238	OG		>640°C†
GD1	Tk7	60.6670	141.5521	I	Ms-Kfs	-
GS4	Loc4	60.5544	141.3030	PG	Ms-Grt-Sil	670±25°C/8.2±1.2 kbar# 670±50°C†
GS5	N9	59.8223	138.8313	PG	Ms	640±30°C/8.2±1 kbar#**, 680°C/9-10 kbar§**, 670±50°C†**

PG=paragneiss, OG=orthogneiss, I=intrusion, *Biotite-garnet thermometry, †Graphite thermometry, §Pseudo-section estimate (Thermocalc), #Average PT (Thermocalc), **PT information is not from sample itself, but from a sample within 1 km in the same continuous zone.

4.3.2 Sample description: field occurrence, whole rock composition and petrography

We selected five metasedimentary gneisses, one meta-igneous gneiss and one granodioritic intrusion for U-Pb geochronology on zircon. The samples cover the gneiss zone of the CMC from W to SE over a distance of ~330 km along strike (Fig. 4.2). Coordinates, mineral assemblages and *PT* estimates for each sample are recorded in Table 4.1.

Sample GS1 was collected in 1991 (V.B. Sisson, pers. comm.), the others by the authors in summer 2008. Samples GS1-GS5 are all layered metasedimentary gneisses typical for the core of the CMC (Fig. 4.3a-c). They are migmatitic gneisses, with mm- to several cm-thick light quartz + plagioclase layers separated from mm- to several cm-thick dark layers consisting of biotite, quartz and plagioclase. Muscovite is present in all samples except for GS1. Garnet is present in GS1, GS3 and GS4. Sillimanite is present in GS4. All gneiss samples contain small amounts of retrograde chlorite, muscovite or epidote. The quartz-plagioclase layers are interpreted as leucosome derived from segregated partial melt, and the dark layers are either melanosome (residuum after certain degree of melt extraction) or paleosome not affected by partial melting. The gneisses are mostly metatexites, formed from relatively low degrees of partial melting (Sawyer, 2008). Since the layering is very dense, both dark and light layers were crushed together for separation of zircons from samples GS1-GS5. Peak metamorphic temperature estimates for the gneiss samples are ~650-720°C, and pressure estimates range from ~7-10 kbar, corresponding to depths of ~25-37 km (Tab. 4.1).

Structurally, the gneisses show a main gneissic foliation defined by biotite (regionally termed S_2 ; Pavlis & Sisson, 1995, 2003), which is isoclinally folded at the cm- to meter-scale into open to isoclinal, upright folds (regionally termed F_3 ; Pavlis & Sisson, 1995, 2003). The thickness of the light layers is often thicker in the fold hinges than on the fold limbs. With increasing intensity of F_3 folding, new biotite grows parallel to the F_3 axial planes and locally, the S_2 foliation is completely transposed into an S_3 foliation, which is subvertical all along the core of the CMC (Figs. 4.3a-c). Compositionally, the samples range from typical calcareous metapelites with high Al_2O_3 , Fe_2O_3 and CaO (samples GS2-GS4, Tab. 4.2) to more quartzofeldspathic metagreywacke with high SiO_2 and low Fe_2O_3 (sample GS5, Tab. 4.2). This compositional variation reflects differences in the composition of the sedimentary protolith which is typical for the Valdez Group in which the CMC is developed (e.g. Nilsen & Zuffa, 1982).

Sample GI1 stems from a small outcrop exposed at the southern border of the gneiss zone in the western part of the CMC (Fig. 4.2). It does not contain the dark and light mm- to cm-thick layers typical for the migmatitic metasedimentary gneisses of the CMC, but is an only slightly foliated, relatively homogenous gneiss consisting mainly of quartz, plagioclase, biotite and very few muscovites. The homogenous and only slightly foliated texture suggests a meta-igneous origin for this gneiss, but the contact to the adjacent metasedimentary gneisses is not exposed and therefore the potential intrusive contact cannot be confirmed from field observations. The whole rock composition of this sample is slightly different from that of the gneisses, with lower SiO_2 , higher Al_2O_3 , CaO and Na_2O (Tab. 4.2).

Sample GD1 is from a granodioritic intrusion exposed in the central northern part of the CMC (Fig. 4.2 and Fig. 4.3d). This intrusion is exposed on ~ 50 km² and cuts unconformably through the outer schist zone of the CMC. It is internally not deformed and cuts the structures in the surrounding schists. In addition it has a narrow contact metamorphic halo indicating that it intruded slightly after the metamorphic peak in the schists. Petrographically, the intrusion consists of quartz, plagioclase, minor K-feldspar and biotite.

Table 4.2: Bulk rock compositions (in wt%)

Nr.	SiO ₂	Al ₂ O ₃	Fe ₂ O ₃	MnO	MgO	CaO	Na ₂ O	K ₂ O	TiO ₂	P ₂ O ₅	LOI ()	Sum
GS2	62.34	17.14	6.31	0.11	2.84	3.30	3.20	2.93	0.86	0.18	1.19	100.70
GS3	65.88	15.43	5.31	0.09	2.25	3.19	3.12	2.21	0.61	0.31	1.01	99.65
GI1	60.43	19.51	4.52	0.07	2.07	5.36	4.83	1.74	0.47	0.86	0.71	100.79
GD1	67.34	17.03	2.88	0.05	1.02	3.29	4.25	2.40	0.34	0.15	0.61	99.59
GS4	66.32	15.28	5.82	0.10	2.28	2.09	2.69	2.38	0.68	0.20	1.81	99.85
GS5	71.44	14.86	2.08	0.04	0.92	3.31	3.61	1.64	0.27	0.14	1.35	99.67

Note: There is no data for Sample GS1.

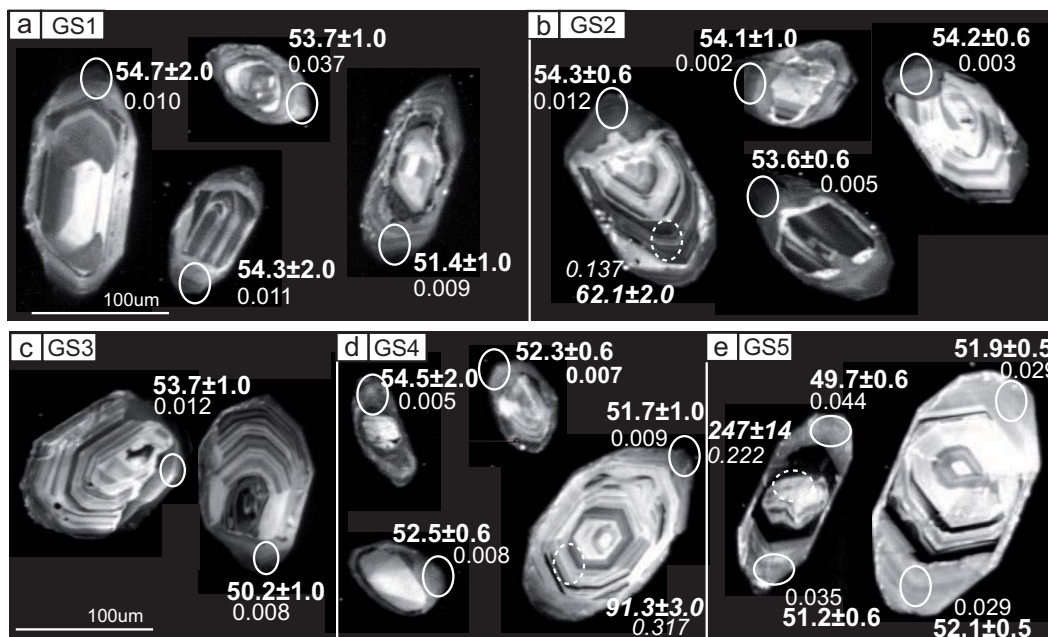


Figure 4.4: CL-images of representative zircon grains from the layered metasedimentary gneisses. SHRIMP spots, corresponding $^{206}\text{Pb}/^{238}\text{U}$ age (in Ma $\pm 1\sigma$ -error) and Th/U ratio are indicated. Age spots in italics are core measurements. Note the irregular shape of the cores compared to the euhedral rims.

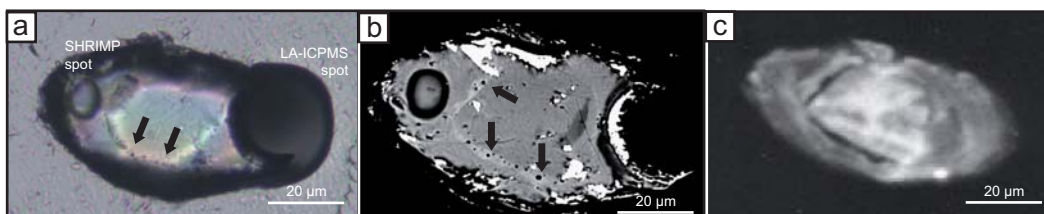


Figure 4.5: (a) Transmitted light image, (b) BSE image, and (c) CL image of zircon crystal from sample GS4. The core-rim boundary in this crystal is marked by small rounded inclusions ($<1\ \mu\text{m}$, dark arrows), accompanied by a light band in BSE (dark in CL). About 5-10% of the zircon grains in the gneisses show such rounded inclusions along the core-rim boundary. The bright spots in (b) represent remnants of the gold coating used for SHRIMP analysis.

4.3.3 Zircon description

Zircon grains separated from all metasedimentary gneiss samples (GS1-GS5) are ~ 50 - $180\ \mu\text{m}$ in length. Whereas GS1, GS2 and GS4 yielded several hundred grains out of fist-sized samples, only a few dozen grains could be obtained from GS3 and GS5. In all gneiss samples the zircons show rounded, sub-rounded and short-prismatic shape, a few long-prismatic types occur. CL-images (Fig. 4.4) reveal that $\sim 90\%$ of the grains consist of a

variably zoned (oscillatory, patchy or sector zoned) core surrounded by a ~5-30 μm wide, CL-bright to dark rim. About 10% of the grains do not show any rim. Some of the cores have regular, prismatic crystal faces, others are slightly rounded or broken, but most cores have an irregular and pitted surface with embayments that truncate the core zoning (Fig. 4.4). Some grains also show a bright CL zone between the cores and the darker rims (e.g. the first three grains in Fig. 4.4b). Similar bright CL-seams at the periphery of detrital cores are often observed in zircons from metasediments (e.g. Vavra et al., 1996). In most grains, the core-rim boundary is sharp, but in some cases the transition is blurry. Most rims are unzoned, but some contain weak concentric zones or mimic weakly the zoning present in the core (Fig. 4.4). In ~5-10% of the crystals, small, rounded inclusions are visible along the core-rim boundary in transmitted light (Fig. 4.5a). The inclusions are accompanied by a slightly lighter band in BSE images (Fig. 4.5b). Unfortunately, the inclusions are too small for electron microprobe analysis, but similar rounded inclusions accompanied by a lighter band in BSE images were identified by Cesare et al. (2003) as representing melt inclusions.

Zircons separated from the meta-igneous sample G11 are ~100-300 μm in length and have prismatic shapes (Fig. 4.6a). About 80% of the grains show a core-rim structure with ~5-30 μm thick rims. Unlike the zircons from the metasedimentary gneisses, the zircon cores of sample G11 have remarkably similar CL-zoning (Fig. 4.6a) with either coarse parallel growth zoning (mostly in the long-prismatic habits) or coarse patchy zoning. No fine oscillatory zoning as observed in the layered gneisses is present. Some cores contain inclusions of up to ~20 μm of quartz, feldspar or biotite. The rims are dark in CL-images and some show weak concentric growth zones.

Zircons separated from the granodiorite GD1 are ~50-150 μm in length and prismatic. Coarse parallel and concentric growth zoning is present (Fig. 4.6b). No rims were observed in these grains.

4.3.4 Zircon composition and Ti-in-zircon thermometry

The trace element compositions of the different zircon domains identified by CL were analysed by LA-ICP-MS. Most analyses correspond to domains previously dated by SHRIMP. The cores and rims of all zircon crystals are easily distinguishable based on their U and Th content: cores contain between 34-536 ppm Th and 143-2347 ppm U (Th/U ratios of 0.1-0.7), whereas rims contain between 2-562 ppm Th and 334-8847 ppm U (Th/U ratios of 0.001-0.1, SHRIMP data, Fig. 4.7a, Tab. 4.3, Tab. 4.4). The zircon rims in the meta-igneous sample G11 show a particularly large scatter in their U and Th contents (Fig. 4.7a).

Ti content in zircon was routinely measured during LA-ICP-MS analyses and can be used to calculate crystallization temperatures of the zircons (Watson & Harrison, 2005; Watson et al., 2006). However, Ti values measured in the zircon rims of samples GS1-GS5 scatter widely between different rims from the same sample (Tab. 4.4). This variation does not



Figure 4.6: (a) Representative CL-images of dated zircon grains from sample G11. Age spots in italics are core measurements. Spots filled grey are measurements excluded in calculating total rim age (see text). (b) Representative CL-images of dated zircon grains from the granodioritic intrusion GD1. In both (a) and (b) SHRIMP spots, corresponding $^{206}\text{Pb}/^{238}\text{U}$ age (1σ -error) and Th/U ratio are reported.

represent a real variation in crystallization temperature of the different rims in the same sample, and two other explanations are possible. (1) The zircon rims formed either not in equilibrium with the local environment or in a system which was not buffered for Ti. In either case the Ti contents would not correlate with T. However, the rather constant MREE and HREE composition of the same zircon rims (Fig. 4.7d) argues against a disequilibrium scenario. (2) Ti measurement was contaminated by inclusions or surface Ti. Contamination was particularly likely given that the zircon rims were particularly thin (Figs. 4.4, 4.5) and inclusions were indeed observed at the core-rim boundary (Fig. 4.5). Despite monitoring the laser signal for inclusions, contamination from micro-inclusions or the crystal surface cannot always be eliminated. The concentration of Ti on the zircon surface or along fractures has been carefully documented by other workers (Hiess et al., 2008; Hofmann et al., 2009). If the scatter in Ti values is the result of contamination, only the lower values of the measured range are significant and indicative of the zircon crystallization temperature. In all the above samples minimum values are around 1-4 ppm. This would correspond to crystallization temperatures of ~620-720 °C (Tab. 4.3, Watson & Harrison, 2005; Watson

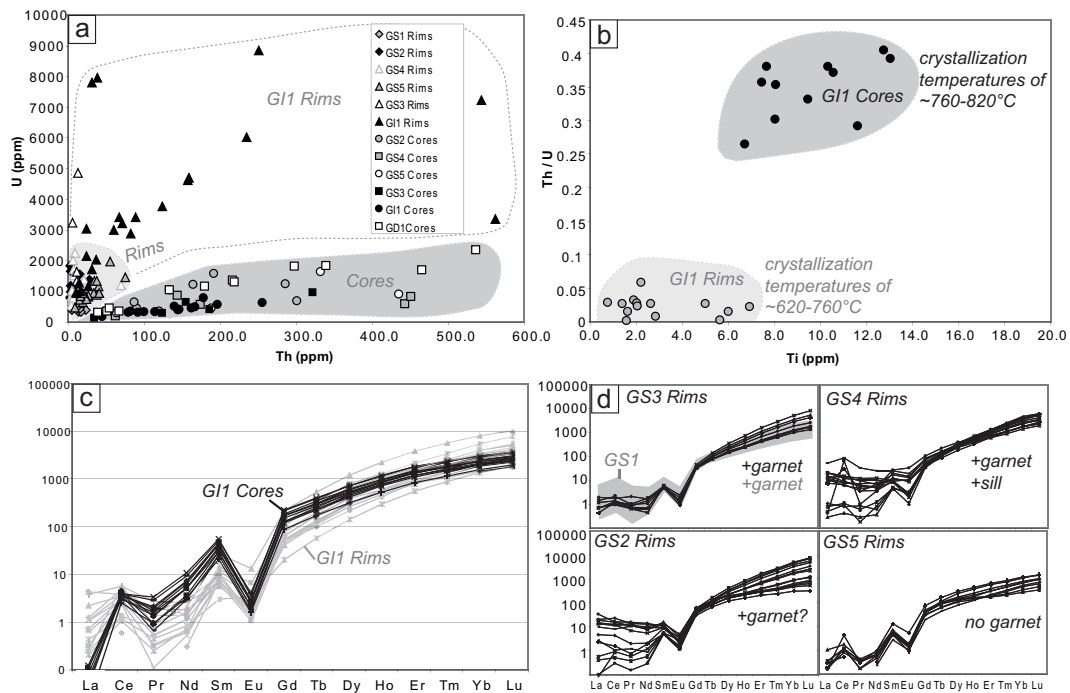


Figure 4.7: Compositional data of zircons from the dated samples. **(a)** Th against U plot that discriminates core and rim compositions. SHRIMP data from table 4.5. **(b)** Ti against Th/U plot of sample G1. Cores and Rims have distinct Th/U and Ti values. Crystallization temperature ranges according to the Ti-in-zircon thermometer of Watson & Harrison (2005). See text for further discussion. **(c)** Chondrite normalized REE pattern for G1. The cores have a homogenous composition, whereas the rims scatter more widely. **(d)** Chondrite normalized REE pattern for zircon rims of GS1-GS5. Data in **(b)**-**(d)** are from LA-ICP-MS analyses, table 4.4.

et al., 2006, including an upward correction of $\sim 50^\circ\text{C}$ for the presence of ilmenite instead of rutile). This is within error of the peak temperatures calculated by other methods for these rocks (Tab. 4.1). The zircon cores of sample GD1 generally have a more homogeneous Ti composition (Tab. 4.4), as expected for measurements not affected by surface contamination, and give crystallization temperatures of $\sim 760\text{-}820^\circ\text{C}$ (Tab. 4.3, Fig. 4.7b). The Ti-values in the rims of sample GD1 are always lower than the values in the cores (except for one outlier in the rims, Tab. 4.4) and give crystallization temperatures of $\sim 620\text{-}760^\circ\text{C}$ (Tab. 4.3, Fig. 4.7b).

The trace element compositions of the rims are generally reproducible within one sample except for the LREE, which scatter considerably between different rims in the same sample (Fig. 4.7c and d; Tab. 4.4). The large scatter in LREE supports the scenario of contamination from LREE-rich micro-inclusions. The chondrite normalised patterns for the zircon rims from samples GS1-GS5 show a moderate to pronounced Eu anomaly (Fig. 4.7d; Eu/Eu^* 0.1-0.05, except for Loc4 that shows Eu/Eu^* 0.6-0.1), and an only very weak positive Ce anomaly. The zircon cores of sample GD1 have a homogeneous trace elemental compo-

sition, with an increase from La to Lu, with a pronounced negative Eu anomaly (Eu/Eu* 0.03-0.04) and a positive Ce anomaly. The rims of sample GD1 scatter more widely in trace element composition and have a less pronounced negative Eu anomaly (Eu/Eu* 0.05-0.4), a less pronounced positive Ce anomaly and a stronger gradient in the HREE (Fig. 4.7c).

Table 4.3: Summary of U-Pb geochronology

Nr	detrital zircon core ages (Ma) _{(m)*}	magmatic zircon core age (Ma) _{(n/m)*}	Th/U core	metamorphic zircon rim age (Ma) _{(n/m)*}	Th/U rim	Ti-in-zircon thermometry (°C)
GS1	-	-	-	52.8±1.0 _(10/12)	0.008-0.060	620-720
GS2	106-61 ₍₈₎	-	0.12-0.45	54.0±0.8 _(15/19)	0.002-0.020	620-720
GS3	107-70 ₍₅₎	-	0.2-0.4	52.6±0.8 _(3/6)	0.002-0.012	620-720
GS4	151-70 ₍₅₎	-	0.17-0.78	53.0±0.7 _(12/14)	0.003-0.060	620-720
GS5	247-67 ₍₄₎	-	0.2-0.5	51.3±0.7 _(12/21)	0.002-0.050	620-720
GI1	-	53.7±0.9 _(14/14)	0.2-0.4	54.0±0.9† _(14/21)	0.008-0.170	760-820§ 620-760#
GD1	-	54.0±0.8 _(11/11)	0.12-0.28	-	-	-

Note: detrital zircon core ages are $^{206}\text{Pb}/^{238}\text{U}$ single spot ages, magmatic and metamorphic zircon ages are Concordia ages except for †. *m=number of total analyses, n=number of analyses included in concordia age calculation. † ^{208}Pb corrected weighed average $^{206}\text{Pb}/^{238}\text{U}$ age, see text for discussion. §Core temperature. #Rim temperature.

4.3.5 SHRIMP U-Pb dating of zircons

Between 4 and 8 zircon cores were analysed from each of the metasedimentary gneisses GS1-GS5. Detailed isotopic measurements are reported in Table 4.5. The core $^{206}\text{Pb}/^{238}\text{U}$ ages scatter widely between 247 and 61 Ma (Tab. 4.3), and are substantially older than the age measured in the rims. This age scatter is expected for detrital grains and is in line with the sedimentary origin of these samples according to field observations, bulk compositions, mineralogy, regional geological context, and the internal zircon structure.

Between 5 and 21 SHRIMP analyses per sample were performed on the thin, CL-bright to dark rims present on the zircon grains of samples GS1-GS5 (Fig. 4.4). Concordia ages were calculated based on ^{208}Pb corrected isotopic ratios (Tab. 4.5, Tab. 4.3, Fig. 4.8a-e). The small size of the zircon rims (Fig. 4.4 and 4.5) required a particularly small spot (down to ~10 μm) and even then overlapping with cores or the epoxy resin in which the zircons are mounted could not always be avoided. As a result, in every sample some analyses are suspected of mixing with the cores (older apparent ages) or yielded young ages due to overlapping with the grain surface or the resin. Such analyses were excluded from the average age calculation and are represented as dashed ellipses in Figures 4.8 and 4.9.

In sample GS1, a tight cluster of 10 analyses gives a Concordia age of 52.8 ± 1.0 Ma (Fig. 4.8a). In sample GS2, 15 analyses give a Concordia age of 54.0 ± 0.8 Ma (Fig. 4.8b). Sample GS3 yielded only few zircons and even fewer with rims, so only 6 analyses could be measured. One analysis is discordant, and another is particularly old and sits partly on epoxy. Of the remaining four analyses, three overlap and define a Concordia age of 52.6 ± 0.8 Ma, which is within error of the aforementioned samples (Fig. 4.8c). In sample GS4 12 rim analyses (two discordant analyses were excluded) yield a Concordia age of 53.0 ± 0.7 Ma (Fig. 4.8d). The 21 analyses on sample GS5 show the most scatter around a major cluster at ~ 51 Ma (Fig. 4.8e). One particularly old analysis was performed on a very small grain lacking a core-rim structure (analysis N9-10R, Tab. 4.5) and was therefore excluded. Four analyses were excluded because they represent pairs of old and young analyses measured on the same rim (compare analysis N9-5.1R with N9-5.2R and N9-1.1R with N9-1.2R, Tab. 4.5). Two analyses yielded ages statistically older than the main cluster and two analyses yielded statistically younger ages than the main cluster, of which one corresponds to a fractured grain (analysis N9-2.2R). The remaining cluster of 12 measurements gives a Concordia age of 51.3 ± 0.7 Ma (Fig. 4.8e). Particularly for this sample the possibility of distinct overgrowths of different age within the same sample, as observed in other migmatites (e.g. Rubatto et al., 2009) can not be ruled out completely. Twelve analyses were performed on the small, long-prismatic zircons from the granodiorite GD1 and a Concordia age of 54.0 ± 0.8 Ma can be calculated from all analyses (Fig. 4.8f).

The cores of sample G11 display a similar, oscillatory internal zoning that is distinct from the variably zoned detrital cores of the gneiss samples (Fig. 4.6a). 14 analyses on the cores define a Concordia age of 53.7 ± 0.9 Ma (Fig. 4.9a). Rims from the same sample show a large scatter in U and Th content with extreme values of up to 9000 ppm U (Fig. 4.7a). The apparent $^{206}\text{Pb}/^{238}\text{U}$ ages scatter significantly and correlate with U content. This indicates that a matrix correction due to the high U content is required as previously documented for zircon with $\text{U} > 2500$ ppm (e.g. Butera et al., 2004; Hermann et al., 2006). Even after correction, the data still scatter significantly, but the major cluster has an average $^{206}\text{Pb}/^{238}\text{U}$ age of 54.0 ± 0.9 Ma (Fig. 4.9b).

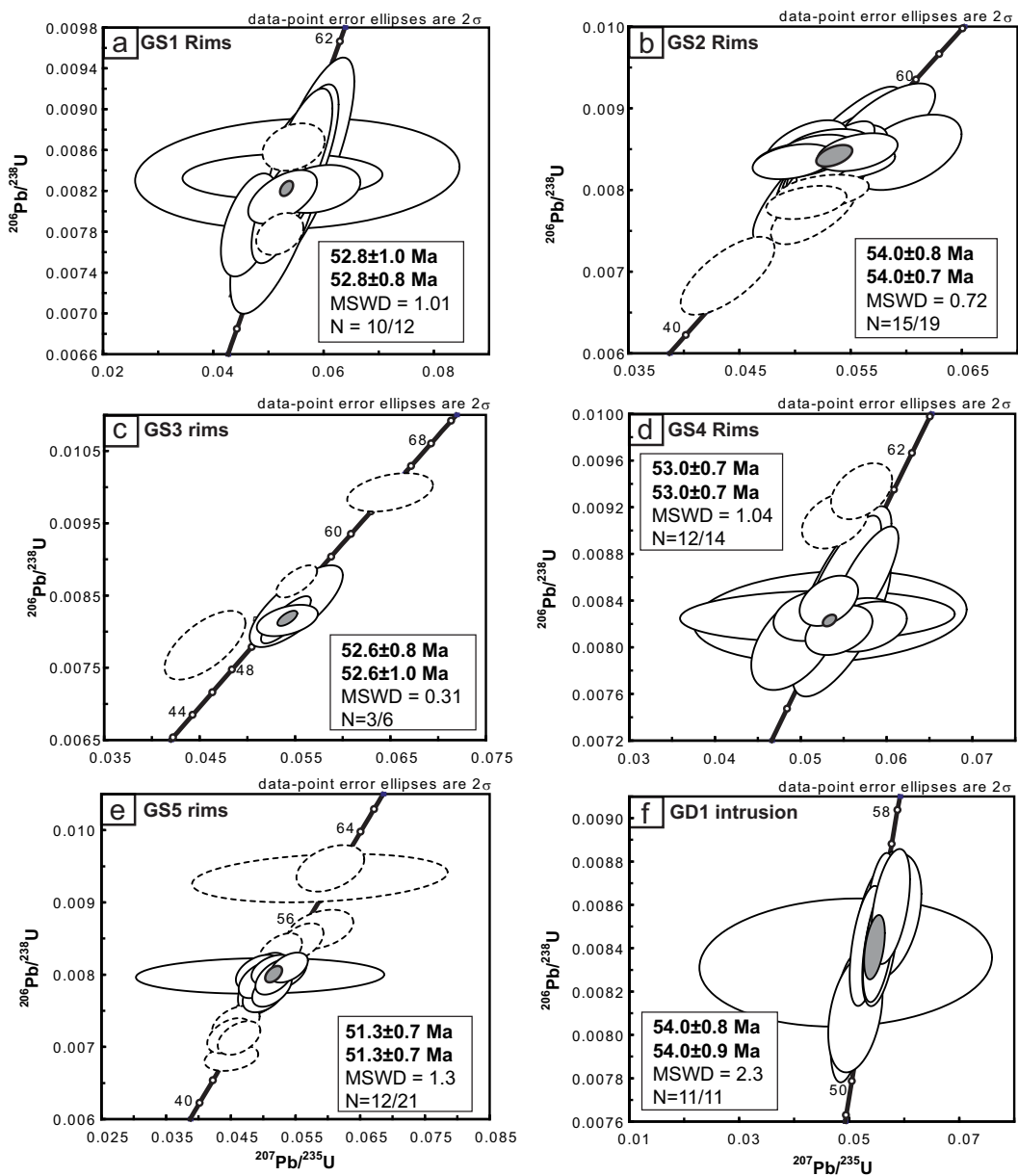


Figure 4.8: Concordia diagrams for ^{208}Pb corrected isotopic ratios of the metamorphic rims of zircons from (a-e) gneiss samples GS1-GS5 and (f) from zircons (cores) of intrusion GD1. In the box, the upper age is the Concordia age (represented in the plot by the grey ellipses), and the lower age is ^{208}Pb corrected, weighted average $^{206}\text{Pb}/^{238}\text{U}$ age with the corresponding MSWD. Errors are at $\pm 95\%$ confidence interval. Isotopic ratios are reported in table 4.5. See text for discussion.

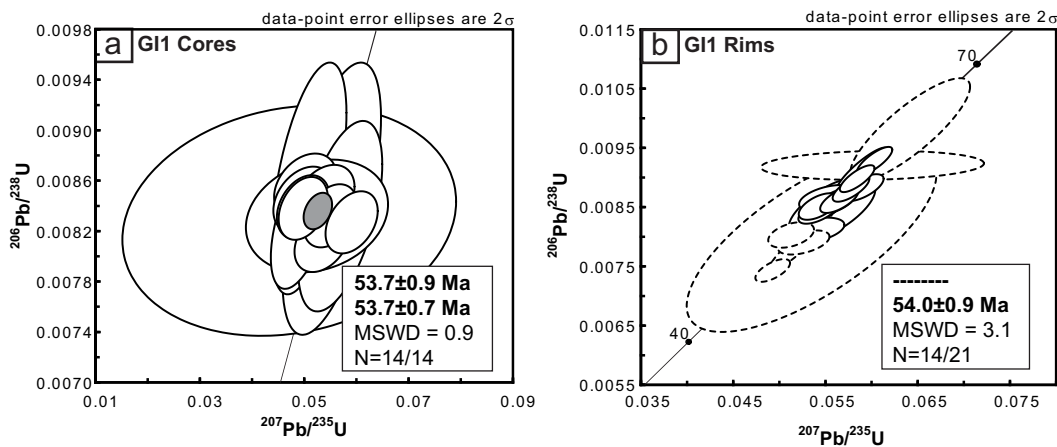


Figure 4.9: Concordia diagrams for ^{208}Pb corrected isotopic ratios of (a) the cores and (b) the metamorphic rims of sample G11. In the box, the upper age is the Concordia age (represented in the plot by the grey ellipses), and the lower age is ^{208}Pb corrected, weighted average $^{206}\text{Pb}/^{238}\text{U}$ age with the corresponding MSWD. Errors are at $\pm 95\%$ confidence interval. Isotopic ratios are reported in table 4.5. See text for discussion.

4.4 Discussion

4.4.1 Growth of metamorphic zircon rims at the metamorphic peak

The metamorphic zircon rims present on the detrital zircon cores in the migmatitic metasedimentary gneisses GS1-GS5 show low Th/U ratios (0.001-0.1) and ages covering a narrow time span of ~ 51 -55 Ma (Tab. 4.3). Different processes have been proposed for the formation of such metamorphic zircon rims: new growth by melting of pre-existing zircon crystals (e.g. Williams et al., 1996; Rubatto et al., 2009), new growth by breakdown of other Zr-bearing phases (e.g. Vavra et al., 1996; Fraser et al., 1997; Bingen et al., 2001), in-situ dissolution-precipitation (Tomaschek et al., 2003), or sub-solidus recrystallization of the zircon lattice (e.g. Hoskin & Black, 2000). It is not always straightforward to distinguish between these different mechanisms (see a discussion in Geisler et al., 2007). However, in the case presented here, several lines of evidence point to an origin of the zircon rims at or close to peak metamorphic conditions during partial melting.

(1) Ti-in-zircon thermometry of the metamorphic rims give crystallization temperatures similar to the peak PT conditions derived for the same samples by conventional thermobarometry (Tab. 4.1, 4.3). (2) The euhedral shape, the weak zoning and the low Th/U ratio of the rims is very typical for metamorphic zircons grown during anatexis (e.g. Hoskin & Schaltegger, 2003). The low Th/U ratio has been interpreted as being the result of contemporaneous growth of a Th-rich phase such as allanite or monazite (Williams et al., 1996; Vavra et al., 1996; Rubatto et al., 2009). Large, complexly zoned monazite is present in

all our investigated samples and is probably the cause for the low Th/U ratios in the zircon rims. (3) The very irregular surface between cores and rims could be the result of chemical corrosion by a fluid or melt during metamorphism prior to rim formation, suggesting that a melt phase was present shortly before rim formation (e.g. Vavra et al., 1996; Cesare et al., 2003). The small, rounded inclusions present along the core-rim boundary in some of the grains probably represent melt inclusions (e.g. Cesare et al., 2003) which again would suggest that melt was present during rim formation. The melt inclusions could also be responsible for the scatter of LREE in the rims of samples GS2, GS1 and GS4 (Fig. 4.7d). (4) All five metasedimentary gneiss samples show a moderate to pronounced Eu anomaly (Fig. 4.7d), which has been attributed in the literature to the co-crystallization of a feldspar phase (e.g. Hinton & Upton, 1991; Rubatto, 2002). Our rocks do not contain K-feldspar, but considerable amounts of plagioclase which also preferably incorporates Eu during melt crystallization. Interestingly, except for sample GS5 and few measurements in GS4 the zircon rims do not show a positive Ce anomaly (which would be typical for magmatic zircon, e.g. Hinton & Upton, 1991). This could again be due to the contamination from microscopic melt inclusions, which would have a high La/Ce ratio.

In conclusion, we interpret our metamorphic zircon rims as having formed at or close to peak metamorphic conditions, where they (re-)crystallized from partial melts contemporaneous with the crystallization of plagioclase and monazite. The zircon rims formed in all lithologies present in the gneissic core of the CMC (metapelites, metasandstones, metaigneous rocks) and they formed in the entire CMC from west to the south-east over a distance of at least ~330 km.

4.4.2 Age and duration of metamorphism in the CMC

The U-Pb zircon ages presented above allow conclusions regarding the age and duration of metamorphism in the CMC (Fig. 4.2; Fig. 4.10a). The metamorphic rim ages in the western and central CMC range from 52.6 ± 0.8 Ma to 54.0 ± 0.9 Ma (Fig. 4.10a). No consistent variation in age along strike is visible on this ~200 km long section of the CMC and the ages are all within error of each other (Fig. 4.10a). This suggests that metamorphism in the western and central CMC occurred simultaneously over a distance of ~200 km along strike during a time span of ~3 Ma (51.8-54.8 Ma). Sample GS5 lies ~150 km south-east of the eastern-most sample from the central CMC and gives a Concordia age of 51.3 ± 0.7 Ma (Fig. 4.8e, Fig. 4.10a). This is within error of the ages of samples GS1 and GS3, and slightly younger (~1.2 Ma) than the ages of samples GS2 and GS4 (Fig. 4.10a). This may suggest that the metamorphism started slightly later in this south-eastern location. However, since single spot measurements in sample GS5 scattered considerably (see section "SHRIMP U-Pb dating of zircons", Fig. 4.8e), and presence of distinct overgrowths of different age within the same sample can not be ruled out completely, it could well be that this single age underestimates the timing and duration of metamorphism in this south-eastern part of the complex.

4.4.3 Relationship between Sanak-Baranof belt magmatism and metamorphism in the CMC

The two U-Pb ages derived from magmatic samples intruding the metamorphic rocks of the CMC lie within error of the ages derived from the metamorphic zircon rims (samples G11 and GD1, Tab. 4.3, Fig. 4.10a). Even within one sample (G11), magmatic cores and metamorphic rims are identical in age. This suggests that magmatism and metamorphism occurred simultaneously over the same small time span of ~ 3 Ma in the western and central parts of the CMC.

U-Pb ages obtained previously for the magmatic rocks of the Sanak-Baranof plutonic belt may give some additional information on the timing and duration of regional-scale magmatism and metamorphism (Fig. 4.10b). For the area examined during our study, U-Pb ages from two magmatic samples are available from the literature (Fig. 4.10b). The first sample is a tonalitic dike from the western end of the CMC (Van Cleve glacier sill, Fig. 4.1, Fig. 4.10b). Sisson et al. (2003) dated xenotime, monazite and zircon from this sample by the U-Pb TIMS method. No Concordia plots, calculated average ages or error estimates for these ages are given, but $^{206}\text{Pb}/^{238}\text{U}$ and $^{207}\text{Pb}/^{235}\text{U}$ ages for different mineral fractions range from 52.2-53.4 Ma for xenotime, 54.0-55.8 Ma for monazite and 59.1-64.3 Ma for zircon. The age ranges for xenotime and monazite are within error of our ages and are considered significant. The zircon age range in contrast is possibly too old and may represent mixing with inherited cores, which cannot be readily separated from the rim during Isotope Dilution TIMS analysis. The second sample comes from a tonalitic pluton exposed ~ 40 km south-east of our GS5 sample (Novatak glacier pluton, Fig. 4.1, Fig. 4.10b). Sisson et al. (2003) give a lower intercept age of 49 ± 7 Ma, based on three discordant multigrain zircon fractions, which is within error of all our ages due to its large error. In addition to these two samples from the CMC area, three U-Pb ages are available from plutons exposed on Baranof Island (Fig. 4.10b). They are 51.6 ± 0.3 Ma for the Redfish Bay pluton (Fig. 4.1, Bradley et al., 2000), and 50.5 ± 0.5 Ma and 50.1 ± 0.1 Ma for the Crawfish Inlet pluton (Fig. 4.1, Bradley et al., 1993, 2000). The first two ages are within error of our sample GS5, and the third age is slightly younger due to its particularly small error.

Regarding the resulting age distribution along the belt (Fig. 4.10b), magmatism and metamorphism seems to have been coeval on a ~ 200 km long section in the western and central CMC during a period of ~ 3 Ma between ~ 52 - 55 Ma, and coeval on a ~ 400 km long section from Nunatak fjord to Baranof Island during a period of ~ 2 Ma between ~ 50 - 52 Ma. A critical age for this interpretation comes from the Mt. Draper pluton, an intrusive body similar to Sanak-Baranof belt rocks but that sticks in the Boundary block, which is a dextrally displaced tectonic sliver of the Chugach terrane with unknown dextral displacement (Figs. 4.1, 4.2). Sisson et al. (2003) give a lower intercept age from three discordant zircon fractions of ~ 54 Ma, without giving an error. We conservatively assign an error of ± 1 Ma, which still could be too small, since Sisson et al. (2003) give an error of ± 7 Ma for a similar lower intercept age based on three discordant zircon fractions from the Novatak

glacier pluton (Fig.4.1, Fig. 4.10b). Depending on the amount of dextral displacement of the sliver parallel to the margin, this age would indicate that no gradient in metamorphism and magmatism would be present over an at least ~800 km long section of the belt, and that metamorphism and magmatism in this section occurred during a period of ~5 Ma between ~50-55 Ma (dashed box in Fig. 4.10b).

Previous workers interpreted the U-Pb ages of the Sanak-Baranof plutonic belt displayed in Fig. 4.10b as best approximated by a linear regression through the data set (e.g. Bradley et al., 1993, 2003; Häussler et al., 2003a; Farris & Paterson, 2009). They interpreted each pluton as the result of a spreading ridge which progressively subducted below the accretionary prism from west to east, and the linear regression was used to calculate a migration rate of this spreading ridge of ~19 cm/year (Farris & Paterson, 2009). However, our data set together with previous U-Pb ages shows that, at least for the eastern part of the belt from the western CMC to Baranof Island, such a progressive age gradient is not present, and the belt is characterized by ~200 to up to ~800 km long sections where metamorphism and magmatism was coeval. A detailed discussion of the ridge subduction model is beyond the scope of this work, but if such a ridge has been present, it must have been subducted with a very small angle or parallel to the south-eastern part of the margin to produce the coeval magmatism and metamorphism observed. This situation would be in agreement with the final subduction of the Resurrection plate at that time as displayed in Häussler et al. (2003a) and Madsen et al. (2006).

4.4.4 Implications for heat transfer into the CMC

The data and discussion presented above limit the duration of peak metamorphism and magmatism in the CMC to ~3 Ma on a ~200 km long section, or, if the age of the Mt. Draper pluton is considered, to ~5 Ma on a ~800 km long section. This short duration of the metamorphic peak is consistent with the very short duration of the orogenic cycle as a whole. The depositional age of the sediments in which the complex is developed is loosely constrained by fossils present in the lower-grade part of the Valdez group to Late Cretaceous to Paleocene (~99-60 Ma, Plafker et al., 1994). In addition, youngest ages of detrital zircon cores may be used to estimate maximum depositional ages of a sedimentary unit (e.g. Dickinson & Gehrels, 2009, Chap. 2). The three youngest detrital core ages from sample GS2 overlap within 1σ and give a mean age of 63 ± 3 Ma, which is according to Dickinson & Gehrels (2009) an acceptable first-order approximation of the maximum depositional age of the unit. This age is in agreement with the youngest detrital zircon grains of a much larger data base of detrital zircons from the Sitka greywacke on Baranof Island, which is correlative along strike with our unit (Häussler et al., 2005). Based on these considerations we assume a ~63 Ma age for the deposition of the sediments in which the CMC developed. This limits the time between sedimentation, accretion, burial to >20 km and heating to >650°C (reached at ~55 Ma) to only ~8 Ma. A short peak of ~3 Ma (~55-52 Ma) is then followed by rapid cooling to below ~300°C, indicated at least in the western

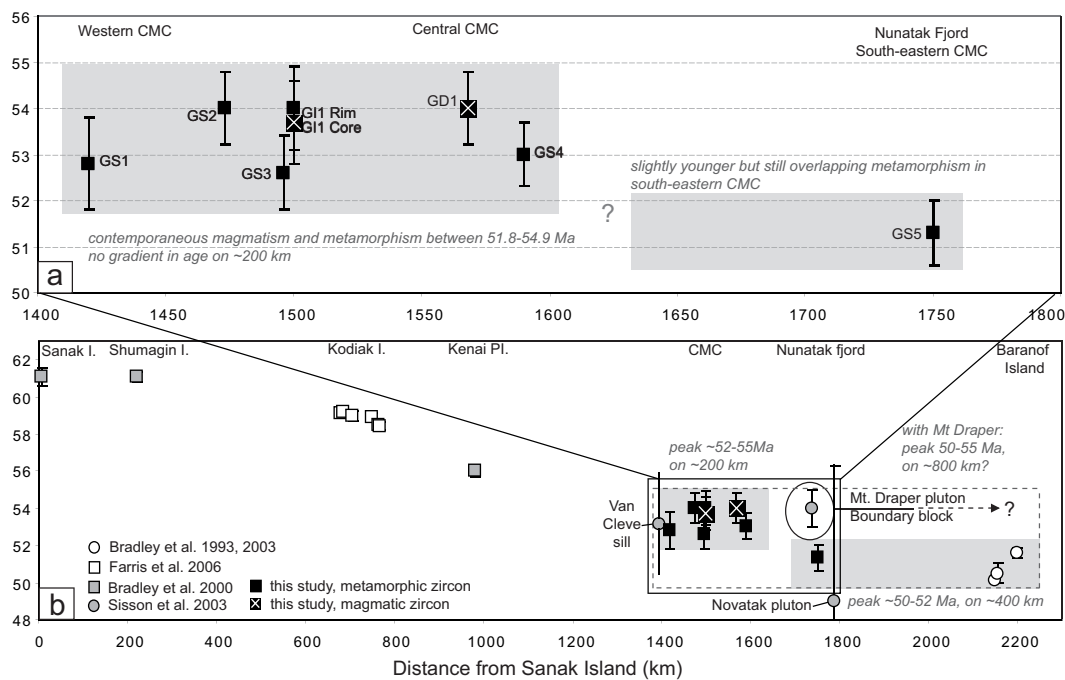


Figure 4.10: (a) Zircon U-Pb ages from the CMC (this study, Tab. 4.3) plotted against distance from Sanak Island (along strike of the CMC). The ages reveal metamorphism and magmatism during a period of ~3 Ma from ~52-55 Ma contemporaneous ~200 km along strike, and a slightly younger but still overlapping metamorphism further to the south-east. (b) U-Pb ages of plutons from previous studies and U-Pb ages from this study plotted against distance from Sanak Island. Ages from Baranof Island are within error of our age from Nunatak (GS5), suggesting a period of magmatism and metamorphism during ~2 Ma from ~52-50 Ma on a section ~400 km along strike. If the age of Mt. Draper pluton is considered, metamorphism and magmatism was contemporaneous between ~55-50 Ma over ~800 km along strike.

and central part of the CMC by ~53-46 Ma cooling ages of magmatic rocks (Hudson et al., 1979; Sisson et al., 1989; Bradley et al., 1993). Therefore, the whole orogenic cycle from (i) initial burial, through (ii) partial melting at 650-700°C and >20 km depth, to (iii) cooling below about 300°C occurred within a short time period of ~10-17 Ma simultaneously over a length scale of more than ~200 km along strike. These timing constraints can be used to discuss possible heat transfer mechanisms into the complex.

(1) Heat transfer by conduction. The short time period available for the formation of the large-scale metamorphic complex is not in agreement with classical conductive heating models of collisional orogens which require 10's of Ma for similar metamorphic conditions to be reached (e.g. England & Thompson, 1984). Moreover, such models predict substantial time lags between metamorphism at different levels in the crust (e.g. Stuewe, 1998a), which is not observed at the different crustal levels currently exposed in the CMC. However, these models were developed for collisional orogens, and may not account for processes which operated in the subduction zone setting in which the CMC formed. In order to test the rel-

evance of heat conduction in a setting more appropriate to the CMC, James et al. (1989) modelled the thermal evolution of the CMC during the subduction of very young oceanic crust (<1.5 Ma) or a spreading ridge, since the CMC has for a long time been interpreted as the result of a subducting spreading ridge below the accretionary prism (e.g. Sisson et al., 1989; Pavlis & Sisson, 1995; Bradley et al., 2003). Based on this modelling, James et al. (1989) concluded that heat conduction alone was not sufficient to produce the metamorphic conditions of the CMC. Their conclusions were based on the lower pressure estimates of Sisson et al. (1989, ~3 kbar, ~10 km depth), but even when considering the newly obtained higher pressure estimates for the gneissic core of the CMC (Tab. 4.1), the plots of James et al. (1989) reveal that also at depths of ~20 km heat conduction alone is not sufficient to produce the temperatures observed. Therefore, heat conduction can be ruled out as a prime mechanism for the formation of the CMC.

(2) Heat transfer by advection. As an alternative, Sisson et al. (1989) proposed that advective transport of heat by rising magmas or fluids from an underlying hot young oceanic crust or spreading ridge could have caused the metamorphism of the CMC. In this scenario, the CMC would have been underlain during the time of metamorphism by rocks related to this subducting ridge, such as underplated mafic melts (e.g. Harris et al., 1996). However, from outcrops along the southernmost part of the Chugach terrane and from a seismic transect located just west of the western end of the CMC (Fuis et al., 1991, 2008), it is known that the accretionary prism is underlain by an up to ~10 km thick package of N-dipping, intercalated mafic and sedimentary rocks. They are interpreted as (a) a primary sequence of sedimentary and basaltic rocks, with the basalts derived from either an intra-oceanic arc (Lull & Plafker, 1990) or an oceanic spreading center (Bradley et al., 2003), or (b) as a secondary tectonic mélange of oceanic crust and sediments which was offscraped from the down-going plate and underplated below the accretionary prism during subduction (Fuis et al., 2008). The presence of mafic underplated melts as suggested by Harris et al. (1996) is relatively unlikely from both the surface outcrops and the seismic information (Fuis et al., 2008). So if a slab window due to ridge subduction was present below the CMC during the time of metamorphism, this slab window probably existed below this ~10 km thick package of alternating sediments and mafic rocks, and any magmas or fluids produced by this slab window originated either at the base or within this thick package and must have risen through it without losing their heat in order to metamorphose the overlying accretionary prism. This must have happened fast and simultaneously over a large area to produce the metamorphism observed in the CMC.

We consider this model as unlikely because the observed intrusive rocks in the CMC area are volumetrically relatively minor (<~20%), and large regions of migmatitic gneiss occur without signs of larger intrusions present which could have heated the metasedimentary rocks (Fig. 4.2). In addition, the intrusions are dominantly felsic, and no larger bodies of mafic intrusions occur, indicating that the melts were not particularly hot and did not release much additional heat during crystallization. Moreover, some of the largest intrusives show contact metamorphic haloes and they cross-cut fabrics which formed in the metasedimentary gneisses at the metamorphic peak (e.g. Fig. 4.3d), indicating that the largest amounts

of melt intruded somewhat after the metamorphic peak at least in the schist zone. In addition, heat transported by magmas is expected to produce temporally separated and spatially localized metamorphic events (e.g. De Yoreo et al., 1991) and not regional metamorphism occurring simultaneously over large areas. Fluids on the other hand are well known to be locally responsible for metasomatism and heating (e.g. Bickle & McKenzie, 1987), but it is equally well known that they are inefficient agents for the transfer of heat on a regional scale (e.g. Connolly & Thompson, 1989; Barr & Dahlen, 1989). We therefore conclude that heat brought by advection of magmas and fluids to the CMC is unlikely to be the main mechanism which formed the CMC.

(3) Alternative mechanisms. We suggest that the metamorphic conditions observed in the CMC which were reached over a short time period could have formed without additional heat input at depth, but as a consequence of the rapid accretion of the complex causing burial and penetrative deformation. It has been shown by theoretical modelling of other accretionary prisms that metamorphic conditions similar to the ones recently obtained for the gneiss zone of the CMC (~650-720°C/ ~7-10 kbar, Tab. 4.1) can be reached in less than 5 Ma, if advective transport of material, frictional heating at the basal decollement and internal strain heating are considered (Dahlen & Barr, 1989; Barr & Dahlen, 1989). Boundary conditions which promote high temperatures inside the wedge are high accretion and erosion rates, large amounts of underplating (duplexing of sediments), high coefficients of basal friction and low fluid/lithostatic pressure ratios (Dahlen & Barr, 1989; Barr & Dahlen, 1989). In addition, amongst others Stuewe (1998b) and Burg & Gerya (2005) showed that if the region of concern pervasively and intensely deformed simultaneously over a large area during a short time period, viscous heating, i.e. the conversion of mechanical work into heat, can not be neglected and contributes significantly to the heat budget of the region.

Such a scenario could indeed be realistic for the setting of the CMC. The accretionary prism within which the CMC developed, formed as a fold-and-thrust belt due to the subduction of the Kula plate (or Resurrection plate, see discussion in Häussler et al., 2003a) below the Alaskan margin. Even though many features of this original fold-and-thrust belt are now obliterated by younger faults and by the accretion of the Yakuat terrane, some constraints on the formation of this fold-and-thrust belt can be made. Plate tectonic reconstructions for the time period of interest show orthogonal to dextral oblique convergence between the Kula/Farallon and North American plates at high velocities of ~10-15 cm/year for all locations from Vancouver Island up to the Gulf of Alaska (Dobrovine & Tarduno, 2008). So independently of on which plate the accretionary prism actually formed, convergence between the down-going and the upper plate was probably very rapid. In addition, erosion rates in the hinterland and accretionary rates in the thrust belt were probably very high, indicated by the large amounts of sediments which were deposited in the trench over a very short time period (e.g. Sample & Reid, 2003). Peak metamorphic conditions in the CMC are accompanied by two intense, pervasive, ductile deformation phases which affected the whole complex (D₂ and D₃ of Pavlis & Sisson, 1995, 2003), suggesting that viscous heating produced by intense internal deformation could have contributed to the peak metamorphic temperatures. In addition, the first of the two fabrics is a subhorizontal flattening fabric

which probably led to vertical thinning and compression of isotherms, and therewith increased the geothermal gradient present at the metamorphic peak (Pavlis & Sisson, 1995).

Based on these qualitative considerations we conclude that neither heat conduction nor heat advection by rising magmas or fluids sufficiently explain the short time scale of metamorphism observed simultaneously over a large area in the CMC. We suggest that rapid advective transport of material in an active fold-and-thrust belt, in combination with viscous heating due to intense internal deformation and thinning of isotherms due to vertical flattening, may be sufficient to explain the short time interval available for reaching the metamorphic conditions observed in the CMC.

4.5 Conclusions

New U-Pb ages of metamorphic and magmatic zircons reveal that metamorphism and magmatism in the western and central CMC occurred during a time period of ~3 Ma between ~52-55 Ma simultaneously on a ~200 km long section. Farther to the south-east, the data set is less dense but suggests that metamorphism and magmatism occurred from Nunatak fjord to Baranof Island during a time period of ~2 Ma between ~52-50 Ma simultaneously on a ~400 km long section. If the age of Mt. Draper pluton is considered, metamorphism and magmatism occurred during a time period of ~5 Ma between ~50-55 Ma simultaneously on a ~800 km long section. The west-east age progression described in the literature for the Sanak-Baranof plutonic belt is therefore at least for the eastern part of the belt not a continuous one, but is characterized by sections of ~200 km up to ~800 km long where metamorphism and magmatism is coeval. The short time period available for large-scale metamorphism and magmatism is not in agreement with conductive heating models and advective heating by magmas or fluids can be excluded for several reasons. We suggest that fast advective transport of material in a fold-and-thrust belt with appropriate boundary conditions, supported by internal heat production due to viscous strain heating and by the compression of isotherms due to vertical thinning during an early phase of deformation, may account for the metamorphic peak conditions reached in the CMC over a short time period simultaneously over a large distance.

Acknowledgments Financial support by the Fonds zur Wissenschaftlichen Förderung FWF project P-19366 is greatly acknowledged. The Electron Microscopy Unit at the Australian National University is thanked for access to the SEM facilities. C. Carson is thanked for field assistance, his hospitality in Canberra and many SHRIMP discussions. U. Klötzli and F. Biedermann are thanked for help with the mount preparation and access to the mineral separation facilities at the University of Vienna. P. Claus is thanked for expert flying in the field.

Table 4.4: Trace element composition of zircons (in ppm)

File name	P	Ti	Sr	Y	Nb	La	Ce	Pr	Nd	Sm	Eu	Gd	Tb	Dy	Ho	Er	Tm	Yb	Lu	Hf	Ta	Th	U	Th/U	Eu/Eu*	Sum REE	
GSI Rims																											
69AR13.D	332	19.0	0.3	621	1.5	1.2	3.8	0.3	2.4	1.2	0.1	9.2	3.5	49	19	99	23	241	47	12211	1.3	120	1114	0.11	0.12	500	
70AR14.D	526	110.2	0.4	531	0.8	0.1	0.4	0.0	0.2	0.8	0.1	7.1	3.2	44	16	78	17	171	31	12648	0.5	7	590	0.01	0.08	370	
71AR1.D	455	3.4	0.3	680	0.6	0.5	1.8	0.2	0.7	0.9	0.1	9.0	4.0	54	21	108	28	299	56	13035	0.7	16	902	0.02	0.09	583	
73AR16.D	216	4.1	0.3	641	1.4	0.1	5.2	0.1	0.7	2.1	0.2	12.4	4.3	54	21	100	22	215	41	9756	0.7	126	476	0.26	0.12	478	
76AR4.D	830	211.5	0.7	456	0.9	1.5	3.3	0.5	1.9	1.2	0.1	8.9	3.1	39	14	65	15	170	37	12285	0.5	17	534	0.03	0.10	361	
77AR17.D	252	12.7	0.2	451	1.0	1.2	5.2	0.2	1.9	1.6	0.3	9.9	3.4	39	14	66	15	157	32	11753	0.7	56	461	0.12	0.22	346	
78AR5.D	384	3.9	0.3	623	0.9	1.0	3.0	0.3	1.1	1.1	0.1	9.3	3.9	52	19	94	23	231	42	11953	1.1	12	674	0.02	0.07	482	
79AR6.D	390	21.2	0.5	1227	4.0	0.1	8.8	0.1	0.7	2.3	0.2	16.7	6.9	91	36	187	44	431	90	14051	3.3	789	2412	0.33	0.08	914	
80AR7.D	336	2.6	0.2	421	0.5	0.6	1.3	0.1	0.8	1.1	0.1	9.4	3.4	40	13	58	12	118	21	11389	0.6	19	525	0.04	0.07	279	
81AR8.D	412	24.7	0.4	601	0.6	0.4	1.0	0.1	0.5	0.7	0.1	6.5	3.0	44	18	95	24	253	52	12592	0.6	8	714	0.01	0.11	498	
82AR9.D	271	2.2	0.2	290	0.5	0.1	0.5	0.0	0.3	0.8	0.1	6.5	2.4	28	9	41	9	90	17	10960	0.4	14	418	0.03	0.10	205	
83AR10.D	497	1.4	0.3	741	0.6	0.5	0.6	0.1	1.1	0.6	0.1	6.7	3.4	53	23	128	33	356	75	11972	0.6	8	907	0.009	0.08	681	
GS2 Rims																											
48B5R1.D	329	13.1	0.2	416	0.9	1.1	2.7	0.2	1.0	1.3	0.2	10.7	4.5	48	13	48	9	86	16	11390	1.0	17	1495	0.01	0.12	241	
49B5R2.D	244	2.1	0.2	280	0.5	0.5	1.0	0.1	0.9	0.8	0.1	6.0	2.5	30	9	33	6	49	8	10905	0.6	9	670	0.01	0.11	147	
50B5R5.D	1031	6.9	0.7	1545	0.8	4.5	9.5	1.0	4.7	2.1	0.3	11.6	5.9	103	45	267	71	807	186	12748	0.9	6	2061	0.003	0.17	1519	
51B5R5-2.D	506	2.0	0.3	659	0.5	0.0	0.5	bdl	0.1	0.8	0.1	7.7	3.9	57	21	104	26	269	54	11404	0.6	4	974	0.004	0.09	544	
52B5R6.D	293	4.9	0.2	377	0.8	3.5	7.2	0.6	2.5	1.4	0.2	7.9	3.3	40	12	46	9	75	13	11651	0.8	15	947	0.02	0.18	220	
55B5R9.D	602	18.4	0.4	733	0.8	8.1	9.8	1.4	6.2	1.6	0.1	7.3	3.7	55	22	122	31	363	83	12322	0.7	7	1168	0.006	0.11	715	
57B5R11.D	366	12.9	0.2	388	0.8	2.3	5.0	1.0	4.3	1.3	0.1	8.8	3.3	39	12	48	9	91	19	11939	0.8	15	995	0.02	0.11	244	
58B5R13.D	588	44.6	0.3	718	0.7	3.2	7.1	1.2	3.6	1.9	0.1	9.6	4.0	57	22	112	27	298	64	12199	0.6	10	980	0.010	0.09	610	
59B5R14.D	470	5.7	0.3	440	0.9	4.9	13.8	1.3	5.8	1.6	0.1	8.0	3.0	40	13	62	14	141	30	12653	0.8	15	1038	0.01	0.09	339	
61B5R12-2.D	374	75.7	0.2	443	1.3	3.2	7.8	1.0	3.6	2.3	0.2	12.3	4.5	49	14	52	10	103	21	11180	1.2	33	1310	0.03	0.12	285	
62B5R52.D	394	26.8	0.2	454	0.8	0.1	0.6	0.1	0.5	0.8	0.1	7.1	3.1	42	14	65	15	149	29	11695	0.9	9	1027	0.009	0.09	326	
63B5R53.D	821	1.5	0.5	1182	0.7	0.1	0.3	0.0	0.3	0.8	0.1	8.6	4.8	82	36	206	56	641	140	12787	0.9	3	1694	0.002	0.10	1176	
67B5R54.D	657	4.2	0.4	989	0.6	0.0	0.2	0.0	0.1	0.7	0.1	8.0	4.4	72	31	173	46	532	118	13660	0.8	3	1559	0.002	0.08	985	
68B5R55.D	859	9.3	0.6	1280	0.8	0.6	0.6	0.1	0.4	0.8	0.2	8.2	4.8	85	38	234	64	754	173	13153	1.1	6	2177	0.003	0.19	1364	
GS3 Rims																											
21T2R6.D	351	2.6	0.3	481	0.5	0.5	1.1	0.2	0.8	0.9	0.1	6.9	2.8	42	15	80	20	209	44	13014	0.5	9	974	0.009	0.08	423	
22T2R5.D	549	1.5	0.5	826	0.6	0.1	0.8	0.1	0.3	0.7	0.1	6.8	3.5	58	25	149	42	473	104	14480	0.8	5	2101	0.002	0.07	865	
23T7R3.D	316	2.3	0.2	433	0.8	0.2	0.8	0.1	0.5	0.8	0.1	6.5	2.7	37	13	67	16	162	33	13212	1.0	11	1038	0.01	0.15	340	
25T2R11.D	669	9.9	0.7	1034	0.7	0.3	0.9	0.1	0.7	0.8	0.1	7.6	4.3	71	31	185	51	571	135	16445	0.9	6	2423	0.002	0.09	1058	
26T2R1.D	839	2.3	0.7	1382	1.0	0.2	0.7	0.1	0.2	0.9	0.1	9.0	5.1	90	41	258	74	855	203	18698	1.6	8	4280	0.002	0.14	1536	
27T2R2.D	321	4.1	0.3	439	0.6	0.3	1.3	0.1	0.9	0.9	0.1	6.8	2.9	37	14	71	18	197	42	13722	0.6	11	1082	0.01	0.10	392	
28T2R4.D	502	1.8	0.4	664	0.6	0.2	0.6	0.1	0.3	0.9	0.1	7.6	3.6	52	21	111	29	307	65	12735	0.7	8	1516	0.006	0.08	598	

Continues on following page

Table 4.4: Trace element composition of zircons (in ppm)

File name	P	Ti	Sr	Y	Nb	La	Ce	Pr	Nd	Sm	Eu	Gd	Tb	Dy	Ho	Er	Tm	Yb	Lu	Hf	Ta	Th	U	Th/U	Eu/Eu*	Sum REE	
GS4 Rims																											
29L4R51.D	645	60.6	0.5	813	1.5	0.3	0.5	0.1	0.3	0.7	0.2	6.8	3.9	64	26	141	37	411	86	12082	1.0	5	1168	0.004	0.26	778	
30L4R54.D	447	26.2	2.2	611	1.3	1.8	19.5	0.3	3.2	1.7	0.6	8.4	3.2	45	18	101	27	299	69	10216	0.7	198	638	0.31	0.45	598	
31L4R52.D	437	4.2	0.7	1057	5.1	0.1	42.0	0.1	1.7	3.0	0.9	16.8	5.9	79	33	182	47	512	106	10332	1.5	1437	1297	1.11	0.36	1030	
32L4R53.D	812	7.7	0.7	1179	1.0	0.1	0.3	0.0	0.2	0.7	0.2	9.4	5.0	90	39	218	61	665	132	11058	1.1	5	1112	0.005	0.22	1222	
33L4R531.D	812	4.8	0.6	1165	0.8	0.1	0.6	0.0	0.4	0.8	0.1	8.7	4.9	89	39	216	60	665	134	12093	1.1	5	1318	0.004	0.17	1219	
36L4R55.D	537	11.7	0.4	718	0.6	0.2	0.7	0.1	0.6	0.7	0.1	7.2	3.9	59	22	106	27	292	59	11709	0.6	7	714	0.009	0.09	578	
37L4R10.D	658	11.2	2.2	1035	0.9	2.7	3.8	0.4	2.4	4.2	1.9	21.3	8.2	100	31	125	28	283	61	12619	1.0	7	1011	0.006	0.61	673	
38L4R7.D	803	34.9	13.7	1091	1.1	1.9	4.2	0.3	1.8	1.4	0.6	10.5	4.7	80	34	200	56	659	148	11582	1.1	9	1319	0.007	0.50	1203	
39L4R13.D	626	16.5	2.5	1139	5.5	3.3	9.2	0.9	3.2	1.5	0.2	8.1	4.5	76	34	208	63	775	159	12797	3.1	31	1438	0.02	0.15	1345	
40L4R6.D	1332	10.6	6.4	1102	4.7	12.6	55.6	3.1	11.5	3.8	1.1	15.1	5.3	75	32	188	51	583	134	10826	1.8	365	1101	0.33	0.45	1172	
41L4R14.D	590	5.9	1.0	880	0.9	3.0	4.8	0.7	3.5	2.6	0.7	15.0	6.0	80	26	119	28	296	58	12202	0.7	20	764	0.03	0.36	643	
42L4R5.D	682	7.4	0.6	949	0.8	5.1	7.4	1.0	4.7	1.3	0.2	8.4	4.2	70	29	156	40	424	93	11906	0.8	20	867	0.02	0.15	843	
43L4R4.D	592	20.6	0.5	792	0.7	2.5	5.1	0.6	2.5	1.9	0.5	12.2	5.0	68	24	100	23	231	48	11563	0.6	7	823	0.008	0.32	524	
46L4R2.D	782	9.8	0.4	1075	0.9	5.1	9.5	1.1	5.8	1.4	0.2	9.1	4.9	78	30	156	38	390	83	11519	0.8	10	1065	0.010	0.13	811	
47L4R1.D	687	14.9	0.5	1023	1.3	3.7	5.7	0.5	2.3	1.3	0.1	8.8	4.8	78	31	161	41	435	84	11846	1.3	10	952	0.01	0.10	855	
GS5 Rims																											
88N9R2.D	265	43.5	0.2	412	0.7	0.1	0.7	0.0	0.3	1.0	0.1	7.8	3.4	38	12	50	12	111	25	12122	0.8	34	1032	0.03	0.10	260	
89N9R3.D	234	4.0	0.2	756	6.1	0.0	2.7	0.0	0.5	2.0	0.3	15.2	6.1	74	25	106	22	196	35	12543	3.3	498	4290	0.12	0.17	484	
90N9R4.D	268	2.1	0.1	348	0.6	0.0	0.5	0.0	0.3	0.8	0.1	8.3	3.5	37	9	31	6	58	12	11717	0.6	21	794	0.03	0.11	166	
91N9R4.D	184	6.8	0.2	471	1.8	0.3	1.1	0.0	0.4	1.1	0.1	10.1	3.9	44	14	64	14	132	26	11322	1.2	67	1547	0.04	0.10	310	
92N9R5.D	213	2.2	0.2	277	0.8	0.0	0.7	0.0	0.3	0.7	0.1	6.5	2.3	27	8	33	7	77	16	11683	0.8	33	988	0.03	0.11	178	
93N9R5.D	275	4.6	0.3	326	0.7	0.1	0.7	0.0	0.3	0.9	0.1	7.8	3.2	33	8	28	5	45	9	12434	0.7	27	1058	0.03	0.10	141	
94N9R7.D	214	12.1	0.2	346	1.0	0.0	0.7	0.0	0.2	0.7	0.1	6.1	2.4	30	11	50	12	116	24	10924	0.8	53	1205	0.04	0.14	253	
96N9R9.D	463	2.2	0.2	723	0.6	0.1	0.3	bdl	0.2	0.7	0.1	8.1	4.4	61	21	92	19	179	38	12893	0.6	13	887	0.01	0.07	424	
97N9R8.D	158	0.9	0.2	232	0.7	bdl	0.6	bdl	0.1	0.4	0.1	3.9	1.6	20	7	36	8	86	18	9876	0.6	37	945	0.04	0.14	183	
GII Cores																											
104T4C1.D	275	10.6	0.3	1567	1.1	0.0	2.2	0.2	3.3	6.6	0.1	36.9	12.1	149	54	238	48	405	74	8727	0.6	148	398	0.37	0.03	1029	
105T4C20.D	282	11.6	0.2	867	1.2	0.0	1.5	0.1	1.4	3.0	0.1	17.5	6.1	77	29	133	28	246	47	8041	0.6	71	244	0.29	0.04	589	
106T4C21.D	443	10.3	0.3	1255	0.9	0.0	1.9	0.1	2.3	5.1	0.1	30.1	9.7	119	42	187	38	320	58	8130	0.4	93	244	0.38	0.04	814	
107T4C22.D	246	7.7	0.3	1403	1.0	0.0	2.2	0.2	3.2	6.2	0.2	33.1	10.7	130	47	212	43	364	67	8896	0.5	126	330	0.38	0.03	919	
108T4C54.D	290	12.8	0.3	1941	1.2	0.0	2.4	0.3	4.8	8.0	0.2	43.5	14.3	179	65	292	59	492	91	8318	0.6	174	430	0.40	0.03	1251	
109T4C55.D	261	9.5	0.3	1160	1.1	0.0	1.9	0.1	2.3	4.4	0.1	23.8	8.1	102	39	177	36	313	59	8670	0.6	113	340	0.33	0.03	767	
110T4C56.D	244	8.1	0.3	1450	1.0	0.0	2.4	0.2	2.9	6.3	0.2	34.0	11.1	135	48	219	44	374	68	9442	0.6	135	381	0.35	0.03	946	
113T4C14.D	352	6.7	0.3	1355	2.0	bdl	2.3	0.1	1.4	3.7	0.1	24.6	9.0	125	45	214	46	398	72	10795	1.2	169	637	0.27	0.03	941	

Continues on following page

Table 4.4: Trace element composition of zircons (in ppm)

File name	P	Ti	Sr	Y	Nb	La	Ce	Pr	Nd	Sm	Eu	Gd	Tb	Dy	Ho	Er	Tm	Yb	Lu	Hf	Ta	Th	U	Th/U	Eu/Eu*	Sum REE	
11474C3.D	328	13.0	0.3	1855	1.4	0.0	2.4	0.3	4.2	7.5	0.2	43.0	14.1	175	63	287	57	489	89	8716	0.6	167	425	0.39	0.04	1231	
11574C22.D	269	7.5	0.3	1526	1.2	bdl	2.8	0.1	2.4	5.6	0.2	34.1	11.2	143	51	229	48	407	73	11876	0.7	151	423	0.36	0.03	1009	
11674C23.D	285	8.0	0.3	1225	1.3	bdl	2.5	0.1	1.6	4.3	0.1	25.7	8.5	112	40	188	40	348	63	11729	0.7	121	403	0.30	0.03	834	
GH Rims																											
04T4R51.D	634	2.8	0.4	1118	1.8	bdl	0.4	bdl	0.1	1.1	0.1	12.4	6.5	97	32	128	26	231	44	11708	2.7	27	3509	0.008	0.10	578	
06T4R53.D	1152	5.6	0.8	2018	4.0	0.1	0.8	0.1	0.8	1.9	0.4	20.8	10.6	161	58	267	62	636	136	13302	7.0	31	10794	0.003	0.18	1356	
07T4R54.D	1186	1.9	1.1	3893	8.4	0.1	3.5	0.1	1.0	4.0	0.7	43.0	19.2	295	121	612	141	1315	253	11811	12.6	362	11021	0.03	0.17	2809	
08T4R55.D	531	0.8	0.5	1293	2.6	0.0	1.5	0.0	0.2	1.1	0.1	12.7	6.1	96	40	204	48	453	86	10454	4.2	93	3204	0.03	0.06	949	
09T4R56.D	300	6.0	0.3	523	1.2	0.1	0.7	0.0	0.4	0.4	0.2	4.1	2.1	35	16	87	22	219	46	12429	2.2	21	1345	0.02	0.43	433	
10T4R57.D	600	38.0	0.8	1481	3.5	1.0	2.4	0.1	0.6	1.7	0.2	16.7	7.3	113	46	223	49	461	91	10859	4.4	148	3857	0.04	0.13	1013	
11T4R1.D	448	6.9	1.4	963	2.0	0.9	3.5	0.2	1.2	1.0	0.1	9.0	4.4	73	29	143	33	320	60	11338	3.2	56	2468	0.02	0.10	679	
12T4R3.D	422	2.0	0.4	1016	2.3	0.3	1.8	0.1	0.5	1.1	0.1	10.8	5.0	77	31	154	35	331	64	11747	3.3	66	2327	0.03	0.08	711	
13T4R4.D	551	2.6	1.5	1413	3.3	0.1	1.5	0.0	0.3	1.1	0.1	12.8	6.1	99	43	227	56	558	109	11044	5.1	76	2865	0.03	0.06	1115	
15T4R9.D	143	2.2	0.5	808	1.5	0.3	3.0	0.2	1.3	1.4	0.2	9.8	3.7	54	23	136	38	440	102	11540	2.2	353	6030	0.06	0.17	813	
16T4R12.D	375	5.0	0.5	1070	2.1	0.1	1.6	0.0	0.3	1.0	0.1	9.9	4.7	77	33	173	42	420	82	12536	3.6	84	3090	0.03	0.06	845	
17T4R21.D	428	1.6	0.4	862	1.9	0.5	2.2	0.2	0.8	0.8	0.1	8.3	4.0	65	25	127	30	292	54	11970	3.3	41	2665	0.02	0.11	610	
18T4R23.D	562	1.4	0.5	1532	3.2	0.3	2.2	0.2	0.7	1.5	0.1	15.5	7.3	115	48	240	56	529	100	11387	5.0	142	5183	0.03	0.05	1116	
19T4R15.D	1235	1.6	0.8	2478	4.7	0.0	0.6	0.0	0.3	2.3	0.2	23.2	12.7	196	71	341	83	886	192	17992	10.2	21	12833	0.002	0.10	1808	
20T4R14.D	501	2.1	0.6	1634	3.9	0.2	1.9	0.0	0.5	1.3	0.1	15.4	7.3	120	50	261	64	642	122	12517	5.9	87	3658	0.02	0.07	1286	

Table 4.5: Zircon U-Pb data

Label	U (ppm)	Th (ppm)	$^{232}\text{Th}/^{238}\text{U}$	% common Pb	$^{207}\text{Pb}/^{235}\text{U}$	$1\sigma\%$	$^{206}\text{Pb}/^{238}\text{U}$	$1\sigma\%$	error corr.	$^{206}\text{Pb}/^{238}\text{U}$ Age	$\pm 1\sigma$
Sample GS1											
ASN-12R*	1074	9	0.0090	0.30	0.0519	3.4	0.00778	1.1	0.32	50.0	0.5
ASN-6R	659	6	0.0088	1.23	0.0464	4.6	0.00787	2.6	0.51	50.5	1.3
ASN-11R	1019	9	0.0091	0.09	0.0518	4.0	0.00800	2.6	0.64	51.4	1.3
ASN-9R	335	13	0.0416	0.15	0.0517	7.0	0.00803	5.2	0.72	51.5	2.7
ASN-4R	392	23	0.0612	0.31	0.0524	4.9	0.00814	1.3	0.54	52.3	0.7
ASN-1R	334	17	0.0515	2.84	0.0589	5.4	0.00822	1.2	0.28	52.8	0.6
ASN-2R	568	5	0.0083	0.05	0.0524	14.2	0.00834	1.1	0.08	53.5	0.6
ASN-7R	430	15	0.0373	0.63	0.0551	22.0	0.00837	2.7	0.12	53.7	1.4
ASN-5R	539	13	0.0258	0.32	0.0567	6.4	0.00847	5.0	0.77	54.3	2.7
ASN-8R	669	7	0.0114	0.20	0.0558	5.0	0.00846	3.8	0.74	54.3	2.0
ASN-10R	741	7	0.0102	0.13	0.0553	4.5	0.00852	3.3	0.71	54.7	1.8
ASN-3R*	386	5	0.0136	0.09	0.0544	4.3	0.00863	1.1	0.26	55.4	0.6
Sample GS2											
KB5-58C	463	90	0.2004	0.03	0.0585	4.7	0.00949	2.6	0.47	60.9	1.6
KB5-52C	658	87	0.1368	0.00	0.0610	4.7	0.00968	2.7	0.55	62.1	1.7
KB5-511C	1239	285	0.2378	0.00	0.0665	2.4	0.00999	1.1	0.40	64.1	0.7
KB5-53C	1039	133	0.1327	0.02	0.0644	2.8	0.01016	1.1	0.37	65.1	0.7
KB5-51C	1578	192	0.1254	0.00	0.0639	2.6	0.01028	1.6	0.55	65.9	1.0
KB5-57C	1228	165	0.1385	0.00	0.0603	16.5	0.01048	8.1	0.48	67.2	5.4
KB5-59C	349	120	0.3545	0.27	0.0704	8.8	0.01202	5.6	0.55	77.0	4.3
KB5-510C	693	301	0.4486	0.18	0.1016	4.6	0.01647	3.8	0.63	105.3	4.0
KB5-3R*	802	2	0.0026	0.00	0.0438	4.0	0.00695	2.8	0.70	44.6	1.3
KB5-6R*	1061	13	0.0125	0.11	0.0510	2.9	0.00785	1.1	0.36	50.4	0.5
KB5-4R*	921	7	0.0077	0.22	0.0525	3.3	0.00798	1.1	0.33	51.2	0.5
KB5-9R	1652	3	0.0020	0.16	0.0523	4.8	0.00820	4.2	0.86	52.6	2.2
KB5-2R	680	6	0.0091	0.14	0.0545	3.4	0.00834	1.1	0.32	53.5	0.6
KB5-10R	1000	10	0.0106	0.00	0.0538	3.5	0.00833	2.3	0.64	53.5	1.2
KB5-5R	844	4	0.0049	0.00	0.0498	3.0	0.00835	1.1	0.35	53.6	0.6
KB5-13R	762	3	0.0046	0.10	0.0542	4.1	0.00839	3.0	0.72	53.8	1.6
KB5-7R	740	8	0.0110	0.00	0.0503	3.3	0.00837	1.1	0.32	53.7	0.6
KB5-12R	1378	28	0.0207	1.14	0.0601	3.4	0.00846	2.2	0.48	54.3	1.2
KB5-8R	787	7	0.0098	0.00	0.0528	3.0	0.00853	1.1	0.35	54.7	0.6
KB5-1R	1553	15	0.0103	0.00	0.0509	3.0	0.00852	1.6	0.53	54.7	0.9
KB5-11R	1015	11	0.0107	0.14	0.0579	3.3	0.00879	2.4	0.70	56.4	1.3

Continues on following page

Table 4.5: Zircon U-Pb data

Label	U (ppm)	Th (ppm)	$^{232}\text{Th}/^{238}\text{U}$	% common Pb	$^{207}\text{Pb}/^{235}\text{U}$	$1\sigma\%$	$^{206}\text{Pb}/^{238}\text{U}$	$1\sigma\%$	error corr.	$^{206}\text{Pb}/^{238}\text{U}$ Age	$\pm 1\sigma$
KB5-56R*	990	4	0.0047	0.24	0.0517	3.1	0.00773	2.1	0.67	49.6	1.0
KB5-51R	1132	10	0.0093	0.02	0.0531	3.2	0.00817	2.1	0.64	52.5	1.1
KB5-55R	1835	3	0.0015	0.00	0.0536	2.7	0.00844	2.0	0.73	54.1	1.1
KB5-52R	928	11	0.0120	0.13	0.0556	2.7	0.00846	1.1	0.38	54.3	0.6
KB5-54R	989	3	0.0031	0.00	0.0517	2.9	0.00845	1.1	0.38	54.2	0.6
KB5-53R	1195	3	0.0029	0.00	0.0539	4.3	0.00851	3.7	0.85	54.6	2.0
Sample GS3											
T27-8C	143	34	0.2471	0.00	0.0755	7.3	0.01100	2.0	0.32	70.5	1.4
T27-7C	644	155	0.2490	0.00	0.0720	3.3	0.01126	1.8	0.46	72.2	1.3
T27-9C	965	322	0.3441	0.00	0.0938	3.8	0.01456	3.1	0.65	93.2	2.9
T27-11C	302	123	0.4211	0.00	0.0995	7.2	0.01629	5.0	0.52	104.2	5.2
T27-10C	409	186	0.4691	0.00	0.0970	23.9	0.01663	2.0	0.11	106.3	2.1
T27-3R*	1346	11	0.0084	0.00	0.0456	3.8	0.00782	2.5	0.64	50.2	1.2
T27-2R	1642	11	0.0071	0.88	0.0542	2.4	0.00817	1.1	0.43	52.4	0.6
T27-5R	4856	13	0.0027	0.26	0.0540	2.0	0.00817	1.6	0.82	52.5	0.9
T27-11R	955	11	0.0118	0.23	0.0551	3.6	0.00836	2.8	0.75	53.7	1.5
T27-1R*	3244	6	0.0018	0.00	0.0552	1.6	0.00871	1.0	0.65	55.9	0.6
T27-10R*	1037	13	0.0125	0.29	0.0649	2.8	0.00993	1.1	0.38	63.7	0.7
Sample GS4											
LOC4-55C	569	174	0.3166	0.00	0.0913	4.5	0.01424	3.7	0.65	91.2	3.3
LOC4-52C	591	443	0.7742	0.00	0.0984	5.5	0.01828	2.4	0.38	116.7	2.7
LOC4-53C	200	63	0.3230	0.39	0.1539	4.1	0.02361	1.4	0.35	150.4	2.1
LOC4-11BR-C	879	143	0.1685	0.31	0.0599	5.4	0.01085	1.2	0.36	69.6	0.8
LOC4-6R-C	823	451	0.5661	0.00	0.0874	5.6	0.01477	2.1	0.49	94.5	2.0
LOC4-1R	991	7	0.0070	0.30	0.0544	3.0	0.00815	1.1	0.36	52.3	0.6
LOC4-3R	765	5	0.0072	0.69	0.0576	3.3	0.00818	1.1	0.32	52.5	0.6
LOC4-8R	612	4	0.0076	0.55	0.0562	3.6	0.00820	1.1	0.31	52.6	0.6
LOC4-5R	822	4	0.0052	0.36	0.0547	4.3	0.00821	3.2	0.72	52.7	1.7
LOC4-4R	720	5	0.0070	0.00	0.0518	12.7	0.00827	1.1	0.09	53.1	0.6
LOC4-10R	562	4	0.0076	0.00	0.0515	3.8	0.00827	1.1	0.29	53.1	0.6
LOC4-9R	1712	7	0.0042	0.00	0.0532	2.6	0.00840	1.0	0.39	53.9	0.6
LOC4-2R	1021	5	0.0046	0.00	0.0547	4.4	0.00849	3.4	0.79	54.5	1.9
LOC4-7R	2260	9	0.0040	0.37	0.0574	2.8	0.00857	2.2	0.78	55.0	1.2
LOC4-55R	781	7	0.0086	0.08	0.0491	4.2	0.00805	2.1	0.48	51.7	1.1
LOC4-53R	1531	7	0.0046	0.11	0.0533	12.3	0.00826	1.9	0.16	53.0	1.0

Continues on following page

Table 4.5: Zircon U-Pb data

Lable	U (ppm)	Th (ppm)	$^{232}\text{Th}/^{238}\text{U}$	% common Pb	$^{207}\text{Pb}/^{235}\text{U}$	$1\sigma\%$	$^{206}\text{Pb}/^{238}\text{U}$	$1\sigma\%$	error corr.	$^{206}\text{Pb}/^{238}\text{U}$ Age	$\pm 1\sigma$
LOC4-51R	2026	6	0.0032	0.00	0.0545	3.6	0.00852	2.9	0.81	54.7	1.6
LOC4-54R*	1204	70	0.0599	0.20	0.0539	2.9	0.00908	1.1	0.35	58.3	0.6
LOC4-52R*	1377	21	0.0158	0.00	0.0570	2.6	0.00934	1.1	0.40	59.9	0.6
Sample GS5											
N9-11C	1632	332	0.2100	0.55	0.0662	7.4	0.01044	1.4	0.45	66.9	0.9
N9-6C	911	435	0.4930	0.00	0.0677	5.2	0.01108	1.4	0.41	71.0	1.0
N9-7C	455	188	0.4270	0.05	0.0886	13.5	0.01412	3.9	0.44	90.4	3.5
N9-4C	296	64	0.2216	1.05	0.1663	6.7	0.03817	6.2	0.75	241.5	14.7
N9-1.1R*	780	20	0.0272	0.42	0.0462	2.9	0.00714	1.3	0.44	45.9	0.6
N9-5.1R*	830	26	0.0326	0.00	0.0447	3.1	0.00717	1.4	0.43	46.1	0.6
N9-6.1R*	629	15	0.0246	0.00	0.0457	3.3	0.00734	1.4	0.40	47.1	0.6
N9-4.1R	947	40	0.0441	0.01	0.0500	2.7	0.00774	1.3	0.41	49.7	0.6
N9-7R	1472	75	0.0528	1.51	0.0513	2.4	0.00782	1.3	0.49	50.2	0.7
N9-2R	880	37	0.0438	0.00	0.0493	2.6	0.00794	1.3	0.48	51.0	0.6
N9-4.2R	1162	40	0.0352	0.02	0.0517	2.3	0.00798	1.2	0.52	51.2	0.6
N9-8R	956	34	0.0364	0.00	0.0495	15.8	0.00799	1.2	0.08	51.3	0.6
N9-9R	753	17	0.0238	0.27	0.0529	2.9	0.00805	1.3	0.43	51.7	0.7
N9-6.2R	643	19	0.0305	0.30	0.0520	3.0	0.00804	1.3	0.41	51.7	0.7
N9-11R	725	15	0.0219	0.04	0.0492	2.8	0.00804	1.2	0.42	51.6	0.6
N9-3R	876	26	0.0312	0.00	0.0503	2.7	0.00805	1.3	0.47	51.7	0.7
N9-12R*	821	23	0.0293	0.16	0.0526	2.6	0.00833	1.2	0.45	53.5	0.7
N9-13R*	958	41	0.0438	0.25	0.0557	2.5	0.00846	1.2	0.47	54.3	0.7
N9-1.2R*	464	9	0.0198	0.77	0.0588	3.5	0.00863	1.3	0.36	55.4	0.7
N9-10R*	742	24	0.0329	0.34	0.0587	13.7	0.00934	1.5	0.24	59.9	0.9
N9-5.2R*	847	16	0.0198	0.11	0.0603	3.5	0.00948	1.4	0.39	60.8	0.8
N9-2.2R*	950	19	0.0206	0.43	0.0450	3.8	0.00687	1.1	0.28	44.1	0.5
N9-2R	1337	34	0.0265	0.00	0.0501	3.3	0.00787	2.1	0.48	50.5	1.1
N9-1.2R	1337	38	0.0290	0.00	0.0515	2.7	0.00808	1.1	0.39	51.9	0.5
N9-1R	1974	55	0.0287	0.15	0.0539	2.2	0.00811	1.0	0.46	52.1	0.5
Sample G11											
T40-51C	521	139	0.2762	0.16	0.0497	4.2	0.00839	1.2	0.32	53.9	0.7
T40-54C	387	144	0.3849	0.00	0.0508	5.9	0.00862	4.4	0.56	55.3	2.4
T40-5C	407	146	0.3698	0.45	0.0534	4.1	0.00813	1.2	0.35	52.2	0.6
T40-34C	454	162	0.3677	0.53	0.0591	3.5	0.00827	1.2	0.37	53.1	0.6
T40-22C	338	99	0.3035	0.93	0.0568	5.8	0.00852	3.7	0.54	53.4	2.0

Continues on following page

Table 4.5: Zircon U-Pb data

Lable	U (ppm)	Th (ppm)	$^{232}\text{Th}/^{238}\text{U}$	% common Pb	$^{207}\text{Pb}/^{235}\text{U}$	$1\sigma\%$	$^{206}\text{Pb}/^{238}\text{U}$	$1\sigma\%$	error corr.	$^{206}\text{Pb}/^{238}\text{U}$ Age	$\pm 1\sigma$
T40-20C	578	196	0.3500	0.06	0.0493	4.8	0.00827	2.6	0.53	53.1	1.4
T40-30C	628	255	0.4199	0.77	0.0549	3.8	0.00832	1.2	0.36	53.4	0.7
T4015C	787	178	0.2334	0.23	0.0523	10.7	0.00832	2.2	0.21	53.4	1.2
T40-25C	183	44	0.2511	0.27	0.0470	28.0	0.00829	4.5	0.17	53.2	2.4
T40-17C	500	167	0.3453	0.05	0.0498	3.9	0.00838	1.2	0.34	53.8	0.6
T40-19C	309	91	0.3051	0.36	0.0552	7.1	0.00846	5.2	0.59	54.3	2.8
T40-3C	362	82	0.2345	0.25	0.0539	4.3	0.00847	1.2	0.32	54.4	0.7
T40-33C	340	114	0.3477	0.26	0.0497	4.8	0.00845	1.3	0.33	54.2	0.7
T40-23C	308	79	0.2655	0.27	0.0502	4.9	0.00855	1.3	0.31	54.9	0.7
T40-51.1R*	3048	24	0.0081	0.75	0.0513	2.0	0.00803	1.1	0.42	51.1	0.6
T40-55R	2159	24	0.0115	0.00	0.0546	2.6	0.00853	2.1	0.78	54.8	1.1
T40-54.1R	4698	159	0.0350	0.07	0.0565	1.5	0.00863	1.0	0.68	53.5	0.6
T40-55.1R	4628	157	0.0350	0.04	0.0561	2.3	0.00864	2.1	0.88	53.6	1.2
T40-52.1R	6020	234	0.0402	0.13	0.0578	1.4	0.00882	1.0	0.72	53.6	0.6
T40-53.2R	8847	250	0.0292	0.08	0.0584	1.3	0.00898	1.0	0.78	52.2	0.6
T40-53R1	7800	31	0.0041	0.00	0.0590	1.9	0.00913	1.7	0.89	54.1	1.0
T40-53.3R	7970	39	0.0050	0.01	0.0603	1.3	0.00928	1.0	0.79	54.9	0.6
T40-56R*	2034	37	0.0186	1.64	0.0642	4.1	0.00981	3.6	0.83	62.9	2.3
T40-4R*	3423	89	0.0268	0.32	0.0493	1.6	0.00743	1.0	0.65	46.9	0.5
T40-9R*	7227	543	0.0777	0.20	0.0522	2.7	0.00790	2.6	0.93	46.7	1.3
T40-6R*	1715	31	0.0185	0.21	0.0526	2.2	0.00790	1.1	0.48	50.7	0.5
T40-23R*	3227	71	0.0227	1.18	0.0535	10.3	0.00795	8.0	0.72	51.0	4.1
T40-8R	1001	16	0.0163	0.26	0.0539	2.5	0.00811	1.1	0.43	52.1	0.6
T40-22R	1287	14	0.0112	1.41	0.0559	3.3	0.00843	2.5	0.71	54.1	1.3
T40-32R	2997	60	0.0207	0.01	0.0543	1.7	0.00844	1.0	0.62	54.2	0.6
T40-31R	3369	562	0.1723	0.27	0.0543	1.6	0.00851	1.1	0.58	53.9	0.6
T40-5R	3418	67	0.0202	0.25	0.0562	1.7	0.00860	1.0	0.62	54.4	0.6
T40-13R	1168	26	0.0234	0.32	0.0553	2.3	0.00865	1.1	0.44	55.5	0.6
T40-14R	3771	124	0.0340	0.24	0.0591	1.5	0.00883	1.0	0.66	55.6	0.6
T40-40R*	974	10	0.0106	0.79	0.0601	8.2	0.00921	1.1	0.14	59.1	0.6
Sample GD1											
TK7-10C	1692	465	0.2840	0.06	0.0500	2.7	0.00808	1.5	0.45	51.9	0.8
TK7-3C	362	51	0.1452	0.00	0.0512	3.9	0.00810	1.4	0.34	52.0	0.7
TK-6C	325	39	0.1243	0.00	0.0494	22.0	0.00834	1.4	0.08	53.5	0.8
TK7-8C	1370	217	0.1633	0.06	0.0556	2.4	0.00841	1.3	0.50	54.0	0.7
TK-5C	1840	339	0.1903	0.16	0.0554	2.1	0.00843	1.3	0.53	54.1	0.7

Continues on following page

Table 4.5: Zircon U-Pb data

Lable	U (ppm)	Th (ppm)	$^{232}\text{Th}/^{238}\text{U}$	% common Pb	$^{207}\text{Pb}/^{235}\text{U}$	$1\sigma\%$	$^{206}\text{Pb}/^{238}\text{U}$	$1\sigma\%$	error corr.	$^{206}\text{Pb}/^{238}\text{U}$ Age	$\pm 1\sigma$
TK7-11C	1818	297	0.1689	0.06	0.0532	2.3	0.00841	1.3	0.50	54.0	0.7
TK7-12C	1164	179	0.1591	0.13	0.0557	3.1	0.00851	1.5	0.47	54.6	0.8
TK-4C	451	54	0.1240	0.42	0.0572	4.2	0.00855	1.4	0.36	54.9	0.8
TK7-7C	1311	219	0.1723	0.24	0.0563	2.6	0.00855	1.4	0.45	54.9	0.8
TK7-9C	2347	536	0.2361	0.25	0.0556	2.1	0.00855	1.4	0.43	54.9	0.7
TK7-1C	1043	133	0.1317	0.13	0.0575	2.5	0.00859	1.3	0.47	55.2	0.7

Note: R denotes rim measurement, C denotes core measurement. *analysis excluded from Concordia age calculation

Chapter 5

Formation of a metamorphic complex along an obliquely convergent margin: Structural and thermochronological evolution of the Chugach Metamorphic Complex, southern Alaska

Abstract The Chugach Metamorphic Complex of southern Alaska formed during Eocene time along an obliquely convergent margin. We present structural analyses, $^{40}\text{Ar}/^{39}\text{Ar}$, Rb/Sr, and zircon fission-track ages along three across-strike transects covering the complex from W to SE. We integrate our results with the metamorphic history and additional geochronology from the literature and derive the following tectonic evolution for the complex: Accretion of sediments to the convergent margin led to D_1 structures and greenschist-facies metamorphism prior to ~55 Ma. At ~55-51 Ma, a margin-parallel stretching phase with vertical thinning (D_2) affected the margin and led to andalusite-sillimanite grade metamorphism and the onset of partial melting. A switch back to dextral transpression (D_3) shortly after D_2 led to rapid cooling of the western and central parts of the complex associated with exhumation of parts of the core of the complex until ~46 Ma. The south-eastern part of the complex cooled and exhumed regularly and slowly until ~5 Ma. An increase in cooling and exhumation occurred after ~10-5 Ma in the entire southeastern part of the complex, associated with the Neogene collision of the Yakutat terrane. Our study describes the evolution of the metamorphic complex in space and time from the accretion of the sediments in which the complex developed to the final exhumation to the surface.

5.1 Introduction

Metamorphic complexes are exposed all over the world in various tectonic settings. In order to produce a metamorphic complex surrounded by lower-grade rocks, differential exhumation and/or differing thermal histories are needed. Exhumation of rocks, i.e. their upward vertical movement relative to the Earth's surface (Stuewe & Barr, 1998) is achieved by at least three general mechanisms: (1) normal faulting, (2) vertical ductile thinning and (3) erosion due to surface uplift (e.g. Ring et al., 1999; Ring & Brandon, 2008). All three mechanisms may be active under both (oblique) divergence and convergence, and, especially in the case of overall convergence, different large-scale tectonic processes such as buoyancy due to density-differences, thermal softening, gravitation-driven extension, extrusion between major fault zones, internal channel flow or ductile shear, magmatic or tectonic underplating, and removal or rollback of lithospheric material have been proposed to facilitate such exhumation (e.g. England & Holland, 1979; Platt, 1993; Selverstone, 2005; Godin et al., 2006; Brun & Faccenna, 2008; Ring & Brandon, 2008). Many models of rock exhumation in convergent settings only consider orogen-perpendicular movements, but others stress the importance of orogen-parallel movements influencing thermal histories and rock exhumation during oblique convergence (e.g. Thompson et al., 1997; Wang & Neubauer, 1998; Koons et al., 2003; Whitney et al., 2007; Goscombe & Gray, 2009; Foster et al., 2009). Thermal histories of metamorphic areas may vary due to processes such as localized advective heat addition by the ascent of magmas or fluids (e.g. Lux et al., 1986; De Yoreo et al., 1991), the in-situ production of radiogenic, mechanical or chemical heat (e.g. Burg & Gerya, 2005), or large-scale processes such as the formation or removal of slab windows below convergent margins (e.g. Thorkelson, 1996).

In this contribution we present the results of a multi-disciplinary study conducted on the Eocene Chugach Metamorphic Complex (CMC) of southern Alaska (Fig. 5.1; Hudson & Plafker, 1982; Sisson et al., 1989; Pavlis & Sisson, 1995). The tectonic history of the southern Alaskan margin has been controlled by the variably oblique convergence between the oceanic plates of the Pacific basin and the North American continent throughout the Cenozoic, which led to the accretion of several distinct tectonic terranes (e.g. Plafker et al., 1994). Active transpression and terrane accretion is still ongoing today, which leads to the formation of the highly glaciated Chugach-St. Elias Mountains along the south-eastern Alaskan coast (e.g. Berger et al., 2008; Meigs et al., 2008; Enkelmann et al., 2010). In addition, the margin experienced an unusual thermal overprint during the Paleocene and Eocene, which is widely interpreted to be the result of the subduction of an oceanic spreading ridge below the margin (e.g. Bradley et al., 1993, 2003; Häussler et al., 2003a). The CMC is a ~10-50 km wide and ~350 km long upper amphibolite facies metamorphic complex which formed in this convergent environment possibly due to heat input from the inferred subducting spreading ridge (e.g. Sisson et al., 1989; Sisson & Pavlis, 1993; Pavlis & Sisson, 1995).

In order to constrain the formation and exhumation mechanisms of this complex further, we present (1) the results of structural field work along three across-strike composite sections covering the western, central and south-eastern parts of the CMC (Fig. 5.2) and (2) the results of $^{40}\text{Ar}/^{39}\text{Ar}$, Rb-Sr and zircon fission-track thermochronology conducted on the three structural transects investigated. Based on these new thermochronological data and data from the literature, we present cooling paths for the different parts of the complex. We then integrate the metamorphic history (Bruand, 2010) with the structural geometry and thermochronology and present a possible tectonic evolution for the entire complex. We then discuss the tectonic evolution of the complex in a regional context.

5.2 Geology of the southern Alaska margin

The CMC is exposed along the southern Alaskan margin (Fig. 5.1b). The southern Alaskan margin is part of the outermost tectonic belt of the North American Cordillera (Fig. 5.1a; Oldow et al., 1989; Dickinson, 2009), which resulted from the (on-going) oblique convergence between oceanic plates of the Pacific Basin and North America. The modern margin is highly curved, which leads to dominantly dextral movement along the active Fairweather fault system in south-eastern Alaska and to thrust-faulting along the Aleutian megathrust farther west (Fig. 5.1b). A block of continental and oceanic crust, the Yakutat terrane, is currently actively colliding into this curved margin (Fig. 5.1b). This collision leads to the formation of the Chugach-St. Elias Mountains, which consist of highly glaciated peaks exceeding 5000 m elevation standing only ~50 km from the coast (e.g. Bruhn et al., 2004; Pavlis et al., 2004; Berger et al., 2008; Meigs et al., 2008).

The rocks inboard of the Yakutat terrane are part of a vast, complexly deformed accretionary prism which extends ~2100 km along the margin from Sanak Island in the west to Baranof Island in the south-east (Fig. 5.1b; Chugach and Prince William terranes). This accretionary prism is emplaced along the Border Range Fault System against the Wrangellia composite terrane to the north (Fig. 5.1b; Plafker et al., 1994; Pavlis & Roeske, 2007). The accretionary prism is built of (1) an inboard narrow belt of Late Triassic to Cretaceous mélangé (e.g. Amato & Pavlis, 2010) and (2) an outboard Late Cretaceous to Eocene marine turbidite sequence consisting of intercalated conglomerates, impure sandstones, marls, claystones and mafic volcanic rocks (Fig. 5.1b; Nilsen & Zuffa, 1982; Plafker et al., 1994). Several local group names were assigned to this turbidite sequence: Shumagin Fm, Kodiak Fm, Valdez Group and Sitka Greywacke for the Cretaceous parts, and Ghost Rock Fm, Sitkalidak Fm and Orca Group for the Eocene parts (Plafker et al., 1994). The accretionary prism is separated into the northern Chugach and the southern Prince William terrane by the Contact fault system, which consists of numerous individual faults which probably developed syn- to post-accretion and show dextral displacement in the eastern and thrust displacement in the western Prince William Sound (Bol & Gibbons, 1992; Bol & Roeske, 1993).

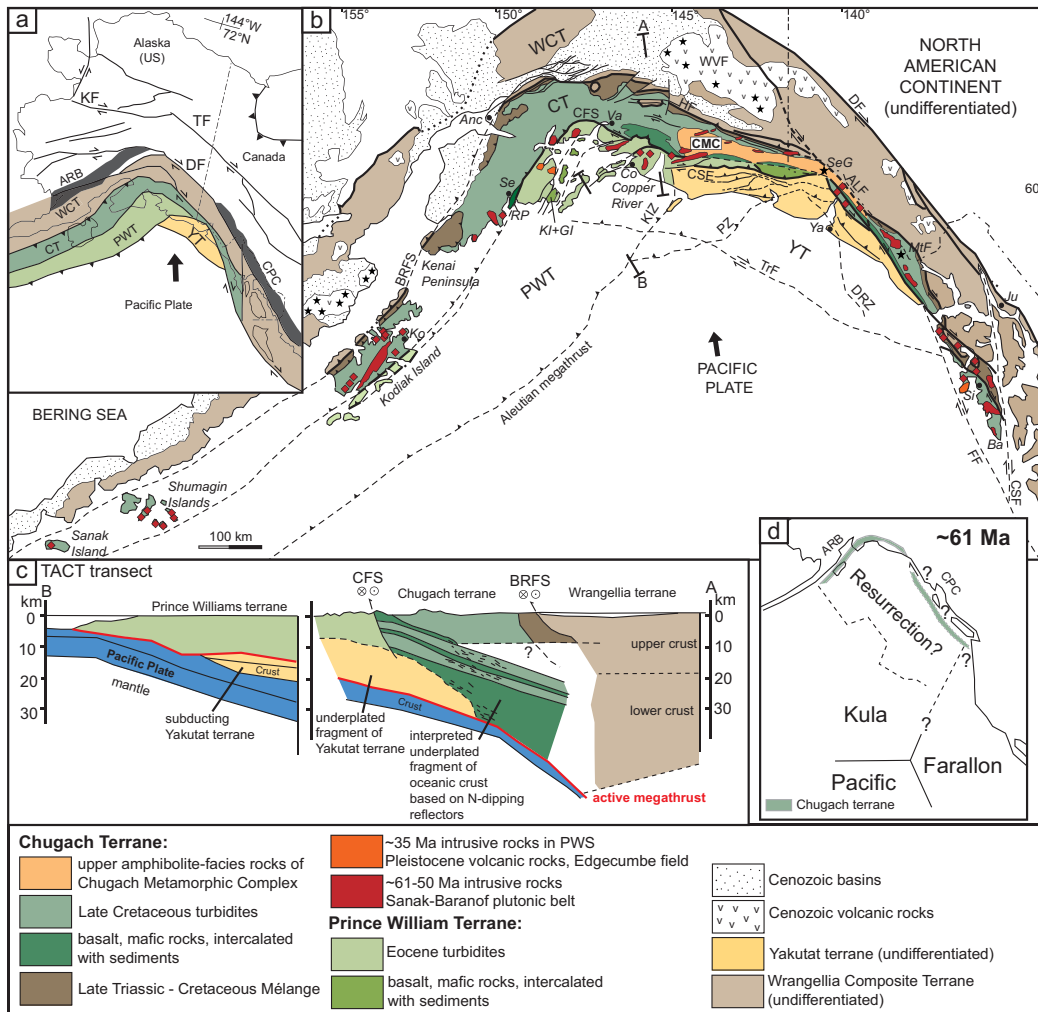


Figure 5.1: (a) Tectonic sketch map of Alaska showing the location of the tectonic terranes relevant for this study and major Neogene faults of the Northern Cordillera. (b) Geological map of the southern Alaska margin, modified from Plafker et al. (1994), faults of the Border Range Fault System after Pavlis & Roeske (2007). (c) Crustal profile through the southern Alaska margin, along the TACT (Trans-Alaska Crustal Transect) route, after Fuis et al. (2008) and Fuis & Plafker (1991). (d) Schematic sketch of the plate tectonic situation in the Pacific Basin during the Late Cretaceous to Eocene period as indicated by magnetic anomalies preserved on the Pacific plate, after Doubrovine & Tarduno (2008). Resurrection plate after Häussler et al. (2003a). Two possible locations of the accretionary prism of the Chugach and Prince William terranes along the margin are indicated. Abbreviations of geographical locations (in italics): Anc=Anchorage, Ba=Baranof Island, Co=Cordova, GI=Glacier Island, Ju=Juneau, KI=Knight Island, Ko=Kodiak, MtF=Mt Fairweather, Se=Seward, SeG=Seward Glacier, RP=Resurrection Peninsula, Si=Sitka, Va=Valdez, Ya=Yakutat. Abbreviations of geological terms: ARB=Alaska Range belt, BRFS=Border Range Fault System, CFS=Contact Fault System, CMC=Chugach Metamorphic Complex, CSE=Chugach-St-Elias-Fault, CSF=Chatham Strait Fault, CT=Chugach terrane, CPC=Coast Plutonic Complex, DF=Denali Fault, DRZ=Dangerous River Zone, FF=Fairweather Fault, KF=Kaltag Fault, KIZ=Kayak Island Zone, PZ=Pamplona Zone, PWT=Prince William terrane, TF=Tintina Fault, TrF=Transition Fault, WCT=Wrangellia Composite terrane, YT=Yakutat terrane.

The turbidite sequence of the accretionary prism contains one large and several smaller belts of mafic volcanic rocks (Fig. 5.1b; Plafker et al., 1994). The large belt stretches in the Chugach terrane from the Prince William Sound in the west to south-eastern Alaska in the south-east and consists of mafic rocks intercalated with sediments (Fig. 5.1b; Lull & Plafker, 1990). Fuis & Plafker (1991) and Fuis et al. (2008) correlate this belt with north-dipping seismic reflectors found below the accretionary prism to the north, and interpret this package of mafic and sedimentary rocks as an offscraped and underplated fragment of the oceanic plate which subducted below the accretionary prism (Fig. 5.1c). Lull & Plafker (1990) interpreted the same mafic rocks as remnants of an accreted intra-oceanic island-arc, whereas Bradley et al. (2003) interpret them as being derived from an oceanic spreading ridge which might have been present close to the margin during sedimentation of the prism. The high velocity layer pointed out by the north-dipping seismic reflectors beneath the Chugach terrane has also been interpreted as a mafic magma underplate, presumably a large gabbroic complex, which would not be related to the mafic rocks cropping out at the surface (e.g. Harris et al., 1996). Other smaller occurrences of mafic rocks, including gabbros and pillow basalts are exposed on Resurrection Peninsula and in Prince William Sound on Knight and Glacier Islands (Fig. 5.1b). They were interpreted as having formed at either a leaky transform fault or at a mid-oceanic spreading center shortly before they were incorporated in the accretionary prism (e.g. Tysdal et al., 1977; Crowe et al., 1992; Kusky & Young, 1999).

Paleocene to Eocene tonalitic, granodioritic and granitic plutons, associated with minor gabbroic plutons, intrude the accretionary prism of the Chugach and the northern part of the Prince William terrane: the so-called Sanak-Baranof plutonic belt (Fig. 5.1b; Hudson et al., 1979; Farris & Paterson, 2009). The mainly calc-alkaline plutons are unusual because they intrude the accretionary prism in an extreme fore-arc position: inferred coeval magmatic arcs are located a few hundred kilometres farther inboard (the Alaska Range and Coast Plutonic belts, Fig. 5.1a; Wallace & Engebretson, 1984; Plafker et al., 1994). The geochemistry of the Sanak-Baranof plutons indicates that they originated mainly from the melting of metasedimentary rocks of the accretionary prism, with a variable contribution from a more mafic end-member (Hudson et al., 1979; Hill et al., 1981; Barker et al., 1992; Harris et al., 1996; Lytwyn et al., 2000; Ayuso et al., 2009). Several possible sources for this mafic component in the plutons exist: It could be derived from the melting of mafic rocks already incorporated into the prism, from melts generated in the mantle wedge below the prism, from melting of the subducting oceanic crust, or from asthenospheric upwelling due to the presence of a slab window related to the subduction of an oceanic spreading center (e.g. Barker et al., 1992; Ayuso et al., 2009). The age of the intrusions ranges from ~61 Ma in the west to ~50 Ma in the east (Bradley et al., 1993, 2000, 2003; Sisson et al., 2003; Farris et al., 2006). Lode-gold deposits associated with brittle faults occur from the Kenai Peninsula down to Baranof Island in the Valdez and Orca groups and are of the same age as the intrusions of the Sanak-Baranof belt (Goldfarb et al., 1986; Häussler et al., 1995). The Chugach Metamorphic Complex is developed in the eastern part of the accretionary prism and is associated closely with the magmatic rocks of the Sanak-Baranof belt. K/Ar and $^{40}\text{Ar}/^{39}\text{Ar}$ ages of metamorphic and magmatic rocks are very similar, and in the

Chugach Metamorphic Complex plutons were emplaced throughout the syn-metamorphic deformational sequence (Pavlis & Sisson, 1995, 2003) indicating that the magmatic and metamorphic events are linked (e.g. Hudson et al., 1979; Sisson et al., 1989; Bradley et al., 1993).

The near-trench position of the Sanak-Baranof plutonic belts, the geochemistry and age distribution of these plutons, the gold mineralizations and the presence of a low-pressure/high-temperature metamorphic complex in the accretionary prism have been interpreted widely as the result of the subduction of an active oceanic spreading ridge below the accretionary prism (Marshak & Karig, 1977; Bradley et al., 1993, 2000, 2003; Sisson & Pavlis, 1993; Pavlis & Sisson, 1995, 2003; Häussler et al., 1995, 2003a; Harris et al., 1996; Madsen et al., 2006; Farris & Paterson, 2009). However, there are two important uncertainties related to the Late Cretaceous to Eocene history which complicate the understanding of the tectonic history of this margin:

(1) The exact location of the prism during accretion and intrusion by the magmatic rocks relative to the inboard terranes is not well known (Fig. 5.1d). The Border Range Fault System inboard of the accretionary prism has a complex Jurassic to Eocene (or younger) deformation history which varies considerably along strike (Roeske et al., 2003; Pavlis & Roeske, 2007). From north of Prince William Sound to the Canadian Border in the east, the fault system consists of a network of dextral strike-slip faults which were active from the Late Cretaceous to the Early Eocene (~50 Ma) with total dextral displacement estimates ranging from ~500 to >1000 km (the Hanagita fault system, Fig. 5.1b; Roeske et al., 2003). Farther to the south-east, faults belonging to the Border Range Fault System could have been active even after ~50 Ma, or have been reactivated by active strike-slip faults belonging to the dextral Fairweather Fault System active probably since ~30 Ma (Fig. 5.1b; Plafker et al., 1994; Pavlis & Roeske, 2007). These structural observations indicate that the prism probably formed considerably to the south of its present position, and that during or after accretion it was transported northwards (Fig. 5.1d). This is supported by the sedimentary petrography, isotopic composition and detrital zircon population ages of the turbidite sequence of the accretionary prism, which point to an origin of the sediments from a rapidly exhuming continental margin magmatic arc (e.g. Nilsen & Zuffa, 1982; Farmer et al., 1993; Sample & Reid, 2003; Häussler et al., 2005). Such a magmatic arc of adequate composition is present in the Coast Plutonic Complex, which is exposed southeast-ward and inboard of the present position of the accretionary prism and which stretches over a distance of ~1700 km along the margin (Fig. 5.1a; e.g. Gehrels et al., 2009). Evidence for considerable northward transport of the accretionary prism after accretion also comes from paleomagnetic studies, which suggest ~13-31° latitudinal northward transport since accretion of the sediments (Plumley et al., 1983; Coe et al., 1985; Bol & Coe, 1992; Roeske et al., 2009), or from geological correlations between similar sedimentary and magmatic rocks now exposed in the area of Vancouver Island (Cowan, 2003). However, similar magmatic rocks related to the Sanak-Baranof belt also intrude crystalline rocks in terranes to the north of the prism, which is cited as evidence that the prism has been in its current position relative to the inboard terranes at least since ~62-50 Ma (e.g. Häussler et al., 2003a).

(2) The plate tectonic configuration in the Pacific Basin during sedimentation and accretion of the prism in the Late Cretaceous and Eocene is not well known because large traces of lithosphere have been consumed in north Pacific trenches (Fig. 5.1d). Therefore there is some uncertainty regarding on which oceanic plate the accretionary prism actually formed. Magnetic anomalies present on the Pacific Plate south of the Aleutian Islands (the Great Magnetic Bight, e.g. Atwater, 1989) suggest that at least during chrons 34-25 (~84-56 Ma, timescale after Mueller et al., 2008) a third plate was present northwest of the Pacific and Farallon plates: the Kula plate (Fig. 5.1d; e.g. Woods & Davies, 1982). The ridge between the Kula and Farallon plates probably intersected the North American margin during this period somewhere between California in the south and Vancouver Island in the north (Fig. 5.1d; e.g. Engebretson et al., 1985; Doubrovine & Tarduno, 2008). The Kula-Farallon ridge has been mentioned as the ridge that produced the Sanak-Baranof plutonic belt (e.g. Bradley et al., 1993; Sisson & Pavlis, 1993; Pavlis & Sisson, 1995; Häussler et al., 1995), but in this case, the entire belt must have been located at least as south as Vancouver Island during intrusion (Fig. 5.1d; Doubrovine & Tarduno, 2008). As an alternative, Häussler et al. (2003a) suggested yet another oceanic plate, the Resurrection plate, was present during the time of Sanak-Baranof-belt magmatism and that the ridge between this Resurrection plate and the Kula plate intersected the southern Alaskan margin in the present-day location of the Sanak-Baranof plutonic belt (Fig. 5.1d). Besides indicating the presence of three plates in the Pacific basin, the magnetic anomalies on the Pacific plate also indicate a major plate tectonic reorganization at chrons 24-21 (~53-48 Ma) which led to a rearrangement of the spreading ridges present in the basin (e.g. Lonsdale, 1988; Atwater, 1989). Pacific-Farallon spreading changed its orientation, but unfortunately most information on Pacific-Kula spreading after this reorganization is lost due to subduction. There are two differing views on what happened after this plate reorganization: (1) Pacific-Kula spreading came to a halt after the reorganization (e.g. Byrne, 1979; Norton, 1995), which would have led to decreased relative motion between the oceanic plates and North America, or (2) Pacific-Kula spreading also changed direction and continued spreading at an increased rate until ~40 Ma (e.g. Lonsdale, 1988; Atwater, 1989), which would have led to increased relative motion between the oceanic plates and North America.

Given the uncertainty in the position of the accretionary prism relative to the inboard crystalline terranes and the uncertainty in the plate tectonic configuration in the Pacific Basin for the period of interest (Late Cretaceous to Eocene), the boundary conditions for the tectonic evolution of the margin are not well constrained. By analysing the internal structural geometry, the metamorphic evolution and thermochronological history of the Chugach Metamorphic Complex in more detail we aim to gain more information about the tectonic environment which shaped the southern Alaskan margin in Late Cretaceous to Eocene times.

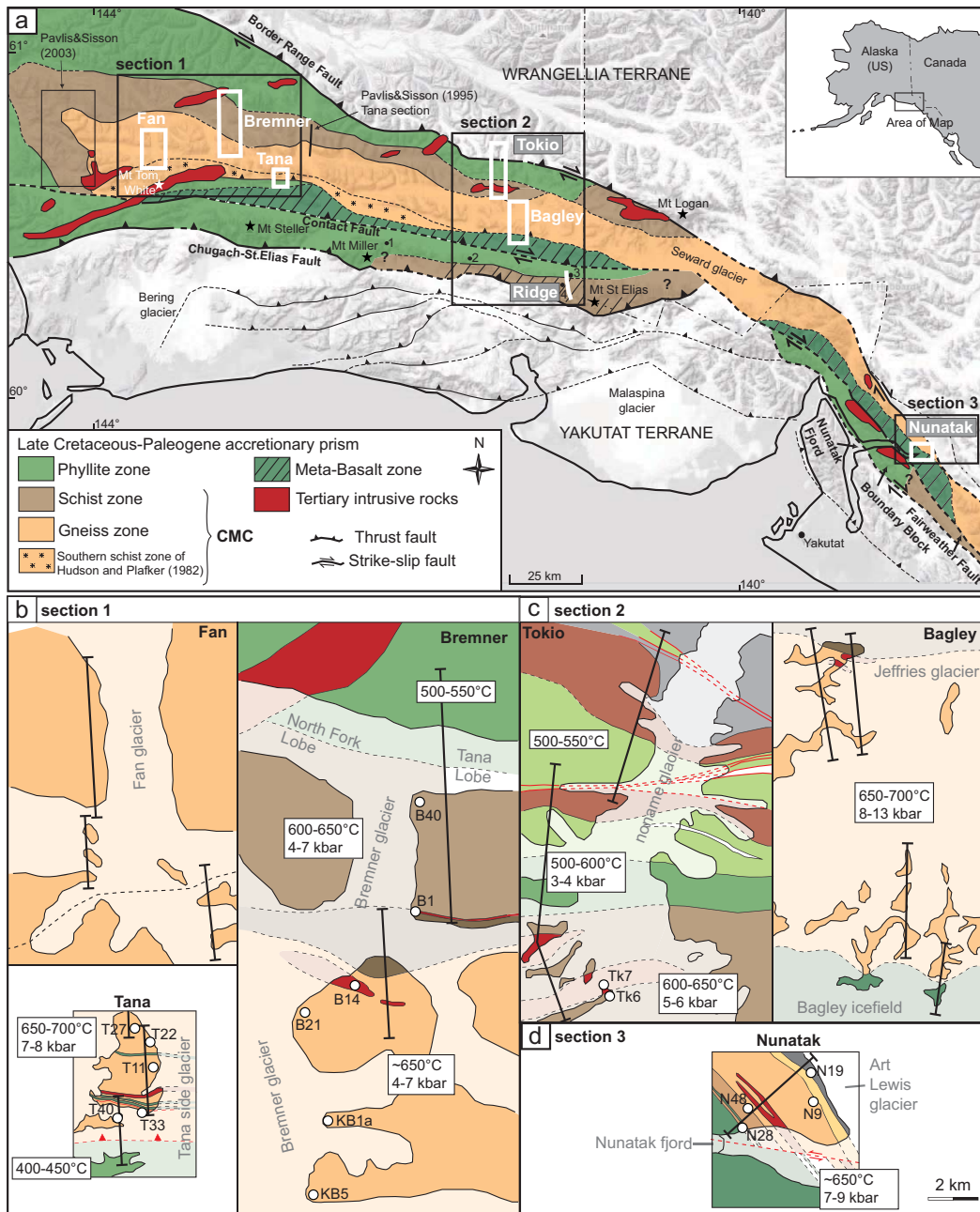


Figure 5.2: (a) Geological map of the Chugach Metamorphic Complex, according to Hudson & Plafker (1982) and results of this study. The locations of the three different sections presented in this study are indicated. Note that Hudson & Plafker (1982) mapped a southern schist zone in the western part of the complex (indicated with stars) which we did not encounter in our sections 1 and 2. (b)-(d) Detailed sketch maps of the different parts of the western, central and south-eastern sections, with the location of the thermochronological samples indicated and with general *PT* conditions from Bruand (2010). Stippled line in the Fan transect of b) indicates the southern gneiss-schist-transition as marked on the map of Hudson & Plafker (1982). Colour code as for Fig. 5.3 for (b) and (c) and Fig. 5.6 for (d).

5.3 Geology of the Chugach Metamorphic Complex

Hudson & Plafker (1982) first described the Chugach Metamorphic Complex based on a reconnaissance study in the area between the Copper River in the west and the US-Canadian border in the east (Fig. 5.1b, Fig. 5.2a). They mapped two macroscopically different metamorphic units: An outer schist zone composed of fine-grained biotite-quartz-plagioclase schist, which surrounds an inner gneiss zone composed of layered migmatitic gneisses (Fig. 5.2a). The complex is intruded by many pre-, syn- and post-metamorphic dikes and plutons associated with the Sanak-Baranof belt (e.g. Sisson & Pavlis, 1993; Pavlis & Sisson, 1995, 2003; Harris et al., 1996). A zone of metabasaltic rocks intercalated with greenschist- to amphibolite facies metasedimentary rocks occurs along the southern border of the complex (Fig. 5.2a; Lull & Plafker, 1990).

Quantitative data on *PT* conditions from the CMC are sparse. Based on samples from five localities distributed throughout the western and narrow northern parts of the complex, Sisson & Hollister (1988) and Sisson et al. (1989) calculated peak pressures of ~2-3 kbar (~10 km depth) and peak temperatures of ~550-650°C. These quantitative *PT* estimates are consistent with regional field observations by Pavlis & Sisson (1995, 2003) and Scharman et al. (subm) which show the ubiquitous occurrence of andalusite and andalusite replaced by sillimanite throughout the northern schist and westernmost gneiss zone.

Based on these observations the CMC has been characterized as an unusual low-pressure/high-temperature complex that developed in the accretionary prism shortly after its accretion. However, quantitative thermobarometry data and the bulk of field observations are limited to the northern part and the western termination of the complex. A recent thermobarometric study obtained a large *PT* dataset along the transects described below and obtained estimates of metamorphic conditions that are surprisingly different than estimates from the northern and western parts of the belt: ~450-550°C and <~3 kbar for the greenschist-facies phyllites outside of the metamorphic complex, ~500-650°C and ~3-7 kbar for the schist zone, and >650°C and ~4-13 kbar for the gneiss zone (Fig. 5.2b-d; Bruand, 2010). These new results suggest that along these transects studied, low pressures similar to the values obtained by Sisson et al. (1989) were only reached in the northern schist zone, associated with lower temperatures, and that the bulk of the complex along these transects experienced considerably higher pressures. According to these new results, rocks of the phyllite, schist and northern gneiss zones reached depths of maximal ~10-25 km whereas rocks of the southern gneissic zone were buried to depths of up to ~30-50 km.

Sisson & Pavlis (1993), Pavlis & Sisson (1995, 2003) and Scharman et al. (subm) conducted focused structural field studies in a series of transects and regional studies throughout the northern half and the western termination of the complex where it plunges westward beneath lower grade rocks (Fig. 5.2a). Their mapping is relatively complete from just west of the Copper River to the Tana River, but is at reconnaissance level from the Tana River to Mt. Logan. Throughout this part of the complex they observe a surprisingly uniform

structural history with three generations of ductile fabrics (Sisson & Pavlis, 1993; Pavlis & Sisson, 1995, 2003): (1) D_1 produced a variably but generally steeply dipping layer-parallel pressure solution foliation (S_1). This early foliation and associated fold-thrust structures are best developed in low-grade phyllites to middle amphibolite facies schists, but are locally recognized into amphibolites facies gneisses. In line with observations in lower grade rocks to the west (e.g. Nokleberg et al., 1989; Fisher & Byrne, 1992) this deformational event is generally interpreted as contemporaneous with accretion. (2) D_2 produced the first syn-CMC metamorphic fabric (S_2) with a pronounced E-W stretching lineation developed in the schists and gneisses. This deformation produced gently-inclined to recumbent, close to isoclinal F_2 folds throughout the schist and gneiss zones, but fades to weak overprints outside the CMC. (3) D_3 produced a steeply-dipping, ~E-W striking foliation (S_3) developed as a crenulation cleavage in the schist zone and as a high-grade foliation contemporaneous with migmatite development in the gneiss zone. Throughout the area of these previous studies, D_3 is associated with the metamorphic peak; e.g. these previous studies showed early metamorphic andalusite pseudomorphs converted to sillimanite and boudinaged with sillimanite pressure shadows. Throughout this zone they documented extensive evidence that D_3 was associated with dextral shear, with localized evidence that D_3 was transpressional.

The CMC is less well known to the east and south of the U.S.-Canadian border. From the core of the St. Elias Mountains through the Fairweather Range the CMC is extensively covered by glacial ice (Fig. 5.2a), but the high grade metamorphism probably extends continuously to at least the Fairweather Range (Fig. 5.1b) and may extend as far as Baranof Island (e.g. Pavlis & Sisson, 1995; Zumsteg et al., 2003).

Previous studies suggest that complications occur along the southern border of the CMC (e.g. Plafker et al., 1994). The area is highly glaciated and mostly covered by the extensive Bagley icefield (Fig. 5.2a). South of this icefield, metabasaltic and metasedimentary rocks crop out along the high-alpine ridge from Mt Steller to Mt St Elias (Fig. 5.2a). Metamorphic grade along this ridge seems to increase from greenschist-facies slates to amphibolite-facies basalt along the ridge from W to E (e.g. Plafker et al., 1994). Felsic and gabbroic plutons intrude the eastern part of the ridge. The entire ridge probably represents a tectonic sliver of the accretionary prism which was dextrally displaced and obliquely exhumed along the Fairweather-Contact fault system, but little is known about the timing and amount of displacement and exhumation (Plafker et al., 1994; Enkelmann et al., 2009, 2010). A similar tectonic sliver is exposed along the Fairweather fault zone in the Nunatak fjord region, the Boundary-Fairweather block (Fig. 5.2a; Hudson et al., 1977a,b; Sisson et al., 2003). The Boundary-Fairweather block consists of a metamorphosed turbidite sequence presumed to be part of the Chugach terrane with metamorphic grade increasing from greenschist facies to amphibolite facies towards the southeast (Hudson et al., 1977b; Sisson et al., 2003).

5.4 Structure of the Chugach Metamorphic Complex

In order to gain more information on the structural geometry of the CMC from W to SE and from N to S, we mapped three composite sections across the complex: (a) a western section 1, (b) a central section 2, and (c) a south-eastern section 3 (Fig. 5.2). Section 1 covers the complex where it is widest, and section 3 where it is narrowest (Fig. 5.2). Access to the sections was by fixed wing aircraft and mapping occurred on foot from central camps. A total of 45 field days were conducted over two summers (2008, 2009). We present structural profiles with stereoplots (Fig. 5.3, Fig. 5.6) field photographs (Figs. 5.4, 5.5, 5.6), and a tectonic sequence diagram (Fig. 5.7; Forster & Lister, 2008) for each section. In order to describe the structural observations as unprejudiced as possible, we do not adopt the D₁-D₃ scheme as developed by Pavlis & Sisson (1995, 2003) in this descriptive part of our contribution, and relate our observations to their structural scheme only in section 5.4.4 and the discussion. In addition we refer to the schist and gneiss zones as macroscopically defined by Hudson & Plafker (1982) and we refer to the lower-grade metamorphic rocks outside the complex as phyllite zone.

5.4.1 Section 1

Section 1 consists of three different field areas: the Fan, Bremner and Tana transects (named after the major glaciers close to the transects, Fig. 5.2, Fig. 5.3a), and overlaps with the area described by Scharman et al. (subm). The section crosses from the phyllite to the gneiss zone in the north (Bremner transect), traverses the gneiss zone (Fan transect) and crosses from the gneiss zone to the phyllite zone in the south (Tana transect, Fig. 5.3a).

Phyllite zone

The Bremner transect starts in the north in the phyllite zone. The rocks are classic Valdez Group metasedimentary rocks comprised of interbedded lithic metasandstones and argilla-

Figure 5.3 (following page): (a) Structural profiles across the Western CMC separated into three parts from N to S: the Fan, Tana and Bremner transects. (b) Structural profiles across the Central CMC separated into three parts from N to S: the Tokio, Bagley and St Elias ridge transects. Stereoplots are lower hemisphere equal area projections, computed with StereoNett software V2.46 of Johannes Duyster. The stereoplots are numbered from 1-14 (SP1-SP14, referenced in the text). Abbreviations: SP=Stereoplot, and=andalusite, S_{ps}=Pressure solution foliation, L_{SedPS}=Intersection lineation between bedding and pressure solution foliation, L_{SPS}=Stretching lineation on pressure solution foliation, S_{Sed}=Sedimentary bedding, S_{bt}=Foliation defined mainly by biotite, L_{Sbt}=Stretching lineation defined by biotite, S_{cr}=Crenulation foliation, S_{melt}=Foliation defined mainly by leucosomes and partly biotite, L_{S_{melt}}=Stretching lineation on S_{melt}, L_{SChl}=late stretching lineation defined by chlorite. Do1-3=Domains with different deformation styles in the gneiss zone (see text for explanation).

aceous rocks consistent with their origin as turbidites. These layered metasedimentary rocks are folded into meter-scale, open to tight folds with straight limbs and narrow hinges. An axial planar foliation to these folds is developed which is defined by thin, dark, pressure solution seams (S_{PS} ; Fig. 5.4a). This S_{PS} dips 5-70° towards the S with flat orientations in the northernmost outcrops of the Bremner transect and steeper orientations towards the Bremner glacier farther south (stereoplot (=SP) 1, Fig. 5.3a). Fold axes and intersection lineations between the bedding and S_{PS} (L_{SedPS}) are E-W horizontal to shallowly W plunging (SP1, Fig. 5.3a). The observed relationship between foliation and bedding in this phyllite zone suggests that the meter-scale folds are parasitic folds to a larger-scale N-vergent antiform as indicated on the profile on Fig. 5.3a.

Schist zone

The transition from the phyllites into the schist zone of the CMC is in the Bremner transect covered by the Tana lobe of the Bremner glacier (Fig. 5.2b, 5.3a). South of the Tana lobe, the sedimentary layering is in general still visible, but it is isoclinally folded on millimeter- to hundreds of meter-scales and attenuated on the limbs. The rocks are generally coarser-grained and schistose, and a continuous cleavage is marked by aligned biotite (S_{bt} , Fig. 5.4b). Moreover, in rocks of appropriate composition, fibrous sillimanite is developed axial planar to the isoclinal folds of the bedding. The S_{bt} foliation is folded on a millimeter- to meter-scale into open to tight folds with sub-vertical axial planes (Fig. 5.4b, c), which leads to variable orientation of the S_{bt} planes (SP2, Fig. 5.3a). The enveloping surface to the upright folds is close to horizontal (Fig. 5.3a), indicating that S_{bt} formed in a nearly flat orientation. A late crenulation cleavage (S_{cr}) is developed parallel to the axial planes of the upright folds (Fig. 5.4b). S_{cr} strikes E-W and dips 50-80° towards the N or S (SP2, Fig. 5.3a). In some cores of the upright folds, steep, brittle faults with cataclasite cores up to 1 m thick are developed.

A pronounced stretching lineation (L_{Sbt}) defined by elongated biotite and elongated quartz nodules is present on S_{bt} . L_{Sbt} plunges 0-25° towards E or W (SP2, Fig. 5.3a). The stretching lineation is parallel to both the fold axes of the isoclinal folds as well as to the fold axes of the open, upright folds. In one locality, top-to-the-east shear senses (sigma-clasts of quartz veins and S-C'-fabrics) were observed parallel to L_{Sbt} and perpendicular to S_{bt} (Coord. 60.8496N/143.2388W). In line with finite strain studies of Pavlis & Sisson (1995, 2003) we interpret that this flat-lying S_{bt} , the E-W stretching lineation L_{Sbt} and the upright folds with E-W fold axes together result in a pronounced constrictional finite fabric throughout the schist zone of the Bremner transect.

Quartz veins are abundant throughout the schist zone. They occur preferably in metapelitic layers, are boudinaged parallel to L_{Sbt} and folded into upright folds, leading to a peculiar bubble-shape on planes oriented perpendicular to S_{bt} and L_{Sbt} (Fig. 5.4b). Felsic dikes and sills up to several meters in thickness intrude the schist zone. The thickest and most

prominent ones are oriented parallel to S_{bt} (Fig. 5.4c), and are interpreted to have intruded prior or synchronous to S_{bt} -deformation.

Gneiss zone

The transition from the schist zone into the gneiss zone (transitional gneiss after Pavlis & Sisson (1995), Figs. 5.2b, 5.3a) is exposed in the Bremner transect and occurs gradually over a distance of ~2-3 km. Large parts of the transition are covered by glacial deposits. Within the transition, the rocks become even coarser grained, and they become segregated parallel to S_{bt} into mm- to several cm-thick light plagioclase-quartz layers separated from dark biotite-sillimanite-garnet-plagioclase-quartz layers. This segregation is interpreted as the onset of partial melting in the rocks (Bruand, 2010). In the Bremner transect, a pluton ~1 km in width occurs close to this schist-gneiss transition (Fig. 5.3a).

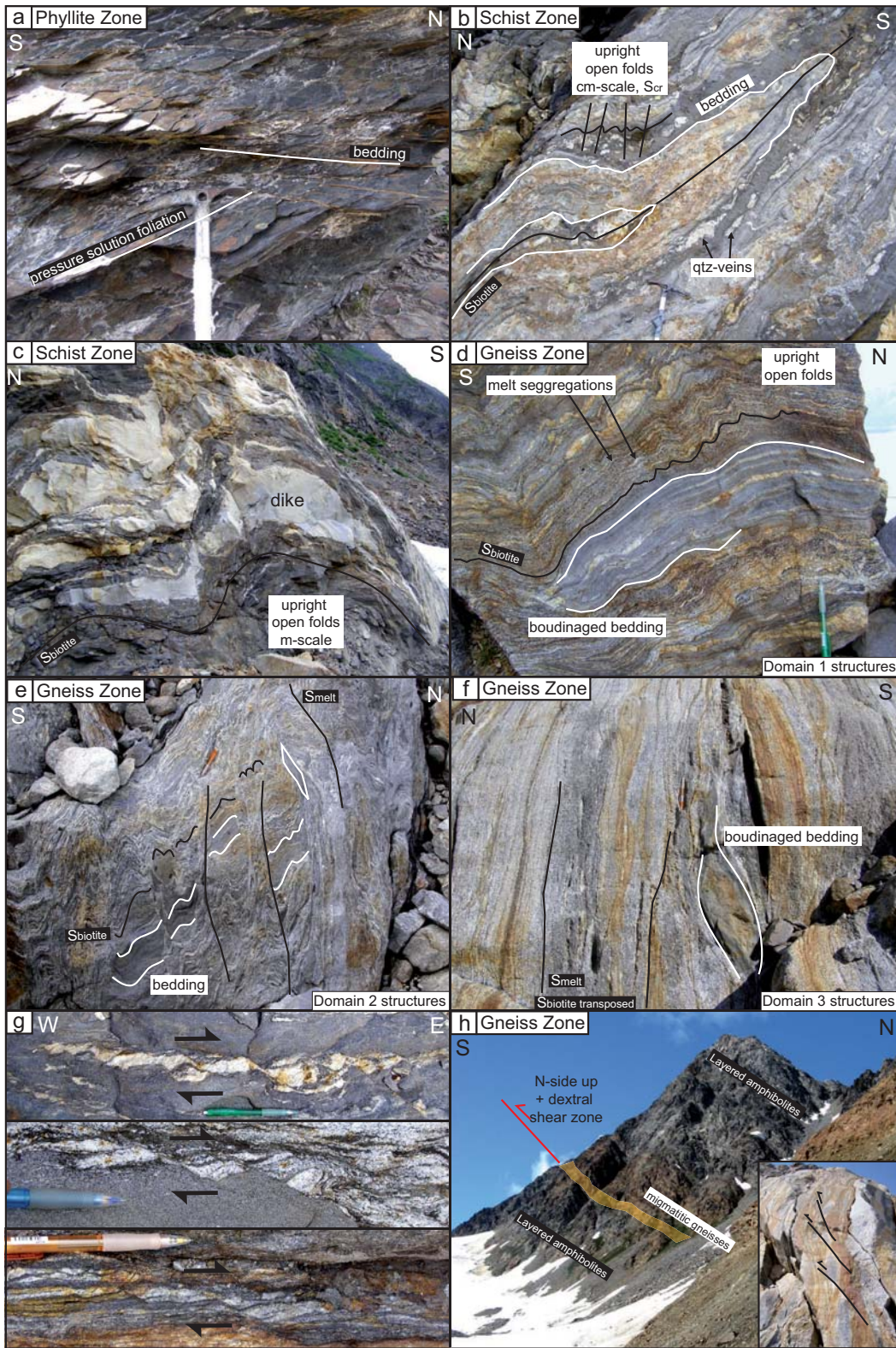
The gneiss zone is exposed in the southern part of the Bremner transect, all along the Fan transect and along parts of the Tana transects (Fig. 5.3a). Three different structural domains which alternate across strike were observed in these gneisses. (1) In Domain 1, the penetrative S_{bt} observed in the schist zone is dominant. Quartzofeldspathic layers, interpreted as leucosomes, occur parallel to this foliation. The sedimentary layering is still visible. The generally flat-lying S_{bt} foliation is crenulated into upright open to tight folds with variable fold intensity (Fig. 5.4d; SP4, Fig. 5.3a). (2) In Domain 2, the S_{bt} foliation is still visible, but the upright folding is much more intense and a new axial plane foliation to these upright folds developed, along which new-grown biotite and mm- to cm-thick quartzofeldspathic layers, interpreted as resulting from partial melting, occur (S_{melt} , Fig. 5.4e). S_{melt} strikes W-E to WNW-ESE and has a fan-shaped dip orientation from north to south over the gneiss zone: it dips predominantly 40-90° towards the south in the north of the gneiss zone (SP3, Fig. 5.3a), is nearly vertical in the central part of the gneiss zone (SP5, Fig. 5.3a) and dips 55-90° towards the north in the south of the gneiss zone (SP7, Fig. 5.3a). (3) In Domain 3, S_{melt} is completely dominant, and S_{bt} has been transposed into the same vertical orientation. Boudinaged lenses of more competent rock types (metasandstones, metabasalts) are still visible, but >50% of the rock consists of light quartzofeldspathic layers (Fig. 5.4f). Transitions between the three different domains are continuous. Domains 1 and 2 are dominant in most of the gneiss zone and alternate on a meter scale. Domain 3 is dominant in the south of the Fan transect and in most of the Tana transect (Fig. 5.3a).

Throughout the gneiss zone, a ductile stretching lineation defined by elongated minerals is present on both the S_{bt} and the S_{melt} ($L_{S_{bt}}$ and $L_{S_{melt}}$). This stretching lineation plunges 0-20° towards W-WNW in the Bremner transect (SP3, Fig. 5.3a), 15-50° towards W in the Fan transect (SP4 and 5, Fig. 5.3a) and 0-60° towards W in the Tana transect (SP6, Fig. 5.3a). The lineation is parallel to the fold axes of the upright folds. We did not observe any asymmetry (e.g. shear sense) parallel to this stretching lineation on planes perpendicular to the main foliation (horizontal planes in the case of S_{melt}), probably partly due to the fact that such outcrop planes were rare on the transects we studied (mostly vertical rock faces along glaciers). However, on a few horizontal planes semi-ductile to brittle, steep dextral shear bands were observed, deforming the high-grade S_{melt} (Fig. 5.4g).

The gneiss zone in the Tana transect is lithologically more variable than the gneiss zone in the Bremner and Fan transects. It consists of a densely layered sequence of migmatitic gneisses, calcsilicate layers, amphibolites and tonalitic to granodioritic intrusions highly foliated in the domain 3 style. In addition to the ductile stretching lineation $L_{S_{melt}}$, a younger stretching lineation defined by retrograde chlorite and muscovite ($L_{S_{chi}}$) is developed on many S_{melt} planes. This lineation plunges 60-80° to the W-NW (SP6, Fig. 5.3a).

The southern part of the CMC in section 1 was different from what we expected based on the map of Hudson & Plafker (1982). On their map, a wide schist zone exists south of the gneiss zone in the Fan transect region, which narrows towards the Tana transect

Figure 5.4 (following page): Field photographs from section 1 of the CMC. **(a)** Greenschist-facies slaty phyllites of the northern Bremner transect. Bedding is clearly recognizable. A 5-70° S-dipping pressure solution foliation is developed which is axial planar to meter-scale folds. Ice axe for scale. Coord. 60.92628088N/143.2129746W. **(b)** The sedimentary layering is isoclinally folded and boudinaged on mm- to m-scale in the schist zone of the CMC. An axial plane foliation defined by biotite and sillimanite is developed to the isoclinal folds (S_{bt}). Late, upright, open folds at mm- to m-scale overprint the isoclinal folds. Boudinaged quartz veins are abundant in more pelitic layers. Ice axe for scale in the lower center of image. Coord. 60.8735N/143.2360W. **(c)** Felsic dikes of up to several meters in thickness intrude the schist zone of the Bremner transect. They are oriented parallel to S_{bt} , and are folded into upright, open folds. Width of image ~5 m. Coord. 60.8735N/143.2360W. **(d)** Domain 1 structure observed in the gneiss zone of the Bremner transect. S_{bt} is the dominant foliation, with melt layers occurring parallel to it. Note the boudinaged sandstone layer in the center of the image, with melt accumulation at the boudin neck. Locally, upright open folds occur. Pencil for scale. Coord. 60.8124N/143.2999W. **(e)** Domain 2 structure observed in the gneiss zone of the Fan transect. S_{bt} is still visible, but is strongly folded into upright, tight to isoclinal folds with mm- to cm-thick melt layers present parallel to the axial plane of these folds (S_{melt}). Pencil for scale. Cord. 60.7546N/143.7217W. **(f)** Domain 3 structure observed in the gneiss zone of the Fan transect. S_{melt} is dominant, and only few layers of competent rock types (metasandstones, metabasalts) occur in a matrix of diffuse gneiss. Pencil in the center of the image for scale. Coord. 60.7282N/143.6351W. **(g)** Dextral shear bands observed on horizontal planes (perpendicular to S_{melt} and parallel to $L_{S_{melt}}$) throughout the gneiss zone. Upper image: transitional gneiss zone, Bremner transect, Coord. 60.8496N/143.2388W. Central image: Gneiss zone, Tana transect, Coord. 60.6840N/142.9220W. Lower image: gneiss zone, Fan transect, Coord. 60.7647N/143.7290W. **(h)** Southern gneiss zone in Tana transect. A 2-4 m wide shear zone is developed in migmatitic gneisses occurring between layered amphibolites. The chlorite-muscovite shear zone reveals N-side up and dextral sense of movement. Height of rock wall 600 m. Coord. 60.6856N/142.9034W. Small insert: Similarly oriented thrusts in the southern part of the gneiss zone on the Fan transect. Coord. 60.7282N/143.6351W.



region (Fig. 5.2a and b). However, we did not encounter a schist zone along either the Fan or Tana transects. On the contrary, in the Fan and Tana transects the proportion of quartzofeldspathic layers, which presumably result from partial melting, increases towards the south across the southern gneiss-schist transition marked by Hudson & Plafker (1982). This observation suggests that metamorphic grade is increasing towards the south within the exposed section. Unfortunately, we could not map the last ~4 km between the southern end of our transect and the Mt Tom White pluton in the Fan transect, since this pluton forms an extremely steep, high-alpine and heavily glaciated ridge which is difficult to access (Fig. 5.2). Nonetheless, only migmatitic gneisses and plutonic rocks are present in the moraine material of the Fan glacier coming from the pluton, making it highly unlikely that a schist zone occurs on these ~4 missing km of detailed mapping. We therefore infer that the gneiss zone continues to the south without an intervening schist zone, and that the transition into the Mt Tom White pluton is continuous with progressively more partial melt present in the rocks. The rugged topography of the Mt. Tom White pluton might be the result of Neogene faults surrounding the massif, which are indicated by much younger (U-Th)/He zircon and apatite ages from the massif than from the surrounding gneisses (Berger and Spotila 2008; Enkelmann et al. 2010).

Transition into the southern phyllite zone

The Tana transect covers the southern border of the CMC into the adjacent phyllite zone. As mentioned above no southern schist zone was encountered on this transect and the gneiss zone is directly juxtaposed against the phyllite zone suggesting the presence of a significant fault between these two zones (Fig. 5.2, Fig. 5.3a). The actual contact with the phyllite zone is unfortunately covered by a glacier (Fig. 5.3a). However, just north of this glacier a shear zone is exposed in the gneiss zone that gives a hint to the nature of the gneiss-phyllite contact in that transect. The shear zone is developed in a layer of migmatitic gneisses which is surrounded by layered amphibolites (Fig. 5.4h). The shear zone is ~2-4 m wide and consists of highly altered gneiss with biotite replaced by chlorite and muscovite. A strong stretching lineation plunges 45-55° towards 270-295°, which lies in the field of L_{SCH1} observed elsewhere in the Tana gneiss zone. Shear sense indicators point to N-side up sense of movement. Thus a dextral-oblique thrust component of movement is suggested across this shear zone. Similarly oriented, smaller-scale brittle reverse faults were observed in the southern gneiss zone of the Fan transect (small inset in Fig. 5.4h).

South of the glacier covering the gneiss - phyllite contact in this transect, greenschist facies phyllites are exposed (Fig. 5.3a). No biotite is present in these rocks. Mm- to cm-thick, ~40-80° N-dipping layers of argillaceous and psammitic metasedimentary rocks are visible which are isoclinally folded and boudinaged into intrafolial folds. A closely spaced, N-dipping pressure solution foliation is developed parallel to this layering and axial planar to the isoclinal folds (Fig. 5.3a). Several generations of veins occur both parallel to the layering/pressure solution foliation and cross-cutting it.

5.4.2 Section 2

Section 2 covers the central part of the CMC and has been studied in three areas: along the northern Tokio transect, along the southern Bagley transect and along the ridge between Mt Miller and Mt St Elias (Fig. 5.2a, Fig. 5.3b). The Tokio transect runs from the Wrangellia terrane in the north into the schist zone of the CMC along an unnamed glacier (Fig. 5.2c). The Bagley transect is separated from the Tokio transect by the ~5 km wide Jeffries glacier and is offset to the east by ~7 km. It runs from transitional gneiss into the gneiss zone and crosses into the southern metabasalt zone (Fig. 5.2c). In addition to these two transects, we conducted four fixed wing aircraft stops along the highly glaciated ridge between Mt Miller and Mt St Elias (Stops 1-4, Fig. 5.2a). Based on these observations we draw a profile across the ridge in the Mt Huxley region (Fig. 5.2a, 5.3b). This profile lies ~11 km south and ~18 km east of the southern end of the Bagley transect. Together, the three transects cover a distance of ~45 km across the CMC and lie roughly 70-90 km east of section 1.

Transition Wrangellia-Chugach terrane

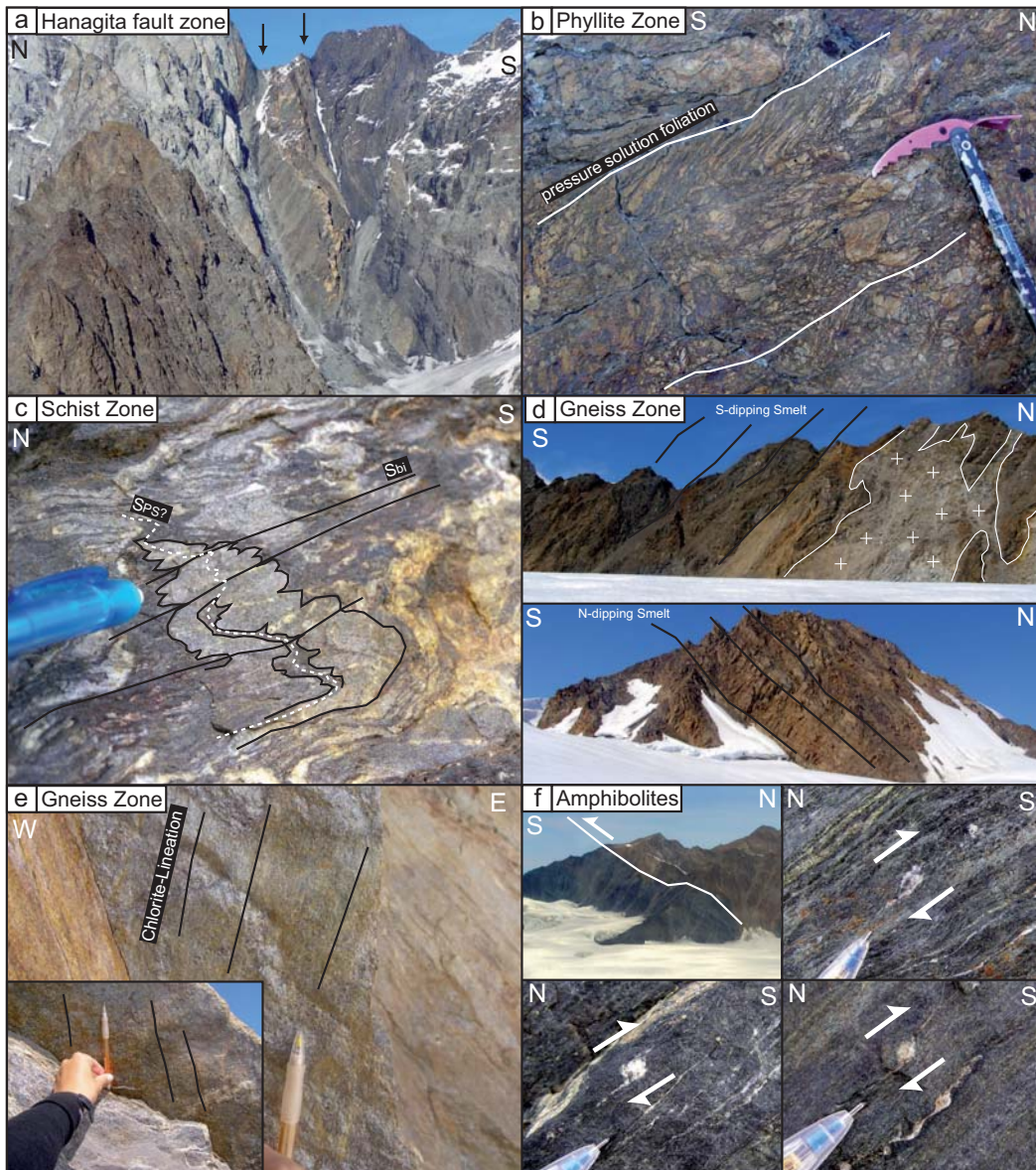
The Tokio transect starts in the Wrangellia terrane in the north (Fig. 5.2c, Fig. 5.3b). The nature and structure of the transition from the Wrangellia into the Chugach terrane has been described in detail by Roeske et al. (2003) in several regions west of the Tokio transect. They described a complex network of generally WNW-ESE striking, steeply dipping ductile to brittle shear zones and faults with predominantly dextral shear senses that juxtapose slivers of rocks from the Wrangellia terrane and slivers of rocks from the Chugach terrane against each other. Our observations from the northern part of the Tokio transect are similar. At the northern end of this transect, garnet-bearing amphibolite-facies metapelitic rocks, which are correlated with the Strelna metamorphics of the Wrangellia terrane by Roeske et al. (2003) are exposed (Fig. 5.2c, Fig. 5.3b). These rocks are intensely folded on mm- to m-scale and a penetrative NW-SE striking and gently SW-dipping foliation is developed. A weakly developed down-dip stretching lineation is observed on this foliation (SP8, Fig. 5.3b). A ~100-200 m wide sliver of greenish-reddish chert is intercalated with the Strelna metamorphics along steep brittle faults at the northern end of the Tokio transect (Fig. 5.2c, Fig. 5.3b). We correlate those steep faults along strike towards the W with the N-strand of the Hanagita fault zone of Roeske et al. (2003). The Strelna metamorphics are intruded by massive hornblende diorite bodies and many felsic dikes (Fig. 5.2c, 5.3b). Dating of similar dioritic rocks farther west reveals a Late Jurassic intrusion age and Cretaceous cooling ages for these diorites (Roeske et al., 2003). The massive diorite is juxtaposed in the south against a series of greenschist facies metasedimentary and metavolcanic rocks. This series consists of a dense intercalation of black slates, greenish metabasalts, light-grey metacarbonates, greyish silt- and sandstones and reddish-greenish cherts, which we interpret as part of the McHugh complex (mélange assemblage of Chugach terrane, Fig. 5.1; Roeske et al., 2003). A penetrative greenschist-facies foliation is developed in these rocks which strikes ~E-W

and dips mainly 25-85° towards the S. A pronounced E-W striking stretching lineation is observed on this foliation, which plunges 0-55° towards the W or E (SP9, Fig. 5.3b). We could not observe any shear sense perpendicular to the main foliation and parallel to the stretching lineation. A second zone of highly altered, massive diorite is juxtaposed against McHugh complex rocks farther south. We correlate the steep, brittle faults exposed on the northern boundary of the diorite intrusion with the S-strand of the Hanagita fault zone of (Roeske et al., 2003, Fig. 5.5a). South of this diorite, steeply foliated rocks of the McHugh complex are exposed (Fig. 5.3b).

Phyllite zone

South of a small side glacier, coherent, isoclinally folded metaconglomerates and metasandstones of the Valdez Group are exposed (Fig. 5.3b, Fig. 5.5b). Thus, for comparison, this side valley occupies the structural equivalent of the Eagle River fault which separates McHugh complex from Valdez Group over large parts of the Chugach terrane farther to the west. An E-W striking, 30-60° south-dipping pressure solution foliation (S_{PS}) parallel to the axial planes of the isoclinal folds is developed in the Valdez Group phyllites. Fold axes and a stretching lineation defined by elongated clasts in metaconglomerates (L_{SPS}) are horizontal and E-W striking (SP10, Fig. 5.3b). The contact to the northern McHugh complex is not exposed along this transect. Farther south the Valdez Group rocks become finer-grained and the pressure solution foliation is not as obvious as in the coarser metasandstones and metaconglomerates (Fig. 5.3b).

Figure 5.5 (following page): Field photographs from section 2 of the CMC. **(a)** South strand of Hanagita fault zone as exposed along the eastern side of the unnamed glacier along which the Tokio transect runs. Steep brittle faults juxtapose massive diorite (light unit to the left) against metasedimentary and metavolcanic rocks of the McHugh complex (dark unit to the right). Height of rock face ~1000 m. Coord. N60.7462/W141.4573. **(b)** Isoclinally folded conglomerate in the phyllite zone of the Tokio transect. A S-dipping pressure solution foliation is developed. Ice axe for scale. Coord. N60.7066/W141.5697. **(c)** Small-scale isoclinally folded bedding is overprinted by a second generation of tight folds which has S_{bt} as axial planar foliation. The first isoclinal fold is probably equivalent to the tight to isoclinal folds in the phyllite zone which have a pressure solution foliation as axial plane foliation. This suggests that S_{bt} is younger than S_{PS} . Pencil for scale. Coord. N60.6642/W141.5488. **(d)** The main foliation in the gneiss zone of the Bagley transect has a fan shape: it dips towards the S in the north (upper image, Coord. N60.6189/W141.4428) and dips towards the N in the south (lower image, Coord. N60.5473/W141.3960). A felsic pluton intrudes the transitional gneiss in the upper image. Both rock faces are ~200 m high. **(e)** A steep, down-dip stretching lineation defined by chlorite and muscovite is developed on S_{melt} -planes especially in the southern part of the Bagley gneiss zone. Pencil for scale. Coord. N60.5362/W141.3958, Small insert: Coord. N60.5473/W141.3960. **(f)** Dark slates intercalated with dark-greenish metabasalts build up the southern border of the CMC in the Bagley transect. The lithological boundary between the orange-brownish gneisses and the dark-green amphibolites is nicely visible from far away (upper left image). A north-dipping foliation with a down-dip lineation is developed in these amphibolitic rocks. Shear sense indicators in these rocks point to a N-side-up sense of shear (upper right and lower images). Coordinates where shear sense indicators were observed: N60.504/W141.3721.



Schist zone

South of another side glacier, massive, fine-grained schistose rocks are exposed with mm- to cm-sized pink andalusite crystals growing across S_{PS} . The fabric appears highly constrictional with a pronounced E-W stretching lineation. South of this outcrop, two felsic plutons each ~500-1000 m in across-strike width intrude the schist zone (Fig. 5.2c, Fig. 5.3b) and are separated by two outcrops of andalusite-bearing schist. In both of these schist exposures, folds of the sedimentary layering with asymmetry to the north are visible with an axial planar pressure solution foliation (S_{PS}), similar to the observations in the phyllite zone farther north, but the orientation of this S_{PS} is much more variable (SP11, Fig. 5.3b). In addition, open upright folds with E-W fold axes accompanied by a crenulation cleavage (S_{cr}) similar to the one in the schist zone of the Bremner transect are locally developed, but this foliation is also more variable in its orientation (SP11, Fig. 5.3b). South of the second pluton, the schists are coarser-grained, and display a pervasive flat-lying foliation defined by biotite and sillimanite (S_{bt} , SP11, Fig. 5.3b), similar to the observations in the schist zone of the Bremner transect. A small-scale observation from isoclinally folded bedding, which is overprinted by a second generation of tight to isoclinal folds with the S_{bt} as axial plane foliation, suggests that S_{bt} is a younger foliation than S_{PS} , which is axial planar to the first generation of folds (Fig. 5.5c). A shallowly W-plunging stretching lineation (L_{Sbt}) is developed on S_{bt} .

Gneiss zone

The Bagley transect starts in the north with transitional gneiss (after Pavlis & Sisson, 1995), which is intruded by an undeformed felsic pluton (Fig. 5.2c, 5.3b). The main foliation defined by biotite (S_{bt}) and rare mm-thick quartzofeldspathic layers is isoclinally folded on mm- to m-scale and a spaced crenulation cleavage (S_{cr}) dipping ~40° to the south is developed. Farther south, quartzofeldspathic layers begin to appear parallel to S_{cr} (= S_{melt}) and structures analogous to Domains 2 and 3 in section 1 are dominant. Across the entire Bagley transect, The S_{melt} foliation defines a similar but more pronounced fan structure as observed in the gneiss zone of section 1: the S_{melt} dips 40-80° towards the S in the northern part of the Bagley gneiss zone (SP12, Fig. 5.3b; Fig. 5.5d) and 30-80° towards the N in the southern part of the Bagley gneiss zone (SP13, Fig. 5.3b; Fig. 5.5d). Distinct from the gneiss zone of section 1 however, the ductile stretching lineation developed on S_{melt} (L_{Smelt}) is not horizontally to shallowly W plunging, but plunges 30-65° towards the W in the northern part of the Bagley transect and 30-60° towards the N-NNE in the southern part of the Bagley transect (SP12, 13, Fig. 5.3b). Moreover, a younger stretching lineation defined by chlorite and muscovite is present in addition to the high-grade stretching lineation on the main foliation planes in the southern Bagley transect (Fig. 5.5e). This lineation plunges 40-80° towards the N and has a similar orientation to the late stretching lineation observed in the Tana transect of section 1 (SP6, 12 and 13, Fig. 5.3b).

Transition into Metabasalt zone

The metabasaltic rocks at the southern end of the CMC are visible from afar due to their dark-green colour which contrasts with the orange-brown gneisses (Fig. 5.5f, Fig. 5.3b). The contact between the gneisses and the amphibolites is exposed in high cliffs but is often covered by ice or debris at the foot of these cliffs and is therefore difficult to reach. Two outcrops were visited in these rocks (60.5044N/141.3720W and 60.5079N/141.4152W). They consist of fine-grained greenschist to amphibolite facies slates interlayered with middle-grained amphibolites. A penetrative, north-dipping foliation is developed in these rocks (SP14, Fig. 5.3b). A N-dipping (down-dip) stretching lineation is developed on the foliation. Parallel to this lineation and perpendicular to the foliation sigma-clasts of thin quartz-veins reveal a N-side-up sense of shear (Fig. 5.5f).

The Mt Miller -Mt St Elias ridge

We visited the ridge between Mt Miller and Mt St Elias on the south-side of the Bagley icefield at four localities (Fig. 5.2a). At stops 1-3 the rocks consist of greenschist-facies metasedimentary rocks where the original bedding is still easily visible. Light-brown, up to 10 meters thick metasandstone layers alternate with dark-grey slates and dark-green metavolcanic rocks. The bedding dips 30-85° towards the N and m-scale to 10's of meter-scale folds that are asymmetric to the south occur. Steep S-dipping faults disrupt the bedding, but displacement directions are not visible. Felsic dikes both parallel to the bedding and parallel to the S-dipping faults also occur. At stop 2, ~45° WNW plunging striae show a dextral and N-side up sense of movement. In summary, stops 1-3 define a narrow strip of low-grade metasediments which crop out just south of the Bagley ice field (Fig. 5.2a). At stop 4, on the N-shoulder of Mt Huxley, highly foliated, dark-green to black middle-grained amphibolites are exposed. The foliation dips steeply towards the N and felsic dikes occur parallel to the foliation. Brittle faults parallel to the foliation with dextral and N-side-up components occur. A felsic intrusion several 100 m in size intrudes the dark amphibolites in the north-face of Mt Huxley.

5.4.3 Section 3

Section 3 lies ~170 km south-east along strike of section 2. The section lies in the glacial valley just above Nunatak fjord and is the first relatively easily accessible transect across the CMC southeast of the high St Elias range. Between this section and section 2 the rocks of the CMC are covered by extensive icefields and crop out only in nunataks and on the south flank of Mt Logan (Fig. 5.2a). The Chugach terrane in section 3 is limited to a narrow strip ~10 km in width between the Border Range fault system in the northeast and the Fairweather fault system in the southwest (Fig. 5.6). In addition to this decrease in total

width, the strike of the Chugach terrane changes from ~W-E in sections 1 and 2 to NW-SE in section 3. Two different lithological units comprise the Chugach terrane in section 3 (Fig. 5.6): a north-eastern, ~4-5 km wide unit of variable gneisses and altered schists and a south-western, ~4-5 km wide unit of fine-grained amphibolites that are interpreted as metabasalts (Figs. 5.2a, 5.6). The transect runs from the Art Lewis glacier in the north-east, which is probably underlain by a Neogene strike-slip fault (Pavlis & Roeske, 2007) to the amphibolites in the south-west (Fig. 5.6).

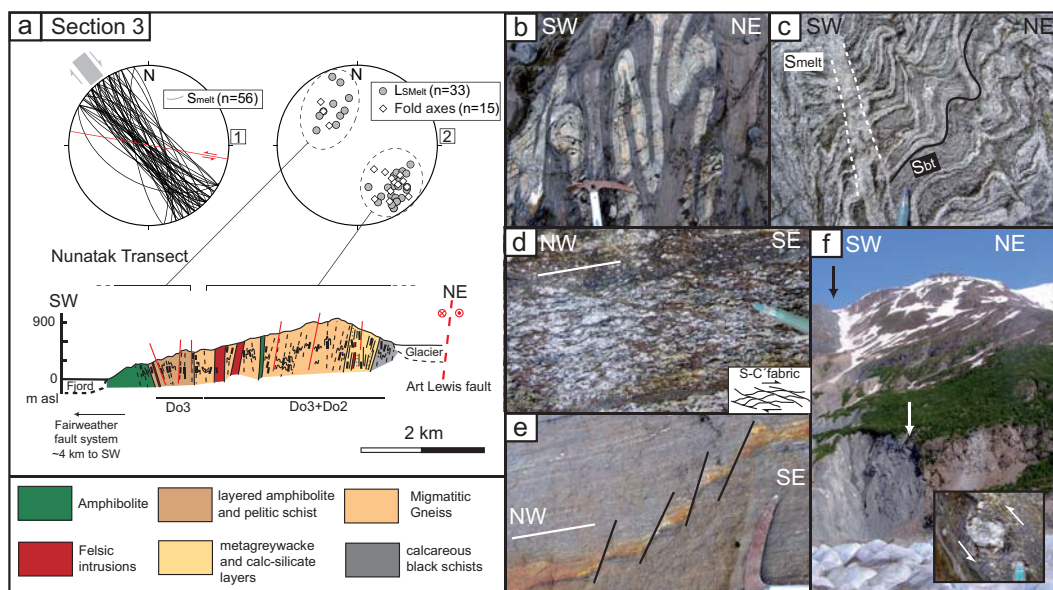


Figure 5.6: Structural profile and field photographs from section 3 at Nunatak fjord. **(a)** Structural profile and stereoplots across the Nunatak transect. Stereoplots are lower hemisphere equal area projections, computed with StereoNett software V2.46 of Johannes Duyster. **(b)** Several cm-thick amphibolite layers are isoclinally folded with metapelitic gneiss ~500 m away from the amphibolite-gneiss contact in the Nunatak transect. Ice axe for scale. Coord. N59.790/W138.8204. **(c)** Domain 2 structures in the gneiss zone of the Nunatak transect. A first foliation defined by biotite and thin melt layers is folded into upright folds with melt layers developed in the axial planes of these folds. Coord. N59.8084/ W138.8266. **(d)** Outcrop plane parallel to SE-plunging stretching lineation and perpendicular to the main foliation in the gneiss zone of the Nunatak transect shows S-C fabrics indicative of dextral shear. Pencil for scale. Coord. N59.8156/W138.8583. **(e)** Brittle WNW-ESE striking faults displace the foliation and a melt layer in the gneiss zone of the Nunatak transect. A large-scale brittle fault with similar orientation and an apparent offset of 1.5 km is located below the East Nunatak glacier. Ice axe for scale. Coord. N59.790/W138.8204. **(f)** The contact between dark amphibolites (left) and reddish gneisses (right) at the south-western end of the Nunatak transect is nicely visible from far. The contact consists of a ~1 m wide mylonite zone which shows NE-side-up and dextral sense of movement (small insert shows delta-clast). The mountainside is ~1000 m high. Coord. N59.8151/W138.8827.

Variable gneiss zone

The variable gneisses and altered schists that underlie most of the transect consist from NE to SW of several different lithological units. Calcareous altered schists are exposed in a narrow strip (~400 m wide) on the northeastern end of the transect along the Art Lewis Glacier (Figs. 5.2d, 5.6). Southwest of these schists, massive metasandstones and calcsilicate layers are exposed. Even farther to the southwest, quartzofeldspathic gneisses typical of the gneiss zone elsewhere in the CMC are exposed. Zones of foliated felsic intrusions alternate with the migmatitic gneisses. About 500 m northeast of the contact with the amphibolites, mm- to m-thick layers of amphibolites are intercalated with the gneisses, due to infolding or primary layering (Fig. 5.6a, b). Structurally, the lithological layering in all units is isoclinally folded and a steep, NW-SE trending foliation is developed, which is defined by mm- to cm-thick quartzofeldspathic layers in the gneisses (S_{melt} , SP1, Fig. 5.6a). In areas where S_{melt} is less dominant, structures analogous to Domain 2 in sections 1 and 2 are visible with an earlier, generally horizontally oriented foliation defined by biotite and thin quartzofeldspathic layers folded into upright open to isoclinal folds (Fig. 5.6c). A pronounced stretching lineation is present on S_{melt} . This lineation plunges 10-45° towards the SE in the northeastern part of the transect and 10-60° towards the NW ~1 km away from the amphibolite contact. Fold axes of intrafolial and isoclinal to open folds in all units are parallel to this stretching lineation (SP2, Fig. 5.6a). On outcrop planes ~parallel to the SE-plunging stretching lineation and perpendicular to the foliation, ductile S-C' fabrics and semi-ductile shear bands are visible which show a dextral sense of movement (Fig. 5.6d). This indicates that on a horizontal plane, the movement had a dextral and SW-side-up component.

Contact to amphibolites

The contact between the gneisses and the amphibolites at the south-western end of the Nunatak transect is sharp and nearly vertical (Fig. 5.6f). A ~1m wide mylonite zone occurs between the amphibolites and the gneisses, where the grain size of both rock types is considerably reduced. Sigma- and delta-clasts observed on vertical planes point to a N-side up sense of movement - however, since these observations were made on planes not parallel to the NW-dipping lineation their significance is uncertain. No shear sense indicators were observed parallel to the NW-dipping lineation due to the lack of correspondingly oriented outcrop planes. However, since the area is located between the dextral Fairweather and the dextral Border Range fault zones, and dextral movement has been observed in the area where the lineation is SW-plunging, the assumption that the movement parallel to this NW-plunging stretching lineation is dextral is reasonable. In this case, the movement on a horizontal plane would have a dextral and NE-side-up component. The SE-plunging stretching lineation farther to the northeast and the NW-plunging lineation farther to the southwest, together with the dextral shear senses point to oblique extrusion of the central zone of the gneisses in a very narrow corridor.

Amphibolites

Although the recent field studies did not extend far into the amphibolites, one of us (Pavlis) conducted field studies in these rocks during the 1990's and part of that effort was summarized by Sisson et al. (2003). Those studies indicated that the structural sequence recognized in the southwestern part of the gneiss extends through the entire zone of amphibolites. That is, a prominent NW plunging mineral lineation is developed on a steeply dipping foliation that is axial planar to isoclinal folds in layering. The origin of the layering in the amphibolites is uncertain, but includes calcsilicate rich bands that are presumably a primary layering; either compositional variations in pillow lavas or entrained sedimentary materials within a submarine volcanic complex. Shear bands are visible locally within these amphibolites on planes parallel to lineation and perpendicular to foliation and consistently show dextral, east-side up, oblique shear. Metamorphic grade also is variable across the amphibolites from epidote-amphibolites to the southwest to amphibolites near the contact with the gneisses.

Brittle faults

On horizontal outcrop planes in the gneisses, steep, brittle dextral faults striking WNW-ESE displace the main foliation with mm- to m-scale offsets (Fig. 5.6e, SP1, red line, Fig. 5.6a). The location of the lithologic boundary between amphibolites and gneisses mapped on both sides of the East Nunatak glacier suggest that there is a similar oriented fault with an apparent offset of ~1.5 km located below this glacier (Fig. 5.2d). This orientation is not a typical Riedel orientation for the dextral Fairweather and Border Range fault zones and the formation of this brittle fault is therefore probably unrelated to the bigger bounding fault zones. Late, muscovite-bearing shear zones and brittle faults which are parallel to the foliation occur all over the Nunatak transect (thin red lines in profile of Fig. 5.6a) and form steep gullies where the rocks weather easily. No shear senses or striae were observed on these shear zones/faults.

5.4.4 Structural summary and relationship with metamorphic grade

A summary of our structural observations is presented in Fig. 5.7 as a tectonic sequence diagram (after Forster & Lister, 2008) where the different observations from each transect are correlated (a) with each other, (b) with the mineral growth events observed in the rocks (Bruand, 2010) and (c) with the deformational sequence observed by Pavlis & Sisson (1995, 2003) in the western and northern part of the complex (Fig. 5.2a). A schematic 3D-sketch of the complex is displayed in Fig. 5.8. Our results together with the observations of Pavlis & Sisson (1995, 2003) and the petrological evolution as described by Bruand (2010) reveal the following structural and metamorphic evolution in the CMC.

Transect		Tectonic sequence					Time
Phyllite Z.	Bremner	S _{sed}	F _{tight-isoclinal} / S _{ps} N-vergent S-dipping E-W fa		Δ bi+chl		
	Tokio	S _{sed}	F _{tight-isoclinal} / S _{ps} N-vergent S-dipping E-W fa				HAF
Schist Z.	Bremner	S _{sed}	F _{isoclinal} / S _{bt} / L _{str} recumbent horizontal EW E-W fa		F _{open} / S _{cr} upright vertical E-W fa	SZ vertical dextral	HAF
	Tokio N	S _{sed}	F _{tight-isoclinal} / S _{ps} N-vergent S-dipping E-W fold axes		Δ And		
	Tokio S	S _{sed}	F _{tight-isoclinal} / S _{ps}		F _{isoclinal} / S _{bt} / L _{str} recumbent horizontal EW E-W fa		
Gneiss Z.	Bremner Fan	S _{sed} (highly boud.)	S _{bt} / L _{str} horizontal EW		F _{isoclinal} / S _{melt} / L _{str} upright vertical EW E-W fa	SZ vertical dextral	
	Tana Bagley	S _{sed} (highly boud.)	S _{bt} / L _{str} horizontal EW		F _{isoclinal} / S _{melt} / L _{str} upright steep N or S dipping E-W fa	SZ N-dipping dextral +N-side up	Δ Ms+Chl
	Nunatak	S _{sed} (highly boud.)	S _{bt} / L _{str} horizontal NW-SE		F _{isoclinal} / S _{melt} / L _{str} upright vertical NW-SE NW-SE fa	SZ vertical dextral	HAF HAF dextral Δ Ms+Chl
			D1 of Pavlis&Sisson (1995, 2003)	D2 of Pavlis&Sisson (1995, 2003)	D3 of Pavlis&Sisson (1995, 2003)		
Metabasalt Z.	Tana	S _{sed}	F _{tight-isoclinal} / S _{ps} S-vergent N-dipping E-W fold axes				
	Bagley	S _{sed}	F _{tight-isoclinal} / S _{ps} S-vergent N-dipping E-W fold axes		S _Z dextral +N-side up		
	St.Elias Ridge	S _{sed}	F _{tight-isoclinal} / S _{ps} S-vergent N-dipping E-W fold axes				HAF

Figure 5.7: Tectonic sequence diagrams after Forster & Lister (2008). The different fabrics observed in each zone on each transect are correlated with each other, with the mineral growth events observed in the rocks and with the structural scheme described by Pavlis & Sisson (1995, 2003). F denotes observed folding phase, with the corresponding geometrical description in subscript (shape of folds, fold vergence, orientation of fold-axes (fa)). S denotes observed planar fabric, with the following subscripts: sed=sedimentary bedding, PS=pressure solution, bt=defined by biotite, cr=crenulation, melt=defined by leucosomes. In addition, the orientation of the planar fabric is given (horizontal vs. vertical). L denotes observed lineation, with str=stretching lineation and the orientation of the lineation indicated. SZ denotes observed shear zone, with orientation and shear sense indicated. HAF denotes high-angle (close to vertical) brittle faults. Slashes between fabric elements indicate that they probably formed simultaneously. Grey bars indicate mineral growth and partial melting events relative to the fabric development.

D₁ In the phyllite zone of sections 1-2 and the northern schist zone of section 2, tight to isoclinal folds with E-W trending fold axes are present, accompanied by an axial planar pressure solution foliation (D₁ after Pavlis & Sisson, 1995, 2003). Since this fabric is the first which developed in the metasedimentary rocks, it is probably related to the accretion of the sediments. However, it is interesting to note that in sections 1 and 2, these early folds are asymmetric to the north, and the corresponding axial planar foliation is south-dipping, contrary to D₁ structures related to accretion described farther west in the area of Prince William Sound which are generally north-dipping and asymmetric to the south (e.g. Plafker et al., 1994). Biotite is growing in the phyllite zone of section 1, whereas only chlorite is present in the southern phyllite zone of section 1 and the entire phyllite zone of section 2. Peak metamorphic conditions reached during that stage in the phyllites are ~400-550°C and ~2-3 kbar in the north and ~400-450°C in the south (Fig. 5.2b and c; Sisson et al., 1989; Bruand, 2010).

D₂ In the southern schist zone of section 2, in the entire schist zone of section 1 and in the entire gneiss zone of all sections an originally flat-lying penetrative foliation defined by biotite ± sillimanite is developed, which dips below the D₁ fabric domain in the northern schist zone and the phyllites of sections 1 and 2 (D₂ after Pavlis & Sisson, 1995, 2003). This fabric is axial planar to isoclinal folds with E-W fold axes, which are parallel to a pronounced E-W subhorizontal stretching lineation. Finite strain analyses of Pavlis & Sisson (1995, 2003) indicate that this D₂-fabric records margin-parallel stretching accompanied by vertical flattening which affected the lower part of the accretionary prism. Besides this well defined pure-shear component the amount of simple shear involved in the formation of the D₂-fabric is not well constrained. Sparse observations of top-to-the-east shear sense perpendicular to the S₂-planes and parallel to the E-W lineation (Pavlis & Sisson, 1995, 2003, and this study) may point to an unknown amount of simple shear deformation during the D₂ deformation. The D₂ fabric development is clearly contemporaneous with biotite, sillimanite and garnet growth in the schist zone and with the onset of partial melting in the gneiss zone. The andalusite crystals observed in the northern schist zone of section 2 occur just above the D₂ fabric front and we interpret this andalusite growth as contemporaneous with the bi±sill±gr growth in the D₂ fabric domain (Fig. 5.7). Peak metamorphic conditions were reached in the schist zone contemporaneous with D₂ and are ~600-650°C and ~5-7 kbar (Figs. 5.2c and d; Bruand, 2010).

D₃ Both the schist and the gneiss zones are overprinted by variably open to isoclinal upright folds with steeply dipping axial planes and E-W fold axes (D₃ after Pavlis & Sisson, 1995, 2003). In the schist zone, a steeply dipping, spaced crenulation cleavage is developed axial planar to the folds and often steep brittle fault zones are developed in the core of these folds. In the schist zone, the D₃ deformation probably set in at or shortly after the metamorphic peak (Fig. 5.7). In the gneiss zone, the D₃ deformation is developed strongly domainal, with domains of low, intermediate and high D₃ strain. In the intermediate and high D₃ strain

domains, a new axial planar foliation to the upright folds is developed, defined by biotite, sillimanite and leucosome layers, indicating that partial melting and metamorphic mineral growth was ongoing during D₃ in the gneiss zone. This newly formed steep foliation defines a large-scale foliation fan in the entire gneiss zone (Fig. 5.8). In the northern gneiss zone the ductile stretching lineation associated with this D₃ fabric is oriented subhorizontal and E-W, whereas in the southern gneiss zone the ductile stretching lineation on the D₃ foliation is plunging steeply to the west-north-west (Fig. 5.3). Finite strain measurements of Pavlis & Sisson (1995, 2003) revealed a horizontal shortening component during D₃-fabric formation. Their observations as well as ours show that dextral shear bands developed simultaneous to and overprinting the D₃ foliation pointing to an important dextral component of simple shear during the D₃ deformation, indicating that D₃ was a dextral transpressive event (Fig. 5.7). The gneiss zone probably reached its metamorphic peak mainly during this D₃ deformation, and experienced temperatures of ~650-700°C and 4-9 kbar in sections 1 and 3 and ~650-700°C and ~8-13 kbar in section 2 (Figs. 5.2b, c and d Bruand, 2010).

Post-metamorphic shear zones and brittle faults in the south of the complex The southern border of the CMC west of the U.S. Canadian Border is made up of a series of ductile to brittle post-metamorphic fault zones which juxtapose high-grade gneisses in the north against low-grade phyllites in the south (Fig. 5.2a, 5.3). The southern schist zone as proposed by Hudson & Plafker (1982) between the gneisses and the phyllites probably has been cut out by these faults and shear zones. Muscovite and chlorite-coated stretching lineations in these shear zones plunge to the west-northwest and shear sense indicators reveal north-side-up and dextral sense of movement along these faults. The presence of these shear zones and faults in the south of the complex, together with the concentration of high D₃ strain domains with down-dip lineations along the southern border produce a highly asymmetric final shape of the complex, with a wide transition from phyllites to gneisses in the north and an abrupt juxtaposition of gneisses against lower-grade phyllites in the south (Fig. 5.8).

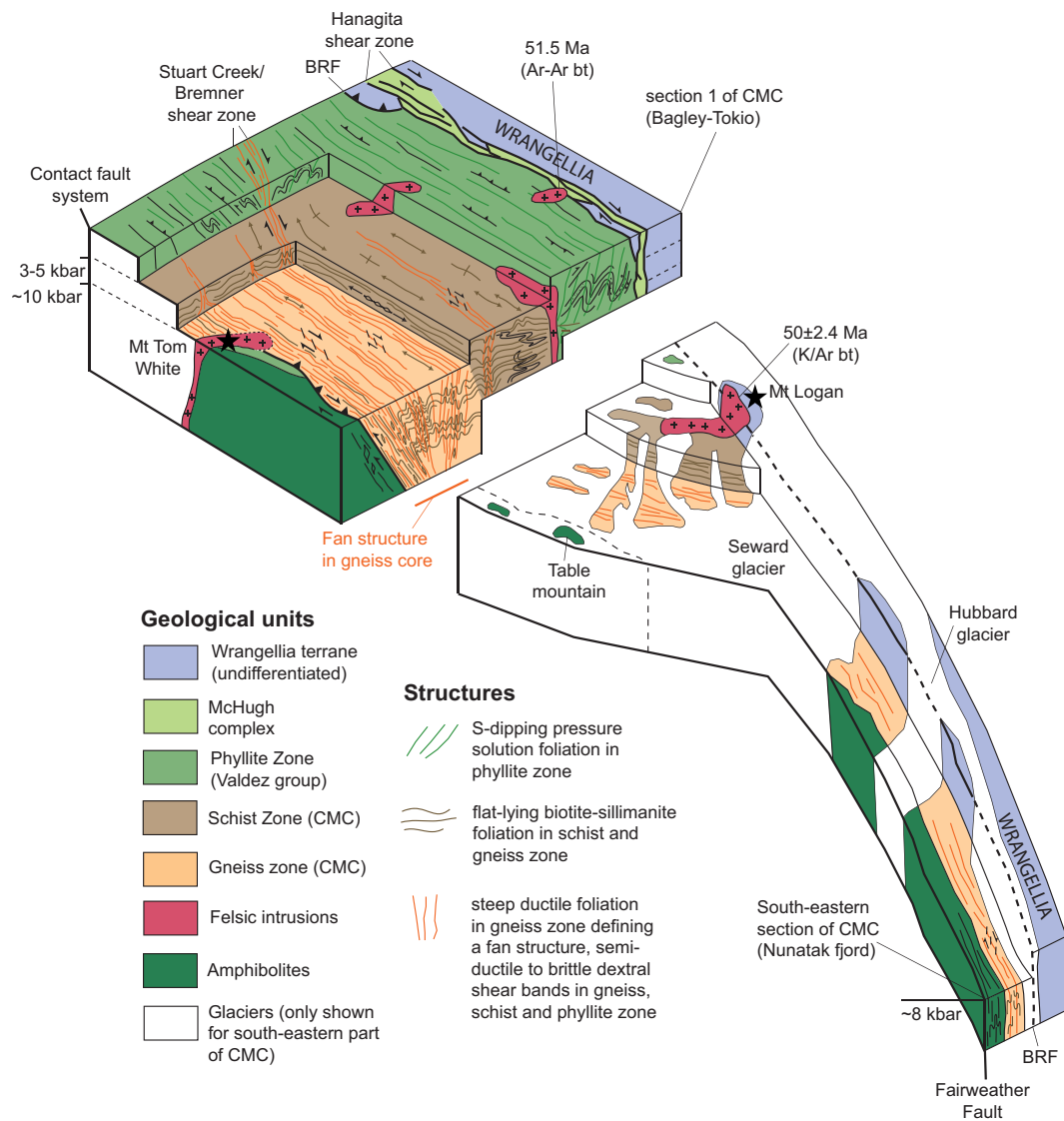


Figure 5.8: Schematic 3D-Sketch of the Chugach Metamorphic Complex with the dominant fabrics indicated. The CMC has a pronounced asymmetric shape with a wide transition from phyllite to gneiss in the north and an abrupt juxtaposition of gneiss against phyllites and metabasalts in the south. Two K/Ar biotite ages from two plutons intruding the Border Range Fault System to the north of the complex are given (from Roeske et al., 2003; Bradley et al., 1993) which indicate that fault activity along these particular fault strands must have occurred before ~52-50 Ma.

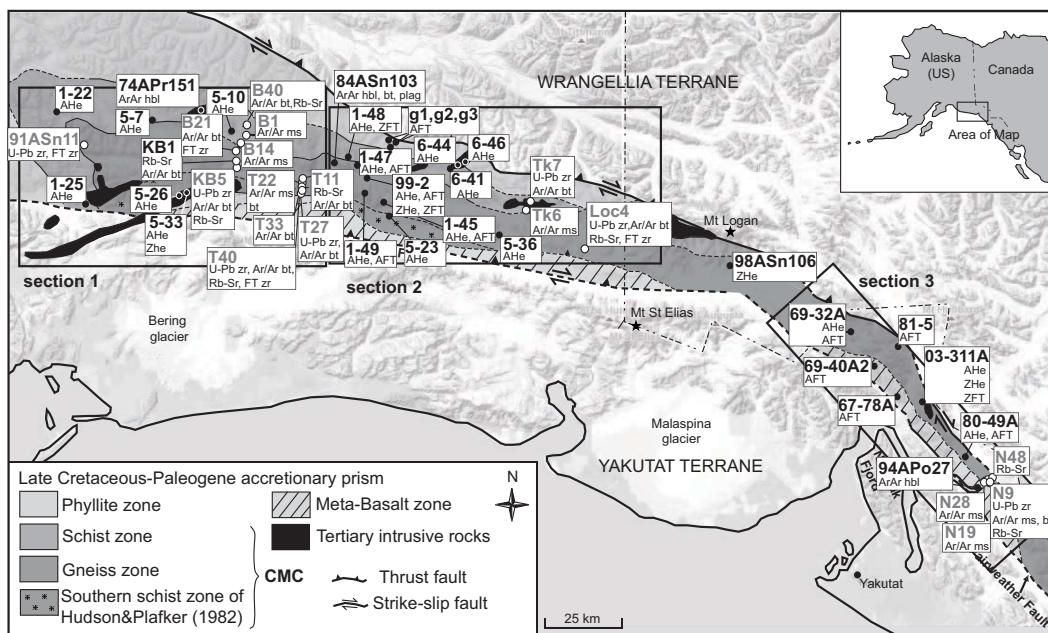


Figure 5.9: Geological map of the CMC with all localities of samples used for thermochronology. Black spots indicate samples from the literature (Tab. 5.2), white spots and grey sample numbers indicate new ages presented in this study or in Chap. 4 (Tab. 5.1). Note that the definitions of sections 1-3 are enlarged compared to Fig. 5.2.

5.5 Thermochronology

The CMC experienced peak metamorphic temperatures of $\sim 600\text{-}700^\circ\text{C}$ at depths of $\sim 10\text{-}20$ km in the schist zone and $\sim 20\text{-}50$ km in the gneiss zone (Bruand, 2010). The timing of this peak metamorphic conditions is revealed by U-Pb dating of metamorphic zircon overgrowths in the gneisses, interpreted to have grown during partial melting in the rocks, which give an age of $\sim 55\text{-}51$ Ma for the peak metamorphism (Tab. 5.1, Chap. 4). Most information on the timing of exhumation and cooling of the complex comes from low-T thermochronological studies aimed at the Neogene history (e.g. Berger et al., 2008; Enkelmann et al., 2008, 2010) with little data on the high-T cooling history of the western (Onstott et al., 1989; Sisson et al., 1989) and south-eastern parts of the complex (Hudson et al., 1977a,b; Sisson et al., 2003). Regional K/Ar data (Hudson et al., 1977a,b) hint at potential variations in the timing of exhumation along- and across-strike with considerably younger K/Ar ages towards the southeast. Thus, to constrain the cooling and exhumation history of the metamorphic complex in time, we used $^{40}\text{Ar}/^{39}\text{Ar}$ dating on muscovite and biotite, Rb/Sr dating on biotite and whole rock and Fission track dating on zircon to samples from sections 1-3 of the metamorphic complex. In addition, we assembled previously obtained $^{40}\text{Ar}/^{39}\text{Ar}$ and low-temperature geochronology available for the same region from the literature.

Table 5.1: Summary of all samples used for geochronology

Nr.	Sect.	Latitude (°N)	Longitude (°W)	Rock type	Mineralogy +Qtz+Plag+Bt	PT conditions	U/Pb zrn (Ma, $\pm 2\sigma$)	$^{40}\text{Ar}/^{39}\text{Ar}$ ms (Ma, $\pm 2\sigma$)	$^{40}\text{Ar}/^{39}\text{Ar}$ bs (Ma, $\pm 2\sigma$)	Rb/Sr (Ma, $\pm 2\sigma$)	FT zrn (Ma, $\pm 2\sigma$)
91Asm11	1	60.8236	144.2500	gneiss	Grt	650 \pm 30°C ^a	52.8 \pm 1.0				30.9 \pm 8.6
B40	1	60.8883	143.2384	schist	Grt-Sil-Ms	*597 \pm 30°C ^b			47.6 \pm 2.3	50.3 \pm 0.5	
B21	1	60.8124	143.3148	gneiss	Ms	-			48.4 \pm 2.1		28.1 \pm 2.8
KB1	1	60.7643	143.2881	gneiss	Ms-Grt-Sil	*666 \pm 30 °C ^a , 5.1 \pm 1.6 kbar ^c			50.0 \pm 2.2	49.9 \pm 0.5	
KB5	1	60.7381	143.3015	gneiss	Ms	>640 °C ^b	54.0 \pm 0.8		47.3 \pm 2.1	48.6 \pm 0.5	
B1	1	60.8496	143.2388	dike	Qtz-Plag-Ms	-		45.8 \pm 2.1			
B14	1	60.8233	143.2777	intrusion	Qtz-Plag-Ms	-		53.4 \pm 2.9			
T27	1	60.7146	142.9147	gneiss	Ms-Grt	~710-720°C/-8-9 kbar ^d	52.6 \pm 0.8		49.2 \pm 2.5		
T22	1	60.7108	142.9036	gneiss	Ms-Grt	-		46.2 \pm 2.3	47.3 \pm 2.0		
T11	1	60.7013	142.9004	gneiss	Ms-Grt	-			47.5 \pm 2.3	49.4 \pm 0.5	
T33	1	60.6856	142.9034	fault rock	Ms-Sil	-			46.9 \pm 2.1		
T40	1	60.6828	142.9238	gneiss	Ms	*679 \pm 30 °C ^a			47.0 \pm 2.0	48.5 \pm 0.5	28.9 \pm 2.4
Tk6	2	60.6642	141.5488	schist	Sil(And)-Ms	*658 \pm 33 °C/6.4 \pm 1.4 kbar ^c	54.0 \pm 0.9	49.0 \pm 2.8			
Tk7	2	60.6671	141.5521	intrusion	Ms	-			49.1 \pm 2.8		
Loc4	2	60.5544	141.3030	gneiss	Grt-Sil-Ms	666 \pm 25 °C/8.2 \pm 1.2 kbar ^c	54.0 \pm 0.8		47.4 \pm 2.1	48.9 \pm 0.5	26.0 \pm 2.8
N9	3	59.8223	138.8313	gneiss	Ms	*>640 °C ^b	53.0 \pm 0.7		15.8 \pm 0.8	14.9 \pm 0.2	
N28	3	59.8151	138.8827	mylonite	Ms-Grt-Sil	*644 \pm 29 °C/8.2 \pm 1.0 kbar ^c	51.3 \pm 0.7	22.6 \pm 1.1			
N48	3	59.8210	138.8783	gneiss	Ms-Grt-Sil	~680°C/~10 kbar ^d		20.0 \pm 1.0			
N19	3	59.8330	138.8314	pegmatite	Qtz-Plag-Ms	-		36.2 \pm 2.2		14.9 \pm 0.2	

PT conditions are from Bruand (2010). U-Pb zircon ages are from Chapter 4. ^aBiotite-Garnet thermometry, ^bGraphite thermometry, ^cAverage PT calculation (Thermocalc), ^dPseudosection estimate (Thermocalc), ^eerror plateau age (see text), *PT information is not from sample itself, but from other sample from the same outcrop.

5.5.1 $^{40}\text{Ar}/^{39}\text{Ar}$ dating of muscovite and biotite

Sample description

Seven muscovite-bearing samples and twelve biotite-bearing samples were selected for $^{40}\text{Ar}/^{39}\text{Ar}$ furnace step heating analyses. The sample locations are displayed on Figures 5.2 and 5.9. Sample coordinates, rock type, mineralogy, *PT* conditions and $^{40}\text{Ar}/^{39}\text{Ar}$ ages are summarized in Table 5.1. Three of the seven muscovite samples come from undeformed igneous rocks (B1, B14 and B19). B1 is derived from an up to ~5 m thick felsic dike intruding the schist zone in the Bremner transect (Fig. 5.2). It is oriented parallel to S_{bt} , but is internally not deformed. B14 is from a several 100 meters wide felsic intrusion in the northern gneiss zone of the Bremner transect (Fig. 5.2). B19 is from a ~20 cm wide cross-cutting pegmatitic dike exposed in the Nunatak transect (Fig. 5.2). In all three igneous samples, coarse muscovite occurs randomly oriented in the matrix and is interpreted to have formed during crystallization of the igneous rocks. One muscovite sample was collected from the schist zone in the Tokio transect and is exposed close to a major intrusion (Tk6, Fig. 5.2c). This sample is affected by contact metamorphism and the development of its muscovite flakes is contemporary to the intrusion: coarse muscovite and fine-grained sillimanite statically replace andalusite crystals and grew at the thermal peak in this sample (Bruand, 2010). The other three muscovite samples (T22, N9, N28) were collected from the gneiss zone in the Tana and Nunatak transects (Fig. 5.2). In all three samples, muscovite is aligned parallel to S_{melt} and probably grew before or at the metamorphic peak.

One of the 12 biotite-bearing samples was collected from the schist zone of the Bremner transect (B40, Fig. 5.2b). In this sample, fine-grained biotite, containing many opaque inclusions, defines S_{bt} . Another biotite-bearing sample was collected from the large intrusion exposed at the southern end of the Tokio transect (Tk7, Fig. 5.2c). In this sample, coarse biotite is randomly oriented in the matrix. The remaining 10 biotite-bearing samples are all from gneisses distributed through the gneiss zone of the CMC (Fig. 5.2, Fig. 5.9). In all of these gneiss samples, biotite mainly defines S_{bt} . In some cases, newly grown biotite also occurs parallel to S_{melt} . All biotites have a relatively constant composition of ~50-60% annite and ~40-50% phlogopite (Bruand, 2010).

Age results

The sample preparation process and the analytical technique is described in Appendix A, detailed isotopic measurements can be found in Tables 5.3 and 5.4, and the results of the step heating experiments are displayed as age spectra on Figures 5.10 and 5.11. Weighted plateau or error plateau ages (Appendix A, Koppers, 2002), the total fusion, normal and inverse isochron ages are given in each diagram. Errors are quoted at 2 sigma.

For the muscovite samples, weighted plateau ages consisting of subsequent degassing steps comprising >50% of the total gas could be calculated for samples B14 and N28 (Fig. 5.10). For sample B1 a weighted plateau age could be calculated after excluding 1 step which had a very high analytical error. Sample T22 gave a more discordant age spectra for which we calculated a weighted mean age after excluding 3 intermediate steps. The other three samples Tk6, N9 and N19 did not yield statistically significant weighted plateau ages, and error plateau ages are reported (calculated using Koppers, 2002). Muscovite ages from sections 1 and 2 of the CMC range from 53.4 ± 2.9 Ma to 45.8 ± 2.1 Ma ($\pm 2\sigma$), but only one sample (B41) is older than ca. 50 Ma, with the remaining samples giving ages less than ca. 49 Ma (Tab. 5.1, Fig. 5.10). Muscovite samples from section 3, however, give significantly younger ages ranging from 36.2 ± 2.2 Ma to 20.0 ± 1.0 Ma (Tab. 5.1, Fig. 5.10).

For the biotite samples, weighted plateau ages consisting of subsequent degassing steps comprising >50% of the total gas could be calculated for samples KB1a, KB5, T40 and N9 (Fig. 5.11). Weighted plateau ages could be calculated for samples B21, T22, T33 and Loc 4 after excluding 1-2 intermediate steps (Fig. 5.11). No statistically meaningful weighted plateau ages could be calculated for samples B40, T11, T27, and Tk7 and error plateau ages are reported (Fig. 5.11). Biotite ages from sections 1 and 2 of the CMC range from 50.0 ± 2.2 Ma to 46.9 ± 2.1 Ma, which is within error of the ages from the muscovites for those regions (Tab. 5.1, Fig. 5.11). The only biotite age from section 3 is much younger with 15.8 ± 0.8 Ma, which is younger than the youngest muscovite age from this region.

5.5.2 Rb/Sr isochron dating

To further evaluate the validity of the $^{40}\text{Ar}/^{39}\text{Ar}$ weighted plateau and error plateau ages as cooling ages, we also dated 7 of the 12 biotite separates used for $^{40}\text{Ar}/^{39}\text{Ar}$ dating and one additional biotite sample from section 3 by the Rb/Sr method, based on two point isochrons derived from biotite and whole rock measurements, respectively. The analytical technique is described in Appendix B, detailed isotopic measurements can be found in Table 5.5, the ages are reported in Table 5.1 and the isochron plots are displayed in Fig. 5.12. Errors are quoted at $\pm 95\%$ confidence interval. The six Rb/Sr ages from sections 1 and 2 vary between 50.3 ± 0.5 Ma and 48.5 ± 0.5 Ma, whereas the two Rb/Sr ages from section 3 are both 14.9 ± 0.2 Ma (Tab. 5.1). All Rb/Sr ages lie within error of the $^{40}\text{Ar}/^{39}\text{Ar}$ ages of the biotites, independently of whether the plateau age was a weighted or an error plateau age (Tab. 5.1), indicating that the $^{40}\text{Ar}/^{39}\text{Ar}$ ages are meaningful and do not represent mixing of different gas reservoirs, inheritance, loss or excess of argon.

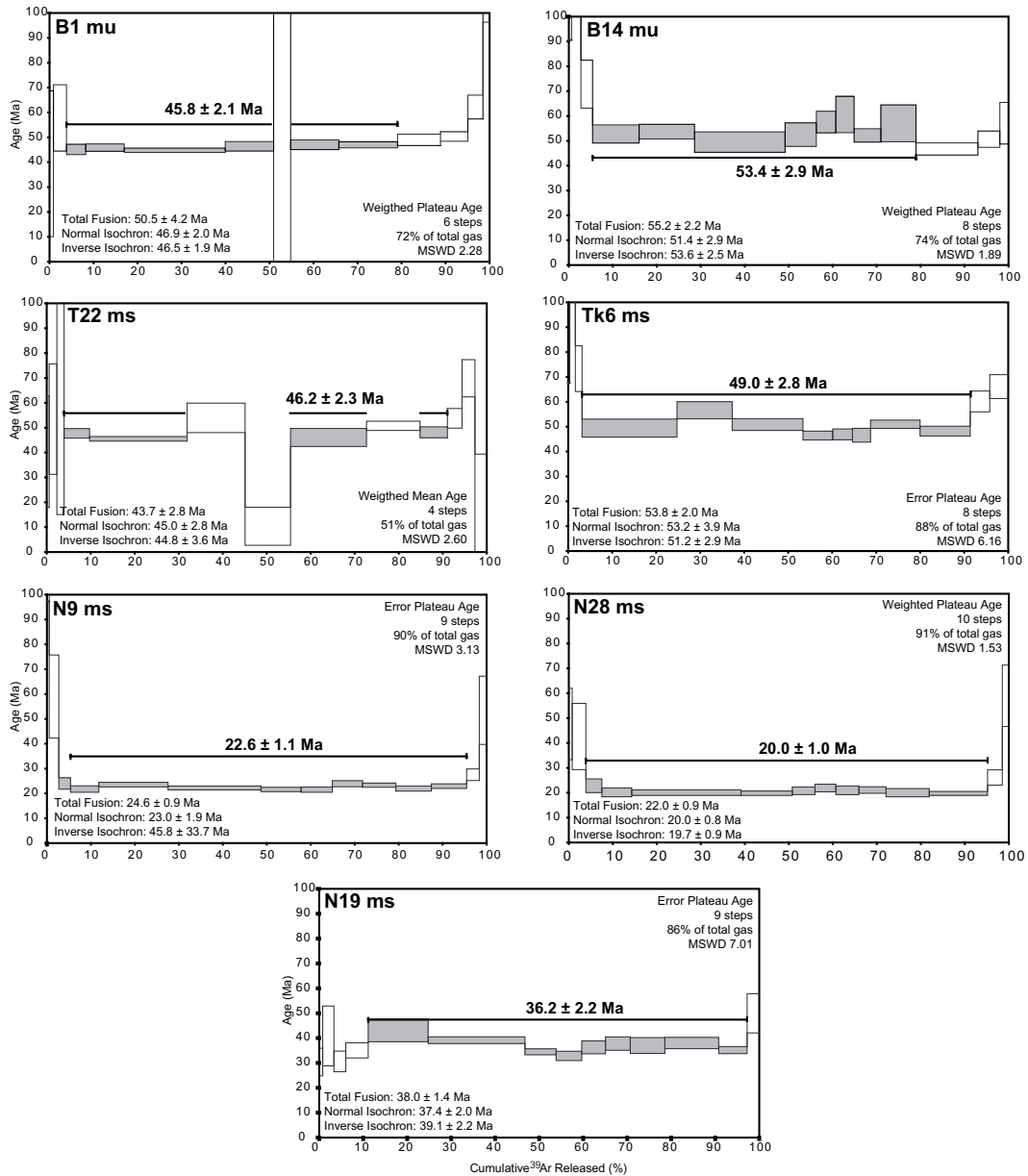


Figure 5.10: $^{40}\text{Ar}/^{39}\text{Ar}$ age spectra from furnace step heating experiments on seven muscovite samples. The bold ages are error-weighted plateau ages or error plateau ages including internal and external errors as described in Appendix A of this chapter. The grey steps are the ones which were included in the age calculation.

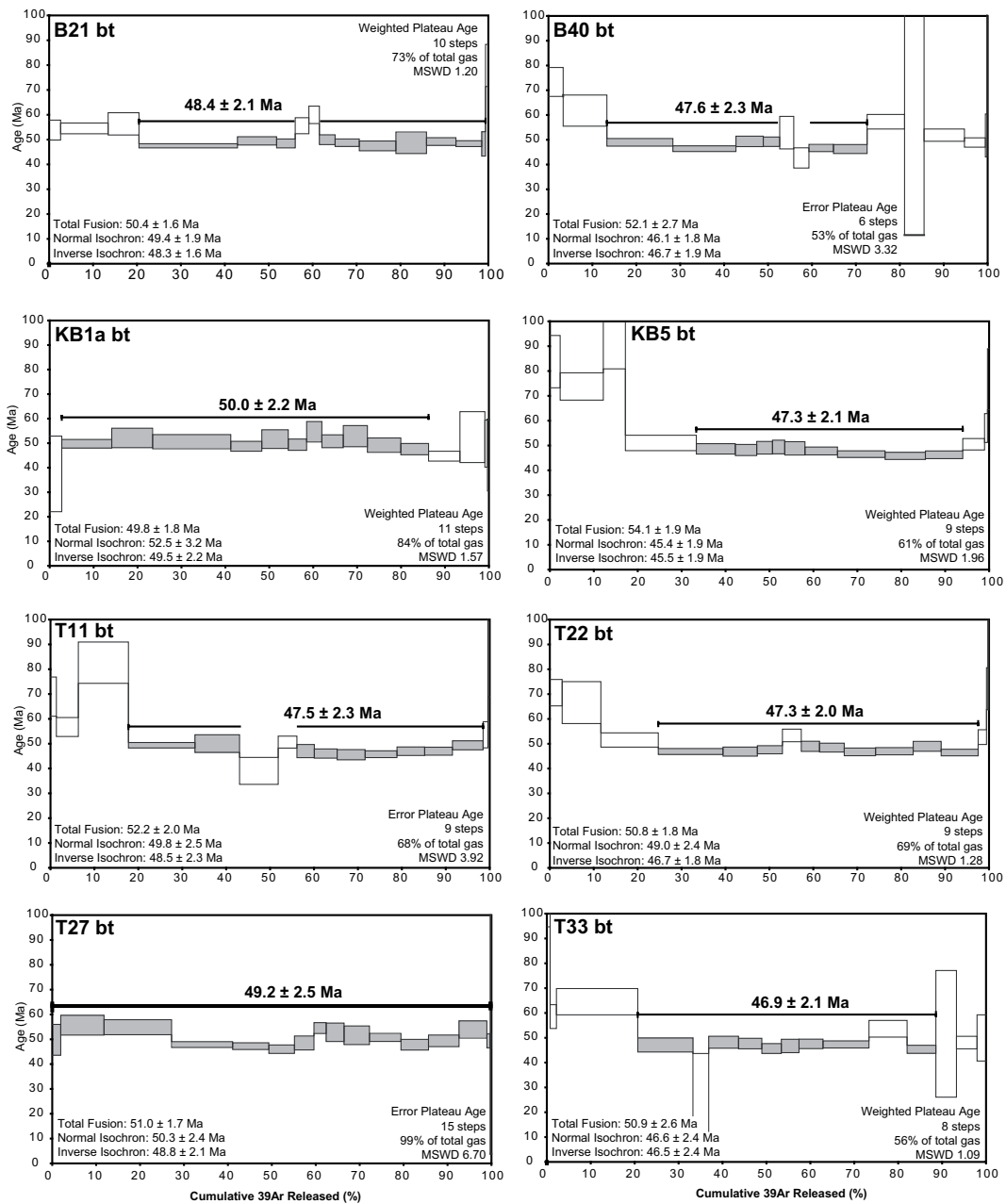


Figure 5.11: continues on following page

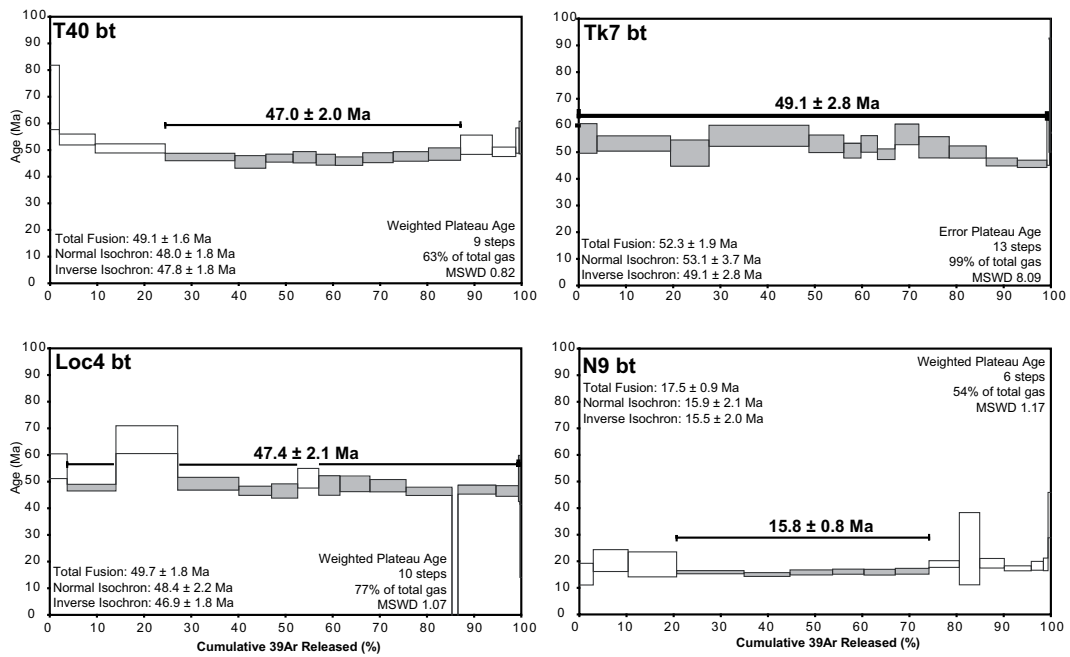


Figure 5.11: ⁴⁰Ar/³⁹Ar age spectra from furnace step heating experiments on twelve biotite samples. The bold ages are error-weighted plateau ages or error plateau ages including internal and external errors as described in Appendix A of this chapter. The grey steps are the ones which were included in the age calculation.

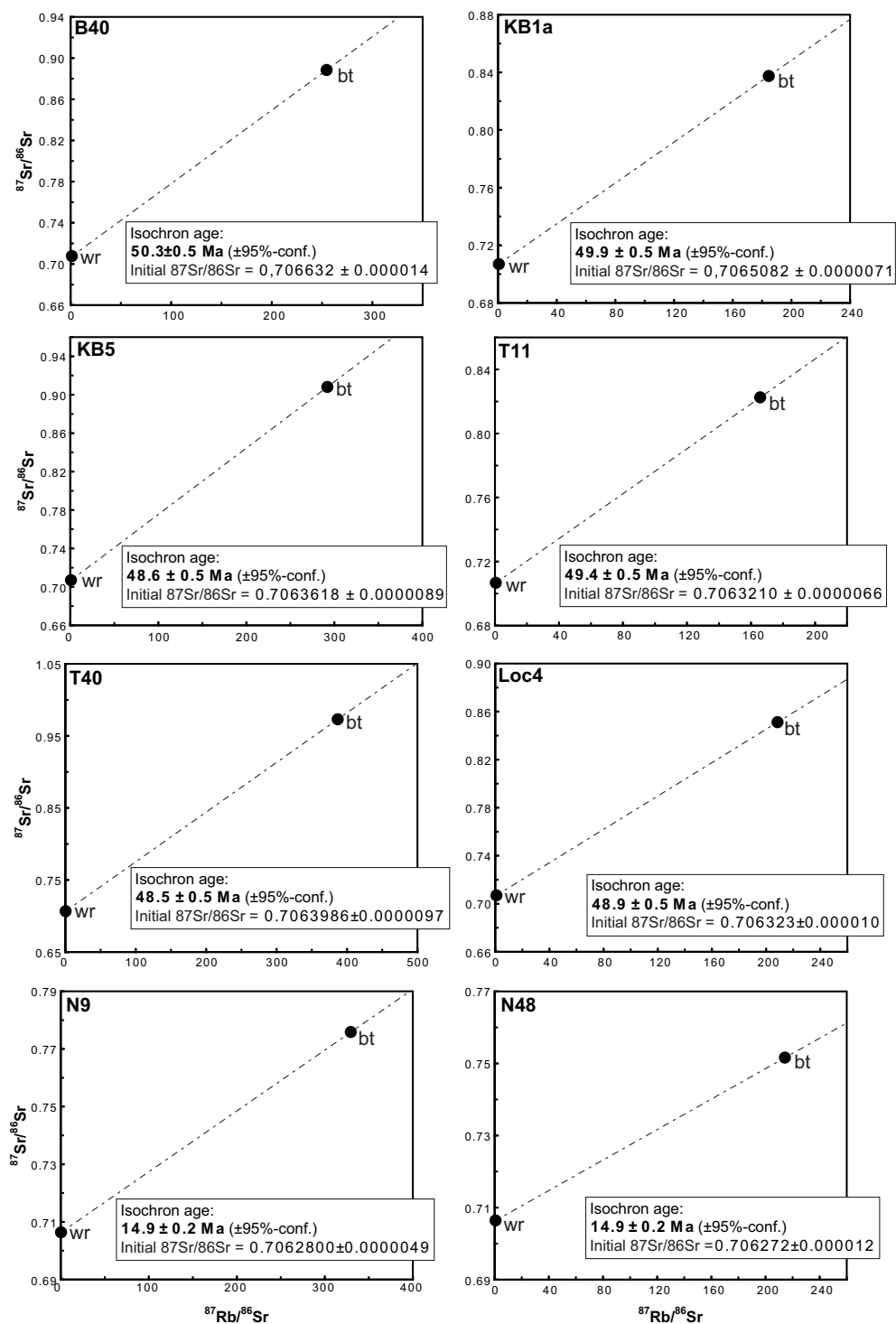


Figure 5.12: Rb-Sr isochrons for biotite (bt) and whole rock (wr) measurements. Isochrons were calculated using Isoplot/Ex (Ludwig, 2003). Analytical techniques are described in Appendix B of this chapter.

5.5.3 Fission track zircon dating

We analyzed four samples from sections 1 and 2 by the zircon fission track method in order to extrapolate between the U/Pb, $^{40}\text{Ar}/^{39}\text{Ar}$ and R/Sr systems and the published low-temperature thermochronology. The analytical technique is described in Appendix C. Ages are reported in Table 5.1, and detailed information is given in Table 5.6. Samples B21, T40 and Loc4 yielded 17-20 datable zircon grains. All three samples pass the χ^2 test, indicating that the grains belong to one single age population, and central ages for all three samples lie within error of each other (26.0 ± 2.8 - 28.9 ± 2.4 Ma; Tab. 5.1). Sample 91ASn11 yielded only two datable grains (36 ± 6 Ma and 24 ± 5 Ma) which fall well within the single grain age range of the three aforementioned samples.

5.5.4 $^{40}\text{Ar}/^{39}\text{Ar}$ and low-temperature geochronology: previous data

A compilation of published $^{40}\text{Ar}/^{39}\text{Ar}$ and low-temperature geochronology data for the three sections of the CMC is displayed in Figure 5.9 and listed separately in Table 5.2. Since the data come from throughout the CMC, we extended our definitions of sections 1-3 to include larger areas (Fig. 5.9).

$^{40}\text{Ar}/^{39}\text{Ar}$ dating Sisson et al. (1989) dated hornblende from the large pluton exposed just north-west of our Bremner transect (Fig. 5.2b) and hornblende, biotite and plagioclase from a tonalitic sill from their Tana transect (Fig. 5.2a) by the $^{40}\text{Ar}/^{39}\text{Ar}$ method (samples 74Apr151 and 84ASn103, Tab. 5.2, Fig. 5.9). Their ages correspond well with the ages we obtained for those regions (Tab. 5.1, Fig. 5.13). Sisson et al. (2003) dated hornblende from the amphibolites exposed at the south-western end of our Nunatak transect (sample 94Apo27), and the age is in agreement with our younger muscovite and biotite ages from this section (Tab. 5.1, Fig. 5.13). These young cooling ages confirm that the relatively young K-Ar ages reported by Hudson et al. (1977a,b) represent a first order, but relatively low-resolution, record of this Miocene medium to high-T cooling history of the Nunatak Fiord region.

Zircon fission track dating Two zircon fission track ages from bedrock samples are available for section 2 (Meigs et al., 2008), as well as a large dataset of detrital zircon fission track ages of modern river sands draining the western and central part of the CMC (Enkelmann et al., 2008, 2010). The two bedrock samples 99-2 and 1-48 come from the gneiss and schist zone, respectively (Fig. 5.9; Meigs et al., 2008). These were analysed using different mounts with different etching times, which allows the revelation of fission tracks in grains with variable radiation damage (e.g. Bernet & Garver, 2005). Both samples failed the χ^2 test, and peak fitting revealed two populations of 28.2 ± 8.2 Ma and 39.6 ± 6.8 Ma for

sample 99-2 and three populations of 30.7 ± 9.8 Ma, 57.5 ± 6.8 Ma and 122.6 ± 57.6 Ma for sample 1-48, respectively. These data indicate that probably different grain populations are present in these samples which reacted differently during metamorphism and cooling. Only the youngest populations are plotted for both samples on Figure 5.13. The zircon fission track ages of modern river sands from the western and central parts of the CMC show a maximum at ~ 20 -35 Ma, corresponding well with the ages derived from the two bedrock samples 99-2 and 1-48 (Enkelmann et al., 2008, 2010). One bedrock zircon fission track age is available for section 3, sample 03-311A (Fig. 5.9), which passes the χ^2 test and yields a well defined age of 4.5 ± 0.6 Ma based on 15 grains, which is considerably younger than the ages from sections 1 and 2 (Tab. 5.2; McAleer et al., 2009). River sand draining the Seward glacier area shows a very young fission track signal (< 3 Ma, with some ages < 1 Ma, Enkelmann et al., 2009). These young ages indicate that the rocks below that glacier only cooled recently below the zircon fission-track annealing temperature, which corresponds well with the young bedrock zircon fission track sample 03-311A from section 3 (Fig. 5.9, Tab. 5.2).

(U-Th)/He zircon/apatite and apatite fission track dating Four (U-Th)/He zircon ages, 12 apatite fission track ages and 19 (U-Th)/He apatite ages are available in the literature (Fig. 5.9, Fig. 5.13, Tab. 5.2; Spotila et al., 2004; Berger & Spotila, 2008; Berger et al., 2008a; McAleer et al., 2009; Enkelmann et al., 2010). Two main trends can be seen (Fig. 5.13). (1) In sections 1 and 2, the ages from all three systems decrease from north to south, with (U-Th)/He apatite ages as old as ~ 28 Ma in the northern phyllite zone, generally ~ 15 -5 Ma in the gneiss zone and as young as 1.7 Ma in the area around Mt Tom White (Figs. 5.2, 5.9, Tab. 5.2). (2) In section 3, a zone of very young ages (< 10 Ma for all three systems) occurs to the east-south-east from Seward glacier down to Nunatak fjord (Fig. 5.9, Fig. 5.13, Tab. 5.2).

Table 5.2: Summary of all $^{40}\text{Ar}/^{39}\text{Ar}$ and low-temperature geochronology from the literature used for Figure 5.13

Sample	Sect.	Location	Method	Age	$\pm 1\sigma$	Reference
5-10	1	Bremner	(U-Th)/He ap	22.8	1.8	Berger et al. 2008
05-7	1	Fan North	(U-Th)/He ap	25.1	0.87	Berger & Spotila 2008
01-22	1	Wernicke North	(U-Th)/He ap	18.9	1.2	Berger & Spotila 2008
01-25	1	Wernicke South	(U-Th)/He ap	10.7	1.31	Berger & Spotila 2008
5-26	1	Tom White pl	(U-Th)/He ap	2.3	0.16	Berger & Spotila 2008
5-33	1	Tom White pl	(U-Th)/He ap	1.7	0.1	Berger & Spotila 2008
5-33	1	Tom White pl	(U-Th)/He zr	8.8	0.3	Enkelmann et al. 2010
74Apr151	1	Bremner pluton	$^{40}\text{Ar}/^{39}\text{Ar}$ hbl	51.2	2.6	Sisson et al. 1989
5-23	2	Juniper Island	(U-Th)/He ap	6.86	1.26	Berger et al. 2008
5-36	2	BagleyS	(U-Th)/He ap	9.03	0.5	Berger et al. 2008
6-41	2	Granite Creek	(U-Th)/He ap	16.9	1.15	Berger et al. 2008
6-44	2	Granite Creek	(U-Th)/He ap	20.7	1.2	Berger et al. 2008
6-46	2	Granite Creek	(U-Th)/He ap	27.8	2.79	Berger et al. 2008
1-45	2	Tana East	(U-Th)/He ap	9.7	1	Spotila et al. 2004
1-49	2	Tana East	(U-Th)/He ap	13	1.3	Spotila et al. 2004
99-2	2	Tana East	(U-Th)/He ap	8.2	0.8	Spotila et al. 2004
01-48	2	Tana East	(U-Th)/He ap	16	1.6	Spotila et al. 2004
01-47	2	Tana East	(U-Th)/He ap	13.3	1.3	Spotila et al. 2004
99-2	2	Tana East	FT ap	13.8	1.4	Meigs et al. 2008
1-49	2	Tana East	FT ap	13.3	1.3	Meigs et al. 2008
1-45	2	Tana East	FT ap	14.5	1.3	Meigs et al. 2008
1-47	2	Tana East	FT ap	27.3	2.7	Meigs et al. 2008
g1	2	Goat Creek	FT ap	29	2.9	Berger et al. 2008
g2	2	Goat Creek	FT ap	30	3	Berger et al. 2008
g3	2	Goat Creek	FT ap	40	4	Berger et al. 2008
99-2	2	Tana East	(U-Th)/He zr	26	2.1	Spotila et al. 2004
99-2	2	Tana East	FT zr	28.2/39.6	4.1/3.4	Meigs et al. 2008
1-48	2	Tana East	FT zr	30.7/57.5/122.6	4.9/3.4/28.8	Meigs et al. 2008
84ASn103	2	Tana Sill	$^{40}\text{Ar}/^{39}\text{Ar}$ hbl	52.8	0.6	Sisson et al. 1989
84ASn103	2	Tana Sill	$^{40}\text{Ar}/^{39}\text{Ar}$ bi	50.1	0.5	Sisson et al. 1989
84ASn103	2	Tana Sill	$^{40}\text{Ar}/^{39}\text{Ar}$ plag	35.3	2.2	Sisson et al. 1989
69-32A	3	Nunatak NW	(U-Th)/He ap	1.9	0.14	McAleer et al. 2009
03-311A	3	Nunatak NW	(U-Th)/He ap	0.89	0.11	McAleer et al. 2009
80-49A	3	Nunatak	(U-Th)/He ap	1.13	0.08	McAleer et al. 2009
69-32A	3	Nunatak NW	FT ap	4.4	1	O'Sullivan et al. 1997
81-5	3	Nunatak NW	FT ap	3.4	1.3	O'Sullivan et al. 1997
69-40A2	3	Nunatak NW	FT ap	1.7	0.4	O'Sullivan et al. 1997
80-49A	3	Nunatak	FT ap	2.7	0.7	O'Sullivan et al. 1997
67-78A	3	Nunatak	FT ap	3.5	1.2	O'Sullivan et al. 1997
98ASn106	3	Seward glacier	(U-Th)/He zr	9.6	2	Enkelmann et al. 2010
03-311A	3	Nunatak NW	(U-Th)/He zr	1.96	0.09	McAleer et al. 2009
03-311A	3	Nunatak NW	FT zr	4.5	0.3	McAleer et al. 2009
94APo27	3	Nunatak	$^{40}\text{Ar}/^{39}\text{Ar}$ hbl	21.5	1.8	Sisson et al. 2003

5.6 Discussion

5.6.1 The cooling history of the Chugach Metamorphic Complex

Closure temperature estimates

The geochronological data presented above (Tab. 5.1, Fig. 5.9) allow constructing cooling paths for the different parts of the metamorphic complex (Fig. 5.13). The interpretation of $^{40}\text{Ar}/^{39}\text{Ar}$ and Rb/Sr ages in deformed metamorphic rocks in terms of cooling is not straightforward (e.g. Jenkin, 1997; Villa, 1998). The isotopic composition of the minerals used for dating may be controlled by two major mechanisms: (1) thermally activated diffusion, which allows isotopic exchange between the mineral and its surroundings above a certain temperature (called closure temperature, e.g. Dodson, 1973), and/or (2) recrystallization of the mineral due to deformation or fluid-rock interaction, which can change the isotopic composition of the mineral even when thermally activated diffusion is slow (e.g. Dunlap, 1997; Villa, 1998). The second case has been documented mainly in mylonitic samples, which deformed below the closure temperature of the system, or samples of low metamorphic grade (e.g. Dunlap, 1997; Foster et al., 1999; Mulch & Cosca, 2004). In our samples, thermally activated diffusion was clearly the main process controlling the isotopic systematics of the samples for two major reasons: 1) the muscovite and biotite ages obtained from undeformed intrusive rocks are indistinguishable from ages in the surrounding country rocks, and these igneous samples show no evidence of retrograde recrystallization or fluid-rock interactions, and 2) most of the samples were obtained from metamorphic rocks with high-grade fabrics which equilibrated at temperatures of $>600^\circ\text{C}$, far above the closure temperatures for muscovite or biotite, and which show no signs of later recrystallization or alteration due to fluid-flow (Tab. 5.1; see description in section 5.1).

The closure temperature of a particular radiogenic system represents the temperature at which diffusion of isotopes out of the crystal becomes insignificant. However, this isotopic closure depends not only on temperature, but also on cooling rate, grain size (i.e. effective diffusion length scales), pressure, and diffusion coefficients which depend on material properties such as mineral structure and chemistry (e.g. Dodson, 1973; Dahl, 1996; Jenkin, 1997; McDougall & Harrison, 1999; Harrison et al., 2009). Due to these different factors exact closure temperatures are difficult to determine and may vary over a considerable temperature range (e.g. McDougall & Harrison, 1999).

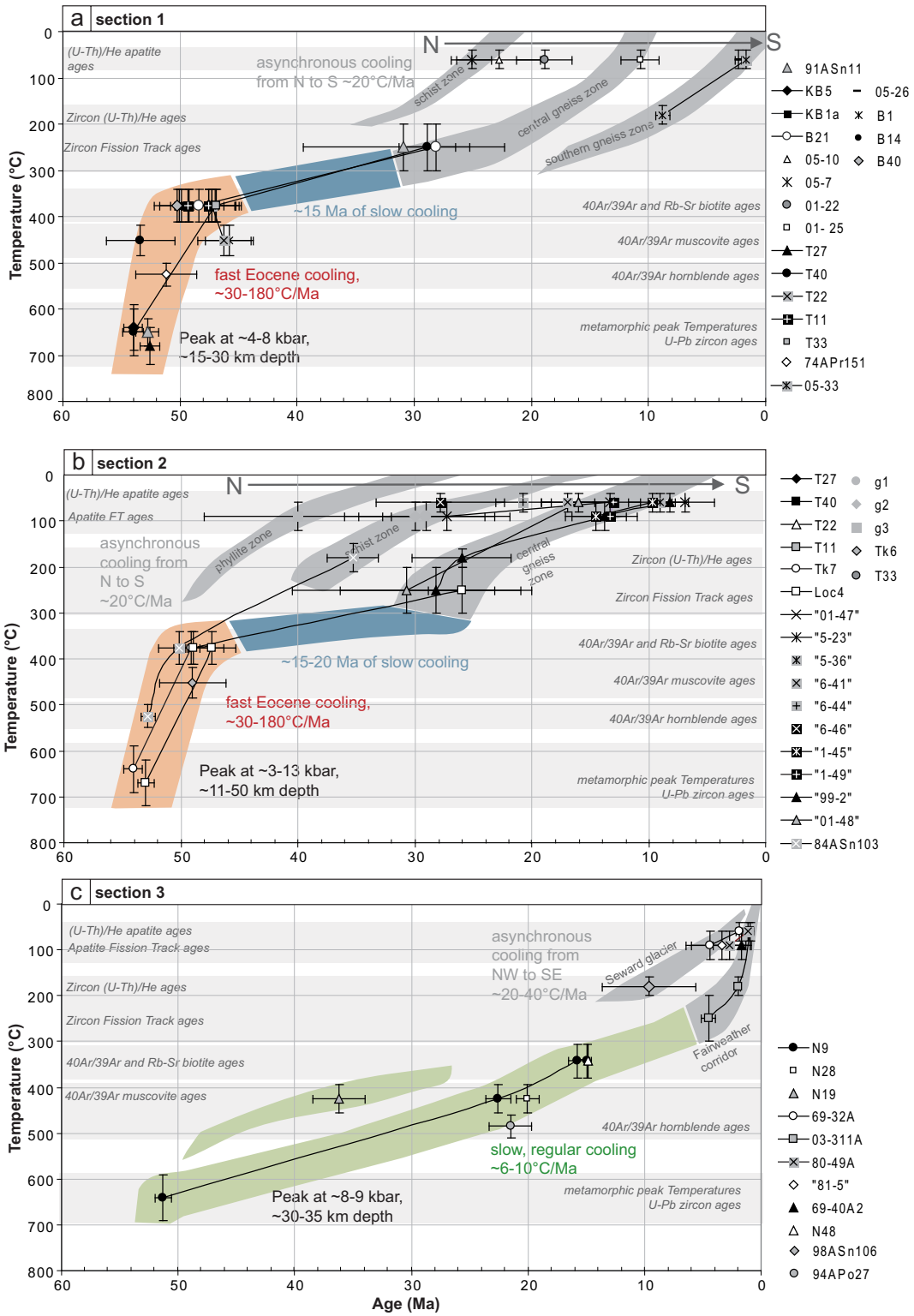
Harrison et al. (2009) conducted ^{40}Ar diffusion experiments on muscovite and calculated a closure temperature of 405°C for a $100\ \mu\text{m}$ grain cooling at $10^\circ\text{C}/\text{Ma}$ at 5 kbar (425°C at 10 kbar, with $E=64\ \text{kcal/mol}$ and $D_0=20\ \text{cm}^2/\text{s}$). Increasing the cooling rate to $100^\circ\text{C}/\text{Ma}$ at 5 kbar increases the closure temperature to 440°C . Increasing the grain size to $500\ \mu\text{m}$ increases the closure temperature to 455°C at $10^\circ\text{C}/\text{Ma}$ cooling rate and to 495°C at $100^\circ\text{C}/\text{Ma}$

at 5 kbar. In our samples, grain sizes for muscovite and biotites in the separates are ~100-500 μm , the maximum metamorphic pressures are ~5-10 kbar, and their chemistry are homogenous (Bruand, 2010). $^{40}\text{Ar}/^{39}\text{Ar}$ cooling ages from section 1 and 2 lie very close to the U/Pb ages for peak metamorphism, suggesting that the first-order cooling rate to mica closure was relatively high, on the order of ~50-100°C/Ma. In contrast, $^{40}\text{Ar}/^{39}\text{Ar}$ ages from section 3 are considerably younger than the peak metamorphic ages estimated from U/Pb methods, suggesting that the high-temperature cooling rate was slower, on the order of ~5-10°C/Ma. Thus, based on Harrison et al. (2009)'s experiments, we assume a closure temperature range for the muscovite samples of section 1 and 2 of 430°C (100 μm grain at 50°C/Ma and 5 kbar) to 495°C (500 μm grain at 100°C/Ma and 5 kbar), and for the samples of section 3 of 395°C (100 μm grain at 5°C/Ma and 5 kbar) to 455°C (500 μm grain at 10°C/Ma and 5 kbar).

For the closure temperature of $^{40}\text{Ar}/^{39}\text{Ar}$ in biotite, we use the equation of Dodson (1973) and the diffusion parameters given in McDougall & Harrison (1999) for biotites of similar composition (~Ann60, $E=47$ kcal/mol, $D_0=0.075$ cm^2/s , cylindrical geometry) to estimate the closure temperature for our samples. For the samples of section 1 and 2 we calculate a closure temperature range of 340°C (100 μm grain at 50°C/Ma) to 412°C (500 μm grain at 100°C/Ma). For the samples of section 3 we calculate a closure temperature range of 307°C (100 μm grain at 5°C/Ma) to 370°C (500 μm grain at 10°C/Ma). Since the Rb/Sr isochron ages lie within error of the $^{40}\text{Ar}/^{39}\text{Ar}$ biotite ages we assume a similar closure temperature range for this system.

For the closure temperatures of the two $^{40}\text{Ar}/^{39}\text{Ar}$ hornblende ages from the literature we assume ranges of 500-550°C for sections 1 and 2 (cooling rates of 50-100°C/Ma, grain size 40-80 μm) and 460-510°C for section 3 (cooling rates of 5-10°C/Ma, grain size 40-80 μm , McDougall & Harrison, 1999). For the only $^{40}\text{Ar}/^{39}\text{Ar}$ plagioclase age we assume a range of 150-210°C (Sisson et al., 1989). Closure temperatures for the low-temperature geochronological systems similarly depend on different factors and vary over certain ranges; we assume the generally accepted values of 200-300°C for zircon fission track ages (e.g. Wagner & Van Den Haute, 1992), 160-200°C for zircon (U-Th)/He ages (e.g. Reiners et al., 2003), 60-120°C for apatite fission track ages (e.g. Green et al., 1986; Carlson et al., 1999), and 40-80°C for apatite (U-Th)/He ages (e.g. Wolf et al., 1996) for all sections.

Figure 5.13 (following page): Cooling curves for the three different sections of the CMC (Fig. 5.9) as derived from the combination of different thermochronological methods. The sample localities are shown in Fig. 5.9. Orange indicates the rapid Eocene cooling phase which occurred in sections 1 and 2 directly after the metamorphic peak. Blue indicates the prolonged period (15-20 Ma) of slow/no cooling in the gneiss zone of sections 1 and 2 of the CMC. Green indicates the slow, regular cooling from peak conditions down to 200-300°C in section 3. Grey indicates cooling curves for the final cooling from 200-300° to surface-near temperatures in all sections. In sections 1 and 2, this grey cooling occurred asynchronous from north to south across the complex.



Cooling history of sections 1 and 2

Figs. 5.13a and 5.13b show the cooling curves for sections 1 and 2 of the CMC. U/Pb zircon ages (Tab. 5.1, Chap. 4) together with peak temperatures derived by classical thermometry for the dated samples (Fig. 5.2) define the starting point for the cooling history. $^{40}\text{Ar}/^{39}\text{Ar}$ hornblende, muscovite and biotite ages define a steep cooling curve right after the metamorphic peak in both sections (red part of cooling curve, Fig. 5.13a and b). During this phase, the rocks cooled from $\sim 650\text{--}700^\circ\text{C}$ at $\sim 55\text{--}52$ Ma to $\sim 350\text{--}400^\circ\text{C}$ at $\sim 50\text{--}46$ Ma. Taking the upper and lower limits of these values, cooling rates were between $29^\circ\text{C}/\text{Ma}$ and $180^\circ\text{C}/\text{Ma}$. The second phase of the cooling history shows an evolution from north to south within the area of sections 1 and 2. Rocks of the phyllite and schist zones in the north of the complex probably cooled relatively rapidly to near-surface temperatures already in the Eocene (oldest apatite fission track ages from the schist zone are ~ 40 Ma). Rocks of the gneiss zone farther south, however, experienced a prolonged period ($\sim 15\text{--}20$ Ma, blue part of cooling history) at temperatures of $\sim 300\text{--}400^\circ\text{C}$ and only started cooling through the zircon fission track closure temperature around $\sim 30\text{--}25$ Ma. Parts of the southernmost gneiss zone even stayed at elevated temperatures of $>200^\circ\text{C}$ until ~ 10 Ma. The slope of the grey cooling curves lies in the range of $\sim 20^\circ\text{C}/\text{Ma}$.

Cooling history of section 3

The cooling history for section 3 is significantly different than that of sections 1 and 2 (Fig. 5.13c). The starting point is defined by a U/Pb zircon age of ~ 51 Ma (Tab. 5.1) corresponding to a maximum temperature of $\sim 600\text{--}700^\circ\text{C}$ (Fig. 5.2). $^{40}\text{Ar}/^{39}\text{Ar}$ hornblende, muscovite, biotite and zircon fission track ages define a slow, regular cooling curve from the peak conditions down to $200\text{--}300^\circ\text{C}$ until ca. 5 Ma (green part of cooling curve, Fig. 5.13c). This corresponds to cooling rates of $\sim 6\text{--}10^\circ\text{C}/\text{Ma}$. The young zircon fission track and zircon and apatite (U-Th)/He ages from the Fairweather corridor indicate a strong increase in cooling rate during the last ~ 5 Ma, with rates of $20\text{--}40^\circ\text{C}/\text{Ma}$, consistent with their locations within the obliquely convergent part of the St Elias orogen (Pavlis et al., 2004; Enkelmann et al., 2010). The slightly older zircon (U-Th)/He age from Seward glacier indicates a somewhat slower cooling, but the <3 Ma zircon fission track ages found in river sands draining the Seward glacier area (Enkelmann et al., 2009, 2010) indicate that the entire strip from Seward glacier down to Nunatak fjord (Fig. 5.2a) experienced rapid cooling during the last ~ 5 Ma.

5.6.2 Interpreting the cooling histories in terms of exhumation

Translating cooling histories into exhumation histories is not always straightforward, especially if independent pressure information for the retrograde part of the metamorphic history is not available. In our case, the only independent information on depth comes from the peak pressures registered in the metamorphic parageneses of the different sections (Fig. 5.2; Bruand, 2010). Generally, cooling histories may be the result of two fundamentally different thermal processes, or a combination of both: (i) passive thermal relaxation from perturbed thermal conditions to a normal geothermal gradient at depth, i.e., without advection of material by tectonics or erosion, or (ii) active cooling by advection of the rocks towards the surface of the Earth; i.e. exhumation by tectonics, erosion, or both. Clearly, discerning between these two origins for certain sections of the cooling histories is essential before an integrated understanding of the tectonic evolution of the region is possible.

Exhumation histories for sections 1 and 2

The cooling histories of both sections 1 and 2 show very fast cooling after the metamorphic peak from ~650-700°C to ~350-400°C at peak pressures of 4-13 kbar (Fig. 5.13; Bruand, 2010). The interpretation that the CMC may be related to the subduction of a spreading ridge below the margin (e.g. Sisson & Pavlis, 1993; Pavlis & Sisson, 1995; Bradley et al., 2003) suggests that the fast cooling reported after the metamorphic peak in sections 1 and 2 could be the result of passive thermal relaxation after the passage of the subducting ridge. In this model, the subducting ridge below the margin causes pervasive heating of the complex, aided by the distribution of heat through magmas which formed above the ridge and intruded higher crustal levels. For this model, cooling sets in once the ridge has passed under the complex and subduction refrigeration together with surface cooling produce rapid cooling. Indeed, this cooling may be substantial as the refrigeration of the complex by the underlying subducting slab may lead to temperature gradients substantially below normal geothermal conditions.

However, if passive thermal relaxation is the reason for the fast cooling from ~650-700°C to ~350-400°C in only ~2-6 Ma at depths of ~20-50 km, a very fast removal of the heat source at depth is required. This is unlikely in a plate geometry as shown by Häussler et al. (2003a) and Madsen et al. (2006) where the Kula-Resurrection ridge is subducting parallel to the margin below the CMC. Moreover, thermal modelling of Groome & Thorkelson (2009) showed that for a slowly migrating triple junction (10 mm/yr), the effect of ridge subduction is characterized by a protracted metamorphic heating followed by slow cooling, particularly at depths of >20 km, which is definitively not observed in sections 1 and 2 of the CMC. Therefore, if a ridge was subducting below the CMC during Eocene times, it must have moved fast, and the plate tectonic geometry must have been in such a way that old and cold lithosphere was subducted shortly after the passage of the ridge in order to

cool the rocks quickly. Since subduction velocities at that time were relatively high (100 mm/yr or more, Doubrovine & Tarduno, 2008), and a major plate tectonic reorganization occurred simultaneously to metamorphism in the CMC, such a scenario with a fast-moving triple junction could have taken place (Sisson & Pavlis, 1993; Pavlis & Sisson, 1995, 2003), but is constrained poorly because there is no constraint on plate geometry.

However, it is unlikely that the fast cooling after the metamorphic peak was the result of only a passive relaxation of the geotherm following ridge subduction for the following reason. Peak pressures reported by these rocks correspond to depths of ~20-50 km, and if only passive cooling would have occurred after the peak, then all of the exhumation from this depth to the surface must have occurred during later stages of the cooling history (from ~350°C to the surface), notably after ~25 Ma (Fig. 5.13). This would imply an unrecognized massive exhumation of parts of the gneiss zone in the Neogene. In addition it would require that exhumation took place during relatively low temperatures and therefore entirely along semi-brittle to brittle faults. However, the ductile penetrative steep foliation with down-dip lineations developed in the gneisses where the highest pressures are recorded indicate that at least parts of the exhumation took place during ductile deformation shortly after the metamorphic peak. Therefore, at least for the zones which report relatively high pressures, the metamorphic peak was followed by exhumation.

The authors of this paper do not entirely agree on the interpretation of the cooling data in terms of ridge subduction and further work is needed to clarify this issue. Some of us infer that a subducting ridge below the complex as additional heat source is not necessarily required, and that the fast cooling of the rocks could solely be the result of fast exhumation aided by a relaxation of isotherms in response to shallow level processes (i.e. in the schist zone). Others prefer an interpretation that a combination of processes led to the rapid cooling: cooling due to exhumation in a rising anticlinorium within the gneissic core (as shown schematically by Pavlis & Sisson, 1995) combined with quenching by subduction refrigeration from below following the passage of a triple junction.

In either case, after the fast cooling phase recorded in section 1 and 2 of the CMC both the gneiss and schist zones were probably at similar depths of ~10-15 km, and the remaining exhumation occurred asynchronously from north to south, with the schist zone reaching relatively shallow depths already in the Eocene, whereas the southern gneiss zone stayed at considerable depths until ~10 Ma ago (e.g. in a mechanism similar to that described by Enkelmann et al., 2008).

Exhumation history for section 3

Despite similar structural observations and similar metamorphic grade, the cooling and exhumation history of section 3 is significantly different from sections 1 and 2. Sections 1 and 2 show a very pronounced cooling and exhumation phase shortly after the metamorphic

peak, whereas cooling and exhumation occurred much slower and more regularly in section 3 from the metamorphic peak until relatively recent times (Fig. 5.13). We suggest that this is the result of the post-metamorphic tectonic configuration of these two segments along the margin - an interpretation which has important implications for the paleo-geometry of the margin. Specifically, it has long been suggested from paleomagnetic data (Coe et al., 1985) and the geology of the southern Alaska margin (Nokleberg et al., 1989) that the Alaskan orocline (i.e. the curvature of the present-day margin) was in existence by Eocene time. Our results provide independent support for this interpretation. If the margin was already curved during cooling and exhumation of the three sections, and the Pacific plate moved northwest-wards relative to North America as indicated by plate tectonic reconstructions (e.g. Doubrovine & Tarduno, 2008), then sections 1 and 2 were under constant convergence after peak metamorphism. This ongoing convergence may have led to the initial formation of topography and rapid exhumation of gneissic rocks shortly after the metamorphic peak, followed by an outward jump of deformation and the accretion of outboard terranes, until the present-day collision with the Yakutat terrane led to final exhumation. Section 3 however would have been located along the transpressional part of the margin, where highly oblique transpressional motion would have led to slow, regular cooling and exhumation in what Koons et al. (in press) refer to as the "oblique orogen". The increased cooling and exhumation rate during the last ~5-10 Ma could be the result of the final collision of the Yakutat terrane with the margin. In our opinion, the different cooling and exhumation histories registered by the three different sections nicely reflect the existence of the Alaskan orocline at least since ~50 Ma.

5.6.3 Integration of the structural record with the metamorphic history of the Chugach Metamorphic Complex

Our study generally supports the structural succession D₁-D₃ for the CMC (Fig. 5.7) that has been recognized previously by Pavlis & Sisson (1995, 2003). D₁ is related to the initial accretion of the sediments, whereas D₂ and D₃ are related to metamorphism in the CMC. In the following, the structural record, the metamorphic evolution and the cooling and exhumation histories of the CMC are integrated and a possible tectonic evolution for the entire complex is presented in a regional context.

D₁ - accretion of sediments

During D₁ deformation a relatively thick accretionary prism formed dominated by convergent D₁ structures such as thrusts and folds. Subduction zone settings are generally relatively cold, with typical geothermal gradients of ~10-15°C/km, leading to blueschist facies metamorphism at depths of ~15-20 km (e.g. Philpotts & Ague, 2009). However, the thermal structure of an accretionary prism depends on many factors such as the amount of accre-

tion and erosion, the coefficient of basal friction, shear heating at the base, internal strain heating and the pore fluid/lithostatic pressure ratio (e.g. Barr & Dahlen, 1989). Examples of relatively high thermal gradients of $\sim 20\text{-}25^\circ\text{C}/\text{km}$ include the Taiwan accretionary prism (Barr & Dahlen, 1989) or the Cascadia accretionary wedge (Booth-Rea et al., 2008), which lead to greenschist facies conditions of $\sim 300\text{-}500^\circ\text{C}$ at depths of $\sim 15\text{-}20$ km ($\sim 4\text{-}6$ kbar). Given the widespread distribution of subgreenschist facies to greenschist facies conditions in the Chugach terrane (e.g. Dusel-Bacon, 1994), the initial geothermal gradient in this accretionary prism was probably on the order of $\sim 20\text{-}25^\circ\text{C}/\text{km}$.

D₂ - vertical flattening and margin-parallel extension

After accretion and D₁ deformation, the deeper parts of the accretionary prism were subjected to D₂ deformation: the presence of the flat-lying D₂ fabric accompanied by a pronounced orogen-parallel stretching lineation indicates that the base of the accretionary prism experienced vertical thinning and margin-parallel stretching (e.g. Pavlis & Sisson, 1995). The D₂ fabric formation was accompanied by andalusite-grade metamorphism just above the D₂ fabric front, sillimanite-grade metamorphism within the schist and parts of the gneiss zone and culminated in the onset of partial melting in the gneiss zone. The vertical thinning during D₂ probably led to the compression of isotherms and to the presence of relatively high geothermal gradients in the schist and gneiss zones. Sisson & Hollister (1988) and Sisson et al. (1989) derived thermal gradients of $\sim 35^\circ\text{C}/\text{km}$ for the edge and $\sim 65^\circ\text{C}/\text{km}$ for the core of the western part of the complex. Farther east, the data of Bruand (2010) indicate an opposite relationship between the northern schist zone ($\sim 35^\circ\text{C}/\text{km}$) and the gneiss zone ($\sim 20\text{-}25^\circ\text{C}/\text{km}$) of sections 1 and 2 of the complex. An increase from $\sim 25^\circ\text{C}/\text{km}$ during D₁ to $\sim 35\text{-}65^\circ\text{C}/\text{km}$ during D₂ at depths of $\sim 10\text{-}20$ km in the lowermost phyllite zone, the schist and western gneiss zone would require a total vertical thinning of $\sim 6\text{-}10$ km of the crustal column. Finite strain modelling of Pavlis & Sisson (1995) showed that depending on the ratio of pure to simple shear during D₂ deformation $\sim 2\text{-}7$ km of vertical thinning could have occurred alone in the D₂ fabric of the schist zone, making a total of $\sim 6\text{-}10$ km thinning in the entire D₂ zone a realistic value. Based on these considerations, we suggest that the D₂ vertical shortening probably was sufficient to produce the high geothermal gradients observed in the lowermost phyllite zone, the schist zone and the western parts of the gneiss zone.

Since the peak metamorphic conditions are constrained to $\sim 55\text{-}51$ Ma by U/Pb dating of metamorphic zircons (Tab. 5.1, Chap. 4), the D₂ deformation must have started at about the same time or shortly before. This period is broadly contemporaneous with the plate tectonic reorganization of the Pacific basin (chron 24-21, $\sim 53\text{-}48$ Ma, Atwater, 1989) suggesting that there might be a relationship between movements of the oceanic plates in the Pacific basin and the strain history along the margin (Sisson & Pavlis, 1993; Pavlis & Sisson, 1995). However, since it is not well constrained what exactly happened during this reorganization, great freedom remains in interpreting the resulting boundary forces which acted on the

margin. D_2 could, for example, be the result of a short-lived transtensional event due to a short-term change in movement direction of the plate segment which was subducting below the margin, related to the plate reorganization. Or it could be the result of forces which acted inside the accretionary prism: after a decrease in convergence rate due to the plate reorganization, gravitational collapse of the overthickened accretionary prism could have occurred leading to the D_2 stretching and vertical thinning. However, in this case extension perpendicular to the margin rather than parallel to it would be expected.

Other possible reasons for D_2 deformation are not directly linked with the plate reorganization. Sisson & Pavlis (1993) and Pavlis & Sisson (1995) for example suggested that the subduction of an oceanic spreading ridge below the margin could have caused the D_2 deformation, with the subduction of the ridge topography inducing the vertical thinning component. The subduction of a ridge below the margin at the time of interest has been inferred by many workers and depending on where to restore the accretionary prism along the margin, potential candidates are the ridge between the Kula and Farallon plates or the ridge between the Kula and Resurrection plates (Fig. 5.1d). Alternatively, Pavlis & Sisson (2003) explored the possibility of D_2 and D_3 actually being the result of the same dextral transpressive deformation, with D_2 representing a mid-crustal decoupling horizon. Or, D_2 could be the result of underplating of a buoyant package of offscraped sedimentary rocks and oceanic crust below the accretionary prism (as it is indicated by seismic profiles crossing Prince William Sound, Fig. 5.1, e.g. Fuis et al., 2008). As a last possibility, the D_2 deformation could have been caused by the geometry of the margin itself: it could be the result of the accretionary prism sliding past a releasing bend in the large-scale strike-slip system bordering the prism.

D_3 - dextral transpression

From D_2 to D_3 , a switch from vertical thinning to horizontal shortening and the onset of dextral shearing occurred. A dextral transpressive shear system developed which inhomogeneously affected the entire area. In the schist zone, open folding, crenulation foliation development and semi-brittle to brittle dextral fault zones developed, probably associated with fast cooling due to a relaxation of the isotherms after the thinning of D_2 ceased. In the gneiss zone, high-temperature deformation continued and domains of high and low D_3 dextral transpressive shear developed. The D_3 deformation is concentrated along the southern border of the CMC in sections 1 and 2: in the southern gneiss zone (southern end of the Fan transect, the entire Tana transect and large parts of the Bagley transect, Fig. 5.3) D_3 is dominant and the D_2 fabric is mostly transposed into the steep D_3 fabric. In addition to the higher intensity, the stretching lineation on the D_3 fabric also plunges 30-60° to the west-northwest in these southern parts, in contrast to the lineation in the northern parts where it is subhorizontal. Simultaneously to the D_3 deformation, partial melting occurred extensively in the gneiss zone and melts rose along the D_3 foliation planes to form bigger plutons which intruded the schist zone, and which locally thermally overprinted the andalusite-grade meta-

morphism present above the D₂ fabric front in the schist zone in section 2.

The domains with high D₃ fabric intensity and down-dip lineations correspond to the domains which registered higher peak pressures than the rest of the complex (~7-8 kbar at the Tana transect, ~8-13 kbar at the Bagley transect, Fig. 5.2b-c), which suggests that the higher pressures are related to this D₃ deformation. We therefore interpret that during this dextral transpressive deformation, rocks of the gneiss zones were partly exhumed along N-dipping D₃ foliation planes with down-dip lineations. This process may represent a narrow extrusion channel in which exhumation occurred due to focused erosion at the surface. Such erosion might have been a consequence of the shortening component of the D₃ deformation, which was concentrated in the southern gneiss zone and along the Contact fault and leading to the formation of topography at the surface. There is, in fact, significant evidence for erosion during the Early Eocene in the Chugach terrane. Approximately 100 km west of the CMC, small Early Eocene non-marine sedimentary basins unconformably overlie the Chugach terrane (e.g. Little & Naeser, 1989). These sedimentary rocks record a proximal metasedimentary and metavolcanic source from the Chugach Mountains, forming large alluvial fan complexes (Little & Naeser, 1989; Trop & Ridgway, 2007).

The D₃ deformation with its dextral transpression is typical for what has been the situation along the margin already during the formation of the accretionary prism during D₁. It therefore represents the switch back after the unusual D₂ event to a normal deformational regime with oblique subduction of oceanic plates below the continental margin. During accretion of the sediments, the strike-slip component of deformation was localized mainly along the Hanagita Fault System inboard of the accretionary prism (Fig. 5.1b; Roeske et al., 2003). During the renewed dextral transpression of D₃, this deformation concentrated farther outboard, along the Contact Fault system and within the gneissic core of the CMC. This outboard jump and concentration of dextral transpression could be related to the fact that the accretionary prism was enlarged due to the accretion of the Prince William terrane which is located outboard of the Chugach terrane.

5.7 Conclusions

Our structural and thermochronological analysis of the Chugach Metamorphic Complex along three across-strike transects reveals the following:

(1) The structural geometry of the CMC is controlled by the presence of three superimposed fabrics consistent with previous work by Sisson & Pavlis (1993) and Pavlis & Sisson (1995, 2003). The first fabric is related to accretion of the sediments and is only recognizable in the phyllite zone surrounding the complex. The second fabric is a flat-lying foliation defined by biotite ± sillimanite with a horizontal E-W stretching lineation. It is present in parts of the schist and in the entire gneiss zone of the complex and indicates vertical

flattening and margin-parallel stretching. The third fabric is a steep foliation defined by biotite \pm melt layers with a horizontal E-W stretching lineation in the northern part and a variably W-NW-dipping stretching lineation in the southern part of the complex. It is heterogeneously developed throughout the gneiss zone and parts of the schist zone, with the most intense deformation concentrated along the southern part of the gneiss zone. In addition, it defines a foliation fan from north to south with south-dipping foliation planes in the north and north-dipping foliation planes in the south. We interpret this fabric as the result of a dextral transpressive deformation. In addition to these three ductile fabrics, the southern part of the gneiss zone is overprinted by numerous semi-brittle to brittle N-dipping faults with N-side-up and dextral sense of movement (Fig. 5.7).

(2) Thermochronology reveals different cooling histories for the western/central and south-eastern sections of the complex. The western and central part of the complex rapidly cooled from peak temperatures of $\sim 650\text{-}700^\circ\text{C}$ at $\sim 55\text{-}52$ Ma to $\sim 350\text{-}400^\circ\text{C}$ around $\sim 50\text{-}46$ Ma, indicating cooling rates of $\sim 30\text{-}180^\circ\text{C/Ma}$ during this time period. This period of rapid cooling was then followed in the gneiss zone by a period of no/slow cooling, before an increase in cooling affected the schist and gneiss zones progressively from north to south. The south-eastern section of the complex cooled much more regularly and slowly, with a cooling rate of $\sim 6\text{-}10^\circ\text{C/Ma}$ from $\sim 51\text{-}5$ Ma, before an increase in cooling rate occurred during the last ~ 5 Ma with rates of $\sim 20\text{-}40^\circ\text{C/Ma}$.

(3) Translation of these cooling histories into exhumation histories is not straightforward. However, based on several considerations we interpret that most likely the fast cooling observed in the western and central sections shortly after the metamorphic peak also corresponds to exhumation of parts of the gneiss zone where the highest pressures are recorded. Exhumation of these parts of the gneiss zone was focused in high D_3 strain zones. Exhumation of the south-eastern section of the complex occurred slowly and regularly simultaneously with cooling.

(4) Integrating the structural record with the thermochronological history suggests the following possible scenario for the development of the CMC. Formation of the accretionary prism in which the CMC developed occurred during dextral transpression which was partitioned into strike-slip along the Hanagita Fault Zone and internal thrusts and folds of the D_1 deformation. The geothermal gradient in this accretionary prism was probably in the order of $\sim 20\text{-}25^\circ\text{C/km}$. Shortly before or at $\sim 55\text{-}52$ Ma, this accretionary prism was affected by D_2 deformation (vertical flattening and margin-parallel stretching) which led to the compression of isotherms, andalusite-sillimanite-grade metamorphism and the onset of partial melting in parts of the complex. This deformation probably led to an increase in the geothermal gradient to $\sim 35\text{-}65^\circ\text{C/km}$ in the schist zone and the western gneiss zone. D_2 was followed by renewed dextral transpression during D_3 , which concentrated along the Contact fault and inside the southern gneiss zone and which led to partial exhumation of the rocks. The already curved margin was probably responsible for the difference in cooling and exhumation timing between the western/central and south-eastern parts of the complex. The collision of the Yakutat terrane led to increased cooling and exhumation in a narrow

zone on the north-side of the Contact/Fairweather fault during the last ~5-10 Ma.

(5) The regional boundary conditions which lead to the margin-parallel stretching phase and the subsequent dextral transpressive deformation at ~55-52 Ma are not well constrained. The incomplete plate tectonic record in the Pacific basin allows a great amount of freedom in assuming the plate forces which acted on the margin at that time. The subduction of a spreading ridge below the complex as it has been suggested in the literature is not uniquely required for the development of the CMC, given our newly obtained metamorphic conditions and the structural history described in this contribution.

Acknowledgments Financial support by the Fonds zur Wissenschaftlichen Förderung FWF project P-19366 is greatly acknowledged. C. Carson and J.D. Champagnac are thanked for help in the field. A. Koppers is thanked for help with the ArArCALC-software. J. Gifford is thanked for help in the ArAr-Lab at the University of Florida. From the University of Vienna we thank U. Klötzli and F. Biedermann for the help with mineral separation and M. Horschinegg for help with the Rb-Sr measurements. P. and J. Claus are thanked for flying in the field.

5.8 Appendix - Analytical techniques

5.8.1 A. $^{40}\text{Ar}/^{39}\text{Ar}$ method

Muscovite and biotite separates were obtained by crushing, sieving, short milling and magnetic separation of fist-sized hand specimens. The separates were then cleaned by hand-picking under a binocular and only transparent, inclusion-free grains were selected. Grain size of the final separates was ~0.1-0.5 mm. The hand-picked separates were cleaned in distilled water in an ultrasonic bath. Approximately ~5 mg of each sample were packed into Al-foil and stacked into a silica glass tube shielded by a 0.2 mm thick cadmium liner. Eight sample splits (each ~5 mg) of flux monitor GA-1550 biotite (K/Ar age 98.5 ± 0.8 1 σ ; Spell & McDougall, 2003) were intercalated in regular intervals between the samples. K glass and CaF₂ salts were included in the tube in order to monitor interfering nuclear reactions on potassium and calcium. The whole tube was irradiated during 15 h in the core of the Oregon State University research reactor facility. Step heating experiments were conducted at the geochronology laboratory at the University of Florida. Samples were loaded into a Modifications Ltd Double vacuum resistance furnace. 14 and 16 heating steps from 600-1350°C were conducted for muscovites and biotites, respectively, with total 15 min heating time per step. The extracted gas was expanded into a stainless steel cleanup line and purified with two 50 L/s SAES getters. Argon isotopes were measured using a MAP215-50 mass spectrometer in electron multiplier mode.

The software ArArCALC v2.4 (Koppers, 2002) was used for data reduction. Data were corrected for system blanks and mass discrimination. Detailed isotopic measurements can

be found in Tables 5.3 and 5.4. We report error-weighted plateau ages when more than three high temperature heating steps containing >50% of the total released $^{39}\text{Ar}_K$ have a MSWD that is smaller than a statistical T-student distribution. If this is not the case, we report error plateau ages (Koppers, 2002). Traditional calculation of plateau ages based on eq. (17) in Koppers (2002) does only account for analytical uncertainty, uncertainty on the J-value determination and uncertainty on the total decay constant of ^{40}K . In order to also consider uncertainties on the individual λ_e and λ_β decay constants, the $^{40}\text{K}/\text{K}$ abundance ratio, the actual measurement of the primary K/Ar standard and the intercalibration of secondary $^{40}\text{Ar}/^{39}\text{Ar}$ standards an alternative set of age equations has to be used (Renne et al., 1998; Min et al., 2000; Scaillet, 2000; Koppers, 2002; Fraser et al., 2008). We therefore applied the recalibration tool incorporated in ArArCALC which calculates plateau ages based on the equations of Karner & Renne (1998), Renne et al. (1998) and Min et al. (2000) which allow incorporating all internal and external errors. The physical constants used for recalculation are given in Min et al. (2000) and Spell & McDougall (2003). Only those recalculated ages are reported in the diagrams, Table 5.1 and the text.

The flux monitor J was determined based on a total of 29 heating steps on 8 sample splits which were distributed over the whole irradiation tube. The obtained J-values scatter considerably and no gradient was detected over the tube. From the 29 heating steps we excluded (a) the steps with the most scatter in isotopic ratio determination, (b) the steps with only very little gas and (c) some visually selected bad steps. We then used the remaining 13 heating steps to calculate an error weighted mean of $J = 0.00369 \pm 0.0001122$ ($\pm 3.04\%$, 2σ , only analytical error considered following Koppers, 2002).

5.8.2 B. Rb/Sr isochron method

The biotite separates prepared for $^{40}\text{Ar}/^{39}\text{Ar}$ step heating experiments (Appendix A) were additionally purified by grinding in an agate mill in alcohol, sieving and magnetic separation. Whole rock powders were obtained by milling of ca. 3 cm^3 -sized samples. Chemical sample preparation was performed at the Geological Survey of Austria in Vienna following the procedure described by Sölvä et al. (2005). Sample weights used for dissolution were about 200 mg for biotite and 100 mg for whole rock. Isotopic measurements were done at the Department of Geological Sciences at the University of Vienna. Spiked Rb ratios were measured at a Finnigan® MAT 262, whereas unspiked Sr ratios were analysed at a ThermoFinnigan® Triton TI TIMS. Sr was run from Re double filaments, whereas Rb was evaporated from a Ta filament. On the ThermoFinnigan® Triton the $^{87}\text{Sr}/^{86}\text{Sr}$ ratio determined for the international standard NBS987 was 0.710248 ± 4 ($n=17$). The error for the calculated $^{87}\text{Rb}/^{86}\text{Sr}$ ratios was taken as $\pm 1\%$ (2σ). Isochron age calculation was performed with Isoplot/Ex (Ludwig, 2003). All data are given in Table 5.5

5.8.3 C. Fission Track zircon method

Zircon grains were extracted by crushing, sieving, magnetic and heavy liquid separation, and finally handpicked. After mounting the zircons in PFA Teflon and polishing them, fossil fission tracks were revealed by etching in a eutectic mixture of NaOH/KOH at 210°C for 4 to 8 hours. External synthetic mica detectors were firmly attached and, after irradiation, etched for 40 minutes in 40%HF at 20°C. Thermal neutron irradiation was performed at the German Technical University München in Garching (FRM-II reactor). Neutron flux was monitored using CN1 dosimeter glasses. All samples have been analysed using the external detector method as described by Naeser (1976) and Gleadow (1981). Ages were calculated using the zeta calibration method (Hurford & Green, 1983) with a zeta factor of 159 ± 3.6 using the software TRACKKEY 4.2.g (Dunkl, 2002). Counting of fission tracks was carried out using a Zeiss Axio Imager A1m microscope equipped with an AUTOSCAN™ stage. Only grains with their prism planes parallel to the polished surface were used for age dating. All data are given in Table 5.6.

Table 5.3: $^{40}\text{Ar}/^{39}\text{Ar}$ furnace step release data for muscovite separates ($J = 0.00369$)

Step T (°C)	$^{36}\text{Ar}(\text{a})$ volt	$^{37}\text{Ar}(\text{cl})$ volt	$^{38}\text{Ar}(\text{cl})$ volt	$^{39}\text{Ar}(\text{k})$ volt	$^{40}\text{Ar}(\text{r})$ volt	Age (Ma)	$\pm 2\sigma$ (Ma)	$^{40}\text{Ar}(\text{r})$ (%)	$^{39}\text{Ar}(\text{k})$ (%)	K/Ca	$\pm 2\sigma$
B1											
600	0.001201	0.002606	0.000085	0.039798	0.237348	39.4	29.3	40.01	0.89	6.6	2.3
700	0.005502	0.002859	0.000136	0.131905	1.161280	57.8	13.3	41.61	2.96	19.8	3.7
750	0.001002	0.000607	0.000094	0.194788	1.334459	45.1	2.1	81.59	4.37	138.1	32.9
800	0.001011	0.000501	0.000089	0.390647	2.720224	45.9	1.5	89.79	8.76	335.5	80.9
850	0.001739	0.000484	0.000386	1.023255	6.955255	44.8	0.9	92.78	22.95	908.5	251.7
900	0.000263	0.000146	0.000205	0.490420	3.454589	46.4	1.9	97.44	11.00	1449.0	1769.5
940	0.061401	0.000368	0.000764	0.172606	2.343523	88.4	95.4	11.44	3.87	201.6	135.1
980	0.000255	0.000264	0.000253	0.488344	3.486493	47.0	1.9	97.53	10.95	794.8	382.2
1020	0.000373	0.000454	0.000013	0.594047	4.237903	47.0	1.2	97.11	13.32	563.1	245.0
1100	0.000102	0.000412	0.000103	0.436056	3.246225	49.0	2.3	98.73	9.78	455.4	150.3
1150	0.000594	0.000299	0.000320	0.276760	2.117574	50.3	1.9	92.05	6.21	397.7	208.4
1200	0.001470	0.000390	0.000127	0.152736	1.448170	62.2	4.8	76.76	3.43	168.5	65.9
1350	0.005289	0.000741	0.000349	0.067281	1.442017	137.6	41.3	47.96	1.51	39.0	12.5
B14											
600	0.000327	0.001178	0.000100	0.028685	0.491646	110.9	20.3	83.48	0.63	10.5	3.6
700	0.003645	0.002106	0.001009	0.097267	2.287860	150.5	11.9	67.94	2.12	19.9	6.6
750	0.000064	0.000212	0.000134	0.121669	1.354788	72.8	9.6	101.16	2.65	246.7	269.6
800	0.000492	0.000504	0.000140	0.484573	3.888232	52.8	3.7	96.09	10.57	413.2	187.3
850	0.000124	0.000275	0.000826	0.578459	4.725706	53.7	3.0	100.44	12.62	905.6	614.8
900	0.000010	0.000190	0.002112	0.943561	7.096891	49.5	4.1	99.61	20.58	2139.9	1258.2
940	0.000070	0.000087	0.000683	0.326367	2.606060	52.5	4.7	100.46	7.12	1605.0	2143.3
980	0.000075	0.000048	0.000327	0.202692	1.777262	57.6	4.4	100.95	4.42	1799.7	3922.8
1020	0.000211	0.000022	0.000314	0.190721	1.761168	60.6	7.3	103.37	4.16	-3648.7	18171.9
1060	0.000003	0.000109	0.000087	0.279736	2.219564	52.2	2.7	99.63	6.10	1106.5	1731.7
1100	0.000035	0.000144	0.000653	0.365784	3.177390	57.1	7.4	100.02	7.98	1089.6	1041.5
1150	0.000428	0.000390	0.000274	0.645871	4.582594	46.7	2.4	96.96	14.09	712.3	292.8
1200	0.000094	0.000301	0.000166	0.228544	1.759886	50.7	3.3	98.12	4.99	326.0	173.2
1350	0.003933	0.001014	0.000023	0.090246	0.784454	57.1	8.4	40.25	1.97	38.3	8.2
T22											
600	0.001227	0.002112	0.000010	0.024813	0.151683	40.3	22.4	29.46	0.55	5.1	1.2
700	0.014884	0.005272	0.000307	0.078754	0.640186	53.4	22.2	12.70	1.76	6.4	0.7
750	0.000245	0.000596	0.000219	0.072798	0.681256	61.4	46.3	90.17	1.63	52.5	41.5
800	0.000652	0.001326	0.000066	0.259141	1.877560	47.7	1.9	90.40	5.79	84.0	22.1
850	0.001109	0.001933	0.000112	0.988961	6.830892	45.5	0.9	95.07	22.11	220.0	26.0
900	0.001909	0.002725	0.001827	0.009838	0.608831	-468.8	879.8	1366.69	0.22	1.6	2.5
940	0.000232	0.000771	0.000600	0.582612	4.781549	54.0	5.9	98.27	13.02	325.1	276.3
980	0.000931	0.001429	0.000187	0.461602	0.719588	10.4	7.7	71.46	10.32	138.9	98.1
1020	0.000574	0.001419	0.001093	0.772691	5.402654	46.1	3.6	96.60	17.27	234.1	53.2
1060	0.000480	0.001130	0.000103	0.544466	4.200304	50.8	1.9	96.41	12.17	207.2	88.2
1100	0.000161	0.001416	0.000130	0.277918	2.032462	48.2	2.2	97.37	6.21	84.4	23.5
1150	0.000230	0.001358	0.000099	0.148520	1.214779	53.8	4.0	94.40	3.32	47.0	15.6
1200	0.000400	0.000030	0.000304	0.131305	1.401922	69.9	7.5	108.92	2.94	-1869.1	39474.2
1350	0.003913	0.004631	0.000292	0.119855	0.342763	19.0	20.4	22.81	2.68	11.1	5.4
Tk6											
600	0.000423	0.001638	0.000008	0.013389	0.179903	87.5	19.9	58.96	0.37	3.5	1.1
700	0.003410	0.002126	0.000360	0.045924	1.460992	200.7	33.9	59.15	1.25	9.3	4.2
750	0.000015	0.000283	0.000104	0.056474	0.633265	73.3	9.2	100.46	1.54	85.7	122.5
800	0.001431	0.000997	0.000547	0.789956	5.934276	49.4	3.6	93.04	21.57	340.6	98.0
850	0.000049	0.000111	0.000582	0.459276	3.956839	56.6	3.4	100.06	12.54	1772.5	1997.8
900	0.000060	0.000359	0.001731	0.588892	4.551462	50.9	2.4	99.27	16.08	705.6	401.3
940	0.000174	0.000763	0.000076	0.247443	1.744336	46.4	1.8	96.79	6.76	139.4	22.2

Continues on following page

Table 5.3: $^{40}\text{Ar}/^{39}\text{Ar}$ furnace step release data for muscovite separates ($J = 0.00369$)

Step T (°C)	36Ar(a) volt	37Ar(cl) volt	38Ar(cl) volt	39Ar(k) volt	40Ar(r) volt	Age (Ma)	$\pm 2\sigma$ (Ma)	40Ar(r) (%)	39Ar(k) (%)	K/Ca	$\pm 2\sigma$
980	0.000319	0.000436	0.000129	0.164863	1.174242	46.9	2.2	92.24	4.50	162.6	55.7
1020	0.000315	0.000701	0.000047	0.149758	1.058487	46.6	2.8	91.60	4.09	91.9	24.4
1100	0.000136	0.001711	0.000922	0.412887	3.199351	51.0	1.7	98.43	11.27	103.8	35.0
1150	0.000129	0.001510	0.000704	0.417077	3.055122	48.2	2.0	98.41	11.39	118.7	39.6
1200	0.000014	0.001000	0.000035	0.162998	1.494072	60.2	4.2	99.43	4.45	70.1	52.1
1350	0.003001	0.008024	0.000300	0.153439	1.548425	66.1	4.8	63.48	4.19	8.2	2.6
N9											
600	0.000100	0.001059	0.000178	0.033824	0.628598	119.9	22.6	104.78	0.52	13.7	9.0
700	0.004520	0.009127	0.000442	0.142724	1.282792	59.0	16.7	48.92	2.18	6.7	1.9
750	0.000089	0.002461	0.000037	0.174616	0.632164	24.0	2.3	95.32	2.67	30.5	6.3
800	0.000286	0.003324	0.000021	0.420795	1.380990	21.8	1.3	93.53	6.43	54.4	7.7
850	0.000554	0.003879	0.000772	1.029682	3.654999	23.5	0.9	95.03	15.74	114.1	20.7
900	0.000528	0.008440	0.000922	1.383073	4.633197	22.2	0.8	96.01	21.14	70.5	16.9
940	0.000370	0.008647	0.000223	0.597214	1.943619	21.6	0.9	93.95	9.13	29.7	5.0
980	0.000428	0.003066	0.000180	0.464416	1.506690	21.5	1.1	91.56	7.10	65.1	13.0
1020	0.000300	0.003241	0.000192	0.451379	1.628229	23.9	1.2	94.18	6.90	59.9	11.2
1060	0.000196	0.005878	0.000077	0.493050	1.734757	23.3	0.8	96.07	7.54	36.1	4.4
1100	0.000276	0.004869	0.000119	0.529612	1.754736	22.0	1.0	94.84	8.09	46.8	7.9
1150	0.000252	0.004687	0.000539	0.525369	1.816930	22.9	0.9	95.36	8.03	48.2	9.9
1200	0.000008	0.003619	0.000025	0.187910	0.781171	27.5	2.3	99.08	2.87	22.3	6.2
1350	0.002675	0.005913	0.000180	0.109088	0.887006	53.5	13.7	52.78	1.67	7.9	2.1
N28											
600	0.000682	0.002322	0.000054	0.034725	0.251182	47.6	14.4	55.37	0.76	6.4	1.1
700	0.006502	0.003003	0.000275	0.141218	0.912566	42.6	13.3	32.16	3.11	20.2	2.8
750	0.000713	0.000903	0.000002	0.165045	0.568074	22.8	2.7	72.55	3.63	78.6	27.7
800	0.000895	0.000502	0.000077	0.308554	0.937426	20.2	1.8	77.46	6.80	264.3	106.6
850	0.000918	0.000794	0.000265	1.127038	3.405043	20.0	1.1	91.87	24.82	610.5	183.1
900	0.000450	0.000676	0.000213	0.530570	1.582824	19.8	0.9	91.50	11.68	337.5	125.0
940	0.000395	0.000417	0.000073	0.232903	0.730049	20.8	1.5	85.58	5.13	239.9	84.8
980	0.000380	0.000501	0.000078	0.216016	0.713518	21.9	1.5	85.79	4.76	185.5	51.3
1020	0.000273	0.000469	0.000007	0.238455	0.753674	21.0	1.7	89.64	5.25	218.4	75.7
1060	0.000204	0.000524	0.000102	0.279761	0.889561	21.1	1.3	92.94	6.16	229.6	69.9
1100	0.000045	0.000414	0.000223	0.445096	1.343148	20.0	1.7	100.10	9.80	462.8	242.3
1150	0.000158	0.000445	0.000310	0.601421	1.788890	19.7	0.8	96.62	13.25	581.0	270.3
1200	0.000232	0.000126	0.000002	0.152043	0.599806	26.1	3.1	112.07	3.35	517.1	616.0
1350	0.000988	0.000803	0.000167	0.067855	0.609708	59.0	12.3	67.49	1.49	36.3	10.0
N19											
600	0.000522	0.001219	0.000015	0.039180	0.180035	30.4	5.5	53.67	0.80	13.8	3.3
700	0.004949	0.001386	0.000236	0.125206	0.775404	40.9	12.0	34.60	2.55	38.9	9.4
750	0.001042	0.000555	0.000127	0.132625	0.613810	30.6	4.2	66.33	2.70	102.8	50.0
800	0.000609	0.000099	0.000093	0.250043	1.326451	35.1	3.0	87.66	5.09	1089.9	1634.9
850	0.000029	0.000182	0.000566	0.669749	4.368302	43.0	4.5	99.79	13.63	-1581.8	1458.2
900	0.000180	0.000052	0.001383	1.081509	6.416690	39.2	1.3	98.74	22.01	8923.4	39917.7
940	0.000147	0.000098	0.000612	0.347358	1.812338	34.5	1.2	97.17	7.07	-1528.8	2494.3
980	0.000340	0.000160	0.000113	0.285812	1.420007	32.9	1.9	92.92	5.82	766.1	988.6
1020	0.000063	0.000097	0.000268	0.265656	1.458694	36.3	2.6	98.27	5.41	1179.1	2698.9
1060	0.000130	0.000059	0.000164	0.276985	1.585372	37.8	2.7	101.99	5.64	-2005.0	6679.9
1100	0.000005	0.000592	0.000512	0.386660	2.167650	37.0	3.2	99.60	7.87	280.6	252.3
1150	0.000194	0.003310	0.000562	0.600671	3.459311	38.0	2.3	97.92	12.22	78.0	19.3
1200	0.000212	0.008907	0.000536	0.317270	1.687382	35.1	1.4	95.95	6.46	15.3	4.3
1350	0.001819	0.121050	0.000013	0.135521	1.029020	50.0	7.9	65.53	2.76	0.5	0.1

Table 5.4: $^{40}\text{Ar}/^{39}\text{Ar}$ furnace step release data for biotite separates ($J = 0.00369$)

Step T (°C)	^{36}Ar (a) volt	^{37}Ar (cl) volt	^{38}Ar (cl) volt	^{39}Ar (k) volt	^{40}Ar (r) volt	Age (Ma)	$\pm 2\sigma$ (Ma)	^{40}Ar (r) (%)	^{39}Ar (k) (%)	K/Ca	$\pm 2\sigma$
B21											
600	0.001508	0.002896	0.000030	0.126360	1.034722	53.8	4.0	69.75	2.61	18.8	3.7
650	0.002701	0.001834	0.000365	0.523828	4.343756	54.5	2.2	84.25	10.82	122.8	25.7
700	0.002752	0.001282	0.000050	0.339942	2.914999	56.3	4.5	78.00	7.02	114.0	28.7
750	0.000502	0.001362	0.000060	1.086027	7.832961	47.5	0.9	97.79	22.43	343.0	51.0
800	0.001021	0.000925	0.000280	0.431398	3.243269	49.5	1.7	91.20	8.91	200.5	36.8
850	0.000326	0.000718	0.000004	0.204937	1.508095	48.4	1.8	93.68	4.23	122.7	24.5
900	0.000290	0.000408	0.000055	0.150567	1.273739	55.6	3.2	93.42	3.11	158.8	71.9
930	0.000109	0.000285	0.000203	0.115830	1.058275	60.0	3.5	96.77	2.39	174.8	70.4
960	0.000011	0.000125	0.000227	0.173592	1.317546	49.9	2.0	99.41	3.59	599.4	495.3
990	0.000041	0.000323	0.000114	0.266125	1.970510	48.7	1.5	99.03	5.50	354.2	111.4
1030	0.000276	0.000419	0.000459	0.403285	2.906499	47.5	2.0	96.92	8.33	413.4	66.4
1060	0.000045	0.000267	0.000641	0.337888	2.499818	48.7	4.3	99.11	6.98	544.6	289.4
1100	0.000021	0.000183	0.000296	0.324654	2.427266	49.2	1.5	99.89	6.71	761.8	736.7
1150	0.000039	0.000915	0.000008	0.284077	2.086887	48.4	1.2	99.09	5.87	133.5	35.1
1200	0.000191	0.000505	0.000000	0.041831	0.306555	48.3	4.9	84.21	0.86	35.6	7.0
1350	0.000120	0.000032	0.000040	0.030996	0.379313	79.9	8.5	110.06	0.64	412.6	2955.6
B40											
600	0.000169	0.001426	0.000050	0.140296	1.577499	73.5	5.9	96.71	3.35	42.3	22.0
650	0.002439	0.001341	0.000211	0.417860	3.944786	61.9	6.3	84.35	9.96	134.0	40.3
700	0.002189	0.003389	0.000600	0.629764	4.696710	49.1	1.5	87.62	15.02	79.9	8.0
750	0.000248	0.000892	0.000428	0.602349	4.252446	46.5	1.2	97.94	14.36	290.4	72.4
800	0.000175	0.000478	0.000227	0.260829	1.960169	49.5	2.1	97.09	6.22	234.6	88.5
850	0.000133	0.000841	0.000118	0.156912	1.175661	49.3	1.9	96.44	3.74	80.2	10.3
900	0.000204	0.000880	0.000002	0.134092	1.080859	53.0	6.6	94.41	3.20	65.5	27.3
930	0.000704	0.001548	0.000202	0.144895	0.939695	42.8	4.1	81.60	3.46	40.2	7.0
960	0.000140	0.000972	0.000018	0.233792	1.660383	46.8	1.5	97.22	5.58	103.4	25.0
990	0.000040	0.000604	0.000141	0.321749	2.264921	46.4	1.8	99.10	7.67	229.2	73.4
1030	0.000142	0.000247	0.000510	0.357513	3.125593	57.4	2.9	101.05	8.53	621.3	588.9
1060	0.000100	0.000919	0.000175	0.185784	1.742645	61.5	50.0	98.05	4.43	86.9	53.4
1100	0.000009	0.000600	0.000159	0.385958	3.051117	52.0	2.5	99.58	9.20	276.5	127.5
1150	0.000103	0.001215	0.000044	0.199605	1.486109	49.0	1.9	97.65	4.76	70.6	18.7
1200	0.000138	0.001768	0.000008	0.016394	0.129271	51.9	8.7	75.83	0.39	4.0	0.3
1350	0.000038	0.001931	0.000023	0.005491	0.135159	157.2	41.3	92.31	0.13	1.2	0.5
KB1											
600	0.001243	0.003429	0.000126	0.105470	0.598702	37.5	15.4	61.81	2.74	13.2	2.0
650	0.001487	0.001754	0.000146	0.437842	3.310648	49.8	1.7	88.01	11.38	107.3	19.4
700	0.002475	0.001424	0.000192	0.358098	2.838608	52.1	4.0	79.30	9.31	108.1	26.8
750	0.000058	0.000352	0.001401	0.684807	5.266836	50.6	2.9	99.34	17.80	835.5	472.1
800	0.000392	0.000381	0.000035	0.271731	2.012066	48.7	2.0	94.23	7.06	307.0	77.3
850	0.000291	0.000156	0.000140	0.232016	1.822044	51.7	3.8	95.18	6.03	638.9	420.0
900	0.000094	0.000223	0.000062	0.160878	1.207074	49.4	2.3	97.41	4.18	309.6	152.3
930	0.000224	0.000242	0.000180	0.133429	1.109648	54.7	4.2	94.08	3.47	236.8	94.2
960	0.000415	0.000303	0.000264	0.187739	1.449136	50.8	2.6	91.91	4.88	266.7	78.0
990	0.000007	0.000055	0.000329	0.211093	1.697444	52.9	4.3	99.55	5.49	1649.3	1936.4
1030	0.000142	0.000132	0.000257	0.292677	2.187998	49.2	2.9	97.77	7.61	953.8	712.1
1060	0.000251	0.000235	0.000038	0.242888	1.754522	47.6	2.3	95.61	6.31	444.1	108.2
1100	0.000464	0.000248	0.000038	0.274817	1.863993	44.7	2.0	92.80	7.14	477.0	195.9
1150	0.000335	0.000225	0.000465	0.218731	1.745103	52.5	10.4	94.34	5.69	418.6	248.1
1200	0.000145	0.000169	0.000040	0.022464	0.170026	49.8	9.6	79.65	0.58	57.1	15.0
1350	0.000371	0.000466	0.000046	0.012820	0.087693	45.1	14.6	44.38	0.33	11.8	3.2
KB5											

Continues on following page

Table 5.4: $^{40}\text{Ar}/^{39}\text{Ar}$ furnace step release data for biotite separates ($J = 0.00369$)

Step T (°C)	36Ar(a) volt	37Ar(cl) volt	38Ar(cl) volt	39Ar(k) volt	40Ar(r) volt	Age (Ma)	$\pm 2\sigma$ (Ma)	40Ar(r) (%)	39Ar(k) (%)	K/Ca	$\pm 2\sigma$
600	0.000683	0.002043	0.000029	0.097494	1.252804	83.8	10.5	85.98	2.33	20.5	10.0
650	0.003356	0.000757	0.001136	0.410536	4.632886	73.8	5.5	82.21	9.82	233.3	51.6
700	0.001214	0.000497	0.000835	0.210418	2.969843	91.8	11.0	89.08	5.03	181.9	83.5
750	0.000447	0.000930	0.001012	0.674903	5.235694	51.0	3.1	97.22	16.14	312.0	146.0
800	0.000449	0.000706	0.000700	0.371487	2.744883	48.6	2.1	95.06	8.89	226.2	67.1
850	0.000468	0.000542	0.000251	0.203882	1.491847	48.2	2.2	91.21	4.88	161.7	32.7
900	0.000264	0.000683	0.000050	0.149801	1.117329	49.1	2.5	93.16	3.58	94.4	16.8
930	0.000369	0.000552	0.000041	0.116528	0.874384	49.4	2.7	88.64	2.79	90.7	15.9
960	0.000248	0.000599	0.000000	0.192569	1.428944	48.8	2.7	94.81	4.61	138.2	25.2
990	0.000281	0.000575	0.000133	0.309411	2.246235	47.8	1.6	96.10	7.40	231.4	49.0
1030	0.000379	0.000599	0.000007	0.453010	3.199850	46.5	1.3	96.26	10.84	325.5	51.5
1060	0.000286	0.000679	0.000199	0.383578	2.666969	45.8	1.4	96.57	9.18	242.7	38.7
1100	0.000270	0.000798	0.000005	0.355758	2.498318	46.3	1.5	96.55	8.51	191.7	41.5
1150	0.000046	0.000601	0.000004	0.207363	1.591352	50.5	2.3	98.81	4.96	148.3	63.8
1200	0.000149	0.001239	0.000020	0.028315	0.245829	57.0	5.8	84.63	0.68	9.8	1.6
1350	0.000049	0.002339	0.000059	0.015290	0.179568	76.7	12.3	92.29	0.37	2.8	1.1
T11											
600	0.000785	0.002690	0.000155	0.068703	0.723648	69.0	7.9	75.59	1.34	11.0	3.3
650	0.000326	0.001038	0.000093	0.255272	2.203691	56.7	3.8	95.52	5.00	105.7	53.5
700	0.006463	0.002557	0.000415	0.582690	7.383411	82.6	8.3	79.32	11.40	98.0	41.2
750	0.000545	0.000926	0.001334	0.774078	5.806218	49.4	1.1	96.97	15.15	359.3	134.9
800	0.000097	0.000377	0.000847	0.518902	3.946306	50.0	3.5	98.93	10.15	591.8	379.6
850	0.000792	0.000930	0.000779	0.449601	2.658971	39.0	5.4	91.53	8.80	207.9	64.7
900	0.000222	0.000306	0.000188	0.218011	1.677592	50.6	2.4	95.92	4.27	306.7	155.8
930	0.000759	0.000488	0.000157	0.202000	1.442185	47.0	2.7	86.26	3.95	177.9	60.2
960	0.000605	0.000698	0.000091	0.265450	1.854970	46.0	1.9	90.89	5.19	163.4	22.9
990	0.000437	0.000280	0.000239	0.325745	2.252218	45.6	2.1	94.23	6.37	500.0	249.4
1030	0.000388	0.000521	0.000050	0.371207	2.578025	45.8	1.4	95.39	7.26	306.4	82.8
1060	0.000276	0.000602	0.000139	0.321838	2.294438	47.0	1.7	96.22	6.30	229.9	58.2
1100	0.000283	0.000866	0.000033	0.322754	2.301536	47.0	1.6	96.15	6.32	160.2	27.4
1150	0.000182	0.001229	0.000007	0.357073	2.676476	49.3	1.8	97.69	6.99	124.9	38.1
1200	0.000042	0.000874	0.000006	0.055565	0.452805	53.6	5.3	97.05	1.09	27.3	14.8
1350	0.000362	0.006204	0.000032	0.021089	0.288898	89.2	20.4	72.88	0.41	1.5	0.5
T22											
600	0.001639	0.002606	0.000436	0.143658	1.549000	70.6	5.3	76.04	2.81	23.7	10.0
650	0.008053	0.002205	0.000136	0.450587	4.578533	66.6	8.4	65.69	8.82	87.9	49.9
700	0.003270	0.004798	0.000031	0.667395	5.225281	51.5	2.9	84.15	13.06	59.8	5.0
750	0.000292	0.001462	0.001458	0.752828	5.357601	46.9	1.2	98.06	14.74	221.4	42.0
800	0.000460	0.001496	0.000200	0.399780	2.842189	46.8	1.8	95.09	7.83	114.9	22.0
850	0.000393	0.001675	0.000068	0.291615	2.107327	47.6	1.6	94.45	5.71	74.9	11.6
900	0.000683	0.001082	0.000000	0.219126	1.777812	53.3	2.5	89.55	4.29	87.1	26.8
930	0.000431	0.001281	0.000052	0.212394	1.579718	49.0	2.0	92.24	4.16	71.3	11.1
960	0.000332	0.001357	0.000109	0.287353	2.114366	48.4	1.8	95.23	5.62	91.1	18.8
990	0.000191	0.001361	0.000345	0.364577	2.585695	46.7	1.5	97.50	7.14	115.2	29.5
1030	0.000257	0.002260	0.000065	0.437531	3.121559	47.0	1.5	97.27	8.56	83.3	9.8
1060	0.000000	0.001554	0.000070	0.325068	2.417353	49.0	2.0	99.64	6.36	89.9	28.0
1100	0.000255	0.002063	0.000160	0.430726	3.037705	46.5	1.3	97.22	8.43	89.8	25.3
1150	0.000053	0.003664	0.000008	0.096801	0.775233	52.7	3.0	97.69	1.89	11.4	3.3
1200	0.000095	0.002896	0.000011	0.020830	0.230035	72.2	8.4	88.92	0.41	3.1	1.0
1350	0.000002	0.002744	0.000052	0.008611	0.160510	120.3	15.8	100.14	0.17	1.3	0.6
T27											
600	0.002170	0.003826	0.000058	0.098358	0.743998	49.8	6.2	53.61	1.94	11.1	2.7
650	0.003866	0.001950	0.000169	0.498439	4.222828	55.7	4.0	78.51	9.85	109.9	30.6
700	0.008461	0.004916	0.000331	0.778735	6.501041	54.9	3.0	72.06	15.38	68.1	15.5

Continues on following page

Table 5.4: $^{40}\text{Ar}/^{39}\text{Ar}$ furnace step release data for biotite separates ($J = 0.00369$)

Step T (°C)	^{36}Ar (a) volt	^{37}Ar (cl) volt	^{38}Ar (cl) volt	^{39}Ar (k) volt	^{40}Ar (r) volt	Age (Ma)	$\pm 2\sigma$ (Ma)	^{40}Ar (r) (%)	^{39}Ar (k) (%)	K/Ca	$\pm 2\sigma$
750	0.000250	0.001405	0.000428	0.704209	5.119520	47.9	1.2	98.22	13.91	215.5	59.9
800	0.000369	0.001073	0.000109	0.417336	2.992334	47.2	1.4	96.14	8.24	167.2	41.5
850	0.000239	0.000953	0.000219	0.295049	2.060565	46.0	1.7	96.33	5.83	133.1	24.4
900	0.000892	0.001040	0.000037	0.224829	1.656349	48.5	2.8	86.00	4.44	92.9	22.7
930	0.000286	0.000534	0.000043	0.140968	1.168922	54.5	2.2	92.98	2.78	113.6	34.5
960	0.000305	0.000480	0.000258	0.206409	1.657659	52.8	3.7	94.54	4.08	184.7	64.8
990	0.000037	0.000360	0.000199	0.292154	2.292639	51.6	3.8	99.19	5.77	348.9	156.6
1030	0.000029	0.000477	0.000463	0.363174	2.800751	50.7	1.6	99.35	7.17	327.6	148.4
1060	0.000037	0.000354	0.000505	0.317896	2.308333	47.8	2.2	99.16	6.28	386.3	166.2
1100	0.000051	0.000452	0.000391	0.351952	2.639366	49.4	2.3	99.09	6.95	335.0	172.5
1150	0.000055	0.000442	0.000092	0.320698	2.631204	53.9	3.5	99.07	6.33	312.3	145.9
1200	0.000129	0.000768	0.000084	0.042552	0.319123	49.4	2.8	89.07	0.84	23.8	4.3
1350	0.000155	0.000461	0.000088	0.009999	0.137825	89.7	85.8	74.99	0.20	9.3	4.3
T33											
600	0.001312	0.001787	0.000164	0.036322	0.672332	119.5	24.8	63.36	0.74	8.7	3.4
650	0.000135	0.000759	0.000019	0.070462	0.628206	58.5	4.8	93.75	1.44	39.9	13.4
700	0.005539	0.001972	0.000100	0.903419	8.894752	64.5	5.3	84.27	18.52	197.0	110.6
750	0.000311	0.000155	0.000249	0.612697	4.380392	47.1	2.8	97.59	12.56	1696.9	3518.3
800	0.000219	0.000496	0.000074	0.174964	0.527094	20.0	23.7	88.36	3.59	151.6	97.4
850	0.000335	0.000324	0.000089	0.331502	2.427056	48.2	2.4	95.75	6.80	439.4	198.9
900	0.000274	0.000497	0.000029	0.258202	1.869714	47.7	2.1	95.51	5.29	223.4	51.9
930	0.000313	0.000402	0.000221	0.216808	1.502950	45.7	2.0	93.86	4.44	232.0	60.6
960	0.000549	0.000332	0.000041	0.196602	1.393968	46.7	2.7	89.27	4.03	255.0	67.8
990	0.000454	0.000267	0.000009	0.266561	1.924360	47.5	1.9	93.16	5.46	428.6	169.8
1030	0.000443	0.000658	0.000056	0.510324	3.666383	47.3	1.4	96.21	10.46	333.5	76.0
1060	0.001018	0.000551	0.000767	0.423143	3.452216	53.6	3.4	91.71	8.67	329.9	144.1
1100	0.000267	0.000343	0.000056	0.319898	2.202258	45.4	1.6	96.18	6.56	401.5	152.0
1150	0.000016	0.000218	0.000960	0.228475	1.792033	51.6	25.5	99.40	4.68	451.3	378.9
1200	0.000001	0.000623	0.000162	0.228454	1.667804	48.1	2.5	99.61	4.68	157.6	69.7
1350	0.001049	0.001146	0.000176	0.100029	0.759176	49.9	9.3	70.82	2.05	37.5	12.9
T40											
600	0.001760	0.001900	0.000020	0.117144	1.248218	69.7	12.1	70.47	1.97	26.5	8.6
650	0.002717	0.001482	0.000485	0.451328	3.704528	54.0	2.0	81.97	7.59	131.0	47.9
700	0.005931	0.002905	0.001672	0.883768	6.797314	50.6	1.7	79.28	14.86	130.8	33.4
750	0.000341	0.000948	0.001001	0.877937	6.317525	47.4	1.4	98.07	14.76	398.2	185.2
800	0.000822	0.001033	0.000186	0.390555	2.699701	45.5	2.4	91.43	6.57	162.5	34.6
850	0.000356	0.001410	0.000027	0.343206	2.447402	47.0	1.5	95.54	5.77	104.7	22.2
900	0.000279	0.001632	0.000073	0.292204	2.098007	47.3	2.1	95.88	4.91	77.0	17.2
930	0.000232	0.000962	0.000363	0.243021	1.710606	46.4	2.0	95.79	4.09	108.6	21.4
960	0.000242	0.000886	0.000314	0.344305	2.395161	45.8	1.6	96.74	5.79	167.2	33.5
990	0.000238	0.000840	0.000280	0.383871	2.747559	47.1	1.9	97.15	6.45	196.4	59.5
1030	0.000090	0.000981	0.000053	0.445949	3.222633	47.6	1.8	98.82	7.50	195.5	50.8
1060	0.000123	0.000782	0.000156	0.404152	2.976667	48.5	2.3	98.44	6.79	222.3	79.5
1100	0.000107	0.001035	0.000889	0.400635	3.167025	52.0	3.6	98.68	6.74	166.5	56.8
1150	0.000170	0.001515	0.000166	0.296035	2.218897	49.3	1.8	97.45	4.98	84.0	20.4
1200	0.000014	0.000349	0.000069	0.042010	0.342143	53.5	4.7	98.48	0.71	51.8	20.4
1350	0.000170	0.000318	0.000056	0.031801	0.264600	54.7	6.1	83.79	0.53	42.9	21.2
Tk7											
600	0.002732	0.003207	0.000073	0.163383	1.370472	55.1	5.5	62.80	3.86	21.9	4.6
650	0.002604	0.001986	0.000050	0.660212	5.348385	53.3	2.9	87.17	15.58	142.9	55.5
700	0.002407	0.000863	0.000445	0.345457	2.605756	49.6	4.9	78.34	8.15	172.1	74.6
750	0.000197	0.000941	0.000772	0.896760	7.661835	56.1	3.9	98.94	21.16	409.6	181.0
800	0.000005	0.000458	0.000349	0.312947	2.528495	53.1	3.3	99.62	7.38	293.7	122.6
850	0.000052	0.000341	0.000180	0.154853	1.189227	50.5	2.7	98.40	3.65	195.3	76.8

Continues on following page

Table 5.4: $^{40}\text{Ar}/^{39}\text{Ar}$ furnace step release data for biotite separates ($J = 0.00369$)

Step T (°C)	$^{36}\text{Ar(a)}$ volt	$^{37}\text{Ar(cl)}$ volt	$^{38}\text{Ar(cl)}$ volt	$^{39}\text{Ar(k)}$ volt	$^{40}\text{Ar(r)}$ volt	Age (Ma)	$\pm 2\sigma$ (Ma)	$^{40}\text{Ar(r)}$ (%)	$^{39}\text{Ar(k)}$ (%)	K/Ca	$\pm 2\sigma$
900	0.000172	0.000331	0.000110	0.147474	1.190327	53.1	3.1	95.60	3.48	191.4	113.7
930	0.000325	0.000579	0.000001	0.157750	1.179726	49.2	2.0	92.17	3.72	117.1	37.0
960	0.000158	0.000397	0.000219	0.213660	1.842167	56.6	3.9	97.24	5.04	231.6	73.8
990	0.000027	0.000327	0.000242	0.272621	2.147673	51.8	4.0	99.30	6.43	358.8	139.7
1030	0.000099	0.000671	0.000459	0.331651	2.522213	50.0	2.3	98.51	7.83	212.4	90.1
1060	0.000277	0.000866	0.000267	0.279927	1.968230	46.3	1.5	95.66	6.61	139.1	24.6
1100	0.000170	0.001464	0.000062	0.265356	1.837442	45.6	1.4	96.98	6.26	77.9	8.7
1150	0.000266	0.001500	0.000040	0.023064	0.188214	53.6	8.6	70.35	0.54	6.6	1.3
1200	0.000021	0.001033	0.000006	0.007184	0.078348	71.3	21.2	92.39	0.17	3.0	0.8
1350	0.000129	0.002395	0.000002	0.005434	0.066050	79.3	22.1	63.31	0.13	1.0	0.2
Loc4											
600	0.000861	0.001938	0.000163	0.159536	1.354527	55.8	4.6	83.96	3.69	35.4	9.1
650	0.000915	0.000922	0.000168	0.447001	3.241199	47.7	1.3	91.99	10.34	208.4	57.8
700	0.001910	0.001575	0.000907	0.566434	5.683338	65.7	5.2	90.75	13.10	154.6	62.2
750	0.000100	0.000656	0.000280	0.560497	4.191489	49.2	2.4	98.95	12.96	367.3	194.9
800	0.000296	0.000463	0.000269	0.300249	2.122773	46.6	1.7	95.70	6.95	278.7	101.4
850	0.000168	0.000260	0.000285	0.239281	1.688684	46.5	2.7	96.79	5.53	395.0	158.8
900	0.000009	0.000101	0.000290	0.193586	1.508683	51.3	3.7	99.84	4.48	824.1	846.3
930	0.000786	0.000464	0.000070	0.194315	1.432955	48.5	3.7	85.79	4.49	180.2	59.6
960	0.000281	0.000255	0.000127	0.274255	2.048068	49.2	2.9	95.78	6.34	463.0	199.1
990	0.000408	0.000225	0.000301	0.331683	2.441769	48.5	2.3	94.97	7.67	633.0	228.0
1030	0.000423	0.000492	0.000109	0.421101	2.962877	46.4	1.6	95.60	9.74	368.3	71.2
1060	0.000249	0.000492	0.002868	0.054850	0.109421	-13.4	10.6	318.83	1.27	48.0	35.7
1100	0.000111	0.000370	0.000196	0.348259	2.483878	47.0	1.7	98.33	8.06	404.5	119.4
1150	0.000172	0.001508	0.000053	0.206201	1.455335	46.5	2.0	96.27	4.77	58.8	10.3
1200	0.000051	0.001469	0.000019	0.013737	0.106889	51.2	8.7	87.42	0.32	4.0	0.7
1350	0.000306	0.001619	0.000060	0.012225	0.051297	27.8	13.7	36.14	0.28	3.2	0.4
N9											
600	0.001671	0.003281	0.000103	0.147253	0.335835	15.2	4.1	40.29	2.96	19.3	4.8
650	0.004608	0.002532	0.000054	0.367574	1.122919	20.3	4.1	45.02	7.38	62.4	10.5
700	0.005669	0.003617	0.000101	0.512579	1.454734	18.8	4.7	46.28	10.29	60.9	9.9
750	0.000415	0.001755	0.000184	0.712370	1.703659	15.9	0.6	92.33	14.30	174.5	32.4
800	0.000390	0.001258	0.000111	0.485050	1.096084	15.0	0.7	89.52	9.74	165.8	28.9
850	0.000441	0.001509	0.000210	0.450064	1.071084	15.8	1.0	88.26	9.04	128.3	24.8
900	0.000277	0.001137	0.000554	0.331297	0.802437	16.1	1.0	89.85	6.65	125.3	39.7
930	0.000175	0.001106	0.000178	0.330826	0.791427	15.9	1.1	92.91	6.64	128.7	26.7
960	0.000252	0.000693	0.000485	0.356395	0.871763	16.2	1.1	91.21	7.16	221.2	95.1
990	0.000025	0.000451	0.000162	0.320333	0.915082	19.0	1.3	98.29	6.43	305.3	161.6
1030	0.000001	0.000567	0.000122	0.215201	0.802902	24.7	13.6	99.24	4.32	163.2	130.9
1060	0.000021	0.000896	0.000269	0.259578	0.753061	19.3	1.8	98.30	5.21	124.5	56.3
1100	0.000209	0.001964	0.000385	0.285287	0.745357	17.3	0.9	91.48	5.73	62.5	12.8
1150	0.000087	0.003425	0.000132	0.128002	0.352808	18.3	1.7	92.40	2.57	16.1	4.4
1200	0.000090	0.002599	0.000011	0.048584	0.137796	18.8	2.4	83.12	0.98	8.0	1.9
1350	0.000045	0.001180	0.000073	0.030114	0.170465	37.4	8.5	92.32	0.60	11.0	5.9

Table 5.5: Rb/Sr isotope data

Sample		Rb (ppm)	Sr (ppm)	$^{87}\text{Rb}/^{86}\text{Sr}$	$^{87}\text{Sr}/^{86}\text{Sr}$	$\pm 2\sigma$	Age (Ma)	$\pm 2\sigma$
B40	wr	144	305	1.364	0.707590	0.000006	50.3	0.5
B40	bi	305	3.52	254.6	0.888406	0.000009		
KB1a	wr	72.3	340	0.616	0.706945	0.000004	49.9	0.5
KB1a	bi	288	4.58	184.6	0.837453	0.000008		
KB5	wr	98.2	343	0.828	0.706934	0.000004	48.6	0.5
KB5	bi	330	3.33	292.0	0.908092	0.000012		
T11	wr	71.1	361	0.571	0.706721	0.000004	49.4	0.5
T11	bi	304	5.36	165.8	0.822514	0.000007		
T40	wr	57.6	397	0.420	0.706688	0.000009	48.5	0.5
T40	bi	297	2.28	386.9	0.973026	0.000068		
LOC4	wr	77.7	251	0.896	0.706945	0.000006	48.9	0.5
LOC4	bi	284	4.00	208.5	0.851165	0.000078		
N9	wr	43.4	352	0.357	0.706355	0.000005	14.9	0.2
N9	bi	372	3.29	329.6	0.775858	0.000065		
N48	wr	72.3	303	0.691	0.706418	0.000012	14.9	0.2
N48	bi	279.3	3.79	214.4	0.751613	0.000042		

Table 5.6: Zircon fission track data

Nr.	Nr. of grains	ρd * 10^6 cm^{-2}	Nd	ρs * 10^6 cm^{-2}	Ns	ρi * 10^6 cm^{-2}	Ni	$P(\chi^2)$ (%)	U (ppm)	Central age (Ma)	Error (2σ)
B21	17	4.82	4798	45.134	1012	61.502	1379	39	500 \pm 265	28.1	\pm 2.8
Loc4	20	4.83	4798	34.636	842	51.049	1241	100	382 \pm 202	26.0	\pm 2.8
T40	20	4.82	4798	57.601	1879	76.331	2490	98	508 \pm 81	28.9	\pm 2.4
91ASn11	2	4.82	4798	2.936	98	3.625	121	16	23 \pm 3	30.9	\pm 8.6

Chapter 6

Conclusions

The Chugach Metamorphic Complex (CMC) of southern Alaska is a large-scale, short-lived metamorphic complex which developed in the fore-arc of an active subduction zone shortly after the accretion of large amounts of sediments to this convergent margin. Structural fieldwork, coupled with a range of different geochronological methods allowed to constrain the spatial and temporal evolution of this complex in more detail. The main results of this thesis and a comparison with previous results are summarized in this chapter.

6.1 Large-scale three-dimensional geometry of the complex

The geometry of the CMC was first described in a reconnaissance study by Hudson & Plafker (1982). They described the complex between the Copper River in the west and the U.S. Canadian border in the east as consisting of an inner high-grade gneiss zone surrounded by an outer schist zone. Contrary to the map of Hudson & Plafker (1982), no schist zone was encountered to the south of the gneiss zone along the two transects mapped during this study in the western and central parts of the complex. According to the results of this thesis, the southern border of the CMC is controlled by steeply north-dipping, semi-brittle to brittle shear zones and fault zones with north-side up and dextral sense of movement. The results of this thesis reveal a strong asymmetry of the western and central parts of the CMC with a wide transition from phyllites to gneisses in the north and an abrupt, fault-bounded juxtaposition of gneisses against phyllites in the south.

Pavlis & Sisson (1995, 2003) studied the transition from the northern phyllite zone to the gneiss zone in the central part of the complex as well as the termination of the complex towards the west. They described three different fabrics, D_1 - D_3 , which control the internal geometry of the complex. The presence of these three fabrics was confirmed during this study. D_1 is dominant in the phyllite zone outside of the complex, D_2 becomes dominant in the southern part of the schist zone and the entire gneiss zone and D_3 is heterogeneously

developed throughout the schist and gneiss zone. D_3 defines a foliation fan in the gneiss zone, with south-dipping foliation planes in the north and north-dipping planes in the south. D_3 is most intensely developed along the southern border of the complex, where the associated ductile stretching lineation is plunging towards the west/northwest, in contrast to the subhorizontal stretching lineation farther north.

The extension of the metamorphic rocks of the CMC towards the south-east was never addressed during previous studies. Rocks belonging to the gneiss zone of the CMC disappear below the extensive Seward glacier east of the U.S. Canadian border. A narrow strip of Chugach terrane rocks extends from this highly-glaciated region south-eastwards to Baranof Island. During this study, a transect was mapped across this narrow strip where the rocks are accessible along the extension of the Nunatak fjord. The metamorphic grade of these rocks is similar to the gneiss zone farther west, the structural geometry is similar with a flat-lying (D_2) fabric and a steep (D_3) fabric, and the metamorphic peak age is identical, suggesting that the metamorphic rocks of the CMC continue around the bend in strike of the Chugach terrane below Seward glacier at least as south-eastward as Nunatak fjord. A study from Baranof Island derived similar metamorphic conditions as we derived for the gneiss zone of the CMC (Zumsteg et al., 2003), but whether the rocks between Nunatak fjord and Baranof Island show continuously a relatively high metamorphic grade is not known.

6.2 Temporal evolution of the complex: rates of tectonic and thermal processes

The temporal evolution of the CMC was so far constrained by (a) the biostratigraphic Late Cretaceous age of sedimentary rocks exposed along-strike of the complex (e.g. Plafker et al., 1994) and (b) limited K/Ar and $^{40}\text{Ar}/^{39}\text{Ar}$ cooling ages of metamorphic and magmatic rocks of the complex (Hudson et al., 1977b, 1979; Sisson et al., 1989; Bradley et al., 1993; Sisson et al., 2003). K/Ar and $^{40}\text{Ar}/^{39}\text{Ar}$ cooling ages of hornblende and biotite from the western and central part of the complex are predominantly ~53-47 Ma, suggesting an Early Eocene age of metamorphism (Hudson et al., 1979; Sisson et al., 1989; Bradley et al., 1993). K/Ar and $^{40}\text{Ar}/^{39}\text{Ar}$ cooling ages of hornblende and biotite from magmatic rocks exposed in the narrow strip of the Chugach terrane between Seward glacier and Baranof Island scatter more widely and are as young as ~18 Ma (Hudson et al., 1977b; Bradley et al., 1993; Sisson et al., 1989), either suggesting a younger metamorphic peak age or a different cooling history compared to the western and central parts of the complex.

The geochronological results obtained during this study allow constraining the temporal evolution of the complex in more detail. Firstly, the depositional age of the sediments in which the complex developed was determined by LA-ICP-MS dating of detrital zircon populations. The depositional ages are ~60-65 Ma for three samples, suggesting a Paleocene depositional age for these parts of the complex, and ~75 Ma for one sample from the deepest

part of the complex, suggesting that Late Cretaceous rocks build up lower parts of the complex. Secondly, the age of peak metamorphism is constrained by the first U-Pb SHRIMP ages of metamorphic zircons and monazites available for the complex to ~55-51 Ma. The only zircon age available for the south-eastern part of the complex is within error of two of seven zircon ages and three of four monazite ages from the western and central parts of the complex, suggesting that the peak metamorphic conditions were reached simultaneously at least ~350 km along strike. Thirdly, the cooling history of the complex is constrained by $^{40}\text{Ar}/^{39}\text{Ar}$ muscovite and biotite dating, Rb/Sr isochron dating and zircon fission track dating for different parts of the complex. Cooling ages for the western and central parts of the complex are relatively old (~50-25 Ma for the different systems), whereas cooling ages for the south-eastern part of the complex are relatively young (~35-15 Ma for the different systems).

Based on these newly obtained geochronological data, thermal and tectonic rates can be calculated. Assuming a starting temperature of the sediments of 20°C at the time of deposition at ~60-65 Ma, and a peak temperature of ~650-700°C derived from thermometry at the metamorphic peak at ~55-52 Ma, heating rates of ~60-140°C/Ma result. Similarly, assuming no burial at time of deposition, and ~15-50 km burial at the metamorphic peak derived from barometry, burial rates of ~1-10 mm/a result. Cooling rates are different for the western/central and the south-eastern part of the complex, respectively. In the western and central parts, cooling ages result in cooling rates of ~30-180°C/Ma shortly after the peak followed by much slower cooling of ~10-20°C/Ma. Cooling ages from the south-eastern part of the complex result in slow, regular cooling rates of ~6-10°C/Ma for most of its cooling history, followed by ~20-40°C/Ma during the last ~5-10 Ma. Exhumation rates are more difficult to constrain. Assuming that the slow regular cooling of the south-eastern section also corresponds to exhumation and that the distribution of isotherms did not change after the metamorphic peak, exhumation rates of ~0.3-0.5 mm/a can be calculated for the first ~40-45 Ma of cooling followed by higher exhumation rates of ~1-2 mm/a during the last ~5-10 Ma. The situation is more complex for the western and central parts of the CMC, since maximum burial depths derived from barometry vary more widely and therefore differential exhumation must have occurred. For the schist zone and parts of the gneiss zone with moderate burial depths, the fast cooling reported shortly after the metamorphic peak could simply represent passive cooling without exhumation due to the relaxation of isotherms after an elevated geothermal gradient. However, the large burial depths derived for parts of the gneiss zone implicate that the fast cooling must have been accompanied by exhumation, which probably was very fast, too.

6.3 Tectonic interpretation: Is a subducting ridge needed?

The structural and geochronological data derived during this thesis have implications for the tectonic interpretation of the complex in a regional context. The presence of andalusite-sillimanite-grade metamorphism in an accretionary prism in the fore-arc of a subduction zone has been attributed by many workers to the subduction of an oceanic spreading ridge below the margin, which acted as an additional heat source for the metamorphism (e.g. Marshak & Karig, 1977; Bradley et al., 1993, 2003; Sisson et al., 1989; Sisson & Pavlis, 1993; Pavlis & Sisson, 1995, 2003; Häussler et al., 1995, 2003a; Madsen et al., 2006; Farris & Paterson, 2009). This interpretation is based on the presence, age distribution and geochemical composition of the Sanak-Baranof plutonic belt in the fore-arc and the low-pressure estimates for the CMC of Sisson et al. (1989; ~2-3 kbar). The Paleocene-Eocene history of southern Alaska has even been increasingly cited as representing the most spectacular ancient example of a ridge subduction event (e.g. Farris & Paterson, 2009). However, results of this thesis and results of the thesis of Bruand (2010) suggest that this model may need to be modified. Several points are exemplarily discussed below.

(1) Age gradient The west-east age gradient which is reported for the Sanak-Baranof intrusions has been interpreted as tracking the location of the subducting ridge from west to east, with a mean migration rate of ~19 cm/a (Farris & Paterson, 2009). U/Pb, $^{40}\text{Ar}/^{39}\text{Ar}$, Rb/Sr and K/Ar ages have been used to define this age trend (e.g. Bradley et al., 1993, 2000, 2003). However, the results of this study show that $^{40}\text{Ar}/^{39}\text{Ar}$, Rb/Sr and K/Ar ages are cooling ages and can be considerably younger than the metamorphic peak / initial crystallization of magmatic rocks. Therefore, only U/Pb ages should be used to study potential age gradients from west to east since these ages are closest to the metamorphic peak / initial crystallization of magmatic rocks and are comparable with each other. An analysis of all available U/Pb ages for the Sanak-Baranof belt including our newly obtained monazite and zircon U/Pb ages reveals that the age gradient is not continuous, but is characterized by sections ~200-400 km wide on which magmatism and metamorphism was coeval. Therefore, if plutonism occurred simultaneously at places ~200-400 km separated from each other, then either several ridges were present, or the ridge moved so fast that the age differences between the plutons are below the resolution of the dating methods, or the ridge might have subducted parallel to the margin. This last possibility is implemented in the models of Häussler et al. (2003a) and Madsen et al. (2006) at least for the eastern part of the belt, where the ridge between the Resurrection and Kula plates is thought to have subducted parallel to the margin.

(2) Fast cooling rates Thermal modelling of the effect of ridge subduction below a margin showed that depending on the migration rate of the subducting ridge parallel to the margin, heating can be relatively fast in the order of a few million years, but cooling generally

occurs over longer time periods due to long thermal decay times along the trailing edge of the slab window (Groome & Thorkelson, 2009). The fast cooling observed at depths of 20-50 km in the western and central parts of the CMC is difficult to explain by fast quenching from below after the passage of a subducting ridge, since such a ridge is bordered by young and hot oceanic lithosphere. Moreover, if the ridge subducted parallel to the margin as indicated by the coeval peak metamorphic ages, it is even more difficult to quickly remove the subducting heat source in order to produce the fast cooling observed after the metamorphic peak. Therefore, the fast cooling rates reported shortly after the metamorphic peak in the western and central parts of the complex are difficult to explain with the model of a subducting ridge below the margin.

(3) Which ridge? One of the drawbacks of the ridge subduction model is the uncertainty about which ridge actually subducted below the margin. Plate tectonic reconstructions based on the magnetic record preserved on the Pacific plate show the presence of three oceanic plates in the Pacific basin during the Paleocene-Eocene: the Kula, Farallon and Pacific plates (e.g. Engebretson et al., 1985; Atwater, 1989; Doubrovine & Tarduno, 2008). The ridge between the Kula and Farallon plates probably intersected the North American margin somewhere between Northern California and British Columbia - an intersection as north as the present location of the Sanak-Baranof belt is unlikely (Doubrovine & Tarduno, 2008). Therefore, there are three possible interpretations for the formation of the Sanak-Baranof belt and the CMC in this context: (a) the entire belt was farther to the south during magmatism and metamorphism, somewhere in the region of Vancouver Island, and the magmatic belt is the result of the intersection with the Kula-Farallon spreading ridge (e.g. Cowan, 2003), (b) the belt was already in its present location during intrusion and metamorphism, and the metamorphic and magmatic event was caused by a spreading ridge between the Kula plate and an additional oceanic plate, which is since then completely subducted (the Resurrection plate, e.g. Häussler et al., 2003a; Madsen et al., 2006), or (c) the magmatic and metamorphic events are not related to the subduction of a spreading ridge but are due to a combination of the geometry of the margin and the relative plate motions between the oceanic plates and the continental margin which led to alternating oblique convergence and divergence.

(4) Alternative model The last possibility from above might be supported by the higher pressure estimates and the structural record reported in Bruand (2010) and this study: the pressure estimates derived by Bruand (2010) for the three transects studied in this thesis are constantly higher than the pressure estimates derived earlier by Sisson et al. (1989) for the northern and western parts of the complex. Given these higher pressure estimates, the metamorphic grade observed is not that unusual and similar to other metamorphic complexes exposed in different parts of the world where no ridge subduction was inferred. In addition, if combined with the structural record, the metamorphic conditions observed might be explained by the following scenario: (1) accretion of large amounts of sediments which

led to relatively high initial geothermal gradients in the accretionary prism, (2) followed by vertical flattening and margin-parallel stretching related to changing boundary conditions leading to compression of isotherms and the onset of andalusite-sillimanite-grade metamorphism, (3) followed by renewed dextral transpression which led, aided by erosion at the surface, to fast cooling and partial exhumation of parts of the gneiss zone. In this scenario, the subduction of a spreading ridge below the complex is not required and the metamorphism is the result of a vertical thinning event which affected the margin.

Given the uncertainties which accompany the ridge subduction model, and given the new thermobarometric, structural and geochronological data, the subduction of a ridge below the Alaskan margin is probably only one of different possible explanations for the tectonic history of the margin, and has, as other models alike, its pitfalls and drawbacks. Therefore, it should be continuously tested against newly emerging field and laboratory data and alternative options should be continuously evaluated as well.

6.4 Outlook

Understanding the tectonic evolution of a complex region such as the southern Alaskan margin probably never comes to an end. In the following, a loose collection of open questions and regional problems is given which is meant to provide the reader possible input for further work.

(1) The metamorphic pressures obtained for rocks from the south-eastern transect along Nunatak fjord belong to the highest pressures reported for the CMC so far (Bruand, 2010). However, the extension of these higher-pressure rocks towards the south-east is unknown. Especially the metamorphic conditions exposed in the Fairweather corridor would be of interest, since large-scale gabbroic bodies intrude these rocks (Loney & Himmelberg, 1983). Neither the metamorphic grade of the country rocks of the plutons nor the age of the gabbroic intrusions is known. Studying structural and metamorphic variations in this narrow corridor of Chugach terrane rocks may give indications on the behaviour of this oblique transpressional orogen.

(2) The metamorphic conditions and temporal evolution of the tectonic slivers present to the south/south-west of the CMC (Boundary block, Mt. Steller-St. Elias ridge) are not constrained at all. Metamorphic grade seems to increase from west to east/north-west to south-east, but neither the exact values nor the timing of burial and exhumation are known. Understanding the evolution of these blocks would help constraining the deformational history of the large-scale Fairweather-Contact fault system, and would reveal the bedrock history of the second highest peak of the United States: Mt St Elias.

(3) The region covered by the Seward glacier, where the strike of the CMC turns from

E-W to NW-SE, has recently revealed zircon fission track ages younger than ~3 Ma (e.g. Enkelmann et al., 2009), indicating that considerable exhumation of rocks occurred below Seward glacier during the last 5 Ma. The maximum pressures experienced by the metamorphic rocks of the CMC increase from west to east (Bruand, 2010), suggesting that the highest pressures might have been recorded by rocks underlying the Seward glacier. It therefore would be interesting to derive thermobarometric data from rocks exposed as small nunataks sticking out of Seward glacier.

(4) Whereas concordant U/Pb ages from the western Sanak-Baranof belt are available (Sanak Island to Kodiak Island, Bradley et al., 2000; Farris et al., 2006), and concordant U/Pb ages from the eastern belt were presented in this thesis, concordant U/Pb ages from the magmatic rocks in Prince William Sound are lacking. This is important, since it has been suggested earlier (e.g. Hudson et al., 1979) that the belt may consist of an older western segment, and a younger eastern segment. Indeed, the concordant ages from the western belt are ~61-59 Ma, whereas the concordant ages from the eastern belt are ~55-50 Ma. Obtaining concordant ages from the plutons in between would reveal whether they belong to one of the two groups or whether they lie in between.

(5) The magmatism of the Sanak-Baranof plutonic belt is always cited as representing fore-arc magmatism relative to a 'real' magmatic arc located farther inboard. Depending on where the Sanak-Baranof belt was located along the margin during the magmatic event, either the Coast Plutonic Belt of British Columbia or the Alaska-Range belt of west-central Alaska are referred to as representing the contemporaneous real magmatic arc. Whereas for the Coast Plutonic Belt a large amount of geochronological data exists (e.g. Gehrels et al., 2009), a modern compilation of age information from the Alaska Range belt is lacking. Such a compilation would be needed in order to evaluate the synchronicity of magmatism in the Sanak-Baranof and Alaska Range belts.

APPENDICES

Appendix A

Tectonic and metamorphic evolution of the Chugach Metamorphic Complex, Alaska: A progress report

Abstract In this contribution we present a progress report of a research project conducted by the authors in the framework of two PhD theses at the Department of Earth Sciences at the University of Graz. In this project, the tectonic and metamorphic evolution of a metamorphic complex is studied by combining different petrological and geochronological approaches. First petrological results constrain the metamorphic conditions in the core to 600-700°C / 4-9 kbar and to <550°C in the outer part of the complex. First geochronological results are expected to be obtained in late 2009. The results will be used to formulate and constrain a geodynamic model for the evolution of this metamorphic complex.

published as: Gasser, D., Bruand, E. (2009) Tectonic and metamorphic evolution of the Chugach Metamorphic Complex, Alaska: A progress report. Erstausgabe, Veröffentlichungen junger WissenschaftlerInnen der Universität Graz, 149-158.

A.1 Introduction

Sediments deposited on the surface of the Earth undergo various processes that change their mineralogical and chemical composition as well as their structure when they are buried and heated up in diverse tectonic settings. These processes are generally summarized under the term “metamorphism” (e.g. Bucher & Frey, 2002). To observe such metamorphic rocks at the Earth’s surface, they have to be exhumed from depth after a metamorphic event. The exact physical conditions (pressure and temperature) and timing of both metamorphism and exhumation events puzzles geologists since the beginning of geological science and understanding them needs a strong co-operation between different sub-fields of geology such as petrology, tectonics and geochronology (e.g. Stuewe, 2007).

In this contribution we present a progress report of two PhD theses conducted by the authors at the department of Earth Science at the University of Graz under the supervision of Prof. Kurt Stüwe. In this project we try to quantify physical conditions and timing of both metamorphism and exhumation of a naturally occurring metamorphic complex in south-eastern Alaska. The project started in October 2007 and is funded by FWF project Nr. 19366-N10 for a period of three years.

A.2 Geological Setting and Project Aims

The Chugach Metamorphic Complex (CMC) is a ~370 km long and ~10-50 km wide zone of metamorphic rocks exposed in the Chugach Mountains in south-eastern Alaska (Hudson & Plafker, 1982, Figs. A.1 and A.2). It developed in meta-sedimentary rocks of the Chugach terrane, which mainly consists of greenschist-facies sandstones, slates and minor basalts of the Valdez group (Nilsen & Zuffa, 1982). The Chugach terrane is bordered by the Border Ranges Fault in the north and the Contact fault in the south, which are both long-lived, complex fault zones with compressional and dextral strike-slip components (Pavlis & Roeske, 2007). The Chugach terrane is part of a group of similar terranes that have all been subsequently accreted to North America in a subduction zone context (eg. Wrangellia, Chugach, Prince William and Yakutat terranes; Fig. A.1). The Yakutat terrane still actively collides with the Prince William and Chugach terranes in the south-eastern corner of Alaska (Fig. A.1; Berger et al., 2008a). The subduction and collision of this terrane leads to active volcanism in the Wrangellia terrane and to the creation of major topography and intense glaciation in the Chugach-St. Elias Mountains (Figs. A.1, A.2 and A.3a).

The CMC itself consists of an outer schist zone of lower amphibolite facies grade and an inner gneiss zone of upper amphibolite facies grade including migmatites that are surrounded by lower grade phyllites (Fig. A.2). Numerous plutonic bodies from few meter to several kilometer size cross-cut both the schist and gneiss zones. The complex is not symmetric in

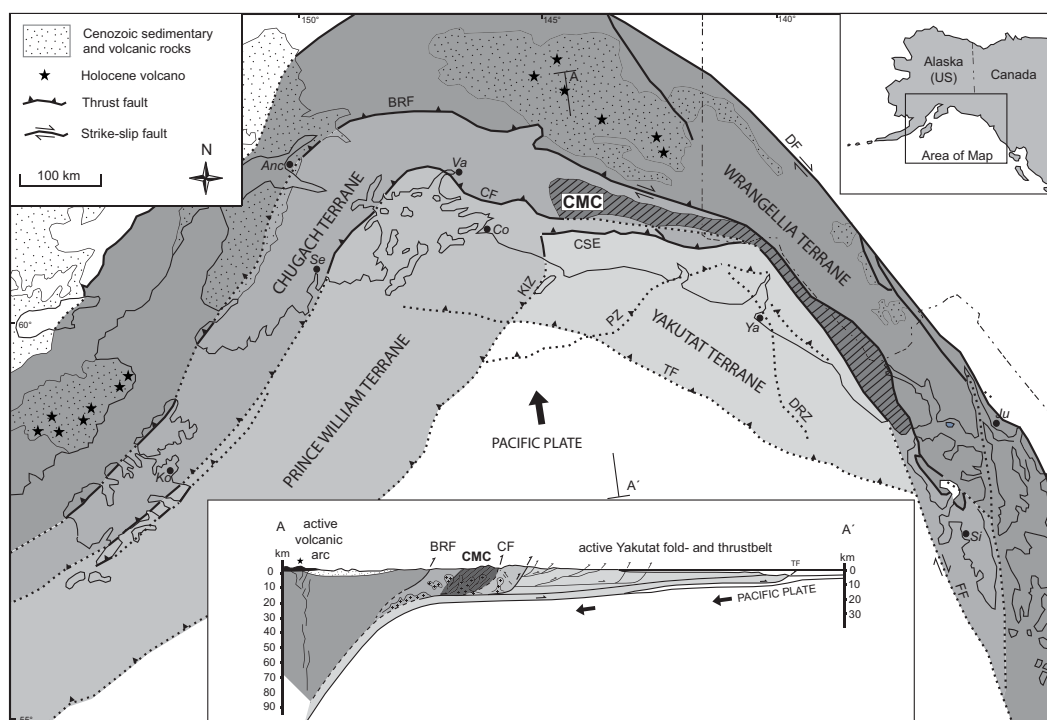


Figure A.1: Tectonic overview map and cross-section of southern Alaska. Abbreviations: TF transition fault, PZ Pamplona zone, KIZ Kayak Island Zone, DRZ Dangerous River Zone, CSE Chugach St Elias Fault, CF Contact Fault, FF Fairweather Fault, BRF Border Ranges Fault, DF Denali Fault.

N-S and E-W direction: it has a much wider schist zone in the north than in the south and gets much narrower from east to west (Fig. A.2).

Due to the rugged topography, high glaciation and inaccessibility of the Chugach-St. Elias mountains, the geology of the CMC is not well known (Fig. A.3a). It was first described by Hudson & Plafker (1982) and was subsequently studied locally by Sisson et al. (1989), Sisson & Pavlis (1993), Pavlis & Sisson (1995), Harris et al. (1996) and Pavlis & Sisson (2003). Despite these local studies, an integrated understanding of the physical conditions and the exact timing of metamorphism in the whole metamorphic complex is lacking. This is insofar important as the CMC is (a) located in an unusual geodynamic setting close to an active subduction zone where normally no metamorphism from the type of the CMC is expected and (b) has a peculiar asymmetric shape that allows studying the metamorphic conditions in areas of different width of the metamorphic zone.

In order to obtain integrated petrological and geochronological informations over the whole complex, our project uses the following approach. In a first step, extensive field work was carried out in selected key areas covering the most important areas of the whole complex (Fig. A.2, black boxes). In a second step, the project is separated in two parts, whereof each

part corresponds to one PhD thesis. The first thesis tries to answer the question: “What are the metamorphic pressure and temperature conditions reached in the CMC from N to S and from E to W?” by combining modern petrological and geochemical analyses using different techniques (electron microprobe, raman spectrometer, XRF) and petrological computer modelling. The second thesis works on the question: “What is the exact timing of heating, peak metamorphism and cooling reached in the CMC from N to S and from E to W?” by applying different radiometric decay systems in minerals to date different geological events in the whole complex. In a third part, the information obtained during the previous two steps is combined in order to construct a coherent geodynamic model that describes the tectonic and metamorphic evolution of the CMC. From this model, geodynamic parameters such as heating and cooling rates and metamorphic field gradients will be extracted.

In the sections below, we describe the actual state of the project, first results and an outlook.

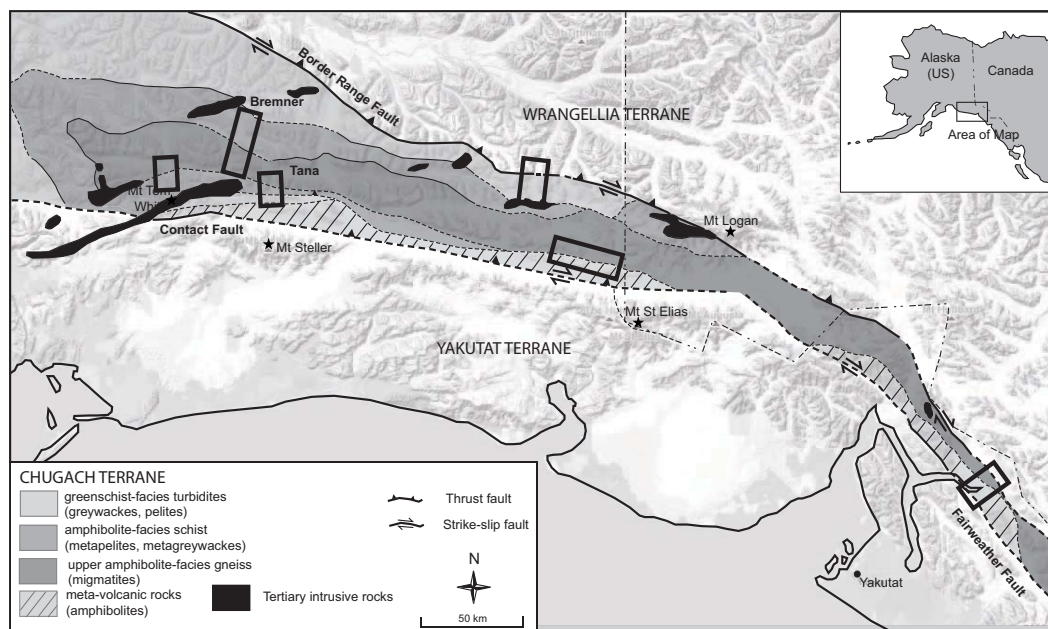


Figure A.2: Geological map of the Chugach Metamorphic Complex (CMC). Black quadrangles are the field areas visited during field seasons 2008 and 2009.

A.3 Field work

Apart from few local geological maps, the only regional geological map available from the CMC is a reconnaissance map at the scale 1:250 000. In order to get more detailed but still regional information on the CMC, seven weeks of field work were conducted in summer 2008 and three weeks of field work in summer 2009. We chose six different areas

covering key localities of the CMC in order to get information from the western, central, eastern, northern and southern parts of the CMC (Fig. A.2). The field areas were only accessible by small bush air planes, and during the 6-10 days camps we stayed in tents on glaciers or moraines. We mapped each field area at the scale of 1:10 000 and collected a total of 182 rock samples in the first field season. The rock types encountered include (a) low-grade phyllites, sandstones and conglomerates (Fig A.3b), (b) greenschists, (c) low- to middle-grade biotite- and andalusite-bearing schists, (d) middle-grade biotite-, garnet-, and/or sillimanite-bearing schists, (e) high-grade biotite-, garnet- and/or sillimanite- and Kfeldspar-bearing (partly migmatitic) gneisses (Fig A.3c), (f) high-grade amphibolites, and (g) magmatic rocks such as granite, tonalite and diorite. The structures observed are (a) a first, low-grade S_1 foliation and corresponding folds in the low-grade phyllites, (b) a second, penetrative, higher-grade flat-lying S_2 foliation in the middle-grade schists, and (c) a steeply dipping, penetrative, high-grade S_3 foliation in the central gneiss zone, that corresponds to a less penetrative steep-dipping S_3 foliation in the schist zone. Lineations on all three foliations are E-W striking and horizontal to shallow-dipping. We summarized all information from the field work on sketches, field maps, cross-sections and stereoplots of structural data from each field area.

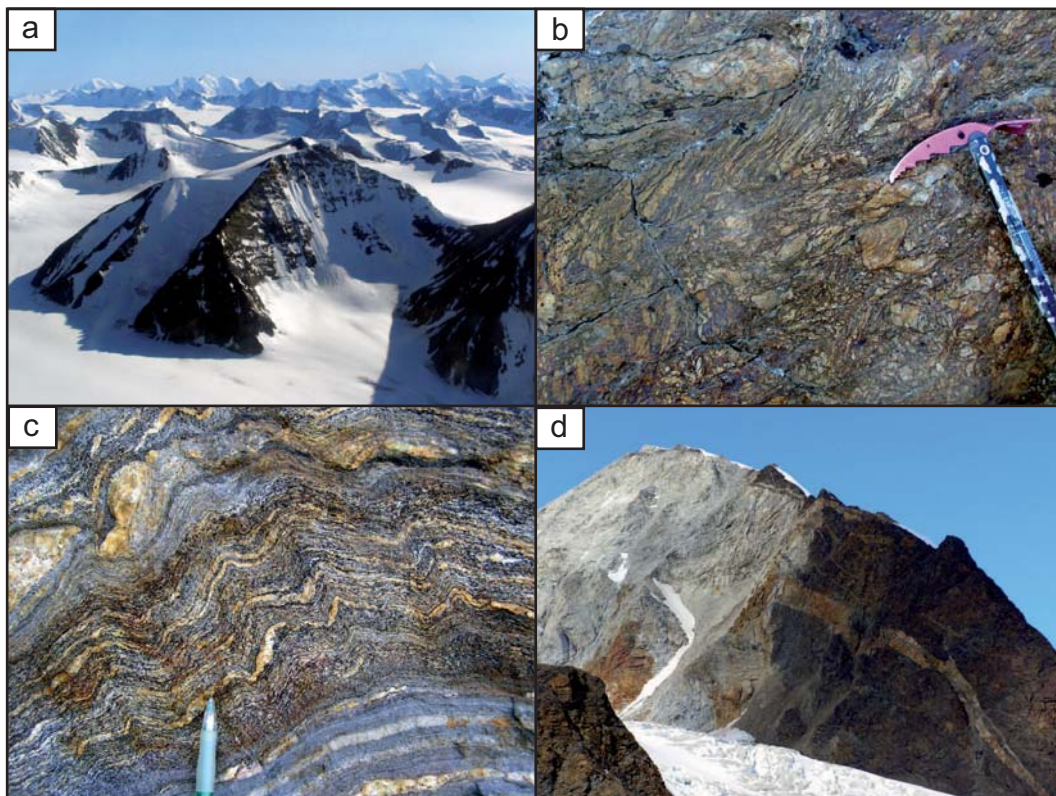


Figure A.3: (a) The highly glaciated eastern Chugach mountains where the CMC is exposed. (b) folded low-grade conglomerate. (c) high-grade folded and foliated gneiss (d) Plutonic rock (white) intruding sedimentary rock (dark).

A.4 Pressure and temperature conditions of metamorphism

In order to constrain the pressure and temperature of peak metamorphism, the mineralogical assemblages and chemical compositions of mineral phases of each rock sample collected during field work are studied in detail. Thin sections of rock slices are investigated both with optical and electron microscopy in order to identify all mineral phases present and to measure their exact chemical composition. With the help of several experimentally calibrated thermometers and geobarometers, we calculated the temperatures and pressures present at the time of mineral crystallization at the metamorphic peak. First temperature results calculated by a biotite-garnet thermometer (Kaneko, 2006) are ~600-650°C in the schist zone and ~650-700°C in the inner gneiss zone (Fig. A.4). Temperatures and pressures calculated with the help of an internally consistent thermodynamic data set using the software THERMOCALC (Holland & Powell, 1998) give as well values of ~600-650°C and ~6.1-6.4 kbar for the schist zone and ~4.4-9.2 kbar for the gneiss zone (Fig. A.4). A trend of increasing pressure in the gneiss zone from W to E is observed as well as a slight increase in temperature from the schist to the gneiss zone. Temperature for greenschist facies rocks (phyllites) as well as for the entire CMC are calculated with the RSCM thermometer (Beysac et al., 2002) based on the crystallization degree of graphite measured by Raman spectroscopy. First results for the phyllites in the northern part of the complex give temperatures in the range of 520-550°C, and 430-450° for the phyllites in the southern part of the complex (Fig. A.4). At the moment of writing, those informations are combined on plots covering the whole CMC in order to better understand the spatial variations of these variables (e.g. Fig. A.4), and in order to densify the sample network where necessary. In addition, the chemical composition of the whole rocks is measured in order to study the influence of the composition of the rock on the mineral reactions occurring.

A.5 Geochronology

In order to constrain the age of peak metamorphism as well as the duration of heating and cooling, a series of radiogenic element decay systems is used to calculate both crystallization as well as cooling ages of certain minerals. In our project we concentrate on the following systems:

U/Th-Pb system in monazite: Monazite is a mineral that generally crystallizes during prograde metamorphism between 550-650°C depending on the bulk chemistry of the sample. Monazite incorporates both U and Th during crystallization, but no Pb. All Pb measured in a monazite crystal therefore results from the radiometric decay of U and Th. With the help of the decay constants and half-lives of these systems the age of crystallization of the monazite grain can be calculated (e.g. Williams et al., 2007).

U/Th-Pb in zircon: This method is based on the same radiometric decay systems as the one described above. The only difference is that the mineral zircon does not grow during prograde metamorphism, but generally during melting of the rocks above about 650-700°. Its age therefore is in general a good proxy for the timing of peak metamorphism (e.g. Rubatto et al., 2001).

$^{40}\text{Ar}/^{39}\text{Ar}$ dating of mica: The ^{40}K isotopes incorporated in micas such as biotite and muscovite decay to ^{40}Ar after crystallization of the mica. At high temperature, the produced ^{40}Ar diffuses out of the crystal and gets lost. However, below a certain temperature (the closing temperature) the ^{40}Ar gets trapped in the crystal structure of the mineral. The concentration of ^{40}Ar measured in a mica crystal is therefore a good proxy for the time at which the crystal cooled below the closure temperature of the system (e.g. ?).

Obtaining such geochronological ages is time-consuming due to the need of separating the datable minerals from their rock matrix (in the case of zircon and micas) or documenting them in detail in thin sections (in the case of monazites). Zircons and monazites are generally very small (10-100 μm) and not easy to handle. Furthermore, expensive mass spectrometers not available at the University of Graz are needed to measure the radiometric element concentrations in the samples. At the stage of writing, ~20 Ar-Ar samples, ~14 zircon samples and ~17 monazite samples are prepared for mass spectrometer analysis. The Ar-Ar samples will be measured by the first author at the geochronology laboratory of the University of Florida and the zircon samples at the sensitive-ion-microprobe (SHRIMP) at the Australian National University in Canberra in summer 2009. The monazite samples will be measured at the Electron microprobe facility at Montan University Leoben and the LA-ICPMS facility at University of Vienna in autumn 2009. Most age results are expected to be obtained in late 2009.

A.6 Outlook

The research project presented in this contribution combines different petrological and geochronological approaches in order to get an integrated interpretation of the tectonic and metamorphic evolution of a naturally occurring metamorphic complex. Half-way through the project, the logistically complex fieldwork, the basic petrological analyses and the mineral separation for geochronology are successfully conducted. In the remaining time, the petrological data will be used to calculate and interpret metamorphic field gradients using phase diagrams, the geochronological ages to calculate and interpret heating and cooling rates. Those informations will help to formulate and constrain geodynamic models to explain the tectonic and metamorphic evolution of the Chugach Metamorphic Complex.

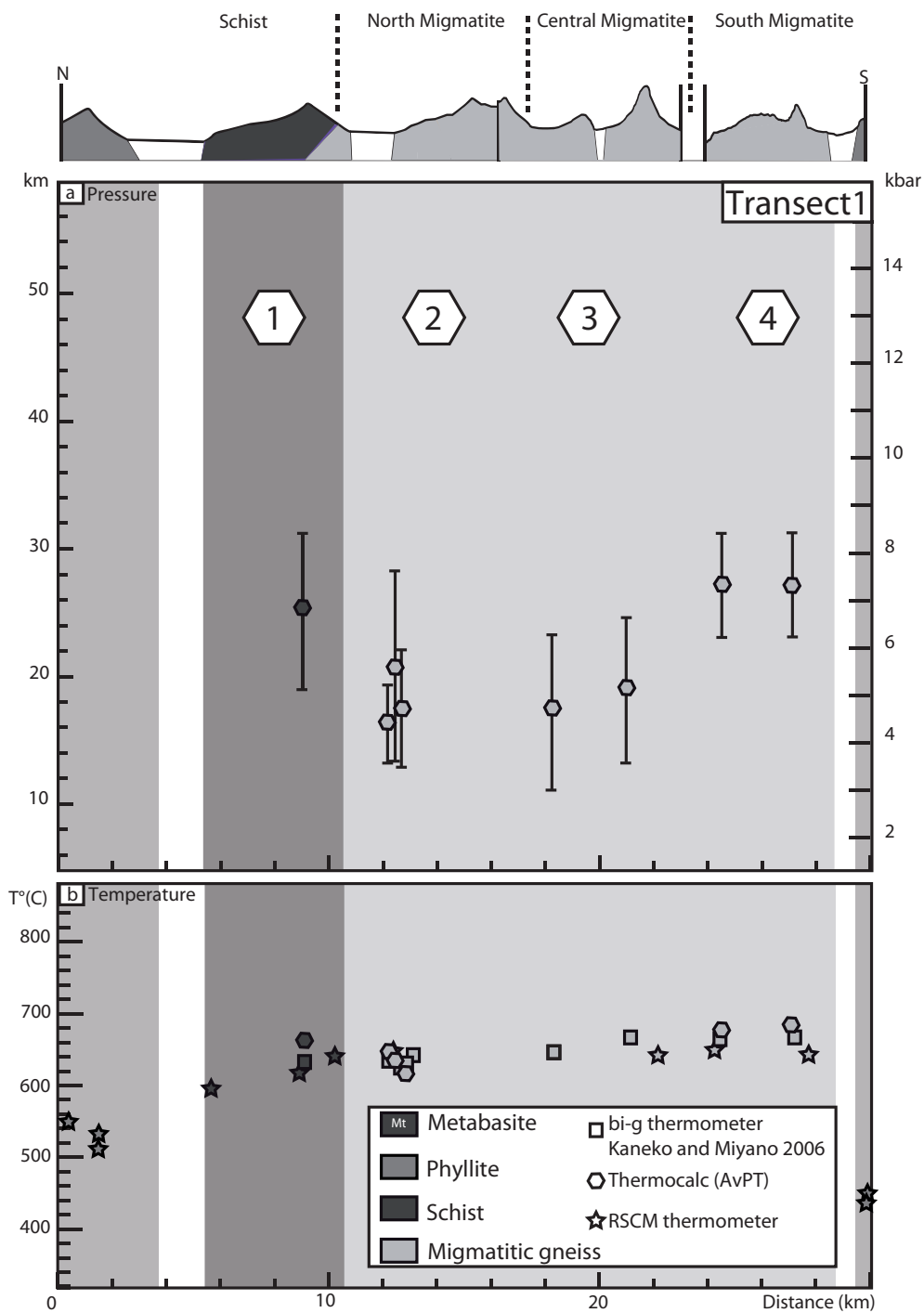


Figure A.4: First pressure-temperature results from Bremner and Tana transects (for location of the transects see Fig. 2). **(a)** Pressures obtained by Thermocalc modelling, **(b)** Temperatures obtained by three independent methods.

Appendix B

Conference abstracts related to this thesis

- Gasser, D., Stüwe, K. (2007) The Chugach Metamorphic Complex of southern Alaska: A test for wedge extrusion models? Geological Society of America Abstracts with Programs, Vol. 39, No. 6, p. 232.
- Gasser, D., Bruand, E., Stüwe, K. (2009) Exhumation of a metamorphic complex in a strike-slip setting: observations from the Chugach Metamorphic Complex (CMC), southern Alaska. Abstract Volume 7th Swiss Geoscience Meeting, Neuchatel, p.79.
- Gasser, D., Bruand, E., Stüwe, K., Rubatto, D., Foster, D., Schuster, R. (2010) Exhuming Metamorphic Rocks: Constraints from Cooling of the Chugach Metamorphic Complex, southern Alaska. Geophysical Research Abstracts Vol. 12, EGU2010-11742, 2010.

B.1 The Chugach Metamorphic Complex of southern Alaska: A test for wedge extrusion models?

High-grade metamorphic rocks are exposed in many orogenic wedges. They form at great depths and were then exhumed to the surface during collision. Several so-called extrusion models have been proposed to explain such exhumation: The rocks may have been extruded (a) as a rigid body between bounding fault zones, (b) by internal ductile channel flow, or (c) by general shear. Each of these models predicts a distinct relationship between the exhumation depth of the rocks and the width of the metamorphic complex at the surface. However, most of these models were developed in the Himalayan crystalline complex, which does not vary enough in width laterally to allow a straight forward testing of the predictions of the different models.

The Chugach Metamorphic Complex (CMC) of southern Alaska consists of high-grade metamorphic rocks (including migmatites) which developed in Cretaceous flysch sediments during an Eocene metamorphic event. The CMC is bound by major reverse and strike-slip fault zones, and its width triples from 25 km in the east to 80 km in the west over a distance of 150 km. The CMC may therefore be an ideal testing ground for different extrusion models.

Despite its interesting geometry, only little is known about the Eocene history, including the metamorphic conditions, the age of metamorphism and the exhumation history of the CMC. In a recently granted project we are currently embarking on a study to investigate transects across the CMC in parts of different width, in order to analyse the structural, chronological and metamorphic field gradients across the wedge. In this contribution we present ideas how along strike variations in field gradients in parts of different widths of the wedge can be used to constrain the different extrusion models.

Gasser, D., Stüwe, K. (2007) Geological Society of America Abstracts with Programs, Vol. 39, No. 6, p. 232.

B.2 Exhumation of a metamorphic complex in a strike-slip setting: observations from the Chugach Metamorphic Complex (CMC), southern Alaska

The exhumation of metamorphic rocks to the surface of the Earth is a much discussed subject in modern geodynamics. Models involving channel flow, pure and simple shear extrusion and others have been postulated based on observations in the Central Himalayan Crystalline Complex or the eclogite complexes in the Alps. Most of these models focus on the vertical component in profile view, not considering horizontal movements in plan view.

The CMC of Southern Alaska consists of low-P high-T gneisses that developed during the Eocene in a Cretaceous accretionary prism. They are exhumed from 20-35 km depth between major crustal-scale dextral shear zones (Fig. 1). Lineations are typically parallel to strike and sub-horizontal, indicating that horizontal movement in plan view is a vital part of the exhumation process. In addition, the complex has a particular triangular shape in plan view, indicating that the exhumation history might not be the same all along the complex but might be different in parts of different width of the complex.

In order to understand the nature of the low-P high-T metamorphism in an accretionary setting and its subsequent exhumation history we are currently working on a project combining extended field work, petrological, structural and geochronological methods. During the summers 2008 and 2009 we mapped six key areas covering the whole complex from north to south and from east to west in order to understand the structural and petrological variations all over the complex. We furthermore calculated detailed pressure and temperature conditions that occurred during metamorphism in the different parts of the complex. In order to better understand the timing and the rates at which heating, cooling and exhumation occurred, we apply several geochronological methods such as U-Pb dating of monazites and zircons, ArAr and RbSr dating of biotite and muscovite and zircon fission track dating to rocks from different parts of the complex.

In this contribution we present an overview of the geology of the CMC, results from our field work as well as first geochronological results.

Gasser, D., Bruand, E., Stüwe, K. (2009) Abstract Volume 7th Swiss Geoscience Meeting, Neuchâtel, p.79.

B.3 Exhuming Metamorphic Rocks: Constraints from Cooling of the Chugach Metamorphic Complex, southern Alaska

Exhumation mechanisms for metamorphic rocks include (a) erosion, (b) extension, (c) extrusion by channel flow, simple or pure shear, and - recently suggested - (d) slab extraction. Distinguishing in a particular case of a metamorphic complex between the different exhumation mechanisms is a much discussed subject in modern geodynamics. In order to add to this discussion, we adopt an interdisciplinary approach combining detailed petrological and structural field work with several geochronological and thermochronological systems.

The Chugach Metamorphic Complex of southern Alaska is a 600 km long and 10-30 km wide zone of upper amphibolite-facies metamorphic rocks. It lies in the outermost tectonic belt of the North American Cordillera, which is a vast and complex Phanerozoic orogen formed from the oblique collision of the Pacific, Kula and Farallon oceanic plates and the North American continent. The Chugach Complex developed in the Eocene in a Cretaceous to Paleocene accretionary prism while the Kula and Pacific plates were obliquely colliding with North America. We conducted detailed field work, U-Pb and ^{40}Ar - ^{39}Ar geochronology and compiled all other geochronological data from the region in order to construct cooling histories for the whole metamorphic complex. These cooling histories vary along strike: The western and central parts of the Chugach Metamorphic Complex, where the metamorphic complex is wide, show very fast cooling to below 300°C between 54-45 Ma, shortly after peak metamorphism, and then slowly cool to surface temperatures over the remaining 45 Ma. In contrast, the south-eastern part; where the metamorphic complex is very narrow, slowly and steadily cooled between 51-5 Ma only to increase its cooling rate in the last few Ma before present. Whether and how these cooling rates can be directly linked with exhumation rates and why they differ so grossly between the wide and the narrow parts of the complex is the current focus of our work.

Gasser, D., Bruand, E., Stüwe, K., Rubatto, D., Foster, D., Schuster, R. (2010) Geophysical Research Abstracts Vol. 12, EGU2010-11742, 2010.



"The scientist does not study nature because it is useful; he studies it because he delights in it, and he delights in it because it is beautiful."

Jules Henri Poincaré in *Science et méthode*, 1908

Appendix C

Internal Structural Geometry of the Paleozoic of Graz

Abstract The Paleozoic of Graz is an isolated nappe complex of about 1500 km² size and belongs to the Austroalpine units of the Eastern European Alps. Despite more than 500 publications on stratigraphy, paleontology and local structure, many aspects of the internal geometry of this complex as a whole remained unclear. In this contribution, we present integrated geological profiles through the entire nappe complex. Based on these profiles we present (i) a simplified lithological subdivision into 13 rock associations, (ii) a modified tectonostratigraphy where we consider only two major tectonic units: an upper and a lower nappe system and where we abandon the traditionally used facies nappe concept, and (iii) a modified paleogeography for the whole complex. Finally, we discuss whether the internal deformation of the Paleozoic of Graz is of Variscan or Eo-Alpine age and which of the published models best explain the tectonic evolution of the Paleozoic of Graz.

Keywords Paleozoic of Graz, Eastern Alps, Austria, geological profiles, structural geology

published as: Gasser, D., Stüwe, K., Fritz, H. (2009) International Journal of Earth Science, DOI: 10.1007/s00531-009-0446-0

C.1 Introduction

The Paleozoic of Graz is a 30 x 50 km sized nappe complex of mostly low grade carbonates, schists and metavolcanics of Paleozoic depositional ages. Together with other low grade Paleozoic sedimentary units such as the Gurktal Thrust System and the Greywacke Zone it builds up large parts of the Upper Austroalpine units of the Eastern European Alps (Fig. C.1a). The Paleozoic of Graz is surrounded by and lies on top of crystalline rocks that experienced high grade metamorphism in the Permian and the Cretaceous (Oberhänsli et al., 2004; Schuster & Stuewe, 2008). It is discordantly overlain by a small Cretaceous Gosau basin and by the Neogene Styrian basin (Fig. C.1b). As such, the Paleozoic of Graz records many of the sedimentological, tectonic and metamorphic events that formed the Eastern Alps since the early Paleozoic. Stratigraphy, paleontology, internal structure and metamorphism of the Paleozoic of Graz were extensively studied over the past 180 years and resulted in over 500 publications (e.g. Schwinner, 1925; Clar, 1935; Boik, 1950; Flügel & Hubmann, 2000, and references therein). However, no geological profiles through the entire Paleozoic of Graz are published. As a consequence, many aspects of the internal structure of the complex are poorly understood.

In this study we present integrated geological profiles through the entire Paleozoic of Graz which we constructed on the base of a simplified lithological subdivision of the complex. Using these profiles, we discuss the internal structure of the Paleozoic of Graz and present a modified tectonostratigraphy for the complex. Within this, we discern only two major nappe systems separated by a single thrust: the Rannach thrust. Based on these results we then discuss the age of internal deformation and metamorphism as well as models proposed in the literature for the final emplacement of the Paleozoic of Graz onto the surrounding crystalline basement.

C.2 Geological setting

The Paleozoic of Graz consists of Silurian to Carboniferous, poly-phase deformed, diagenetic to greenschist facies rocks. In the literature, five sedimentary facies associations are discerned: The Rannach, Hochlantsch, Laufnitzdorf, Kalkschiefer and Schöckl facies. Each facies has been ascribed to one tectonic nappe (Fig. C.1b; Fritz et al., 1991, 1992; Ebner et al., 2000). These nappes are attributed to an upper (Rannach and Hochlantsch), an intermediate (Laufnitzdorf and Kalkschiefer) and a lower nappe system (Fig. C.1b; Fritz et al., 1992). In general, deformation intensity is lowest in the upper nappe system and highest in the lower nappe system. The fact that the same names have been applied to both sedimentary facies as well as tectonic units led to some confusion in the literature, because some of the facies occur in more than one tectonic nappe.

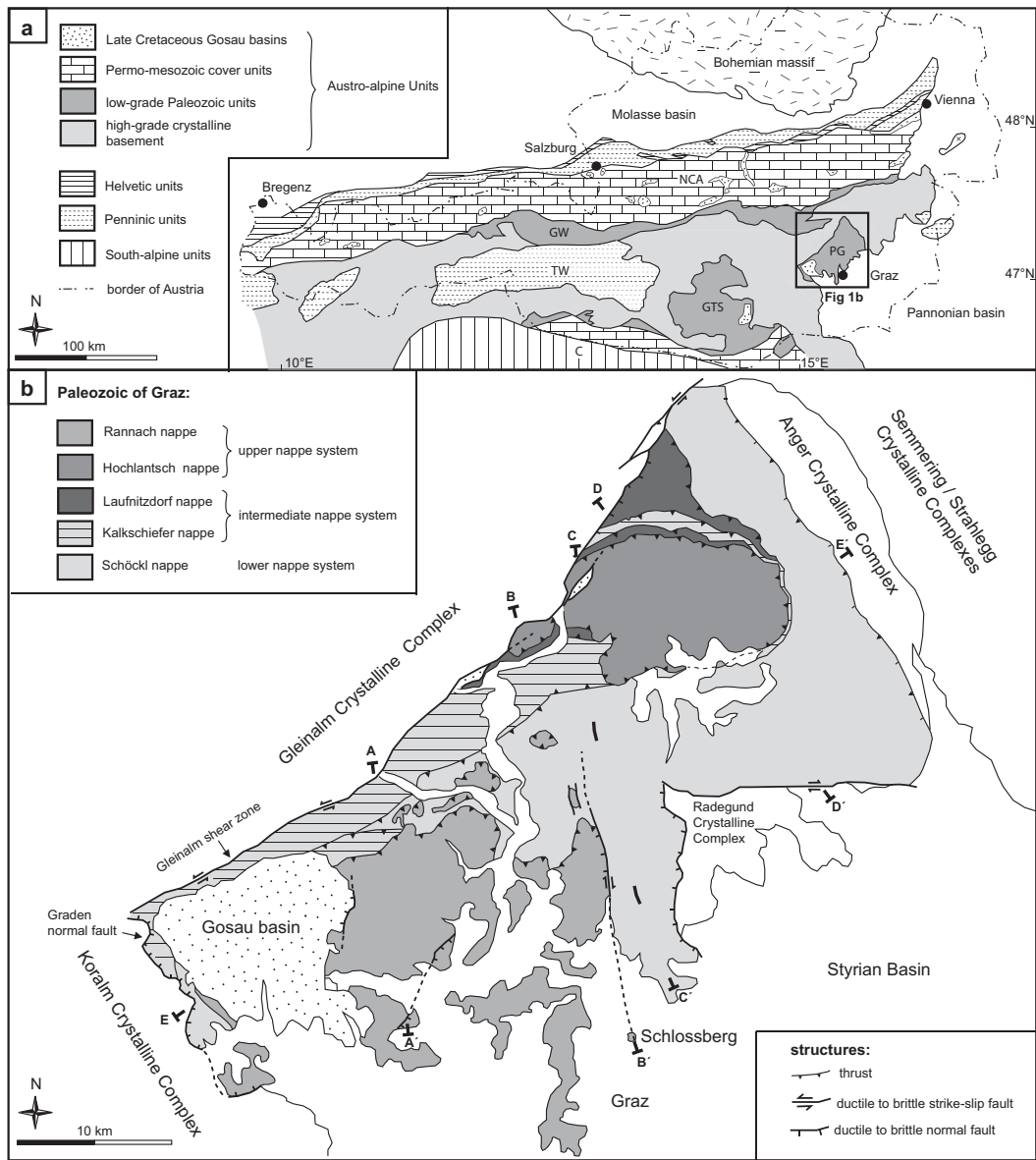


Figure C.1: (a) Geological sketch map of the Eastern Alps. PG: Paleozoic of Graz, GTS: Gurktal Thrust System, TW: Tauern Window, GW: Grauwacken Zone, NCA: Northern Calcareous Alps. (b) Tectonic map of the Paleozoic of Graz after Fritz et al. (1991). Profile traces from Fig. C.4 are indicated.

The borders of the Paleozoic of Graz consist of ductile to brittle shear zones including the sinistral Gleinalm shear zone in the north-west (Neubauer, 1988a; Neubauer et al., 1995), the Graden normal fault in the south-west (Rantitsch, 2006) and un-named ductile to brittle normal and strike-slip faults against the Radegund Crystalline in the south and the Anger

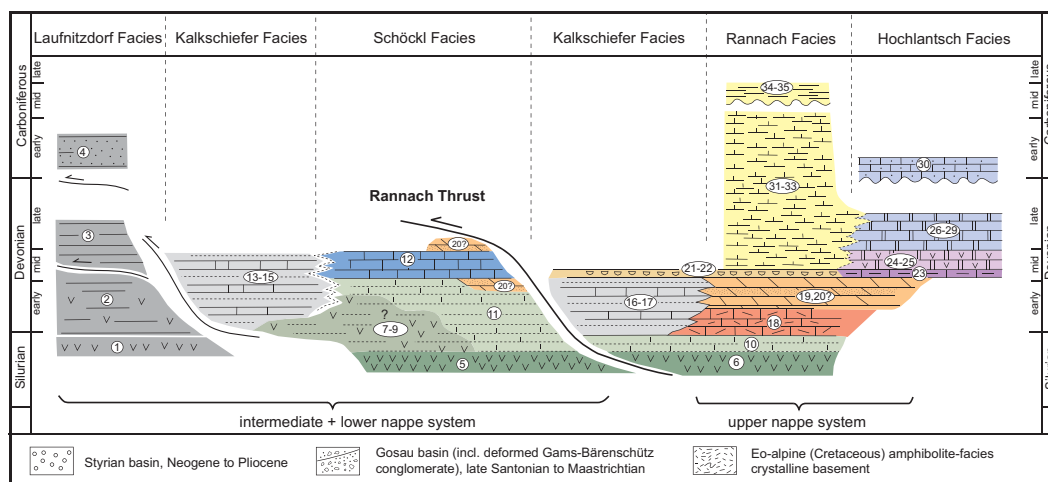


Figure C.2: Stratigraphic relationships as they are observed today in the major tectonic units of the Paleozoic of Graz. Also legend to figure C.4. Formation numbers: 1: Hackensteiner Fm, 2: St. Jakob Fm, 3: Harrberger Fm, 4: Dornerkogel Fm, 5: Taschen Fm, 6: Kehr Fm, 7: Semriach Phyllite Fm, 8: Heilbrunn Phyllite Fm, 9: Hirschkogel Phyllite Fm, 10: Kötschberg Fm, 11: Schönberg Fm, 12: Schöckl Fm, 13: Kogler Fm, 14: Hochschlag Fm, 15: Hubenhalt Fm, 16: Bameder Fm, 17: Heigger Fm, 18: Parmasegg Fm, 19: Flösserkogel Fm, 20: Raasberg Fm, 21: Plabutsch Fm, 22: Draxler Fm, 23: Osser Fm, 24: Tyrnaueralm Fm, 25: Rotmüller Fm, 26: Zachenspitz Fm, 27: Hochlantsch Fm, 28: Schweinegg Fm, 29: Fahrneck Fm, 30: Bärenschütz Fm, 31: Kollerkogel Fm, 32: Steinberg Fm, 33: Sanzenkogel Fm, 34: Höchkogel Fm, 35: Hahngraben Fm. Drawn according to Flügel & Hubmann (2000), Hubmann & Messner (2007) and the results of this study.

Crystalline in the north-east (Fig.C.1b; Krenn et al., 2008). The Paleozoic of Graz is discordantly overlain in its south-western part by a late Cretaceous (85 - 65 Ma) Gosau basin (Fig. C.1b). This basin contains a basal, reddish conglomerate, limestone, marls and a >1000 m thick sequence of sand-, silt- and claystones. These sediments show an evolution from a coarse alluvial facies, through a lacustrine shallow-water facies, to a marine delta system (Neubauer et al., 1995; Ebner & Rantitsch, 2000). Clasts in the basal conglomerate are derived from the Northern Calcareous Alps, the Southern Alps, the Paleozoic of Graz as well as reworked clasts from the Gosau itself. Interestingly, clasts from the surrounding crystalline basement are missing. The transport direction of the sediments was mainly from north and northeast (Gollner et al., 1987; Ebner & Rantitsch, 2000). In the south, both the Gosau basin and the Paleozoic of Graz are discordantly overlain by the Neogene Styrian basin. Sedimentation in this basin took place between the lower Miocene and the Pliocene (19 - 1.8 Ma; Piller et al., 2004).

Detailed stratigraphical and paleontological work in the Paleozoic of Graz led to the definition of 35 sedimentary formations (Fig. C.2; Flügel & Hubmann, 2000). The oldest rocks are Silurian, volcano-clastic sediments which are interpreted to be the result of intracontinental rifting (Fritz & Neubauer, 1988; Loeschke, 1989). From the Early Devonian on, several distinct facies associations developed. Rocks in the Rannach and Hochlantsch nappes represent the most proximal facies. Early Devonian sandy limestones and dolomites,

deposited in a coastal environment, are overlain by Middle Devonian platform carbonates and Late Devonian to Carboniferous pelagic limestones. Erosion and carstification occurred in the Late Devonian and Early Carboniferous (Fig. C.2; Flügel & Hubmann, 2000; Ebner et al., 2000; Hubmann & Messner, 2007). Rocks in the Kalkschiefer and Laufnitzdorf nappes and in the Schöckl nappe experienced epizonal to greenschist facies metamorphism. The internal stratigraphy of those nappes is therefore less well known. The Laufnitzdorf nappe contains carbonates, radiolarites, clay- and sandstones of Devonian age, which were deposited in a pelagic environment. The Kalkschiefer nappe consists of a uniform sequence of marls, limestones and sandstones of Devonian age. In the Schöckl nappe, the Silurian volcano-clastic rocks are overlain by dark-grey carbonates and black schists which were probably deposited in a euxinic basin. They are in turn overlain by Middle Devonian platform carbonates (Fig. C.2; Flügel & Hubmann, 2000; Ebner et al., 2000). The Schöckl nappe also contains large amounts of greenschist facies phyllites and chlorite schists of unknown age (Fig. C.2, Fm 10-12). However, their close association with Silurian volcano-clastic rocks and Early Devonian black schists make a pre-Middle-Devonian age probable.

Metamorphic conditions in the Paleozoic of Graz were revealed by illite crystallinity, vitrinite reflectance and Raman spectroscopy (Hasenhüttl, 1994; Russegger, 1996; Rantitsch et al., 2005). In the upper nappe system, estimated metamorphic temperatures lie in the range of 200-300°C. In the intermediate and lower nappe system, rocks of the Laufnitzdorf nappe show temperatures below 300°C, rocks of the Kalkschiefer and Schöckl nappes above 300°C. Raman spectroscopy revealed a temperature aureole roughly parallel to the normal faults along the north-eastern, southern and south-western margins of the Paleozoic of Graz (Rantitsch et al., 2005). At the south-western margin, metamorphic temperatures rise over only a few kilometres from < 250°C in the Gosau basin to ~500°C in the Paleozoic of Graz and 500-600°C in the Koralm Crystalline (Rantitsch et al., 2005). Krenn et al. (2008) calculated conditions of ~500-600°C and ~6-9 kbar at the north-eastern border to the Anger Crystalline. Surprisingly, there is no temperature aureole parallel to the north-western margin to the Gleinalm Crystalline, where temperatures in the crystalline also reached ~500°C.

C.3 Simplified lithological subdivision

In order to construct integrated structural profiles through the entire Paleozoic of Graz it is necessary to reduce the 35 formations described by Flügel & Hubmann (2000) to much fewer distinct rock associations (Fig. C.2). Each of the rock associations defined here is displayed in one colour on figure C.2 and contains one or more formations. We assembled (a) formations that are identical in age and sedimentary facies but occur in different tectonic units, and (b) formations that are part of a continuous sedimentary sequence but vary slightly in composition. The following groupings are performed to obtain rock associations which are displayable on the scale of the profiles:

- *Dark grey (Fm 1 - Fm 4)*: The Hackensteiner (Fm 1), St. Jakob (Fm 2), Harrberger (Fm 3), and Dornerkogel (Fm 4) formations correspond to the Laufnitzdorf group of Flügel & Hubmann (2000). They all occur only in the northern part of the Paleozoic of Graz. Formations 1-3 build a Silurian to late Devonian sequence of pelagic, fine-grained clastic sediments intercalated with volcanic ashes and limestones. Their ages overlap; they received their different names mainly from different workers who observed them in different places and different structural positions. The Dornerkogel formation (Fm 4) is lithologically different: it consists of coarser-grained silt- and sandstones which were deposited in a turbiditic environment. Detrital micas in this formation are of Variscan age and it is therefore interpreted as a Flysch deposit in front of the Variscan orogen (Neubauer et al., 2007). However, because it occurs only in the northernmost part of the Paleozoic of Graz in close proximity and probably in sedimentary contact with Fm 1, we assembled it together with Fm 1-3.
- *Dark green (Fm 5 - Fm 6)*: The Taschen (Fm 5) and Kehr (Fm 6) formations are both basic metavolcanic rocks of Silurian age. They occur geographically in different regions: near Taschen in the central part, and near Kehr in the western part of the Paleozoic of Graz (Fig. C.3). They occur in two different structural levels: the Kehr formation in the upper Rannach nappe and the Taschen formation in the lower Schöckl nappe. The Taschen formation is slightly higher metamorphosed than the Kehr formation. Despite these geographical, structural and metamorphic differences, their lithology and age are very similar and we therefore assume them to be originally part of the same rock association.
- *Intermediate green (Fm 7 - Fm 9)*: The Semriach (Fm 7), Hirschkogel (Fm 8) and Heilbrunn (Fm 9) formations correspond to the Passail group of (Flügel & Hubmann, 2000). They are all greenschist facies, sericite and chlorite bearing phyllites of unknown age. However, their close proximity to the Taschen, Schönberg and Schöckl formations make a Silurian to Early Devonian age probable. They are grouped based on their position within the sedimentary succession and their lithological similarity. The Semriach and Hirschkogel formations occur both in the region of Semriach and the Heilbrunn formation crops out in a structurally lower level parallel to the eastern border of the Paleozoic of Graz (Fig. C.3).
- *Light green (Fm 10 - Fm 11)*: The Kötschberg (Fm 10) and Schönberg (Fm 11) formations are both dark limestones and black schists. They occur in sedimentary contact on top of the Kehr and Taschen formations respectively. Grouping them followed the same logic as grouping the Kehr and Taschen formations (Fm 5-6).
- *Blue (Fm 12)*: The Schöckl formation (Fm 12) consists of a peculiar blue-white banded limestone of several 100 m thickness. This limestone is lithologically very distinct. It is therefore not grouped with other formations.
- *Light grey (Fm 13 - Fm 17)*: The Kogler (Fm 13), Hochschlag (Fm 14), Hubenhalt (Fm 15), Bameder (Fm 16) and Heigger (Fm 17) formations are what has traditionally been referred to as Kalkschiefer facies. They are layered calcareous schists, slaty

limestones, and minor clay-, silt- and sandstones of early to middle Devonian age. They occur all over the Paleozoic of Graz in different tectonic positions and are internally folded and imbricated. Their different formation names mainly originate from their occurrence in different geographical areas and tectonic levels. Because they are lithologically and stratigraphically similar, we assembled them into one group.

- *Dark orange (Fm 18)*: The Parmasegg formation (Fm 18) is a distinct rock association consisting of coastal crinoidal limestones, sandy marls and minor silt- and sandstones with a thickness of up to 200 meters. It is therefore left ungrouped.
- *Medium orange (Fm 19 - Fm 20)*: The Flösserkogel formation (Fm 19) consists of early diagenetic, yellow dolomites, limestones and sandstones. It reaches 500 - 1000 m thickness and builds up substantial parts of the upper Rannach and Hochlantsch nappes. The Raasberg Fm (Fm 20) occurs around Raasberg (Fig. C.3) and consists of highly deformed and metamorphosed dolomites, limestones and sandstones. Its stratigraphic and tectonic position is unclear (Fig. C.2; Flügel & Hubmann, 2000). However, because it consists of very similar rocks as the Flösserkogel Fm and because it is located on top of the Schöckl Fm we group it together with the Flösserkogel Fm and interpret it as a sheared relict of the upper nappe system on top of the lower nappe system.
- *Light orange (Fm 21 - Fm 22)*: The Plabutsch (Fm 21) and Draxler (Fm 22) formations are dark, fossil-rich limestones intercalated with marls and claystones of well defined middle Devonian age. They occur in two different geographic locations but are grouped for their lithological and age equivalence.
- *Dark purple (Fm 23)*: The Osser formation (Fm 23) is lithologically similar to Fm 21 and Fm 22 but contains less fossils, is more marly, much more deformed and of slightly higher metamorphic grade. It is therefore kept separate and is not grouped.
- *Light purple (Fm 24 - Fm 25)*: The Tyrnauer Alm (Fm 24) and Rotmüller (Fm 25) formations consist of limestones, sand- and siltstones and intercalated volcanics. They occur in close geographic proximity in the upper Hochlantsch nappe and are of the same age, they are therefore grouped together.
- *Light blue (Fm 26 - Fm 30)*: The Zachenspitz (Fm 26) and Hochlantsch (Fm 27) formations build up a classical carbonate platform sequence of late Devonian age with massive to bedded light-grey limestones constituting the major cliffs of the Hochlantsch massif. The Schweinegg (Fm 28) and Fahrneck (Fm 29) formations are both very local occurrences of fossil rich limestones only tens of metres in thickness. Both have previously been suggested to correspond to the Zachenspitz and/or Hochlantsch formations and they are therefore grouped with them here. The Bärenschütz formation (Fm 30) only occurs locally south of Hochlantsch (Fig. C.3) where it discordantly overlies Fm 27. It consists of bedded limestones and is significantly younger than formations 26-29, but it is grouped with them here as it is too small to feature as a mappable association of its own.

- *Yellow (Fm 31 - Fm 35)*: The Kollerkogel (Fm 31), Steinberg (Fm 32) and Sanzenkogel (Fm 33) formations are all variegated, pelagic limestones and shales of late Devonian to Carboniferous age. Each formation is less than 100 meters thick and they occur in an undisturbed stratigraphic sequence in the upper Rannach nappe. The Höchkogel (Fm 34) and Hahngraben (Fm 35) formations are separated from the others by an erosional unconformity. They consist of limestones and shales and contain detrital mica of Variscan age. They are therefore - similar to the Dornerkogel Fm (Fm 4) - interpreted as Variscan flysch deposit (Neubauer et al., 2007). However, they are very thin and are therefore grouped together with formations 31-33.

In summary, figure C.2 shows the simplified stratigraphic relationships as they are observed today in the Paleozoic of Graz in the different tectonic units. The groupings we performed show clearly the first-order stratigraphic features that are typical for this complex. The sedimentation started with Silurian metavolcanic rocks. In the early and middle Devonian, platform carbonates and sandy coastal deposits interfinger with fine-grained siliclastic sediments, volcanic layers point to an ongoing volcanic activity. In the late Devonian, the environment changes from a platform setting to more pelagic sedimentation, which - interrupted by two erosional unconformities - continued up to the Carboniferous and finished with the deposition of flysch-type clastic sediments. The paleogeographical implications of these observations are discussed further below.

C.4 Structural geometry

Using this simplified lithological subdivision, we assembled a structural map (Fig. C.3) and constructed a series of geological profiles through the entire nappe complex (Fig. C.4). The topography for the profiles was extracted from a digital elevation model. Geological information such as detailed maps, local profiles, drillhole data and written descriptions of structure and stratigraphy was taken from many detailed publications listed in Flügel & Hubmann (2000) and the published geological map sheets 133 Leoben, 134 Passail, 135 Birkfeld, 162 Köflach, 163 Voitsberg, 164 Graz and 165 Weiz of the 1:50 000 map series of the Geological Survey of Austria, which are available for download at <http://www.geologie.ac.at/>. The traces from the profiles in figure C.4 are indicated on figure C.1 and C.3. Profiles A to D run north-south to northwest-southeast and are chosen to be perpendicular to the major fold axis orientation in the Paleozoic of Graz. Profile E runs southwest-northeast and is parallel to the late Cretaceous stretching direction reported by Krohe (1987), Neubauer et al. (1995) and Krenn et al. (2008).

Rannach thrust The most prominent tectonic feature in the Paleozoic of Graz is the thrust at the base of the Rannach and Hochlantsch nappes (Fig. C.3 and Fig. C.4, profiles B-E). The thrust, here called Rannach thrust, can be traced through much of the Paleozoic of

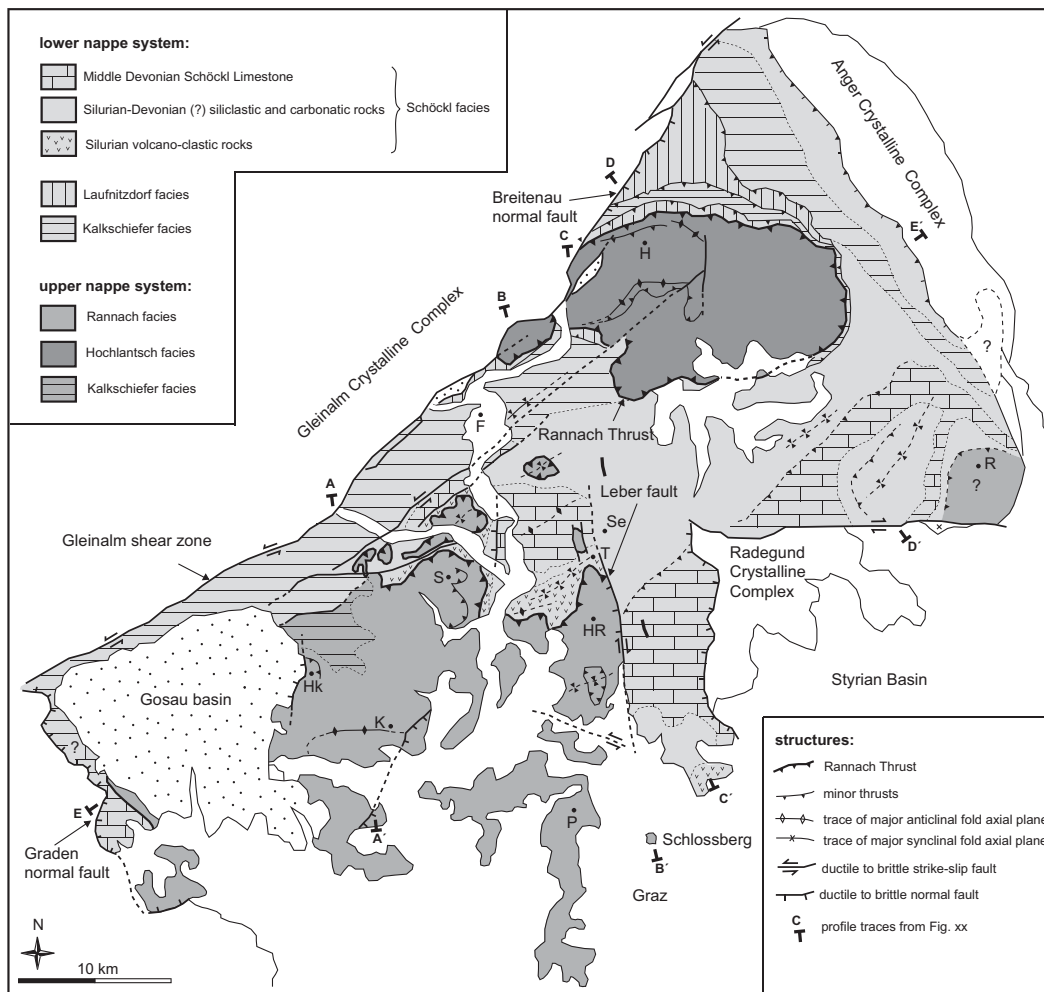
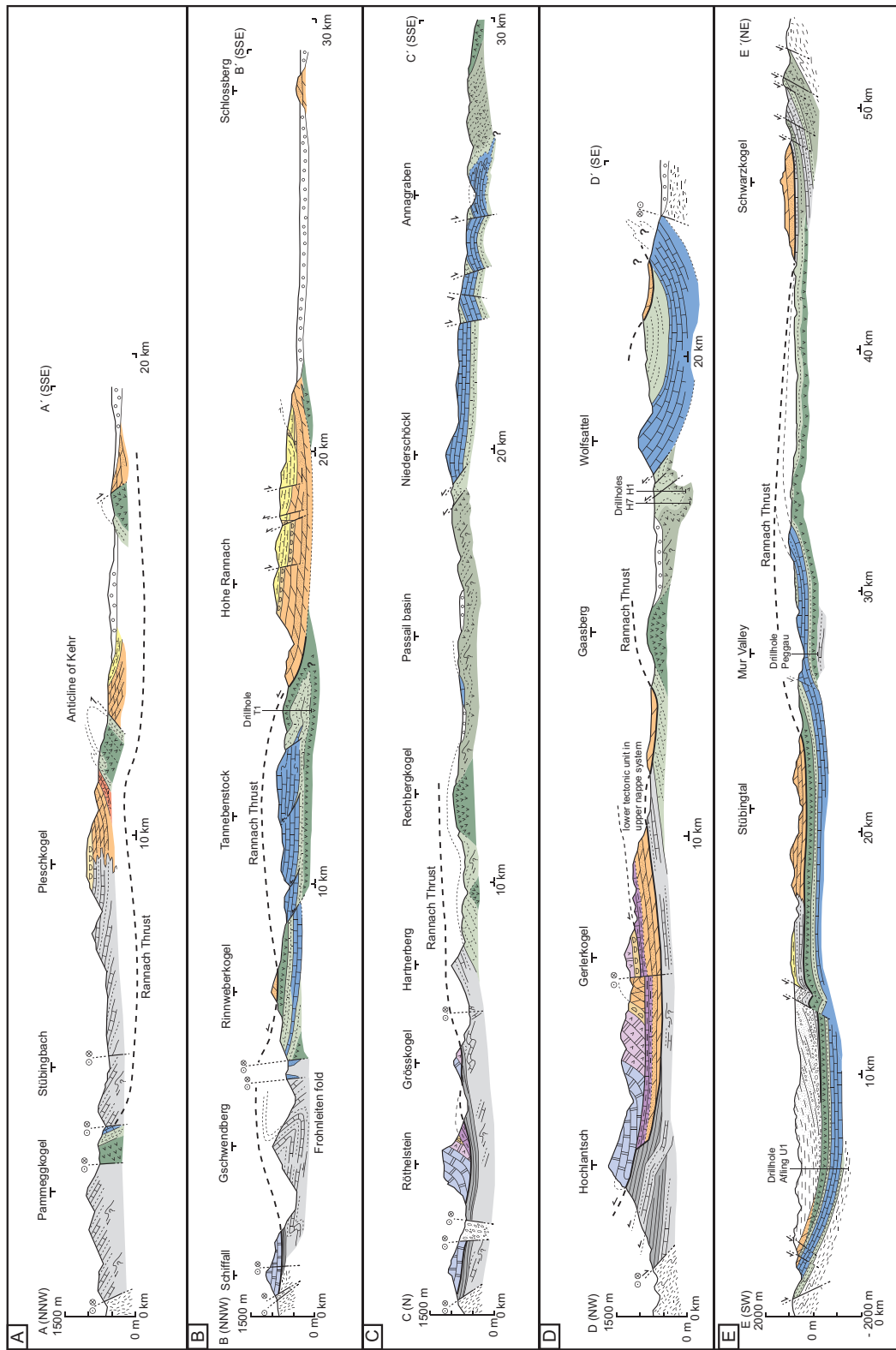


Figure C.3: Structural map of the Paleozoic of Graz. The profile traces of figure C.4 are indicated. Locations mentioned in the text are: Hk: Höllerkogel, S: Schartnerkogel, HR: Hohe Rannach, T: Tannebenstock, F: Frohnleiten, H: Hochlantsch, R: Raasberg, P: Plabutsch, T: Taschen, K: Kehr, Se: Semriach.

Graz and separates rocks of the Rannach and Hochlantsch facies above from rocks of the Kalkschiefer, Schöckl and Laufnitzdorf facies below. The thrust itself is best exposed in the central part of the Paleozoic of Graz. Below Schartnerkogel (Fig. C.3) it separates relatively undeformed, low grade rocks of the Rannach facies from highly deformed, greenschist facies rocks of the Schöckl facies. The thrust itself is a several meters thick high strain zone at the base of the Parmasegg formation (Fritz, 1988, 1991). It contains asymmetric pressure

Figure C.4 (following page): Geological profiles through the Paleozoic of Graz. No vertical exaggeration. Informations on drillhole T1, H7 and H1 are from Weber (1990), on drillhole Peggau from Fritz (1986) and on drillhole Afling U1 from Kröll & Heller (1978).



shadows around pyrite showing a stretching lineation progressively turning from east-west to southeast-northwest with generally top-west to top-northwest shear sense. Below Hohe Rannach (Fig. C.4, profile B) the thrust separates rocks of the Rannach facies from highly-deformed greenschist facies rocks of the Schöckl facies. The thrust consists of an up to 100 m thick sheared zone with strongly interleaved rock slices of the Laufnitzdorf and Rannach facies (Neubauer, 1989). Similarly-sheared Laufnitzdorf facies rocks occur below the Rannach thrust at Schiffall and Röthelstein (Fig. C.4, profiles B- C). Below Schiffall, Grösskogel and north of Gaasberg (Fig. C.4, profiles B-D) the Rannach thrust cuts straight through highly folded units of the Schöckl and Kalkschiefer facies; it therefore represents a thrust that is younger with respect to the internal deformation of the lower nappe system.

In other parts of the Paleozoic of Graz, the location of the Rannach thrust is less obvious. In the northwestern part north of Höllerkogel and Stübingbach (Fig. C.3, Fig. C.4 profile A), rocks of the Kalkschiefer and Schöckl facies are juxtaposed against rocks of the Rannach and Kalkschiefer facies along steep, semi-brittle sinistral strike slip zones (Fritz, 1991). The original geometry of the Rannach thrust is therefore obliterated. In the southwest around Kehr the oldest rocks of the Rannach facies crop out in a southeast-verging antiform, but a thrust zone which could correspond to the Rannach thrust is not exposed (Neubauer, 1991). In the northeastern part around Hochlantsch (Fig. C.3) the location of the Rannach thrust is obvious below Schiffall, Röthelstein and Grösskogel (Fig. C.4, profiles B-C). In the north of Hochlantsch the undeformed and low grade Hochlantsch formation is thrust over imbricated and highly deformed Kalkschiefer and Laufnitzdorf facies rocks and the Rannach thrust is clearly developed. However, south of Gerlerkogel (Fig. C.4, profile D) a tectonic unit of higher deformed rocks consisting of the Flösserkogel and Osser formations (Fm 19 and 23) reveals a similar metamorphic grade as the underlying Kalkschiefer and Laufnitzdorf facies rocks and the Rannach thrust could therefore be also located on top of this unit (Hasenhüttl, 1994). Because the Flösserkogel and equivalents of the Osser formation are elsewhere clearly located above the Rannach thrust, we interpret this tectonic unit as a local thrust inside the upper nappe system. The Raasberg formation occurs in the southeastern part around Raasberg on top of and sheared together with rocks of the Schöckl facies (Fm 20; Fig. C.3 and C.4, profile D). We interpret it as an equivalent of the Flösserkogel formation and therefore as a small relict of the Rannach thrust zone on top of Schöckl facies rocks.

Despite some local difficulties in determining the location of the Rannach thrust, it is a major first-order tectonic boundary in most of the Paleozoic of Graz. It splits the Paleozoic of Graz into an upper nappe system and a lower nappe system which differ from each other significantly in deformation style and metamorphic grade. Rocks of different sedimentary facies occur both above and below this thrust: Rannach, Hochlantsch and Kalkschiefer facies rocks above, Schöckl, Kalkschiefer and Laufnitzdorf facies rocks below.

Upper nappe system Deformation in the upper nappe system above the Rannach thrust is characterised by large scale open folds, local imbrications and steep brittle faults. Variable

fold axis orientations occur but the general trend of the axes is E-W to NE-SW. A prominent fold example is the southeast-verging anticline of Kehr (Fig. C.4, profile A; Neubauer, 1991). Other large scale folds occur in the Hochlantsch massif (Fig. C.4, profile D; Gollner & Zier, 1985). The Hochlantsch massif consists of two smaller thrust sheets which we both assign to the upper nappe system: an upper, less deformed unit which contains formations 26-30 and a lower more deformed unit consisting of formations 19 and 23. Smaller local imbrications in the upper nappe system are known from east of Schartnerkogel (Fig. C.3; Fritz, 1991), from south of Hohe Rannach (Fig. C.4, profile B) and around Höllnerkogel (Fig. C.3). Steep brittle normal and strike slip faults cross-cut the whole upper nappe system.

Lower nappe system Deformation in the lower nappe system is much more intense and differs in style from deformation in the upper nappe system. The Schöckl facies rocks in the lower nappe system are intensely deformed and show a penetrative foliation with a pronounced, asymmetric E-W stretching lineation with top-W shear sense. At micro- to meso-scale, two generations of isoclinal folds occur: (i) isoclinally folded quartz veins which have the penetrative foliation as axial plane foliation, and (ii) isoclinal folds of the penetrative foliation itself with a spaced second cleavage developed in the hinges. The stretching lineation is folded around these second generation folds (Agnoli, 1987; Fritz, 1988, 1991; Reisinger, 1988; Neubauer, 1989, 1991).

Apart from this strong deformation at micro- and meso-scale, also large-scale repetitions of stratigraphy occur. In the northern part, rocks of the Kalkschiefer and Laufnitzdorf facies are imbricated and thrust on top of each other. At the eastern border of the Paleozoic of Graz, phyllites of the Heilbrunn formation (Fm 9), calcareous schists of the Hochschlag formation (Fm 8), phyllites of the Semriach formation (Fm 7) and limestone of the Schöckl formation (Fm 12) lie on top of each other (Fig. C.4, profile E). In the central part of the Paleozoic of Graz, the Schöckl formation is symmetrically both under- and overlain by the Taschen (Fm 5) and Schönberg (Fm 11) formations (eg. south of Tannebenstock, south of Annagraben and below Schartnerkogel, Fig. C.3 and C.4). Schwinner (1925) interpreted this repetition of stratigraphy as the result of multiple thrusting. Clar (1933) and Boik (1950) proposed the existence of large-scale isoclinal folds with the Schöckl formation in the core of the folds. The symmetric occurrence of the same lithologies below and above the Schöckl formation, as well as isoclinal folds at micro- and meso-scale point to the possible existence of such large-scale folds. That is why we draw this possibility on Fig. C.4, profiles B-D, Fig. C.5 and Fig. C.6d. However, hinges of such possible large-scale folds are nowhere exposed and no proofs for overturned sequences in the inverted limbs such as top-bottom criteria are known. In addition, it is not known if the repetition of stratigraphy occurred prior to, contemporaneously with, or after the formation of the penetrative foliation, the stretching lineation and the two generations of micro- to meso-scale isoclinal folds.

These isoclinally folded and foliated rocks are further overprinted by open to tight, NW to

SE-verging folds with a steep axial planar crenulation cleavage and NE-SW trending axes. These folds are associated with brittle fore- and backthrusts. Rocks underlying the basin of Passail (Fig. C.4, profile C) as well as the northern border of the Schöckl limestone (Fig. C.4, profile C and D) are strongly overprinted by such tight folds and thrusts. The large-scale open synform south of Wolfsattel belongs to this generation of folds (Fig. C.4, profile D).

C.5 Modified tectonostratigraphy and paleogeography

Our tectonostratigraphic interpretation is displayed in figure C.6. In this interpretation, the structure of the Paleozoic of Graz is described in terms of an upper, less deformed nappe system, which is separated by the Rannach thrust from a lower, more deformed and generally higher metamorphic nappe system. The upper nappe system consists of weakly deformed Rannach, Hochlantsch and Kalkschiefer facies rocks. The lower nappe system consists of complexly and poly-phase deformed Laufnitzdorf, Kalkschiefer and Schöckl facies rocks, where several repetitions of stratigraphy occur. The reason for this large-scale repetition of stratigraphy is not well-known - it could be either thrusting or isoclinal folding.

Our tectonostratigraphy differs from the one previously published in the literature. Traditionally, the Kalkschiefer and Laufnitzdorf facies rocks were attributed to an intermediate nappe system (Fig. C.1b, Fig. C.6c; Fritz et al., 1991, 1992). However, no first-order tectonic boundary such as the Rannach thrust is observed between the Kalkschiefer and Laufnitzdorf facies rocks on one side and the Schöckl facies rocks on the other side. A close investigation of existing maps and our profiles reveals that the Kalkschiefer facies rocks lie stratigraphically on top of the Schönberg formation (Fm 11) and laterally replace rocks of the Schöckl formation (Fm 12). This can be seen for example on figure C.4, profile C south of Hartnerberg. Rocks of the Schöckl formation are nowhere overthrust by rocks of the Kalkschiefer and Laufnitzdorf facies and a tectonic boundary between them (except for late steep sinistral strike slip faults on Fig. C.4, profile B) is not known. We therefore prefer to interpret the Kalkschiefer and Laufnitzdorf facies rocks as lateral facies equivalents of the Schöckl formation and not as an own intermediate tectonic nappe system.

Traditionally, tectonic nappes in the Paleozoic of Graz (and in other low-grade sedimentary units of the Alps) have been defined on the basis of sedimentary facies with each identified facies being ascribed to an own tectonic nappe. In the Paleozoic of Graz, the terms Laufnitzdorf, Kalkschiefer, Schöckl, Rannach and Hochlantsch have been used interchangeably for sedimentary facies as well as tectonic units. Here, we have shown that rocks of the Kalkschiefer facies occur both in the upper and lower nappe system. It is therefore confusing to use the term Kalkschiefer nappe in a tectonic sense because it is not explicit. Similarly, the terms Rannach and Hochlantsch nappes do not really describe tectonic units, but different facies associations occurring on the same tectonic level, namely in the upper

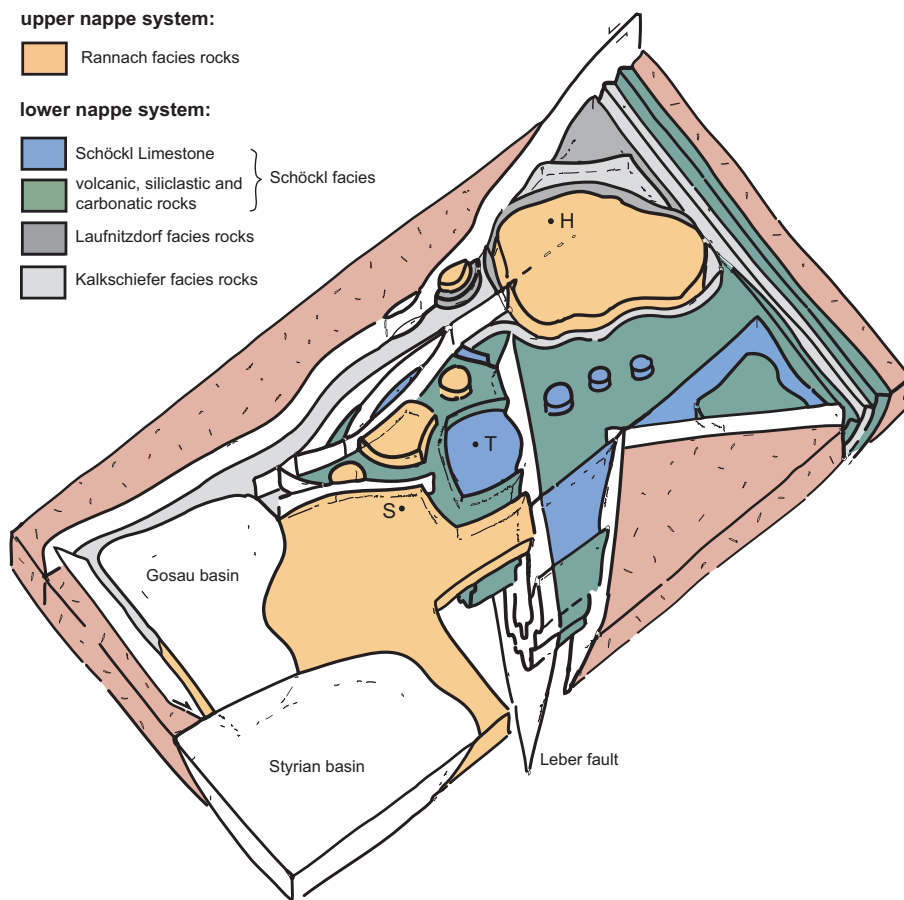


Figure C.5: 3D Sketch of the Paleozoic of Graz. Location abbreviation as in figure C.3.

nappe system. We therefore propose to only use upper and lower nappe system in a tectonic context.

The analysis of the profiles also leads to a slightly modified paleogeography for the Paleozoic of Graz. Such a paleogeographical model has to explain that (a) the Kalkschiefer facies rocks occur in the lower nappe system and are closely imbricated with Laufnitzdorf facies rocks and (b) the Kalkschiefer facies rocks occur in the upper nappe system in sedimentological contact with Rannach facies rocks. Hubmann (1993) proposed the arrangement displayed in figure C.6a for the Middle Devonian. In this scenario, the Rannach and Hochlantsch facies represent a proximal, coastal facies which is separated from the Schöckl limestone by a Kalkschiefer facies basin. The pelagic Laufnitzdorf facies directly borders the Schöckl limestone towards a more pelagic environment. This scenario makes it difficult to explain the close imbrication of Kalkschiefer and Laufnitzdorf facies rocks that is observed today in the northern part of the Paleozoic of Graz. The Kalkschiefer facies rocks would have needed to overthrust the Schöckl limestone in order to get adjacent with

the Laufnitzdorf facies rocks. We therefore propose a modified arrangement which does not require such a complicated deformation (Fig. C.2 and Fig. C.6b). We suggest that there were two basins of Kalkschiefer facies rocks that flanked the Schöckl facies on both sides and were therefore - in part - adjacent to the Laufnitzdorf facies rocks. This is sedimentologically reasonable as the Kalkschiefer facies represents an intermediate facies between the pelagic Laufnitzdorf facies and the carbonate platform of the Schöckl facies. However, the two Kalkschiefer facies basins are postulated entirely on tectonic considerations. A second difference between the model proposed by (Hubmann, 1993, Fig. C.6a) and the model proposed here (Fig. C.6b) is that we do not directly link the stratigraphy we observe in the upper tectonic nappe system with the stratigraphy in the lower tectonic nappe system. We do not know how much displacement occurred along the Rannach thrust and if the two nappe systems were directly adjacent during sedimentation or not. The stratigraphy in the two nappe systems shows some differences: Whereas in the upper nappe system dolomitic, carbonaceous, sandy and marly sediments dominate, the lower nappe system is dominated by fine-grained siliclastic rocks and more pelagic sediments. However, both nappe systems share the volcanic rocks at the base. In fact, these basal volcanic rocks may have served as a detachment horizon for the later Rannach thrust.

Despite these modifications in the paleogeographical interpretation and the uncertainties that remain due to later deformation, we suggest that the Paleozoic of Graz nicely fits in other larger-scale models for the paleogeographical evolution of the Austroalpine during the Paleozoic. In the Silurian, the Paleozoic of Graz was located at the northern border of Gondwana, where spreading led to volcanism and the deposition of volcano-clastic rocks. In the Devonian, the Paleotethys opened and shallow-water, carbonate platform and basin sediments were deposited, followed by deeper-water and more pelagic sediments in the upper Devonian. In the Carboniferous, a change from an extensional setting towards a compressional setting occurred with the deposition of flysch-type deposits, erosion and carstification. Similar evolutions are observed in several other low-grade Paleozoic units such as the Carnic Alps or the Greywacke Zone (e.g. Fritz & Neubauer, 1988; Schönlaub, 1992; Neubauer & Sassi, 1993; Schönlaub & Histon, 1999; Von Raumer & Stampfli, 2008).

C.6 Tectonic evolution of the Paleozoic of Graz: A discussion

According to the profiles and structural map shown in figure C.3 and C.4, the internal geometry of the Paleozoic of Graz is best described in terms of an upper and a lower nappe system separated by the Rannach thrust. Deformation in the lower nappe system is dominated by a ductile penetrative foliation, isoclinal folds and an E-W stretching lineation. Deformation in the Rannach thrust zone is dominated by a stretching lineation that progressively turns from E-W to SE-NW. In both the lower and upper nappe systems open folds with NE-SW trending fold axes occur. Several brittle strike-slip faults cross-cut the Paleozoic of Graz, but major normal faults inside the complex are not known. The whole complex is bordered

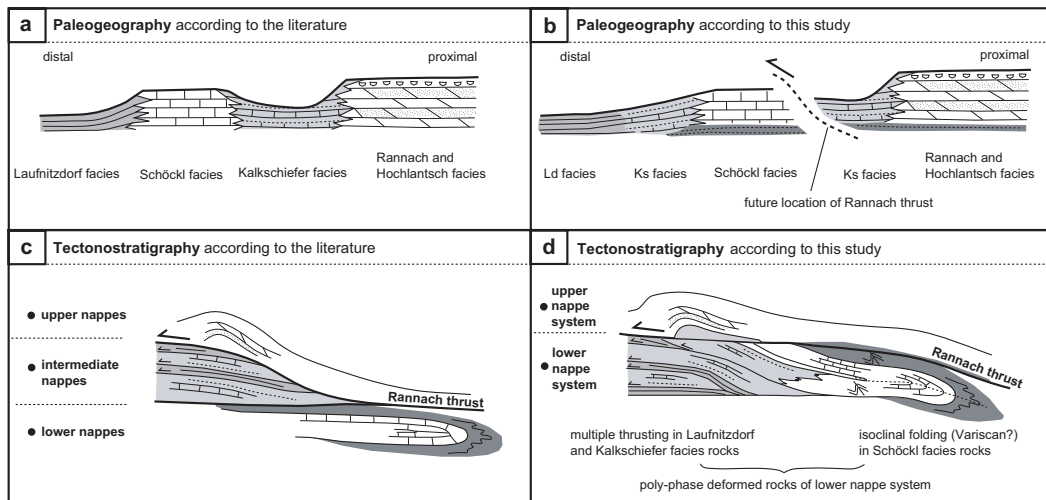


Figure C.6: (a) Simplified tectonostratigraphy as presented by Fritz et al. (1991, 1992). (b) Simplified tectonostratigraphy as proposed in this study. (c) Simplified paleogeography as proposed by Hubmann (1993). (d) Simplified paleogeography as proposed in this study.

by a normal fault in the west, a strike-slip fault in the northwest and several complex strike-slip, normal and thrust faults in the south and east. In the following, we discuss what we know and what we do not know about the events which led to this actual internal geometry of the complex.

C.6.1 Age of internal deformation and metamorphism - Variscan or Eo-Alpine?

The internal deformation of the Paleozoic of Graz is loosely-constrained by the Upper Carboniferous age of the youngest sediments incorporated into the deformed complex and by the Late Cretaceous Gosau basin which unconformably overlies the deformed complex (Fig. C.2). Within this large age bracket both the Variscan (Carboniferous) and the Eo-Alpine (Cretaceous) orogeny occurred, which are both well-known in large parts of the Eastern Alps. Variscan deformation is documented for the Carnic Alps and the Greywacke zone (Fig. C.1a) by late Carboniferous to Permian rocks which discordantly overlie deformed pre-late-Carboniferous sequences (Neubauer, 1988b; Schönlaub & Histon, 1999; Neubauer & Handler, 1999). In the Carnic Alps rocks of the same age as the Höchkogel and Hahngraben Fm (Fm 34-35) from the Rannach facies are incorporated in isoclinal, complex Variscan deformation (Schönlaub & Histon, 1999, their Fig. 7 and 9). Correspondingly, in the Gurktal nappe system, Variscan deformation is indicated by Carboniferous $^{40}\text{Ar}/^{39}\text{Ar}$ muscovite ages from mylonites (Neubauer & Handler, 1999). It is therefore possible that Variscan deformation also affected the Paleozoic of Graz. In the upper nappe system, a hint for Variscan tectonics in the Graz Paleozoic is evident from carstification of previous deep

marine limestones (Sanzenkogel. Fm.) followed by deposition of clastic sediments containing Variscan mica (Hahngraben Fm.; Fig. C.2). Conversely, Eo-Alpine deformation is well-documented in large parts of the Eastern Alps by deformed Permo-Mesozoic sediments, for example below the Greywacke zone or below the Gurktal nappe system (Ratschbacher, 1986). In these zones a similar top-W to top-NW thrusting as in the Paleozoic of Graz occurred which may indicate that deformation in the Paleozoic of Graz is also of Eo-Alpine age. In addition, recent studies in the Northern Calcareous Alps showed that the onset of Eo-Alpine thrusting in these units already started in the late Jurassic (ca 150 Ma: Frisch & Gawlick, 2003; Fritz et al., 2006). This was most likely associated with closure of the Meliata oceanic basin, blue-schist metamorphism of oceanic sediments, and nappe imbrication of footwall units (Dallmeyer et al., 2008). Unfortunately, Permo-Mesozoic sediments - used elsewhere in the Eastern Alps to differentiate between Variscan and Eo-Alpine orogeny - are absent in the Paleozoic of Graz. So neither Variscan nor Eo-Alpine deformation can be proven in the Paleozoic of Graz with the help of sediments.

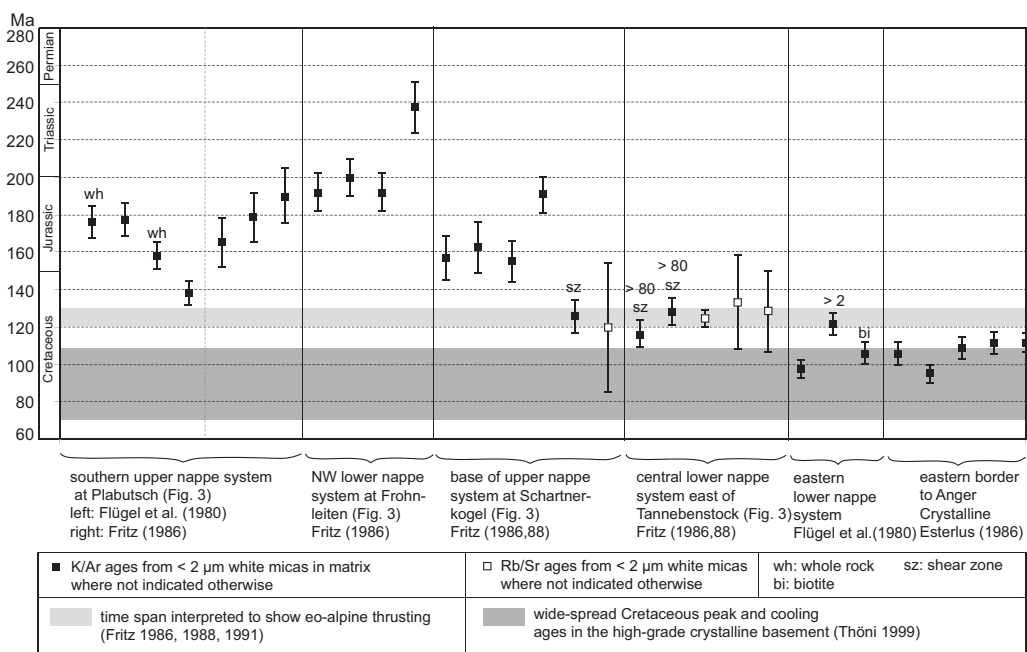


Figure C.7: Geochronological ages from the Paleozoic of Graz (from Flügel et al. (2000); Fritz (1986, 1988, 1991) and Esterlus (1986). Fritz (1986, 1988, 1991) interpreted the ages in the time interval 130-115 Ma as showing Eo-Alpine thrusting. However, the ages scatter over a larger time interval from 240 - 100 Ma and do not necessarily show the time of deformation (Thöni, 1999), see also text for discussion. Timescale after Ogg et al. (2008).

The age of the low-grade metamorphism in the Paleozoic of Graz is similarly controversial. Earlier studies suggested Silurian to Early Devonian rifting and volcanism (Hasenhüttl, 1994) and the Variscan orogeny (e.g. Fritz, 1986; Russegger, 1996) as the causes for meta-

morphism. In view of the rising evidence for a Permian thermal event (Schuster & Stuewe, 2008) ? also suggested that the overall metamorphism of the Paleozoic of Graz could be the result of Permian burial. Fritz (1988, 1991) interpreted K/Ar and Rb/Sr ages from white micas in both pressure shadows and the matrix as being the result of an Eo-Alpine thrusting event around 125 Ma and concluded, that all deformation in the Paleozoic of Graz took place during the Cretaceous. However, a plot of all published isotopic ages from the Paleozoic of Graz shows that they scatter over a large time interval from ~240 Ma down to ~90 Ma (Fig. C.7) and that only a few ages lie in the range Fritz (1988, 1991) attributed to the age of deformation. A similar scatter of ages was recorded from other low-grade Upper Austroalpine Units in the Eastern Alps such as the base of the Northern Calcareous Alps and the Greywacke Zone (Kralik et al., 1987; Thöni, 1999). The interpretation of all these scattering ages is difficult: They could (a) represent mixed ages between an old, Variscan and a younger (~100 Ma) Eo-Alpine event, (b) be related to hot fluids circulating after Triassic-Jurassic spreading, or (c) represent crystallisation ages during a Jurassic to Early Cretaceous deformation (Thöni, 1999). In view of these difficulties in interpreting isotopic ages in low grade rocks we are not convinced that the few isotopic ages that lie in the range of 130-115 Ma in the Paleozoic of Graz are sufficient to conclude that all deformation in the Paleozoic of Graz took place during the Cretaceous. We suggest that the actual state of knowledge about deformation and metamorphism and the lack of a modern, detailed geochronological analysis of the region do not allow judging unequivocally which of the two major events (Variscan or Eo-Alpine) was (and to which extent) responsible for the actual internal geometry of the Paleozoic of Graz.

C.6.2 Deformation along the borders in the Late Cretaceous and Tertiary

The Paleozoic of Graz is not only internally deformed and metamorphosed; it is also spectacularly juxtaposed against high grade crystalline units such as the Koralm Crystalline along its south-western and the Gleinalm Crystalline along its north-western borders (Fig. C.1b). Several models have been proposed to explain the emplacement of the Paleozoic of Graz on top of these crystalline units. The following observations have to be included in these models:

(i) the Paleozoic of Graz is only 1-2 km thick: the crystalline rocks below the Paleozoic of Graz were reached in a drill hole in the Gosau basin at a depth of only about 1000 m below sea level (Kröll & Heller, 1978, Fig. C.4, profile E). Based on the very low grade metamorphism of the uppermost units it can be argued that the complex was never more than 5-8 km thick.

(ii) Geochronological data from the surrounding crystalline units constrain the age of amphibolite to eclogite facies metamorphism to around 100-80 Ma and subsequent cooling to below 100°C to around ~60-50 Ma (Neubauer et al., 1995; Heijl, 1997; Thöni, 1999).

(iii) Simultaneously to metamorphism and cooling, sedimentation occurred in the alluvial to marine Gosau basin on top of the Paleozoic of Graz. This suggests that exhumation of the crystalline units was not accompanied by major topography.

iv) The profiles in Fig. C.4 show that the internal structure of the Paleozoic of Graz is dominated by compressional structures; apart from brittle normal and strike slip faults along the borders extensional structures inside the Paleozoic of Graz are rare.

(v) The Paleozoic of Graz is bounded by several ductile to brittle fault zones: The north-western border towards the Gleinalm Crystalline is made up by a sinistral fault zone dipping 50-80° towards SSE and showing a stretching lineation dipping ~10° towards the NE (Neubauer, 1988a; Neubauer et al., 1995). The south-western border towards the Koralm Crystalline is a steep, brittle, NE dipping normal fault (Graden normal fault) which overprints a gently NE dipping mylonitic foliation with a down-dip lineation and top-NE shear sense in the crystalline rocks (Krohe, 1987; Rantitsch, 2006). The eastern border to the Radegund Crystalline is made up of a several 100 m broad zone of highly-deformed rocks of the Paleozoic of Graz which show both top-E and top-W shear sense (Krenn, 2001). The southern border towards the Radegund Crystalline consists of a steep, brittle dextral strike slip fault (Krenn, 2001). The north-eastern border towards the Anger Crystalline is less pronounced and the metamorphic grade increases continuously. A tectonic foliation is developed, which dips 35-55° towards SW and shows both top-NE and top-SW shear sense. This foliation is overprinted by steep SW dipping brittle normal faults (Neubauer, 1981, 1982; Gsellmann, 1987; Krenn, 2001; Krenn et al., 2008).

Ratschbacher et al. (1991) interpret the mylonitic fault rocks found in several of the border faults as part of a single belt of mylonitic rocks which underlie the Paleozoic of Graz. According to them, exhumation of the surrounding crystalline rocks took place due to a gravitational instability caused by the thickened Early Cretaceous orogenic wedge, and the entire nappe stack of the Paleozoic of Graz was sheared off from its basement along a basal, spoon-shaped high-strain zone towards the north-east. In contrast, Neubauer et al. (1995) proposed that the Glein- and Koralm Crystalline were exhumed in an overall transpressional setting in a sinistral wrench corridor, where the Paleozoic of Graz and the Gosau basin were located in a releasing bend of this corridor. This model does not require a connected shear zone at the base of the whole Paleozoic of Graz and interprets the extensional structures at the borders and the Gosau basin formation as the result of oblique shortening rather than gravitational collapse. In consistency with that, Rantitsch et al. (2005) modelled the thermal influence of the exhuming crystalline rocks onto the Paleozoic of Graz and the Gosau basin along the Graden normal fault and concluded that a normal fault which roots in a flat lying detachment at ~20 km depth best fits the observations. Consequently, from a thermal point of view no shallow flat lying detachment along the base of the Paleozoic of Graz is needed. Krenn et al. (2008) returned to the model proposed by Ratschbacher et al. (1991) and refined it to a two stage process: in a first event the Paleozoic of Graz extruded as a block together with the underlying crystalline rocks to the NE. In a second event the Paleozoic of Graz decoupled from the underlying crystalline rocks and pure extension led

to the formation of normal faults at the borders whereas the underlying crystalline rocks were ductilely stretched.

The models explaining the exhumation of the surrounding crystalline basement either invoke a continuous shear zone at the base of the Paleozoic of Graz (which decouples it from the underlying crystalline rocks) or brittle to ductile faults which go much deeper than the actual base of the Paleozoic units. Considering the internal geometry of the Paleozoic rocks (Fig. C.4), we suggest that decoupling along the base in an overall extensional setting (as suggested by Ratschbacher et al., 1991; Krenn et al., 2008) is mechanically highly unlikely. If extension and stretching of the underlying crystalline basement occurred, the whole internal Paleozoic of Graz would have dismembered. In contrast, no substantial extensional structures are observed in the Paleozoic of Graz and the profiles on figure C.4 suggest that there is a minimum of extensional strain. We therefore suggest that exhumation of the Kor- and Gleinalm Crystalline in an overall transpressional regime (as suggested by Neubauer et al., 1995) provides a good explanation that is consistent with the observations in the Paleozoic of Graz.

C.7 Conclusions

Re-evaluation of an abundance of local literature and the compilation of this information in form of integrated profiles leads to the following conclusions about the internal structure of the Paleozoic of Graz: (1) The 35 sedimentary formations defined by Flügel & Hubmann (2000) can be summarized into 13 distinct rock associations belonging to five different sedimentological facies termed the Laufnitzdorf, Kalkschiefer, Schöckl, Rannach and Hochlantsch facies. (2) The Paleozoic of Graz consists of an upper and a lower nappe system which are separated by a thrust, the Rannach thrust. Kalkschiefer, Rannach and Hochlantsch facies rocks occur in the upper nappe system, Kalkschiefer, Laufnitzdorf and Schöckl facies rocks occur in the lower nappe system. Upper and lower nappe system differ in deformation style and metamorphic grade. (3) In the literature, the same names were applied for both sedimentary facies as well as tectonic units. Because sedimentary facies and tectonic units do not correlate this should be avoided. (4) The age of internal deformation remains badly constrained. Compared with other Paleozoic units of the Eastern Alps, both Variscan and Eo-Alpine events may have contributed to the internal structure of the Paleozoic of Graz. (5) The exhumation of the surrounding crystalline basement during the Late Cretaceous led to deformation along the borders of the Paleozoic of Graz. For mechanical reasons we favour models that invoke a deep-seated detachment in the crystalline rocks relative to models that invoke a shallow, flat-lying detachment at the base of the Paleozoic of Graz.

C.8 Acknowledgments

The project was funded by Project Nr. 19366-N10 of the Fonds zur Förderung der wissenschaftlichen Forschung FWF. We thank K. Krenn and R. Schuster for helpful discussions and W. Frisch and J. von Raumer for constructive reviews.

Appendix D

Conference abstract related to Appendix C

- Gasser, D., Stuewe, K., Fritz, H. (2008) Geological profiles through the poly-phase deformed Paleozoic of Graz. *Journal of Alpine Geology*, Vol. 49, p. 29, PANGEO 08 conference, Vienna.

D.1 Geological profiles through the poly-phase deformed Paleozoic of Graz

The Upper Austroalpine / Upper Central Austroalpine Paleozoic of Graz consists of a 30 x 50 km sized nappe complex built up mainly of low-grade carbonates and schist of Silurian to Carboniferous age. It lies on top of high-grade Middle Austroalpine / Lower Central Austroalpine crystalline basement, and it is discordantly overlain by a small Cretaceous Gosau Basin and by the Neogene Styrian Basin. As such, the Paleozoic of Graz records many of the sedimentological, tectonic and metamorphic events that formed the present Eastern Alps since the early Paleozoic.

Stratigraphy, palaeontology, internal structure and metamorphism of the Paleozoic of Graz were extensively studied over the past 180 years, and resulted in over 500 publications (eg. Flügel and Hubmann, 2000 and references therein). However, remarkably no geological profiles through the entire Paleozoic of Graz are published and the complex, poly-phase tectonic history is still not fully understood. We present geological profiles through the entire Paleozoic of Graz in order to understand the actual 3D geometry of this complex. As a base, we use 1:50 000 geological maps, a 10 m digital elevation model, local detailed maps and profiles, drillhole data and descriptions of structure and stratigraphy from various publications listed in Flügel and Hubmann (2000).

The structure of the Paleozoic of Graz, as revealed by the profiles, is dominated by the following elements: (i) a probably Variscan (?) large-scale isoclinal fold with an E-W trending axis in the lower nappe complex bringing Silurian schist on top of Devonian limestone, (ii) early Cretaceous W to NW directed thrusts and open to tight folds separating the Paleozoic of Graz into an upper and a lower nappe system, and (iii) late Cretaceous to Tertiary ductile to brittle normal and strike-slip faults defining the borders against the surrounding crystalline basement. Which of these events could have led to the emplacement of the Paleozoic of Graz on top of the crystalline basement is discussed

Gasser, D., Stüwe, K., Fritz, H. (2008) Journal of Alpine Geology, Vol. 49, p. 29, PANGEO 08 conference, Vienna.

Appendix E

Geology of Styria: An overview

Abstract In 2009 the Styrian Doctoral School of Earth Sciences organised a field workshop on the geology of Styria. The field trip was led by PhD students of the three participating universities: KFU Graz, TU Graz and MU Leoben. As an outcome of this field trip, we present here the geology of the entire province in a simplified way, taking into account modern concepts of the tectonic evolution. In a first part, the tectonic units building up Styria are presented; in a second part the geodynamic evolution of these units through time is described. A third part deals with the economic significance of mineral resources in Styria. The figures of this contribution are available online on the pages of the naturwissenschaftlicher Verein and at <http://wegener.uni-graz.at>.

published as: Gasser, D., Gusterhuber, J., Krische, O., Puhr, B., Scheucher, L., Wagner, T. and Stüwe, K. (2009) Mitteilungen des naturwissenschaftlichen Vereins Steiermark 139, 5-36.



Figure E.1: Group photo of participants of the first field excursion with the topic "Geology of Styria" of the joint doctoral school "Earth Sciences" of the three universities KF Graz, TU Graz and MU Leoben. The rock boulder consists of a Permian gabbro eclogitized during the Cretaceous orogeny, Koralmpe, Styria. Participants: 1 Thomas Wiedel (KF), 2 Dr. Prof. Roland Bakker (MU) 3 Latif Yalcinoglu (MU), 4 Lorenz Scheucher (MU), 5 Bernhard Hubinger (KF), 6 Patrick Grunert (KF), 7 Andrea Kern (KF), 8 Stefan Hausegger (TU), 9 Emilie Bruand (KF), 10 Florian Mittermeyer (TU), 11 Oliver Krische (MU), 12 Jürgen Gusterhuber (MU), 13 Muhammad Imran (MU) 14 Omar Mohammed (KF), 15 Nantasin Prayath (KF), 16 Ivana Cuperova (MU), 17 Barbara Pühr (KF), 18 Nina Gegenhuber (MU), 19 Dr. Prof. Kurt Stüwe (KF), 20 Rhamat Ali Gakkhar (MU), 21 Nicolas Legrain (KF), 22 Thomas Wagner (KF), 23 Deta Gasser (KF), 24 Tamer Abu-Alam (KF), 25 Esam Abu El-Siba (MU).

E.1 Introduction

Styria, the second largest province of Austria, has a very rich and diverse geological history. Located at the transition from the European Alps in the west to the Pannonian Basin in the east, it contains rocks that tell a fascinating story of mountain building and basin formation that covers at least the last 500 million years of Earth's history. Indeed, the capital of Styria, Graz, can probably boast with the fact of having a more variable geology within 50 km radius than just about any other state capital in the world: from volcanism to high-grade metamorphic rocks, from young limestones to ancient marbles, from active mountain

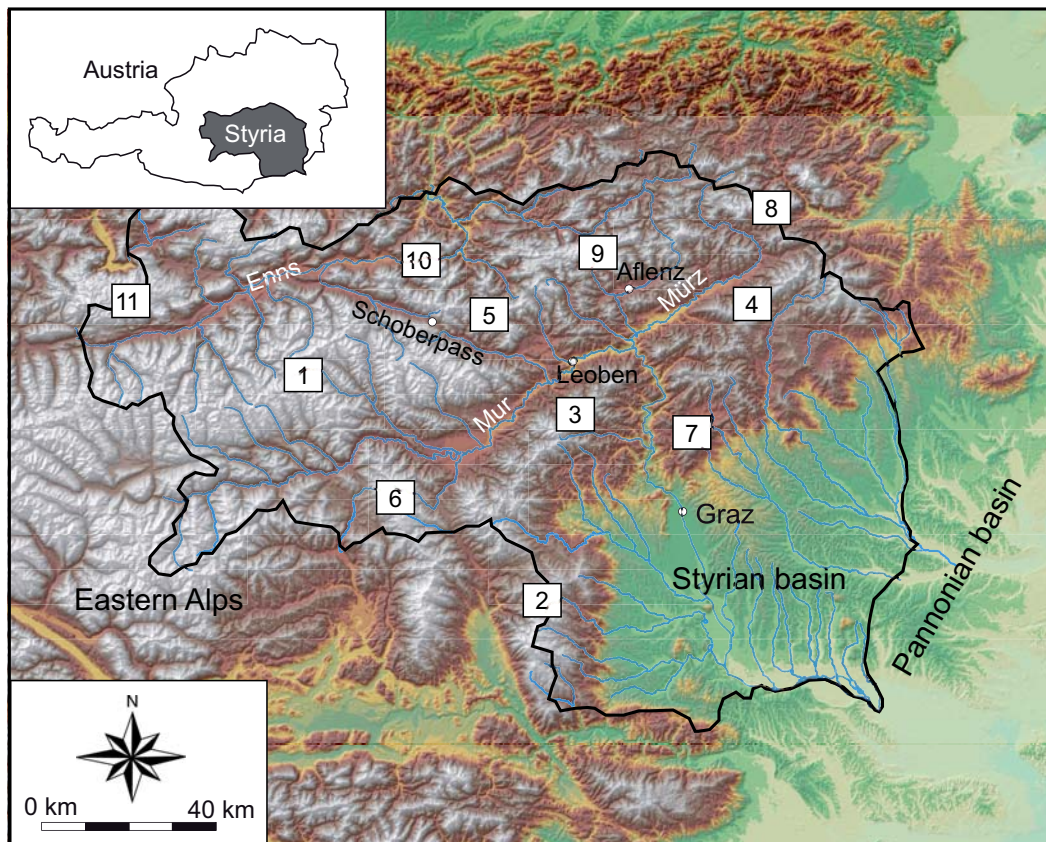


Figure E.2: Topographic map derived from a digital elevation model of Styria with the transition from the Eastern Alps into the Styrian/Pannonian Basin nicely visible. The Alpine part of Styria is divided into several regions, whereof the most important ones are: (1) Niedere Tauern, (2) Koralpe, (3) Gleinalpe, (4) Fischbacher Alpen, (5) Eisenerzer Alpen, (6) Seetaler Alpen, (7) Grazer Bergland, (8) Rax, (9) Hochschwab, (10) Gesäuse, (11) Dachstein. More detailed topographic maps of Styria are online at: www.austrianmap.at.

building to sedimentary basin formation, all can be found within an hours drive in Styria.

Earth Sciences in general and the processes that shaped the geological history of Styria in particular can be studied at three universities in Styria: the Karl Franzens University Graz (KFU), the Technical University Graz (TUG) and the Montan University Leoben (MUL). As part of the newly founded joint Doctoral School of Earth Sciences of the three universities, a geological field trip for PhD students took place in May 2009 (Fig. E.1). The aim was to introduce the (partly international) students to the geology of Styria and to provide an overview of the complex geological history of this area. The excursion was led by PhD students who work on geological projects in different parts of Styria and was coordinated by K. Stüwe. During the field trip, the idea was born to present the geology of Styria to a wider audience. This contribution is the outcome of a combined effort of the involved PhD students to present a simplified, modern overview of the geological history of Styria

to professional earth scientists and non-professionals alike. Our contribution presents an overview over the different tectonic units building up the province, the different rock types occurring in these units, the evolution of these units through time as well as the economic significance of ore deposits in the state.

Around 200 years of geological research in Styria led to the formulation of many different models and concepts explaining its geological history. A milestone in the understanding of the geological history of Styria was the contribution by Flügel & Neubauer (1984). However, since then, many debates were led about the exact tectonic relationship between different units, or about which rocks actually belong to which units and which do not. Some of these debates are still ongoing (fortunately for the active geologists!). There are debates of only local importance; others deal with the large-scale origin of huge areas in Styria. We are aware of these controversies, but a short overview contribution like ours can never cope with all of them. We therefore decided to closely follow the two recent contributions of Schmid et al. (2004) and Froitzeim et al. (2000), except for the Northern Calcareous Alps where we follow Frisch & Gawlick (2003). In addition we would like to point to the contribution by Neubauer et al. (2000) where a different nomenclature and tectonic interpretation is used. In addition, we selected a small number of the most recent/relevant contributions on each geological unit. Clearly, this selection is our personal choice and meant to give the reader only a starting-point.

E.2 Geographical division of Styria

On a topographic map derived from a digital elevation model (Fig. E.2), a first-order geographic division of Styria is immediately obvious: whereas the northern, western and south-western parts of Styria are built up of rugged mountains, the south-eastern part is made up of relatively flat lowlands with only minor topographic relief. This transition is spectacular: it marks the passage from the Alps, which extend hundreds of kilometres westward all the way to Nice, to the Pannonian Basin, which extends hundreds of kilometres eastward all the way to the Carpathian arc. Three main rivers drain the Alpine part of Styria to either side of the principal Alpine divide (located at the Schoberpass, Präbichl and Semmering): the Enns towards the north-west and the Mur and Mürz towards the south-east (Fig. E.2). The valleys formed by these three river systems divide the Alpine part of Styria into several smaller massifs, of which the most important ones are the Niederen Tauern, Koralpe, Gleinalpe, Fischbacher Alpen, Eisenerzer Alpen, Seetaler Alpen, Grazer Bergland, Rax, Hochschwab, Gesäuse and Dachstein (Fig. E.2). The part of the Pannonian Basin exposed in Styria is called the Styrian Basin. Typical photographs of different Styrian landscapes are shown on Fig. E.3. Each of these landscapes has its own geological history, which will be discussed in the following chapters.



Figure E.3: Air photographs of typical Styrian landscapes as controlled by their geology. **(a)** The crystalline rocks of the Austroalpine Units form sharp ridges with regular slopes. Rottenmanner Tauern in the fore-ground, Seckauer Tauern in the background. **(b)** The low-grade Paleozoic sedimentary rocks of the uppermost Austroalpine Units form wooded hills and sharp limestone cliffs: the Grazer Bergland with Röthelstein/Rote Wand in the foreground and Hochlantsch in the background. **(c)** The Paleozoic rocks of the Greywacke Zone build up sharp, steep mountains. Erzberg mine in Upper Devonian limestones with the village of Eisenerz in the foreground. The mine is the largest siderite mine in the world and the largest open-pit mine in Central Europe. **(d)** The Northern Calcareous Alps are dominated by Triassic and Upper Jurassic carbonate platforms building up major cliffs intercalated with more soft sediments forming the flatter slopes below the cliffs. The Hoher Dachstein in the foreground, with 2995 m the highest peak in Styria, consists of Upper Triassic limestone. **(e)** The Neogene sediments of the Styrian Basin form relatively flat low-lands with good agricultural land. In the background small hills of Tertiary volcanic rocks. **(f)** The Riegersburg in south-eastern Steiermark is built upon very young, Plio-Pleistocene basaltic lava. All photos by R. Homberger, Arosa.

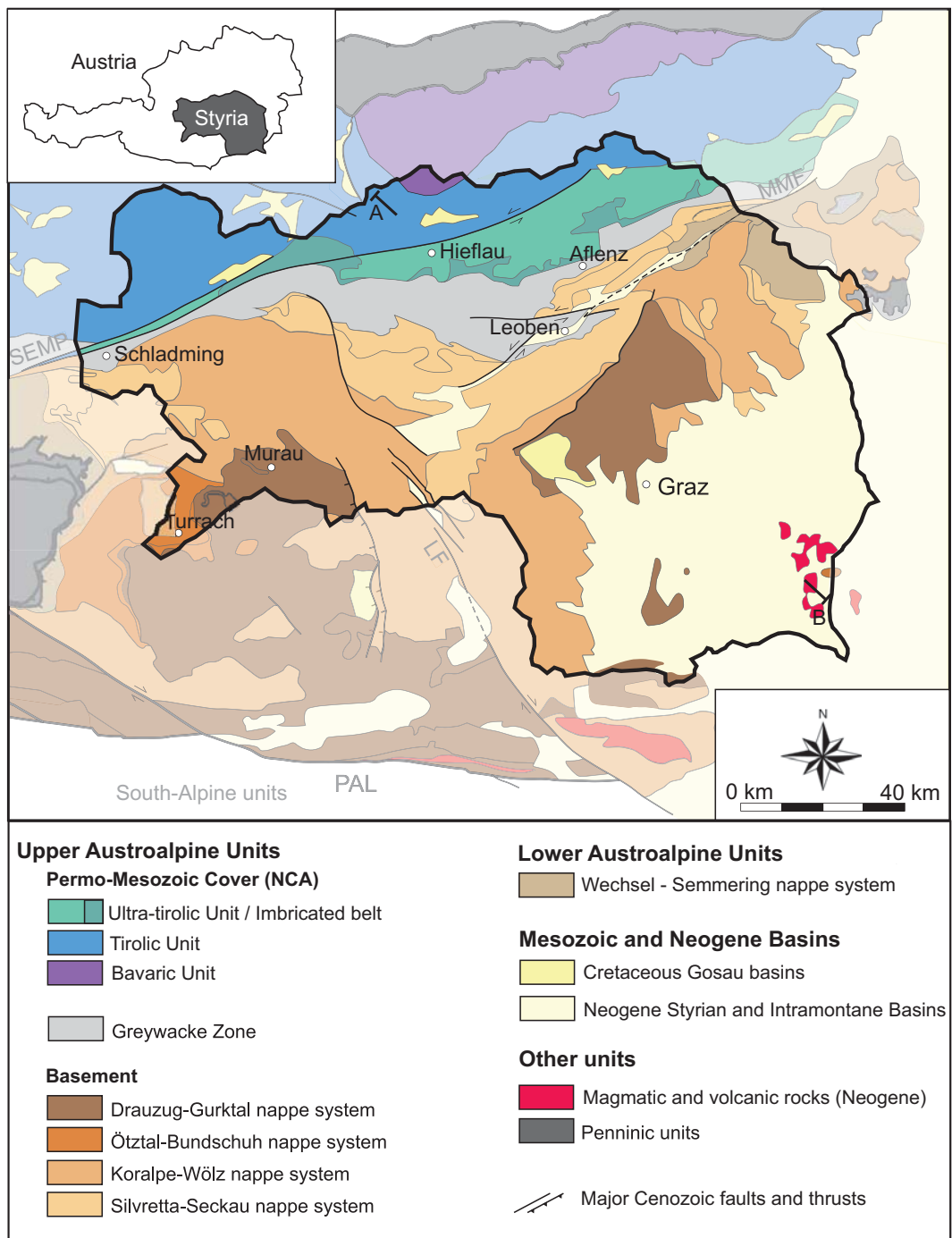


Figure E.4: Tectonic overview map of Styria, after Schmid et al. (2004) and Frisch & Gawlick (2003) for the NCA. A-B = Profile trace of Fig. E.5. Abbreviations: NCA = Northern Calcareous Alps, SEMP = Salzach-Ennstal fault system, MMF = Mur-Mürz fault system, LF = Lavantal fault system, PAL = Periadriatic Lineament. Geological maps of Styria are for download at www.geologie.ac.at/.

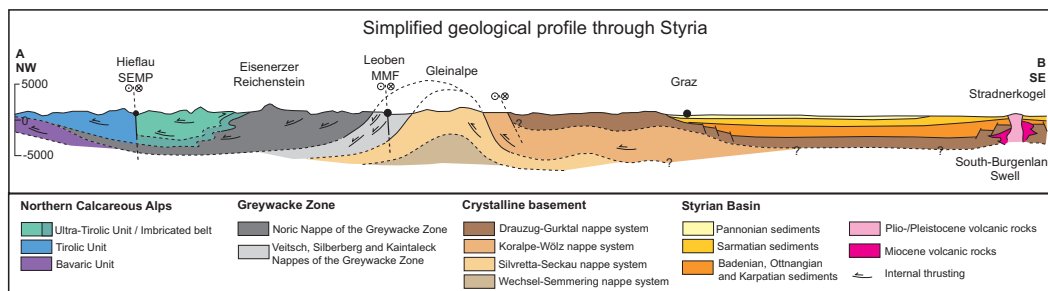


Figure E.5: Simplified geological profile through Styria. Abbreviations: SEMP = Salzach-Ennstal fault system, MMF = Mur-Mürz fault system. Profile trace is indicated on Fig. E.4.

E.3 Geological division of Styria

The first-order geographic division of Styria into Eastern Alps and Styrian Basin is also a geological division (Fig. E.4 and E.5). The Alpine part consists of poly-phase deformed and partly metamorphosed sedimentary and crystalline rocks of the Austroalpine Units, whereas the Styrian Basin consists of less deformed and unmetamorphosed sediments that overlie the Austroalpine Units.

E.3.1 The Austroalpine units

All geological units exposed in the Alpine part of Styria belong to the so-called Austroalpine nappe complex. They consist of several nappe systems stacked on top of each other and separated by either flat-lying shear zones or by major steep strike-slip faults from each other. North of a line Enns valley – Schoberpass – Leoben – Aflenz – Rax (Fig. E.2 and Fig. E.4) Paleozoic to Mesozoic sediments and low-grade metamorphic metasediments of the Greywacke Zone and the Northern Calcareous Alps (NCA) are exposed. South of this line, a series of low- to high-grade Paleozoic and Mesozoic metamorphic rocks with complex poly-phase tectonic and metamorphic histories is exposed. A schematic tectonostratigraphy according to Frisch & Gawlick (2003) (for the NCA), Schmid et al. (2004) and Froitheim et al. (2000) is displayed in Fig. E.6 and the different units are discussed in more detail below.

Crystalline basement units

The Crystalline basement units to the south of a line Enns valley – Schoberpass – Leoben – Aflenz – Rax (Fig. E.2, Fig. E.4) can be separated into several nappe systems. They

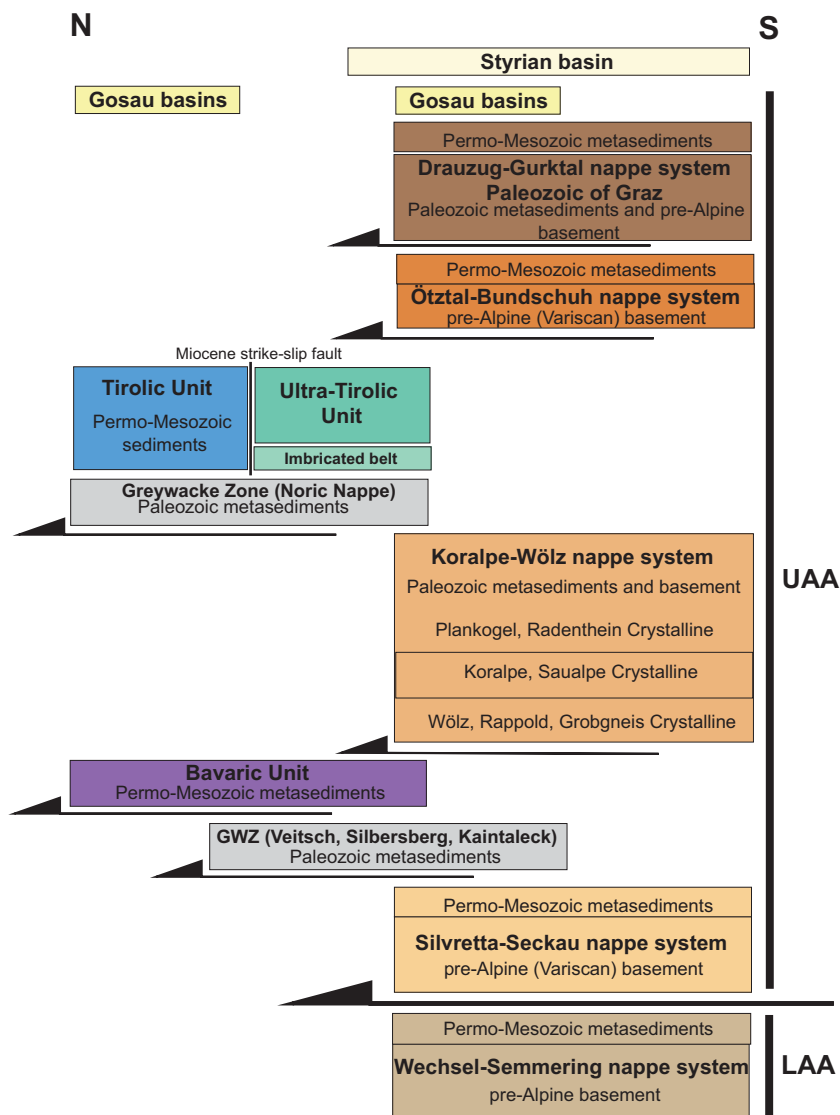


Figure E.6: Schematic tectonostratigraphic relationships as they are observed today between the different tectonic units in Styria. This tectonostratigraphy is the result of mainly three different orogenies: Upper Jurassic thrusting in the NCA, Cretaceous nappe stacking in all Austroalpine Units, and Miocene strike-slip tectonics. After Frisch & Gawlick (2003) for the NCA, Schmid et al. (2004) and Froitzheim et al. (2000). Abbreviations: UAA = Upper Austroalpine Units, LAA = Lower Austroalpine Units.

are from bottom to top the Semmering-Wechsel, Silvretta-Seckau, Koralm-Wölz, Ötztal-Bundschuh and Drauzug-Gurktal nappe systems (after Schmid et al., 2004; Froitzheim et al., 2000). A simplified geological map with the different rock types occurring in this nappe systems is displayed in Figure E.7 (except for the uppermost Drauzug-Gurktal nappe system, which is displayed in Fig. E.9). A metamorphic map indicating the peak metamorphic grade reached during the last two important metamorphic events (Permian and

Eo-Alpine) is displayed on Figure E.8. The different nappe systems are described in more detail below.

Semmering-Wechsel nappe system (Lower Austroalpine Units LAA) The Semmering-Wechsel nappe system is only exposed in a small area in northwestern Styria close to the Semmering pass and in the Wechsel mountains (Fig. E.2, Fig. E.4). It consists mainly of paragneisses and phyllitic micaschists, but orthogneisses, greenschists, amphibolites and quartzites are also present (Fig. E.7). Permo-Mesozoic carbonaceous, siliciclastic and volcanoclastic metasediments partly overlie and are folded into the crystalline basement. As in all crystalline units of the Austroalpine nappe stack the metamorphic history in the Semmering-Wechsel nappe system is complex. Relics of a Variscan (Carboniferous) and a Permo-Triassic metamorphic event are overprinted by a greenschist facies Eo-Alpine event (Fig. E.8; Schuster et al., 2001, 2004).

Silvretta-Seckau nappe system (Upper Austroalpine Units UAA) The Silvretta-Seckau nappe system builds up a small region south of Schladming, the Rottenmanner and Seckauer Tauern which are part of the Niedere Tauern, the Gleinalpe region in central Styria and an elongated region north of the Mürz valley between Kapfenberg and Rax (Troiseck-Floning Zug) (Fig. E.2; Fig. E.4). It consists of biotite-plagioclase gneisses and mica schists, hornblende gneisses, amphibolites and orthogneisses (Fig. E.7). Migmatites and ultramafic complexes locally occur. Remnants of Permo-Mesozoic cover sequences, such as siliciclastic, volcanoclastic and carbonaceous sediments are locally present. Variscan tectonics and metamorphism is widely distributed in this nappe system, but no Permo-Triassic metamorphism is recorded (Fig. E.8a). The whole nappe system is overprinted by a greenschist to epidote-amphibolite facies Eo-Alpine metamorphism (Fig. E.8b; Scharbert, 1981; Schermaier et al., 1997; Neubauer et al., 1995; Faryad et al., 2002; Faryad & Hoinkes, 2003).

Koralpe-Wölz nappe system (UAA) The Koralpe-Wölz nappe system is exposed in much of the western Niedere Tauern, the Seetaler Alpen, the Koralpe and the Fischbacher Alpen and therefore builds up large parts of Styria (Fig. E.2, Fig. E.4). In contrast to the other crystalline units, it lacks Permo-Mesozoic metasediments (Fig. E.6, E.7). It consists mainly of micaschists and paragneisses, pegmatites and orthogneisses. Locally marbles, amphibolites and eclogites occur (Fig. E.7). A wide-spread Permo-Triassic metamorphic imprint up to amphibolite facies and local anatexis is recorded, accompanied by Permian gabbros, granites and volcanic rocks (Fig. E.8a). The Eo-Alpine imprint rises from north to south from greenschist/epidote-amphibolite facies (Wölz complex, Fig. E.6) to eclogite facies (Koralpe complex, Stuewe & Powell, 1995; Bruand et al., 2010). Across the so-called BUP (base of the Eo-Alpine upper plate) on top of the Koralpe-Wölz nappe system a decrease in metamorphic grade down to lower greenschist facies is recorded (Fig. 8b; Tenczer & Stuewe, 2003; Schmid et al., 2004; Schuster et al., 2004).

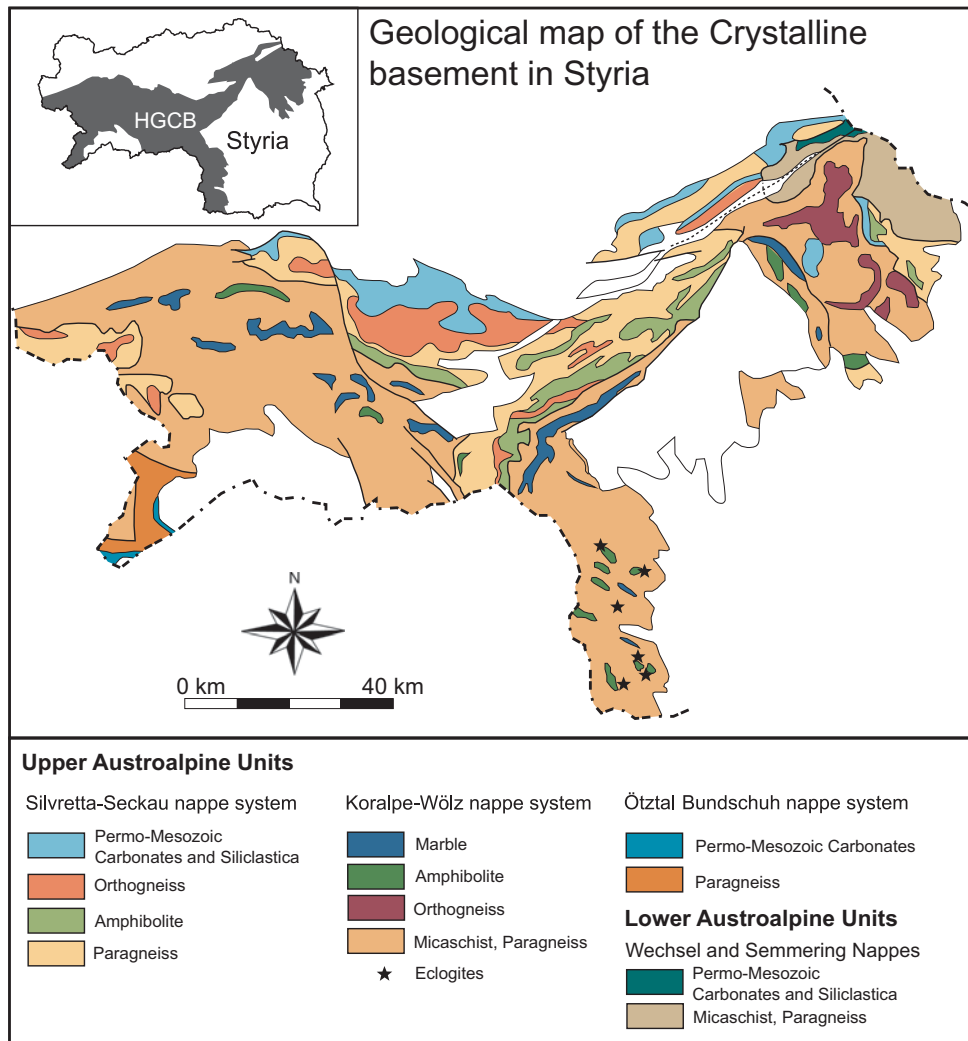


Figure E.7: Geological map of the medium- to high-grade metamorphosed units of Styria. Simplified after Flügel & Neubauer (1984) and Egger et al. (1999) with the tectonic division of Schmid et al. (2004).

Ötztal-Bundschuh nappe system (UAA) The Bundschuh Nappe of the Ötztal-Bundschuh nappe system is only exposed in a small area in westernmost Styria around Turrach (Fig. E.4). It contains mainly biotite-plagioclase gneisses, mica schists, amphibolites and orthogneisses. Remnants of Permo-Mesozoic cover sequences are present (Fig. E.7). Up to amphibolite facies metamorphism occurred during the Variscan event, overprinted by an Eo-Alpine greenschist to amphibolite facies metamorphism (Fig. E.8b; Miller & Thöni, 1995; Koroknai et al., 1999; Schuster et al., 2004).

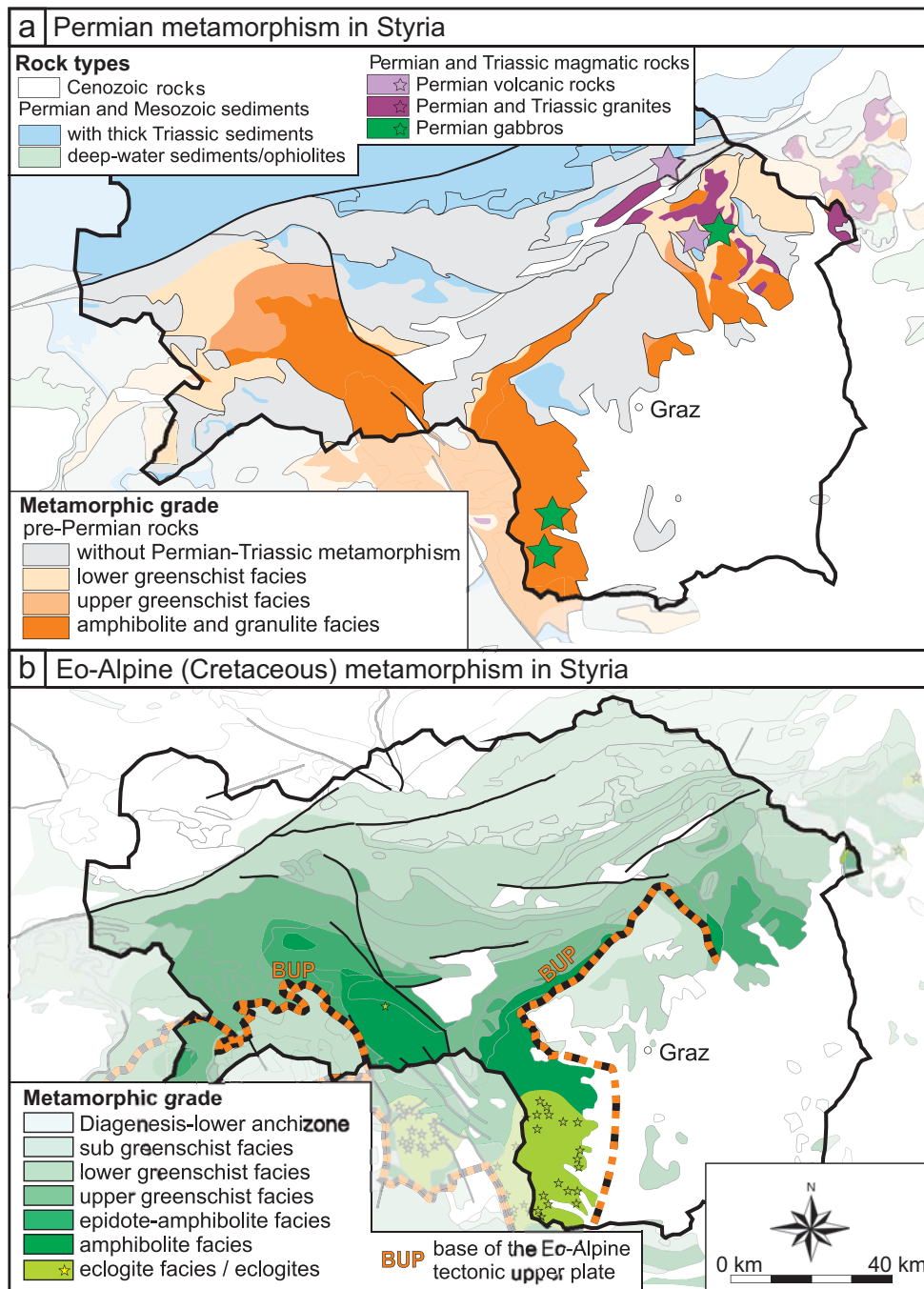


Figure E.8: Metamorphic map of Styria: (a) peak metamorphic grade reached during the Permian metamorphic event, (b) peak metamorphic grade reached during the Eo-Alpine event. Note that the colour code is only valid inside Styria. After Schuster (unpublished).

Drauzug-Gurktal nappe system (incl. Paleozoic of Graz) (UAA) The Drauzug-Gurktal nappe system represents the uppermost unit of the Austroalpine nappe stack in Styria. Remnants of it are exposed in two isolated areas: The Paleozoic of Graz in central Styria north of Graz (Grazer Bergland, Fig. E.3b, Fig. E.9) and the Gurktal nappes in western Styria (in the region of Murau; Fig. E.2, Fig. E.4). Both occurrences show similar sedimentary and tectonic features. In general, they consist of low-grade metamorphic Paleozoic sedimentary rocks with a few relics of Permo-Mesozoic cover occurring in the Gurktal nappes. The Gurktal nappes consist from bottom to top of the Murau Nappe, the Stolzalpe Nappe and the very small Ackerl Nappe (Flügel & Neubauer, 1984). The Murau Nappe is dominated by low-grade black schists and calcareous phyllites of probably Silurian age overlain by carbonates of Lower Devonian age. The Stolzalpe Nappe consists of (a) basal Upper Ordovician to Silurian volcanics, overlain by (b) carbonaceous, sandy and pelitic sediments of Silurian and Lower Devonian age that are in turn overlain by (c) Upper Devonian to Lower Carboniferous pelagic carbonates (Neubauer & Pistotnik, 1984; Koroknai et al., 1999).

The Paleozoic of Graz also consists of a lower and an upper nappe group (Fig. 9; Gasser et al., 2009). Both nappe groups are built up of several different sedimentary facies zones (Fig. E.10). The northern part of the lower nappe group around Breitenau (Fig. E.9) in the Grazer Bergland is dominated by Devonian to probably Carboniferous calcareous schists and pelitic sediments of the Kalkschiefer and Laufnitzdorf facies. The central and southern part of the lower nappe group south and east of the Passail Basin is dominated by basal Silurian volcanic rocks, overlain by Silurian to Devonian siliciclastic and carbonaceous rocks and Middle Devonian limestones (Fig. E.10). The upper nappe group is also characterized by basal Silurian volcanic rocks, exposed around Kehr. They are overlain by Devonian to Carboniferous carbonaceous schists, sandstones and limestones of the Kalkschiefer facies and Rannach facies exposed west of the Mur valley and in the Hohe Rannach, and of the Hochlantsch facies exposed in the Hochlantsch massif. Upper and lower nappe groups are separated by a major out-of-sequence thrust, the Rannach thrust (Figs. E.9 and E.10; Gasser et al., 2009; Flügel, 2000).

Greywacke Zone (UAA)

The Greywacke Zone represents an up to 23 km wide zone of Paleozoic rocks between the sedimentary rocks of the Northern Calcareous Alps in the north and the higher-grade crystalline basement units to the south (Fig. E.3c, Fig. E.11). This zone extends from Innsbruck in the west to Lower Austria in the east, where it plunges beneath Tertiary cover of the Vienna Basin (Fig. E.4). The Styrian and Lower Austrian parts are named the Eastern Greywacke Zone (Schönlaub, 1980). Akin to the crystalline basement units, the Greywacke Zone has a complex internal structure and consists of several tectonic nappes stacked on top of each other. They are from bottom to top the Veitsch, Silbersberg, Kaintaleck and Noric nappes (Neubauer et al., 1993, Figs. E.11, E.12).

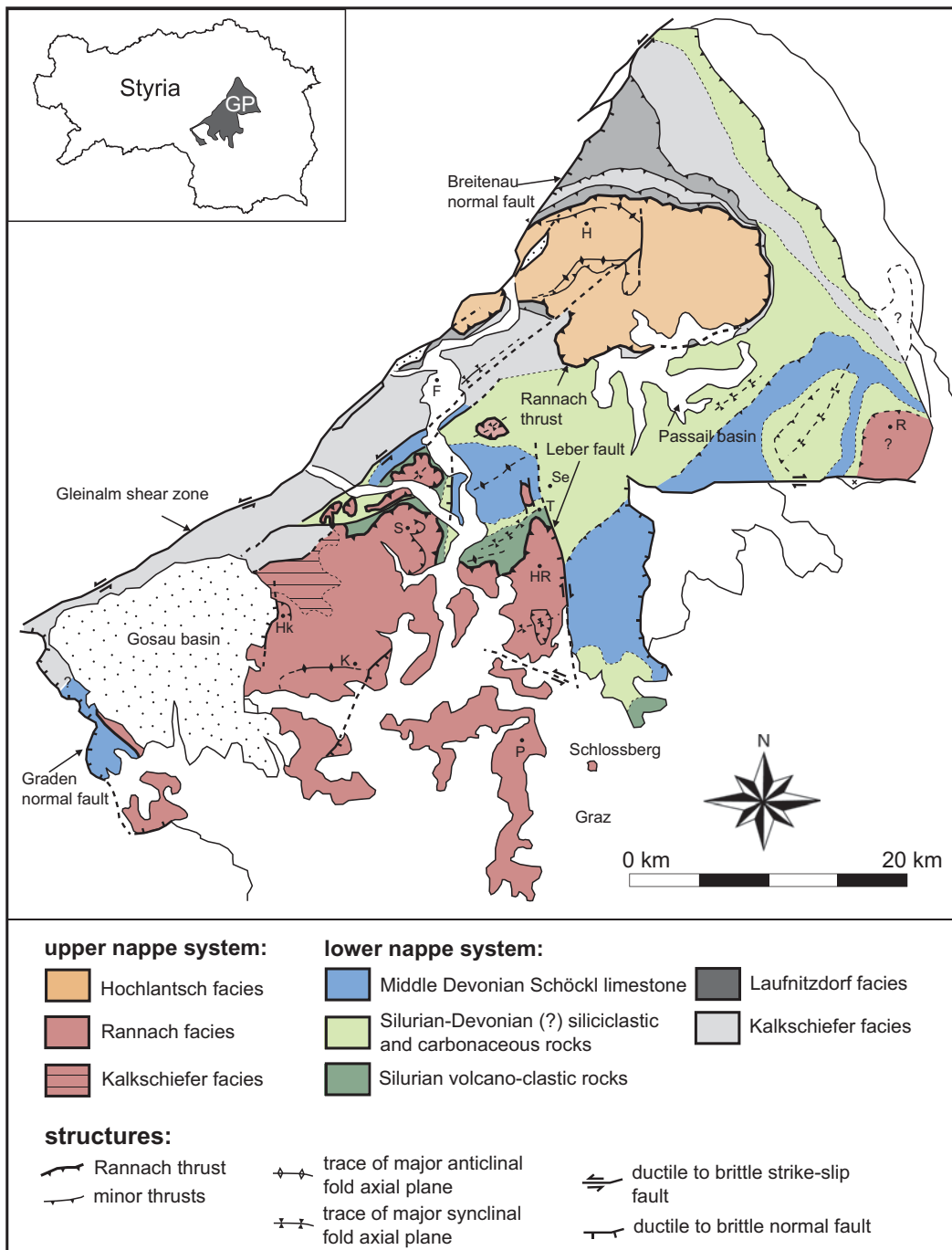


Figure E.9: Structural map of the Paleozoic of Graz. Geographic locations: P = Plabutsch, K = Kehr, Hk = Höllerkogel, S = Schartnerkogel, HR = Hohe Rannach, F = Frohnleiten, H = Hochlantsch, R = Raasberg, T = Taschen, Se = Semriach. Modified from Gasser et al. (2009).

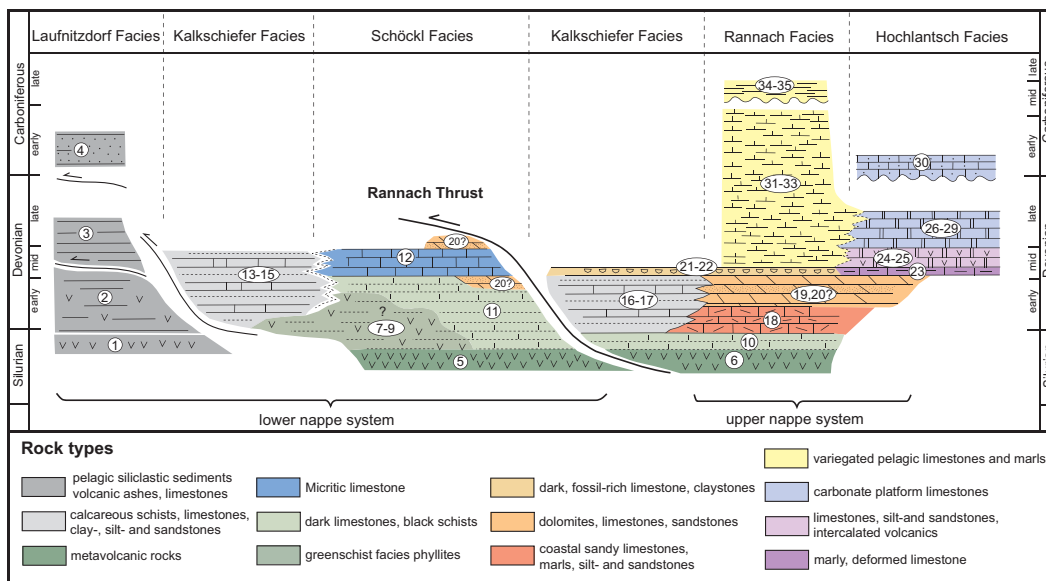


Figure E.10: Stratigraphic relationships as they are observed today in the major tectonic units of the Paleozoic of Graz. Formation numbers: 1 = Hackensteiner Fm, 2 = St. Jakob Fm, 3 = Harrberger Fm, 4 = Dornerkogel Fm, 5 = Taschen Fm, 6 = Kehr Fm, 7 = Semriach Phyllite Fm, 8 = Heilbrunn Phyllite Fm, 9 = Hirschkogel Phyllite Fm, 10 = Kötschberg Fm, 11 = Schönberg Fm, 12 = Schöckl Fm, 13 = Kogler Fm, 14 = Hochschlag Fm, 15 = Hubenhalt Fm, 16 = Bameder Fm, 17 = Heigger Fm, 18 = Parmasegg Fm, 19 = Flösserkogel Fm, 20 = Raasberg Fm, 21 = Plabutsch Fm, 22 = Draxler Fm, 23 = Osser Fm, 24 = Tyrnaueralm Fm, 25 = Rotmüller Fm, 26 = Zachenspitze Fm, 27 = Hochlantsch Fm, 28 = Schweinegg Fm, 29 = Fahrneck Fm, 30 = Bärenschtütz Fm, 31 = Kollerkogel Fm, 32 = Steinberg Fm, 33 = Sanzenkogel Fm, 34 = Höchkogel Fm, 35 = Hahngraben Fm. Modified from Gasser et al. (2009).

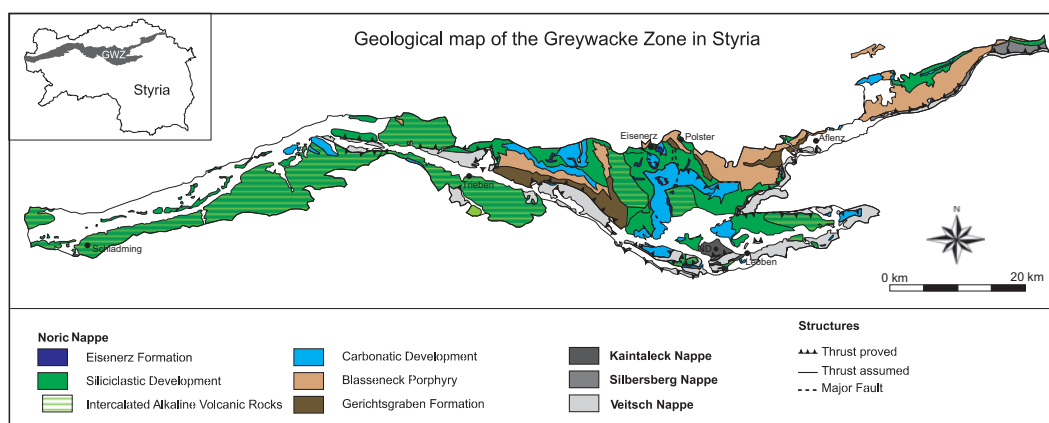


Figure E.11: Geological map of the Greywacke Zone in Styria, after Flügel & Neubauer (1984) and Neubauer et al. (1993). Abbreviation: ND = Niederung mountain.

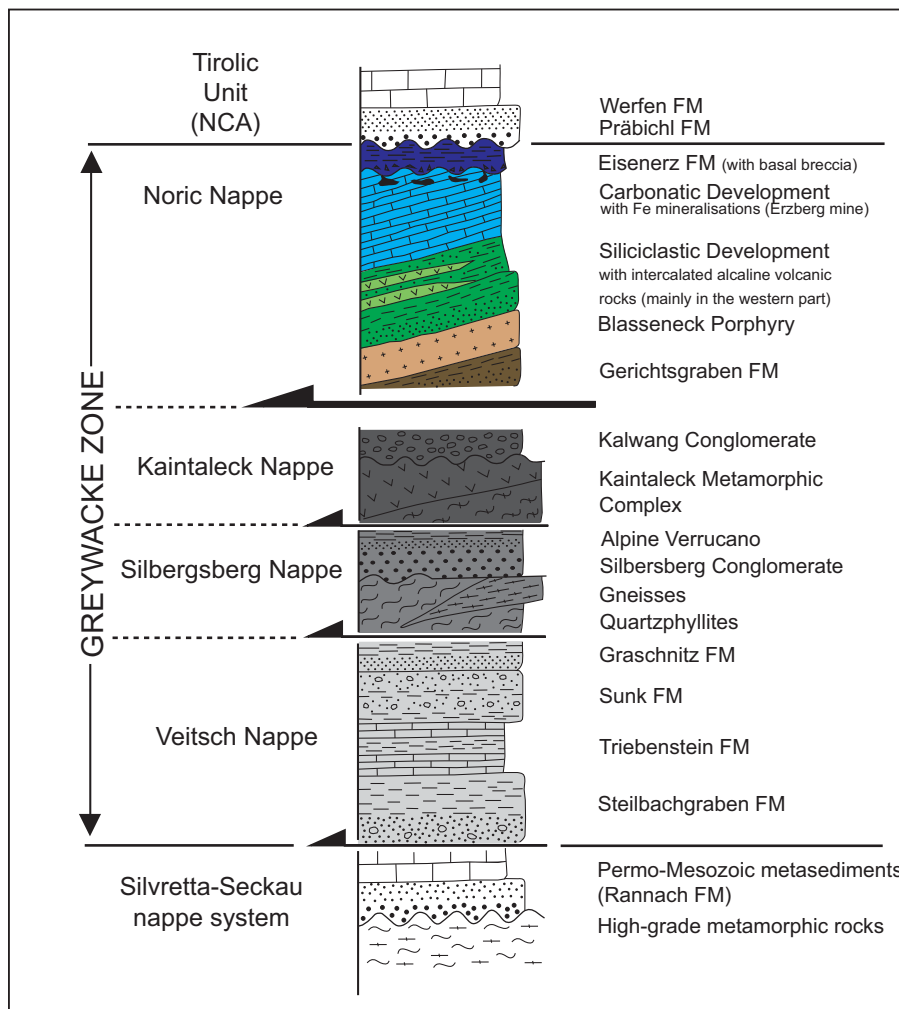


Figure E.12: Schematic tectonostratigraphy of the Greywacke Zone. Thickness of units is not for scale. Colours correspond to colours on Fig. E.9. Modified after Neubauer et al. (1993). Note that according to Frotzheim et al. (2000) the Veitsch, Silbergsberg and Kaintaleck Nappes originate from the Silvretta-Seckau nappe system, whereas the Noric Nappe originates from the Koralpe-Wölz nappe system.

Veitsch Nappe The Veitsch Nappe is exposed in a long but narrow strip at the southern border of the Greywacke Zone extending from Bruck a.d. Mur towards Leoben and St. Michael, and further along the northern margin of the Palten-Liesing valley. It consists of Carboniferous metasediments with metamorphosed coal intercalations and magnetite (Neubauer et al., 1993). Locally, Permian clastic sediments are present (Neubauer & Vozarova, 1990). In the region of Hohentauern south of Trieben (Fig. E.11), Ratschbacher (1987) subdivided the sequence of the Veitsch Nappe into three formations (from bottom to top): (1) the Steilbachgraben Formation, composed mainly of clastics and minor carbonates, (2) the Triebenstein Formation with carbonates and some greenschists, and (3) the

Sunk Formation with quartz conglomerates and anthracite/graphite deposits (exploited in the Sunk mine). Locally, in the Mürz valley close to St. Marein, the hanging wall of the Sunk Formation is built up by the Graschnitz Formation (Neubauer & Vozarova, 1990), which contains brownish to reddish sandstones and phyllites (Fig. E.12).

Silbersberg Nappe The Silbersberg Nappe is only exposed in a narrow strip in the easternmost part of the Greywacke Zone in Styria (Fig. E.11). As well as the other nappes, the Silbersberg Nappe consists of a number of formations that are clearly tectonically separated from all other footwall and hanging wall formations. At the base, these formations include early Paleozoic carbonate-chlorite schists, quartz phyllites and gneisses. The main constituents of the Silbersberg Nappe are the Silbersberg conglomerate and the Alpine Verucano Formation (light-coloured greenish quartzitic phyllites) on the top. The Silbersberg conglomerate is characterized by interspersions of reddish coloured quartz pebbles (Hermann, 1992). After Neubauer et al. (1993) the succession of the Silbersberg Nappe is probably of Permian age.

Kaintaleck Nappe The Kaintaleck Nappe is exposed north-west of Leoben on the mountain Nieder-ung (Fig. E.11). Different structural and geochronological investigations suggest that the Kaintaleck Nappe consist of various allochthonous flakes from over- and underlying stratigraphic members. The subdivision was introduced after studies of Neubauer & Frisch (1993): the succession starts with mica schists, amphibolites and paragneisses and passes into the transgressive overlying Kalwang Conglomerate (Fig. E.12). The crystalline rocks in the lower part of the nappe show an early Variscan amphibolite facies imprint at around 360 Ma (Neubauer et al., 1993).

Noric Nappe The Noric Nappe constitutes the main part of the Greywacke Zone in Styria. It forms a sedimentary-volcanogenic nappe stack (Hermann, 1992). At the base, The Gerichts-graben Formation is composed of greyish sandy, phyllitic and mica bearing schists, sandstones quartzites and banded limestones (Fig. E.12). Conodonts investigations within these limestones indicate a Middle Ordovician age. The overlying lower Upper Ordovician Blasseneck porphyry is of ignimbritic origin (rhyolitic rock), mainly composed of quartz, sericite and chlorite (as conversion products of feldspars and biotite). It reaches thicknesses of up to 1000 m. During the Upper Ordovician, Silurian and Devonian both a carbonaceous and a siliciclastic development was deposited. Within the siliciclastic sequence, Silurian alkaline volcanic rocks, predominantly in the western part of the Greywacke Zone in Styria, are intercalated. The Devonian limestones are occasionally mineralized with siderite (mined at the Erzberg, Fig. E.3c). After an erosional event during the Lower Carboniferous with thin karst filling breccias, the Eisenerz Formation was deposited. It represents the uppermost stratigraphic member of the Variscan succession, before Variscan orogeny started at the Lower/upper Carboniferous border (Schönlaub, 1982). The Noric Nappe is

transgressively overlain by the Tirolic Unit of the Northern Calcareous Alps (Fig. E.12). The Präbichl area near Eisenerz is a classic region where all units of the Noric Nappe are in close proximity and can be studied on walks up the Polster mountain (Fig. E.11).

Northern Calcareous Alps (NCA, UAA)

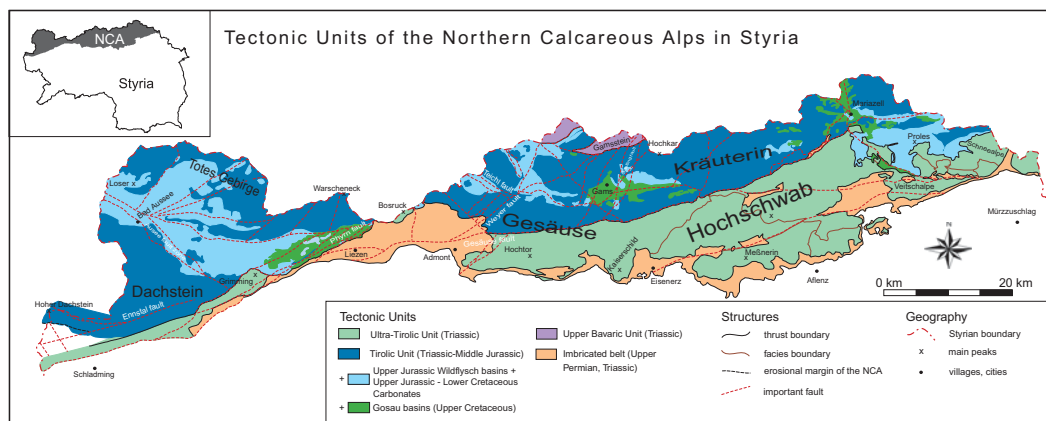


Figure E.13: Geological map of the Northern Calcareous Alps in Styria. Modified after Flügel & Neubauer (1984), Gawlick et al. (1994), Gawlick et al. (1999a), Mandl (2001) and Byrda (2009).

The NCA are an elongated thrust belt of more than 500 km length from the Rhein valley in the west to Vienna in the east. They are located north of the Greywacke Zone and south of the Penninic flysch zone. They build up the northern part of Styria (Upper Styrian region). Some cities and villages inside the NCA are Mariazell, Eisenerz, Gams, Admont, Liezen and Bad Aussee (Fig. E.4 and Fig. E.13). In the eastern part of Styria, the NCA are exposed in a forest-rich low mountain range with moderate altitudes around 800–1800 m. In the Hochschwab and Gesäuse the NCA reaches more than 2000 m and shows a real high mountainous character with karstified plateaus and steep, exposed ridges. The Salzkammergut area in northwestern Styria is a hilly area with isolated high plateaus of 1800–2700 m altitude (Totes Gebirge, Dachsteinplateau). The highest peak of Styria, the Hoher Dachstein with 2995 m, is built up of rocks belonging to the Northern Calcareous Alps (Fig. E.3d).

Geologically, the Northern Calcareous Alps consist of Permo-Mesozoic sediments affected by several tectonic and metamorphic events, which led to a complex internal structure. In Styria, the following tectonic units can be distinguished according to Frisch & Gawlick (2003): The Upper Bavaric Unit, the Tirolic Unit with the Hallstatt Mélange, the Ultra Tirolic Unit and an imbricated belt (Fig. E.6, Fig. E.13).

Upper Bavaric Unit According to Krystyn et al. (2008) the Upper Bavaric Unit is only exposed in a small tectonic isolated area around the Gamsstein in northern Styria (Fig. E.13). It consists of a sedimentary sequence from lower Middle Triassic carbonate ramp sediments (Gutenstein and Steinalm Formations), overlain by the Middle Triassic Reifling Formation (hemipelagic carbonates) and the Partnach Formation (marls, claystones, platy limestones), to the lower Upper Triassic Wetterstein Platform (allodapic limestones of the Raming Formation), foreereef, reef and lagunal facies of the Wetterstein Formation). The siliciclastic sediments in the hanging wall show the drowning of the Wetterstein platform during the so-called Lunz Event. The Gamsstein was brought into its actual position during younger, tectonic movements because its sedimentary features and the facies conditions do not fit with the surrounding Tirolic blocks (Krystyn et al., 2008).

Tirolic Unit The Tirolic Unit builds up the northern half of the NCA in Styria (Fig. E.4, E.13). It consists of two Upper Jurassic nappes: the upper and the lower Tirolic Unit (Frisch & Gawlick, 2003), but the database in central and eastern Styria is too scarce to differentiate them on the map scale (Fig. E.13). In general the sedimentary succession of the Tirolic Units can be separated into a Permo-Triassic to Middle Jurassic part deposited on a passive continental margin, and an Middle Jurassic to Eocene part dominated by convergent tectonics (Fig. E.13).

The Permo-Triassic to Middle Jurassic succession starts with Permian siliciclastics and Upper Permian evaporites (anhydrite, salt, gypsum; generally known under the term “Alpines Haselgebirge”). These Permian evaporites formed preferential shear horizons during younger tectonic movements and are therefore today mostly found tectonically separated from their surroundings. The Upper Permian evaporites, mined today in the Salzkammergut (see section E.5) were transferred into Upper Jurassic basins during the Upper Jurassic deformation (see section E.4) and occur now in a matrix of Upper Jurassic radiolarites (Wildflysch basins, Fig. E.13). In the Lower Triassic, red, green and violet siliciclastic rocks with an increasing amount of shallow-marine carbonates towards the hanging wall were deposited (Werfen Formation). The Werfen Formation is overlain by shallow marine carbonate ramp sediments of the Gutenstein and Steinalm Formations (dolomites and limestones), which are in turn overlain by pelagic carbonates intercalated with volcano-clastic rocks (Reifling Formation). In Middle and Upper Triassic times sediments of a classically structured carbonate-dominated continental margin build up the succession. A shallow-marine carbonate platform (Wetterstein Formation) and hemipelagic carbonates from the deeper shelf (Hallstatt Formation) occur. Upper Triassic siliciclastic and mixed siliciclastic-carbonatic rocks (Raibl and Leckkogel Formation) drowned the platform and lie between the Wetterstein Platform and the Upper Triassic Hauptdolomit and Dachstein Platform. The Tirolic succession can be observed in the steep cliffs of the Gesäuse and the Dachstein mountains. In the hemipelagic shelf to the SE of the platform the Pötschen (dolomites, limestones) and Hallstatt Formations (limestones) were sedimented. The Hauptdolomit-Dachstein Platform is again overlain by fine-grained siliciclastic rocks of the Kössen Formation, and in

the basin the sediments changed to the Zlambach Formation (marls, marly limestone). The Triassic/Jurassic boundary is marked by the transition from the Triassic shallow-marine carbonate platform to Lower Jurassic hemipelagic grey and red limestones and marls (e.g. Adnet and Allgäu Formation, Dürnberg Formation, to name only a few). Lower Jurassic breccias related to contemporaneous normal faults occur (e.g. Adneter Scheck). The Middle Jurassic rocks are characterized by hardgrounds (gaps) or condensed limestones (e.g. Klaus Formation).

In the upper Middle Jurassic the sedimentation changed rapidly from a calcareous to a radiolaritic one. Typical sediments are red, black and grey radiolarites and cherty limestones. In front of the Upper Jurassic nappe stack (see section E.4) different radiolaritic Wildflysch basins such as the Sandlingalm (Gawlick et al., 2007), Lammer (Gawlick, 1996) and the Tauglboden Basin (Gawlick et al., 1999a) were deposited. Simultaneously with thrusting and syn-deformational basin formation, isolated carbonate platforms of Upper Jurassic to Lower Cretaceous age occur (Plassen Carbonate Platform, Fritz et al., 2006) with adjacent sediments (mass flows: Barmstein Formation, pelagic micrites: Oberalm Formation) deposited in the former radiolaritic basins. They are in turn overlain by Lower Cretaceous siliciclastic molasse-type rocks that coarsen upwards (Schrambach Formation, Rossfeld Formation). Above a Middle Cretaceous unconformity Upper Cretaceous to Eocene, terrestrial to deep marine sediments of the Gosau group were deposited (Wagreich et al., 2009). These Gosau sediments are today only preserved along younger tectonic faults and in front of overthrusts, for example along the Miocene Salzach-Ennstal fault north of Liezen or in the area of Gams in the central NCA of Styria (Fig. E.13).

Ultra-Tirolic Unit The Ultra-Tirolic Unit builds up the southern half of the NCA in Styria (Fig. E.4, E.13). It consists of strongly deformed nappes with olistholitic megablocks in a melange like matrix affected by greenschist facies metamorphism in Upper Jurassic times (Gawlick et al., 1994; Frisch & Gawlick, 2003) or in late Early Cretaceous times (e.g. Frank & Schlager, 2005). It lies on top of an imbricated belt (described below) and is separated from the Tirolic Unit by Miocene strike slip faults or Eocene southvergent thrusts. In the western part between Schladming and Grimming, the Ultra-Tirolic Unit is termed the Mandling Unit, whereas in the eastern part (southern part of the Gesäuse, Hochschwab, Veitsch and Schneealpe) the name Mürzalpen Nappe is in use (Fig. E.13). The Ultra-Tirolic Unit consists of Middle Triassic Gutenstein dolomite, Reifling dolomite, Upper Triassic Wetterstein dolomite, Leckkogel beds and Waxeneck dolomite up to Dachstein limestone and Aflenz Formation. It shows a thermal overprint investigated by Conodont Alteration Indices (CAI) values from 5.5 to 6.0. Some parts in the Mürzalpen Nappe reach CAI values of 6.5–7.0 (300 °C).

Imbricated belt This tectonic unit is part of the Hallstatt Mélange (Frisch & Gawlick, 2003) crops out in a small narrow zone at the southern rim of the NCA and in some windows

in between the Ultra Tirolic unit, building up the flat slopes and the hilly area at the foot of the overlying platform carbonates. These rocks are beautifully visible along this southern margin of the Hochschwab (Tragöss, St. Ilgen) and at the base of the Dachstein in the Ramsau. The boundaries to the GWZ in the footwall and to the Ultra Tirolic Unit in the hanging wall are of tectonic nature. The belt consists of diverse sedimentary successions with different metamorphic grades occurring in a *mélange* like architecture. Quartzites, sand-, silt-, claystones and carbonates of the Werfen Formation are brought together with un- and metamorphosed clays, salt and gypsum of Upper Permian age. In some parts un metamorphosed Hallstatt limestones and Zlambach marls can be found.

E.3.2 Neogene basins

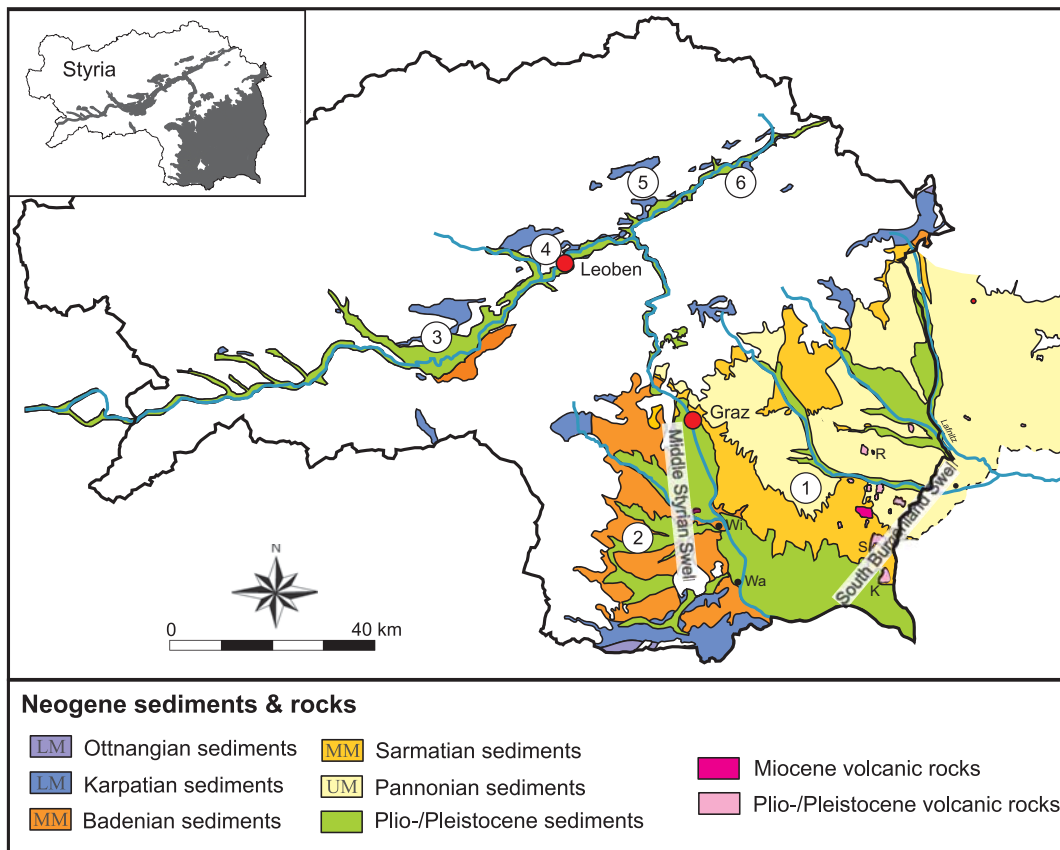


Figure E.14: Geological map of Neogene sediments and volcanic rocks in Styria. Modified after Gross et al. (2007). Abbreviations: MMS = Middle Styrian Swell, SBS = South Burgenland Swell, LM = Lower Miocene, MM = Middle Miocene, UM = Upper Miocene, Wa = Wagner, Wi = Wildon, R = Riegersburg, S = Straden, K = Klöch. (1) Eastern Styrian Basin, (2) Western Styrian Basin, (3) Fohnsdorf Basin, (4) Trofaiach Basin, (5) Kapfenberg Basin, (6) Krieglach Basin.

Several basins filled with Neogene sediments occur in Styria (Fig. E.14). They range from Otnangian to Badenian and rarely to Upper Pannonian in age with partial Plio-/ Pleistocene cover sediments (Fig. E.15). There are marine, brackish and limnic-fluviatile developments. The Styrian Basin is the largest of the Neogene basins in Styria. It represents the western-most lobe of the Pannonian Basin at the south-eastern margin of the Eastern Alps and forms the orogen – basin transition zone. It is separated from the Pannonian Basin by the northeast-southwest striking South Burgenland Swell. It is an east-west elongated basin, where the easternmost part is situated in the province of Burgenland. Whereas in the Styrian Basin thick Miocene and minor Pliocene sediments occur, the adjacent Western Pannonian Basin shows the contrary: thin Miocene and thick (up to 2 km) Pliocene sediments are deposited. The Styrian Basin itself can be subdivided into a deep (~4 km) Eastern and a rather shallow (~1km) Western Styrian Basin, separated by the Middle Styrian Swell. The Eastern Styrian Basin shows three distinctive depocentres. A hilly landscape characterizes the topography of the basin, showing a general south-east trending drainage system. Some volcanic cones of Plio- and Pleistocene age in south-eastern Styria (Fig. E.3f) add to the basins special geomorphological appearance which attracted researchers at all times (e.g. Winkler-Hermaden, 1957; Ebner & Sachsenhofer, 1995; Sachsenhofer et al., 2000; Gross et al., 2007).

There are a number of other smaller intramontane Neogene basins in Styria, for example the Fohnsdorf and Seckau Basin, the Trofaiach Basin, the Kapfenberg Basin and the Krieglach Basin. All of these basins are exposed along the Mur-Mürz fault system (Fig. E.14; Sachsenhofer et al., 2000). In contrast to the Styrian Basin, the Intramontane Basins only contain the syn-extensional sediments of Karpatian – Badenian age (Fig. E.14, E.15). Many of them contain coal deposits (see section E.5). Other related pull-apart basins outside of Styria are the Tamsweg and the Vienna Basin and the Ennstal and Lavanttal depressions. All show a rather similar evolution related to Miocene brittle tectonics (see section E.4). Today's drainage pattern is mostly governed by these prominent and still active strike-slip fault systems highlighting their importance for shaping the present landscape.

E.4 Geodynamic evolution of Styria

All the geological units described in the previous chapter allow reconstructing the evolution of Styria over at least the last 500 million years from the beginning of the Paleozoic to today. The processes of plate tectonics changed the distribution of continents and oceans: continents broke apart and oceans formed; continents collided and mountain chains grew. Several distinct time periods influenced the evolution of Styria in particular – a simplified summary of what happened where and when is given in Fig. E.16 and is discussed in detail below. The amount of knowledge clearly increases towards the present: whereas not much is known about the oldest events at the beginning of the Paleozoic, detailed reconstructions of landscape evolution are possible for the last few millions of years.

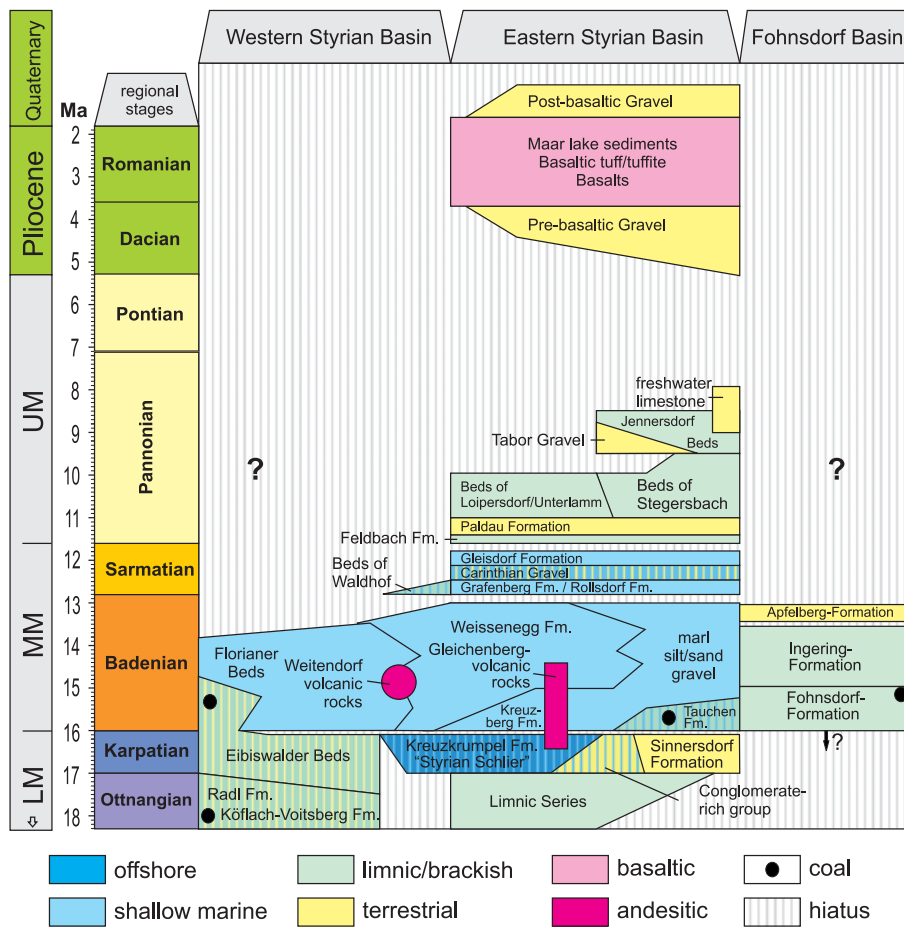


Figure E.15: Stratigraphic chart of the Neogene basins in Styria. Modified after Piller et al. (2004).

Ordovician to Devonian sedimentation Plate tectonic reconstructions show that during Late Ordovician and Silurian time, the world was dominated by the presence of a large landmass, Gondwana, located around the present south pole, and several smaller landmasses, such as Laurentia, Siberia and Baltica that were located at and north of the equator (plate tectonic maps can be downloaded at www.scotese.com). Between these landmasses, the so-called Rheic ocean existed. Paleomagnetic and stratigraphic studies show that the low-grade Paleozoic sediments present in the Greywacke Zone as well as in the Drauzug-Gurktal nappe system were deposited on the shelf of this Rheic ocean, at the northern margin of Gondwana. They were probably part of smaller terranes that broke off from the northern margin of Gondwana in Upper Ordovician to Silurian times at a southern latitude of up to 60° and drifted northward towards the landmasses of Laurentia during Devonian times. During this time period, terrestrial sequences were deposited, intercalated with volcanic rocks; shallow-water carbonate platforms developed on shelf margins and pelagic sequences were deposited in deeper basins (e.g. Schönlaub, 1992; Von Raumer & Stampfli, 2008).

Variscan orogeny during the Carboniferous During Late Devonian to Carboniferous time, the situation changed. The terranes originally broken-off from the southern Gondwana continent were located close to the equator and collided with the landmass of Laurentia. This collision led to a belt of complex deformation and metamorphism that can be followed through entire Central Europe: the Variscan orogen. The low-grade Paleozoic rocks of the Greywacke Zone and the Drauzug-Gurktal nappe systems escaped serious metamorphic and magmatic overprint during this collision and sedimentation partly went on into the Lower Carboniferous. But erosional unconformities, a low-grade metamorphic overprint and deformation structures such as thrusts and folds related to the Variscan orogen are present. The higher-grade crystalline basement units below the Drauzug-Gurktal nappe system show a more intense overprint related to the collision: high pressure – low temperature metamorphism occurred around 350 Ma, followed by a thermal peak at around 340 Ma and cooling until 310 Ma. Intrusions of Variscan age also occur. However, the metamorphic and tectonic overprint related to two later events (Permo-Triassic and Eo-Alpine, see below) make an unequivocal interpretation of the Variscan history of the crystalline basement units difficult (e.g. Tait et al., 1997; Neubauer & Handler, 2000; Schuster et al., 2004).

Permo-Triassic metamorphism and Permo-Mesozoic sedimentation At the beginning of the Permian, terrestrial to shallow-marine sediments (e.g.: siliciclastics, carbonates and evaporites), today exposed at the base of the NCA and as remnants on the crystalline basement units, were deposited in graben structures on top of the eroded Variscan nappe stack Neubaueretal:2007. They indicate that Variscan deformation ceased and topography decreased to sea level. Today, these units are exposed as the monometamorphic units found along the northern margin of the Seckauer Tauern and in the Schladminger Tauern. Simultaneously, low pressure – high temperature metamorphism affected the basement, especially the future Koralpe-Wölz nappe system (Fig. E.8a). This metamorphism was accompanied by mafic intrusions and abundant pegmatites, indicating that the basement was thinned and stretched in north-south direction. At the beginning of the Triassic, this thinning and stretching finally led to the opening of a new oceanic basin, the Meliata ocean, and the subsidence of the adjacent margins (e.g. Schuster et al., 2001, 2004; Schuster & Stuewe, 2008).

On the northwestern passive margin of this new Meliata ocean, the Triassic to Middle Jurassic sedimentary succession of the NCA developed. Remnants of this succession are also locally present on the crystalline basement units. During the Triassic, siliciclastic and volcanic sediments were shed onto this margin from a continental landmass to the northwest, carbonate platforms developed on the shelf and were drowned again, marls and pelagic limestones were deposited in deeper parts of the margin towards the southeast. A global mass extinction at the Triassic/Jurassic boundary marked the transition into more pelagic

Figure E.16 (following page): Geodynamic evolution of Styria through time with the most important sediment accumulation events (light grey) and metamorphic and deformational events (dark grey) indicated. Abbreviation: IMB = Intramontane Basins.

sedimentation with less continental input during the Jurassic. Normal faulting and breccia formation, followed by deep-water pelagic sediments on northwestern parts of the margin (today represented by the Bavaric nappes) documented the opening of another oceanic basin to the north: the Penninic ocean. This ocean began to separate a northern European continent from the southern African continent, including the Adriatic micro-continent which separated from Africa during the Cretaceous (Schmid et al., 2008). On the central and southern parts of the shelf, pelagic carbonates are typical in Lower and Middle Jurassic times. In Middle Jurassic times also sedimentary omissions, hardgrounds and condensed sediments are common (Frisch & Gawlick, 2003).

Middle to Upper Jurassic deformation In the upper Middle Jurassic, conditions on the shelf described above changed completely. Compressive to transpressive deformation affected the sediments deposited on this shelf progressively from SE towards NW. An accretionary prism formed with the deposition of elongated, syn-orogenic basins in front of the advancing nappe stack. These basins were filled with small to huge (up to km-sized) blocks of eroded Triassic to Middle Jurassic carbonatic and siliciclastic rocks of the former passive margin which was now broken into pieces and thrust on top of each other. Multiple sets of erosion, deposition, re-erosion and re-deposition of such basins can be documented (Fig. E.13, Upper Jurassic Wildflysch basins; Gawlick, 1996). Parts of the nappe stack were affected by an up to greenschist facies metamorphism according to Gawlick et al. (1994, 1999a) (Ultra Tirolic Unit). The compressional structures (nappe piles, thrust fronts, basins) are sealed by uppermost Jurassic to Lower Cretaceous carbonate platforms and basinal sequences. Gawlick et al. (1999a) and Frisch & Gawlick (2003) interpret this deformation as the result of subduction of the shelf sediments below oceanic crust or below an unknown part of continental crust. In contrast, Frank & Schlager (2005) interpret this deformation as being the result of a transpressive regime along major-scale strike-slip zones.

Cretaceous (Eo-Alpine) orogeny Compressional tectonics re-started on the previously deformed shelf in the Lower Cretaceous and now also seriously affected the underlying crystalline basement. An intra-continental subduction zone started inside the Adriatic micro-continent around 145 Ma between the later Koralpe-Wölz nappe system and the Ötztal Bundschuh nappe system. It successively consumed more and more parts of the Adriatic plate until ultimately the Penninic ocean in the north started to subduct in the Upper Cretaceous (e.g. Froitzheim et al., 2000; Stuewe & Schuster, in press). The main nappe stack of the Austroalpine Units as displayed in Fig. E.6 formed. The Drauzug-Gurktal nappe system thrust on top of the Koralpe-Wölz nappe system. The Koralpe-Wölz nappe system was subducted and metamorphosed up to eclogite-facies grade (Fig. E.8b). During this time one of the largest shear zones of the Alps formed as one of the major shear horizons during nappe stacking: the Plattengneiss shear zone inside the Koralpe-Wölz nappe system. The already formed nappe stack of the Tirolic and Ultratirolic Units together with the underlying Paleozoic rocks of the Noric nappe were sheared off from the Koralpe-Wölz nappe system. The

Silvretta-Seckau nappe system was thrust on top of the Lower Austroalpine Semmering-Wechsel nappe system. The lower nappes of the Greywacke Zone (Veitsch, Silbersberg, Kaintaleck) as well as the Bavaric nappes were sheared off from the Silvretta-Seckau nappe system and transported northwestwards. Molasse-type sediments were deposited in front of the Tirolic nappe systems.

The whole nappe stacking process is reflected in the metamorphic gradient developed (Fig. E.8b; Tenczer & Stuewe, 2003). The peak of this activity is marked by the peak metamorphic conditions in the Koralpe-Wölz nappe system that were reached around 92 Ma in the central Koralpe. After about 90 Ma, cooling and exhumation of the high-grade rocks occurred between 90–60 Ma during the Upper Cretaceous. Final exhumation of the metamorphic rocks occurred around 40–50 Ma. Simultaneously to cooling and exhumation, the entire region was warped on a 10 km long wavelength (Putz et al., 2006) and normal and strike-slip faults formed. These faults are associated with sedimentary basins filled with terrestrial to marine sediments (Gosau group, Wagneich et al., 2009). These basins are located on top of the Tirolic Unit and the Drauzug-Gurktal nappe system north and east of the Dachstein region and west of Graz, respectively. In the Upper Cretaceous, the Penninic ocean located to the north of the Adriatic continent entered the subduction zone and nappe stacking and exhumation in the Austroalpine Units ceased. The Bavaric, Tirolic, Ultra Tirolic Units and the imbricated belt at their base were thrust out of sequence to the north and also simultaneously backthrust to the south. Only the Bavaric Unit was finally thrust over the northern Rhenodanubian flysch zone in Eocene times. This thrusting was followed by peneplanisation and deposition of the Oligocene to Lower Miocene fluvatile sediments of the Augenstein Formation (Frisch & Gawlick, 2003).

Miocene tectonics and Neogene basin formation In the Lower Miocene, north-south convergence between the Adriatic and the European continent in the Penninic domain was still ongoing. However, beside continuing nappe stacking (in the Molasse zone in the north and in the Klagenfurt Basin), the convergence was compensated by strike-slip faults along which individual blocks could escape eastwards towards the Pannonian realm where space was created by a retreating subduction zone in the Carpathians (Ratschbacher et al., 1991; Frisch et al., 1998). Thus, the Miocene is generally considered to be the period of lateral extrusion. Major conjugated fault systems developed such as the Mur-Mürz fault system (MMF), the Lavanttal fault system (LF), the Salzach-Enns fault system (SEMP) and the Periadric Lineament (PAL) (Fig. E.4). The nappe stack of the NCA was fragmented into individual smaller fault-bounded blocks with rotations and displacements in the order of tens of kilometres during this phase (paleostress analysis by Peresson & Decker, 1997; Decker et al., 1994). Along these fault systems, the formation of intramontane pull-apart basins led to local subsidence. These basins were filled with syn-rift sediments (Marton et al., 2000) and bear the coal deposits of Styria. Especially along the MMF, the so-called Noric Depression developed (Sachsenhofer et al., 2000). The most important of these small pull-apart basins are the Fohnsdorf Basin (at the junction between Lavanttal fault system

and MMF), the Leoben Basin, the Krieglach Basin and several others along the Mur-Mürz lineament. The Styrian Basin evolved simultaneously to the Intramontane basins on top of one of the extruding blocks due to extensional normal faulting (Ebner & Sachsenhofer, 1995). Extension favored the ascent of magmas, which generated andesitic shield volcanoes during Lower and up to Middle Miocene times. Volcanic rocks from this time are found today in Weitendorf near Wildon and Bad Gleichenberg (Fig. E.14).

At the Karpatian/Badenian boundary (Fig. E.14, Fig. E.15), strike-slip and extensional faulting ceased and an unconformity due to a tectonic event and contemporaneous sea level low stand developed: the so-called “Styrian Phase” may be observed in quarries near Wagna in western Styria. In the Badenian, post-extensional regional subsidence due to cooling of the lithosphere was ongoing in the Styrian Basin and marine sediments were deposited. One of the last fully marine sediments that were deposited in the basin was the ~13 Ma old Leitha limestone that builds up the white limestone cliffs near Wildon and Leibnitz. During Sarmatian and Pannonian times, the basin experienced a transition from marine to brackish and eventually to terrestrial sedimentation. The reconstruction of the depositional history for this time interval is complicated by the fact that there are no Sarmatian and Pannonian sediments present in the Western Styrian Basin or the Noric depression (Fig. E.15). It is not known if such sediments were deposited and if they were eroded subsequently or no deposition happened at this time. Indications for the erosion of at least some hundreds of meters of sediments suggest the former (Dunkl & Frisch, 2002; Dunkl et al., 2005). In Pliocene to Pleistocene times a major change in the stress field led to basin inversion, and consequential young tectonic uplift of the whole Styrian Basin and erosion of a few hundred meters of sediments. A contemporaneous tilting of the basin by 1–2 degrees to the east leads to the map scale distribution of the sedimentary units with the oldest being exposed at the western margin of the basin and the youngest in the very east of the state (Fig. E.14). During the Pliocene to Early Pleistocene a second (basaltic) volcanic phase erupted forming volcanoes for example at Riegersburg (Fig. E.3f), Straden and Klöch (Fig. E.14). An elevated heat flow since Sarmatian times is related to thinned lithosphere below the Styrian Basin and is currently being exploited in terms of thermal springs and spas in south-eastern Styria. In the last few million years karstification of the mountains dominated by limestones in Styria (Grazer Bergland, NCA) led to the formation of large caves (f.ex. Lurgrotte, north of Graz). The youngest sediments present in Styria are glaciation-related Pleistocene deposits mostly present along the major drainage pattern. The Pleistocene ice sheets itself never reached beyond Judenburg in the Mur Valley and Völkermarkt in the Drau Valley leaving much of Styria ice-free during the entire Pleistocene.

E.5 Mining in Styria

Styria has many natural resources of economic importance which are currently mined. Table E.18 and Fig. E.17 show an overview of all raw materials mined in Styria in 2007 and corresponding locations of the mines (data from Österreichisches Montanhandbuch 2008). Production data of 2006, including information on historical mining in Styria back to 1950, are given by Ebner (2008). There are several raw materials where Styria has a leading position in Austria. In the case of iron, all of the Austrian production is mined in Styria (The small specularite mine near Waldenstein (Carinthia), which produces a few thousand tons of platy hematite is not regarded as an iron mine because specularite is not used as a source for iron). In addition, more than 50 percent of the total Austrian production of talc/leucophyllite, magnesite, quartz/quartzite, basaltic rocks and ultramafic rocks are mined in Styria. Styria also produces the majority of gypsum/anhydrite, limestone and diabase in Austria. Production data and percentages of the most important natural resources mined in Styria are shown in Table E.18 and a short description of the deposits is given below. Further information on Austria's natural resources (with corresponding geologic framework) can be found in Ebner (1997) and Weber et al. (1997).

Iron The only Fe-mine in Austria is located at the “Steirischer Erzberg” in Eisenerz (Fig. E.3c). The Erzberg is the largest siderite mine of the world and the largest open-pit mine on metallic ores in Central Europe (according to 2007 production; the siderite mine in Bakal (Russia) produced 1.7 Mio. t of siderite in 2007, compared to 2.15 Mio. t produced at the Erzberg). The main Fe-bearing minerals are siderite, ankerite and Fe-dolomite. Other minerals like pyrite, hematite and magnetite only occur in very small proportions (Schönlaub, 1982). The host rocks of the iron ores are Devonian limestones of the Noric Nappe (Fig. E.12). In 2007, the Voest Alpine Erzberg mined approx. 5.6 Mio. t of crude ore. After processing, about 2.15 Mio. t of iron ore, containing about 34 percent Fe, were produced. A recent overview of the Fe-mineralisation and the genesis of the Erzberg deposit (and also other Fe-mineralisations within the Noric Nappe and the Northern Calcareous Alps) is given by Prochaska & Henjes-Kunst (2009).

Evaporites Gypsum, anhydrite and salt deposits, which are economically important, occur in the “Alpines Haselgebirge” in the Northern Calcareous Alps (see section E.3, NCA). In Styria, salt (halite) is mined at the underground mine in Altausee. The halite is extracted from the host rock using water, which dissolves the salt. About 1.16 Mio. m³ of brine were produced in 2007. In addition, 1172 t of solid salt were mined at Altausee. Gypsum and anhydrite are mined in the areas of Grundlsee, Tragöß and Admont. Together, these mines produced 477201 t of gypsum and 13 448 t of anhydrite in 2007. Schauburger (1986) gives an overview of evaporitic deposits in the Eastern Alps.

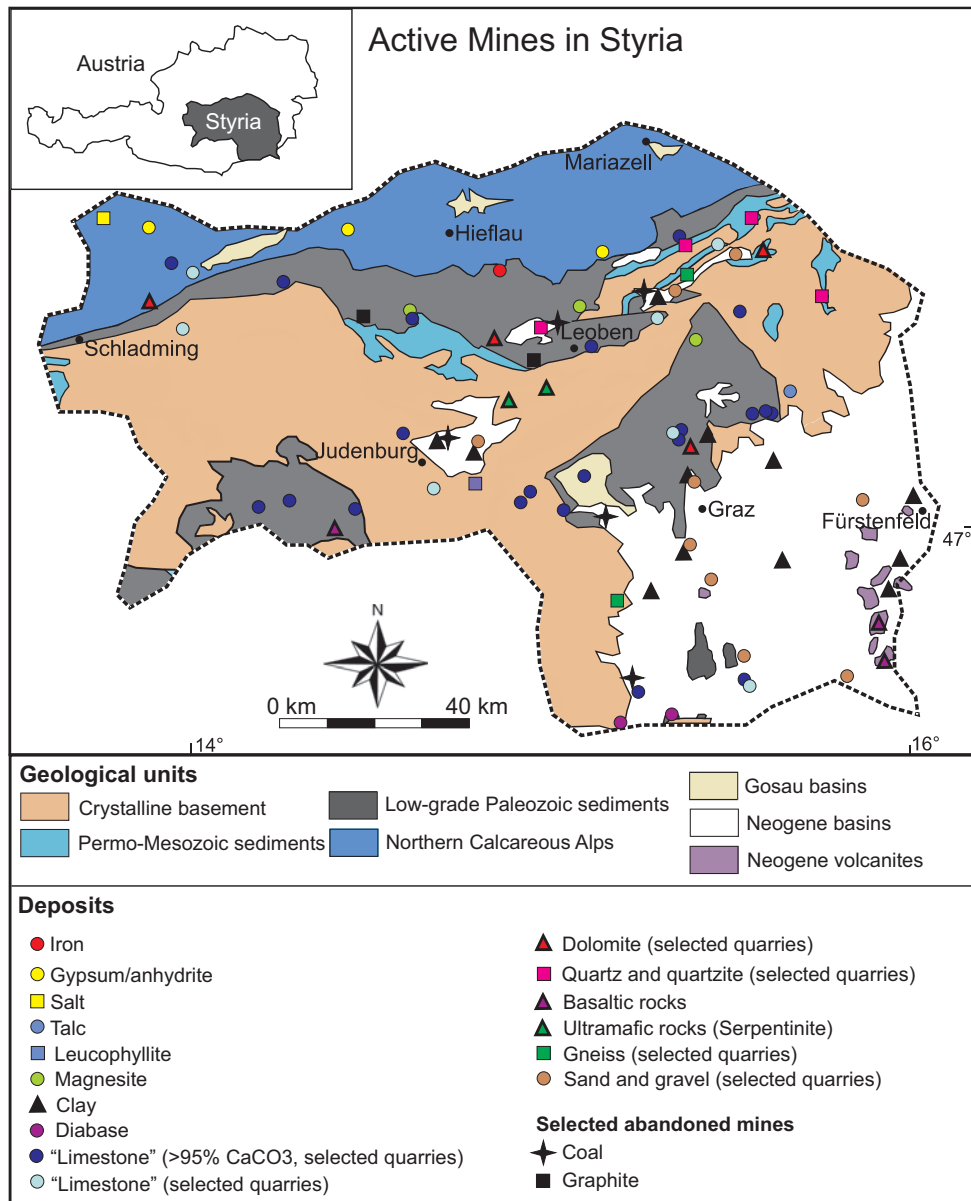


Figure E.17: Simplified geological map of Styria with locations of active mines (data from Österreichisches Montanhandbuch, 2008).

Talc and leucophyllite These ores occur in crystalline basement units. Talc and leucophyllite were formed in alpidic shear zones by hydrothermal fluids (leucophyllite is defined as mixture of quartz, muscovite and chlorite which was formed by hydrothermal influence (Prochaska, 1991). Talc is mined at the open-pit mine Rabenwald near Weiz, which is located in the Strallegg Complex of the Koralpe-Wolz nappe system (Fig. E.6). A sum-

<u>Raw material</u>	2007 production [t]	Percentage of total Austrian production
Iron	2 150 000	100
Gypsum and anhydrite	490 649	46
Salt (brine)	1 158 490 m ³	47
Talc and leucophyllite	119 815	78
Magnesite	557 183	67
“Limestone” (≥ 95 % CaCO₃)	3 620 238	25
“Limestone”	2 175 921	31
Clay	605 708	26
Diabase	898 407	40
Dolomite	484 206	12
Quartz and quartzite	204 311	67
Basaltic rocks	1 607 969	85
Ultramafic rocks	1 142 770	62
Gneiss	72 388	8
Sand and gravel	1 573 347	7

Figure E.18: List of all raw materials mined in Styria in 2007 (data from Österreichisches Montanhandbuch, 2008).

mary of talc (and also magnesite) deposits in Austria, including genetic models, is given by Prochaska (2000). The leucophyllite deposit Kleinfestritz near Zeltweg is located in the Silvretta-Seckau nappe system. Detailed investigations of the Kleinfestritz deposit have been carried out by Prochaska (1991). In total, these two mines produced 119.815 t of talc and leucophyllite in 2007, which corresponds to 78 percent of the total Austrian production.

Magnesite Magnesite of economic importance only occurs in the low-grade Paleozoic units. They host a number of Veitsch-type sparry magnesite deposits. Austria’s largest magnesite mine in Breitenau/Hochlantsch is located in the lower nappe system (Laufnitzdorf facies) of the Paleozoic of Graz (Fig. E.9). With a production of 385 500 t crude magnesite in 2007, the Breitenau mine produced nearly 50 percent of Austria’s total magnesite production. The other Styrian magnesite mines are located in the Veitsch Nappe of the Greywacke Zone near Wald/Schoberpass and St. Katharein/Laming (4 mines). Detailed geological and geochemical information on the “Veitsch type” magnesite deposits in the Greywacke Zone can be found in Ebner et al. (2004). With a total production of 555183 t, Styria produced 67 percent of the total Austrian magnesite production in 2007.

Carbonates (“limestone” and dolomite) Deposits of “limestone” occur in different geologic units in Styria. In Fig. E.17, the “limestone” mines are divided in those which are assigned as “bergfrei” (i.e. containing more than 95 percent CaCO₃) and those which do

not fulfil this criterion. Most of the mines are located in the low-grade Paleozoic units (Paleozoic of Graz, Greywacke Zone and Gurktal nappes). However, “limestone” deposits also occur in other geologic units like the Styrian Basin, the Northern Calcareous Alps and the Crystalline Basement (including their Permo-Mesozoic cover). In the Crystalline Basement the “limestones” are metamorphosed and should therefore be named as marbles (for that reason the term “limestone” was put in quotation marks). Dolomite of economic importance mainly occurs in the low-grade Paleozoic units, but also in the Northern Calcareous Alps and the Permo-Mesozoic cover of the Crystalline Basement. In total, 5796159 t of “limestone” and 484206 t of dolomite were mined in Styria in 2007.

Clay Clay pits occur in the sedimentary sequences of the Neogene basins (Styrian Basin, Fohnsdorf Basin, Mürz valley). Several pits in these basins mined 605708 t of clay in 2007.

Diabase Diabase, which is defined as a low-grade metamorphosed basaltic rock, is mined in two quarries at the southern Styrian border (Lieschengraben near Oberhaag and Radlpass). Both are located in low-grade Paleozoic units of the Gurktal nappe system. Styria produced 898407 t of diabase in 2007.

Quartz and quartzite The bulk of the quartzite mines are located in the Permo-Mesozoic cover of the Crystalline basement in northeastern Styria. The quarry located near Trofaiach mines quartz from the low-grade Greywacke Zone. 204311 t of quartz/quartzite were mined in Styria in 2007, which is about two third of the total Austrian production.

Basaltic and ultramafic rocks Mines for basaltic rocks are located in Neogene volcanites of the Styrian Basin in southeastern Styria (e.g.: Klöch) and in the Gurktal nappes. Ultramafic rocks (serpentinite, dunite) are mined in the area of Kraubath, where they occur in ophiolite-like sequences of the Speik-Complex (Silvretta-Seckau nappe system). In 2007, 1607969 t of basaltic rocks and 1142770 t of ultramafic rocks, which corresponds to 85 percent and 62 percent of the total Austrian production, respectively, were mined.

Gneiss Gneiss is mined in several quarries in two areas, near Stainz and near St. Marein / Mürztal. Both areas are located in the crystalline basement, but in different units. In the area of Stainz, gneisses from the Koralpe complex (Koralpe-Wölz nappe system) is mined. In the area of St. Marein, the quarries are located in the Silvretta-Seckau nappe system. In total, 72388 t of gneiss were mined in 2007.

Sand and gravel Sand and gravel deposits of economic importance occur in fillings of the Neogene basins (most of them in the Styrian Basin) and in Quaternary sediments. There are more than 20 quarries mining sand and gravel in Styria with a total production of 1 573 347 t in 2007.

E.6 Final remarks

Styria has a rich and diverse geological history, and the mineral resources mined in Styria are an important economic sector in the province. The three Styrian universities which offer studies in Earth Sciences are ideally located to learn more about the geological formation and evolution of that fascinating region on our doorstep.

E.7 Acknowledgments

The joint Doctoral School of Earth Sciences in combination with GASS (Graz Advanced School of Science) and UZAG (Universitätszentrum für angewandte Geowissenschaften Steiermark) is thanked for financial support of the field trip 2009. R. Schuster (GBA Vienna) is thanked for many discussions and a thorough review of this article. R. Bakker, H.-J. Gawlick, S. Matthäi and W. Kurz are thanked for attending and leading parts of the field trip. F. Ebner, H.-J. Gawlick, G. Hoinkes, R. Sachsenhofer and W. Vortisch are thanked for support and advice during writing. All PhD students that attended the workshop are thanked for their interest and support.

Bibliography

- AGNOLI, F. (1987) *Geologie des Stross nordwestlich von Weiz*. PhD thesis, Graz, 144 p.
- AGUE, J.; BAXTER, E. (2007) Brief thermal pulses during mountain building recorded by Sr diffusion in apatite and multicomponent diffusion in garnet. *Earth and Planetary Science Letters*, 261:500–516.
- ALEINIKOFF, J.N.; SCHENCK, W.; PLANK, M.; SROGI, L.; FANNING, C.; KAMO, S.; BOSBYSELL, H. (2006) Deciphering igneous and metamorphic events in high-grade rocks of the Wilmington Complex, Delaware: Morphology, cathodoluminescence and backscattered electron zoning, and SHRIMP U-Pb geochronology of zircon and monazite. *Geological Society of America Bulletin*, 118:39–64.
- AMATO, J.; PAVLIS, T. (2010) Detrital zircon ages from the Chugach terrane, southern Alaska, reveal multiple episodes of accretion and erosion in a subduction complex. *Geology*, 38:459–462.
- ANCZKIEWICZ, R.; THIRLWALL, M. (2003) Improving precision of Sm-Nd garnet dating by H₂SO₄ leaching: a simple solution to the phosphate inclusion problem. *Geological Society of London, Special Publication*, 220:83–91.
- ANDERSEN, T. (2005) Detrital zircons as tracers of sedimentary provenance: limiting conditions from statistics and numerical simulation. *Chemical Geology*, 216:249–270.
- ATWATER, T. (1989) The Eastern Pacific Ocean and Hawaii. E. Winterer; D. Hussong; R. Decker, (eds.), *Geology of a transpressional orogen developed during ridge-trench interaction along the North Pacific margin*, Boulder, Colorado, Geological Society of America, The Geology of North America, Vol. N:21-72.
- AYUSO, R.; HÄUSSLER, P.; BRADLEY, D.; FARRIS, D.; FOLEY, N.; WANDLESS, G. (2009) The role of ridge subduction in determining the geochemistry and Nd–Sr–Pb isotopic evolution of the Kodiak batholith in southern Alaska. *Tectonophysics*, 464:137–163.
- BARBEAU, D.; DUCEA, M.; GEHRELS, G.; KIDDER, S.; WETMORE, P.; SALEEBY, J. (2005) U-Pb detrital-zircon geochronology of northern Salinian basement and cover rocks. *Geological Society of America Bulletin*, 117:466–481.
- BARKER, F.; FARMER, G.; AYUSO, R.; PLAFKER, G.; LULL, J. (1992) The 50 Ma granodiorite of the Eastern Gulf of Alaska: Melting in an accretionary prism in the Forearc. *Journal of Geophysical Research*, 97:6757–6778.
- BARR, T.; DAHLEN, F. (1989) Brittle Frictional Mountain Building 2. Thermal structure and heat budget. *Journal of Geophysical Research*, 94:3923–3947.
- BELTRANDO, M.; HERMANN, J.; LISTER, G.; COMPAGNONI, R. (2007) On the evolution of orogens: Pressure cycles and deformation mode switches. *Earth and Planetary Science Letters*, 256:372–388.
- BERGER, A.; BURRI, T.; ALT-EPPING, P.; ENGI, M. (2008) Tectonically controlled fluid flow and water-assisted melting in the middle crust: An example from the Central Alps. *Lithos*, 102:598–615.
- BERGER, A.; ROSENBERG, C.; SCHALTEGGER, U. (2009) Stability and isotopic dating of monazite and allanite in partially molten rocks: Examples from the Central Alps. *Swiss Journal of Geosciences*, 102:15–29.
- BERGER, A.; GULICK, S.; SPOTILA, J.; UPTON, P.; JAEGER, J.; CHAPMAN, J.; WORTHINGTON, L.; PAVLIS, T.; RIDGWAY, K.; WILLEMS, B.; MCALEER, R. (2008b) Quaternary tectonic response to intensified glacial erosion in an orogenic wedge. *Nature Geoscience*:doi:10.1038/ngeo334.

- BERGER, A.; SPOTILA, J. (2008) Denudation and deformation in a glaciated orogenic wedge: The St. Elias orogen, Alaska. *Geology*, 36:523–526.
- BERGER, A.; SPOTILA, J.; CHAPMAN, J.; PAVLIS, T.; ENKELMANN, E.; RUPPERT, N.; BUSCHER, J. (2008a) Architecture, kinematics, and exhumation of a convergent orogenic wedge: A thermochronological investigation of tectonic-climatic interactions within the central St. Elias orogen, Alaska. *Earth and Planetary Science Letters*, 270:13–24.
- BERNET, M.; GARVER, J. (2005) Fission-Track Analysis of detrital Zircon. *Reviews in Mineralogy and Geochemistry*, 58:205–237.
- BEYSSAC, O.; GOFFÉ, B.; CHOPIN, C.; ROUZAUD, J. (2002) Raman spectra of carbonaceous material in metasediments: a new geothermometer. *Journal of Metamorphic Geology*, 20:859–871.
- BICKLE, M.; MCKENZIE, D. (1987) The transport of heat and matter by fluids during metamorphism. *Contributions to Mineralogy and Petrology*, 95:384–392.
- BINGEN, B.; AUSTRHEIM, H.; WHITEHOUSE, M. (2001) Ilmenite as a source for zirconium during high-grade metamorphism? Textural evidence from the Caledonides of western Norway and implications for zircon geochronology. *Journal of Petrology*, 42:355–375.
- BLACK, L.; KAMO, S.; WILLIAMS, I.; MUNDIL, R.; DAVIS, D.; KORSCH, R.; C., F. (2003) The application of SHRIMP to Phanerozoic geochronology: a critical appraisal of four zircon standards. *Chemical Geology*, 200:171–188.
- BOIK, H. (1950) Zum Bau der Grazer Decken. *Zeitschrift der Deutschen Gesellschaft für Geowissenschaften*, 102/1:247–271.
- BOL, A.; COE, R. (1992) Paleomagnetism of the Resurrection Peninsula, Alaska: Implications for the tectonics of southern Alaska and the Kula-Farallon Ridge. *Journal of Geophysical Research*, 97:17213–17232.
- BOL, A.; GIBBONS, H. (1992) Tectonic implications of out-of-sequence faults in an accretionary prism, Prince William Sound, Alaska. *Tectonics*, 11:1288–1300.
- BOL, A.; ROESKE, S. (1993) Strike-slip faulting and block rotation along the contact fault system, eastern Prince William Sound, Alaska. *Tectonics*, 12:49–62.
- BOOTH-REA, G.; KLAESCHEN, D.; GREVEMEYER, I.; RESTON, T. (2008) Heterogeneous deformation in the Cascadia convergent margin and its relation to thermal gradient. *Tectonics*, doi:10.1029/2007TC002209.
- BRADLEY, D.; HÄUSSLER, P.; KUSKY, T. (1993) Timing of Early Tertiary ridge subduction in southern Alaska. *US Geological Survey Bulletin*, 2068:163–177.
- BRADLEY, D.; KUSKY, T.; HÄUSSLER, P.; GOLDFARB, R.; MILLER, M.; DUMOULIN, J.; NELSON, S.; KARL, S. (2003) Geologic signature of early Tertiary ridge subduction in Alaska. V. Sisson; S. Roeske; T. Pavlis, (eds.), *Geology of a transpressional orogen developed during ridge-trench interaction along the North Pacific margin*, Geological Society of America Special Paper, 371: 5–21.
- BRADLEY, D.; PARRISH, R.; CLENDENEN, W.; LUX, D.; LAYER, P.; HEIZLER, M.; DONLEY, T. (2000) New geochronological evidence for the Timing of Early Tertiary Ridge Subduction in Southern Alaska. *US Geological Survey Professional Paper*, 1615:5–21.
- BRUAND, E. (2010) *Petrology of the Chugach Metamorphic Complex, southern Alaska*. PhD, University of Graz.
- BRUAND, E.; STUEWE, K.; PROYER, A. (2010) Pseudosection modelling for a selected eclogite body from the Koralpe (Hohl), Eastern Alps. *Mineralogy and Petrology*, doi 10.1007/s00710-009-0097-7.
- BRUHN, R.; HÄUSSLER, P. (2006) Deformation driven by subduction and microplate collision: Geodynamics of Cook Inlet basin, Alaska. *Geological Society of America Bulletin*, 118:289–303.
- BRUHN, R.; PAVLIS, T.; PLAFKER, G.; SERPA, L. (2004) Deformation during terrane accretion in the St. Elias orogen, Alaska. *Geological Society of America Bulletin*, 116:771–787.
- BRUN, J.; FACCENNA, C. (2008) Exhumation of high-pressure rocks by slab-rollback. *Earth and Planetary Science Letters*, 272:1–7.

- BUCHER, K.; FREY, M. (2002) *Petrogenesis of Metamorphic Rocks*. Springer Verlag, 341 p.
- BURG, J.; GERYA, T. (2005) The role of viscous heating in Barrovian metamorphism of collisional orogens: thermomechanical models and application to the Lepontine Dome in the Central Alps. *Journal of Metamorphic Geology*, 23:75–95.
- BUTERA, K.; WILLIAMS, I.; BLEVIN, P.; SIMPSON, C. (2004) Zircon U-Pb dating of Early Palaeozoic monzonitic intrusives from the Goonumbla area, New South Wales. *Australian Journal of Earth Sciences*, 48:457–464.
- BYRDA, G. (2009) *Arbeitstagung der Geologischen Bundesanstalt Blatt 101 Eisenerz, Leoben, 31.08 - 04.09.2009*. Wien, 252 p.
- BYRNE, T. (1979) Late Paleocene demise of the Kula-Pacific spreading center. *Geology*, 7:341–344.
- CAMACHO, A.; LEE, J.; HENSEN, B.; BRAUN, J. (2005) Short-lived orogenic cycles and the eclogitization of cold crust by spasmodic hot fluids. *Nature*, 435:1191–1196.
- CARLSON, W.D.; DONELICK, R.A.; KETCHAM, R.A. (1999) Variability of apatite fission track annealing kinetics: I. Experimental Results. *American Mineralogist*, 84:1213–1223.
- CARRAPA, B. (2010) Resolving tectonic problems by dating detrital minerals. *Geology*, 38:191–192.
- CESARE, B.; GOMEZ-PUGNAIRE, M.; RUBATTO, D. (2003) Residence time of S-type anatectic magmas beneath the Neogene Volcanic Province of SE Spain: a zircon and monazite SHRIMP study. *Contributions to Mineralogy and Petrology*, 146:28–43.
- CHAMBERLAIN, C.; RUMBLE, D. (1988) Thermal Anomalies In A Regional Metamorphic Terrane: An Isotopic Study of the Role of Fluids. *Journal of Petrology*, 29:1215–1232.
- CHERNIAK, D.; WATSON, E. (2003) Diffusion in Zircon. J. Hanchar; P. Hoskin, (eds.), *Zircon*, Reviews in Mineralogy and Geochemistry, 53: 113–139.
- CHRISTESON, G.; GULICK, S.; AVENDONK, H.; WORTHINGTON, L.; REECE, R.; PAVLIS, T. (in press) The Yakutat terrane: Dramatic change in crustal thickness across the transition fault, Alaska. *Geology*.
- CLAR, E. (1933) Zur Geologie des Schöcklgebietes bei Graz. *Jahrbuch der Geologischen Bundesanstalt*, 83:113–136.
- CLAR, E. (1935) Vom Bau des Grazer Paläozoikums östlich der Mur. *Neues Jahrbuch Min Geol Paläont Abt, B* 73:1–39.
- CLENDENEN, W.; FISHER, D.; BYRNE, T. (2003) Cooling and exhumation history of the Kodiak accretionary prism, southwest Alaska. V. Sisson; S. Roeske; T. Pavlis, (eds.), *Geology of a transpressional orogen developed during ridge-trench interaction along the North Pacific margin*, Geological Society of America Special Paper, 371:71–88.
- COE, R.; GLOBERMAN, B.; PLUMLEY, P.; THRUPP, G. (1985) Paleomagnetic results from Alaska and their tectonic implications. D. Howell, (ed.), *Tectonostratigraphic terranes of the Circum-Pacific region*, Earth Science Series 1, 85–108.
- COE, R.; GLOBERMAN, B.; THRUPP, G. (1989) Rotation of central and southern Alaska in the early Tertiary: oroclinal bending by megakinking? C. Kissel; C. Laj, (eds.), *Tectonostratigraphic terranes of the Circum-Pacific region*, Paleomagnetic rotations and continental deformation, 327–342.
- CONEY, P.; JONES, D.; MONGER, J. (1980) Cordilleran suspect terranes. *Nature*, 288:329–333.
- CONNOLLY, J.; THOMPSON, A. (1989) Fluid and enthalpy production during regional metamorphism. *Contributions to Mineralogy and Petrology*, 102:346–366.
- COWAN, D. (2003) Revisiting the Baranof-Leech River hypothesis for early Tertiary coastwise transport of the Chugach-Prince William terrane. *Earth and Planetary Science Letters*, 213:463–475.
- CROWE, D.; NELSON, S.; BROWN, P.; SHANKS, W.; VALLEY, J. (1992) Geology and Geochemistry of volcanogenic massive sulfide deposits and related igneous rocks, Prince William Sound, South-Central Alaska. *Economic Geology*, 87:1722–1746.
- DAHL, P. (1996) The crystal-chemical basis for Ar retention in micas: inferences from interlayer partitioning and implications for geochronology. *Contributions to Mineralogy and Petrology*, 123:22–39.

- DAHLEN, F.; BARR, T. (1989) Brittle Frictional Mountain Building. I. Deformation and Mechanical Energy Budget. *Journal of Geophysical Research*, 94:3906–3922.
- DALLMEYER, R.; NEUBAUER, F.; FRITZ, H. (2008) The Meliata suture in the Carpathians: regional significance and implications for the evolution of high-pressure wedges within collisional orogens. S. Siegesmund; B. Fügenschuh; N. Froitzheim, (eds.), *Tectonic Aspects of the Alpine-Dinaride-Carpathian System*, Geological Society, London, Special Publications, 298, 101-115.
- DAVIS, A.; PLAFKER, G. (1986) Eocene basalts from the Yakutat terrane: Evidence for the origin of an accreting terrane in southern Alaska. *Geology*, 14:963–966.
- DE YOREO, J.; LUX, D.; GUIDOTTI, C. (1991) Thermal modelling in low-pressure/high-temperature metamorphic belts. *Tectonophysics*, 188:209–238.
- DECELLES, G.; B., C.; GEHRELS, G. (2007) Detrital zircon U-Pb ages provide provenance and chronostratigraphic information from Eocene syn-orogenic deposits in northwestern Argentina. *Geology*, 35:323–326.
- DECKER, K.; PERESSON, H.; FAUPL, P. (1994) Die miozäne Tektonik der östlichen Kalkalpen: Kinematik, Paläospannungen und Deformation-saufteilung während der "lateralen Extrusion" der Zentralalpen. *Jahrbuch der Geologischen Bundesanstalt*, 137/1:5–18.
- DEWEY, J. (2005) Orogeny can be very short. *Proceedings of the National Academy of Science*, 102:15286–15293.
- DICKINSON, W. (2009) Anatomy and global context of the North American Cordillera. S. Kay; V. Ramos; W. Dickinson, (eds.), *Backbone of the Americas: Shallow subduction, plateau uplift, and ridge and terrane collision*, Geological Society of America Memoir 204:1-29.
- DICKINSON, W.; GEHRELS, G. (2009) Use of U-Pb ages of detrital zircons to infer maximum depositional ages of strata: A test against a Colorado Plateau Mesozoic database. *Earth and Planetary Science Letters*, 288:115–125.
- DODSON, M. (1973) Closure temperature in cooling geochronological and petrological systems. *Contributions to Mineralogy and Petrology*, 40:259–274.
- DOUBROVINE, P.; TARDUNO, J. (2008) A revisited kinematic model for the relative motion between Pacific oceanic plates and North America since the Late Cretaceous. *Journal of Geophysical Research*, 113, B12101:doi:10.1029/2008JB005585.
- DUNKL, I. (2002) Trackkey: a Windows program for calculation and graphical presentation of fission track data. *Computers and Geosciences*, 28:3–12.
- DUNKL, I.; FRISCH, W. (2002) Thermochronological constraints on the Late Cenozoic exhumation along the Alpine and West Carpathian margins of the Pannonian Basin. *EGU Stephan Mueller Special Publication Series*, 3:135–147.
- DUNKL, I.; KUHLEMANN, J.; REINECKER, J.; FRISCH, W. (2005) Cenozoic relief evolution of the Eastern Alps - constraints from apatite fission track age-provenance of neogene intramontane sediments. *Austrian Journal of Earth Sciences*, 98:92–105.
- DUNLAP, W. (1997) Neocrystallization or cooling? $^{40}\text{Ar}/^{39}\text{Ar}$ ages of white micas from low-grade mylonites. *Chemical Geology*, 143:181–203.
- DUSEL-BACON, C. (1994) Metamorphic history of Alaska. G. Plafker; H. Berg, (eds.), *The Geology of Alaska*, Boulder, Colorado, Geological Society of America, The Geology of North America G-1, 495-533.
- EBERHART-PHILLIPS, D.; CHRISTENSEN, D.; BROCHER, T.; HANSEN, R.; RUPPERT, N.; P.J., H.; ABERS, G. (2006) Imaging the transition from Aleutian subduction to Yakutat collision in central Alaska, with local earthquakes and active source data. *Journal of Geophysical Research*, 111:B11303, doi:10.1029/2005JB004240.
- EBNER, F. (1997) Die geologischen Einheiten Österreichs und ihre Rohstoffe. *Archiv für Lagerstättenforschung der Geologischen Bundesanstalt*, 19:49–229.
- EBNER, F. (2008) Die aktuelle Produktion mineralischer Rohstoffe in der Steiermark. *Joannea Geol. Paläont.*, 10:39–48.
- EBNER, F.; HUBMANN, B.; WEBER, L. (2000) Die Rannach- und Schöckl-Decke des Grazer Paläozoikums. *Mitt Ges Geol Bergbaustud Österr.*, 44:1–44.

- EBNER, F.; PROCHASKA, W.; TROBY, J.; M AZIM ZADEH, A. (2004) Carbonate hosted sparry magnesite of the Greywacke zone, Austria/Eastern Alps. *Acta Petrologica Sinica*, 20(4):791–802.
- EBNER, F.; RANTITSCH, G. (2000) Das Gosaubecken von Kainach - ein Überblick. *Mitt Ges Geol Bergbaustud Österr*, 44:157–172.
- EBNER, F.; SACHSENHOFER, R. (1995) Paleogeography, subsidence and thermal history of the Neogene Styrian Basin (Pannonian Basin System, Austria). *Tectonophysics*, 242:133–150.
- EGGER, H.; KRENMAYR, H.; MANDL, G.; MATURA, A.; NOWOTNY, A.; PASCHER, G.; PESTAL, G.; PISTONIK, J.; ROCKENSCHAUB, M.; SCHNABEL, W. (1999) *Geologische Uebersichtskarte der Republik Österreich 1:1.500.000*. Geologische Bundesanstalt, Wien.
- ENGBRETSON, D.; COX, A.; GORDON, R. (1984) Relative motions between oceanic plates of the Pacific basin. *Journal of Geophysical Research*, 89:10291–10310.
- ENGBRETSON, D.; COX, A.; GORDON, R. (1985) Relative motions between oceanic and continental plates in the Pacific basin. *Geological Society of America Special Paper*, 206:1–59.
- ENGLAND, P.; HOLLAND, T. (1979) Archimedes and the Tauern eclogites: the role of buoyancy in the preservation of exotic eclogite blocks. *Earth and Planetary Science Letters*, 44:287–294.
- ENGLAND, P.; THOMPSON, A. (1984) Pressure-Temperature-Time Paths of regional metamorphism I. Heat transfer during the evolution of regions of thickened continental crust. *Journal of Petrology*, 25:894–928.
- ENKELMANN, E.; GARVER, J.; PAVLIS, T. (2008) Rapid exhumation of ice-covered rocks of the Chugach-St. Elias orogen, southeast Alaska. *Geology*, 36:915–918.
- ENKELMANN, E.; ZEITLER, P.; GARVER, J.; PAVLIS, T.; HOOKS, B. (2010) The thermochronological record of tectonic and surface process interaction at the Yakutat-North American collision zone in southeast Alaska. *American Journal of Science*, in press.
- ENKELMANN, E.; ZEITLER, P.; PAVLIS, T.L. AND GARVER, J.; RIDGWAY, K. (2009) Intense localized rock uplift and erosion in the St. Elias orogen of Alaska. *Nature Geoscience*, doi:10.1038/NGEO502.
- ESTERLUS, M. (1986) *Kristallisationsgeschichte und Strukturprägung im Kristallin E des Grazer Paläozoikums*. PhD thesis, University of Vienna, 187 p.
- FARMER, G.; AYUSO, R.; PLAFKER, G. (1993) A Coast Mountains provenance for the Valdez and Orca groups, southern Alaska, based on Nd, Sr and Pb isotopic evidence. *Earth and Planetary Science Letters*, 116:9–21.
- FARRIS, D.; HÄUSSLER, P.; FRIEDMAN, R.; PATERSON, S.; SALTUS, R.; R., A. (2006) Emplacement of the Kodiak batholith and slab-window migration. *Geological Society of America Bulletin*, 118:1360–1376.
- FARRIS, D.; PATERSON, S. (2009) Subduction of a segmented ridge along a curved continental margin: Variations between the western and eastern Sanak-Baranof belt, southern Alaska. *Tectonophysics*, 464:100–117.
- FARYAD, S.; HOINKES, G. (2003) P-T gradient of Eo-Alpine metamorphism within the Austroalpine basement units east of the Tauern Window (Austria). *Mineralogy and Petrology*, 77:129–159.
- FARYAD, S.; MELCHER, F.; HOINKES, G.; PUHL, J.; MEISEL, T.; FRANK, W. (2002) Relics of eclogite facies metamorphism in the Austroalpine basement, Hochgrössen (Speik complex), Austria. *Mineralogy and Petrology*, 74:49–73.
- FERRIS, A.; ABERS, G.; CHRISTENSEN, D.; VEENSTRA, E. (2003) High-resolution image of the subducted Pacific (?) plate beneath central Alaska, 50–150 km depth. *Earth and Planetary Sciences Letters*, 214:575–588.
- FINGER, F.; BROSKA, I.; ROBERTS, M.; SCHERMAIER, A. (1998) Replacement of primary monazite by apatite-allanite-epidote coronas in an amphibolite facies granite gneiss from the eastern Alps. *American Mineralogist*, 83:248–258.
- FISHER, D.; BYRNE, T. (1992) Strain variations in an ancient accretionary complex: implications for forearc evolution. *Tectonics*, 11:330–347.

- FITZSIMONS, I.; KINNY, P.; HARLEY, S. (1997) Two stages of zircon and monazite growth in anatectic leucogneiss: SHRIMP constraints on the duration and intensity of Pan-African metamorphism in Prydz Bay, East Antarctica. *Terra Nova*, 9:47–51.
- FITZSIMONS, I.; KINNY, P.; WETHERLEY, S.; HOLLINGSWORTH, D. (2005) Bulk chemical control on metamorphic monazite growth in pelitic schists and implications for U-Pb age data. *Journal of Metamorphic Geology*, 23:261–277.
- FLÜGEL, H.; HUBMANN, B. (2000) *Das Paläozoikum von Graz: Stratigraphie und Bibliographie*. Österr Akad Wiss Schr der Erdw Komm 13, 118 p.
- FLÜGEL, H.; MAURITSCH, H.; HEINZ, H.; FRANK, W. (2000) Paläomagnetische und radiometrische Daten aus dem Grazer Paläozoikum. *Mitt Ges Geol Bergbaustud Österr*, 44:1–44.
- FLÜGEL, H. (2000) Die lithostratigraphische Gliederung des Paläozoikums von Graz (Österreich). H. Flügel; B. Hubmann, (eds.), *Das Paläozoikum von Graz, Stratigraphie und Bibliographie*, Österreichische Akademie der Wissenschaften, Schriftenreihe der Erdwissenschaftlichen Kommissionen 13, 7–59.
- FLÜGEL, H.; NEUBAUER, F. (1984) *Erläuterungen zur Geologischen Karte der Steiermark, 1:200 000*. Geologische Bundesanstalt, Wien.
- FORSTER, M.; LISTER, G. (2005) Several distinct tectono-metamorphic slices in the Cycladic eclogite-blueschist belt, Greece. *Contributions to Mineralogy and Petrology*, 150:523–545.
- FORSTER, M.; LISTER, G. (2008) Tectonic sequence diagrams and the structural evolution of schists and gneisses in multiply deformed terranes. *Journal of the Geological Society of London*, 165:923–939.
- FOSTER, D.; GOSCOMBE, B.; GRAY, D. (2009) Rapid exhumation of deepcrust in an obliquely convergent orogen: The Kaoko Belt of the Damara Orogen. *Tectonics*, 28:TC4002, doi:10.1029/2008TC002317.
- FOSTER, D.; GRAY, D.; BUCHER, M. (1999) Chronology of deformation within the turbidite-dominated Lachlan orogen: implications for the tectonic evolution of eastern Australia and Gondwana. *Tectonics*, 18:452–485.
- FOSTER, G.; GIBSON, H.; PARRISH, R.; HORSTWOOD, M.; FRASER, J.; TINDLE, A. (2002) Textural, chemical and isotopic insights into the nature and behaviour of metamorphic monazite. *Chemical Geology*, 191:183–207.
- FOSTER, G.; KINNY, P.; VANCE, D.; PRINCE, C.; HARRIS, N. (2000) The significance of monazite U-Th-Pb age data in metamorphic assemblages; a combined study of monazite and garnet chronometry. *Earth and Planetary Science Letters*, 181:327–340.
- FOSTER, G.; PARRISH, R. (2003) Metamorphic monazite and the generation of P-T-t paths. D. Vance; W. Müller; I. Villa, (eds.), *Geochronology: Linking the Isotopic record with Petrology and Textures*, Geological Society of London Special Publication 220, 25–47.
- FOSTER, G.; PARRISH, R.; HORSTWOOD, M.; CHENERY, S.; PYLE, J.; GIBSON, H. (2004) The generation of prograde P-T-t points and paths; a textural, compositional, and chronological study of metamorphic monazite. *Earth and Planetary Science Letters*, 228:125–142.
- FRANK, W.; SCHLAGER, W. (2005) Jurassic strike-slip versus subduction in the Eastern Alps. *Int J Earth Sci*, 95:431–450.
- FRASER, G.; ELLIS, D.; EGGINS, S. (1997) Zirconium abundance in granulite-facies minerals, with implications for zircon geochronology in high-grade rocks. *Geology*, 25:607–610.
- FRASER, G.; HUSSEY, K.; COMPSTON, D. (2008) Timing of Paleoproterozoic Au-Cu-Bi and W-mineralization in the Tennant Creek region, northern Australia: Improved constraints via intercalibration of $^{40}\text{Ar}/^{39}\text{Ar}$ and U-Pb ages. *Precambrian research*, 164:50–65.
- FRISCH, W.; GAWLICK, H.J. (2003) The nappe structure of the central Northern Calcareous Alps and its disintegration during Miocene tectonic extrusion—a contribution to understanding the orogenic evolution of the Eastern Alps. *Int J Earth Sci*, 92:712–727.
- FRISCH, W.; KUHLEMANN, J.; DUNKL, I.; BRÜGEL, A. (1998) A Palinspastic reconstruction and topographic evolution of the Eastern Alps during late Tertiary tectonic extrusion. *Tectonophysics*, 297:1–15.

- FRITZ, H. (1986) *Zur Geologie des nordwestlichen Grazer Paläozoikums (im Bereich Schartnerkogel - Parmaseggkogel)*. PhD thesis, University of Graz, 202 p.
- FRITZ, H. (1988) Kinematics and geochronology of Early Cretaceous thrusting in the northwestern Paleozoic of Graz (Eastern Alps). *Geod Acta*, 2/2:53–62.
- FRITZ, H. (1991) Stratigraphie, Fazies und Tektonik im nordwestlichen Grazer Paläozoikum (Ostalpen). *Jahrb der Geol Bundesanst*, 134/2:227–255.
- FRITZ, H.; EBNER, F.; NEUBAUER, F. (1992) The Graz Thrust-Complex (Paleozoic of Graz). *Alpaca field guide, KFU Graz*:83–92.
- FRITZ, H.; EBNER, F.; NEUBAUER, F. (2006) Berrisian drowning of the Plassen carbonate platform at the type-locality and its bearing on the early Eoalpine orogenic dynamics in the Northern Calcareous Alps (Austria). *Int J Earth Sci*, 95:451–462.
- FRITZ, H.; NEUBAUER, F. (1988) Geodynamic aspects of the Silurian and Early Devonian Sedimentation in the Paleozoic of Graz (Eastern Alps). *Schweiz Mineral Petrogr Mitt*, 68:359–367.
- FRITZ, H.; NEUBAUER, F.; RATSCHBACHER, L. (1991) Compression versus extension in the Paleozoic of Graz (Eastern Alps, Austria). *Zbl Geol Paläont*, 1/1:55–68.
- FROITZHEIM, N.; PLASIENKA, D.; SCHUSTER, R. (2000) Alpine tectonics of the Alps and Western Carpathians. T. McCann, (ed.), *The Geology of Central Europe*, Volume 2: Mesozoic and Cenozoic. - Geological Society, London, 1141-1232.
- FUIS, G.; AMBOS, E.; MOONEY, W. (1991) Crustal structure of accreted terranes in southern Alaska, Chugach Mountains and Copper River Basin, from seismic refraction results. *Journal of Geophysical Research*, 96:4187–4227.
- FUIS, G.; MOORE, T.; PLAFKER, G.; BROCHER, T.; FISHER, M.; MOONEY, W.; NOKLEBERG, W.; PAGE, R.; BEAUDOIN, B.; CHRISTENSEN, N.; LEVANDER, A.; LUTTER, W.; SALTUS, W.; RUPPERT, N. (2008) Trans-Alaska Crustal Transect and continental evolution involving subduction underplating and synchronous foreland thrusting. *Geology*, 36:267–270.
- FUIS, G.; PLAFKER, G. (1991) Evolution of deep structure along the Trans-Alaska Crustal Transect, Chugach Mountains and Copper River Basin, southern Alaska. *Journal of Geophysical Research*, 96:4229–4253.
- GASSER, D.; STÜWE, K.; FRITZ, H. (2009) Internal structural geometry of the Paleozoic of Graz. *Int J Earth Sci*, DOI 10.1007/s00531-009-0446-0.
- GAWLICK, H. (1996) Die früh-oberjurassischen Brekzien der Strubbergsschichten im Lammerthal - Analyse und tektonische Bedeutung (Nördliche Kalkalpen, Österreich). *Mitteilungen der Gesellschaft der Geologie- und Bergbaustudenten Österreich*, 39/49:119–186.
- GAWLICK, H.; FRISCH, W.; VECSEI, A.; STEIGER, T.; BÖHM, F. (1999a) The change from rifting to thrusting in the Northern Calcareous Alps as recorded in Jurassic sediments. *Int J Earth Sci*, 87:664–657.
- GAWLICK, H.; KRYSZYN, L.; LEIN, R. (1994) Conodont colour alteration indices: Palaeotemperatures and metamorphism in the Northern Calcareous Alps - a general view. *Int J Earth Sci*, 83:660–664.
- GAWLICK, H.; SCHLAGINTWEIT, F.; SUZUKI, H. (2007) Die Ober-Jura bis Unter-Kreide Schichtfolge des Gebietes Höherstein-Sandling (Salzkammergut, Österreich) - Implikationen zur Rekonstruktion des Block-Puzzles der zentralen Nördlichen Kalkalpen, der Gliederung der Radiolaritflyschbecken und der Plassen-Karbonatplattform. *Neues Jahrbuch für Geologie und Paläontologie Abhandlungen*, 243/1:1–70.
- GEHRELS, G.; RUSMORE, M.; WOODSWORTH, G.; CRAWFORD, M.; ANDRONICOS, C.; HOLLISTER, L.; PATCHETT, J.; DUCEA, M.; BUTLER, R.; KLEPEIS, K.; DAVIDSON, C.; FRIEDMAN, R.; HAGGART, J.; MAHONEY, B.; CRAWFORD, W.; PEARSON, D.; GIRARDI, J. (2009) U-Th-Pb geochronology of the Coast Mountains batholith in north-coastal British Columbia: Constraints on age and tectonic evolution. *Geological Society of America Bulletin*, 121:1341–1361.
- GEISLER, T.; SCHALTEGGER, U.; TOMASCHEK, F. (2007) Re-equilibration of zircon in aqueous fluids and melts. *Elements*, 3:43–50.
- GIBSON, H.; CARR, S.; BROWN, R.; HAMILTON, M. (2004) Correlation between chemical and age

- domains in monazite, and metamorphic reactions involving major pelitic phases: an integration of ID-TIMS and SHRIMP geochronology with Y-Th-U X-ray mapping. *Chemical Geology*, 211:237–260.
- GLEADOW, A. (1981) Fission-track dating methods: what are the real alternatives? *Nuclear Tracks*, 5:3–14.
- GODIN, L.; D., G.; LAW, R.; SEARLE, M. (2006) Channel flow, ductile extrusion and exhumation in continental collision zones: An introduction. R. Law; M. Searle; L. Godin, (eds.), *Channel flow, ductile extrusion and exhumation in continental collision zones.*, Geological Society of London Special Publication 268, 1-23.
- GOLDFARB, R.; LEACH, D.; MILLER, M.; PICKTHORN, W. (1986) Geology, metamorphic setting, and genetic constraints of epigenetic lode-gold mineralization within the Cretaceous Valdez Group, south-central Alaska. *Geological Association of Canada Special Paper*, 32:87–105.
- GOLLNER, H.; SCHIRNIK, D.; TSCHELAUT, W. (1987) The Problem of the Southalpine Clasts in the "Mittelsteirische Gosau". H. Flügel; P. Faupl, (eds.), *Geodynamics of the Eastern Alps*, Deuticke, Vienna (1987), pp. 156–163.
- GOLLNER, H.; ZIER, C. (1985) Zur Geologie des Hochlantsch (Grazer Paläozoikum, Steiermark). *Jahrb der Geol Bundesanst*, 128/1:43–73.
- GOSCOMBE, B.; GRAY, D. (2009) Metamorphic response in orogens of different obliquity, scale and geometry. *Gondwana Research*, 15:151–167.
- GRADSTEIN, F.; OGG, J.; SMITH, A. (2004) *A Geologic Time Scale 2004*. Cambridge University Press, Cambridge. 589 pp.
- GREEN, P.; DUDDY, I.; GLEADOW, A.; TINGATE, P.; LASLETT, G. (1986) Thermal annealing of fission tracks in apatite 1. A qualitative description. *Chemical Geology*, 59:237–253.
- GREGORY, C.; RUBATTO, D.; ALLEN, C.; WILLIAMS, I.; HERMANN, J.; IRELAND, T. (2007) Allanite micro-geochronology: A LA-ICP-MS and SHRIMP U-Th-Pb study. *Chemical Geology*, 245:162–182.
- GROOME, W.; THORKELESON, D. (2009) The three-dimensional thermo-mechanical signature of ridge subduction and slab window migration. *Tectonophysics*, 464:70–83.
- GROSS, M.; FRITZ, I.; PILLER, W.; SOLIMAN, A.; HARZHAUSER, M.; HUBMANN, B.; MOSER, B.; SCHOLGER, R.; SUTTNER, T.; BOJAR, H. (2007) The Neogene of the Styrian Basin: Guide to Excursion. *Joannea - Geologie und Paläontologie*, 9:117–193.
- GSELLMANN, H. (1987) *Zur Geologie am Nordoststrand des Grazer Paläozoikums*. PhD thesis, University of Graz, 202 p.
- GULICK, S.; LOWE, L.; PAVLIS, T.; GARDNER, J.; MAYER, L. (2007) Geophysical insights into the Transition Fault debate: Propagating strike-slip in response to stalling Yakutat block subduction in the Gulf of Alaska. *Geology*, 35:763–766.
- HARRIS, N.; SISSON, V.; WRIGHT, J.; PAVLIS, T. (1996) Evidence for Eocene mafic underplating during fore-arc intrusive activity, eastern Chugach mountains, Alaska. *Geology*, 24:263–266.
- HARRISON, T.; CATLOS, E.; MONTEL, J. (2002) U-Th-Pb dating of phosphate minerals. *Reviews in Mineralogy and Geochemistry*, 48:523–558.
- HARRISON, T.; CÉLÉRIER, J.; AIKMAN, A.; HERMANN, J.; HEIZLER, M. (2009) Diffusion of ⁴⁰Ar in muscovite. *Geochimica et Cosmochimica Acta*, 73:1039–1051.
- HASENHÜTTL, C. (1994) *Eine Wärmegeschichte des Grazer Berglandes. Inkohlung, Illitkristallinität, Tonmineralogie und Condont Color Alteration Index im nördlichen Teil des Grazer Deckenkomplex*. PhD thesis, University of Graz, 192 p.
- HEIJL, C. (1997) 'Cold spots' during the Cenozoic evolution of the Eastern Alps: thermochronological interpretation of apatite fission-track data. *Tectonophysics*, 272:159–173.
- HERMANN, J. (2002) Allanite: thorium and light rare element carrier in subducted crust. *Chemical Geology*, 192:289–306.
- HERMANN, J.; RUBATTO, D.; TROMMSDORFF, V. (2006) Sub-solidus Oligocene zircon formation in garnet peridotite during fast decompression and fluid infiltration (Duria, Central Alps). *Mineralogy and Petrology*, 88:181–206.

- HERMANN, S. (1992) *Die Steirische Grauwackenzone am Kaintaleck: Geologie, Petrographie, Struktur, Geochemie und Rb-Sr-Datierungen*. Diplomarbeit, Graz, 225 p.
- HETHERINGTON, C.; JERCINOVIC, M.; WILLIAMS, M.; MAHAN, K. (2008) Understanding geological processes with xenotime: composition, chronology and a protocol for electron probe microanalysis. *Chemical Geology*, 254:133–147.
- HIESS, J.; NUTMAN, A.; BENNETT, V.; HOLDEN, P. (2008) Ti-in-zircon thermometry applied to contrasting Archean metamorphic and igneous systems. *Chemical Geology*, 247:323–338.
- HILL, M.; MORRIS, J.; WHELAN, J. (1981) Hybrid granodiorites intruding the accretionary prism, Kodiak, Shumagin, and Sanak Islands, southwest Alaska. *Journal of Geophysical Research*, 86:10569–10590.
- HINTON, H.; UPTON, B. (1991) The chemistry of zircon: Variations within and between large crystals from syenite and alkali basalt xenoliths. *Geochimica et Cosmochimica Acta*, 55:3287–3302.
- HOFMANN, A.; VALLEY, J.; WATSON, E.; CAVOSIE, A.; EILER, J. (2009) Sub-micron scale distributions of trace elements in zircon. *Contributions to Mineralogy and Petrology*, 158:317–335.
- HOLLAND, T.; POWELL, R. (1998) An internally consistent thermodynamic data set for phases of petrological interest. *Journal of Metamorphic Geology*, 16:309–343.
- HOSKIN, P.; BLACK, L. (2000) Metamorphic zircon formation by solid-state recrystallization of protolith igneous zircon. *Journal of metamorphic geology*, 18:423–439.
- HOSKIN, P.; SCHALTEGGER, U. (2003) The composition of zircon and igneous and metamorphic petrogenesis. J. Hancher; P. Hoskin, (eds.), *Zircon*, Reviews in Mineralogy and Geochemistry, 53: 27–55.
- HUBMANN, B. (1993) Ablagerungsraum, Mikrofazies und Paläoökologie der Barrandeikalk-Formation (Eifelium) des Grazer Paläozoikums. *Jahrb der Geol Bundesanst*, 136/2:393–461.
- HUBMANN, B.; MESSNER, F. (2007) "Stein im Bild", die fazielle Entwicklung der Rannachdecke (Grazer Paläozoikum). *Jahrb der Geol Bundesanst*, 147:277–299.
- HUDSON, T.; PLAFKER, G. (1982) Paleogene metamorphism of an accretionary flysch terrane, eastern Gulf of Alaska. *Geological Society of America Bulletin*, 93:1280–1290.
- HUDSON, T.; PLAFKER, G.; LANPHERE, M. (1977a) Intrusive rocks of the Yakutat-St. Elias area, south-central Alaska. *U.S. Geological Survey Journal of Research*, 5:155–172.
- HUDSON, T.; PLAFKER, G.; LANPHERE, M. (1977b) Metamorphic rocks of the Yakutat-St. Elias area, south-central Alaska. *U.S. Geological Survey Journal of Research*, 5:173–184.
- HUDSON, T.; PLAFKER, G.; PETERMAN, Z. (1979) Paleogene anatexis along the Gulf of Alaska margin. *Geology*, 7:573–577.
- HUERTA, A.; ROYDEN, L.; HODGES, K. (1996) The interdependence of deformational and thermal processes in mountain belts. *Science*, 273:637–639.
- HURFORD, A.; GREEN, P. (1983) The zeta age calibration of fission track dating. *Isotope Geoscience*, 1:285–317.
- HÄUSSLER, P.; BRADLEY, D.; GOLDFARB, R.; SNEE, L.; TAYLOR, C. (1995) Link between ridge subduction and gold mineralization in southern Alaska. *Geology*, 23:995–998.
- HÄUSSLER, P.; BRADLEY, D.; GOLDFARB, R. (2003b) Brittle deformation along the Gulf of Alaska margin in response to Paleocene-Eocene triple junction migration. V. Sisson; S. Roeske; T. Pavlis, (eds.), *Geology of a transpressional orogen developed during ridge-trench interaction along the North Pacific margin*, Geological Society of America Special Paper, 371:119–140.
- HÄUSSLER, P.; BRADLEY, D.; WELLS, R.; MILLER, M. (2003a) Life and death of the Resurrection plate: Evidence for its existence and subduction in the northeastern Pacific in Paleocene-Eocene time. *Geological Society of America Bulletin*, 115:867–880.
- HÄUSSLER, P.; GEHRELS, G.; KARL, S. (2005) Constraints on the Age and Provenance of the Chugach Accretionary Complex from detrital zircons in the Sitka Greywacke near Sitka, Alaska. *Studies by the U.S. Geological Survey in Alaska, 2004, U.S. Geological Survey Professional Paper*, 1709-F:1–11.

- HÄUSSLER, P.; NELSON, S. (1993) Structural evolution of the Chugach-Prince William terrane at the hinge of the orocline in Prince William Sound, and implications for ore deposits. C. Dusel-Bacon; A. Till, (eds.), *Geological Studies in Alaska by the U.S. Geological Survey, 1992*, U.S. Geological Survey Bulletin 2068:143-162.
- JAFFEY, A.; FLYNN, K.; GENDENIN, L.; BENTLEY, W.; ESSLING, A. (1971) Precision measurement of half-lives and specific activities of ²³⁵U and ²³⁸U. *Physical Review C*, 4/5:1889–1906.
- JAMES, T.; HOLLISTER, L.; MORGAN, W. (1989) Thermal modelling of the Chugach Metamorphic Complex. *Journal of Geophysical Research*, 94:4411–4423.
- JAMIESON, R.; BEAUMONT, C.; FULLSACK, P.; LEE, B. (1998) Barrovian regional metamorphism: where's the heat? C. Beaumont; P. Fullsack, (eds.), *What drives metamorphism and metamorphic reactions?*, Geological Society of London Special Publication, vol. 138, p. 23-51.
- JANOTS, E.; BRUNET, F.; GOFFÉ, B.; POINSSOT, C.; BURCHARD, M.; CEMIC, L. (2007) Thermochemistry of monazite-(La) and dissakite-(La) : implications for monazite and allanite stability in metapelites. *Contributions to Mineralogy and Petrology*, 154:1–14.
- JANOTS, E.; ENGI, M.; BERGER, A.; ALLAZ, J.; SCHWARZ, J.; SPANDLER, C. (2008) Prograde metamorphic sequence of REE minerals in pelitic rocks of the Central Alps: implications for allanite-monazite-xenotime phase relations from 250 to 610°C. *Journal of metamorphic Geology*, 26:509–526.
- JANOTS, E.; ENGI, M.; RUBATTO, D.; BERGER, A.; GREGORY, C.; RAHN, M. (2009) Metamorphic rates in collisional orogeny from in situ allanite and monazite dating. *Geology*, 37:11–14.
- JANOTS, E.; NEGRO, F.; BRUNET, F.; GOFFÉ, B.; ENGI, M.; BOUYBAOUENE, M. (2006) Evolution of the REE mineralogy in HP-LT metapelites of the Sebti complex, Rif, Morocco: Monazite stability and geochronology. *Lithos*, 87:214–234.
- JENKIN, G. (1997) Do cooling paths derived from mica Rb-Sr data reflect true cooling paths? *Geology*, 25:907–910.
- JOHNSTON, S. (2001) The Great Alaskan Terrane Wreck: reconciliation of paleomagnetic and geological data in the northern Cordillera. *Earth and Planetary Science Letters*, 193:259–272.
- JONES, J.; CONNELLY, J.; KARLSTROM, K.; WILLIAMS, M.; DOE, M. (2009) Age, provenance, and tectonic setting of Paleoproterozoic quartzite successions in the southwestern United States. *Geological Society of America Bulletin*, 121:247–264.
- KANEKO, Y., M.T. (2006) Erratum to “recalibration of mutually consistent garnet-biotite and garnet-cordierite geothermometers”. *Lithos*, 86:347.
- KARNER, D.; RENNE, R. (1998) ⁴⁰Ar/³⁹Ar geochronology of Roman volcanic province tephra in the Tiber river valley: age calibration of middle Pleistocene sea-level changes. *Geophysical society of America Bulletin*, 110:740–747.
- KIM, Y.; YI, K.; CHO, M. (2009) Parageneses and Th-U distributions among allanite, monazite, and xenotime in Barrovian-type metapelites, Imjingang belt, central Korea. *American Mineralogist*, 94:430–438.
- KINGSBURY, J.; MILLER, C.; WOODEN, J.; HARRISON, T. (1993) Monazite paragenesis and U-Pb systematics in rocks of the eastern Mojave desert, California, USA: implications for thermochronometry. *Chemical Geology*, 110:147–167.
- KOHN, M.J.; CATLOS, E.; RYERSON, F.; HARRISON, T. (2001) Pressure-temperature-time path discontinuity in the Maine Central thrust zone, central Nepal. *Geology*, 29:571–574.
- KOHN, M.J.; MALLOY, M. (2004) Formation of monazite via prograde metamorphic reactions among common silicates: Implications for age determinations. *Geochimica et Cosmochimica Acta*, 68:101–113.
- KOHN, M.; WIELAND, M.; PARKINSON, C.; UPRETI, B. (2005) Five generations of monazite in Langtang gneisses: implications for chronology of the Himalayan metamorphic core. *Journal of Metamorphic Geology*, 23:399–406.
- KOONS, P.; HOOKS, B.; PAVLIS, T.; UPTON, P.; BARKER, A. (in press) Three dimensional mechanics of Yakuat convergence in the southern Alaskan plate corner. *Tectonics*.

- KOONS, P.; NORRIS, R.; CRAW, D.; COOPER, A. (2003) Influence of exhumation on the structural evolution of transpressional plate boundaries: An example from the Southern Alps, New Zealand. *Geology*, 31:3–6.
- KOPPERS, A. (2002) ArArCALC - software for $^{40}\text{Ar}/^{39}\text{Ar}$ age calculations. *Computers Geosciences*, 28:605–619.
- KOROKNAI, B.; NEUBAUER, F.; GENSER, J.; TOPA, D. (1999) Metamorphic and tectonic evolution of Austroalpine Units at the western margin of the Gurktal nappe complex, Eastern Alps. *Schweiz. Mineral. Petrogr. Mitt.*, 79:277–295.
- KRALIK, M.; KRUMM, H.; SCHRAMM, J. (1987) Low grade and very low grade metamorphism in the Northern Calcareous Alps and in the Greywacke Zone: Illite-Crystallinity data and isotopic ages. H. Flügel; P. Faupl, (eds.), *Geodynamics of the Eastern Alps*, Deuticke, Vienna (1987), pp. 164–178.
- KRENN, E.; USTASZEWSKI, U.; FINGER, F. (2008) Detrital and newly formed metamorphic monazite in amphibolite-facies metapelites from the Motajica massif, Bosnia. *Chemical Geology*, 254:164–174.
- KRENN, K. (2001) *Structural and thermal control of ore deposits in the Graz Paleozoic*. PhD thesis, University of Graz, 115 p.
- KRÖLL, A.; HELLER, R. (1978) Die Tiefbohrung Afling U1 in der Kainacher Gosau. *Verh der Geol Bundesanst*, 2:23–34.
- KROHE, A. (1987) Kinematics of Cretaceous nappe tectonics in the Austroalpine basement of the Koralpe region (eastern Austria). *Tectonophysics*, 136:171–196.
- KRYSTYN, L.; LEIN, R.; RICHOSZ, S. (2008) Der Gamsstein: Werden und Vergehen einer Wettersteinkalk-Plattform. *Journal of Alpine Geology*, 49:157–172.
- KUSKY, T.; BRADLEY, D.; HÄUSSLER, P. (1997b) Progressive deformation of the Chugach accretionary complex, Alaska, during a Paleogene ridge-trench encounter. *Journal of Structural Geology*, 19:139–157.
- KUSKY, T.; BRADLEY, D.; HÄUSSLER, P.; KARL, S. (1997a) Controls on accretion of flysch and mélange belts at convergent margins: Evidence from the Chugach Bay thrust and Iceworm mélange, Chugach accretionary wedge, Alaska. *Tectonics*, 16:855–578.
- KUSKY, T.; GANLEY, R.; LYTWYN, J.; POLAT, A. (2004) The Resurrection Peninsula ophiolite, mélange and accreted flysch belts of southern Alaska as an analog for trench-forearc systems in Precambrian orogens. T. Kusky, (ed.), *Precambrian ophiolites and related rocks*, Developments in Precambrian Geology, Vol. 13:627–674.
- KUSKY, T.; YOUNG, C. (1999) Emplacement of the Resurrection Peninsula ophiolite in the southern Alaska forearc during a ridge-trench encounter. *Journal of Geophysical Research*, 104:29025–29054.
- LANCASTER, P.; BAXTER, E.; AGUE, J.; BREEDING, C.; OWENS, T. (2008) Synchronous peak Barrovian metamorphism driven by syn-orogenic magmatism and fluid flow in southern Connecticut, USA. *Journal of Metamorphic Geology*, 26:527–538.
- LITTLE, T.; NAESER, C. (1989) Tertiary tectonics of the Border Ranges Fault System, Chugach Mountains, Alaska: Deformation and Uplift in a forearc setting. *Journal of Geophysical Research*, 94:4333–4359.
- LOESCHKE, J. (1989) Lower Paleozoic volcanism of the Eastern Alps and its geodynamic implications. *Geol Rundsch*, 78:599–616.
- LONEY, R.; HIMMELBERG, G. (1983) Structure and Petrology of the La Perouse Gabbro Intrusion, Fairweather Range, Southeastern Alaska. *Journal of Petrology*, 24:377–423.
- LONSDALE, P. (1988) Paleogene history of the Kula plate: Offshore evidence and onshore implications. *Geological Society of America Bulletin*, 100:733–754.
- LUDWIG, K. (1998) On the treatment of concordant uranium-lead ages. *Geochimica et Cosmochimica Acta*, 62:665–676.
- LUDWIG, K. (2003) Isoplot/Ex version 3.0. A geochronological toolkit for Microsoft Excel. *Berkeley Geochronological Centre Special Publication*:70 p.

- LULL, J.; PLAFKER, G. (1990) Geochemistry and Paleotectonic Implications of Metabasaltic Rocks in the Valdez Group, Southern Alaska. J. Dover; J. Galloway, (eds.), *Geological Studies in Alaska by the U.S. Geological Survey, 1989*, U.S. Geological Survey Bulletin 1946: 29-38.
- LUX, D.; DE YOREO, J.; GUIDOTTI, C.; DECKER, E. (1986) Role of plutonism in low-pressure metamorphic belt formation. *Nature*, 323:794–797.
- LYTWYN, J.; CASEY, J.; GILBERT, S.; KUSKY, T. (1997) Arc-like mid-ocean ridge basalt formed seaward of a trench-forearc system just prior to ridge subduction: An example from subaccreted ophiolites in southern Alaska. *Journal of Geophysical Research*, 102:10225–10243.
- LYTWYN, J.; LOCKHART, S.; CASEY, J.; KUSKY, T. (2000) AGeochemistry of near-trench intrusives associated with ridge subduction, Seldovia Quadrangle, southern Alaska. *Journal of Geophysical Research*, 105:27957–27978.
- MADSEN, J.; THORKELSON, D.; FRIEDMAN, R.; MARSHALL, D. (2006) Cenozoic to Recent plate configurations in the Pacific Basin: Ridge subduction and slab window magmatism in western North America. *Geosphere*, 2:11–34.
- MANDL, G. (2001) *Geologische Bundesanstalt Arbeitstagung 2001 Blatt 103/Kindberg, Blatt 104/Mürzzuschlag, Neuberg a.d. Mürz, 3. - 7. September*. Wien, 351 p.
- MARSHAK, R.; KARIG, D. (1977) Triple junctions as a cause for anomalously near-trench igneous activity between the trench and volcanic arc. *Geology*, 5:233–236.
- MARTON, E.; KUHLEMANN, J.; FRISCH, W.; DUNKL, I. (2000) Miocene rotations in the Eastern Alps - paleomagnetic results from intramontane basin sediments. *Tectonophysics*, 323:163–182.
- MCALEER, R.; J.A., S.; ENKELMANN, E.; BERGER, L. (2009) Exhumation along the Fairweather fault, southeastern Alaska, based on low-temperature thermochronometry. *Tectonics*, 28:TC1007, doi:10.1029/2007TC002240.
- MCDOUGALL, I.; HARRISON, T. (1999) *Geochronology and Thermochronology by the $^{40}\text{Ar}/^{39}\text{Ar}$ Method*. Oxford University Press, 2nd edition, 269 pp.
- MEIGS, A.; JOHNSTON, S.; GARVER, J.; SPOTILA, J. (2008) Crustal-scale structural architecture, shortening, and exhumation of an active, eroding orogenic wedge (Chugach/St.Elias Range, southern Alaska. *Tectonics*, 27:TC4003, doi:10.1029/2007TC002168.
- MEZGER, K.; HANSON, G.; BOHLEN, S. (1989) U-Pb systematics of garnet: dating the growth of garnet in the Late Archean Pikwitonei granulite domain at Cauchon and Natawahunan Lakes, Manitoba, Canada. *Contributions to Mineralogy and Petrology*, 101:136–148.
- MILLER, C.; THÖNI, M. (1995) Origin of eclogites from the Austroalpine Ötztal basement (Tirol, Austria): geochemistry and Sm-Nd vs. Rb-Sr isotope systematics. *Chemical Geology*, 122:199–225.
- MIN, K.; MUNDIL, R.; RENNE, P.; LUDWIG, K. (2000) A test for systematic errors in $^{40}\text{Ar}/^{39}\text{Ar}$ geochronology through comparison with U/Pb analysis of a 1.1-Ga rhyolite. *Geochimica et Cosmochimica Acta*, 64/1:73–98.
- MUELLER, R.; SDROLIAS, M.; GAINA, C.; ROEST, W. (2008) Age, spreading rates, and spreading asymmetry of the worlds ocean crust. *Geochemistry, Geophysics, Geosystems*, 9:doi:10.1029/2007GC001743.
- MULCH, A.; COSCA, M. (2004) Recrystallization or cooling ages: In situ UV-laser $^{40}\text{Ar}/^{39}\text{Ar}$ geochronology of muscovite in mylonitic rocks. *Journal of the Geological Society of London*, 161:573–583, doi:10.1144/0016-764903-110.
- NAESER, C.W. (1976) Fission-track dating. *US Geol. Surv. Open File Report*, 76-190:1–65.
- NEUBAUER, F. (1981) Untersuchungen zur Geologie, Tektonik und Metamorphose des "Angerkristallins" und des E-Randes des Grazer Paläozoikums. *Jber Hochschulschwerpkt*, S15:114–121.
- NEUBAUER, F. (1982) Untersuchungen zur Tektonik, Metamorphose und Stellung des Grazer Paläozoikum-Ostrand. *Jber Hochschulschwerpkt*, S15:93–101.
- NEUBAUER, F. (1988a) Bau und Entwicklungsgeschichte des Rennfeld-Mugel- und des Gleinalmkristallins (Ostalpen). *Abh der Geol Bundesanst*, 42:128 p.

- NEUBAUER, F. (1988b) The Variscan orogeny in the Austroalpine and Southalpine domains of the Eastern Alps. *Schweiz Mineral Petrogr Mitt*, 68:339–349.
- NEUBAUER, F. (1989) Lower Paleozoic volcanism of the Eastern Alps and its geodynamic implications. *Geol Rundsch*, 78:599–616.
- NEUBAUER, F. (1991) Stratigraphie und Struktur der Rannachdecke bei Kehr (Grazer Paläozoikum). *Jahrb der Geol Bundesanst*, 134/1:101–116.
- NEUBAUER, F.; DALLMEYER, R.; DUNKL, I.; SCHIRNIK, D. (1995) Late Cretaceous exhumation of the metamorphic Gleinalm dome, Eastern Alps: kinematics, cooling history and sedimentary response in a sinistral wrench corridor. *Tectonophys*, 242:79–98.
- NEUBAUER, F.; FRIEDL, G.; GENSER, J.; HANDLER, R.; MADER, D.; SCHNEIDER, D. (2007) Origin and tectonic evolution of the eastern Alps deduced from dating of detrital white mica: A review. *Mitt Österr Geol Ges*, 100:8–23.
- NEUBAUER, F.; FRISCH, W. (1993) The Austroalpine metamorphic basement east of the Tauern Window. J. von Raumer; F. Neubauer, (eds.), *Pre-Mesozoic Geology in the Alps*, Springer-Verlag, Berlin, 515–536.
- NEUBAUER, F.; GENSER, J.; HANDLER, R. (2000) The Eastern Alps: the result of a two-stage collision process. *Mitt Österr Geol Ges*, 92:117–134.
- NEUBAUER, F.; HANDLER, R. (1999) Variscan orogeny in the Eastern Alps and Bohemian Massif: How do these units correlate? *Mitt Österr Geol Ges*, 92:35–59.
- NEUBAUER, F.; HANDLER, R. (2000) Variscan orogeny in the Eastern Alps and Bohemian Massif: How do these units correlate? *Mitt Österr Geol Ges*, 92:35–59.
- NEUBAUER, F.; HANDLER, R.; HERMANN, S.; PAULUS, G. (1993) Revised Lithostratigraphy and Structure of the Eastern Greywacke Zone (Eastern Alps). *Mitt. Österr. Geol. Ges*, 86:61–74.
- NEUBAUER, F.; PISTOTNIK, J. (1984) Das Altpaläozoikum und Unterkarbon des Gurktaler Deckensystems (Ostalpen) und ihre paläogeographischen Beziehungen. *Geol. Rundschau*, 73/1:143–174.
- NEUBAUER, F.; SASSI, F. (1993) The Austro-Alpine Quartzphyllites and Related Paleozoic Formations. J. von Raumer; F. Neubauer, (eds.), *Pre-Mesozoic Geology in the Alps*, Springer Verlag, 423–440.
- NEUBAUER, F.; VOZAROVA, A. (1990) The Noetsch-Weitsch-North Gemic Zone of Alps and Carpathians: correlation, paleogeography and significance for Variscan orogeny. D. Minarikova; H. Lobitzer, (eds.), *Thirty Years of Geological Cooperation between Austria and Czechoslovakia*, Federal Geological Survey Vienna, Geological Survey Prague, 167–171.
- NILSEN, T.; ZUFFA, G. (1982) The Chugach terrane, a Cretaceous trench-fill deposit, southern Alaska. J. Laggett, (ed.), *Trench-forearc Geology: Sedimentation and Tectonics on Modern and Active Plate Margins*, Blackwell Science, p. 213–227.
- NOKLEBERG, W.; PLAFKER, G.; LULL, J.; WALLACE, W.; WINKLER, G. (1989) Structural Analysis of the southern Peninsular, southern Wrangellia, and northern Chugach terranes along the Trans-Alaska Crustal Transect, Northern Chugach Mountains, Alaska. *Journal of Geophysical Research*, 94:4297–4320.
- NORTON, I. (1995) Plate motions in the North Pacific: the 43 Ma nonevent. *Tectonics*, 14:1080–1094.
- ÖBERHÄNSLI, R.; BOUSQUET, R.; ENGI, M.; GOFFÉ, B.; GOSSO, G.; HANDY, M.; KOLLER, F.; LARDEAUX, J.; POLINO, R.; ROSSI, P.; SCHUSTER, R.; SCHWARTZ, S.; SPALLA, I.; AGARD, P.; BABIST, J.; BERGER, A.; BERTLE, R.; BUCHER, S.; BURRI, T.; HEITZMANN, P.; HOINKES, G.; JOLIVET, L.; KELLER, L.; LINNEN, M.; LOMBARDO, B.; MARTINOTTI, G.; MICHARD, A.; PESTAL, G.; PROYER, A.; RANTISCH, G.; ROSENBERG, C.; SCHRAMM, J.; SOELVA, H.; THOENI, M.; ZUCALI, M. (2004) *Metamorphic structure of the Alps*. 1:1'000000. Paris, CGMW.
- OGG, J.; OGG, G.; GRADSTEIN, F. (2008) *The concise geologic time-scale*. Cambridge University Press, 184 p.
- OLDOW, J.; BALLY, A.; LALLEMANT, H.; W.P., L. (1989) Phanerozoic evolution of the North American Cordillera; United States and Canada. A. Bally; A. Palmer, (eds.), *The Geology of North America - An overview*, Boulder, Colorado, 139–232.

- ONSTOTT, T.; SISSON, V.; TURNER, D. (1989) Initial argon in amphiboles from the Chugach Mountains, southern Alaska. *Journal of Geophysical Research*, 94:4361–4372.
- PARRISH, R. (1990) U-Pb dating of monazite and its applications to geological problems. *Canadian Journal of Earth Sciences*, 27:1431–1454.
- PAVLIS, T.; MARTY, K.; SISSON, V. (2003) Constrictional flow within the Eocene forearc of southern Alaska: An effect of dextral shear during ridge subduction. V. Sisson; S. Roeske; T. Pavlis, (eds.), *Geology of a transpressional orogen developed during ridge-trench interaction along the North Pacific margin*, Geological Society of America Special Paper, 371:171-190.
- PAVLIS, T.; PICORNELL, C.; SERPA, L.; BRUHN, R.; PLAFKER, G. (2004) Tectonic processes during oblique collision: Insights from the St. Elias orogen, northern North American Cordillera. *Tectonics*, 23:TC3001,doi:10.1029/2003TC001557.
- PAVLIS, T.; ROESKE, S. (2007) The Border Range Fault System, southern Alaska. K. Ridgway; J. Trop; J. Glen; J. O'Neill, (eds.), *Tectonic Growth of a Collisional Continental Margin: Crustal Evolution of southern Alaska*, Geological Society of America Special Paper 431:95-128.
- PAVLIS, T.; SISSON, V. (1995) Structural history of the Chugach metamorphic complex in the Tana River region, eastern Alaska: A record of Eocene ridge subduction. *Geological Society of America Bulletin*, 107:1333–1355.
- PAVLIS, T.; SISSON, V. (2003) Development of a sub-horizontal decoupling horizon in a transpressional system, Chugach metamorphic complex, Alaska: Evidence for rheological stratification of the crust. V. Sisson; S. Roeske; T. Pavlis, (eds.), *Geology of a transpressional orogen developed during ridge-trench interaction along the North Pacific margin*, Geological Society of America Special Paper 371:191-216.
- PEARCE, N.; PERKINS, W.; WESTGATE, J.; GORTON, M.; JACKSON, S.; NEAL, C.; CHENERY, S. (1996) A compilation of new and published major and trace element data for NIST SRM 610 and NIST SRM 612 glass reference materials. *Geostandard Newsletter*, 21:115–144.
- PERESSON, H.; DECKER, K. (1997) The Tertiary dynamics of the northern Eastern Alps (Austria): changing palaeostresses in a collisional plate boundary. *Tectonophysics*, 272:125–157.
- PERRY, S.; GARVER, J.; RIDGWAY, K. (2009) Transport of the Yakutat terrane, southern Alaska: Evidence from sediment petrology and detrital zircon fission-track and U/Pb double dating. *Journal of Geology*, 117:156–173.
- PHILIPPOT, P.; BLICHERT-TOFT, J.; PERCHUK, A.; COSTA, S.; GERASIMOV, V. (2001) Lu-Hf and Ar-Ar chronometry supports extreme rate of subduction zone metamorphism deduced from geospeedometry. *Tectonophysics*, 342:23–38.
- PHILPOTTS, A.; AGUE, J. (2009) *Principles of Igneous and Metamorphic Petrology*. Cambridge University Press, Second Edition, 667 p.
- PILLER, W.; EGGER, H.; ERHART, C.; GROSS, M.; HARZHAUSER, M.; HUBMANN, B.; VAN HUSEN, D.; KRENMAYR, H.; KRYSSTYN, L.; LEIN, R.; LUKENEDER, A.; MANDL, G.; RÖGL, F.; ROETZEL, R.; RUPP, C.; SCHNABEL, W.; SCHÖNLAUB, H.; SUMMESBERGER, H.; WAGREICH, M. (2004) *Die Stratigraphische Tabelle von Österreich 2004 (sedimentäre Schichtfolgen)*. Österr strat Komm und Komm für die paläont und strat Forsch Österr.
- PLAFKER, G.; MOORE, J.; WINKLER, G. (1994) Geology of the southern Alaska margin. G. Plafker; H. Berg, (eds.), *The Geology of Alaska*, Geological Society of America, The Geology of North America, v G-1, p. 389-449.
- PLATT, J. (1993) Exhumation of high-pressure rocks: a review of concepts and processes. *Terra Nova*, 5:119–133.
- PLUMLEY, P.; COE, R.; BYRNE, T. (1983) Paleomagnetism of the Paleocene Ghost Rock Formation, Prince William terrane, Alaska. *Tectonics*, 2:295–314.
- PROCHASKA, W. (1991) Leukophyllitbildung und Alteration in Scherzonen am Beispiel der Lagerstätte Kleinfestritz (Steiermark). *Archiv für Lagerstättenforschung der Geologischen Bundesanstalt*, 13:111–122.
- PROCHASKA, W. (2000) Magnesite and talc deposits in Austria. *Mineralia Slovaca*, 32:543–548.

- PROCHASKA, W.; HENJES-KUNST, F. (2009) Genese der Sideritvererzungen der Östlichen Grauwackenzone - aktueller Stand der Forschung. *Arbeitstagung 2009 der Geologischen Bundesanstalt Blatt 101 Eisenerz*:153–169.
- PUTZ, M.; STÜWE, K.; JESSEL, M.; CALCAGNO, P. (2006) Three-dimensional model and late-stage warping of the Plattengeiss shear zone in the Eastern Alps. *Tectonophysics*, 412:87–103.
- PYLE, J.; SPEAR, F. (2003) Four generations of accessory-phase growth in low-pressure migmatites from SW New Hampshire. *American Mineralogist*, 88:338–351.
- PYLE, J.; SPEAR, F.; RUDNICK, R.L.; MCDONOUGH, W. (2001) Monazite-xenotime-garnet equilibrium in metapelites and a new monazite-garnet thermometer. *Journal of Petrology*, 42:2083–2107.
- RANTITSCH, G.; SACHSENHOFER, R.; HASENHÜTTL, C.; RUSSEGGER, B.; RAINER, T. (2005) Thermal evolution of an extensional detachment as constrained by organic metamorphic data and thermal modelling: Graz Paleozoic Nappe Complex (Eastern Alps). *Tectonophysics*, 411:57–72.
- RANTITSCH, G. MALI, H. (2006) The geological structure of the Late Cretaceous Graden normal fault (Eastern Alps). *Mitt Naturwiss Ver Steiermark*, 135:25–31.
- RASMUSSEN, B.; FLETCHER, I.; MUHLING, J.; MUELLER, A.; HALL, G. (2007) Bushveld-aged fluid flow, peak metamorphism, and gold mobilization in the Witwatersrand basin, South Africa: Constraints from in situ SHRIMP U-Pb dating of monazite and xenotime. *Geology*, 35:931–934.
- RASMUSSEN, B.; MUELLER, A.; FLETCHER, I. (2009) Zirconolite and xenotime U-Pb age constraints on the emplacement of the Golden Mile Dolerite sill and gold mineralization at the Mt Charlotte mine, Eastern Goldfields Province, Yilgarn Craton, Western Australia. *Contributions to Mineralogy and Petrology*, 157:559–572.
- RASMUSSEN, B.; MUHLING, J.; FLETCHER, I.; WINGATE, M. (2006) In situ SHRIMP U-Pb dating of monazite integrated with petrology and textures: Does bulk composition control whether monazite forms in low-Ca pelitic rocks during amphibolite facies metamorphism? *Geochimica et Cosmochimica Acta*, 70:3040–3058.
- RATSCHBACHER, L. (1986) Kinematics of austroalpine cover nappes: changing translation path due to transpression. *Tectonophysics*, 125:335–356.
- RATSCHBACHER, L. (1987) Stratigraphy, tectonics and paleogeography of the Veitsch Nappe (Greywacke Zone, Eastern Alps): A rearrangement. H. Flügel; F. Sassi; P. Grecula, (eds.), *Pre-Variscan and Variscan events in the Alpine-Mediterranean mountain belts*, Bratislava (Alfa), 407-414.
- RATSCHBACHER, L.; WENK, H.; SINTUBIN, M. (1991) Calcite textures: examples from nappes with strain-path partitioning. *J Struct Geol*, 13/4:369–384.
- REDFIELD, T.; SCHOLL, D.; FITZGERALD, P.; BECK, M. (2007) Escape tectonics and the extrusion of Alaska: Past, present, and future. *Geology*, 35:1039–1042.
- REINERS, W.; ZHOU, Z.; EHLERS, T.; XU, C.; BRANDON, M.; DONELICK, R.; NICOLESCU, S. (2003) Post-orogenic evolution of the Dabie Shan, Eastern China, from (U Th)/He and Fission track thermochronology. *American Journal of Science*, 303:489–518.
- REISINGER, J. (1988) *Geologie des Hirschkogel - Landscha Berges nördlich von Weiz*. PhD thesis, Graz, 176 p.
- RENNE, P.; SWISHER, C.; DEINO, A.; KARNER, D.; OWENS, T.; DEPAOLO, D. (1998) Intercalibration of standards, absolute ages and uncertainties in $^{40}\text{Ar}/^{39}\text{Ar}$ dating. *Chemical Geology*, 145:117–152.
- RICHTER, D.; SMITH, J.; LANPHERE, M.; DALRYMPLE, G.; REED, B.; SHEW, N. (1990) Age and progression of volcanism, Wrangell volcanic field, Alaska. *Bulletin of Volcanology*, 53:29–44.
- RING, U.; BRANDON, M. (2008) Exhumation Settings, Part 1: Relatively simple cases. *International Geology Review*, 50:97–120.
- RING, U.; BRANDON, M.; WILLET, S.; LISTER, G. (1999) Exhumation processes. U. Ring; M. Brandon; G. Lister; S. Willet, (eds.), *Exhumation Processes: Normal faulting, ductile flow and erosion*, Geological Society of London Special Publication 154, 1-27.

- ROESKE, S.M.; HOUSEN, B.A.; O'CONNELL, K.; GALLEN, S. (2009) Paleocene - early Eocene displacement of terranes along the northern Cordillera margin. *Geological Society of America Abstracts with Programs*, 41/7:518.
- ROESKE, S.; SNEE, L.; PAVLIS, T. (2003) Dextral-slip reactivation of an arc-forearc boundary during Late Cretaceous-Early Eocene oblique convergence in the northern Cordillera. V. Sisson; S. Roeske; T. Pavlis, (eds.), *Geology of a transpressional orogen developed during ridge-trench interaction along the North Pacific margin*, Geological Society of America Special Paper 371:141-169.
- ROWE, C.; MENEGHINI, F.; MOORE, C. (2009) Fluid-rich damage zone of an ancient out-of-sequence thrust, Kodiak Islands, Alaska. *Tectonics*, 28:doi:10.1029/2007TC002126.
- RUBATTO, D. (2002) Zircon trace element geochemistry: partitioning with garnet and the link between U-Pb ages and metamorphism. *Chemical Geology*, 184:123-138.
- RUBATTO, D.; HERMANN, J. (2001) Exhumation as fast as subduction? *Geology*, 29:3-6.
- RUBATTO, D.; HERMANN, J.; BERGER, A.; M., E. (2009) Protracted fluid-induced melting during Barrovian metamorphism in the Central Alps. *Contribution to Mineralogy and Petrology*, DOI 10.1007/s00410-009-0406-5.
- RUBATTO, D.; HERMANN, J.; BUICK, I. (2006) Temperature and Bulk Composition Control on the Growth of Monazite and Zircon during Low-pressure Anatexis (Mount Stafford, Central Australia). *Journal of Petrology*, 47:1973-1966.
- RUBATTO, D.; WILLIAMS, I.; BUICK, I. (2001) Zircon and monazite response to prograde metamorphism in the Reynolds Range, central Australia. *Contributions to Mineralogy and Petrology*, 140:458-468.
- RUPPEL, C.; HODGES, K. (1994) Pressure-temperature-time paths from two-dimensional thermal models: Prograde, retrograde, and inverted metamorphism. *Tectonics*, 13:17-44.
- RUSSEGGER, B. (1996) Niedrigst- bis niedriggradige Metamorphose im südlichen Grazer Paläozoikum (Ostalpen). *Jahrb der Geol Bundesanst*, 139/1:93-100.
- SACHSENHOFER, R.; KOGLER, A.; POLESNY, H.; STRAUSS, P.; WAGREICH, M. (2000) The Neogene Fohnsdorf Basin: basin formation and basin inversion during lateral extrusion in the Eastern Alps (Austria). *International journal of Earth Sciences*, 89:415-430.
- SAMPLE, J.; MOORE, J. (1987) Structural style and kinematics of an underplated slate belt, Kodiak and adjacent islands, Alaska. *Geological Society of America Bulletin*, 99:7-20.
- SAMPLE, J.; REID, M. (2003) Large-scale, latest Cretaceous uplift along the northeast Pacific Rim: evidence from sediment volume, sandstone petrography, and Nd isotope signatures of the Kodiak Formation, Kodiak Islands, Alaska. V. Sisson; S. Roeske; T. Pavlis, (eds.), *Geology of a transpressional orogen developed during ridge-trench interaction along the North Pacific margin*, Geological Society of America Special Paper, 371:51-70.
- SAWYER, E. (2008) *Atlas of Migmatites*. The Canadian Mineralogist, Special Publication 9, 317 p.
- SCAILLET, S. (2000) Numerical error analysis in $^{40}\text{Ar}/^{39}\text{Ar}$ dating. *Chemical Geology*, 162:269-298.
- SCHARBERT, S. (1981) Untersuchungen zum Alter des Seckauer Kristallins. *Mitt. Ges. Geol. Bergbaustud. Österr.*, 27:173-188.
- SCHAUBERGER, O. (1986) Bau und Bildung der Salzlagerstätten des ostalpinen Salinars. *Archiv für Lagerstättenforschung der Geologischen Bundesanstalt*, 7:217-254.
- SCHERMAIER, A.; HAUNSCHMID, B.; FINGER, F. (1997) Distribution of Variscan I- and S-type granites in the Eastern Alps: a possible clue to unravel pre-Alpine basement structures. *Tectonophysics*, 272:315-333.
- SCHMID, S.; BERNOULLI, D.; FÜGENSCHUH, B.; MATENCO, R.; SCHEFER, S.; SCHUSTER, R.; TISCHLER, M.; USTASZEWSKI, K. (2008) The Alps-Carpathians-Dinarides-connection: a correlation of tectonic units. *Swiss Journal of Geosciences*, 101:139-183.
- SCHMID, S.; FÜGENSCHUH, B.; KISSLING, E.; SCHUSTER, R. (2004) Tectonic map and overall architecture of the Alpine orogen. *Eclog. Geol. Helv*, 97:93-117.

- SCHÖNLAUB, H. (1980) Die Grauwackenzone. R. Oberhauser, (ed.), *Der geologische Aufbau Österreichs*, Springer Verlag, Wien, 265-289.
- SCHÖNLAUB, H. (1982) Die Grauwackenzone in den Eisenerzer Alpen (Österreich). *Jahrbuch der Geologischen Bundesanstalt*, 124/2:361–423.
- SCHÖNLAUB, H. (1992) Stratigraphy, biogeography and paleoclimatology of the Alpine Paleozoic and its implications for plate movements. *Jahrb der Geol Bundesanst*, 135/1:381–418.
- SCHÖNLAUB, H.; HISTON, K. (1999) The Paleozoic evolution of the Southern Alps. *Mitt Österr Geol Ges*, 92:15–34.
- SCHUSTER, R.; KOLLER, F.; HOECK, V.; HOINKES, G.; BOUSQUET, R. (2004) Explanatory notes to the map: Metamorphic structure of the Alps - Metamorphic evolution of the Eastern Alps. *Mitteilungen der Österreichischen Geologischen Gesellschaft*, 149:175–199.
- SCHUSTER, R.; SCHARBERT, S.; ABART, R.; FRANK, W. (2001) Permo-Triassic extension and related HT/LP metamorphism in the Austroalpine - Southalpine realm. *Mitt. Geol. Bergbau Stud. Österr*, 44:111–141.
- SCHUSTER, R.; STUEWE, K. (2008) Permian metamorphic event in the Alps. *Geology*, 36/8:603–608.
- SCHWINNER, R. (1925) Das Bergland nordöstlich von Graz. *Sitzungsber Akad Wiss Wien*, 134:219–276.
- SELVERSTONE, J. (2005) Are the Alps collapsing? *Annual Reviews in Earth and Planetary Sciences*, 33:113–133.
- SHAW, D. (1956) Geochemistry of pelitic rocks. Part III: Major elements and general geochemistry. *Bulletin of the Geological Society of America*, 67:919–934.
- SISSON, V.; HOLLISTER, L. (1988) Low-pressure facies series metamorphism in an accretionary sedimentary prism, southern Alaska. *Geology*, 16:358–361.
- SISSON, V.; HOLLISTER, L.; ONSTOTT, T. (1989) Petrologic and age constraints on the origin of a low-pressure/high-temperature metamorphic complex, southern Alaska. *Journal of Geophysical Research*, 94:4392–4410.
- SISSON, V.; PAVLIS, T. (1993) Geologic consequences of plate reorganization: An example from the Eocene southern Alaska fore-arc. *Geology*, 21:913–916.
- SISSON, V.; POOLE, A.; HARRIS, N.; BURNER, H.; COPELAND, P.; RAYMOND, A.; MCLELLAND, W. (2003) Geochemical and geochronologic constraints for genesis of a tonalite-trondhjemite suite and associated mafic intrusive rocks in the eastern Chugach Mountains, Alaska: A record of ridge transform subduction. V. Sisson; S. Roeske; T. Pavlis, (eds.), *Geology of a transpressional orogen developed during ridge-trench interaction along the North Pacific margin*, Geological Society of America Special Paper, 371: 293-326.
- SLÁMA, J.; KOSLER, J.; CONDON, D.; CROWLEY, J.; GERDES, A.; HANCHAR, J.; HORSTWOOD, M.; MORRIS, G.; NASDALA, L.; NORBERG, N.; SCHALTEGGER, U.; SCHOENE, B.; TUBRETT, M.; WHITEHOUSE, M. (2008) Plesovice zircon - A new natural reference material for U-Pb and Hf isotopic microanalysis. *Chemical Geology*, 249:1–35.
- SÖLVA, H.; GRASEMANN, B.; THÖNI, M.; THIEDE, R.; HABLER, G. (2005) The Schneeberg normal fault zone: normal faulting associated with Cretaceous SE-directed extrusion in the Eastern Alps (Italy/Austria). *Tectonophysics*, 401:143–166.
- SMART, K.; PAVLIS, T.; SISSON, V.; ROESKE, S.; SNEE, L. (1996) The Border Range fault system in Glacier Bay National Park, Alaska: evidence for major early Cenozoic dextral strike-slip motion. *Canadian Journal of Earth Sciences*, 33:1268–1282.
- SMITH, H.; BARREIRO, B. (1990) Monazite U-Pb dating of staurolite-grade metamorphism in pelitic schists. *Contributions to Mineralogy and Petrology*, 105:602–615.
- SPEAR, F. (1993) *Metamorphic phase equilibria and pressure-temperature-time paths*. Mineralogical Society of America Monograph, 799 pp.
- SPEAR, F.; PYLE, J. (2003) Apatite, Monazite and Xenotime in metamorphic rocks. M. Kohn; J. Rakovan; J. Hughes, (eds.), *Phosphates. Geochemical, geobiological and materials importance*, Reviews in Mineralogy and Geochemistry 48: 293-335.

- SPELL, T.; MCDOUGALL, I. (2003) Characterization and calibration of $^{40}\text{Ar}/^{39}\text{Ar}$ dating standards. *Chemical Geology*, 198:189–211.
- SPOTILA, J.; BUSCHER, J.; MEIGS, A.; REINERS, P. (2004) Long-term glacial erosion of active mountain belts: Example of the Chugach-St.Elias Range, Alaska. *Geology*, 32:501–504.
- STACEY, J.; KRAMERS, J. (1975) Approximation of terrestrial lead evolution by a two-stage model. *Earth and Planetary Science Letters*, 26:207–221.
- STEVENSON, A.; SCHOLL, D.; VALLIER, T. (1983) Tectonic and geologic implications of the Zodiac fan, Aleutian Abyssal Plain, northeast Pacific. *Geological Society of America Bulletin*, 94:259–273.
- STOWELL, H.; TINKHAM, D. (2003) Integration of phase equilibria modelling and garnet Sm-Nd chronology for construction of P-T-t paths: examples from the Cordilleran Coast Plutonic Complex, USA. *Geological Society of London Special Publication*, 220:119–145.
- STUEWE, K. (1998a) Tectonic constraints on the timing relationships of metamorphism, fluid production and gold-bearing quartz vein emplacement. *Ore Geology Reviews*, 13:219–228.
- STUEWE, K. (1998b) Heat sources of Cretaceous metamorphism in the Eastern Alps - A discussion. *Tectonophysics*, 287:251–269.
- STUEWE, K. (2007) *Geodynamics of the Lithosphere*. Springer Verlag, 2nd edition, 493 p.
- STUEWE, K.; BARR, T.D. (1998) On uplift and exhumation during convergence. *Tectonics*, 17:80–88.
- STUEWE, K.; POWELL, R. (1995) Geothermobarometry from modal proportions. Application to a PT path of the Koralm complex, Eastern Alps. *Contributions to Mineralogy and Petrology*, 119:83–93.
- STUEWE, K.; SCHUSTER, R. (in press) Initiation of subduction in the Alps: Continent or Ocean? *Geology*.
- SURPLESS, K.; GRAHAM, S.; COVAULT, J.; WOODEN, J. (2006) Does the Great Valley Group contain Jurassic strata? Reevaluation of the age and early evolution of a classic foreland basin. *Geology*, 34:21–24.
- TAIT, J.; BACHTADSE, V.; FRANKE, W.; SOFFEL, C. (1997) Geodynamic evolution of the European Variscan fold belt: paleomagnetic and geological constraints. *Geologische Rundschau*, 86:585–598.
- TENCZER, V.; STUEWE, K. (2003) The metamorphic field gradient in the eclogite type locality. *Journal of Metamorphic Geology*, 21:377–393.
- THÖNI, M. (1999) A review of geochronological data from the Eastern Alps. *Schweiz Mineral Petrogr Mitt*, 79:209–230.
- THOMPSON, A.; SCHULMANN, K.; JEZEK, J. (1997) Thermal evolution and exhumation in obliquely convergent (transpressive) orogens. *Tectonophysics*, 280:171–184.
- THORKELOSON, D.J. (1996) Subduction of diverging plates and the principles of slab window formation. *Tectonophysics*, 255:47–63.
- TOMASCHEK, F.; KENNEDY, A.; VILLA, I.; LAGOS, M.; BALLHAUS, C. (2003) Zircon from Syros, Cyclades, Greece - Recrystallization and Mobilization of zircon during high-pressure metamorphism. *Journal of Petrology*, 44:1977–2002.
- TOMKINS, H.; PATTISON, D. (2007) Accessory phase petrogenesis in relation to major phase assemblages in pelites from the Nelson contact aureole, southern British Columbia. *Journal of Metamorphic Geology*, 25:401–421.
- TREOLAR, P. (1997) Thermal controls on early-Tertiary, short-lived, rapid regional metamorphism in the NW Himalaya, Pakistan. *Tectonophysics*, 273:77–104.
- TROP, J.; RIDGWAY, K. (2007) Mesozoic and Cenozoic tectonic growth of southern Alaska: A sedimentary perspective. K. Ridgway; J. Trop; J. Glen; J. O'Neill, (eds.), *Tectonic Growth of a collisional continental margin: Crustal evolution of southern Alaska*, Geological Society of America Special Paper 431, 55-94.
- TYSDAL, R.; CASE, J.; WINKLER, G.; CLARK, S. (1977) Sheeted dikes, grabbro, and pillow basalt in flysch of coastal southern Alaska. *Geology*, 5:377–383.
- TYSDAL, R.; PLAFKER, G. (1978) Age and continuity of the Valdez Group, southern Alaska. N. Sohl; W. Wright, (eds.), *Changes in stratigraphic nomenclature by the U.S. Geological Survey 1977*, U.S. Geological Survey Bulletin 1457-A, 120-131.

- VANCE, D.; HARRIS, N. (1999) Timing of prograde metamorphism in the Zaskar Himalaya. *Geology*, 27:395–398.
- VANCE, D.; MAHAR, E. (1998) Pressure-temperature paths from P-T pseudosections and zoned garnets: potential, limitations and examples from the Zaskar Himalaya, NW India. *Contributions to Mineralogy and Petrology*, 132:225–245.
- VANCE, D.; MÜLLER, W.; VILLA, I. (2003) Geochronology: linking the isotopic record with petrology and textures - an introduction. M.W.V.I. Vance D., (ed.), *Geochronology: Linking the isotopic record with petrology and textures*, Geological Society of London Special Publication 220: 1-24.
- VAVRA, G.; GEBAUER, D.; SCHMID, R. (1996) Multiple zircon growth and recrystallization during polyphase Late Carboniferous to Triassic metamorphism in granulites of the Ivrea Zone (Southern Alps): and ion microprobe (SHRIMP) study. *Contributions to Mineralogy and Petrology*, 122:337–358.
- VERMEESCH, P. (2004) How many grains are needed for a provenance study? *Earth and Planetary Science Letters*, 224:441–451.
- VILLA, I. (1998) Isotopic closure. *Terra Nova*, 10:42–47.
- VON RAUMER, J.; STAMPFLI, G. (2008) The birth of the Rheic Ocean - Early Paleozoic subsidence patterns and subsequent tectonic plate scenarios. *Tectonophysics*, 461:9–20.
- WAGNER, G.; VAN DEN HAUTE, P. (1992) *Fission Track Dating*. Enke Verlag, Stuttgart, Germany, 285 p.
- WAGREICH, M.; KOLLMANN, H.; SUMMESBERGER, H.; EGGER, H.; SANDERS, D.; HOBIGER, G.; MOHAMED, O.; PRIEWALDER, H. (2009) *Stratigraphie der Gosau Gruppe von Gams bei Hieflau (Oberkreide-Paläogen, Österreich)*. Geologisches Kartenblatt 101 Eisenerz, Arbeitstagung der Geologischen Bundesanstalt 2009 - Leoben, 81-105, Wien.
- WALL, F.; NIKU-PAAVOLA, V.; C., S.; MÜLLER, A.; JEFFERIES, T. (2008) Xenotime-(Y) from carbonatite dykes at Iofdal, Namibia: unusually low LREE:HREE ratio in carbonatite, and the first dating of xenotime overgrowths on zircon. *The Canadian Mineralogist*, 46:861–877.
- WALLACE, W.; ENGBRETSON, D. (1984) Relationships between plate motions and late Cretaceous to Paleogene magmatism in southwestern Alaska. *Tectonics*, 3:295–315.
- WANG, X.; NEUBAUER, F. (1998) Orogen-parallel strike-slip faults bordering metamorphic core complexes: the Salzach-Enns fault zone in the Eastern Alps. *Journal of Structural Geology*, 20:799–818.
- WATSON, E.; HARRISON, T. (2005) Zircon thermometer reveals minimum melting conditions on earliest Earth. *Science*, 308:841–844.
- WATSON, E.; WARK, D.; THOMAS, J. (2006) Crystallization thermometers for zircon and rutile. *Contributions to Mineralogy and Petrology*, 151:413–433.
- WEBER, L. (1990) *Die Blei-Zinkerzlagertstätten des Grazer Paläozoikums und ihr geologischer Rahmen*. Arch für Lagerstättenforsch der Geol Bundesanst Bd 12, 289 p.
- WEBER, L.; GÖTZINGER, M.; GÖD, R.; SCHULZ, O.; EBNER, F.; SACHSENHOFER, R.; VATAR, F.; PAAR, W.; BRIEGLEB, D.; HÖLL, R.; EICHHORN, R.; SEEMANN, R.; KIRCHNER, E.; CERNY, I.; SCHROLL, E.; RAITH, J.; PROCHASKA, W.; TUFAR, W.; MALI, H.; GÜNTHER, W.; SPIELER, A.; MELCHER, F.; GRÄF, W. (1997) Die metallogenetischen Einheiten Österreichs. L. Weber, (ed.), *Archiv für Lagerstättenforschung der Geologischen Bundesanstalt*, 19:230-394.
- WHITNEY, D.; EVANS, B. (2010) Abbreviation for names of rock-forming minerals. *American Mineralogist*, 95:185–187.
- WHITNEY, D.; TEYSSIER, C.; HEIZLER, M. (2007) Gneiss domes, metamorphic complexes, and wrench zones: thermal and structural evolution of the Nidge massif, central Anatolia. *Tectonics*, 26:doi:10.1029/2006TC002040.
- WIJBRANS, J.; MCDUGALL, I. (1987) ⁴⁰Ar/³⁹Ar dating of white micas from an Alpine high-pressure metamorphic belt on Naxos (Greece): the resetting of the argon isotopic system. *Contributions to Mineralogy and Petrology*, 93:187–194.
- WILLIAMS, I. (1998) U-Th-Pb geochronology by ion microprobe. M. McKibben; W. Shanks; W. Ridley, (eds.), *Application of microanalytical techniques to understanding mineralizing processes*, Reviews in Economic Geology, vol. 7, p. 1-35.

- WILLIAMS, I.; BUICK, I.; CARTWRIGHT, I. (1996) An extended episode of early Mesoproterozoic metamorphic fluid flow in the Reynolds Range, central Australia. *Journal of Metamorphic Geology*, 14:29–47.
- WILLIAMS, M.; JERCINOVIC, M.; GONCALVES, P.; MAHAN, K. (2006) Format and philosophy for collecting, compiling and reporting microprobe monazite ages. *Chemical Geology*, 225:1–15.
- WILLIAMS, M.; JERCINOVIC, M.; HETHERINGTON, C. (2007) Microprobe Monazite Geochronology: Understanding Geologic Processes by integrating composition and chronology. *Annual Reviews in Earth and Planetary Sciences*, 35:137–175.
- WILLIAMS, M.; JERCINOVIC, M.; TERRY, M.P. (1999) Age mapping and dating of monazite on the electron microprobe: deconvoluting multistage tectonic histories. *Geology*, 27:1023–1026.
- WING, B.; FERRY, J.; HARRISON, T. (2003) Prograde destruction and formation of monazite and allanite during contact and regional metamorphism of pelites: petrology and geochronology. *Contributions to Mineralogy and Petrology*, 145:228–250.
- WINKLER-HERMADEN, A. (1957) *Geologisches Kräftespiel und Landformung*. 822 p., Springer-Verlag, Wien.
- WOLF, R.; FARLEY, K.; SILVER, L. (1996) Helium diffusion and low temperature thermochronometry of apatite. *Geochim. Cosmochim. Acta*, 60:4231–4240.
- WOODS, M.; DAVIES, G. (1982) Late Cretaceous genesis of the Kula plate. *Earth and Planetary Science Letters*, 58:161–166.
- ZENG, L.; ADIMOW, D.; SALEEBY, J. (2005) Coupling of anatexis reactions and dissolution of accessory phases and the Sr and Nd isotope systematics of anatexis melts from a metasedimentary source. *Geochimica et Cosmochimica Acta*, 69:3671–3682.
- ZUMSTEG, C.; HIMMELBERG, G.; KARL, S.; HÄUSSLER, P. (2003) Metamorphism within the Chugach accretionary complex on Baranof island, southeastern Alaska. V. Sisson; S. Roeske; T. Pavlis, (eds.), *Geology of a transpressional orogen developed during ridge-trench interaction along the North Pacific margin*, Geological Society of America Special Paper, 371: 253-267.

THANKS TO...

"L'union des talents dépasse leur simple addition."

anonymous

This thesis would not have been possible without the help of numerous people. Thanks to:

Kurt Stüwe: for initiating this project and introducing me to his way about thinking of "Kristallingeologie", for always supporting my financial, material and travelling wishes (including an all-around-the-world-trip), for letting me work independently and for letting me ski on Bagley icefield!

Emilie Bruand: without her this thesis would have never been the same. She did all the detailed petrology on the CMC, on which I based large parts of my work and interpretation. Her generosity in sharing her results with me, and her continuous interest in discussing possible interpretations of the tectonic history made working on this thesis a pleasure. Merci Emilie pour les derniers trois années, pour bavarder, manger, sortir, voyager, rigoler, faire des randonnées, camper, chanter, balader, parler français, nager, cuisiner, danser, râler, souffrir avec moi!

T. Pavlis: for continuous interest in the outcome of this work, for extended email-discussions, for prompt replies, for a few joint days in the field, for sharing my interest for the regional geology of southern Alaska and for examining the final thesis.

U. Klötzli, D. Rubatto, R. Schuster, B. Fügenschuh, D. Foster and A. Koppers: for scientific discussions, both in person and via extended email-contact, for help in the lab, for introducing me to the world of geochronology and for correcting parts of my thesis.

My office mates Tom, Tamer and Nico, as well as Alex, Angela, Flo and Patrick for discussions and shared lunches, and the staff of the Department of Earth Sciences for technical support: J. Neubauer for help with the SEM, G. Zmugg and A. Pock for thin sections, W. Becke for assistance in the lab, E. Kober for printing and S. Umschaden for administration. F. Biedermann from the University of Vienna for help with mineral separation and mount preparation.

On my trip around the world the following people were of great help: P. and J. Claus, our pilots in Alaska, C. Carson, JD Champagnac, T., T. and K. Stüwe assisted in the field, J. Gifford hosted me in Florida, learnt me how to crochet and assisted in the ArAr-Lab, C. Carson hosted me in Canberra and bought a great birthday cake for me, D. Rubatto spent hours at the SHRIMP with me and rescued my zircon mounts, and T. Ewing took me out for climbing - thank you all for that!

The last months were lightened by Unionbad, Augartenpark, Murradweg, Juice to Choose, Asiamensa, Posaune Pizza and the Spar supermarket in the Hans-Sachs-Gasse which is open until 21.

My friends Bas and Sabine were always there for me - even though they are currently spread all over the world. Thanks!

Andri, Bernd, Cecile, Conny and Conae, Dani, Ellinore, Johanna, Lars Axel, Laurent, Lea, Lilli, Marco, Markus, Martin, Roland, Sämi, Stoffi - thanks for visiting me, climbing with me, skiing with me, skypeing with me, hosting me, travelling with me over the past three years.

And finally, my family, Anna-Katharina, Ulrich, Nora and Nina (with Sofie, Samuel and Martin) for love and support!

SHORT CV



Personal information

Full name: Deta Gasser
Date of birth: 26.09.1982
Place of birth: Frauenfeld, Switzerland
Citizenship: Swiss

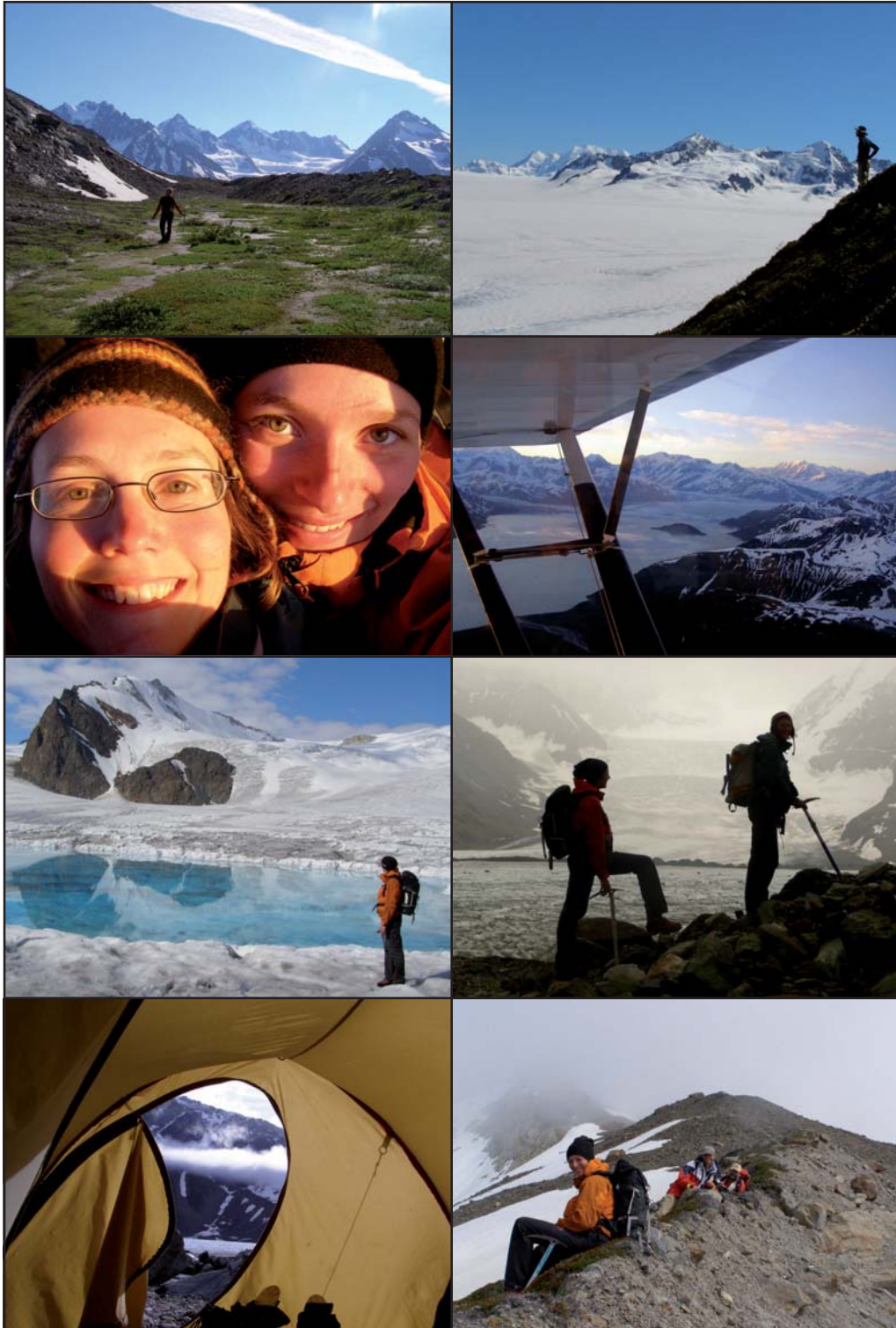
Education

2007-2010: PhD student, University of Graz, Austria
Thesis title: "Evolution of the Chugach Metamorphic Complex of southern Alaska in space and time"
Supervisor: Dr. Prof. Kurt Stuewe

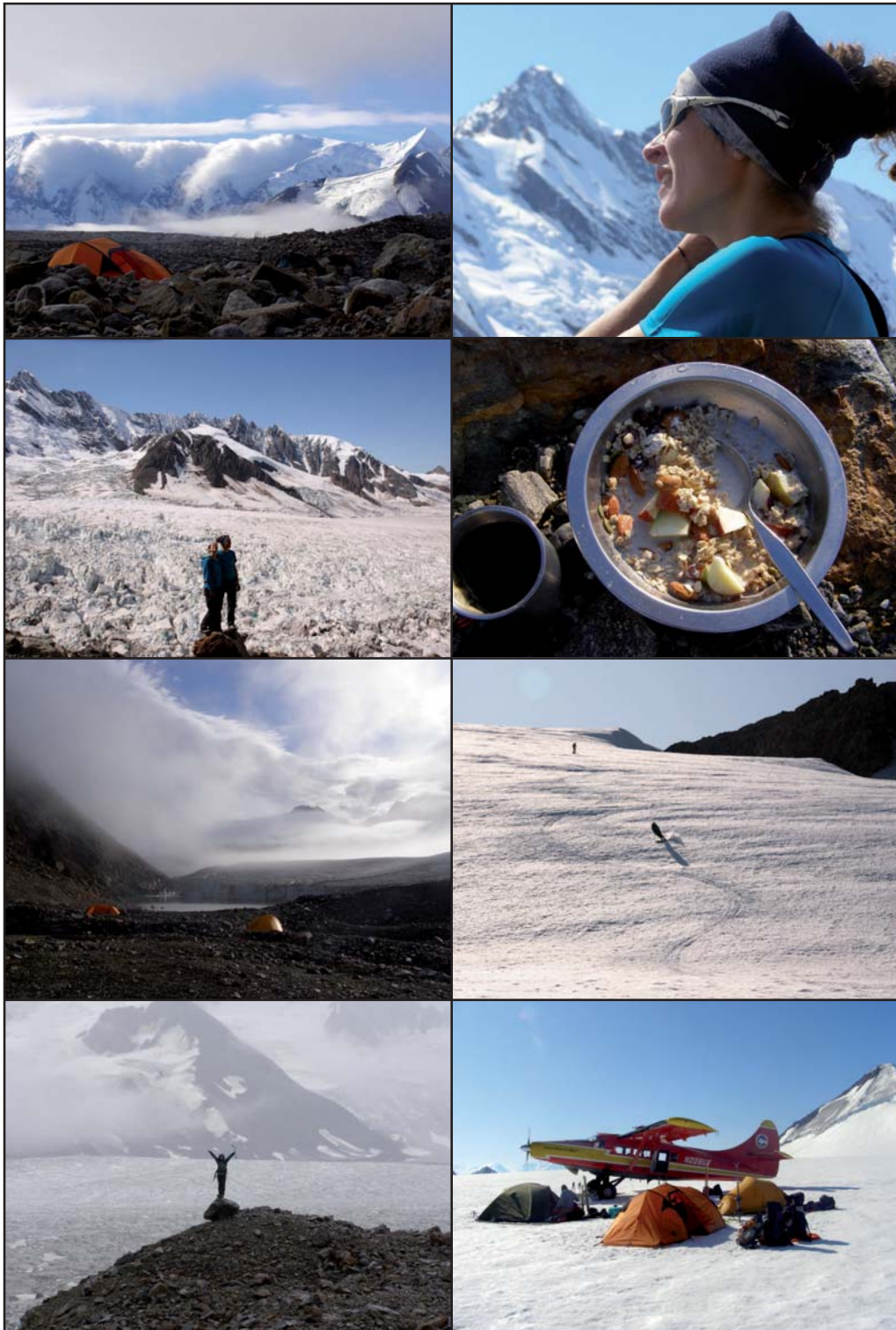
2006-2007: PhD student and teaching assistant, University of Neuchatel, Switzerland
Project title: "Deep penetration of meteoric waters into the rising Alps"
Supervisor: Dr. Prof. Martin Burkhard †

2001-2006: MSc studies of Earth Science, ETH Zurich, Switzerland
Master thesis: "From the seafloor to the roof top: Tectonic evolution of the Engi Slates, Glarus Alps, Switzerland"
supervisors: Dr. Prof. Neil Mancktelow, Dr. Bas den Brok

2004-2005 ERASMUS exchange year, NTNU Trondheim, Norway
Graduate studies in Engineering Geology and Petroleum Geology



Perfect moments 2008



Perfect moments 2009